IntechOpen

# Solar Cells

## Research and Application Perspectives

*Edited by Arturo Morales-Acevedo*

# SOLAR CELLS - RESEARCH AND APPLICATION PERSPECTIVES

Edited by **Arturo Morales-Acevedo**

**Solar Cells - Research and Application Perspectives**
http://dx.doi.org/10.5772/3418
Edited by Arturo Morales-Acevedo

**Contributors**

Chunfu Zhang, Foozieh Sohrabi, Arash Nikniazi, Hossein Movla, Tayyar Dzhafarov, Parag Vasekar, Tara P Dhakal, Wen-Cheng Ke, Shuo-Jen Lee, Xingzhong Yan, Minlin Jiang, Hyung-Shik Shin, Sadia Ameen, Alessio Bosio, Daniele Menossi, Alessandro Romeo, Nicola Romeo, Mu-Kuen Chen, Purnomo Sidi Priambodo, Egbert Rodriguez Messmer, Xiang-Dong Gao, Kazuma Ikeda, Yoshio Ohshita



**Notice**



First published in Croatia, 2013 by INTECH d.o.o.
eBook (PDF) Published by IN TECH d.o.o.
Place and year of publication of eBook (PDF): Rijeka, 2019.
IntechOpen is the global imprint of IN TECH d.o.o.
Printed in Croatia

Legal deposit, Croatia: National and University Library in Zagreb

Additional hard and PDF copies can be obtained from orders@intechopen.com

Solar Cells - Research and Application Perspectives
Edited by Arturo Morales-Acevedo
p. cm.
ISBN 978-953-51-1003-3
eBook (PDF) ISBN 978-953-51-6313-8

# Meet the editor

Dr. Arturo Morales-Acevedo is currently a full professor at the Electrical Engineering Department at Centro de Investigación y de Estudios Avanzados del Instituto Politécnico Nacional (CINVESTAV del IPN) in Mexico city, México. Following his graduate studies at Purdue University (USA), Université Pierre et Marie Curie (France) and CINVESTAV (México), he has worked in the physics and technology of solar cells for more than 30 years, becoming a leading scientist on solar photovoltaic energy research in the Latin-American region. He has collaborated with different universities such as Havana University in Cuba and the National University of Colombia. His work has been exposed in numerous scientific articles in specialized journals and international conferences around the world with about 600 citations to his work. Dr. Morales-Acevedo has been Photovoltaic Systems Associate Editor of the Solar Energy Journal for more than 10 years. He is also a Senior Member of the Institute of the Electrical and Electronics Engineers (IEEE), where he was a Distinguished Lecturer of the Electron Devices Society (EDS-IEEE). Dr. Morales-Acevedo continues his research actively, both in the theoretical and the experimental development of thin film solar cells and photovoltaic systems, with the help of several PhD students and the support of different scientific agencies.

# Contents

# Preface

Over the last decade, PV technology has shown the potential to become a major source of power generation for the world – with robust and continuous growth even during times of financial and economic crisis. That growth is expected to continue in the years ahead as worldwide awareness of the advantages of PV increases. At the end of 2009, the world's PV cumulative installed capacity was approaching 23 GW. One year later it was 40 GW. In 2011, more than 69 GW are installed globally and could produce 85 TWh of electricity every year. This energy volume is sufficient to cover the annual power supply needs of over 20 million households. PV is now, after hydro and wind power, the third most important renewable energy in terms of globally installed capacity. The growth rate of PV during 2011 reached almost 70%, an outstanding level among all renewable technologies.

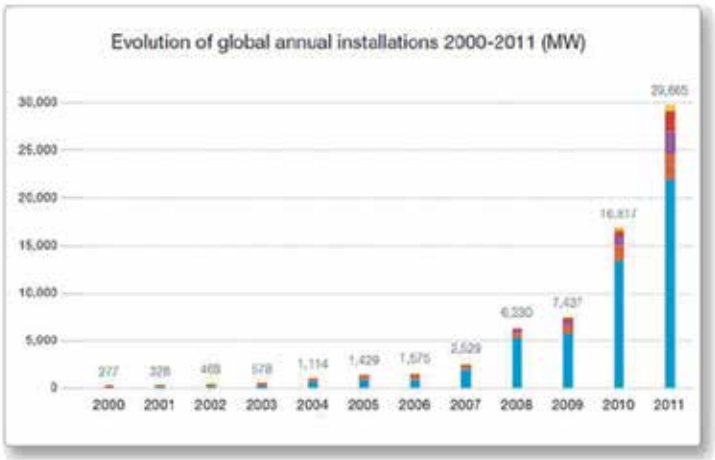


**Figure 1.** Evolution of global annual PV installations (European Photovoltaic Industries Association)

However, cost remains as the greatest barrier to further expansion of PV-generated power, and therefore cost reduction is the prime goal of the PV sector. Current PV production is dominated by single-junction solar cells based on silicon wafers including single crystal (c-Si) and multi-crystalline silicon (mc-Si). These types of single-junction, silicon-wafer devices are now commonly referred to as the first-generation (1G) technology. Half of the cost of first-generation photovoltaic cells is the cost of the 200–250-μm-thick silicon wafer—a cost incurred for largely mechanical reasons since the majority of solar absorption occurs in the top few tens of microns. So reduction of wafer thickness offers cost-reduction potential. Pro-

duction costs will also be reduced over the next decade by the continued up-scaling of production, smarter processing and shorter manufacturing learning curves.

The obvious next step in the evolution of PV and reduced $/W is to remove the unnecessary material from the cost equation by using thin-film devices. Second-generation (2G) technologies are single-junction devices that aim to use less material while maintaining the efficiencies of 1G PV. 2G solar cells use amorphous-Si (a-Si), $CuIn(Ga)Se_2$ (CIGS), CdTe or polycrystalline-Si (p-Si) deposited on low-cost substrates such as glass. These technologies work because CdTe, CIGS and a-Si absorb the solar spectrum much more efficiently than c-Si or mc-Si and use only 1–10 μm of active material. Meanwhile, in very promising work, thin film polycrystalline-Si has demonstrated to produce 10% efficient devices using light-trapping schemes to increase the effective thickness of the silicon layer.

As 2G technology progressively reduces the active material cost with thinner films, eventually even the low-cost substrate will become the cost limit and higher efficiency will be needed to maintain the $/W cost-reduction trend. The possible future is for third-generation (3G) devices, which exceed the limits of single-junction devices and lead to ultra-high efficiency for the same production costs of 1G/2G PV, driving down the $/W. 3G concepts can be applied to thin films on low-cost substrates to retain material cost savings, but there is also benefit in applying 3G concepts using thin films on c-Si as active substrates. This is an attractive proposition as this may allow current 1G PV manufacturing plants to access the step-change efficiencies of 3G without necessarily undertaking a change in production tools. The emergence of 3G approaches are already showing up commercially in highly efficient thin-film GaInP/GaAs/Ge triple-junction space-PV for satellites. These are too expensive for terrestrial applications, but nevertheless they demonstrate the viability of the 3G approach, particularly when combined with high solar radiation concentration (above 400X with cell efficiencies above 40%). Lower-cost 3G PV is also appearing, such as micromorph a-Si/mc-Si hetero-structure solar cells.

Further progress in PV technology should also be measured in $/W, and many scientific advances, as fascinating as they might be, will only be relevant to the industry if they can be implemented at affordable costs. In this sense, there are two routes to cheaper photovoltaic energy. The first is based on the use of new technology to improve the performance or decrease the cost of current devices. The second possibility might involve new whole-device concepts. Indeed, in recent years we have seen the emergence of dye-sensitized and polymer-based solar cells (including organic/inorganic hybrids) as fundamentally new types of device.

We must remember, however, that currently solar cells and modules represent only about 50% of the total cost of a PV system. The cost of the modules will continue their reduction by the above cell technology evolution, and then the cost of the other components, known as the balance of system (BOS), will become even more important and will limit the price reduction of PV energy. Hence, PV system technology development and system sizing strategies are also very important for achieving the global deployment of PV energy. In other words, the technology evolution of the BOS components such as inverters, battery charge controllers and sun trackers is also needed in order to attain an appropriate $/W cost of the installed PV systems.

In this book, all of the above topics are seen as important and they can give direction of the future research in the solar cell field. Therefore, the chapters compiled in this book by highly experienced researchers, from all over the world, will help the readers understand the de-

velopment which is being carried out today, so that photovoltaic energy becomes an appropriate source of electrical energy that satisfies the demand of a growing population, in a less polluted environment, and in a more equitative world with less climate variation.

In chapter 1, the authors explain some ways to use nano-structured silicon as the basis for 3G solar cells. For Si quantum dots (QD) they explain that there is an optimum separation (spacing) between these dots in order to favor the photo-generated carrier transport. In addition, the matrix material is also important in order to have the most appropriate barrier at the interface between the QDs and the matrices. In this regard, they explain that the formation of Si QDs in a-Si/SiNx layers is preferred over SiC layers due to the smaller thermal budget required for the first case, despite the smaller barrier at the SiC interface. The authors also explain that Si nanowires (NWs) might be better than Si QDs because Si NWs are well-defined doped nanocrystals during their synthesis. Moreover, Si NWs demonstrate ultra-high surface area ratio, low reflection, absorption of wideband light and a tunable bandgap. In order to optimize Si NWs, the wire diameter, surface conditions, crystal quality and crystallographic orientation along the wire axis should be investigated, but there is a long way to achieve optimum values experimentally.

In chapter 2, the different factors that affect the efficiency of conventional silicon solar cells are briefly reviewed by the author. One of the most important efficiency losing effects is due to the silicon reflectance. Nanoporous silicon (PS) may help in this aspect, and then the structural features of PS layers, the reflectance characteristics and the band gap of PS as a function of porosity, in addition to the experimental results about preparation of PS layers with different thickness and porosity are discussed here by the author. He makes a comparative analysis of studies published for the last 10-15 years, concerning the photovoltaic characteristics of silicon solar cells with and without a PS layer. A wide-band gap nanoporous silicon (up to 1.9 eV) resulting in the widening of the spectral region of the cell response to the ultraviolet part of solar spectrum may promote the increased efficiency of silicon solar cells with a PS layer. The internal electric field of porous silicon layer with a variable band gap (due to decrease of porosity deep down) can stimulate an increase the short-circuit current. Additionally, the intensive photoluminescence in the red-orange region of the solar spectrum observed in porous silicon under blue-light excitation can also increase the concentration of photo-excited carriers. It is necessary to take into account the passivation and gettering properties of Si-H and Si-O bonds on pore surfaces which can increase the lifetime of minority carriers. The author concludes that in agreement with the results presented in the review and taking into account the simplicity of fabrication of porous silicon layers on silicon, nanoporous silicon is a good candidate for making low cost silicon solar cells with high efficiency.

Hydrogenated amorphous silicon (a-Si:H) thin-film solar cells have emerged as a viable substitute for solid-state silicon solar cells. The a-Si:H thin-film solar cells gained importance primarily due to their low production cost, but these cells have the inherent disadvantage of using glass as a substrate material. Replacing the glass substrate with a stainless steel (SS) substrate makes it possible to fabricate lightweight, thin, and low-cost a-Si:H thin-film solar cells using roll-to-roll mass production; however, the surface morphology of a SS substrate is of poorer quality than that of the glass substrate as discussed by the authors in chapter 3. It has been suggested that diffusion of detrimental elements, such as Fe from stainless steel, into the a-Si:H layer as a result of high temperatures during the a-Si:H processing, deteriorate the cell's efficiency. In the work presented here, a thick (exceeding 2-μm) metal Mo buf-

fer layer is used to reduce the diffusion of Fe impurities from 304 SS substrates. The influence of the Fe impurities on the cell's performance was investigated carefully. Additionally, Electro-polishing (EP) and Electrical chemical mechanical polish (ECMP) processes have been used to improve the surface roughness of the stainless steels, and make them more suitable as a substrate for a-Si:H thin-film solar cells. SIMS results showed that the Fe impurities can be blocked effectively by increasing the thickness of the Mo buffer layer to more than 2 μm. The increased Voc and Jsc of a-Si:H solar cells on a Ag/Mo/304 SS substrate was due to an increased Rsh and a decreased Rs which related to the reduction of the Fe deep-level defects density. EP and ECMP surface treatment techniques were also used to smooth the 304 SS substrate surface. A decreased surface roughness of untreated 304 SS substrate as a result of being subjected to the EP or ECMP process increased the total reflection (TR) rate. It is suggested that due to the dense and hard Cr-rich passivation layer that was formed on the ECMP processed 304 SS substrate, the Cr impurity was nearly entirely prevented from diffusing into the a-Si:H layer, resulting in a decreased Rs and increased Rsh of the cell. The smooth surface and the low level of diffusion of impurities of the ECMP processed 304 SS substrate play an important role in improving the conversion efficiency of the a-Si:H thin-film solar cells.

Second generation (2G) polycrystalline thin film solar cells are treated in chapter 4. In this chapter, the authors report the state of the art of second-generation solar cells, based on $CuInGaSe_2$ (CIGS) thin film technology. This type of cells have reached, on the laboratory scale, photovoltaic energy conversion efficiencies of about 20.3%; which is the highest efficiency ever obtained for thin film solar cells. In particular, the materials, the sequence of layers, the characteristic deposition techniques and the devices that are realized by adopting CIGS as an absorber material are fully described. Particular emphasis is placed on major innovations developed in the authors' laboratory, that have made it possible to achieve high efficiencies, in addition to showing how the thin-film technology is mature enough to be easily transferred to industrial production. The fabrication procedure proposed by the authors is a completely dry process, making use of the sputtering technique only for the deposition of all the layers, including CdS, and the high temperature treatment in pure selenium for the selenization of the $CuInGaSe_2$ film. At the end of this chapter, the authors also discuss the perspectives for solar cells based on $Cu_2ZnSnS_4$ (CZTS) absorber layers. CZTS is a new alternative material, which has in the last ten years seen a huge improvement; a lot has been done to study the physical properties and to control the stoichiometry, especially secondary phases that are still a strong limitation to high efficiency. High series resistance and short minority carrier lifetime generally reduce the current of these devices and the tendency to form a great number of detrimental defects decreases the open circuit voltage.

In chapter 5, the $Cu_2ZnSnS_4$ (CZTS) solar cell development is reviewed in a more complete way by the authors. In this chapter, the recent progress in both material development and device fabrication is summarized and analyzed. The future prospects of the CZTS thin film solar cells, which will boost PV technologies, are discussed. Typical properties of CZTS films such as structural, optical and electrical properties are presented. Then, the solar cell structures fabricated with this material are described. A variety of results are obtained when different techniques are used for the CZTS deposition. Vacuum evaporation, sputtering and pulsed laser deposition are compared with non-vacuum techniques such as electro-deposition, sol-gel, nano-particle based and screen printing techniques for CZTS layer deposition. The authors discuss that in order to have good CZTS layer properties and solar cells, defect

engineering and control of the secondary phases in the film are needed. Band-gap engineering is also a tool for improved performance. Other important aspects for making better solar cells are also discussed. For example, the use of non-toxic chemicals, the avoidance of Se treatments and CdS as a buffer layer can be very important for the massive application of CZTS solar cells, as explained by the authors in this chapter. The chapter is concluded with a proposal of new nano-structured CZTS solar cells based on Mo nanorods covered with CZTS layers deposited by the sol-gel technique.

It is explained by the author in chapter 6, that current research trends are inclined towards thin film solar cells using earth-abundant materials. Thin film solar technologies such as CIGS and CdTe are already mature and have reached the commercialization stage. However, as explained above, there are toxicity issues associated with some of the elements such as selenium and cadmium; and also scarcity issues with other elements such as indium and tellurium. Futuristic technologies for p-type candidates using earth-abundant materials include CZTS, discussed previously, $Zn_3P_2$, $FeS_2$, SnS, etc. Basic material properties and current status of these technologies are discussed in this chapter. CZTS deposition techniques such as spray pyrolysis and solution based methods are discussed, in addition to those presented in the two preceding chapters. Deposition methods for other abundant solar cell materials such as $Zn_3P_2$ and $FeS_2$ are also reviewed, including a discussion on the optimization of these layers. Apart from these, there are several other promising materials that can be synthesized using earth-abundant constituents, such as SnS, $Cu_2FeSnS_4$ (CFTS) and $Cu_2SnS_3$, and these potentially can be used in solar cells due to their photovoltaic properties, as explained by the author of this chapter.

Dye-sensitized solar cells (DSCs) have been receiving continuous research interest and industrial attention as a potential low-cost, clean, and renewable energy source, since their inception in 1985. In chapter 7, the authors assert that DSC is the only photovoltaic device that uses molecules to absorb photons and convert them to electric charges without the need of intermolecular transport of the electronic excitation. According to them, it is also the only photovoltaic device that separates two functions: light harvesting and charge-carrier transport, mimicking the photo-synthesis found in green leaves. The chapter starts with a brief description of the basic concept of the light-harvesting efficiency (LHE), and then give a review on five typical branches representing the significant advances in this area, including (1) the mesoporous photoanodes with high surface area, (2) the hierarchically nanostructured photoanodes, (3) the dual-function scattering layer on the top of nanocrystalline (nc) electrode, (4) the plasmonic photoanodes, and (5) the photonic crystal photoanode and others. The basic principles of these novel nanostructures/methods enhancing the light-harvesting capacity of DSC, together with their mutual effects on the electrical and photo-electrochemical properties of the nanoporous electrode, are discussed in detail. Based on the in-depth analysis of literature and the authors' experience, a perspective will be presented, shedding a light on the future research road. The authors conclude that the light-harvesting capacity (LHE) of the photoanode film has very important effects on the power conversion efficiency of DSC. The deliberate modulation of the internal surface area of the nanoporous electrode and the optical path of the incident light are currently the main way to enhance the LHE of DSC. A wide range of novel materials or techniques have been utilized to improve the LHE of the electrode, including the high-surface area mesoporous nanostructures, scattering-enhanced hierarchical nanostructures, up-conversion materials, plasmonic core-shell structures, and photonic crystals. While most of reported work realized obvious enhancement on

one or more specific capacities of DSC, such as the dye-loading properties, optical scattering, or improved harvesting of near-infrared light, very a few studies can demonstrate high device performance comparable with the state-of-the-art nc-$TiO_2$ cell. The intrinsically different particle size, microstructures, preparation strategy of these novel materials from the traditional nc-$TiO_2$ electrode will inevitably result in significant change in the microstructure or the optical/electrical properties of the photoanode, which may greatly impair the final performance of the device. How to balance the advantageous and disadvantageous factors involved in these new-type photoanodes and realize the solid improvement of the overall performance of DSC will be emphasised by scientists in the near future. After all, the photoanodes based on these novel materials or structures are still in an infant stage, containing infinite possibilities to improve or even revolutionize the basic principle and performance of the traditional DSC.

In chapter 8, the authors discuss briefly the different conducting polymers, metal oxides and their application for the improved performance of DSSCs. The chapter includes a brief literature survey on the photovoltaic properties of various metal oxides nanomaterials, nanofillers in polymer electrolytes and conducting polymers. Additionally, the latest research advancements are surveyed for the development of efficient conducting polymers to be used as p-type semiconducting nanomaterials for counter electrode materials and efficient nanofillers in the solid polymers of DSSCs. Moreover, the doping and the use of $TiO_2$ and ZnO nanomaterials for enhancing the performance of DSSCs is also discussed. It is seen that the preparation methods, doping, morphologies, and the sizes of conducting polymers and metal oxides have shown considerable impact on the electrical properties of the nanomaterials and performance of DSSCs. The study also demonstrates the enhanced properties of inorganic metal oxides like ZnO and $TiO_2$ with different sizes and morphologies for achieving the efficient photovoltaic properties of DSSCs such as Jsc, Voc, FF and the conversion efficiency. The Polyaniline (PANI) nanocomposites with semiconductor materials, such as CdS, have shown improved optoelectronic properties and they have been applied to diodes and solar cells. The uniform distribution of CdS effectively improves the electronic states of PANI such as polarons and bipolarons which enhance the charge transfer. The unique conducting polymers, particularly PANI nanomaterial have been used as hole transporting materials and as counter electrodes for DSSCs. Properties of metal oxide semiconductors, particularly $TiO_2$ and ZnO, are summarized in terms of morphology, surface properties, dye absorption and application in DSSCs. Metal oxides with different morphologies and sizes enhance the surface-to-volume ratio and produce highly advanced photoanodes for efficient DSSCs. The morphologies of metal oxides considerably influence the dye absorption, light harvesting and results in increased electron transfer and reduce the recombination rate during the operation of DSSCs. The photovoltaic properties such as Jsc, Voc, FF, and conversion efficiency have been significantly improved by modifying the sizes and shapes of the metal oxides. The chapter also summarizes the use of various metal oxide nanomaterials as nanofillers in polymer electrolytes and describes their effect on the properties of polymer electrolytes and the performance of DSSCs. The introduction of metal oxide nanomaterials into the polymer matrix has significantly improved the amorphicity, mechanical, thermal and ionic conductivity of polymer electrolytes. At the end, some of the polymer composite electrolytes and their photovoltaic properties for DSSCs are also reviewed.

Low in cost, light in weight and mechanical in flexibility, the solution processed organic solar cells have aroused worldwide interest and have been the promising alternative to the

traditional silicon-based solar cells, but they are still not ready for massive commercialization because of their low power conversion efficiency (PCE). In chapter 9, the authors explain that PCE of standalone organic solar cells is improved continuously, but some bottlenecks still appear because of the drawbacks of molecular and macromolecular materials: First, organic solar cells are dominated by excitonic effects, and the relatively short lifetime and low mobility of charge carriers, limit the maximum thickness of the active layer for light absorption. Second, most organic semiconducting materials show discrete absorption behaviour and cover only a fraction of the solar spectrum leading to inefficient light harvest. To overcome these drawbacks, the realization of organic tandem solar cells based on complementary thin absorber materials provides a reasonable solution to the above obstacles. The working principle of this kind of photovoltaic devices can simply be described as a process of "light in-current out". This process consists of seven parts: (1) in-coupling of photon, (2) photon absorption, (3) exciton formation, (4) exciton migration, (5) exciton dissociation, (6) charge transport, and (7) charge collection at the electrodes. The first two parts are optical mechanisms and the other parts constitute electrical aspects. The optical phenomena play a significant role because more incident photons and absorbed photons are the base for a better performance of organic solar cells. It has been reported that the internal quantum efficiency (IQE) of organic bulk hetero-junction solar cells can reach 100%. And the external quantum efficiency (EQE) can be approximately described as the product of IQE and the ratio of the number of absorbed photons in the active layer to the number of incoming photons. As a result, the optical optimization of organic solar cells is highly important. This is why the device performance of standalone and tandem organic solar cells is investigated in this chapter. The contents of the chapter includes a comparison of the performance of standalone conventional and inverted organic solar cells, and a further discussion about optimizing organic tandem solar cells by considering the current matching of the sub-cells. At first, active layer thickness of the tandem cell is optimized by considering the current matching for normal and reversed structures. Owing to the different spectral ranges of the two blend materials (P3HT:PCBM and pBBTDPP2:PCBM) and device structures, it is noted that the reversed tandem cell allows a larger matching Jsc when the total device is relatively thin. When the thickness of the active layer increases, the normal tandem solar cell begins to present its superiority in performance. Then, the authors assert that we can choose a thinner reversed tandem cell to achieve the Jsc needed in some cases, saving cost in this case.

In chapter 10, the new 3G multi-junction solar cells are studied by the authors. InGaAsN is a candidate material to realize ultra-high efficiency multi-junction solar cells because this material has a band gap of 1 eV, and the same lattice constant as GaAs or the common Ge substrate. So far, Solar Junction has reported a 3-junction lattice-matched solar cell, GaInP/GaAs/GaInNAs, with a conversion efficiency of 43.5% under 418-suns. By realizing InGaP/InGaAs/InGaAsN/Ge, 4-junction solar cell, the conversion efficiency is expected to be 41% under AM1.5G 1-sun and 51% under AM1.5D 500-suns. Here, 9% In and 3% N compositions are required to realize the 1 eV band gap and lattice matching. To achieve the expected super high efficiency, the conversion efficiency of InGaAsN solar cell should be high with the short circuit current of 18 mA/cm$^2$ under a GaAs filter. However, the present conversion efficiency of InGaAsN is still low. The highest conversion efficiency reported is 6.2% (AM1.5 1-sun) with a short circuit current (Jsc) of 26 mA/cm$^2$ (10.9 mA/cm$^2$ under AM0 and GaAs filter), open circuit voltage (Voc) of 0.41 V, fill factor (FF) of 0.577. This result indicates that the minority carrier diffusion length is very short. The electrical properties such as minority carrier mobility and lifetime should be improved to realize more than 1 μm diffusion length

at 3% N composition. Hence, in this chapter the authors show the improvement in the mobility and minority carrier lifetime of GaAsN by using the chemical beam epitaxy (CBE) technique. Good crystalline quality of GaAsN was obtained by using this technique. There are three regions in the relationship between the temperature and the growth rate. In the lower temperature region (340 – 390 ºC), the growth rate increases with increasing temperature. In the middle temperature region (390 – 445 ºC), the growth rate decreases with increasing temperature. In the higher temperature region (445 – 480 ºC), the growth rate is only slightly changed. The hole mobility and electron lifetime of p-GaAsN was improved by controlling the growth rate in CBE. The electron lifetime of p-GaAsN was also improved by controlling the GaAs substrate orientations. The defect properties that limit the minority carrier life time was studied by using deep level transient spectroscopy (DLTS). Their analysis indicates that N-related centers are the dominant scattering centers.

Chapter 11 deals with an alternative kind of modules to be used under concentrated sunlight. In the past few years Concentrating Photovoltaics (CPV) has moved from R&D and pilot projects (typically installations below 500 kilowatts) to multi-megawatt power plants. A CPV module consists typically of a high-efficient solar cell and a concentrator that concentrates light and that can be made out of a mirror, a parabolic dish or lenses. These modules are then mounted on a 2-axis tracking system to make sure that the module is always perpendicular to the sun, so that the light spot reaches the active area of the solar cell. A CPV system is therefore more complex than a conventional PV system, and, in order to be commercially competitive with standard systems, it is important to control its cost figure. When making a cost analysis of a CPV system, from manufacturing of solar cells to a finished installation, the cost figure is given in terms of a monetary unit per Watt (€/W or $/W). There are two possibilities to reduce the value of this cost figure, which are either reducing the cost of the system, which is typically done reducing the cost of the raw materials or optimizing production processes, or by increasing the output power of the CPV module, which can be achieved by reducing possible sources of losses inside a module (these can be optical, electrical or thermal). The advantage of increasing the output power of a module is that this has an important impact to other related costs, since also the manufacturing and installation costs are reduced due to the need of fewer modules or even trackers for a CPV power plant of a given size. The output power of a CPV module can be optimized by reducing the internal losses that appear in the module design. Therefore a good match of the materials from which the module is made should be aimed. The need of a good match is especially true for the interaction between the solar cell and the optical system, where the solar cell can be adapted in size, light spectrum, concentration ratio and interface to the optical system. A solar cell can be designed to have either a maximum efficiency when it is measured as a stand-alone device (having air as the surrounding medium) or to have maximum efficiency when it is surrounded in any other optical medium that is used inside the CPV module (e.g. glass or an optical encapsulant). In order to explain better how the embedding medium affects the solar cell performance and to quantify this effect, a series of simulations has been done with a simulation program that has been developed by the author in collaboration with the University of Granada (Spain). This program is called ISOSIM and is able to simulate the performance of a multi-junction solar cell, including its anti-reflection coating (ARC) and taking into consideration the concentration and the medium in which the solar cell is used (e.g. air or an optical gel to couple the light from the lens to the solar cell). It is also possible to add optical layers on top of the solar cell structure and simulating thereby a CPV module. With ISOSIM it is also possible to understand and predict experimental behaviour

of solar cells under real operating conditions. The results obtained in this chapter can be extrapolated to triple-junction solar cells, since typically the third junction is made out of germanium and is far from limiting the multi-junction solar cell. It is shown that in order to obtain maximum module power output, a solar cell and optical system should match each other well, in a way that the design of the solar cell should take into account the optical system of the CPV module or the other way around, the design of the optical system should be adapted to a given solar cell. It is also shown that a small variation in efficiency of a solar cell has a big impact on CPV module power output and therefore also on the installation cost of a CPV power plant.

A Photovoltaic (PV) solar cell system as an autonomous energy source unit must have an energy management control unit that is embedded in the system. In general, there are 5 elements that exist in an autonomous PV system: (1) The solar cell array; (2) The energy management control unit; (3) the energy storage subsystem; (4) the DC to AC converter and (5) the delivery bus. In chapter 12, the authors explain that these parts should be designed such that the whole system is very efficient managing the electrical energy at low cost. In chapter 12, the authors make a review of the required energy management control systems. Electrical energy management and engineering for solar PV systems is started by designing the system requirements to fulfill the electrical energy needs, the technical specifications of solar cell modules and batteries, and also information of solar radiation energy in the zone of installation. The characterization of the solar modules and batteries are very important to support the system design. Furthermore, the system´s electrical energy management and engineering must deal with 4 tasks: First of all, current flow-in and flow-out monitoring from the battery bank. The second one is measuring the electrical energy content inside the battery bank. The third one is an evaluation of the internal energy condition based on energy capacity and availability, and deciding whether or not integrating with an external system (grid). The fourth one, when this integration is needed, is frequency, phase and voltage synchronization. Those four tasks require an algorithm and procedure, which can be very complex for electronic analog circuits. To cover these 4 tasks, a processing system based on a microprocessor or even a computer system has to be developed. If several units exist they can be coordinated to build a grid that maintains the electrical energy service, as explained by the authors.

In chapter 13, the authors study the hybrid operation of a small wind and photovoltaic (PV) energy power system. Theoretically, source impedances of the wind generator and solar cell pose problems for simultaneous battery charging by both wind and solar energy. A battery in under-charged condition can be charged by both energy sources; but with increase in the battery voltage, it can be charged by only one energy source. To enhance energy utilization, a switch circuit can be employed to adjust the charging duty cycle of the two energy sources. During solar energy charging, the mechanical energy generated by inertia of the wind turbine will be stored and employed to charge the battery during wind energy charging. On the other hand, solar energy cannot be stored but will be lost during wind energy charging. Hence, by shortening the wind energy charging cycle can help reduce energy loss. To overcome the above problem, a microprocessor-based controller is utilized to control the charging system. Depending on the weather condition, wind or solar energy may charge one or both batteries. If there is only one energy source, it charges both batteries. When there are two energy sources, each charges an individual battery, respectively. Nevertheless, when the wind speed is high, the wind energy charges both batteries. In the study presented in

this chapter, a 250-W permanent magnet generator (PMG) and a 75-W solar cell panel were used to validate the feasibility of the proposed charging system. The results show that with the two energy sources better utilized, the fluctuations in wind power system can be reduced and the reliability of both power systems can be improved.

I hope the topics discussed in the above chapters give a whole perspective of the future development of solar cell research and application. If this objective is achieved, the purpose of this book will be fully accomplished.

**Dr. Arturo Morales-Acevedo**
Electrical Engineering Department,
Centro de Investigación y de Estudios Avanzados del
Instituto Politécnico Nacional (CINVESTAV del IPN),
Ciudad de Mexico, México

Chapter 1

# Optimization of Third Generation Nanostructured Silicon-Based Solar Cells

Foozieh Sohrabi, Arash Nikniazi and Hossein Movla

Additional information is available at the end of the chapter

http://dx.doi.org/10.5772/51616

## 1. Introduction

Recently, the demand of solar cells has rapidly been growing with an increasing social interest in photovoltaic energy. Improving the energy conversion efficiency of solar cells by developing the technology and concepts must be increasingly extended as one of the key components in our future global energy supplement, but, the main problem of photovoltaic modules are their rather high production and energy cost.

Third generation solar cell is an alternative type of the promising device, which aims to achieve high-efficiency devices with low cost in comparison with expensive first generation solar cells and low-efficiency second generation solar cells. One of the prominent types is Si-based third generation solar cells which benefit from thin film processes and abundant, nontoxic materials. To gain efficiencies more than Shockley and Queisser limit which states the theoretical upper limit of 30% for a standard solar cell and overcome the loss mechanisms in this generation, different methods have been proposed:

1. Utilization of materials or cell structures incorporating several band gaps:
   - Si-based multi-junction solar cells
2. Modification of the photonic energy distribution prior to absorption in a solar cell:
   - Photon energy down-conversion
   - Photon energy up-conversion
3. Reducing losses due to thermalization:
   - Hot carrier solar cells
   - Impact ionization solar cells

This chapter mainly brings out an overview of the optimization of the first strategy and briefly the second and third strategies accompanying nanostructures. Multijunction solar cells are stacks of individual solar cells with different energy threshold each absorbing a different band of the solar spectrum. Si-based tandems based on quantum dots (QDs) and quantum wires (SiNWs) allowing band gap engineering and their optimization methods influencing their optical and electrical properties such as suitable Si QDs and SiNWs fabrication methods in various matrixes, interconnection between QDs, optimized impurity doping, etc. will be discussed. Moreover, the effects of the spacing and the size of Si QDs and SiNWs and their efficient amounts considering the latest researches will be introduced.

Another important process is multiple exciton generation (MEG) in QDs due to the current scientific interest in efficient formation of more than one photoinduced electron-hole pair upon the absorption of a single photon for improving solar devices.

Afterwards, the structural and superficial effects on the optimization of Si-based third generation solar cellslike light concentration and use of forming gas will be presented.

Finally, the outlook concerning the mentioned methods will be suggested.

## 2. Principle of third generation solar cells based on silicon

The main aim of third generation solar cell is obtaining high efficiency. To achieve such efficiency improvements, devices aim to circumvent the Shockley-Queisser limit for single-bandgap devices that limits efficiencies to either 31% or 41%, depending on concentration ratio (Fig. 1).

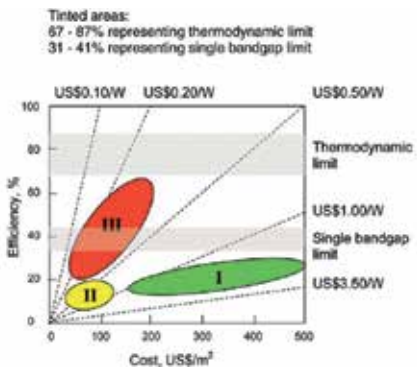


**Figure 1.** Efficiency and cost projections for first- (I), second- (II), and thirdgeneration (III) PV technologies (wafer-based, thin films, and advanced thin films, respectively) [2].

The two most important power-loss mechanisms in single band gap cells are the inability to absorb photons with energy less than the bandgap (1 in Fig. 2) and thermalization of photon energies exceeding the bandgap in which the excess energy is lost as heat because the elec-

http://dx.doi.org/10.5772/51616

tron (and hole) relaxes to the conduction (and valence) band edge. The amounts of the losses are around 23% and 33% of the incoming solar energies, respectively (2 in Fig. 2) (1). Eventually, these two mechanisms alone cause the loss of about half of the incident solar energy in solar cell conversion to electricity. Other losses are junction loss, contact loss, and recombination loss which is shown in Fig. 2[1].

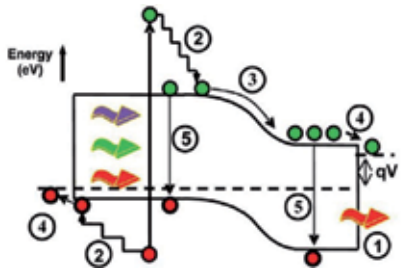


**Figure 2.** Loss processes in a standard solar cell: (1) non absorption of below bandgap photons; (2) lattice thermalization loss; (3) and (4) junction and contact voltage losses; (5) recombination loss (radiative recombination is unavoidable) [2].

Three families of approaches have been proposed for applying multiple energy levels:

1. increasing the number of energy levels;
2. multiple carrier pair generation per high energy photon or single carrier pair generation with multiple low energy photons; and
3. capturing carriers before thermalization.

Of these, tandem cells, an implementation of strategy (a), are the only ones that have, as yet, been realized with efficiencies exceeding the Shockley-Queisser limit [2].

In this chapter, firstly the concept of tandem solar cell or multijunction solar cell will be discussed and then Si nanostructured tandems will be explained precisely. However, amorphous silicon (a-Si) tandems will not be investigated in this chapter due to their lower efficiency in comparison with Si nanostructured tandem solar cells.

*Multiple- Junction solar cell*

One of the promising methods to enhance the efficiency of solar cells is to use a stack of solar cells, in which each cell has a band gap that is optimized for the absorption of a certain spectral region [3]. In fact, by stack layers, the number of energy levels is increased. This method was suggested for the first time by Jackson in 1955.

Solar cells consisting of p-n junctions in different semiconductor materials of increasing bandgap are placed on top of each other, such that the highest bandgap intercepts the sunlight first [2].

The importance of multijunction solar cell is that both spectrum splitting and photon selectivity are automatically achieved by the stacking arrangement.

To achieve the highest efficiency from the overall tandem device, the power from each cell in the stack must be optimized. This is done by choosing appropriate bandgaps, thicknesses, junction depths, and doping characteristics, such that the incident solar spectrum is split between the cells most effectively. Moreover two configurations are used for extracting electrical power from the device effectively which are reviewed by Conibeer: either a 'mechanically stacked' cell, in which each cell in the stack is treated as a separate device with two terminals for each; or an 'in-series' cell with each cell in the stack connected in series, such that the overall cell has just two terminals on the front and back of the whole stack. For a fixed solar spectrum and an optimal design, these two configurations give the same efficiency. But for a real, variable spectrum, the mechanically stacked design gives greater flexibility because of the ability to optimize the I-V curve of each cell externally and then connect them in an external circuit.

The reduced flexibility of just optimizing the I-V curve for the whole stack, because the same current must flow through each cell, makes the in series design more sensitive to spectral variations. Furthermore, they become increasingly spectrally sensitive as the number of bandgaps increases. For space-based cells this is not a great problem because of the constant spectrum, but for cells designed for terrestrial use, it is significant because of the variability of the terrestrial solar spectrum. This is particularly the case at the beginning and end of the day when the spectrum is significantly red shifted by the thickness of the atmosphere. Nonetheless, the much greater ease of fabrication of in-series devices makes them the design of choice for most current devices [2].

The efficiency depends on the number of subcells [1]. The efficiency limit for a single pn junction cell is 29%, but this increases to 42.5% and 47.5% for 2-cell and 3-cell tandem solar cells, respectively. However, these values are a little bit more for concentrated light.

For example, the radiative efficiency of bulk silicon (Si) solar cells under the AM1.5G spectrum is limited theoretically to 29% due to the incomplete utilization of high energy photons and transmission of photons with less energy than the Si band gap [3]. But, the theoretical efficiency of tandem solar cells with a bulk Si bottom cell increases to 42.5 % when one additional solar cell with 1.8 eV band gap is used and to 47.5 % with two further solar cells with band gaps of 1.5 and 2 eV placed on top of the bulk Si cell.

*Si nanostructure tandems*

Silicon is not suitable for optoelectronic applications because of its indirect bandgap and poor light emission properties. However, silicon bandgap tuning above bulk silicon bandgap (1.12eV) is possible in the nanometer regime (sizes less than 10nm) enabling a revolutionary control over its properties [4].Therefore, use of nanostructures in tandem solar cells can create bandgap engineering besides improving the efficiency. Improved optical and electrical properties of silicon can be found in different forms of silicon, for example, porous silicon, silicon superlattices and Si-QD embedded in dielectric [4].

In silicon based tandem solar cells, this bandgap engineering can be done using either quantum wells (QWs) or quantum dots (QDs) of Si sandwiched between layers of a dielectric based on Si compounds such as $SiO_2$, $Si_3N_4$, SiON or SiC which taking advantages of the

http://dx.doi.org/10.5772/51616

widening of absorption spectrum in the UV range [5]. As a whole, Si nanotechnology is the best choice to improve the metastabilities and to increase the quantum efficiency [6].

By restricting the dimensions of silicon to less than Bohr radius of bulk crystalline silicon (almost 5 nm), quantum confinement causes its effective bandgap to increase. If these dots are close together, carriers can tunnel between them to produce QD superlattices. Such superlattices can then be used as the higher bandgap materials in a tandem cell [1]. In fact, the idea is to add one or more layers of nano-structured materials on the top of a solar cell for which the optical absorption covers different domains of the solar spectrum (Fig. 3 is an example of "all silicon" tandem solar cell).

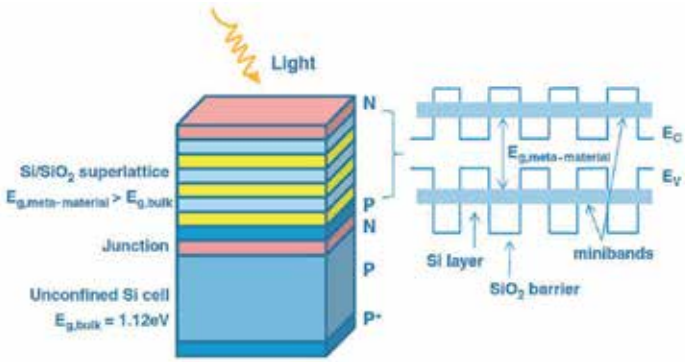


**Figure 3.** Schematics of an "all silicon" tandem solar cell with a top cell based on a nanostructured meta-material stacked on an unconfined Si cell [7].

All tandem solar cells offer the advantages of using silicon which is an abundant material, stable, non-toxic and capable to diversify in order to obtain both a medium bandgap material (~1 eV) and high a bandgap material (~1.7 eV) [7]. It should be mentioned that combining two tandem cell bandgaps (1.12 eV and 1.7 eV) achieve a conversion efficiency factor up to 42%.Another significant advantage of Si is its well developed technology in the world which paves the way for experimental and optimization studies of tandem solar cells. Moreover, strong optical absorption and high photocurrent have been found in nc-Si films and attributed to the enhancement of the optical absorption cross section and good carrier conductivity in the nanometer grains [8].

An approach to prepare silicon quantum dot superlattices by depositing alternating layers of stoichiometric oxide followed by silicon-rich oxide also appears promising in a potentially low cost process, with the control of dot diameter and one spatial coordinate [9].In detail, these layers are grown by thin-film sputtering or CVD processes followed by a high-temperature anneal to crystallize the Si QWs/QDs. The matrix remains amorphous, thus avoiding some of the problems of lattice mismatch [2]. For sufficiently close spacing of QWs or QDs, a true miniband is formed creating an effectively larger bandgap. For QDs of 2 nm (QWs of 1 nm), an effective bandgap of 1.7 eV results – ideal for a tandem cell element on top of Si [2].

Because of the charge carrier confinement in Si quantum dots it is possible to adjust the band gap by a control of the Si quantum dot size [3].

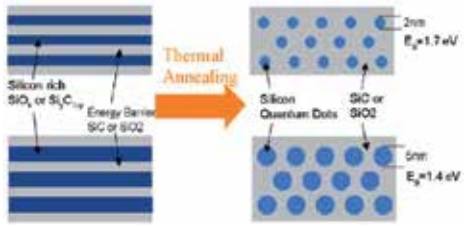


**Figure 4.** Schematic of the procedure to achieve size control of Si NC in Si based dielectric matrices. Layers with silicon excess are deposited alternately between stoichiometric layers. The stoichiometric layers act as a diffusion barrier for the silicon atoms and therefore limit the growth of silicon nanocrystals during the annealing step [3].

Generally, there are two ways for observing and estimating the size [1]:

1. The dot size of the Si QDs can be evidenced by high-resolution transmission electron microscopy (HRTEM). We can clearly see black dots due to contrast difference between Si and $SiO_2$ in Fig. 5.
2. Raman spectroscopy can also be used to estimate the dot size. (Fig. 6.)

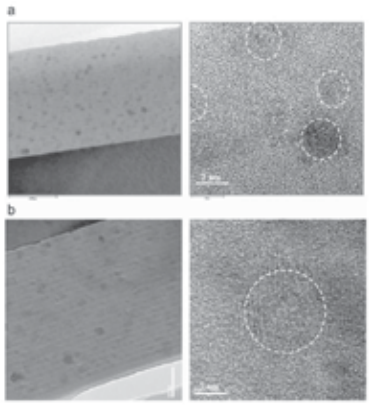


**Figure 5.** Transmission electron microscopy (TEM) images of Si quantum dots in $SiO_2$ matrix with low-magnification and high-resolution lattice images for (a) 5 nm Si QDs and (b) 871 nm Si QDs[1].

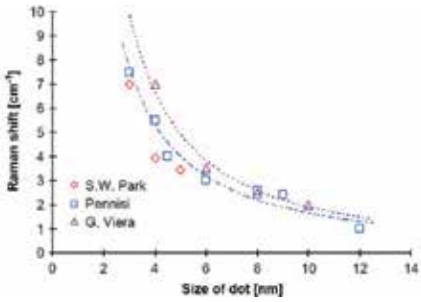


**Figure 6.** Raman peaks shifts to lower energy for Si QDs with 3,4, and5 nm. Reference data are adapted from Pennisi and co-workers [8] and Viera et al[1].

To realize all-silicon tandem solar cells, Park et al., fabricated phosphorus-doped Si QDs superlattice as an active layer on p-type crystalline Si (c-Si) substrate as shown in Fig. 7. The phosphorous doping in n-type Si QDs superlattice was realized by $P_2O_5$ co-sputtering during the deposition of silicon-rich oxide (SRO, Si and $SiO_2$ co-sputtering), which forms Si QDs upon high-temperature post-annealing. The n-type region typically includes 15 or 25 bi-layers formed by alternating deposition of P-doped QDs and $SiO_2$ [1].

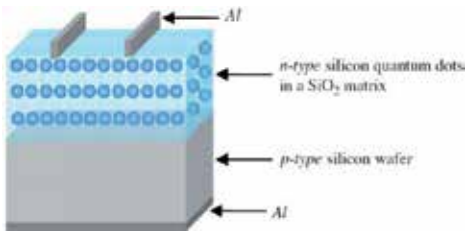


**Figure 7.** Schematic diagram of (n-types) Si QDs and (p-type) c-Si heterojunction solar cell [1].

In the next section the optimization methods for nanostructured silicon based solar cell will be discussed in detail.

## 3. Optimization method in nanostructures

### 3.1. Silicon quantum dots solar cells

The main challenge for a nanostructure engineered material in a tandem cell is to achieve sufficient carrier mobility and hence a reasonable conductivity. For a nanostructure, this generally requires formation of a true superlattice with overlap of the wave function for adjacent quantum dots; which in turn requires either close spacing between QDs or a low barrier height. Moreover, the quantum confinement, achieved by restricting at least one dimension of silicon less to the Bohr radius of the bulk crystalline silicon (around 5 nm), causes the effective bandgap to increase [10] which also results in increased absorption. The strongest quantum confinement effect is obtained if the silicon is constrained in all three dimensions, as in quantum dots, such that the same increase in effective bandgap can be achieved with a much less stringent size constraint [10]. Different technological approaches allowing formation of Si QDs. Generally, perfect (ideal) QD arrays can have the following characteristics [11]:

1. Absolutely accurate positioning and control for nucleation site of individual QD;
2. Uniformity of size, shape and composition;
3. Large-area (~$cm^2$), long-range ordering QDs;
4. The ability to control the QDs size;
5. The ability to achieve both ultra-high dense QD arrays and sparse QD arrays

In this part we will discuss on optimum properties of Si QDs that include size, spacing and dielectric matrix of Si QDs which also have great influences on the band structure [9].

*3.1.1. Optimum size of Si QDs*

A control of the Si nanocrystal size allows the adjustment of essential material parameters such as bandgap and oscillator strengths due to size quantization effects [3]. Experimental results have shown that the size of the QDs can be quite well controlled by selecting an appropriate thickness for the SRO layer and the density of the dots can be varied by the composition of the SRO layer. In detail, the size and crystallization of the Si nanocrystals are dependent on a number of factors, including the annealing method and the barrier thickness [12].

In 2006, Gavin Conibeer et al., at the University of NSW, used the energy confinement of silicon based quantum dot nanostructures to engineer wide band gap materials to be used as upper cell elements in Si based tandem cells. HRTEM data shows Si nanocrystal formation in oxide and nitride matrixes with a controlled nanocrystal size, grown by layered reactive sputtering and layered PECVD [13].

The data shown in Fig. 8 are measured from HRTEM images for samples at several deposition times. There is a sharp decrease in the nanocrystal size distribution on reduction in layer thickness from 4.7 to 3.5 nm. This indicates a transition from a bulk diffusion mechanism of Si atoms during precipitation to a constrained two dimensional diffusion regime, such that the nanocrystal size is defined by the layer thickness [13].

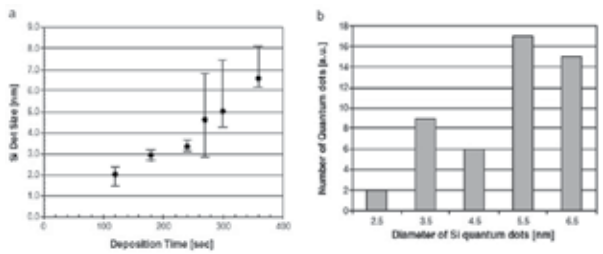


**Figure 8.** a) Dependence of quantum dot size distribution on deposition time as measured by HRTEM (other sputtering parameters optimized). b) QD size distribution for deposition time of 280 s [13].

This is an important self-regulation effect which gives much greater uniformity in nanocrystal optoelectronic properties, at least in the growth direction, as indicated for photoluminescence (PL). PL results indicate quantum confined properties as evidenced by the increase in the photo-luminescent energy in PL experiments [13].

Fig. 9a shows an increase in PL energy as nanocrystal size decreases, thus demonstrating quantum confinement and hence formation of quantum dots. It also shows a dramatic increase in PL intensity on going from a dot diameter of 4.7 to 3.5 nm. This correlates well with the greatly increased uniformity in Si quantum dot size as the deposited layer goes from 4.7 to 3.5 nm, as shown in Fig.8a on change of diffusion mechanism (see above). The

http://dx.doi.org/10.5772/51616

large increase in PL energy is due to the much greater signal at a given energy with good dot size uniformity. (The fact that this intensity drops again is discussed below.) An increase in PL intensity is also to be expected as dot size decreases because of the increase in spatial localization of electrons and holes that will increase the probability of recombination [13].

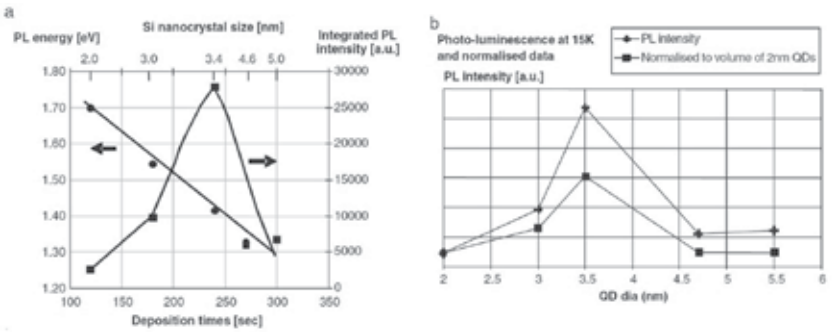


**Figure 9.** a) PL energy and integrated intensity (15 K) as a function of deposition time, showing quantum confined energy in silicon quantum dots. Deposition time is also calibrated for dot diameter by TEM. b) PL intensity data normalized for decreasing volume [13].

Eun-Chel Cho et al. in 2007 in Australia show that there is a large increase in PL intensity as the QD size decreases, which is consistent with the increase in radiative efficiency with the onset of pseudodirectbandgap behavior. The photoluminescence peaks from Si QDs in nitride are more blue-shifted than that of Si QD in oxide. Figure 10 shows the PL peak energies from Si QD dispersed in oxide and nitride. PL peak energies of Si QDs in oxide are less than 2.0 eV, while Si QDs in nitride have peak energies less than 3.0 eV [10].

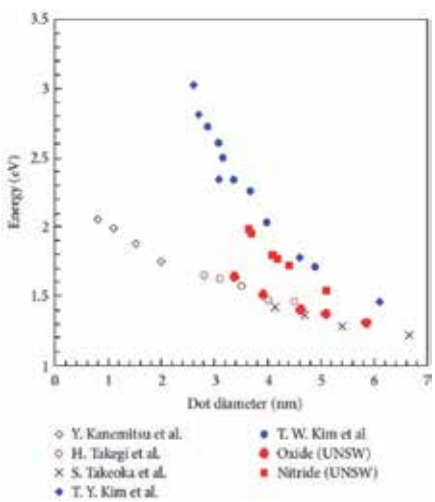


**Figure 10.** Energy gaps of three-dimensionally confined Si nanocrystals in $SiO_2$ and $SiN_x$ (300°K) [10].

Puzder et al. in 2002 have explained that the main reason for the PL peak energy reduction in oxide matrix is the distortion of the local $sp^3$ network by double-bonded oxygen. However, Yang et al. in 2004 claimed that the reason for the stronger blue shift in nitride is better passivation of Si QDs by nitrogen atoms, eliminating the strain at the $Si/Si_3N_4$ interface nearly completely [10]. Generally, it can be concluded that the optimum size of Si QDs is 2-3nm.

*3.1.2. Optimum spacing of Si QDs*

If QDs dots are spaced close enough and there is a significant overlap of the wave function, carriers can tunnel between them to produce a true quantum dot superlattice. Such a superlattice can then be used as the higher bandgap material in a tandem cell [10]. In other words, one common strategy to boost the performance of photovoltaic device structures is incorporating closely packed 3D QD array into device structures. When QDs in different size are formed into an ordered 3D array, there will be strong electron coupling between them so that excitons will have a longer life, facilitating the collection and transport of ''hot carriers'' to generate electricity at high voltage [11]. In addition, such an array makes it possible to create more than one electron-hole pair from a single absorbed photon, and thus enhance photocurrent, through the process of impact ionization [14]. This process happens when the energy of the photon is far greater than the semiconductor bandgap; while in bulk semiconductors the excess energy is simply dissipates away as heat, in QDs the charge carriers are confined within an infinitesimal volume, thereby increasing their interactions and enhancing the probability for multiple exciton generation [14].

The transport properties of the ensembles of disordered Si QDs in insulating matrix could be explained in terms of the percolation theory, which has already been successfully implemented to explain the transport processes in granular metals by Abeles et al. in 1975. Indeed, this theory describes the effect of the system's connectivity on its geometrical and physical properties [15].

To what concerns the ensemble of Si QDs, there can be distinguished five different structural-electrical regimes, such that in each of them we may expect a different transport mechanism to dominate. These regimes are

1. Spherical QDs isolated by uniformly dispersed in insulating matrix
2. Some of the QDs starts to "touch" their neighbors named as Transition regime
3. Forming of clusters of "touching" QDs named as Intermediate regime
4. Clusters of regime 3 form a global continuous network named as Percolation transition regime
5. Well forming of percolation cluster of "touching" QDs and disappearance of geometrically non-"touching" QDs.

Fig.11 (a), (b) and (c) present typical examples of ensembles of Si QDs corresponding to regimes 1, 3 and 5, respectively. Usually there are narrow (no more than 0.5 nm wide) boundaries formed between the nanoparticles, which involves at least a different crystallographic orientation of the touching crystallites. In a literature the charge transfer process between such "touching" QDs was termed as "migration".

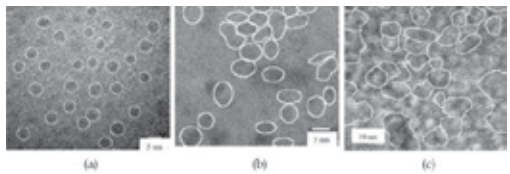

**Figure 11.** HRTEM images of the ensembles of Si QDs corresponding to different structuralelectrical regimes: (a) uniformly dispersed isolated spherical QDs (regime 1), (b) clusters of "touching" QDs (regime 3) and (c) percolation clusters of "touching" QDs (regime 5)[15].

The effect of the connectivity on the transport properties (dark and photoconductivity) of the ensembles of Si QDS is illustrated in Fig. 12. As one can see, the global picture of transport in Si QDs ensembles is reminiscent of that of granular metals, but the details are quite different. As long as Si QDs or clusters of Si QDs are small enough, they "keep" the carrier that resides in them and become charged when an excess charge carrier reaches them. Hence, the transport through the system can take place only if a corresponding charging (or Coulomb) energy is provided [15]. Balberg et al. in 2004 reported this topic for the samples with low number of Si QDs in the ensemble, which are characterized by the QDs of regime 1, the local conductivity is determined by the tunneling of charge carriers under Coulomb blockage between adjacent nanocrystallites similar to the case encountered in granular metals in the dielectric regime.

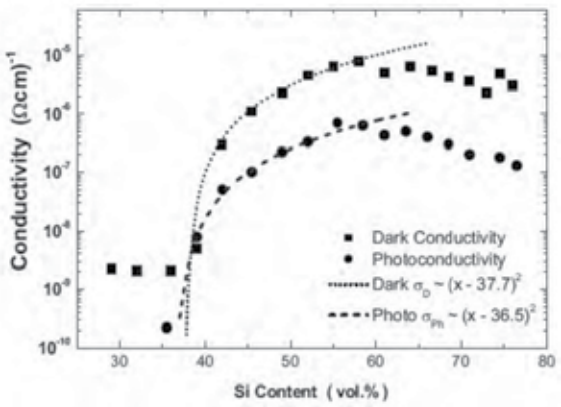


**Figure 12.** Dependence of the dark conductivity and the photoconductivity on the Si content [15].

With increasing of Si content (Figure 11b), the interparticle distance decreases and the tunneling-connected quantum dot clusters grow in size. The "delocalization" of the carrier from its confinement in the individual quantum dot to larger regions of the ensemble will take place, i.e., the charge carrier will belong to a cluster of QDs rather than to an individual QD. Correspondingly, this will also yield a decrease in the local charging energy in comparison with that of the isolated QD and the distance to which the charge carrier could wander will increase and as a consequence the conductivity of the ensemble will increase as well. The

charge carrier transport in the case of regime 3 is thus determined by the intracluster migration and by the intercluster tunneling.

Finally we can conclude from Fig. 12 that the maximal possible conductivity is assured regime 5 and the highly percolating system of Si QDs will ensure the most favorable conditions for the electronic transport between the nanocrystals and the bandgap value in such structures can be adjusted in the large range covering the major part of the solar spectrum.

Also transport properties are expected to depend on the matrix in which the silicon quantum dots are embedded. As shown in Figure 13, different matrices produce different transport barriers between the Si dot and the matrix, with tunneling probability heavily dependent on the height of this barrier. $Si_3N_4$ and SiC give lower barriers than $SiO_2$ allowing larger dot spacing for a given tunneling current [13].

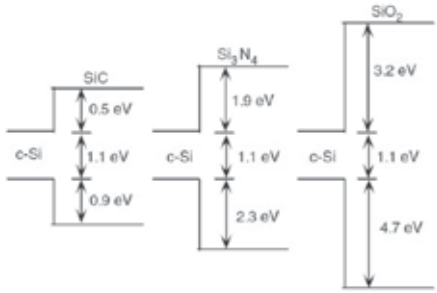


**Figure 13.** Bulk band alignments between crystalline silicon and its carbide, nitride and oxide [13].

The results suggest that dots in a $SiO_2$ matrix would have to be separated by no more than 1-2 nm of matrix, while they could be separated by more than 4 nm of SiC [10]. It is also found that the Bloch mobilities do not depend strongly on variations in the dot spacing but do depend strongly on dot size within the QD material [16].

Hence, transport between dots can be significantly increased by using alternative matrices with a lower barrier height, $\Delta E$. The spacing of dots would have to be closest in the oxide, nitride and carbide, in that order. Similar deposition and quantum dot precipitation approaches should work for all [16].

*3.1.3. Optimum dielectric matrix of Si QDs*

In recent years it emerged that the Si QD interface with its surrounding dielectric matrix plays a decisive role in determining the optical absorption gap and the optical activity of the Si QD on both experimental and theoretical grounds [17].

Generally, as mentioned above, three types of dielectric matrices $SiO_2$, $Si_3N_4$, or SiC are used to form all tandem silicon solar cell.

It should be considered that lower barrier heights will give a greater tunneling probability between adjacent Si QDs and hence greater conductance [18]. Therefore, $Si_3N_4$ and SiC have

http://dx.doi.org/10.5772/51616

greater conductance than $SiO_2$. In detail, SiC has the lowest barrier height among these dielectrics. However, the low barrier height also limits the minimum size of QDs to about 3nm or else the quantum-confined levels are likely to rise above the level of the barrier, which should be around 2.3 eV for amorphous SiC. In addition, although $SiO_2$ matrix has higher barrier height (3.2eV) comparatively, many attempts were made to fabricate Si-QD in Si-rich $SiO_2$ thick layers or superlattices since $SiO_2$ is a frequently used dielectric and compatible in microelectronics processes [4].

Si ion implantation into an oxide layer can be used to produce Si QDs at an irregular position with a relatively large size distribution. Si QDs can fabricate by solution synthesis, mechanical milling, and particle selection from porous silicon, but it is difficult to control the size uniformity of distributed QDs or an additional process to select the particle with the same size [15].

The material requirements for the dielectric layers are ease of thin-film growth and use of abundant nontoxic materials, hence it is most likely to be an oxide, nitride, or carbide of silicon. It is also necessary that carriers from the quantum dot layers have a high probability of tunneling through the dielectric layers [10]. It is worth noting that these devices must be thin to limit recombination due to their short diffusion lengths, which in turn means they must have high absorption coefficients [18].For layers of thickness less than about 4 nm, the precipitation enters a regime of 2D diffusion in which the dot size is accurately controlled by the layer thickness [13]. This is achieved by creating each dielectric layer with a thickness in the range of 1.5 to 2.5 nm for the case of oxide [10].

Si QD fabrication by various vacuum deposition techniques is preferable because of the greater potential of integration into conventional devices [10]. These include sputtering and plasma enhanced chemical vapor deposition (PECVD). The most successful and hence most commonly used technique is sputtering, because of its large amount of control over deposition material, deposition rate and abruptness of layers. This uses a new multi-target remote plasma sputtering machine with two independent RF power supplies as well as an additional DC power supply [16].

Si precipitation from a Si-rich layer, high temperature annealing of excess Si in an inert atmosphere is necessary to form Si nanocrystals with a few nm diameters, for example, Si QD precipitation in oxide, nitride, and carbide (Figure 14.a) and Equation (1) describes this Si precipitation mechanism [10]:

$$Si(O,\ N,\ C)_x \rightarrow \left(\frac{x}{2}\right)Si\left(O_2,\ N_{\frac{4}{3}},\ C\right) + \left(1 - \frac{x}{2}\right)Si\left(1\right) \quad (1)$$

It should be mentioned that in particular the amount of excess silicon in the Si-rich layer is an important parameter to study the nucleation of the QDs. If the Si concentration in the Si-rich layer film before annealing exceeds a certain limit, dots can merge together during the coalescence phase of the growth process, affecting the quantum confinement properties of the structures [25].

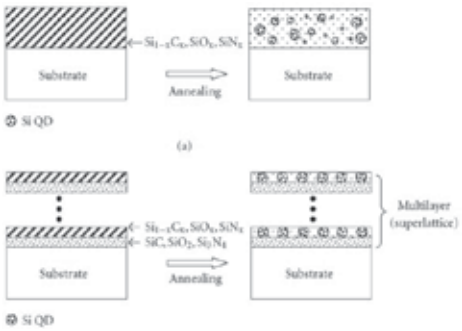


**Figure 14.** Si QDs from phase separation of a) a single silicon-rich precursor layer and b) a multilayer structure [10].

More accurate size control and a narrow size distribution are achieved by growth of a Si QD multilayer structure, which is fabricated by alternating layers of stoichiometric insulating materials and silicon-rich layers shown in Figure 14 b. Depending on the annealing conditions, silicon precipitates from the silicon-rich layers as approximately spherical QDs of a diameter close to the original layer thickness. Hence controls of the diameter and of one spatial coordinate of the dots are possible.

As mentioned above, $SiO_2$ is a frequently used dielectric and compatible in microelectronics processes.Therefore, Si-QD is generally fabricated in Si-rich $SiO_2$ thick layers or superlattices. Another dielectric option is $SiN_x$ dielectrics. Due to low barrier height, highest Si-QD growth density in Si3N4 and less silicon requirement in $Si_3N_4$ during deposition, this dielectric is replaced instead of $SiO_2$. Moreover, the formation of Si-QD in $SiN_x$ is preferable, because the formation of 3–7 nm Si-QD in Si-rich SiC film requires higher thermal budget (1100 1C) than Si-QD formation in a-Si/$SiN_x$ layer structure that requires lower annealing temperature (800-850°C) [4].

Efficient photoluminescence (PL) has also been observed from So-rich $SiN_x$ films, a single Si-QD layer sandwiched between two a-$SiN_x$ layers and structured layers of Si-QD in a-$SiN_x$. In addition, for the same Si-QD size and PL excitation wave length, Si-QDs in $SiN_x$ film show PL peak in shorter wavelengths (450-620 nm) than Si-QDs in $SiO_2$ film (650-950 nm) [4]. TEM images in Figure 8 show Si QDs interspersed in the oxide matrix [10].

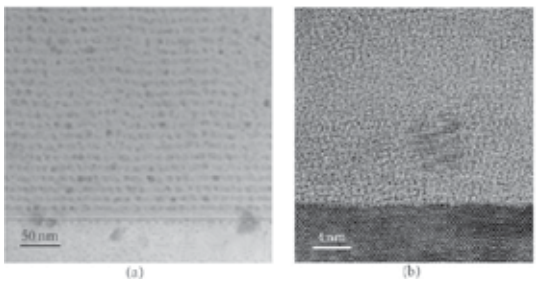


**Figure 15.** Transmission electron microscopy (TEM) images of Si QDs in SiO2 matrix with (a) low magnification and (b) HRTEM lattice image of Si quantum dots [10].

http://dx.doi.org/10.5772/51616

The bandgap of $Si_3N_4$ is significantly lower than that of $SiO_2$. Hence Si QDs in the nitride offer a lower barrier height and much increased carrier tunneling probability between quantum dots. (SiC offers a lower barrier still.) For this reason, Si QDs have explored transferring the technology in $SiO_2$ to the growth of Si nanocrystals in silicon nitride by both sputtering and PECVD [10].

Layered Si QDs have also extended the in nitride technology to gas phase in situ deposition. Figure 16 shows in situ Si QD dispersed in a nitride matrix. A stoichiometric $Si_3N_4$ layer and an in situ Si QD layer are alternately deposited on a Si substrate. This technique allows QDs to form during deposition without a postdeposition annealing. This technique is a low temperature process and may be potentially beneficial to doping of Si QDs owing to high equilibrium temperature of the plasma and free of high temperature postannealing described in Figure 14 [16].

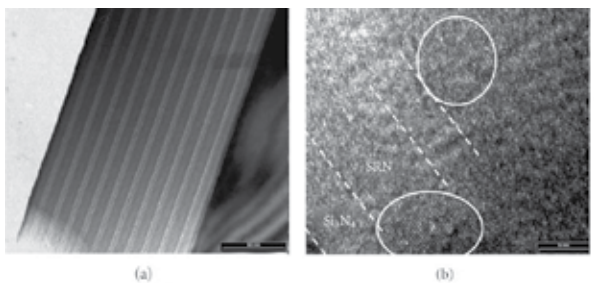


**Figure 16.** Si QDs dispersed in a $Si_3N_4$ matrix fabricated by gas phase in situ deposition: a) low-magnification TEM and b) high-resolution TEM [10].

Another dielectric for growing Si-QD is SiC. Although the electron tunneling conductivity is higher in SiC compared to $Si_3N_4$ and $SiO_2$ due to the lower barrier height (0.5eV) of SiC; the formation of Si-QD in $SiN_x$ is preferable, because the formation of 3–7 nm Si-QD in Si-rich SiC film requires higher thermal budget (1100°C) than Si-QD formation in a-Si/$SiN_x$ layer structure that requires lower annealing temperature (800-850°C) [4].

After annealing above 1000°C, indicating formation of amorphous graphitic carbon is indicated. Hence the best data so far for Si nanocrystals in a SiC matrix are obtained for a $Si_{0.75}C_{0.25}$precursor composition [10]. $Si_{1\_x}C_x$/SiC multilayers have also been deposited by sputtering to give better control over the Si QD as with oxide and nitride matrices [18].

Raman, TEM and XRD spectra for a silicon-rich $Si_{0.75}C_{0.25}$precursor layer grown on a quartz substrate with subsequent annealing are shown in Figure 17. There is clear evidence for the formation of nano-crystalline Si at an annealing temperature greater than 1000°C. This is shown in the Raman peak at ~ 508 $cm^{-1}$ (red shifted from 520 $cm^{-1}$ due to a nanocrystalline folded Brillouin zone dispersion in k-space); TEM lattice fringe spacing consistent with {111} Si planes; and XRD peaks at $2\theta$ = 28.40 with peak broadening indicating nanocrystal of 3-7nm (estimated using the Scherrer equation). It should be noted that here the nanocrystal size determined by TEM is slightly smaller than that determined by XRD[10].

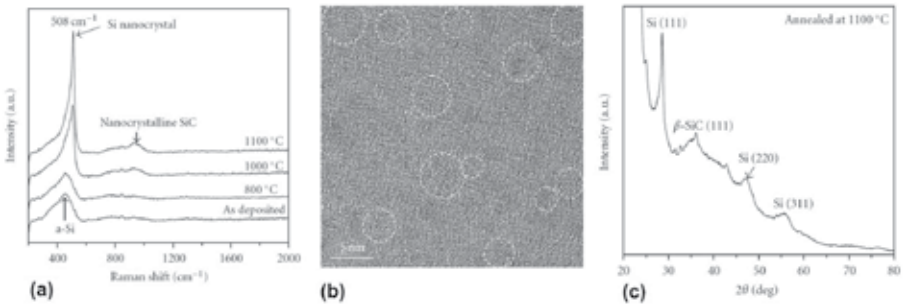


**Figure 17.** Silicon-rich SiC precursor layer: (a) Raman spectra for various annealing temperatures; Cross-sectional HRTEM image; and (c) X-ray diffraction[10].

Other Si and C concentrations were tried. As the concentration of C in $SiC_x$ is increased to the nearly stoichiometric $Si_{0.495}C_{0.505}$, Raman evidence for the stretching vibration modes of Si-C and C-C bonds can be easily identified. With increasing annealing temperature, which shows increasing intensities of both TO and LO bands, the formation of crystalline SiC during annealing is indicated. In addition, there is a dramatic decrease in the intensity of Si-Si vibration modes indicating the formation of far fewer Si nanocrystals. There is also evidence for free carbon at ~1400 $cm^{-1}$ in as deposited film, splitting into two bands at ~1360 (D band) and 1590 $cm^{-1}$ (G band) [16].

As before, a multilayer approach was used to fabricate Si QDs in carbide of uniform size. A multilayer with stoichiometric SiC and silicon-rich $Si_{1-x}C_x$ precursor layer was fabricated, as shown in Figure 17.a, and annealed at a high temperature to selectively precipitate Si nanocrystals in a carbide matrix. However, the lattice fringes in HRTEM image correspond to β-SiC {111} crystalline planes (Figure 17.b). One possible reason for SiC QDs, instead of Si QDs, is that the C/Si ratio in layered structure has an increase, compared to the original design.

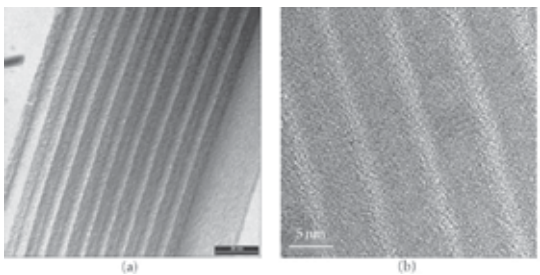


**Figure 18.** TEM images of SiC/Silicon-rich SiC multilayer a) deposited and b) annealed at 1100°C for 20 minutes [10].

The decay length $L_d$ is determined by the barrier height of the material in which the dot is embedded, which in the present case is either a silicon carbide, nitride, or oxide matrix [10]. In the simplest case, the decay length ($L_d$) is given by:

$$L_d = \frac{1}{\sqrt{2m^*(V_0 - E_n)}} \quad (2)$$

The latter expression holds when ΔE, the difference between the conduction band edge of the matrix and the confined energy level, is in eV.m* and $m_0$ are the effective mass and electron mass in the matrix material, respectively. $V_0$ is the corresponding band offset and $E_n$ is the confined energy level in a quantum dot. Without considering the confined energy of QDs, energy difference ΔE are 3.2 eV, 1.9 eV, and 0.5 eV for the conduction edge of bulk Si and $SiO_2$, $Si_3N_4$, and SiC, respectively. Electrons effective masses of $SiO_2$, $Si_3N_4$, and 3C–SiC are 0.86, 0.05–0.13 [19], and 0.24 ± 0.1, respectively. Following this line of argument, the results suggest that dots in an SiO2 matrix would have to be separated by no more than 1-2 nm of matrix for a reasonable overlap of the wave function and hence of conductivity, while they could be separated by more than 4nm of SiC [10].

### 3.2. Silicon nanowire solar cells

The semiconductor nanostructures are hence proposed to combine with the organic materials to provide not only a large interface area between organic and inorganic components for exciton dissociation but also fast electron transport in semiconductors. Therefore, many research groups combined organic materials with semiconductor nanostructures to overcome the drawbacks of the organic solar cells. Many inorganic nanowires had been experimented for this purpose, including CdTe, CdS, CdSe,ZnO, and TiO2 nanowires [20]. To overcome this Silicon nanowires (SiNWs) have attracted much attention for photovoltaic applications because of their unique optical and electrical properties [21] and have the potential to impact many different technologies either through improved material properties or by offering a new geometry not possible with bulk or thin film devices [22]. It is known that SiNW arrays demonstrate excellent antireflection (AR) properties due to their broadband optical absorption by multiple scattering incidents, and therefore can be used as solar cell absorbers for trapping light [21]. In practical applications, a bunch of SiNWs are more useful than a single SiNW. The usage of SiNW arrays can be categorized into two types. The first one is for anti-reflection purposes. SiNW arrays are used to replace the conventional anti-reflection coating layer. The second one is SiNW-array core-sheath p–n junction solar cells. In particular, the second type combines the advantages of the first type, that is, a large junction area, a high anti-reflection ability, and a high light-trapping effect [23].

SiNWs can be prepared by fabricated by various techniques, including chemical vapor deposition (CVD), physical vapor deposition (PVD), reactive ion etching (RIE) combined with lithography techniques [22], dry etching, laser ablation,and vapor–liquid–solid(VLS) [20]. Among these, the metal-assisted chemical etching (MACE) technique is more facile and more economical to fabricate SiNW arrays since it avoids high temperature or high vacuum [22].

Fabrication of nanowire based solar cells with nanowire arrays formed on the entire wafer by the wet etch process has obtained a very reasonably good energy conversion efficiency. However, with the formation of SiNW arrays by VLS process on the entire silicon wafer, the solar cell performance is very poor and has an energy conversion efficiency of only 0.1% [24] due to improper doping condition used.

The SiNW arrays have been demonstrated as an efficient antireflection film for silicon solar cell by proper growth of density and length of wires [24]. Fabrications of these wires on si substrate, nanowire length has linear behave by etching time. Zeng et al. confirmed this with their experiments.The SEM observation clearly revealed that the lengths of the produced SiNWs increased with the etching time, ranging from 340nm to 1700nm, which indicates that the length of the SiNWs can effectively be tailored by prolonging the etching time. Fig. 19(f) shows the SiNW length as a function of the etching time. An excellent linear behavior can be obtained.

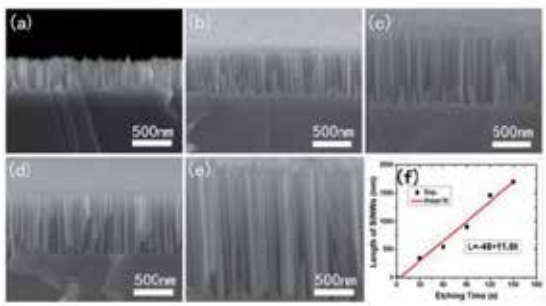


**Figure 19.** a-e) demonstrates the cross-sectional SEM micrographs of SiNW arrays with different length fabricated at 0.2 M H2O2 and room temperature for 30s, 60s, 90s, 120s, and 150s, respectively. (f) shows the SiNW length as a function of the etching time [21].

Also the thickness of SiNWs has impressive on solar cell spectrum absorption and the optimum length of nanowires for 350 to 620 nm. Huang et al. in 2009 was confirmed on that by combination of the SiNWs and P3HT:PCBM blend is an attractive route to obtain high $J_{sc}$ and efficiencies by improving the optical absorption, dissociation of excitons, and the electron transport.The P3HT:PCBM film exhibits little absorption beyond 650nm.The SiNWs/P3HT:PCBM film has improved light harvesting from 650 to 1100 nmbecause the cut off wavelength of Si is about 1100nm (Figure 20(Left)) [20].

Zeng et al. also shows that the as-grown SiNW arrays exhibit not only a large suppression of the reflectance over the entire light wavelength range, but also a very different reflection behavior from polished Si. The reflectance decreases with the wavelength increasing. As shown in figure 20(b), the reflectance is smaller than 18%, 9%, 5%, 2% and 1% at the nanowires length of 340nm, 542nm, 908nm, 1460nm and 1700nm, respectively. This can be attributed to the three important properties of SiNW arrays [21]:

1. The extremely high surface area of the SiNW arrays.
2. The suppression of the reflectance over a wide spectral bandwidth due to the subwavelength-structured (SWS) surface of the SiNW arrays.
3. A gradual change in the refractive index with depth due to a porosity gradient throughout the SiNW arrays which closely resembles a multi-antireflection layer coating.

It should also be mentioned that the interference peaks in the reflectance spectra of the SiNW arrays are related to the periodic nanostructure nature to some extent.

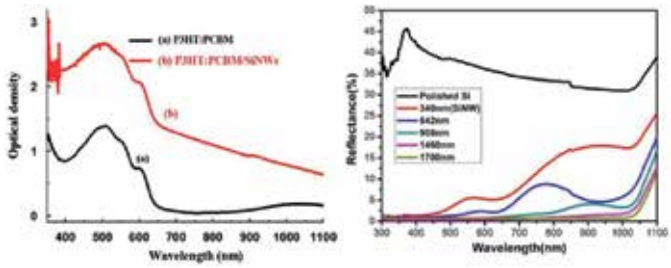


**Figure 20.** Left) UV–visible absorption of P3HT:PCBM blend on the ITO glass (a) with SiNWs and (b) without SiNWs. Right) Reflectance of SiNWs and polished wafer as a function of light wavelength, nanowires length of 340nm, 542nm, 908nm, 1460nm and 1700nm [20,21].

Also the SiNW arrays grown on the silicon substrate with SiH4:$N_2$ gases exhibit good optical characteristic of antireflection with same result as mentioned [24]. On the other hand, it is also expected that the long SiNWs willhave more light-trapping effect than the short SiNWs. The reflectance measurement does confirm this speculation because the reflectance decreases with the wire's length, as shown in Figure 20. However, this is not consistent with the devices' performance because the device with the shortest wire length has much better performance than the one with the longest length [23].

In addition, the reflectance decreases as the wire length increases. The reason can be easily explained by the enhanced light-trapping effect caused by the increasing wire length. However, this cannot explain the better performance of the device with a shorter wire length than that with a longer SiNWs [23].

Comparison of the photovoltaic performance for SiNW solar cells with SiNWs grown at different conditions. Figure21 show the device parameters, including the cell areas, and current density-to-voltage (J-V) curves under 1 sun AM 1.5 G illumination. The 0.37 μm-SiNW/PEDOT:PSS solar cell has the highest PCE of 8.40%, highest $J_{sc}$ of 24.24 mA/cm$^2$, and highest $V_{oc}$ of 0.532 V. When the SiNWs' length extends to 5.59 μm, PCE reduces from 8.40% to 3.76%, $J_{sc}$ decays from 24.24mA cm 2 to 13.06 mA cm$^2$, $V_{oc}$ decreases from 0.532 V to 0.435 V, and $R_s$ increases from 2.95 O cm$^2$ to 4.25 O cm$^2$. Only fill factor (FF) stays in the range between 63% and 67% [23].

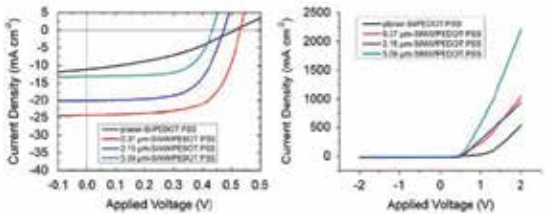


**Figure 21.** Current density-to-voltage curves of each SiNW devices and planar Si devices under the illuminance condition of 1 sun AM 1.5 G. (Left) Curves around fourth quarter. (Right) Curves in the range of -2 V to 2 V [23].

However, the I–V characteristic measurements of this SiNW-based photovoltaic cell still indicate a much lower short circuit current, leading to much lower energy conversion efficiency in comparison with planar or textured Si solar cell. The much lower short circuit current is attributed to the lower density of the nanowire grown by the current VLS process, which could not provide efficient light trapping and causes large series resistance in the SiNW network [24].

At least the current SiNWs based solar cells have a much better performance than the ones reported in the literature, there is still much room to improve the performance by growing denser arrays of nanowires, which provide enough light trapping and reduce series resistance, and by growing nanowires with less amount of metal catalysts or other catalysts that do not cause recombination centers [24].

## 4. Structural and superficial optimization

There are a number of structural optimization methods that can improve the efficiency besides process optimization which is discussed in previous section. Such as surface texturing, anti-reflection coating, defect passivating by forming gas, use of concentrator system, etc. In this section the last two methods will be discussed more.

### 4.1. Concentrator Photovoltaics

To moderate the price of multijunction solar cells and also to increase the efficiency, optical concentrator systems are proposed. The key elements of a photovoltaic concentrator are low-cost concentrating optics (a system of lenses or reflectors) to focus sunlight on a small area of solar cells, mounting, single or dual-axis tracking to improve performance of the system, and high-efficiency solar cells[14].

Theoretical maximum efficiencies of multi-junction solar cells without concentration and for concentration ratio of 500x have large difference. For example, the efficiency is 30.8% and 49.3% at one sun for one and three junction solar cell respectively, but it increases to 40.8% and 63.8% under concentration [14].

The first concentrator photovoltaic system was proposed in the mid 1970's by Sandia Labs. Despite the advantages of concentrating technologies, their application has been limited by the costs of focusing, tracking and cooling equipment. Optimization of a concentrator system is a complex problem: as all its components like solar cells, optics and tracking systems have to be specifically optimized, and all the interactions have to be regarded [14]. Natalya V. Yastrebova has reported several effective concentrator designs: Amonix is installing 250x concentrators using Fresnel lenses; Solar Systems, Spectrolab and Concentrating Technologies are installing reflective dishes; SunPower is designing a high-concentration, thin (flat-plate-like) concentrator; the Ioffe and Frauhofer Institutes are developing a 130x glass-Fresnel concentrator (Figure 22).

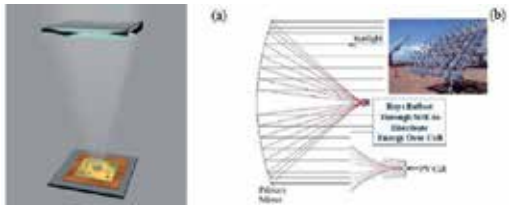

**Figure 22.** a) Concentrix concentrator using Fresnel lenses b) Spectrolab's reflective-optics concentrator module [14].

However, it should be taken into account that concentrators require direct sunlight and hence do not work with an overcast sky. Therefore, the concentrators are suitable for areas where cloud cover is low. The most appropriate time for operation is the middle of the day when the sunlight is strongest because at this time, the spectrum is least variable and hence spectral sensitivity is less significant [13].

### 4.2. Passivating the interfacial defects

One of the methods to enhance photoluminescence properties of nanostructured silicon based solar cells is passivating the non-radiative defects at the Si–barrier ($SiO_2$, $Si_3N_4$,…) interface by a forming gas (FG) post hydrogenation process performed on structures previously annealed in $N_2$ for different durations as proposed by Aliberti et al. A significant enhancement of the PL intensity has been observed for the samples with QD nominal size larger than 4nm, whereas a moderate enhancement is shown for the samples with QD size smaller than 4nm (Figure 23.a)[25].

Figure 23 b shows the PL spectra for two samples with a single layer of Si QDs in $SiO_2$ before and after FG hydrogenation. One sample has nominally 6 nm Si QDs and the other has 3.6 nm Si QDs. In addition to the intensity increase, which is more pronounced for the sample with larger QDs, no significant variation of the PL peak energy, or appreciable difference of the shape of the PL signal, can be observed in any of the samples [25].

The fact that the PL peak energy remains unmodified after the FG hydrogenation is an indication that, for sputtered single layer Si QDs in $SiO_2$, the PL cannot be attributed to defects. Therefore, the PL of these structures relies entirely on the quantum confinement effect of Si QDs[25].

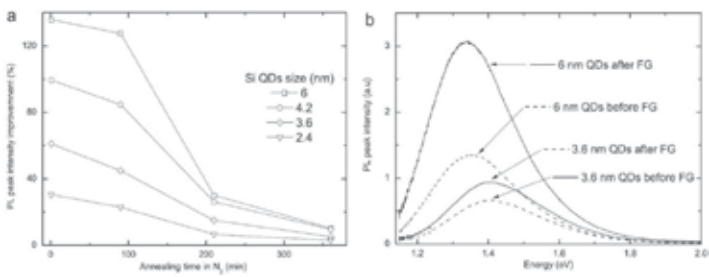


**Figure 23.** a) Relative improvement of the PL peak intensity for single layer Si QDs in SiO2 samples after FG post-hydrogenation versus annealing time in N2 (before FG) b) PL signal of two samples with different QDs nominal size (6 and 3.6 nm) before and after FG post-hydrogenation (samples have been annealed in $N_2$ at 1100°C for 5 min) [25].

## 5. Conclusions and outlook

Third generation nanostructured silicon based solar cells offer significantly lower cost per Watt by applying multiple energy levels with abundant and nontoxic material that also benefits from thin film processes.

Therefore, optimization of these high efficient solar cells is a demand which should be satisfied by detailed researches. Then, in this chapter, various optimization methods have been taken into account.

The first is optimization in silicon quantum dot solar cells. We conclude that the control over QD size is possible for layer thicknesses less than about 7nm, within which Si migration to nucleating sites is dominated by a 2D rather than a 3D diffusion regime. For this layer thickness, the optimum size for Si QDs is 2-3 nm.

Moreover, to ensure favorable electronic transport, the optimum spacing should be satisfied. We conclude that in lower spacing, the possibility of percolation is enhanced; then the prominent regime will be charge transfer which is called migration instead of electron tunneling. It should be paid attention that different matrices produce different transport barriers between the Si QDs and the matrices, because tunneling strongly depends on the height of barrier. So, $Si_3N_4$ and SiC allow larger spacing for a given tunneling current in comparison with $SiO_2$ because they give lower barriers.

Although the electron tunneling conductivity is higher in SiC compared to $Si_3N_4$ and $SiO_2$ due to the lower barrier height (0.5eV) of SiC; the formation of Si-QD in SiNx is preferable, because the formation of 3-7 nm Si-QD in Si-rich SiC film requires higher thermal budget (1100°C) than Si-QD formation in a-Si/SiNx layer structure that requires lower annealing temperature (800-850°C).

Also, we conclude that Si QD fabrication by various vacuum deposition techniques is preferable because of the greater potential of integration into conventional devices.

The second is optimization in silicon nanowire solar cell which explains that in some aspects, Si NW is preferable in comparison with Si QD. The most important feature of SiNW is its crystallinity invariance under introduction of impurity atoms during the growth. In other words, SiNW is well-defined doped nanocrystal during synthesis. Moreover, it demonstrates ultra-high surface area ratio, low reflection, absorption of wideband light and tunable bandgap.

In addition, the absorption in Si NW is more than solid Si film. And in order to optimize SiNW, wire diameter, surface conditions, crystal quality and crystallographic orientation along the wire axis should be investigated. In practice, radial p-n junction NW cells tend to favor high doping levels to produce high cell efficiencies (up to 11%). Therefore, solar cells based on arrays of Si wires are a promising approach to reducing the cost of solar cell production.

However, SiNW has some disadvantages. For example, the probe light used in the optical measurement cannot be focused solely onto the nanowire.

In addition to above mentioned process optimization, structural optimization is discussed briefly. As a result, concentrator systems and forming gas can ensure the high efficiency nanostructured Silicon based solar cells.

This chapter brings an overview about various optimization methods which can be done over third generation nanostructured silicon based solar cells, however, there is a long way to achieve optimum values experimentally. So, more experimental researches in this area are required.

## Acknowledgements

The authors want to thank INI (Iran Nanotechnology Initiative) Council and Student Scientific Association of University of Tabriz for their support. And, also they are very grateful to Dr. Rostami, Dr. Rasouli and Dr. Baghban who help them to do research in this field of photovoltaics.

## Author details

Foozieh Sohrabi[1*], Arash Nikniazi[2] and Hossein Movla[2]

*Address all correspondence to: F.sohrabi90@ms.tabrizu.ac.ir

1 School of engineering emerging technologies, University of Tabriz, Tabriz, Iran

2 Faculty of Physics, University of Tabriz, Tabriz, Iran

## References

[1] Park, S, Cho, E, Song, D, Conibeer, G, & Green, M. A. (2009 ). Cells n -Type silicon quantum dots and p-type crystalline silicon heteroface solar cells. *Solar Energy Materials & Solar*, 93684-690.

[2] Conibeer, G. (2007). Third-generation photovoltaics. *Material Today*, 10(11), 44-50.

[3] Löper, P, Hiller, D, Janz, S, Hermle, M, Glunz, S.W., & Zacharias, M. (2011). 23rd Workshop on Quantum Solar Energy Conversion. 20-26 March 2011, Bad Hofgastein, Austria.

[4] Panchal, A.K., & Solanki, C.S. (2011). Fabrication of silicon quantum dots in $SiN_x$ multilayer using hot-wire CVD. *Journal of Crystal Growth*, 3112659-2663.

[5] Gourbilleau, F., Dufour, C., Rezgui, B., & Brémond, G. (2009). Materials Science and Engineering B. 15970-73.

[6] Shen, W. Z. (2011). Silicon Quantum Dots: Photoluminescence Controlling and Solar Cell Application. *Seventh International Conference on Thin Film Physics and Applications*.

[7] Munteanu, D, & Autran, J. L. (2011). Modeling of energy bands in ultra-thin layer quantum nanostructures for solar cell applications. *Journal of Non-Crystalline Solids*, 357, 1884-1887.

[8] Xu, C., Li, Z. P., Pan, W., & Shen, W. Z. (2011). Tuning photoresponse through size distribution control of silicon quantum dots. *Applied Surface Science*, 2578409-8412.

[9] Jiang, C, & Green, M. A. (2006). Silicon quantum dot superlattices: modeling of energy bands, densities of states, and mobilities for silicon tandem solar cell application. *Journal of applied physics*, 99114902.

[10] Cho, E., Green, M. A., Conibeer, G., Song, D., Cho, Y., Scardera, G., Huang, S., Park, S., Hao, X. J., Huang, Y., & Dao, L. V. (2007). Silicon Quantum Dots in a Dielectric Matrix for All-Silicon Tandem Solar Cells. *Advances in OptoElectronics*.

[11] Lan, H., & Ding, Y. (2012). Ordering, positioning and uniformity of quantum dot arrays. *Nano Today*, 7, 94-123.

[12] Di, D, Perez-Wurfl, I, Conibeer, G, & Green, M. A. (2010). Formation and photoluminescence of Si quantum dots in $SiO_2/Si_3N_4$ hybrid matrix for all-Si tandem solar cells. *Solar Energy Materials & Solar Cells*, 94, 2238-2243.

[13] Conibeer, G., Green, M., Corkish, R., Cho, Y., Cho, E., Jiang, C., Fangsuwannarak, T., Pink, E., Huang, Y., Puzzer, T., Trupke, T., Richards, B., Shalav, A., & Lin, K. (2006). Silicon nanostructures for third generation photovoltaic solar cells. *Thin Solid Films*, 511-512, 654-662.

[14] Yastrebova, N. V. (2007). High-efficiency multi-junction solar cells: Current status and future potential. *Centre for Research in Photonics*.

[15] Nychyporuk, T., & Lemiti, M. (2011). Silicon-Based Third Generation Photovoltaics. In: Kosyachenko L.A. (ed.), *Solar Cells- Silicon Wafer-Based Technologies*, Rijeka: Intech, 139-176, Available from, http://www.intechopen.com/books/solar-cells-silicon-wafer-based-technologies, accessed 2 November 2011.

[16] Green, M. A., & Conibeer, G. (2007). Nanostructured Silicon-Based Tandem Solar Cells. *PhD thesis. University of New South Wales, Sydney, Australia*.

[17] Konig, D., Rudd, J., Green, M. A., & Conibeer, G. (2009). Impact of interface on the effective band gap of Si quantum dots. *Solar Energy Materials & Solar Cells*, 93, 753-758.

[18] Pavesi, L., & Turan, R. (2010). Silicon Nanocrystals: Fundamentals, Synthesis and Applications. *Rijeka:WILEY-VCH Verlag GmbH & Co.*

[19] Goodey, A. P., Eichfeld, S. M., Lew, K., Redwing, J. M., & Mallouk, T. E. (2007). Silicon Nanowire Array Photoelectrochemical Cells. *Journal of American Chemical Society*, 12912344-12345.

[20] Huang, J., Hsiao, C., Syu, S., Chao, J., & Lin, C. (2009). Well-aligned single-crystalline silicon nanowire hybrid solar cells on glass. *Solar Energy Materials & Solar Cells*, 93, 621-624.

[21] Zeng, L., Yu, X., Han, Y., & Yang, D. (2011). Performance of silicon nanowire solar cells with a phosphorus diffused emitter. *PhD thesis. Zhejiang University, Hangzhou, China*.

[22] Garnett, E. C., & Yang, P. (2008). Silicon Nanowire Radial p-n Junction Solar Cells. *Journal of American Chemical Society*, 130, 9224-9225.

[23] Syu, H., Shiu, S., & Lin, C. (2012). Silicon nanowire/organic hybrid solar cell with efficiency of 8.40%. *Solar Energy Materials & Solar Cells*, 98, 267-272.

[24] Kuo, C. Y., Gau, C., & Dai, B. T. (2011). Photovoltaic characteristics of silicon nanowire arrays synthesized by vapor-liquid-solid process. *Solar Energy Materials & Solar Cells*, 95, 154-157.

[25] Aliberti, P., Shrestha, S. K., Li, R., Green, M. A., & Conibeer, G. J. (2011). Single layer of silicon quantum dots in silicon oxide matrix: Investigation of forming gas hydrogenation on photoluminescence properties and study of the composition of silicon rich oxide layers. *Journal of Crystal Growth*, 32784-88.

Chapter 2

# Silicon Solar Cells with Nanoporous Silicon Layer

Tayyar Dzhafarov

Additional information is available at the end of the chapter

http://dx.doi.org/10.5772/51593

## 1. Introduction

Today's photovoltaic solar panels are widely used to supply the power and buildings. The account of total solar cell product in 2010 was about 20 GW. Over 95% of all solar cells produced world wide are composed of the silicon (single crystal, polycrystalline, amorphous, ribbon etc.) and domination of silicon-based solar cell market probably will be do so in the immediate future. The main reason for dominant role of silicon solar cells in word market is high quality silicon that produced in large quantities for microelectronic industry. Additionally silicon solar cell processing does not burden the environment.

The main requirements for ideal solar cell material are (a) direct band structure, (b) band gap between 1.1 and 1.7 eV, (c) consisting of readily available and non-toxic materials, (d) good photovoltaic conversion efficiency, (e) long-term stability [1]. Silicon is the second most abundant element in the earth's crust (35 %) after oxygen. It is the base material for photovoltaic conversion of solar spectrum radiation ranging from ultraviolet to the near infrared, however it can absorb the small portion of solar radiation, i.e. can convert photons with energy of the silicon band gap. The theoretical curve for conversion efficiency of solar cell materials versus band gap for single junction cell (Figure 1) shows that silicon (1.1 eV) is not at the maximum of the curve (about 1.4-1.5 eV) but relatively close to it [2]. The efficiency for ideal silicon solar cell can reach about 30% (for AM1.5 at 300K).

Photoelectron properties related with indirect band structure and high reflectance of crystalline silicon (about of 30-35%) are still a challenger for creation solar cells with high conversion efficiency. High refractive index of crystalline silicon (about 3.5) in solar spectrum

region of 300-1100 nm creates large optical losses which can be reduced by using antireflection coating (ARC). Although highly efficient double and triple antireflection coatings are available, most manufactured crystalline silicon solar cells employ simple and inexpensive single-layer ARC with relatively poor antireflection properties.

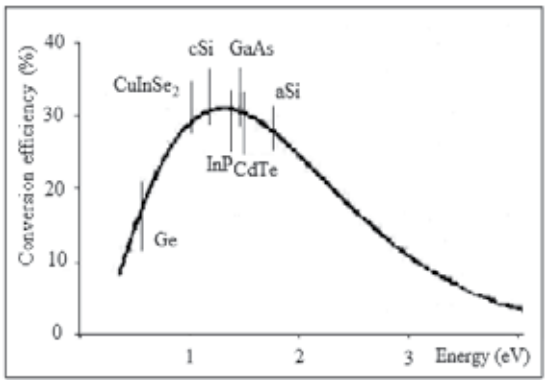


**Figure 1.** Conversion efficiency depending on semiconductor band gap (AM1.5, 300K).

The first observation of a visible photoluminescence at room temperature in nanostructured porous silicon opened the possibilities of wide range photonic and biologic applications due to tunable refractive index, large surface/volume ratio an biocompatibility of porous silicon [3]. Today the porous silicon is quickly becoming very import and versatile material for solar cell technology.

The crystalline structure, chemical, electrical, photoluminescence and optical properties of porous silicon have been extensively studied by various experimental techniques [4]. Porous silicon can be formed by chemical etching, electrochemical etching and photo-electrochemical etching of silicon in HF-based solutions at room temperature. Therefore the chemical technology can be more adapted to industrial fabrication of solar cells due to its simplicity and lower cost. Porosity, thickness, refractive index of layer, pore size etc. depend on formation parameters (electrolytes contents, current density, temperature, crystal orientation, doping type and concentration, time etching etc.). Sizes of pore and pores walls can be varied from 5-10 nm to hundreds micrometers dependent on fabrication parameters. Possibilities of minimization of reflectance (due to light trapping in pores), increase of band gap of porous silicon layer (due to quantum confinement of charges in the PS microcrystallites) by changing of porosity allow to use PS layer as both ARC and wide-band gap photosensitive layer. Last years the porous silicon layers are widely used in silicon solar cell applications.

This chapter has focused on review of investigations concerning using of porous silicon layers in silicon solar cells and also characterization of structure and properties of porous layers.

http://dx.doi.org/10.5772/51593

## 2. Photovoltaic characteristics of solar cells

For the solar cell with the series resistance $R_s$ and shunt (or parallel) resistance $R_{sh}$ current-voltage characteristic is determined as [5]

$$I = I_0\left\{\exp\frac{qV - IR_s}{AkT} - 1\right\} + \frac{V - IR_s}{R_{sh}} - I_l \tag{1}$$

Here $I_o$ is the reverse saturation current, $A$ is diode ideality factor, $q$ is elementary charge, $k$ is Boltzmann's constant, $T$ is absolute temperature, $I_l$ is photo-generated current. Figure 2 shows the representation of the dark and the illuminated characteristics of the *p-n* junction.

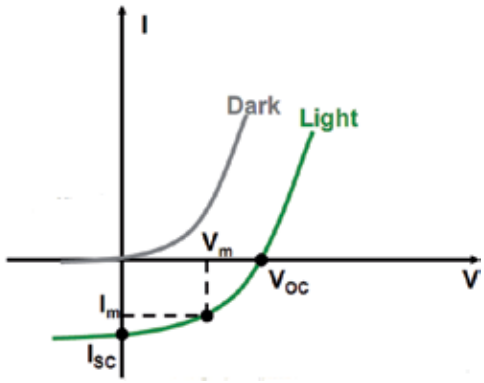


**Figure 2.** The dark and light current-voltage characteristics of the *p-n* junction.

The reverse saturation current is given

$$I_0 = \frac{qD_n n_i^2}{L_n N_A} + \frac{qD_p n_i^2}{L_p N_D} \tag{2}$$

Here $L_n$ and $L_p$ are diffusion length, $D_n$ and $D_p$ are diffusion coefficient of minority carriers (electrons and holes, respectively), $n_i$ is intrinsic carrier concentration, $N_A$ and $N_d$ are concentration of acceptor and donor impurities, respectively.

When the solar cell is operated at open circuit ($I$=0, i.e. the shunt resistance is high) then the open-circuit voltage is give

$$V_{OC} = \frac{AkT}{q}\ln\left(\frac{I_l}{I_0} + 1\right) \approx \frac{AkT}{q}\ln\frac{I_l}{I_0} \tag{3}$$

Very low values of $R_{sh}$ produces a significant reduction of $V_{oc}$. An increase in reverse saturation current $I_o$ produces a reduction in $V_{oc}$. The reverse saturation current is determined by

the leakage current of carriers across the *p-n* junction under reverse bias. The leakage current is a result of recombination of carriers on either side of the junction. For the solar cell working at short circuit ($V$=0, i.e. low $R_s$ and $I_o$, and high $R_{sh}$) the short-circuit current is equal to photocurrent $I_{sc} \approx I_l$.

The series resistance of cell depends on concentration of carriers in *n*- and *p*-region, depth of *p-n* junction, resistance and construction of frontal and back ohmic contacts. Increase of series resistance produces a significant reduction in $I_{sc}$.

The conversion efficiency of the solar cell is defined as the percentage of incident of solar power, which the can convert in electrical power

$$\eta = \frac{P_m}{E_l S} \tag{4}$$

Here $P_m = I_m V_m$ (in Watt) is maximum electrical power, $I_m$ and $V_m$ values of current and voltage corresponding the maximum output power (Fig. 2), $E_l$ (in W/m$^2$) is light irradiance and $S$ is the surface area of the solar cell.

The fill factor (FF) defines the portion of electrical power produced in solar cell in load. The fill factor is the ratio of the maximum electrical power divided by the open-circuit voltage and the short-circuit current

$$FF = \frac{P_m}{I_{sc} V_{oc}} = \frac{I_m V_m}{I_{sc} V_{oc}} \tag{5}$$

Substituting $P_m$ from Eq.(4) in Eq. (5) gives for the efficiency

$$\eta = \frac{V_{oc} I_{sc}}{E_l S} FF \tag{6}$$

The series and shunt resistance of solar cell influence on the fill factor. Increase of shunt resistance and decrease of series resistance result in to higher fill factor and thereby to larger efficiency.

For crystalline silicon solar cells efficiency about 25% in laboratory and 14% commercially is reached. A theoretical limit of efficiency of crystalline solar cell is about 30%. Comparison efficiency of industrially produced silicon solar cells with theoretical efficiency shows that about 85% power losses occur in commercially cells.

The present efficiency and cost of the silicon solar cell in comparison with conventional energy sources limit the wider using of silicon cells. To improve the performance of solar cells, the power losses must be reduced. The maximum absorption (i.e. minimum reflectance), minimum recombination and series resistance are most conditions for reaching a high efficiency solar cell. The reduction of different energy losses in crystalline silicon solar cells is the most problem of improvement of the conversion efficiency and thereby of reduction of cost.

http://dx.doi.org/10.5772/51593

## 3. Losses in solar cells

The losses in silicon solar cells can be related with: (a) recombination losses, (b) series resistance losses, (c) thermal losses, (d) metal/semiconductor contact losses,(e) reflection losses [6].

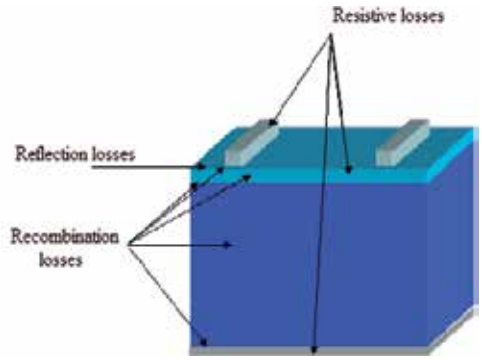


**Figure 3.** Schematic representation of energy losses in solar cell.

*(a) Recombination losses* can be caused as result of surface and bulk recombination, recombination in depletion region and recombination at metal/semiconductor contact (Figure 3). Recombination losses mainly influence on the open-circuit voltage.

The incomplete chemical bonds presenting on the surface of semiconductor play role of traps for photo-excited carriers and therefore recombination on traps can result in reduction on photocurrent. The surface recombination velocity $S$ is expressed as

$$S = \sigma v N_t \tag{7}$$

Where $\sigma$ and $v$ are capture cross section for carriers and thermal velocity of carriers, respectively, $N_t$ is the number of surface traps. The decrease of surface recombination velocity is usually reached by deposition of thin passivation films on top surface of cell (for example $SiO_2$ or $Si_3N_4$ films) by chemical vapor deposition (CVD), plasma enhance chemical vapor deposition (PECVD) or thermal oxidation technique). The standard technique for the reduction of the surface state density of Si is thermal oxidation at 800°C for 15 min in dry oxygen [7]. Passivation of silicon surface results in significant reduction of surface recombination velocity (from $8x10^4$ to $1.6x10^2$ cm/s).

Impurities and crystalline defects, presenting in bulk region of semiconductor can play role of traps for carriers. Reduction of concentration of rest impurities in bulk of semiconductor, according to Schockey and Read model, will decrease the trap-assisted recombination velocity. Using the bulk semiconductor material having lower concentration impurities and defects can increase the diffusion length of minority carriers and thereby can decrease the recombination losses in bulk of solar cells.

*(b) Series resistance* of a solar cell consists of several components, such as top grid and busbar resistance, emitter resistance; semiconductor bulk resistance and metal/semiconductor

contact resistance (see Figure 3). The series resistance controlled by the top contact design and emitter resistance must be carefully designed for each type of solar cell in order to optimize efficiency of solar cell. The semiconductor bulk resistance is low (about $10^{-3}$ Ω) due to its high conductivity. High values of series resistance will produce a significant reduction in short-circuit current. Losses caused by series resistance are given by $P = V_{Rs}I = I^2R_s$ and increase quadratic with photocurrent and therefore they most important at high illumination intensities. Very low values of shunt resistance $R_{sh}$ will produce a significant reduction in open-circuit voltage. A low shunt resistance is a processing defect rather than a design parameter. Both series and shunt resistance losses decrease the fill factor and efficiency of a solar cell.

The characteristic equation for solar cell described by Eq. (3) shows that an increase in reverse saturation current $I_o$ produces a reduction in open-circuit voltage. Increase of reverse saturation current means rising of leakage of carriers across the *p-n* junction under reverse bias due to recombination of carriers in depletion regions on either side of junctions. Recombination proceeding in the depletion regions is less significant as compared to the surface recombination due to the electrical field of *p-n* junction that separates the photo-generated electrons and holes.

Reduction of emitter layer resistance is reached by optimization of the doping concentration of layer and the *p-n* junction depth. For ($n^+$-*p*) silicon solar cell the optimal values of junction thickness and doping concentration about of $d_{pn} \approx 0.8$ μm and $n^+ \approx 2x10^{19}$ $cm^{-3}$ respectively.

*(c) Thermal losses* consist of a significant portion of losses in photovoltaic solar cells. The excess energy formed at absorption of the solar photons that is larger than the band gap energy of semiconductor is realized in the form heat. The temperature rise of solar cell results in increase in the reverse saturation current $I_o$ due to an increase concentration of the intrinsic carriers $n_i$ and diffusion length of minority carriers (Eq. (2)). The increase in reverse saturation current reduces the open-circuit voltage (Eq. (3)). Increase in $I_o$ means the rising the "leakage" of carriers across the *p-n* junction under reverse bias due to recombination of carriers in the neutral regions on neither side of the junction.

*(d) Metal/semiconductor contacts* placed on the frontal and back surfaces of solar cell cause considerable losses. The screen-printed technique is often used for deposition metallic contacts to silicon solar cells[8]. The frontal contact has form of fine grid lines and the back contact is a metal plate covering entire back surface of cell. Ag and Ag-Al pastes are used in conventional silicon solar cells by deposition of frontal and back ohmic contacts by screen-printed technique. Reduction of resistance of metal/semiconductor contacts is one of major means decrease of power losses for cells. Presence of acceptor type impurity (Al) in back contact (Ag-Al) results in decrease the resistance of near-back contact region of *p*-type silicon substrate due to diffusion penetration of aluminum during thermal treatment. Moreover, the heavy doping forms the near-surface electric field that reduces the recombination losses at metal/semiconductor contact.

*(e) Reflection losses*. A large portion of energy losses during solar cell operation could be attributed to optical losses caused by large value of reflectance (about 35%) in the spectral

http://dx.doi.org/10.5772/51593

range where silicon is photosensitive [9]. Traditional techniques of texturing and antireflection coating (ARC) have been applied widely to decrease the reflectance of silicon surface. This technology is most used in industrial production of silicon solar cells [10]. The texturisation adds micrometer-scale tilted pyramid structure to the silicon surface, which reduces reflection of the incident light (Figure 4) [11].

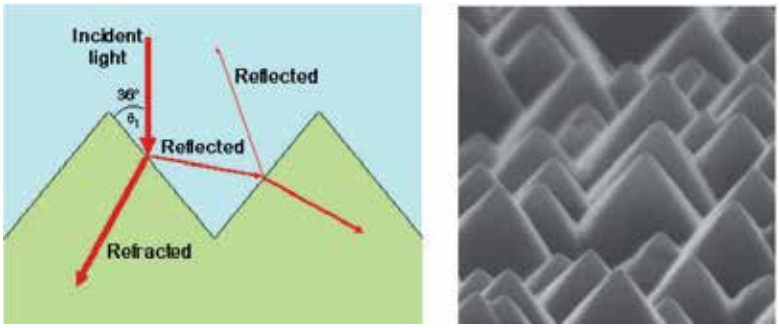


**Figure 4.** The schematic representation of multiple light reflection (on left) and optical microscopy image of textured silicon surface (on right).

Pyramids are usually formed by etching the surface with acid ($H_2SO_4$, $HNO_3$:$H_2O$ etc.) or with alkaline etch (NaOH, KOH etc.). The light bouncing from pyramid to pyramid increases the optical path and increases absorption of visible light in silicon, thus increasing the efficiency of solar cell. Antireflection coating presents thin film of a transparency material with refractive index ($n$) between those of air ($n_o$=1) and silicon ($n_{Si}$ = 3.84). ARC reduces the Fresnel reflection caused from light penetration from a medium of one refractive index to another (for example air/semiconductor).

The optimization of parameters (the refractive index and thickness) of ARC was based on the stratified medium theory and Bruggeman effective medium approximation [12]. The zero-reflection for normal incidence of light on ARC/Si system is given [13]

$$n_{arc} = (n_o n_{Si})^{1/2} \tag{8}$$

Here $n_{arc,}$ $n_o$and $n_{Si}$are the refractive indexes of antireflection coating, the ambient media (air) and silicon, respectively.

The optimal single-layer ARC (SLARC) thickness ($d_{arc}$) for minimum reflection for wavelength $\lambda$ is given [14]

$$d_{arc} = \lambda / 4n_{arc} \tag{9}$$

If conditions (8) and (9) for air/SLARC/Si system are to be satisfied ($n_o$ = 1, $n_{Si}$ = 3.84), then the optimal values of refractive index and thickness (a quarter of wavelength) of SLARC must be (for $\lambda$=650 nm) $n_{arc}$= 1.96 and $d_{arc}$=80 nm. For glass/SLARC/Si system (where a glass is protecting layer) optimal values for $n_{arc}$ = 1.55 and $d_{arc}$= 65 nm.

For double-layer antireflection coating (DLARC) with refractive index of top and bottom layers $n_1$ and $n_2$, respectively, on silicon (air/ARC(top)/ARC(bottom)/Si system) the zero-reflectance at normal incident light is realized at conditions [15]

$$n_1 = (n_o n_2)^{1/2} \quad \text{and} \quad n_2 = (n_1 n_{Si})^{1/2} \tag{10}$$

Here $n_1$ and $n_2$ are refractive index of top layer 1 and bottom layer 2, respectively. For air/layer 1/layer 2/Si system, the ideal values for top layer are $n_1$= 1.57 and $d_1$ = 102 nm, whereas the bottom layer parameters are $n_2$ = 2.46 and $d_2$ = 65 nm.

Different types of SLARC ($SiO_2$, ZnS, $Al_2O_3$, $Ta_2O_3$), DLARC ($MgF_2$/ZnS, $SiO_2/TiO_2$, $MgF_2/TiO_2$, $MgF_2/CeO_2$, $SiO_2$/SiH etc.) and multilayer ARCs are used for reduction for reflectance of silicon solar cells. Optimal values refractive index and thickness for single-layer ARCs on silicon surface (air/ARC/Si system, for $\lambda$ = 650 nm) are presented in Table 1.

| ARCs | $n_{arc}$ | $d_{arc}$ (nm) |
|---|---|---|
| $SiO_2$ | 1.4 | 116 |
| $Si_3N_4$ | 2 | 81 |
| ZnS | 2.25 | 72 |
| ZnO | 2 | 81 |
| $MgF_2$ | 1.4 | 116 |
| $TiO_2$ | 2.5 | 65 |
| $SnO_2$ | 1.9 | 86 |
| $SiN_x$:H | 1.9-2.4 | 68-86 |
| Por.Si | (1.2-2.2)* | 74-135 |

* For porosity from 52% to 80%

**Table 1.** Optimal values of refractive index and thickness of the single-layer ARCs on silicon.

As stated above ARCs are generally fabricated by chemical vapor deposition, plasma-enhanced chemical deposition, thermal oxidation processes. They are carried out at high temperatures resulting in an increase in the cost of solar cells [16]. Traditional antireflection coating and surface texturing may reduce reflection efficiently (up to 10-15%) at low wavelength in the visible spectrum (about 400-800 nm), but they are less efficient at harvesting light in the near infrared spectrum (more than 800 nm). The significant of portion of solar radiation, penetrating through the atmosphere, lies at wavelength greater than 800 nm, therefore solar cells with traditional ARC and surface textures leave a huge amount of potential energy out of the using.

Use the single layer ARCs is most simple, low cost and suitable for silicon solar cell technology as compared to expensive and impractical double- or multilayer ARCs. A single layer ARC allows a reduction of reflectance (up to 11%) only in a narrow wavelength range of so-

http://dx.doi.org/10.5772/51593

lar spectrum. A single-layer coating cannot reduce the reflection in a wide wavelength because of neighboring interference maxima. A wider spectral range may be obtained either by increasing the number of layers or by using an inhomogeneous layer with gradient of refractive index. Usage of such inhomogeneous layer allows to suppress the interference maxima narrowing the spectral range. Using the ARC with monotonous changeof the refractive index on the depth can raise the performance of silicon solar cells. ARCs with a graded refractive index constituted from silicon and titanium oxides mixtures were studied in [17]. 3.7% average reflectance between wavelength from 300 to 1100 nm and 48% improvement of the photocurrent was reached on using silicon and titanium oxides mixtures as graded ARC on silicon. It is believed that the porous silicon with tunable refractive index can be adapted production of silicon solar cells due to the simple and cheap technology.

## 4. Fabrication and Properties of Porous Silicon

Porous silicon layer on monocrystalline Si substrate and its manufacture by the technique of electrochemical etching of silicon substrate in HF solution or by chemical etching in HF-$HNO_3$ mixture are known as early as from 1956 [3,18]. Electrochemical etching of silicon is attractive because of the possibility to tune the pore size from a few nanometers to a few tens of micrometers, just by choosing wafer doping level and etching conditions. Moreover, a wide range of porous layer thickness, porosities, surface areas and morphologies can be formed depending on the etching conditions. The bulk silicon was shown modifies during the etching to sponge-like structure with silicon columns and hydrogen covered pores.

The simplest electrochemical cell is shown in Figure 5. The Si wafer acts as the anode and the platinum is the cathode. The thickness of porous silicon layer on Si substrate is determined by duration of etching. The porosity, i.e. the void fraction in the porous layer is determined by the current density (about 10 - 100 mA/cm$^2$), composition electrolyte, resistance and the doping density of Si substrate.

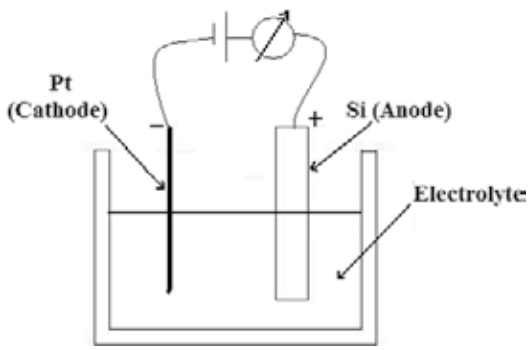


**Figure 5.** Cross-sectional view of lateral anodization cell.

The anodic reaction on the Si substrate can be written during pore formation as [19]

$$Si + 6HF \rightarrow H_2SiF_6 + H_2 + 2H^+ + 2e^- \quad (11)$$

Silicon atoms are dissolved as $SiF_6^{2-}$ require the presence of $F^-$ ions (from HF solution) and positively charges holes (from the silicon wafer) at the silicon interface. Concentration of holes in *p*-Si is sufficiently high (about $10^{14}$ - $10^{18}$ $cm^{-3}$) and this case the nano-size pores were formed. Concentration of holes in *n*-Si is very small (about $10^2$-$10^6$ $cm^{-3}$) and therefore generation of holes is possible due to illumination of *n*-Si substrate.

The porous silicon layers are often prepared in composition of $HF:H_2O$, $HF:C_2H_5OH$, $HF:C_2H_5OH:H_2O$, $HF:HNO_3$, $HF:HNO_3:H_2O$. Fabrication of porous silicon layers on *n*-type silicon substrates is usually produced under illumination. Before the etching process the silicon substrate are dipped in $HF:H_2O$ (1:50) solution for remove the native oxide film on silicon surface.

The structure and size of pores in porous silicon layer formed on *n*-Si substrate differ from those for layer on *p*-Si. If electrochemical etching was carried out at relatively low current density (10-80 $mA/cm^2$), then the local dissolution of silicon surface takes place. Herewith, pore formation begins on surface defects of Si and further growth of pores into silicon substrate proceeds due to the holes diffusion to Si-electrolyte interface. In the case of large current density (0.5 - 0.8 $A/cm^2$) when the amount of holes moving to Si-electrolyte interface is very high, the etching of top regions of Si substrate is preferred. It ensures the uniform etching of silicon surface and formation a smooth surface of substrate (the so-called the electro-polishing process). The raising the current density above the critical value at the end of anodization process results in a detachment of the porous silicon film from Si substrates. The behavior at high current densities turns out to be useful to produce porous silicon free-standing layers. The anodic reaction during the electro-polishing can be written as

$$Si + 6HF \rightarrow H_2SiF_6 + 4H^+ + 4e^- \quad (12)$$

Pores, depending on the diameter, denoted as micropores ($R < 2$ nm), mesopores ($2\ nm < R < 50$ nm) and macropores ($R > 50$ nm). Under illumination the pore size dependent on doping density and anodization conditions, with diameters in the range 100 nm - 20 μm (macropores).

The average porosity (*P*), i.e. the avoid fraction in the porous layer, can be obtained by gravimetric using the equation

$$P = \left\{ \frac{m_1 - m_2}{m_1 - m_3} \right\} 100(\%) \quad (13)$$

Here $m_1$ is Si sample mass before the anodization etching, $m_2$ just after etching and $m_3$ after the removal of the porous layer by electro-polishing or after a rapid dissolution of the whole porous layer in a 3% KOH solution. Guessing the porous silicon mass $m_{PS}$, the average porosity can be also determined by using the equation

http://dx.doi.org/10.5772/51593

$$P = \frac{1 - m_{PS}}{\rho s d} = \frac{m_1 - m_{ps}}{m_1} \tag{14}$$

One can also get the porous silicon layer thickness $d$ using the equation

$$d = \frac{m_1 - m_3}{\rho S} \tag{15}$$

Here $\rho$ is the Si density (2.33 g/cm$^3$) and $S$ is the etched surface.

The inhomogeneity in porosity and thickness of porous of the porous layers is often observed on fabrication with electrochemical anodization cell. They are most probably due to the bubbles that form and stick on silicon surface. The inhomogeneity in porous and thickness must be removed and the concentration of the HF has to be locally constant on the surface of the silicon substrate. Removal of the bubbles on the surface of the silicon and thereby preparation of homogeneous porous silicon layers is realized with using a stirrer. The distance between the silicon wafer and the platinum cathode also influences on the homogeneity, whereas the shape of platinum cathode almost does not influence on homogeneity. There is a certain distance for given cell when the porous silicon layers are homogeneous.

The thickness of the porous silicon layers mainly depends on duration of anodization process, whereas the porosity depends on the current density. It is be noted that the character of the thickness-etching time and porosity-current density relations depend on orientation, type and concentration level in silicon and conditions anodization process ( the electrolyte composition, distance between silicon wafer and platinum electrode, illumination etc.).

The thickness-etching time dependence for porous silicon layer fabricated on *p*-type (100) silicon substrates in 3HF:1$C_2H_5OH$ solution at current density 20 mA/cm$^2$ is given in Figure 6 [20]. It is seen that the average growth kinetics of porous silicon layer is about 14 nm/s.

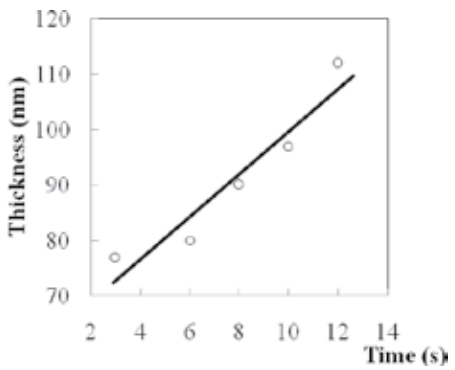


**Figure 6.** Thickness vs. etching time for porous silicon growth at constant current density of 20 mA/cm$^2$.

The porosity of the porous silicon layer almost linearly increases with the current density once the other etching parameters are kept fixed (Figure 7).

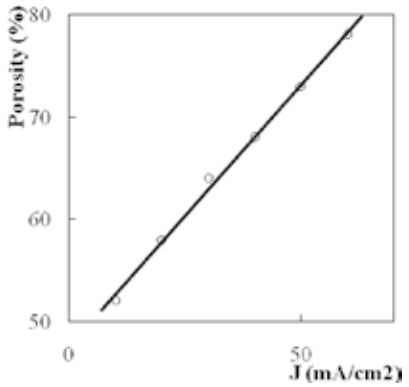


**Figure 7.** The porosity as a function of current density.

Porous silicon is a particular form of crystalline silicon. The crystalline structure of porous silicon presents a network of silicon in nano (micro)-sized regions surrounded by void space with a very large surface-to-volume ration (up to $10^3$ $m^2/cm^3$) [13]. The structure of porous silicon is like a sponge or columnar where quantum confinement effects play fundamental role [4]. The pore surfaces are covered by silicon hydrides (Si-H) and silicon oxides (Si-O).

Figure 8 shows Fourier transform infrared (FTIR) spectrum of free-standing PS film of thickness of 12 μm measured at room temperature [21]. The peaks related with absorption on vibration of Si-H (2100 $cm^{-1}$) and Si-O bonds (1100 $cm^{-1}$) located on pore surfaces were observed from Figure 8. These bonds play an important role in regulating optical, electrical and gas sensing properties of porous silicon.

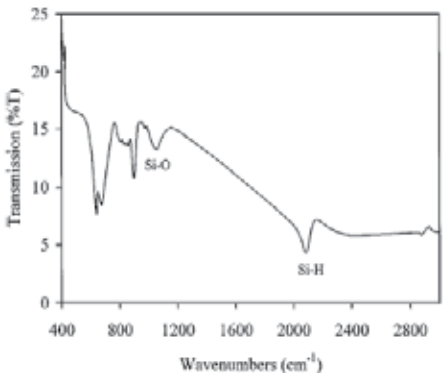


**Figure 8.** FTIR spectrum of porous silicon film (300 K).

The effect of isothermal annealing of free-standing PS films on changes of intensity of absorption coefficient of Si-H (2100 $cm^{-1}$) and Si-O (1100 $cm^{-1}$) peaks is used for estimation of diffusion coefficient [22]. Results of these measurements showed that in the range of 65-185°C the temperature dependence of hydrogen and oxygen diffusion coefficient along the porous surfaces are described as

http://dx.doi.org/10.5772/51593

$$D(H) = 5x10^{-10} \exp(-0.37\ eV/kT) \quad (16)$$

$$D(O) = 1.3x10^{-8} \exp(-0.50\ eV/kT) \quad (17)$$

The activation energy for diffusion of hydrogen along the porous surfaces estimated from response (or recovery) $V_{oc}$ - $t$ curves for Au/PS/Si cells under humid ambient (90%RH) is 0.34 eV [23].

The thermal oxidation of free-standing PS films in the range from 400 to 900°C is accompanied the structural phase transition [24]. The crystalline nanostructured silicon partly converts into amorphous and polycrystalline silicon, if temperature is about 500°C. At higher temperatures three Si structures (crystalline, polycrystalline and amorphous) produce $SiO_2$ (combination of cristobolite and quartz) due to the oxygen diffusion and absorption in PS. An optimal oxygen-absorption temperature is about 700°C.

The characterization of the lattice deformation of porous silicon carried out by X-ray diffraction has been described in [25, 26]. Crystalline structure of porous silicon layers is equivalent to that of nearly perfect silicon. Porous silicon may be considered as an assembly of small silicon crystallites. These crystallites have two different dimensions, the bigger one being oriented perpendicular to the surface. Typical values seem to be about 1000 Å and 10-100Å. Lattice parameter of the porous silicon of 54% porosity prepared on $p^+$-Si (100) substrate was slightly bigger (the difference ($\Delta a$) is $2.3x10^{-3}$ Å) than that of intrinsic silicon ($a$= 5.4306 Å).

A linear increase in the lattice parameter expansion (the lattice mismatch parameter $\Delta a$ / $a$) for porous silicon going from 4 to $7x10^{-4}$ when the porosity increases from 34 to 72% has been measured [25]. The same behavior for lattice mismatch parameter ($\Delta a$ / $a$)$x10^4$ between porous silicon layer and $p^+$-type silicon substrate depending on porosity has been found in [27].

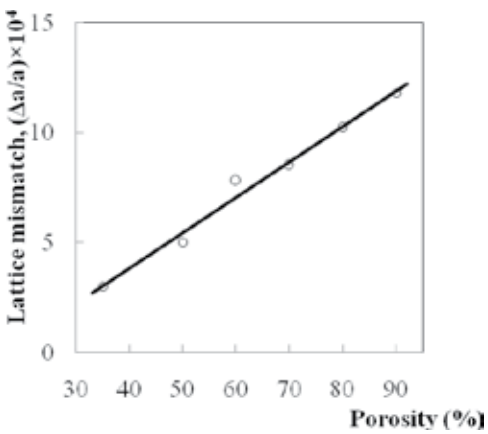


**Figure 9.** Relation for lattice mismatch parameter *Δa/a* between the PS layer and $p^+$-type Si substrate.

The origin expansion is attributed to the hydrogen-silicon bonds at the inner surface of the porous silicon. The hydrogen desorption results in a sharp contraction of the lattice parameter of porous silicon layer.

The pores on the surface of silicon increases absorption of light by increasing the effective thickness of emitter layer of solar cell (see Figure 4). Therefore the refractive index of the emitter layer, which strongly influences on efficiency of the solar cell depends on porosity of porous silicon. The current density applied during the formation process determines the porosity of the porous silicon layer and consequently its refractive index. We can say that the porosity-current density profile is transferred to the refractive index versus current density profile.

The reflectance can be calculated from refractive index. For film with parallel surfaces when light moves from a medium with refractive index $n_1$ to one with refractive index $n_2$ reflectance for normal incident is given as

$$R = (n_1 - n_2 / n_1 + n_2)^2 \tag{18}$$

The reflectance spectrum of the porous silicon film is characterized by the multiple interference fringes caused by the air-porous silicon and porous silicon-silicon interfaces. A simple method for evaluating the refractive index on a thin film is to measure the interference fringes resulting from multiple reflections

$$n = 1/2d\,(\lambda_1\lambda_2 \,/\, \lambda_2 - \lambda_1) \tag{19}$$

Here $\lambda_1$ and $\lambda_2$ are the wavelength for two consecutive maxima, $d$ is the thickness of the film. The main advantage of this method determination of the refractive index is its rapidity and simplicity. This method has been used by different authors for normal incidence. Figure 10 illustrates the refractive index as a function of current density for low resistivity silicon substrate [28].

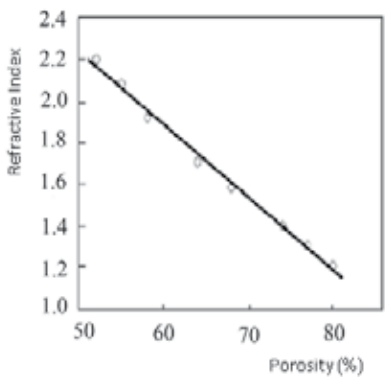


**Figure 10.** Refractive index as a function of current density for $p^+$-type doped substrate.

Three type of porous silicon layer with different refractive index profile along the thickness are used in solar cells as antireflection coating: *(a)* the refractive index is constant, *(b)* the refractive index profile smoothly changes, and *(c)* it changes in stepped form. The *(b)* type of porous silicon layer is fabricated by smooth change the current density during anodization process and *(c)* type porous silicon presents the multilayer structure which can be prepared by stepped variation of the current density during growth process.

http://dx.doi.org/10.5772/51593

As stated above the porous silicon consists of a network of nano-sized silicon walls and voids that formed when crystalline silicon wafer are etched electrochemically in HF-based electrolyte. Porous silicon presents the quantum system in which the charge carriers located in narrow crystalline silicon wall separating the pore walls. One of features of nanoporous silicon in comparison to the bulk silicon is shifting of fundamental absorption edge into the short wavelength of the visible region of the solar spectrum. It was confirmed by the measuring the optical absorption in the free-standing porous silicon layers [29].

PS layers with a thickness of 10-20 μm and an average porosity of 40 to 80% were prepared on *n*-type (111) Si substrates (ϱ =1×$10^{-2}$ Ω cm) by anodic etching in HF:$H_2O$ = 1:3 solution at a *dc* current of about 10-60 mA $cm^{-2}$ under white-light illumination [30]. For optical and electrical measurements, the PS films were then detached from the Si substrate by electro- polishing in the same solution with a current density of 0.8-1.0 A $cm^{-2}$. The free-standing PS films were characterized by porosity, thickness, optical and resistance measurements. The average porosity was measured by a gravimetric technique. Resistance and charge carrier concentration measurements were carried out on the free-standing PS layers attached to a dielectric substrate (glass) by using the Van der Pauw technique.

Figure 11 shows the effective energy gap in dependency on porosity of the free- standing PS films, calculated from extrapolation of the high energy part of {$\alpha^2$ ($h\nu$) $^2$- $h\nu$} spectra [29]. Near linear increase of band gap from 1.4 to 1.9 eV with rising of porosity of PS films in the range of 30-90 % is observed.

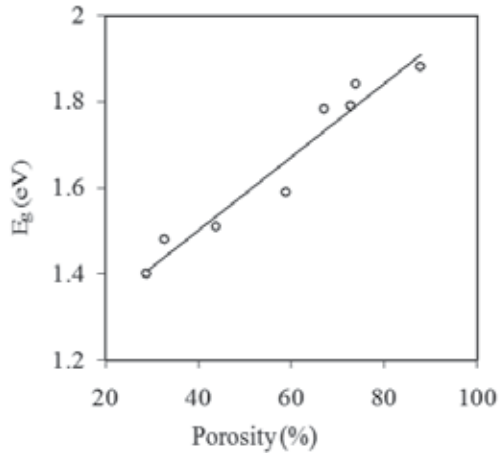


**Figure 11.** Energy band gap in depending on porosity of PS film (40% RH, 300 K).

Data on Figure 11 concerning increase of the energy gap in dependency on porosity of PS films can be explained by a model including the quantum confinement of carriers in the PS microcrystallites, causing the widening of the Si band gap.

The electrical measurements of the free-standing PS layers with 65% porosity (300 K, 45% RH) gave values of ϱ = 1.8×$10^6$ Ω cm for resistance, $p$ = 9.6×$10^{12}$ $cm^{-3}$ for hole concentration, and μ = 0.36 $cm^2$/(V s) for hole mobility.

## 5. Porous silicon layers in silicon solar cells

As stated above the features of porous silicon (a quantum system, a sponge or columnar structure and an extremely large pore surfaces) provide many possible applications, such as light emitting diode, chemical and biological sensor, hydrogen fuel cell, photovoltaic cell, antireflection coating in solar cells etc.

Decrease of reflectance (between 30 and 3%) and increase of band gap of porous silicon layer (between 1.1 and 1.9eV ) with increase of porosity makes nanoporous silicon as a promising material for use in the solar cell technology. Therefore formation of nanoporous layer on frontal surface of PS/Si solar cell with lower reflectance and larger band gap, expanding the spectral range of photosensitivity, will contribute to increasing of conversion efficiency. Moreover,formation of Si-H and Si-O bonds on silicon surfaces followed by electrochemical etching in HF-based solution will provide passivation the pore surfaces.

Thus, the room temperature fabrication only nanoporous silicon layer on frontal surface of ready silicon solar cell, instead of three-step process (texturization, antireflection layer deposition and passivation), performed at high temperatures on standard technology can essentially improve the photovoltaic parameters and decrease the cost of silicon solar cells.

*The potential advantages of porous silicon in silicon solar cells include:*

(1) Use as antireflection coating due to a lowering of the reflectance in the sensitivity range of silicon solar cell and possibility of formation PS layer with smooth change the refractive index between those Si and air

(2) Use as a wide-band optical window (the band gap shifts from 1.1 eV to 1.9 eV as the porosity is increased from 30 to 85% [29,31] that can broad the photosensitive region of the solar cell

(3) Use as front semiconductor layer with a variable band gap that can result in increase of photocurrent

(4) Possibility of the conversion of high energy ultra-violet and blue part of the solar spectrum into long wavelength radiations due to photoluminescence in nanocrystalline porous silicon

(5) Surface passivation and gettering role of porous silicon [32]

(6) Simplicity and lower cost fabrication technology of nanoporous silicon due to electrochemical modification of silicon

The theoretical requirements for the design of single- and double-layer porous silicon as antireflection coating on silicon solar cells are given in [33]. It is shown that the effective reflectance of $(n^+\text{-}p)$Si solar cell with shallow $n^+$-emitter depth (about 0.3 μm) can be reduced to 7.3% with a single porous silicon layer (of 80-90 nm thickness) formed a few seconds under current density of 50 mA/cm$^2$. Taking account of the possibility to modulate optical properties of porous silicon by changing the electrochemical parameters during formation (dura-

tion of etching, current density etc.) to reduce the reflectance, structural parameters of double-layers porous silicon are calculated and lower reflectance double-layer porous silicon ARC is realized in [33]. The lowest value of the effective reflectance (below 3%) of a double-layer PS ARC on *($n^+$-p)* Si cell with 0.5 μm-thick emitter have been obtained under 1 mA/cm$^2$ for 1 s (bottom layer of 47 nm thickness and 37% porosity) and under 50 mA/cm$^2$ for 100 s (top layer of 77 nm thickness and 71% porosity). It is experimentally shown that multiple PS layers ARCs can be formed in a single step procedure by changing the current density during its electrochemical preparation.

The significant reducing of the effective reflectance (up to 3%) was observed for monocrystalline silicon with porous silicon layer formed on previously texturized surface of sample [34]. Porous silicon layer was fabricated by electrochemical or chemical etch (stain etching) in HF:$HNO_3$:$H_2O$ for 3-60 s on *p*-type monocrystalline silicon (Cz) or multicrystalline silicon samples. The monocrystallne wafers were previously texturised by anisotropic etching in alkaline solution.

Data of integral reflectance (for $\lambda$ = 650 nm) of silicon samples without and with texturized layer, porous silicon layer or antireflection layer are presented in Table 2. The main conclusion which can be made from Table 2 is the effective reflectance for silicon samples with porous silicon layer is significantly smaller than that for samples without porous silicon layer. Moreover, the minimal effective reflectance (about of 3 %) is reached for porous silicon layer formed on previously texturized surface of silicon. The efficiency of PS/($n^+$-*p*)Si solar cell with PS formed after phosphorus diffusion (12.1%) is larger compared to reference silicon solar cell without PS layer (9.4%).

| Samples | Effective reflectance (%) |
|---|---|
| Polished surface | 33.9 |
| mc-Si with ARC ($SnO_x$) | 9.4 |
| PS by stain etching (mc-Si) | 6.6 |
| Texturisation by alkaline etching (Cz-Si) | 12.6 |
| Texturisation by alkaline etching + PS by electrochemical etching (Cz-Si) | 3.4 |
| Texturisation by alkaline etching + PS by stain etching (Cz-Si) | 3.1 |
| PS by electrochemical etching (Cz-Si polish surface) | 9.7 |

**Table 2.** The effective reflectance for different silicon surfaces [34].

The porous silicon layer formed on the textured surface of crystalline silicon by using silicon-dissolved tetramethylammonium hydroxides (TMAH) method results in significant decrease of reflectance [35]. Formation of porous silicon on textured surface of silicon allowed reduce reflectance up to 5% over spectral region from 400 to 1020 nm as compared to that for textured surface without porous silicon (about 15 %). In addition, a slight increase of the effective carrier lifetime is also observed for samples with porous silicon layer.

Antireflection properties of nanoporous silicon layer on *p*-type silicon were investigated in [36]. PS layers were prepared by electrochemical etching of silicon in 1HF: $1C_2H_5OH$ solution. The average reflectance between wavelengths 300-1000 nm was 10.3 % for the optimal PS layer. The analysis of the internal quantum efficiency of *($n^+$-p)* silicon solar cell with porous silicon layer as antireflection coating showed that quantum efficiency was comparable to that of a solar cell with a $SiN_x$ antireflection coating prepared using plasma-enhanced chemical vapour deposition.

*There are two technology of formation of porous silicon layer on silicon solar cells: (1) the thin porous silicon is formed on final step on surface of ready Si solar cell with metal contacts and (2) the relatively thick porous silicon layer is formed prior to emitter diffusion and metal contact deposition.* In the first case the thickness of porous layer (70-150 nm) must be less than depth of $n^+$-*p* (or $p^+$-*n*)-junction (300-800 nm), $d_{PS} < d_{pn}$ and duration of electrochemical etching is short (about 5-15 s). In the second case the thickness of the porous layer (5-15μm) is significantly large than the depth of location of $n^+$-*p* (or $p^+$-*n*) junction ($d_{PS}>d_{pn}$) and duration formation of porous layer is significantly larger (about 10-30 min). It can be expected that the profile of $n^+$-p junction must be a flat in the first case and non-flat (it is similar to profile of porous layer surface) in the second case.

*At first bellow will be considered results on photovoltaic properties of silicon solar cells with thin porous layer* formed on final step fabrication of cells.

The surface modification of silicon solar cells was used for improvement of photovoltaic characteristics of silicon solar cells in [37]. *p*-type boron-doped monocrystalline silicon wafers with orientation of (100), resistivity about of 3 Ω cm and thickness of 250-380 μm were used for fabrication of solar cells by screen-printed process [8, 38]. $n^+$-emitter layer with 0.5-1.0 μm thickness and 15-20 Ω/□ sheet resistance was formed as a result of phosphorus diffusion. Formation of porous silicon layer on $n^+$-surface of the device was performed on the final step of the solar cell fabrication sequence. Fabrication of PS layer on $n^+$-*p* junction was carried out at galvanostatic condition (constant current) in an electrolyte solution $HF:C_2H_5OH:H_2O$ (1:1:1 in volume) under illumination. Choice of optimal thickness of porous silicon layer as ARC on surface of ($n^+$-*p*) silicon solar cell and choice of the refractive index, which strongly depends on porosity (see Figure 9), were defined from conditions presented above.

If conditions (8) and (9) for air/ARC/Si system are to be satisfied ($n_0$=1 for air and $n_{Si}$=3.84 for Si), then the optimal values of refractive index and thickness (a quarter of wavelength) of the porous silicon layer, acting as ARC must be (for $\lambda$= 650 nm) $n_{arc}$=1.96 and $d_{arc}$=83 nm, respectively. Taking into account the refractive index depends on porosity of porous silicon (Figure 9) one may conclude that the porous silicon layer of 80-90 nm thickness and about 55% porosity (n=2) may act as ARC having minimum reflectance, that in turn will improve the photovoltaic parameters of PS/($n^+$-*p*)Si solar cells.

The growth rate of porous silicon on Si substrate, measured in this run for a current density of 60 mA/cm$^2$, was about 8 nm/s. Therefore, the time of electrochemical etching under a constant current of 40, 50 or 60 mA/cm$^2$ was 8-15 seconds. As a result, a blue colored PS layer between the grid fingers on the surface of the $n^+$-emitter silicon solar cell has been obtained. For some measurements, the PS layers were then detached from the Si substrate by electropolishing process [30]. Free-standing PS layers were characterized by porosity, thickness, re-

sistivity, photoluminescence and reflectance measurements. Resistivity measurements, carried out by the Van der Pauw technique on the free-standing porous silicon layer of 60% porosity, gave $3x10^4$ Ω cm.

A SEM micrograph of the front PS surface obtained by using scanning electron microscopy (SEM) (JSM-5410LV) is shown in Figure 12. Cross cut representation of silicon layer showed that the pores have a conical form.

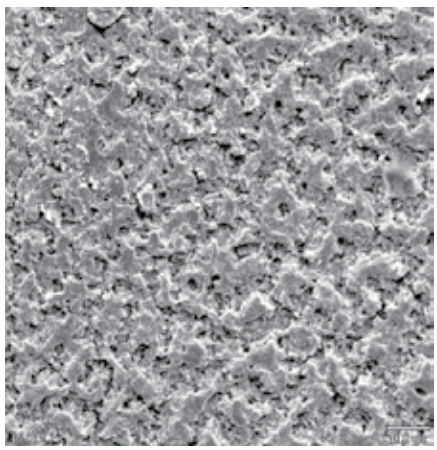

**Figure 12.** Scanning electron microscopy of porous silicon layer surface.

Figure 13 shows the photoluminescence spectrum of the PS layer (60% porosity) on Si substrate, where the spectrum illustrates the peak at $\lambda$=580 nm (the orange region of the solar spectrum). Measurements of distribution of photoluminescence intensity along the thickness of the PS layer (of thickness 10 μm) showed that the intensity approximately linearly decreasesfrom the surface deep down. Similar results were also obtained by investigations of samples with PS layers of different thicknesses. Observation of photoluminescence in PS at visible region of the spectrum can be interpreted by quantum confinement effect causing the confinement of the charge carriers in nanocrystalline silicon wall separating the pore [39].

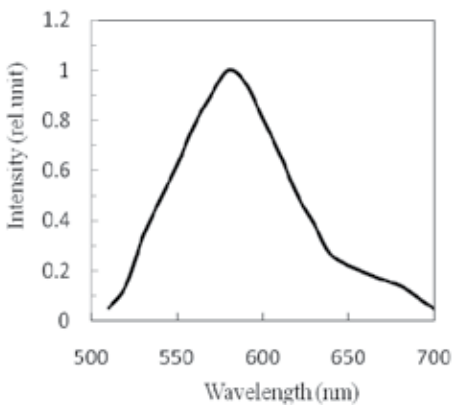


**Figure 13.** The photoluminescence spectrum for porous silicon layer.

The integrated reflectance spectra of the polished silicon surface before and after porous silicon layer (of 60% porosity) formation showed the significant lowering of the reflectance (to 4%) as compared to polished silicon (about 38-45%). These data show that PS on ($n^+$-$p$) silicon solar cell can be used as effective antireflection coating.

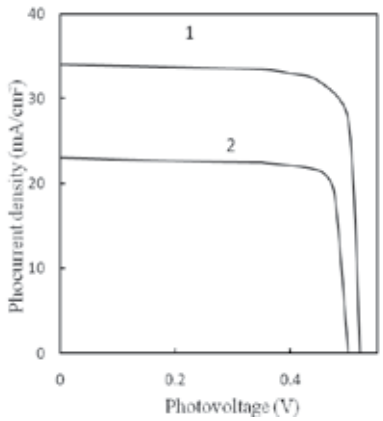


**Figure 14.** Photocurrent density-voltage chracteristics of ($n^+$-$p$) silicon solar cell (1) with and (2) without PS layer.

The current-voltage characteristics of $n^+$-p silicon solar cells without and with porous silicon layer of 60% porosity (($n^+$-$p$)Si and PS/($n^+$-$p$)Si structures respectively), measured under AM1.5 illumination, have been presented in Figure 14. As a result, due to the PS coating, the short-circuit current density increased from 23.1 to 34.2 mA/cm$^2$ and the open-circuit voltage increased from 500 to 520 mV. The experimental results on the photovoltaic parameters for thirty solar cells before and after formation of the PS layer on $n^+$-emitter surface showed that the mean increment of photocurrent density is about 48% (Table 3). At the same time, the open-circuit voltage increase is about 4%. The fill factor remains approximately the same for cells with porous layer (FF=0.75) as compared to the solar cells without porous layer (FF=0.74). The mean efficiency of photovoltaic conversion for solar cells with PS layer increased from 12.1 to 14.5%, what equals a relative increment of about 20%.

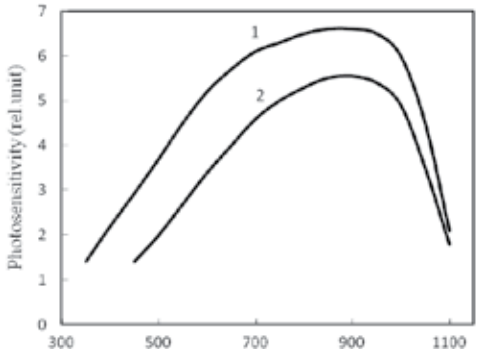


**Figure 15.** The photosensitivity spectra of (1) PS/($n^+$-$p$)Si and (2) ($n^+$-$p$) Si solar cells.

The photosensitivity spectra of the solar cells with and without PS layer were presented in Figure 15. The value of photosensitivity for the PS/($n^+$-$p$)Si cell is larger (by about 25%) and

http://dx.doi.org/10.5772/51593

the spectral photosensitivity region is considerably wider than those for ($n^+$-$p$) Si cell without the PS layer. The significant improvement of photovoltaic characteristics of the PS/($n^+$-$p$)Si solar cell was attributed mainly to the two-fold role of the porous silicon layer on surface of the $n^+$-emitter. Firstly, it behaves as a antireflection coating, increasing the incident photon flow on the $p^+$-$n$ junction and secondly, it plays the role of a wide-band gap optical window (about of 1.8-1.9eV for PS of 60% porosity), broadening the spectral region of photosensitivity of the cell to the ultraviolet part of solar spectrum.

| Solar cell | $J_{sc}$ (mA/cm$^2$) or I (mA) | $V_{oc}$ (mV) | FF | Eff. (%) | Reflectance (λ=650 nm) | Reference |
|---|---|---|---|---|---|---|
| ($n^+$-p) Si | 23.1 | 500 | 0.74 | 12.1 | 28 | [37] |
| PS/($n^+$-p) Si | 34.2 | 520 | 0.75 | 14.5 | 4 | |
| ($n^+$-p) Si | 21.5 | 580 | 0.55 | 7.5 | 12 | [40] |
| PS/($n^+$-p) Si | 28.4 | 585 | 0.74 | 12.5 | 3 | |
| ($n^+$-p) Si | 95 mA | 580 | | 10.3 | | [41] |
| PS/($n^+$-p) Si | 137 mA | 570 | | 13.5 | | |
| ($n^+$-p) Si | 17.2 | 598 | 0.74 | 7.6 | 7 | [42] |
| PS/($n^+$-p) Si | 20.1 | 606 | 0.75 | 9.5 | 12 | |
| Text. ($n^+$-p) Si | 23.3 | 592 | 0.70 | 9.6 | 3 | |
| PS/Text. ($n^+$-p) Si | 25.5 | 595 | 0.74 | 11.2 | | |
| ($n^+$-p) Si | 18.5 | 580 | 0.73 | 7.85 | 7 | [43] |
| PS/($n^+$-p) Si | 27.2 | 601 | 0.77 | 12.54 | | |
| PS/ ($n^+$-p) Si | 33.4 | 460 | | | 9 | [44] |
| $SiO_x$/( $n^+$-p) Si | 34.8 | 530 | | | 3.8 | |
| ($p^+$-n)PS/Si (100) | 15.9 mA | 480 | 0.81 | 15.4 | 7 | [45] |
| ($p^+$-n)PS/Si (111) | 12.4 mA | 440 | 0.82 | 11.2 | 16 | |
| ($n^+$-p)PS/Si (111) | 12.4 mA | 440 | 0.82 | 11.2 | | [47] |
| $SiO_2$/($n^+$-p)Si (111) | 6.04 mA | 370 | 0.79 | 4.4 | | |
| (ZnO-$TiO_2$)/($n^+$-p)Si | 10.2 mA | 410 | 0.81 | 8.4 | | |
| ($p^+$-n)PS/Si PS on one side | 8.8 mA | 430 | 0.78 | 7.4 | 16 | [48] |
| ($p^+$-n)PS/Si/PS PS on both sides | 12.4 mA | 490 | 0.84 | 12.75 | 6 | |
| ($n^+$-p)PS/Si | 28.9 | 627 | 0.76 | 13.8 | 9 | [49] |
| PS/($n^+$-p) Si | 26.3 | 602 | 0.76 | 12 | 10 | [50] |
| SiN/($n^+$-p) Si | 28.4 | 606 | 0.75 | 13 | | |
| ($n^+$-p) mc-Si | 26.6 | 572 | 0.75 | 11.3 | 15 | [51] |
| PS/ ($n^+$-p) mc-Si | 28.9 | 582 | 0.76 | 12.7 | 5 | |
| ($n^+$-p) mc-Si | 29.8 | 577 | 0.5 | 12.9 | 8 | [7] |
| ($n^+$-p)PS/mc-Si | 30.2 | 587 | 0.76 | 13.5 | | |

**Table 3.** Photovoltaic parameters of silicon solar cells without and with porous silicon layer.

Change the porosity deep down to PS layer can also stimulates the improvement of the photovoltaic parameters of solar cells. Experimentally observed decrease of intensity of the photoluminescence peak at 580 nm deep down to PS layer, which consists of pores of conical form, can be circumstantial evidence for decrease of porosity deep down. Taking into account that the band gap energy of nanoporous silicon increases with increment of porosity due to quantum confinement of carrier charges (see Figure 11), one can assume that the porous silicon layer on the ($n^+$-$p$)Si cell is a semiconductor with variable band gap width (changing from about 1.8-2.0 eV on the front PS surface to 1.1 eV on the PS/$n^+$Si interface). As a result, the internal electrical field of the porous layer with variable band gap can also increase of the photocurrent generated in the PS/($n^+$-$p$)Si solar cell.

The original formation technique of porous silicon layer on silicon solar cells was used in [40]. $n^+$-$p$ junctions were obtained by phosphorus diffusion into monocrystallinep-type silicon wafers. PS layer was formed after deposition of front grid contact. New method PS layer formation consisted in deposition a thin Al film on front surface silicon cell and then HF-spray-etching. Advantage of method is use HF solution only, instead HF:$HNO_3$ composition, since HF-spray-etching does not influence on front grid metallic contact. Hydrogen-rich PS prepared by HF-spray-etching method plays role of a passivation layer and decreases the surface reflectance from 12% for textured surface to 3% for textured surface in the presence of a thin porous silicon layer. Formation of PS layer prepared under optimized HF-spraying conditions improves the conversion efficiency from 7.5 to 12.5% (Table 3). The observed results were discussed throughout increase of light absorption due to reflectance lowering and band gap widening. Unfortunately, data on thickness, porosity and other parameters of porous layers are not presented in [40].

The porous silicon as ARC in ($n^+$-$p$) silicon solar cells was used in [41]. Thin porous silicon layer (of thickness about 100 nm) on $n^+$-emitter was formed on final stage of ($n^+$-$p$) solar cell fabrication. 1HF : 1$C_2H_5OH$ and 1HF : 1$C_2H_5OH$ : $H_2O$ solutions were used as electrolyte during anodization modification of silicon (for 3-12 s). $n^+$-$p$ junction with $n^+$-emitter of 400 nm thickness was formed by phosphorus diffusion in monocrystalline p-type (100) silicon of 1.5 Ω cm resistivity.The reflection spectra of porous layer prepared on the polished surface of $n^+$-emitter showed that the average reflectance is about 7.6% in the wavelength range 400-700 nm with minimum value of 1.4% at 580 nm. The photovoltaic parameters of ($n^+$-$p$)Si solar cells before and after formation of PS layer are presented in Table 3. It is seen that the efficiency of solar cell increased from 10.3 to 13.5% as result of fabrication of porous layer on front surface of the cell. The significant increasing for the short-circuit current (from 95 to 137 mA) and very small decreasing of the open-circuit voltage were observed for cells with porous silicon coating. Authors [41] supposed that the formation of porous silicon layer on silicon solar cells does not ensure necessary level of passivation and also does not have sufficient temporal stability.

The photovoltaic parameters of ($n^+$-$p$) Si solar cells with and without thin porous silicon layer prepared by standard screen-printed technique are studied in [42]. *P*-type Si (100) wafers of 1.5 Ω cm resistivity and 20 $cm^2$ surface were used. Formation of porous silicon layer on n $^+$-surface of cells was performed by electrolytic anodization in 1HF: 4$C_2H_5OH$ solution with

http://dx.doi.org/10.5772/51593

a current density of 10 mA/cm$^2$ during short time 10 s. Data on characteristics of solar cells, prepared on base of polished monocrystalline and textured monocrystalline silicon without and with porous layer are presented in Table 3. The main conclusion from results presented in Table 3 consists in increasingthe short-circuit current density and efficiency of silicon solar cells with porous layer. For both group cells prepared on polished and textured silicon with porous layer efficiency increases by about 20-25% compared to a cells without porous silicon layer. However the open-circuit voltage and fill factor for cells with porous layer remain almost same with those for cells without porous silicon. The minimum reflectance and the best photovoltaic parameters have the solar cells with porous silicon layer prepared on textured surface.

A significant improvement in efficiency of ($n^+$-$p$) Si solar cells with the thin porous silicon layer has been achieved in [43]. Float-zone (100) oriented $p$-type silicon with 1Ω cm resistance was used as starting material. Formation of the porous silicon layer was made on finished solar cell during chemical etching in HF: $HNO_3$:$H_20$ solution for 20 s. The reflectance of polished Si sample is significantly lowered after porous layer formation from 36 to 9.5%.The silicon solar cell with porous layer leads to a 46% and 38% relative improvement in photocurrent density and efficiency respectively (Table 3). The observed enhancement in the photovoltaic parameters was attributed to both the antireflection and passivation properties of porous silicon. The passivation capabilities of PS accompanied with lowering of recombination velocity of charge that can arise from the presence of Si-hydrides and Si-hydroxides on pore surfaces.

Double layers $SiO_x$/PS structure as antireflection coating in ($n^+$-$p$) Si solar cells prepared the screen-printing technique was studied in [44]. Then porous silicon layers were fabricated on the front surface of screen-printing ($n^+$-$p$) Si solar cells by electrochemical etching in 1HF: $3C_2H_5OH$ solution at a current density of 20 mA/cm$^2$ for 4-12 s. The silicon oxide films of different thickness (70-105 nm) were deposited on porous silicon by PECVD method. Decrease of reflectance and improvement of photovoltaic parameters of double layer $SiO_x$/PS/($n^+$-$p$) Si cells were received compared to the single PS/($n^+$-$p$) Si cells. Best results were obtained when the thickness of $SiO_x$ film and PS layer (P=60%) are 105 and 60 nm respectively (Table 3). An improvement in the open-circuit voltage of 14% for double-layer ARC authors [44] attribute to enhancing the surface passivation of the pores due to diffusion of hydrogen from $SiO_x$ film.

*There are a number of studies on silicon solar cells with thick porous silicon coating in which the porous layer is formed before fabrication of $n^+$-$p$ (or $p^+$-$n$) junction.*

The orientation of porous silicon influences of performance of silicon solar cells [45]. ($p^+$-$n$) silicon solar cells were prepared on base of n-type Si of (111) and (100) orientation (0.75 Ω cm). $p^+$-type doping was achieved by boron diffusion. Porous silicon layer on $p^+$-silicon was fabricated by electrochemical anodization in 1HF: $3C_2H_5OH$ solution at a current density of 50 mA/cm$^2$ for 20 min. The surface reflectance of porous silicon on (100) Si is significantly less (8 %) than that for (111) Si (16%). The photovoltaic parameters for (100) Si and (111) Si-based solar cells presented in Table 3 show that the conversion efficiency of (100) Si-based cells is larger (15.42%) than that of (111) Si-based cells (12.4%). The observed results authors

explain formation higher pyramids on (100) Si surface compared to (111) Si surface that results in lower reflectance.

It is to be noted that for thick porous silicon layer when it thickness is larger than that of $p^+$*(or* $n^+$*)*-emitter, non-uniformity of $p^+$-$n$ (or $n^+$-$p$) junction profile can make worse the parameters of cells. Influence of different PS layer thickness on photovoltaic properties of $n^+$-$p$ silicon solar cells showed that both external and internal quantum efficiencies are improved as far as PS/Si interface does not overpass the $n^+$-$p$ junction [46]. It can mean that when the thickness of PS layer is larger than that of $n^+$emitter region, i.e. the space-charge region locates in PS layer, the surface defects of PS layer stimulate the increase the recombination rate of photocarriers.

The comparative investigations of ($n^+$-$p$) Si (111) solar cells with single layer ARC ($SiO_2$), double layers ARC ($ZnO/TiO_2$) and the porous silicon layer are carried out in [47]. The porous silicon layers were formed on phosphorus-doped $n^+$-layer of solar cells in 1HF: $3C_2H_5OH$ solution at current density 60 mA/cm$^2$ for 30 min. The best photovoltaic characteristics showed the silicon solar cells with porous layer (see Table 3). From SEM micrograph presented in the work it is seen that thickness of porous silicon is significantly larger than the depth of $p^+$-$n$ junction in silicon. It can make worse the characteristics of the $p^+$-$n$ cells.

Above we considered the results of studies on silicon solar cells with porous layer formed only on front side of cell. Interesting data for silicon solar cells with porous layers prepared *on both sides of the (111) n-type Si wafers* (of 0.75 Ω cm resistivity and of 283 μm thickness) are given in [48]. The porous silicon layers on the polished front side and the unpolished backside were obtained by electrochemical process in 1HF : 4 $C_2H_5OH$ solution under 60 mA/cm$^2$ for 15 min for each side (before boron diffusion and metal contact deposition). SEM images showed that the porous surface formed on the front polished side has discrete pores, whereas the porous silicon surface created on unpolished backside is shaped in small pores which are attributed to an increase in surface roughness. The reflectance of the PS front and back sides in the spectral range 400-1000 nm are about 16% and 6% respectively. As is seen from Table 3 the efficiency of ($p^+$-n)PS/nSi/PS solar cell with PS layer on both sides of Si is increased to 12.75% compared to solar cell with PS layer on the unpolished side (7.4%).

The formation of PS layer during the normal cleaning sequence at the beginning of the solar cell process was carried out in [49]. Porous silicon layers on p-type silicon wafer prepared by stain etching in HF:$HNO_3$ showed reflectance as low as 9 %. Photovoltaic characteristics of the best porous silicon cells fabricated by screen-printed technique are given in Table 3. The high values of photovoltaic parameters of ($n^+$-$p$)PS/$p$Si solar cells are attributed to lower reflectance and passivation properties of PS layer.

Thin porous silicon layer formed on dendritic web and string ribbon silicon by chemical etching in HF:$HNO_3$:$H_2O$ solution for a few seconds increases the lifetime of the minority carriers by a factor 3.3 [50]. The additional heat treatment (860°C, 2 min) or simultaneous phosphorus and aluminum diffusion after PS layer formation results in lifetime enhancement by a factor 8.3 or 5.8 respectively. In opinion of authors [50] porous silicon induced lifetime enhancement can be caused by the gettering properties of PS layer. Photovoltaic

http://dx.doi.org/10.5772/51593

characteristics of ($n^+$-$p$) silicon solar cells with porous silicon layer and SiN antireflection coating are given in Table 3. It is seen that both type solar cells have almost same parameters.

The improvement of photovoltaic parameters of *multicrystalline*($n^+$-$p$) Si solar cells with porous silicon layer is observed in [51]. Formation of porous silicon layer on textured surface of p-type mc-Si (1Ω cm) was performed by two-step chemical etching of silicon before phosphorus diffusion. It is shown that macroporous silicon layer formed before phosphorus diffusion results in texturisation of mc-Si with the larger angle than that obtained classical texturisation based in KOH. The surface reflectance of mc-Si with PS layer with phosphorus glass drops up to 5% compared to that for mc-Si with phosphorus silica glass but without PS layer (16%). The main parameters of ($n^+$-$p$) mc-Si based solar cells (of 25 $cm^2$ size) without and with PS layer were presented in Table 3. Formation of PS layer on mc-Si allows enhance the efficiency up to 12.7% that is close the efficiency limit of the mc-Si solar cells with $TiO_x$ antireflection coating. Additional etching of ($n^+$-$p$) mc-Si solar cell in $98HNO_3$:2HF solution for 300 s (after PS formation) improves its photovoltaic parameters [7] (see Table 3).

Gettering behavior of PS layer on silicon leading to enhancement of the lifetime of the non-equilibrium minority carriers and improvement of silicon solar cell characteristics have been considered in [52-54]. The porous silicon containing a large number of small pores with diameter between 4-50 nm shows very large the surface area-to-volume ratio (about of 500 $cm^2/m^3$). The extremely large pore surfaces and their very chemical activity ensure possibilityof application related with gettering of impurities and defects. The high-temperature annealing of the chemical etched porous silicon surface can enhance the impurity diffusion into the porous silicon network and thereby acting as an efficient external gettering site. The oxidation rate of porous silicon due to its mesapore structure is significantly larger (by 10-20 times) than that for single-crystalline silicon surface [52]. Gettering by porous silicon consists of oxidizing the porous silicon layer in wet oxygen ambient condition followed by the removal oxide in a dilute HF solution. The lattice mismatch between porous layer and silicon substrate can stimulate the gettering of impurities and defects.

The gettering-induced enhancement in the minority carrier diffusion length in multicrystalline silicon (mc-Si) with porous silicon layer on its surface was studied in [53]. The PS/Si/Al structures prepared by formation of porous layer in front surface of silicon and by vacuum evaporation of aluminum layer (2 μm) on the other side of sample were exposed to the wet oxidation of the porous silicon (950°C). Measurements showed that the minority carrier diffusion length for Si in such structure (about 190 nm) is larger than that for reference Si sample (about 100 nm). Co-gettering effect for PS/Si/Al consists in out-diffusion of impurities throughout the porous silicon layer and the aluminum. For {phosphorus layer/silicon/aluminum layer} structures (without porous layer) usually used for fabrication of silicon solar cell influence of co-gettering on the diffusion length of minority carriers is less (about 100 nm).

The PS/Si/Si structures prepared by forming porous silicon layers on both sides of Si wafer and then coated with phosphorus dopant ($POCl_3$) and heat treated at 900°C for 90 min discovered the improvement of the electrical and recombination characteristics of silicon [54]. Diffusion of phosphorus into PS layer is accompanied by gettering of eventual impurities towards the phosphorus doped PS layer. As a result of removal of impurities, increasing the

mobility of the majority carriers and the diffusion length of minority carriers are observed. Removal of eventual impurities and defects away from the device active regions allowed to improve output characteristics of silicon solar cells.

Above, the results of influence of the porous silicon as an active element in thick crystalline silicon solar cells have been considered. It is shown the porous silicon as antireflection coating significantly improves the performance of silicon solar cells. In last year's porous silicon layer were also used as sacrificial layer for fabrication of thin-film silicon solar cells. As known the monocrystalline silicon which intensively are used in commercial solar cell applications is high cost material. The reduction in the amount of high-quality expensive silicon material per solar cell is one of ways of lowering the cell coat. At present one of the technologies developed to fulfill the aim of reduction the cost of silicon solar cell is porous silicon (PSI)-transfer process [55]. The thickness of monocrystalline silicon solar cell prepared by PSI-process (about 5-50 μm) is significantly lower than that of crystalline silicon cell fabricated by standard technology (250-300 μm). The PSI-transfer process consists of four steps. *First*, double layers of porous silicon are fabricated by electrochemical etching on surface of monocrystalline silicon: the 1-2 μm-thickness low-porosity layer (20%) at the top and 350 nm-thickness high-porosity layer (50-60%) beneath. *Second*, thin monocrystalline silicon layer (about 5-50 μm thickness) epitaxial grows on top (low-porosity) layer. Low-porosity layer is of monocrystalline quality which allows the growth of a high quality epitaxial layer of silicon. *At third step* the epitaxial silicon layer is detached from silicon substrate through a high-porosity layer by lift-off technique and then it is transferred onto a foreign substrate. *At final step* thin-film silicon solar cell is fabricated by standard or other technology. Shortly after using of PSI-process cell efficiency gradually increased from 12.5% (in 1997) to 16.9% (in 2009). Today the record value of efficiency of 19.1% (S=4 $cm^2$,$V_{oc}$=650 mV, $J_{sc}$=37.8 mA/cm2, FF=0.78) for monocrystalline silicon solar cell of 43 μm thickness prepared by porous silicon transfer technique was demonstrated [56]. It should be noted that porous silicon transfer process is certainly complex for industrial application. Nevertheless it shows the high efficiency potential of the porous silicon transfer process.

## 6. Conclusion

The review of investigations of the use of the nanoporous silicon in silicon solar cell showed that an increase in the conversion efficiency (about of 25-30%) is achieved for PS/Si solar cell compared to a cell without a PS layer. At the same time, the performance of silicon solar cells with PS layer is more than that of silicon solar cells with conventional ARC. The lower value of effective reflectance (up to 3%) for nanoporous silicon layer that significantly reduces the optical losses is one of main reasons of improvement of performance of PS/Si solar cell. A wide-band gap nanoporous silicon (up to 1.9 eV) resulting in widening of the spectral region of photosensitivity of the cell to the ultraviolet part of solar spectrum may promote the increase the efficiency of silicon solar cells with PS layer. The internal electric field of porous silicon layer with variable band gap (due to decrease of porosity deep down) can stimulate an increase in short-circuit current (Figure 16).

http://dx.doi.org/10.5772/51593

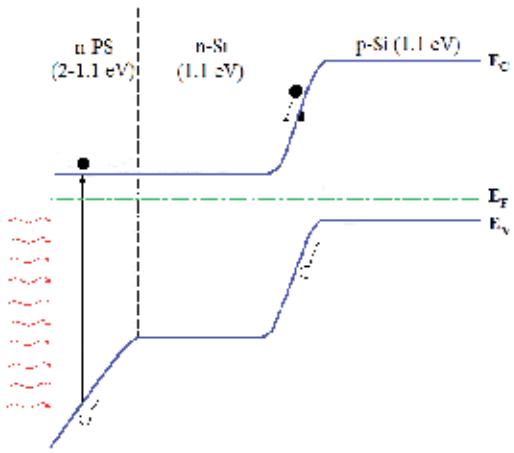


**Figure 16.** Energy band diagram of *n*PS/(*n*⁺-*p*) Si solar cell.

Additionally, the intensive photoluminescence in the red-orange region of the solar spectrum observed in porous silicon under blue-light excitation can increase the concentration of photo-exited carriers. It is necessary to take into account the passivation and gettering properties of Si-H and Si-O bonds on pore surfaces which can increase the lifetime of minority carriers.

Porous silicon, along with above advantages, in some cases e.g. due to its high resistivity can reduce the output parameters of PS/Si solar cells. Contribution of resistance (about $5x10^{-2}$ Ω) of thin porous silicon layer (about 100 nm) in total series resistance of the solar cell (about 0.5-1.0 Ω) is negligible and therefore it must not influence on parameters of cells. The resistance of thick PS layer (5-15 μm) can essentially increase the total series resistance and thereby it can reduce the photovoltaic parameters of silicon solar cell. However, as is seen from Table 3 reducing of parameters of PS/Si solar cells with thick PS layer was not observed. It tentatively can be explained that formation $n^+$or $p^+$-emitter layer by phosphorus or boron diffusion in PS is accompanied with decrease of layer resistance. Moreover, the non-flatprofile of $n^+$-$p$ (or $p^+$-$n$) junction in PS/Si cells with thick PS layer (prepared before junction formation) does not result in reducing of efficiency (see Table 3). Explanation of this problem demands of further investigations.

Note should be taken that properties of PS layer and thereby photovoltaic characteristics of solar cell can change on running under illumination, heating etc. At present, as far as our knowledge goes, publications on temporal stability of PS-based solar cells are almost absent in literature.Works related with degradation phenomena in PS/Si solar cells is the matter of topical interest for further researches.

Judging by the results presented in this review and taking into account the simplicity of fabrication of porous silicon layer on silicon we can safely draw to the conclusion that the nanoporous silicon is a good candidate for use on preparation of low cost silicon solar cells with high efficiency. It gives hope for the industrial production of PS-based silicon solar cells.

## Author details

Tayyar Dzhafarov*

Address all correspondence to: caferov@physics.ab.az

Department of Solar and Hydrogen Cells, Institute of Physics, Azerbaijan National Academy of Sciences, Azerbaijan

## References

[1] Goetzberger, A., & Hebling, C. (2000). Photovoltaic Materials, Past, Present, Future. *Solar Energy Materials and Solar Cells*, 62, 1-19.

[2] Sze, S. (1990). Physics of Semiconductor Devices. New York: John Wiley & Sons.

[3] Canham, L., editor. (1997). Properties of Porous Silicon. London: IEE-Inspec.

[4] Bisi, O., Ossicini, S., & Pavesi, L. (2000). Porous Silicon: A Quantum Sponge Structure for Silicon Based Optoelectronic. *Surface Science Reports*, 38, 1-126.

[5] Fahrenbruch, A., & Bube, R. (1983). Fundamentals of Solar Cells, New York.

[6] Gupta, S., Srivastaya, M., & Gupta, A. Mathematical Formulation Comparative Analysis of Losses in Solar Cells. http://www.tutorialspoint.com/white-papers.

[7] Lipinski, M., Panek, P., & Ciach, R. (2003). The Industrial Technology of Crystalline Silicon Solar Cells. *J. Optoelectronics and Advanced Materials*, 5, 1365-1371.

[8] Neuhaus, D., & Munzer, A. (2008). Industrial Silicon Wafer Solar Cells. *Advances in Electronics*, 4, 2-15.

[9] Moller, H. J. (1993). Semiconductor for Solar Cells. Boston: Artech House.

[10] Green, M. (1999). Limiting Efficiency of Bulk and Thin-film Silicon Solar Cells in Presence of Surface Recombination. *Progress in Photovoltaic*, 1999, 7(3), 327-330.

[11] Neizvestny, I. (2011). Nano-technologies in Solar Cells. *International Association of Academies of Sciences, Scientific Council on New Materials, conference proceedings*, October 5-7, 2011, Kiev.

[12] Born, M., & Wolf, E. (1970). Principles of Optics. London: Pergamon Press.

[13] Goodman, A. (1978). Optical Interference Method for the Approximate Determination of Refractive Index and Thickness of a Transparent Layer. *Applied Optics*, 17(17), 2779-2789.

[14] Sopori, B., & Pryor, R. (1983). Design of Antireflection Coatings for Textured Silicon Solar Cells. *Solar Cells*, 1983, 8, 249.

[15] Jayakrishnan, R. (2009). Dielectric Coating Agents for Passivation and Anti-reflection. *Photovoltaic International*, 6, 83-86.

[16] Chen, Z., Sana, P., & Salami, J. (1993). A Novel and Effective PECVD $SiO_2$/SiN Antireflection Coating for Si Solar Cells. *IEE Trans. Electron Device*, 40(6), 1161-1165.

[17] Mahdjoub, A. (2007). Graded Refractive Index Antireflection Coatings Based on Silicon and Titanium Oxides. *Semiconductor Physics, Quantum Electronics and Optoelectronics*, 10(1), 60-66.

[18] Feng, Z., & Tsu, R. (1994). Porous Silicon. Singapore: World Scientific.

[19] Beale, M., Uren, J., Chew, N., & Cullis, A. (1985). An Experimental and Theoretical Study of the Formation and Microstructure of Porous Silicon. *Journal of Crystal Growth*, 73, 622-636.

[20] Remache, L., Mahdjoub, A., Fourmond, E., Dupuis, J., & Lemiti, M. (2010). Design of Porous Silicon/PECVD $SiO_x$Antireflection Coatings for Silicon Solar Cells. *Intern. Conference on Renewable Energies and Power Quality (ICREPQ-2010)*, Granada, Spain, 23-25 March.

[21] Dzhafarov, T. D., & Can, B. (2000). The Diffusion Distribution of Hydrogen and Oxygen in Porous Silicon Films. *Journal of Materials Science Letters*, 19, 287-289.

[22] Abdullaev, G. B., & Dzhafarov, T. D. (1987). Atomic Diffusion in Semiconductor Structures. New York: Harwood Academic Press.

[23] Dzhafarov, T., & Aydin, S. (2010). Diffusion of Hydrogen in Porous Silicon-based Sensors. *Journal of Porous Media*, 13(2), 97-102.

[24] Cisneros, R., Pfeiffer, H., & Wang, C. (2010). Oxygen Absorption in Free-Standing Porous silicon: A Structural, Optical and Kinetic Analysis. *Nanoscale Res. Lett*., 5(4), 686-691.

[25] Barla, K., Herino, R., Bomchil, G., Pfister, J., & Freund, A. (1984). Determination of Lattice Parameters and Elastic Properties of Porous Silicon by X-ray Diffraction. *Journal of Crystal Growth*, 8, 727-732.

[26] Barla, K., Herino, R., Bomchil, G., Pfister, J., & Baruchel, J. (1984). X-ray Topographic Characterization of Porous Silicon Layers. *Journal of Crystal Growth*, 68, 721-726.

[27] Bellet, D., & Dolino, G. X. (1996). X-Ray Diffraction Studies of Porous Silicon. *Thin Solid Films*, 276(1), 778-782.

[28] Perez, E. (2010). Design, Fabrication and Characterization of Porous Silicon Multilayer Optical Devices. Ph.D. thesis, Universitet Rovirai Virdali.

[29] Dzhafarov, T., & Aydin, S. (2009). Nano-Porous Silicon for Gas Sensors and Fuel Cells Applications. *Journal of Qafqaz University*, 25, 20-35.

[30] Dzhafatov, T., Oruc, C., & Aydin, S. (2004). Humidity-Voltaic Characteristics of Au-Porous Silicon Interfaces. *Journal of Physics D: Applied Physics*, 37, 404-408.

[31] Pickering, C., Beale, M., Robbins, D., Pearson, R., & Greef, R. (1984). Optical Studies of the Structure of Porous Silicon Films Formed in p-type Degenerate and Non-degenerate Silicon. *J. Phys. C*, 17, 6535-6552.

[32] Schirone, L., Sotgiu, G., Montecchi, M., & Parisini, A. (1997). Porous Silicon in High Efficiency Large Area Solar Cells. *Conference proceedings, Progr.14 European PV Solar Energy Conf.*, Barcelona, Spain, 1479-1482.

[33] Strehlke, S., Bastide, S., Guillet, J., & Levy-Clement, J. (2000). Design of Porous Silicon Antireflection Coatings for Silicon Solar Cells. *Materials Science and Engineering*, B69-70, 81-86.

[34] Lipinski, M., Panek, P., Beilanska, E., Weglowska, J., & Czternastek, H. (2000). Influence of Porous Silicon on Parameters of Silicon Solar Cells. *Opto-Electronics Review*, 8(4), 418-420.

[35] Weiying, O., Lei, Z., Hongwei, D., Jun, Z., & Wenjing, W. (2011). Optical and Electrical Properties of Porous Silicon Layer Formed on the Textured Surface by Electrochemical Etching. *Journal of Electronics*, 32(5), 1-5.

[36] Kim, J. (2007). Formation of a Porous Silicon Antireflection Layer for a Silicon Solar Cell. *Journal of Korean Physical Society*, 50(4), 1168-1171.

[37] Dzhafarov, T., Aslanov, S., Ragimov, S., Sadigov, M., & Aydin Yuksel, S. (2012). Effect of Nanoporous Silicon Coating on Silicon Solar Cell Performance. *Vacuum*, 86(12), 1875-1879.

[38] Green, M. (1999). Limiting Efficiency of Bulk and Thin-film Silicon Solar Cells in the Presence of Surface Recombination. *Progress in Photovoltaic*, 7, 327-338.

[39] Canham, L. (1990). Silicon Quantum Wire Array Fabrication by Electrochemical and Chemical Dissolution of Wafers. *Appl. Phys. Lett.*, 57, 1046.

[40] Saadoun, M., Ezzaaoia, H., Bassais, B., Boujmil, M., & Bennaceur, R. (1999). Formation of Porous Silicon for Large-area Silicon Solar cells: A New Method. *Solar Energy Materials and Solar Cells*, 59, 377-385.

[41] Yerokhov, V., Melnik, I., Tsisaruk, A., & Semochko, I. (2000). Porous Silicon in Solar Cell Structures. *Opto-Electronics Review*, 8(4), 414-417.

[42] Panek, P., Lipinski, M., & Czternastek, H. (2000). Porous Silicon Layer as Antireflection Coating in Solar Cells. *Opto-Electronics Review*, 8(1), 57-59.

[43] Chaoui, R., & Messaoud, A. (2007). Screen-Printed Solar Cells with Simultaneous Formation of Porous Silicon Selective Emitter and Antireflection Coating. *Desalination*, 209, 118-121.

[44] Remache, L., Mahdjoub, A., Fourmond, E., Dupuis, J., & Lemiti, M. (2010). Design of porous silicon/PECVD $SiO_x$ antireflection coatings for silicon solar cells. *International Conference on Renewable Energies and Power Quality (ICREPQ-2010)*, 23-25 March, Granada.

[45] Aziz, W., Ramizy, A., Ibrahim, K., Omar, K., & Hassan, Z. (2009). Effect the Orientation of Porous Silicon on Solar Cell Performance. *Optoelectronics and Advances Materials*, 3(12), 1368-1370.

[46] Bastide, S., Albu-Yaron, A., Strehlke, S., & Levy-Clement, C. (1999). *Formation and Characterization of Porous Silicon Layers for Application in Multicrystalline Silicon Solar Cells*, 57, 393-417.

[47] Ramizy, A., Aziz, W., Hasan, Z., Omar, K., & Ibragim, K. (2000). The Effect of Porosity on the Properties of Silicon Solar Cells. *Microelectronic International*, 27(2), 117-120.

[48] Ramizy, A., Hassan, Z., Omar, K., Al-Douri, Y., & Mahdi, M. (2001). New Optical Features to Enhance Solar Cell Performance Based on Porous Silicon Surfaces. *Applied Surface Science*, 257, 6112-6117.

[49] Ludemann, R., Damiani, B., & Rohatgi, A. (2000). Novel Processing of Solar Cells with Porous Silicon Texturing. *In: Proceedings of the 28-th IEEE Photovoltaic Specialists Conference*, 15-22 September, Anchorage, Alaska, 299-301.

[50] Hilali, M., Damiani, B., & Rohatgi, A. Lifetime Enhancement During Processing of Porous Silicon Cells. http://smartech.gatech.edu/jspui/bitstream.

[51] Panek, P. (2004). Effect of Macroporous Silicon Layer on Opto-Electrical Parameters of Multicrystalline Silicon Solar Cells. *Opto-Electronics Review*, 12(1), 45-48.

[52] Hirscheman, K., Tsybeskov, L., Duttagupta, S., & Fauchet, P. (1996). Silicon-based Visible Light-Emitting Devices Integrated into Microelectronic Circuits. *Nature*, 384, 338-340.

[53] Vinod, P. (2007). Porous Silicon and Aluminum Co-gettering Experiment in p-Type Multicrystalline Silicon Substrates. *Science and Technology of Advanced Materials*, 8, 231-236.

[54] Khedher, N., Hajji, M., Ben Jaballah, A., & Quertani, B. (2005). Gettering of Impurities from Crystalline Silicon by Phosphorus Diffusion Using a Porous Silicon Layer. *Solar Energy Materials & Solar Cells*, 87(1-4), 605-611.

[55] Solanski, C., Bilyalov, R., Poortmans, J., Nijs, J., & Mertens, R. (2004). Porous Silicon Layer Transfer Processes for Solar Cells. *Solar Energy Materials and Solar Cells*, 83, 101-113.

[56] Petermann, H., Zielke, D., Schmidt, J., Haase, F., Rojas, E., & Brendel, R. (2012). Efficient and 43μm-Thick Crystalline Si Solar Cell from Layer Transfer Using Porous Silicon. *Progress in Photovoltaic: Research and Application*, 20(4), 1-5.

Chapter 3

# Influence of Surface Treatment on the Conversion Efficiency of Thin-Film a-Si:H Solar Cells on a Stainless Steel Substrate

Wen-Cheng Ke and Shuo-Jen Lee

Additional information is available at the end of the chapter

http://dx.doi.org/10.5772/51531

## 1. Introduction

Over the past decade, hydrogenated amorphous silicon (a-Si:H) thin-film solar cells have emerged as a viable substitute for solid-state silicon solar cells. The a-Si:H thin-film solar cells gained importance primarily due to their low production cost, and eco-friendly nature [1-3]. However, these cells have the inherent disadvantage of using glass as a substrate material, which makes the cells unsuitable for use in a round shaped product, are heavy and have a high material cost. Replacing the glass substrate with a stainless steel (SS) substrate makes it possible to fabricate lightweight, thin, and low-cost a-Si:H thin-film solar cells using roll-to-roll mass production [4,5]. However, the surface morphology of a SS substrate is of poorer quality than that of the glass substrate. For the past several years flexible solar cells fabricated on a stainless steel substrate are being widely used for the building of integrated photovoltaics (BIPVs). Stainless steel has many advantages, such as low cost, high extension, ease of preparing etc. Thus it was commonly believed that the wide application of BIPVs especially rooftop applications, would be the biggest market for flexible PV technology [1-4], especially since these flexible products are very light, and quick and easy to install. Indeed, BIPV products did see a rapid growth in recent years, with more companies going into production. However, the main challenge of BIPVs remains. The question of how to improve the conversion efficiency has not been resolved.

The main limitation of thin-film solar cell efficiency is the long absorption length of the long wavelength photons and the thinness of the absorbing layer. The absorption length of a-Si:H with a bandgap of 1.6 eV, for the red and infrared solar photons, exceeds 1 μm and 100 μm, respectively [6,7]. In addition, for a-Si:H the hole diffusion length is 300–400 nm, which lim-

its the solar cell absorber layer thickness to less than the hole diffusion length [8]. This makes it exceedingly difficult to harvest these photons since the absorber thickness of a p-i-n single junction solar cell is limited to only a few hundred nanometers for efficient carrier collection. Thus, increasing the light absorption is essential for the design of thin-film solar cells [9–12]. Maximum light absorption is achieved using several different techniques including back-reflector or light trapping configurations. Enhanced light-trapping in thin-film solar cells is typically achieved by a textured oxide layer on the metal back-reflector that scatters light within the absorbing layer and increases the optical path-length of the solar photons. In our latest research [13,14], we fabricated a textured SS substrate using the photolithography method to increase the light scattering. Unfortunately, the electrical properties of a-Si:H thin-film solar cells deposited on these micro-size textured SS substrates are not stable. There are many deep etching pits on the textured SS substrate surface, resulting in a non-uniform thickness of the a-Si:H thin-film deposited on the whole textured SS substrate surface. This non-uniform coverage of the a-si:H layer on the textured 304 SS usually fails to perform its function in the thin-film solar cells. Thus, the surface morphology of the SS substrate plays an important role in achieving the stable electrical properties of the a-Si:H thin-film solar cells.

In addition, it is well known that defects in thin-film solar cells increase the series resistance (Rs) and decrease the shunt resistance (Rsh), resulting in a decreased open voltage ($V_{OC}$) and short current density ($J_{sc}$) of the thin-film solar cells. Although a number of investigations were carried out to study the properties of the defects in crystalline Si solar cells [15,16], a detailed understanding of a-Si:H thin-film solar cells is still lacking. Iron (Fe), one of the most common impurities in crystalline Si solar cell materials, has a detrimental effect on the minority carrier lifetime due to the defect states introduced by Fe and its complexes with acceptors in the band gap of silicon [17,18]. It has been suggested that diffusion of detrimental elements, such as Fe from stainless steel, into the a-Si:H layer as a result of high temperatures during the a-Si:H processing, deteriorate the cell's efficiency. In this study, a thick (exceeding 2-μm) metal Mo buffer layer is used to reduce the diffusion of Fe impurities from the 304 SS substrate. The influence of the Fe impurities on the cell's performance was investigated carefully. Additionally, Electro-polishing (EP) and Electrical chemical mechanical polish (ECMP) processes have been used to improve the surface roughness of the stainless steels, and make them more suitable as a substrate for a-Si:H thin-film solar cells. The EP and ECMP dissolve metal ions electrochemically by applying an anodic potential on the SS substrate surface in an aqueous electrolyte [19-22]. It should be noted that the ECMP also removes a passivation layer by the mechanical abrasion of the polishing pad and the abrasives in the electrolyte. After the EP or ECMP process is finished, the SS substrate surface forms a hard and dense Cr-rich passivation layer which is expected to block the diffusion of metal impurities from the SS substrate into a-Si:H layer. We carefully investigated the conversion efficiency of a-Si:H thin-film solar cells based on the surface morphology and impurity diffusion of 304 SS substrate treated by the EP and ECMP processes.

http://dx.doi.org/10.5772/51531

## 2. Surface-treated process of 304 stainless steel substrate

### 2.1. Electro-polishing process

In the 1980's, most of the research reports indicated that the EP process of the stainless steel substrate began by forming a viscous layer on the substrate surface resulting in the formation of a passivation layer. Generally, the high spike has a higher dissolve velocity in the viscous layer providing the initial polish of the stainless steel substrate. Once the EP process has ran for a long enough time, a dense passivation layer or metal-rich oxidation layer will form at the bottom of the viscous layer on the surface of the substrate resulting in a smooth surface. The viscous layer formation mechanism in the EP pricess is a key parameter for achieving a smooth surface stainless steel substrate. There are some conditions, such as solution convection, ion diffusion, electrical current distribution and electron migration will determine the EP results. Thus, the applying voltage, current, gap between the anode and cathode, reaction time, cathode design must be controlled carefully. The schematic diagrams of the EP system are shown in Fig. 1. In this study, the 304 stainless steel substrate with thickness of 1 mm was clipped by the anode clamp. The stainless steel net was used as the cathode plate. The important parameter lists of the EP process are listed in Table 1. After the EP process, the mirror-like surface of the 304 stainless steel substrate can be achieved (Fig. 2).

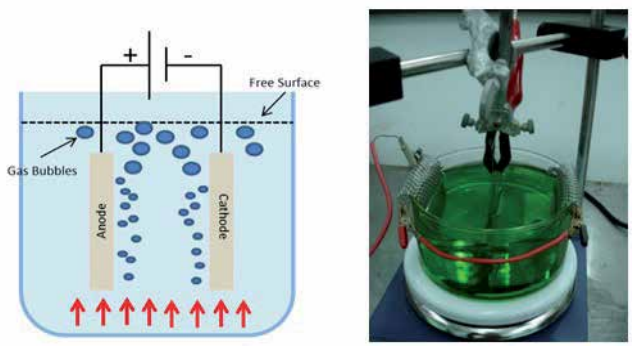


**Figure 1.** The schematic diagram of the EP system.

| EP process | Parameters |
|---|---|
| Reaction time | 1 min |
| Voltage/current | 3.3 V/4.5 A |
| Temperature | 70˚C |
| Electrolyte | $C_3H_5(OH)_3$:$H_2O$ = 1:1<br>$H_2SO_4$:$H_3PO_4$ = 0.29 |

**Table 1.** The key parameters of the EP process.

**Figure 2.** The image of the mirror-like 304 stainless steel substrate after the EP process.

### 2.2. Electrical chemical mechanical polish process

The schematic diagrams of the ECMP system are shown in Fig. 3 and Fig. 4. The ECMP process consists of both electrochemical and mechanical polishing mechanisms, electrolysis and physical polishing, to repair the irregular surface morphology of the 304 SS substrate. In addition, the mechanical friction between the polishing pad and the 304 SS substrate induces an interactive force that removes the surface oxidation layer or passivation layer that forms during the electrolysis process. It should be noted that no peeling force is generated during the ECMP process, and thus there is no need to consider any mechanical deformation of the substrate. The ECMP process base on the fundamental electrochemical reaction terms as following:

Anode chemical reaction:

$$M^{+} + OH^{-} \rightarrow \grave{e}MOH \tag{1}$$

Cathode chemical reaction:

$$2H^{+} \rightarrow \grave{e}H_{2} \tag{2}$$

The important parameters of ECMP process are described in the list below.

http://dx.doi.org/10.5772/51531

1. The 304 stainless steel substrate was first cleaned by acetone and DI water in order to remove the oil and particle contaminant.
2. Polishing solution with 50g of 1μm $Al_2O_3$ powder in 0.5 L DI water.
3. Electrolyte solution ($NaNO_3$) with concentration of 3 wt%.

The other important parameter lists of the ECMP process are listed in Table 2. In Fig. 5, the mirror-like surface of the 304 stainless steel substrate can be achieved after the ECMP process.

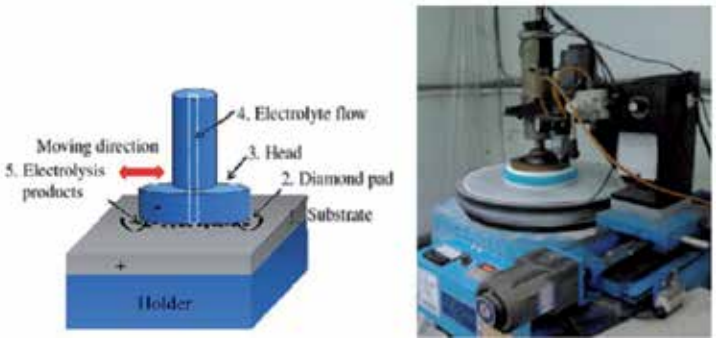


**Figure 3.** The schematic diagram of the ECMP system.

## 3. Effect of Mo blocking layer on the conversion efficiency of a-Si:H solar cells

### 3.1. Experimental details

In this study, a series of p-i-n solar cells were deposited on a 304 SS substrate by high frequency plasma enhanced chemical vapor deposition (HF-PECVD), in an ultrahigh-vacuum, single-chamber, load-locked system at a constant temperature of 200 °C. The

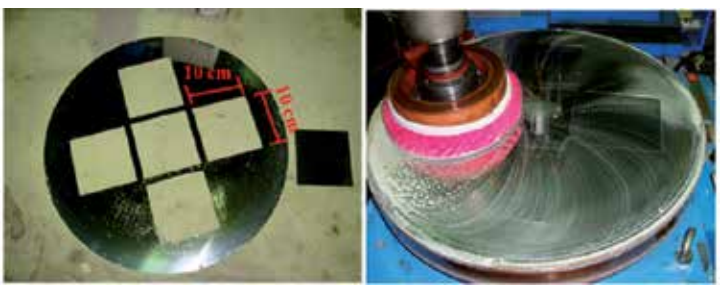

**Figure 4.** The sample holder and polishing process image of the ECMP system.

| ECMP process | Parameters |
|---|---|
| Polishing time | 20 min |
| Voltage/current | 7 V/1 A |
| Rotation speed (anode holder) | 30 rpm |
| Rotati speed (Cathode head) | 40 rpm |

**Table 2.** The key parameters of the ECMP process.

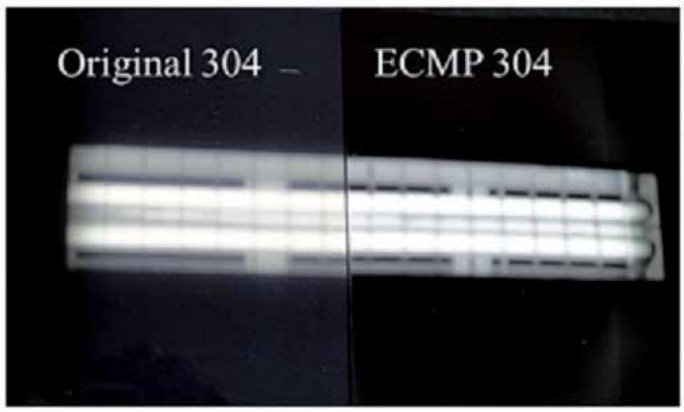


**Figure 5.** The image of the mirror-like 304 stainless steel substrate after the ECMP process.

thickness of the p-i-n layers in the solar cell structure were 10, 300, and 20 nm respectively. In order to avoid diffusion by Fe impurities diffusing from the 304 SS substrate into Si solar cells and to study its influence on cell efficiency (see Fig. 6), we designed a series of cell structures including Ag/AZO/n-i-p/SS, Ag/AZO/n-i-p/Ag/SS, Ag/AZO/n-i-p/Ag/0.5-μm-thick Mo/SS, and Ag/AZO/n-i-p/Ag/2.0-μm-thick Mo/SS. It was crucial that no alumina-zinc-oxide (AZO) layer would grow between the 304 SS substrate and the a-Si:H cell so that we could clearly observe the change in cell performance as a result of preventing the diffusion of Fe impurities. All metal and transparent conductive oxide layers in the structure of the cells were deposited by radio frequency (RF) magnetron sputtering. The thickness of the back reflection metal Ag and AZO layers were 200 and 150 nm, respectively. It should be noted that the metal Mo layers, 0.5-μm-thick and 2-μm-thick were deposited on a 304 SS substrate by adjusting the sputtering power to 100 W and 500 W, respectively. The Ar gas flow rate was kept at 30 sccm, and the deposition time was kept at 30 min. In general, high sputtering power can achieve a higher metal deposition rate. The solar cell performance was determined using a calibrated AM 1.5G solar simulator under illumination, and operating at a light intensity of 100 mW/cm$^2$. The current-voltage (I-V) curves were obtained using the Keithley 2400 SourceMeter. The optical properties of the raw 304 SS substrate and the 304 SS

http://dx.doi.org/10.5772/51531

substrate coated with Ag and Ag/Mo films were measured by a UV-visible(Vis)-near IR (NIR) spectrophotometer (Perkin Elmer Lambda 750s) in the 400-700 nm wavelength range. The samples were measured with a secondary ion mass spectroscope (SIMS) in order to analyze the diffusion of Fe impurities from the 304 SS substrate into the cell structure.

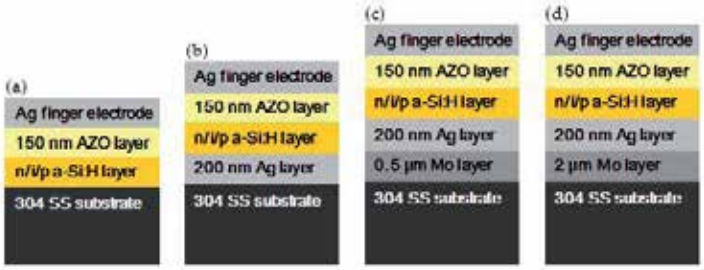


**Figure 6.** Cross-sectional schematic diagrams for the samples of this study.

### 3.2. Morphological properties

Figure 7 shows the SEM images of a metal Mo buffer layer with varying thickness on a 304 SS substrate. In Fig. 7(a), the small size of the Mo grains and the grain direction are a random distribution when the sputtering power is low (i.e. low deposition rate = 0.28 nm/sec). In contrast, the long ridge and the ordered arrangement of the large Mo grains was achieved by a high-power sputtering process (i.e. deposition rate = 1.11 nm/sec). In addition, the grain boundary decreased due to the increased merging of the Mo grains into the high-power sputtered sample.

### 3.3. Optical properties

The total reflection (TR) and the diffuse reflection (DR) rates versus the wavelength curves for the raw 304 SS substrate, Ag/304 SS substrate, 0.5-μm-thick Mo/304 SS substrate and 2-μm-thick Mo/304 SS substrate are shown in Fig. 8. The TR rate is defined as the ratio of the reflection light to the incident light. When the incident light angle is zero, any reflection light with an angle larger than 8° over the incident light is called the DR rate. The TR and DR rates are very important indexes for monitoring the light-trapping in thin-film solar cells. In general, high TR and DR rates indicate that the light path can be increased in the cell structure. Thus, scattered light within the absorbing layer increases the optical path length of the solar photons. The TR and DR rates of the Mo coating on the 304 SS substrate, whether being a 0.5-μm-thick or a 2-μm-thick Mo buffer layer were smaller than that of the raw 304 SS substrate. In addition, the TR and DR rates showed a slightly decreasing trend when the Mo buffer layer thickness increased from 0.5 μm to 2 μm. The cross-sectional SEM images in Figs. 7(c) and (d), show the roughened surface (large grain size and deep V-shaped trench) of the 2-μm-thick Mo buffer layer, which is believed to be the main reason for the low TR and DR rates of the thick Mo buffer layer. It was also found that the TR/DR rate at a

wavelength of 550 nm increased from 54.3%/7.7% of a raw 304 SS substrate to 84.2%/11.4% for the Ag coated 304 SS substrate. Previous work performed by our group showed that the surface texturing of different types of SS substrates after coating with Ag film revealed high TR and DR rates [13-14]. Coating an Ag film on the 304 SS substrate as a back reflector can help light absorption and further improve cell efficiency.

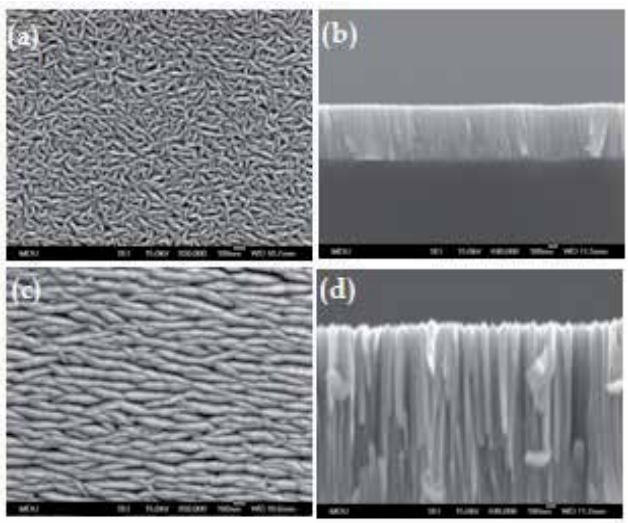


**Figure 7.** SEM images of the Mo buffer layer on a 304 SS substrate with a thickness of (a) 0.5-μm (b) 2-μm and cross sectional images of the Mo buffer layer with (c) 0.5-μm (d) 2-μm.

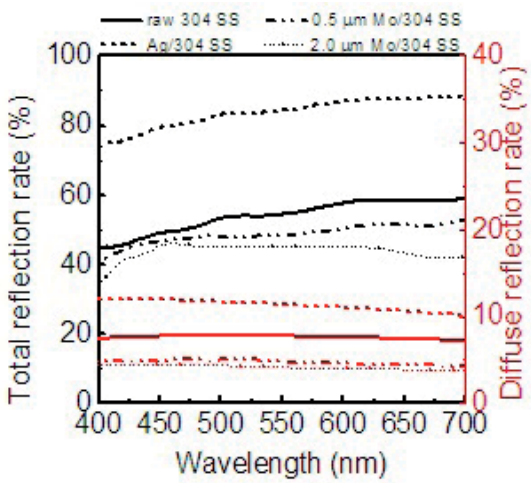


**Figure 8.** The TR and DR rates versus the wavelength curves of all the studied cells.

http://dx.doi.org/10.5772/51531

### 3.4. Current-voltage characteristics

Figure 9 shows the light J-V characteristics of all studied cells. The cell structure of Ag/AZO/n-i-p/Ag/SS has poor performances with η=0.78%, FF = 29%, $V_{oc}$ = 0.44 V and $J_{sc}$ = 6.18 mA/cm$^2$. This poor cell efficiency may be due to several reasons, including incomplete absorption of incident light, and the presence of intrinsic or processing-induced defects. The light absorption of thin film solar cells can be enhanced by using the surface textured 304 SS substrate as a back-reflector. Since the DR and TR rates of the raw 304 SS substrate is low, a 200 nm thick Ag film was coated on the 304 SS substrate as a back-reflector. In Fig. 8, the increased TR and DR rates of the Ag coated 304 SS substrate was helpful for increasing the $V_{oc}$ and $J_{sc}$ of the a-Si:H thin film solar cell. However, the cell conversion efficiency of 1.3% is still too low for a-Si:H thin film solar cells, and the increased cell efficiency by using a metal Ag back-reflector is limited. On the other hand, the Fe impurities or iron-boron complex are deep-level defects in Si [23,24], and are known to have serious detrimental effects on the efficiency of crystalline Si solar cells. Thus, we suggest that these Fe impurities diffused from the 304 SS substrate into the a-Si:H thin film solar cells also form deep-level defects that deteriorates the cell's performance. A detailed and comprehensive understanding is necessary to address this process. In addition, a diffusion blocking layer is necessary to prevent the Fe impurities diffused from the 304 SS substrate to enter the a-Si:H thin film solar cells.

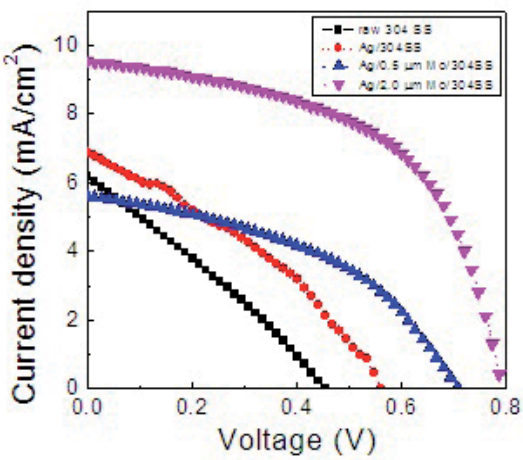


**Figure 9.** The J-V characteristics for all the studied cells.

### 3.5. Impurity diffusion in a-Si:H films

In order to study this Fe diffusion, we performed a SIMS analysis. Figure 10 shows the SIMS depth profile of the p-i-n a-Si:H thin film cells on the Ag/ 304 SS substrate and the Ag/2-μm-thick Mo/304 SS substrate. In Fig. 10(a), the Fe atom was detected in the whole p-i-n cell structure. In particular, the maximum signal intensity of the Fe atom was found at a depth of 500 nm in the Ag/AZO/n-i-p/Ag/SS substrate sample. The driving force of the Fe diffusion

from the 304 SS substrate into the p-i-n a-Si:H solar cells was believed to be due to the high temperature of the PECVD a-Si:H deposition process. The 200 nm Ag back-reflector can't prevent the Fe diffusion from the 304 SS substrate. In Fig. 10(b), the Fe atom signal intensity from the 304 SS substrate decreased with the increase in the thickness of the Mo buffer layer. In addition, almost no Fe atoms were detected in the p-i-n a-Si:H solar cells. It should be mentioned that few Fe atoms can diffuse through the 0.5-μm-thick Mo film into the a-Si:H layer. In Fig. 10(c), the cross-sectional SEM image indicates that the low sputtering rate of the Mo film has a dense columnar structure. High density, thin Mo films may be useful to suppress the diffusion of Fe atoms. However, we must consider the time-cost estimation. A 2-μm thick Mo film deposited at the low sputtering rate (0.28 nm/sec) requires 2 hrs, and at the high sputtering rate (1.11 nm/sec) it only requires 30 min. In addition, a 2-μm thick Mo film deposited at the high sputtering rate can effectively suppress the diffusion of Fe atoms into the a-Si:H layer. Thus, the optimal deposition condition for the Mo buffer layer is believed to be a thicker layer deposited at a high sputtering rate.

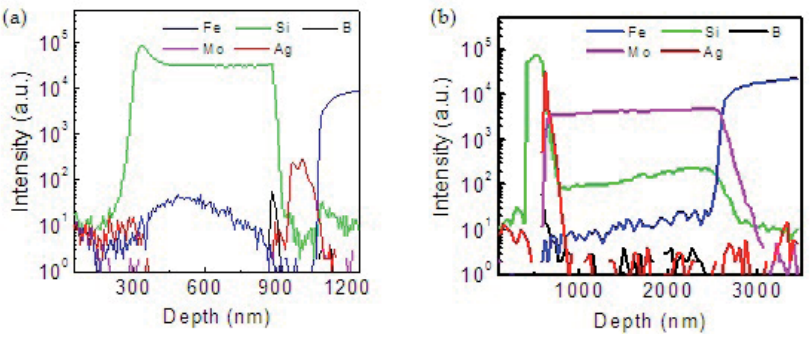


**Figure 10.** The SIMS depth profile of a-Si:H solar cells grown on (a) an Ag/304 SS substrate and (b) an Ag/2-μm Mo/304 SS substrate.

### 3.6. a-Si:H thin-film solar cells performance

Table 3 summarizes the relative cell performance of all studied cells. The best cell structure (i.e. Ag/AZO/n-i-p/Ag/2.0-μm-thick Mo/ SS) has a performance of η=4.12%, FF = 55%, $V_{oc}$ = 0.78V and $J_{sc}$ = 9.54 mA/cm$^2$. The $R_{sh}$ was 119.1 Ω and 290.6 Ω for a-Si:H solar cell on the Ag coated 304 SS substrate and the Ag/2-μm-thick Mo film/304 SS substrate, respectively. In addition, the series resistance ($R_s$) of the Ag/AZO/n-i-p/Ag/ SS cell decreased from 53.3 Ω to 16.7 Ω for the Ag/AZO/n-i-p/Ag/2.0-μm-thick Mo/ SS cell. There are many reasons for the series resistance, including the resistance of the semiconductor bulk, contacts, interconnections, etc. Shunt resistance is believed to be caused mainly by lattice defects or leakage current at the edge of the solar cell. Based on the SIMS results, we believe that the high conversion efficiency was due to the effective prevention of the diffusion of Fe impurities. Fe impurities in the Si thin films will form deep-level defects that degenerate the junction interface in each layer of the cell structure thereby decreasing the $R_{sh}$ of the solar cell. In addition, the Fe induced deep-level defects will increase the resistivity of the intrinsic a-Si:H layer which may raise the Rs. The high $V_{oc}$ and $J_{sc}$

http://dx.doi.org/10.5772/51531

were due to an increase of Rsh and a decrease of Rs as a result of coating a thick Mo buffer layer on the 304 SS substrate. This effectively prevented Fe impurities from diffusing into the a-Si:H solar cells thereby improving the conversion efficiency of the solar cells. The improvement of the conversion efficiency of a-Si:H thin film solar cells on a 304 SS substrate by using a Mo buffer layer is still an open question. Some possible reasons might explain the improvement in cell efficiency by using a thick Mo buffer layer. For example, a thick Mo buffer layer decreases the surface roughness of the raw 304 SS substrate. The decrease in interface defect density of the a-Si:H thin-film solar cells due to the improved interface flatness results in an increased conversion efficiency as the Mo buffer layer thickness increases. However, we have to keep in mind that the thermal expansion coefficients of Si, Mo and stainless steel are $2.5\times10^{-6}$/K, $5.2\times10^{-6}$/K and $1.4\times10^{-5}$/K, respectively. Consequently, the a-Si:H layer grown directly on the stainless steel substrate will induce structural defects because of the severe mismatch in thermal expansion coefficients. The low thermal expansion coefficient of Mo film onto a stainless steel substrate can minimize the mismatch in thermal expansion coefficients between the a-Si:H layer and the 304 SS substrate. The density of the structural defects in the a-Si:H thin-film solar cells can be reduced, resulting in a high conversion efficiency of thin-film a-Si:H solar cells on the 304 SS substrate. More detailed experiments must be carried out in the future to allow us to understand the precise mechanism involved in improving cell efficiency by using a Mo buffer layer.

| | $V_{oc}$ (V) | $J_{sc}$ (mA/cm²) | P (mW) | FF (%) | η (%) | $R_s$ (Ω) | $R_{sh}$ (Ω) |
|---|---|---|---|---|---|---|---|
| Raw 304SS | 0.44 | 6.18 | 0.78 | 29 | 0.78 | 58.1 | 82.5 |
| Ag/304SS | 0.54 | 6.88 | 1.3 | 35 | 1.3 | 53.3 | 119.1 |
| Ag/0.5 μm Mo/ 304SS | 0.7 | 5.6 | 1.75 | 44 | 1.75 | 49.1 | 286.3 |
| Ag/2 μm Mo/ 304SS | 0.78 | 9.54 | 4.12 | 55 | 4.12 | 16.7 | 290.6 |

**Table 3.** AM 1.5G output parameters of the a-Si:Hthin-film solar cells.

## 4. Surface treatment of the 304 stainless steel substrte to improve the conversion efficiency of a-Si:H solar cells

### 4.1. Experimental details

The a-Si:H thin-film solar cells were grown on 1-mm-thick 304 SS substrates by high-frequency plasma enhanced chemical vapor deposition (HF-PECVD) in an ultrahigh-vacuum, single-chamber, load-locked system at a constant temperature of 200 °C. The cell structures (see Fig. 11), consisting of Ag finger electrode/AZO/n-i-p/Ag/304 SS substrates were used to study the cells' performance on the EP and ECMP processed 304 SS substrate. The 60 nm Ag layer was deposited on the 304 SS substrate as a back reflector layer and back contact by radio frequency (RF) sputtering. The thickness of the n-i-p layers in the solar cell structure were 20, 300 and 10 nm, respectively. The 150-nm-thick AZO films were then grown on the

a-Si:H active layer by RF-sputtering. The EP process is an anodic dissolution of the surface polishing process. The 304 SS substrate was immersed in the electrolyte, and then a current of 4.5 A and voltage of 3.3 V was applied for 1 minute. For the ECMP process, the 304 SS substrate was treated with 3%wt $NaNO_3$ solution and 1 μm diameter alumina powders. The formation of the passivation layer on the 304 SS substrate during the initial ECMP process led to spikes on the sample surface that were readily removed by powder polishing. The ECMP process required roughly 5 minutes to achieve a mirror-like surface on the 304 SS substrate. The solar cell performance was measured using a calibrated AM 1.5G solar simulator under illumination, and operating at a light intensity of 100 $mW/cm^2$. The current density-voltage (J-V) curves were obtained using the Keithley 2400 Source Meter. The optical properties of the untreated 304 SS substrate and the EM/ECMP processed 304 SS substrate were measured by a UV-visible(Vis)-near IR (NIR) spectrophotometer (Perkin Elmer Lambda 750s) in the 300-1000 nm wavelength range. The samples were measured with a secondary ion mass spectroscope (SIMS) in order to analyze the diffusion of iron (Fe) and chromium (Cr) impurities from the 304 SS substrate into the cell structure.

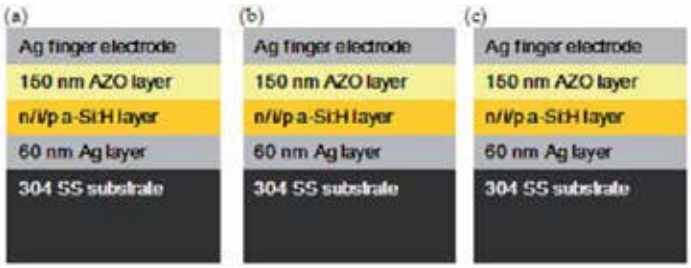


**Figure 11.** Cross-sectional schematic diagrams for the samples of this study.

### 4.2. Morphological properties

Fig. 12 shows the SEM and optical microscopy images of the untreated 304 SS substrate and the 304 SS substrate treated by EP and ECMP process. Fig. 12(a), shows many voids and scratches on the untreated 340 SS substrate surface. The surface roughness measured by 3D confocal microscopy, shows an average roughness (Ra) of ~ 330 nm for a surface area of 300×300 $\mu m^2$ for the untreated 304 SS substrate. Fig. 12(b), shows that the voids and scratches on the surface of the 304 SS substrate can be readily removed after the EP process. The smooth surface of the 304 SS substrate by means of the EP process was accomplished using the anode electrolysis mechanism that places the 304 SS substrate in the electrolyte and then applies the optimal voltage and current between the anode and the cathode electrode. In the 1980's, most of the research reports indicated that the EP process of the stainless steel substrate began by forming a viscous layer on the substrate surface resulting in the formation of a passivation layer. Generally, the high spike has a higher dissolve velocity in the viscous layer providing the initial polish of the stainless steel substrate. Once the EP process has ran for a long enough time, a dense passivation layer or metal-rich oxidation layer will form at

http://dx.doi.org/10.5772/51531

the bottom of the viscous layer on the surface of the substrate resulting in a smooth surface. However, the shortcoming of the EP process is that some small scratches and pin holes may remain that it cannot remove completely. Thus, this study used the ECMP process in an attempt to achieve a smoother surface of the 304 SS substrate. The ECMP process consists of both electrochemical and mechanical polishing mechanisms, electrolysis and physical polishing, to repair the irregular surface morphology of the 304 SS substrate. In addition, the mechanical friction between the polishing pad and the 304 SS substrate induces an interactive force that removes the surface oxidation layer or passivation layer that forms during the electrolysis process. It should be noted that no peeling force is generated during the ECMP process, and thus there is no need to consider any mechanical deformation of the substrate. Our experimental results indicated that the surface roughness of the 304 SS substrate can be reduced to 22 nm after having been treated by the ECMP process, as shown in Fig. 12(c).

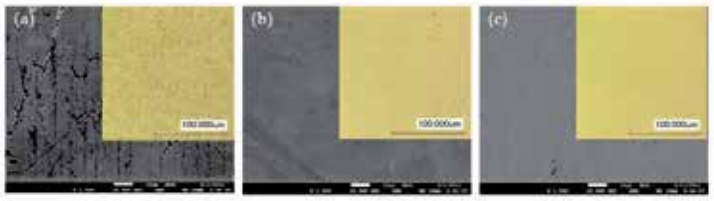


**Figure 12.** SEM and OM images of the (a) untreated 304 SS substrate, (b) EP, and (c) ECMP processed 304 SS substrate.

### 4.3. Optical properties

The effect of the surface morphology of the 304 SS substrate, treated by the EP and ECMP processes, on the light reflection properties were measured with a UV-visible-nIR spectrometer in the wavelength range of 300-1000 nm. As shown in Fig. 13, the average total reflection (TR) rate in the wavelength range of 300-1000 nm increased from 65.6 % for the untreated 304 SS substrate to 74.2 % and 73.7% respectively for the EP and ECMP processed 304 SS substrate. The average diffuse reflection (DR) rate was 3.8% for the untreated 304 SS substrate and decreased to 0.9% and 0.8% for the EP and ECMP processed 304 SS substrate, respectively. The high TR rate and low DR rate of the EP and ECMP processed 304 SS substrate were consistent with the SEM results. Thus, the EP and ECMP processes can achieve a smooth surface of the 304 SS substrate.

### 4.4. Current-voltage characteristics

Figure 14 shows the light current density and voltage (J-V) characteristics of all cells studied. The cell structure of the Ag finger electrode/AZO/n-i-p/Ag/untreated 304 SS substrate performed poorly with $\eta$=1.7 %, FF = 0.39, $J_{sc}$ = 5.1 mA/cm$^2$, and $V_{oc}$ = 0.79 V. Compared to the electrical properties of the a-Si:H thin-film solar cells grown on the glass substrate, the $J_{sc}$ (i.e. ~ 15 mA/cm$^2$) is a key electrical property that needs to be improve in order to achieve a high con-

version efficiency of the a-Si:H thin-film solar cells on the 304 SS substrate. We first considered the incomplete absorption of incident light by the a-Si:H layer. It is known that the light absorption of thin-film solar cells can be enhanced by using a high reflectance metal as a back-reflector. Fig. 13 shows that the increased TR rate of the EP and ECMP processed 304 SS substrate was helpful to increase the $J_{SC}$ of the a-Si:H thin-film solar cells. Compared with the a-Si:H thin-film solar cells on the untreated 304 SS substrate, the $J_{sc}$ can be increased by about 35% and 43% for cells on EP and ECMP processed 304 SS substrates, respectively.

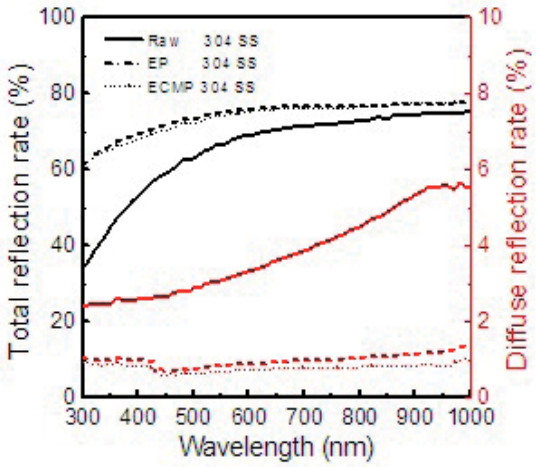


**Figure 13.** The TR and DR rates versus the wavelength curves of all the studied SS substrate samples.

It is worth noting that the difference of the average TR rates between the EP and ECMP processed 304 SS substrate was about 0.5%. However, the $J_{sc}$ increased to 7.9 mA/cm$^2$ for cells on the EP processed 304 SS substrate, and to 9.0 mA/cm$^2$ for cells on the ECMP processed 304 SS substrate. Thus, another way to improve the $J_{sc}$ of cells was associated with the intrinsic or processing-induced defects. In our previous study, we found that the Fe impurities that diffused from the 304 SS substrate into the a-Si:H layer deteriorated the cells' performance. The Fe impurities of the iron-boron complex are deep-level defects in Si, and are known to have serious detrimental effects on the efficiency of crystalline Si solar cells [25,26]. Thus, we believe that the impurities diffused from the 304 SS substrate into the a-Si:H thin-film solar cells form deep-level defects that deteriorate the cell's performance. A detailed and comprehensive understanding of the process is required to address this issue.

### 4.5. Impurity diffusion in a-Si:H films

In order to study the diffusion of impurities from the 304 SS substrate, we performed a SIMS depth profile analysis of the cell structure. Fig. 15 shows the SIMS depth profile of the p-i-n a-Si:H thin-film solar cells on the Ag/untreated 304 SS substrate, the Ag/EP processed 304 SS substrate and the Ag/ECMP processed 304 SS substrate. In Fig. 15(a), the Fe and Cr atoms

http://dx.doi.org/10.5772/51531

were detected in the whole p-i-n cell structure. The driving force of the Fe and Cr atoms diffusion from 304 SS substrate into the p-i-n a-Si:H solar cells was believed to be due to the high temperature of the PECVD a-Si:H layer deposition process. Fig. 15(b) shows that the intensity of the Fe and Cr atoms signals from the 304 SS substrate can be decreased by three orders of magnitude in the p-i-n a-Si:H layers. The dense Cr-rich passivation layer formed on the surface of the 304 SS substrate by the EP process is believed to act as a blocking layer to suppress the continual diffusion of Fe and Cr atoms from the 304 SS substrate during the high-temperature PECVD deposition process. The passivation layer can be a thin layer of oxidized metal that forms during the EP process. However, there remain some small scratches on the EP processed 304 SS substrate (see Fig. 12(b)) that provide the impurities diffusion with a channel into the a-Si:H layer. Thus, a small amount of Cr and Fe impurities can still diffuse into the a-Si:H layer. On the other hand, Fig. 15(c) shows that almost no Cr atoms are detected in the p-i-n a-Si:H layer. The ECMP process includes a mechanical polishing mechanism, and the mechanical friction between the polishing pad and the 304 SS substrate induces an interactive force that removes the Cr-rich passivation layer which formed during the electrolysis. Thus, we believe that the thickness of the Cr-rich passivation layer or oxidation layer on the ECMP processed 304 SS substrate is thinner than that of the EP processed 304 SS substrate. This thinner Cr-rich passivation layer may allow Fe atoms to diffuse into the a-Si:H layer. However, the dense and hard Cr-rich passivation layer on the 304 SS substrate which is generated during the electrolysis process will suppress the Cr atoms of the 304 SS substrate diffused into the a-Si:H layer.

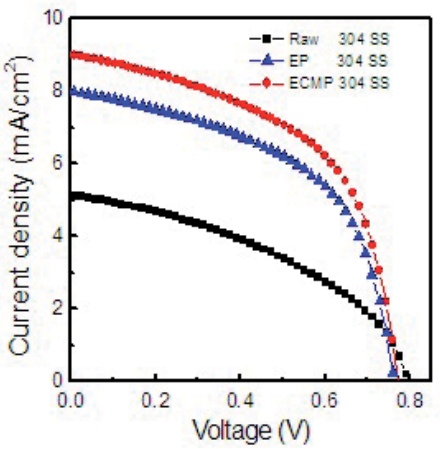


**Figure 14.** The J-V characteristics for all the studies cells.

### 4.6. a-Si:H thin-film solar cells performance

Table 4 summarizes the relative cell performance of all cells studied. The best cell for the a-Si:H grown on the ECMP processed 304 SS substrate had a performance of $\eta$ =3.7 %, FF = 0.52, $J_{sc}$ = 9.0 mA/cm$^2$, and $V_{oc}$ = 0.78 V. The $R_{sh}$ was 923 Ω and 1269 Ω for a-Si:H solar cells

grown on the untreated 304 SS substrate and ECMP processed 304 SS substrate, respectively. In addition, the series resistance ($R_s$) of the untreated 304 SS substrate cell decreased from 136 Ω to 72 Ω for the ECMP processed 304 SS substrate cell. There are many reasons for the series resistance, including the resistance of the semiconductor bulk, contacts, interconnections, etc. The shunt resistance is believed to be caused mainly by lattice defects or leakage current at the edge of the solar cell. Based on the SIMS results, we believe that the high conversion efficiency was due to the effective prevention of the diffusion of Cr and Fe impurities. The Cr and Fe impurities in the Si thin films form deep-level defects that degenerate the junction interface in each layer of the cell structure thereby decreasing the $R_{sh}$ of the solar cell. In addition, the Cr and Fe induced deep-level defects increased the resistivity of the intrinsic a-Si:H layer which could increase the Rs. The high $J_{sc}$ was due to an increase in $R_{sh}$ and a decrease in $R_s$ as a result of EP and ECMP processed 304 SS substrate. These processes effectively prevented Cr and Fe impurities from diffusing into the a-Si:H solar cells thereby improving the conversion efficiency of the solar cells.

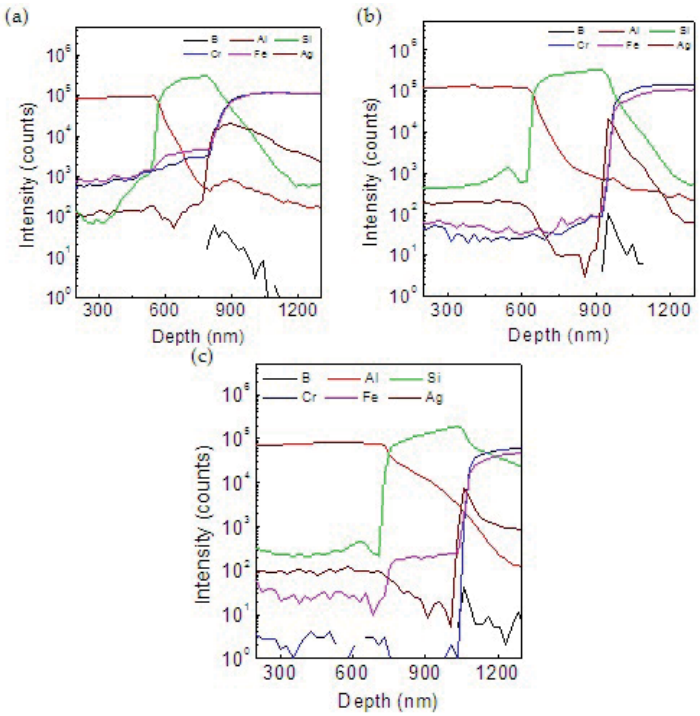


**Figure 15.** The SIMS depth profile of a-Si:H thin-film solar cells grown on (a) untreated 304 SS substrate, (b) EP and (c) ECMP processed 304 SS substrate.

In addition, the surface morphology and the diffusion of impurities into the 304 SS substrate influence the electrical performance of the a-Si:H thin-film solar cells. We must also keep in mind that the thermal expansion coefficients of Si, Ag and stainless steel are $2.5\times10^{-6}$/K, $1.95\times10^{-5}$/K and $1.4\times10^{-5}$/K, respectively. Consequently, the a-Si:H layer grown directly on the

http://dx.doi.org/10.5772/51531

Ag/stainless steel substrate will induce structural defects as a result of the severe mismatch in thermal expansion coefficients. In order to improve the thermal expansion mismatch issue, we inserted the ZnO:Al buffer layer between the a-Si:H layer and Ag/304 SS substrate. The thermal expansion coefficient of ZnO:Al is $5.3\times10^{-6}$/K. The low thermal expansion coefficient of ZnO:Al film onto a Ag/304 SS substrate can minimize the mismatch in thermal expansion coefficients between the a-Si:H layer and the 304 SS substrate. This reduces the density of the structural defects in the a-Si:H thin-film solar cells, resulting in a higher conversion efficiency of 4.5 % for a-Si:H thin-film solar cells on the ECMP processed 304 SS substrate. More detailed experiments including putting n-type a-Si:H down on the SS substrate side, adjusting the thickness of the ZnO:Al & Ag back-reflector must be carried out in the future to allow us to further improve cell efficiency.

| | $V_{oc}$ (V) | $J_{sc}$ (mA/cm$^2$) | FF (%) | η (%) | $R_s$ (Ω) | $R_{sh}$ (Ω) |
|---|---|---|---|---|---|---|
| Ag/Raw 304SS | 0.79 | 5.1 | 39 | 1.7 | 136 | 923 |
| Ag/EP 304SS | 0.77 | 7.9 | 52 | 3.2 | 105 | 1286 |
| Ag/ECMP 304SS | 0.78 | 9.0 | 52 | 3.7 | 72 | 1269 |

**Table 4.** AM 1.5G output parameters of the a-Si:H thin-film solar cells.

## 5. Conclusions

This study presented the influence of the thickness of the metal Mo buffer layer on a 304 SS substrate on the performance of a-Si:H solar cells. The SIMS result showed that the Fe impurities can be blocked effectively by increasing the thickness of the Mo buffer layer to more than 2 μm. The increased $V_{oc}$ and $J_{sc}$ of a-Si:H solar cells on a Ag/Mo/304 SS substrate was due to an increased Rsh and a decreased $R_s$ which related to the reduction of the Fe deep-level defects density. The Mo buffer layer functioning as an Fe impurities blocking layer plays an important role in improving the a-Si:H thin-film solar cells on a 304 SS substrate.

EP and ECMP surface treatment techniques were also used to smoothen the 304 SS substrate surface. A decreased surface roughness of untreated 304 SS substrate as a result of being subjected to the EP or ECMP process increased the TR rate. We believe that the high TR rate due to the smooth surface of the 304 SS substrate after undergoing the EP or ECMP process increased the short current density and as a result increased the cell conversion efficiency. In addition, the SIMS analysis indicated that the diffusion of Fe and Cr impurities from the 304 SS substrate into the a-Si:H solar cell can be suppressed by using the EP process. We suggested that due to the dense and hard Cr-rich passivation layer that was formed on the ECMP processed 304 SS substrate, the Cr impurity was nearly entirely prevented from diffusing into the a-Si:H layer, resulting in a decreased $R_S$ and increase Rsh of the cell. The smooth surface and the low level of diffusion of impurities of the ECMP processed 304 SS

substrate play an important role in improving the conversion efficiency of the a-Si:H thin-film solar cells.

## Acknowledgements

The authors gratefully acknowledge the financial support from the National Science Council of Taiwan, R.O.C. under contract nos. NSC-98-2112-M155-001-MY3 and NSC-99-2221-E-155-065.

## Author details

Wen-Cheng Ke and Shuo-Jen Lee

Department of Mechanical Engineering, Yuan Ze University, Chung-Li, 320, Taiwan, R.O.C.

## References

[1] Hsu, . M., Tathireddy, P., Rieth, L., Normann, A. R., & Solzbacher, F. (2007). *Thin Solid Films 516 34.*

[2] Fan, Q. H., Chen, C., Liao, X., Xiang, X., Zhang, S., Ingler, W., Adiga, N., Hu, Z., Cao, X., Du, W., & Deng, X. M. (2010). *Sol. Energy Mater. Sol. Cells 94 1300*.

[3] Huran, J., Hotovy, I., Pezoltd, J., Balaykin, N. I., & Kobzev, A. P. (2006). *Thin Solid Films 515 651*.

[4] Deng, X. M., Liao, X. B., Han, S. J., Povolny, H., & Agarwal, P. (2000). *Sol. Energy Mater. Sol. Cells 62 89*.

[5] Kolodziej, A., Krewniak, P., & Nowak, S. (2003). *Opto-electronics Review, 11 281*.

[6] Ferlanto, A. S., Ferreira, G. M., Pearce, J. M., Wronski, C. R., Collins, R. W., Deng, X., & Ganguly, G. (2002). *J. Appl. Phys. 92 2424*.

[7] Zhou, D., & Biswas, R. (2008). *J. Appl. Phys. 103 093102*.

[8] Curtin, B., Biswas, R., & Dalal, V. (2009). *Appl. Phys. Lett. 95 231102*.

[9] Anna, J. A., Selvan, A. E., Delahoy, S., Guo, , & Li, Y. M. (2006). *Sol. Energy Mater. Sol. Cells, 90 3371*.

[10] Llopis, F., & Tobías, I. (2005). *Sol. Energy Mater. Sol. Cells, 87 481*.

[11] Sőderstrőm, T., Haug, F. J., Terrazzoni-Daudrix, V., & Ballif, C. (2008). *J. Appl. Phys. 103 114509*.

http://dx.doi.org/10.5772/51531

[12] Müller, J., Rech, B., Springer, J., & Vanecek, M. (2004). *Sol. Energy, 77 917*.

[13] Lee, S. J., Chen, S. L., Peng, C. W., Lin, C. Y., & Ke, W. C. (2007). *Mate. Chem. Phys. 118 219*.

[14] Lee, S. J., Lin, C. Y., Cheng, S. L., & Ke, W. C. (2011). *Mate. Chem. Phys. 130 733*.

[15] Reehal, H. S., Lesniak, M. P., & Hughes, A. E. (1996). *J. Phys. D: Appl. Phys. 29 934*.

[16] Ali, A., Gouveas, T., Hasan, M. A., Zaidi, S. H., & Asghar, M. (2011). *Sol. Energy Mater. Sol. Cells 95 2805*.

[17] Macdonald, D., Roth, T., Deenapanray, P. N. K., Bothe, K., Pohl, P., & Schmidt, J. (2005). *J. Appl. Phys. 98 083509*.

[18] Lim, S. Y., & Macdonald, D. (2007). *Sol. Energy Mater. Sol. Cells 95 2485*.

[19] Abbott, A. P., Capper, G., Mc Kenzie, K. J., & Ryder, K. S. (2006). *Electrochimica Acta. 51 4420*.

[20] Andrade, L. S., Xavier, S. C., Rocha-Filho, R. C., Bocchi, N., & Biaggio, S. R. (2005). *Electrochimica Acta. 50 2623*.

[21] Lin, C. C., & Hu, C. C. (2008). *Electrochimica Acta. 53 3356*.

[22] Hryniewicz, T. (1994). Surf. Coat Technol. 64 75

[23] Reehal, H. S., Lesniak, M. P., & Hughes, A. E. (1996). *J. Phys. D: Appl. Phys. 29 934*.

[24] Abdelbarey, D., Kveder, V., Schröter, W., & Seibt, M. (2010). *J. Appl. Phys. 108 043519*.

[25] Pickett, M. D., & Buonassisi, T. (2008). *J. Appl. Phys. 92 122103*.

[26] Macdonald, D., Roth, T., & Deenapanray, P. N. K. (2006). *Appl. Phys. Lett. 89 142107*.

Chapter 4

# Polycrystalline Cu(InGa)$Se_2$/CdS Thin Film Solar Cells Made by New Precursors

Alessio Bosio, Daniele Menossi,
Alessandro Romeo and Nicola Romeo

Additional information is available at the end of the chapter

http://dx.doi.org/10.5772/51684

## 1. Introduction

In the last five years photovoltaic modules production continued to be one of the rapidly growing industrial sectors, with an increase well in excess of 40% per year. This growth is driven not only by the progress in materials and technology, but also by incentives to support the market in an increasing number of countries all over the world. Besides, the increase in the price of fossil fuels in 2008, highlighted the necessity to diversify provisioning for the sake of energy security and to emphasize the benefits of local renewable energy sources such as solar energy. The high growth was achieved by an increase in production capacity based on the technology of crystalline silicon, but in recent years, despite the already very high industrial growth rates, thin film photovoltaics has grown at an increasingly fast pace and its market share has increased from 6% in 2006 to over 12% in 2010. However, the majority of photovoltaic modules installed today are produced by the well-established technology of monocrystalline and polycrystalline silicon, which is very close to the technology used for the creation of electronic chips. The high temperatures involved, the necessity to work in ultra-high vacuum and the complex cutting and assembly of silicon "wafers", make the technology inherently complicated and expensive. In spite of everything, silicon is still dominating the photovoltaic market with 90% of sales. Other photovoltaic devices based on silicon are produced in the form of "thin films" or in silicon ribbons; these devices are still in the experimental stage. Amorphous silicon is a technology that has been on the market for decades and it is by now clear that it does not keep the promises of change and development that were pledged when it was initially launched.

Without resorting to sophisticated photovoltaic devices such as multi-junction solar cells, where the cost of production is high, thin film silicon modules were generally poor in conversion efficiency and demonstrated low stability. On the other hand, silicon is not an appropriate material for implementation as a thin film, both for the difficulties of processing (necessity of high temperatures) and the inherent characteristics of the semiconductor which, being an "indirect gap" material has a low absorption coefficient in the visible radiation region. Because of this, silicon must either be deposited in thick layers or it is necessary to use complex light trapping techniques. Beyond the use of silicon, thin film technology has the advantage to provide large-scale productions, in which the panel is the final stage of inline processes and not the assembly of smaller cells, as in the case of crystalline silicon or polysilicon wafer-based modules. The highest rates of production (in terms of square meters of modules per minute) have assumed since the '70s, that, in the future, in order to compete with traditional energy sources, there will be just thin film modules. However the effective start of industrial production of thin film modules was delayed until 2000 due to problems with the reproducibility of the results, the stability over time and scalability of the layer deposition on large areas. Overcoming these problems, the photovoltaic modules that use $CuInGaSe_2$ (CIGS) and CdTe thin film technology are already being produced with a high quality and conversion efficiency (12-14%), with expected values up to 15% for the near future. The cell interconnection integrated into large area modules (0.6 x 1.2 $m^2$), with very limited use of raw materials, can minimize the production cost, so that the thin film modules will soon be able to compete with conventional modules based on the silicon wafer.

In addition to lowering the cost/$m^2$ of the cell area, thin film technology offers the possibility to produce devices on flexible substrates. This extends the opportunity to installing modules by adapting them to the shape of the surface thereby achieving complete architectural integration.

Moreover, $Cu(InGa)Se_2$polycrystalline thin film modules have successfully passed the long-term tests in outdoor conditions, demonstrating a very good stability over time.

Beyond the potential benefits as sociated with terrestrial applications we must also consider that the $Cu(InGa)Se_2$ showed good resistance to ionizing radiation, much more if compared with crystalline silicon cells; furthermore, the cells can also be made on very light weight flexible substrates. For these reasons, this material is very promising for space applications. From this point of view, $Cu(InGa)Se_2$ is one of the most promising materials used in thin-film technology; not only for the reasons mentioned above, but perhaps more importantly, because it has reached very high efficiencies comparable to that obtained, up to now, with the best Silicon solar cells, at both cell and module level.

The highest $Cu(InGa)Se_2$ solar cell efficiency of 20,3% with 0,5 $cm^2$ total area was gained in 2010 by Jackson et al. [1] from Zentrum fuer Sonnenenergie of Wasserstoff-und-Forschung Baden-Wuerttemberg (ZSW), Germany. In addition, many companies have made modules with efficiencies above 12% up to the fantastic world record of 17,8 % obtained with $30x30cm^2$ modules by the "Solar Frontier" research group from Showa Shell Sekiyu KK (Japan), which exceeds the previous record of 17,4% achieved by the Q-Cells subsidiary company, Solibro Gmb H.

http://dx.doi.org/10.5772/51684

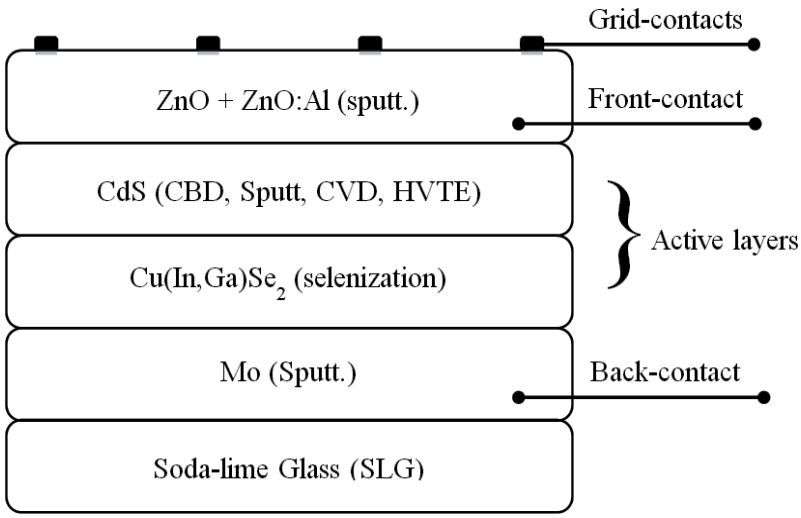


**Figure 1.** Schematic structure of a Cu(In,Ga)$Se_2$-based solar cell.

As we can see in figure 1,the $CuInGaSe_2$/CdS thin film solar cell consists of 6 layers; this implies that in the overall structure there are at least 7 interfaces.

This made very complicated to understand the behavior of the final device and several research groups have tried to explain the properties of the cell by studying these interfaces in detail. On the other hand, when two different materials are put in contact there is an inter-diffusion of chemical elements from the one to the other and a sub sequent formation ofa new thin layer between the two. This new layer is known as *hetero-interface*. The most important hetero-interface is the metallurgical hetero-junction between Cu(InGa)$Se_2$ and CdS, but all the other interfaces have also an important role in the final performance of the cell.

Despite all efforts aimed to understand the behavior of the interfaces, Cu(InGa)$Se_2$/CdS hetero-junction still exhibits quite a few open problems and it is therefore subject to a margin of uncertainty in its progress. For this reason more detailed studies are needed to reach a complete understanding of all the phenomena regarding this remarkable device.

In this chapter we will describe the current state and the degree of understanding of the Cu(InGa)$Se_2$ solar cells construction technology. In particular, after presenting a brief history of this device we will discuss the material and consider both the cells and the modules; after that we will focus particularly on the manufacturing techniques which have led to high-efficiency devices (cells and modules) and consequently, the different problems in herent to this material with particular attention to the scalability at an industrial level of the production process. Then we arrive at conclusions also talking about future perspectives.

## 2. A brief history

The history of $CuInSe_2$ begins with the research carried outin the Bell Telephone laboratories in the early 70'seven thoughits synthesis and characterization have already been studied by Hahn in 1953 [2]. Along with new ternary chalcopyrite materials, it was also characterized by other groups [3]. The Bell Labs had grown crystals of a wide selection of these materials reporting their structural and electro-optics properties [4, 5]. In that period, a solar cell with an efficiency of 12% based on CdS evaporated onto a *p*-type $CuInSe_2$ single crystal was realized [6]. In 1977, depositing by flash-evaporation a CdS thin film onto a single crystal of *p*-type $CuGaSe_2$, a solar cell that exhibited an energy conversion efficiency of up to 7 % was realized [7].

$CuInSe_2$ is a semiconducting compound of the I-III-$VI_2$ family with a direct band gap of 1,05 eV. Its chalcopyrite structure makes a good match to wurtzite CdS with only 1,2% lattice mis match. This explains the good efficiency for the first time obtained with $CuInSe_2$ single crystal and put in evidence that $CuInSe_2$/CdS was the sixth system, along with junctions based on Si, GaAs, CdTe, InP, and $Cu_xS$ that showed energy conversion efficiency up to 10%. Besides, $CuInSe_2$ is a direct band gap semiconductor, which minimizes the requirements for minority carrier diffusion length, and exhibits the highest absorption coefficient ($3x10^5$ $cm^{-1}$) in the visible region of the solar spectrum. These considerations make $CuInSe_2$ the best-suited material for the fabrication of an all polycrystalline thin film solar cell.

There has been relatively little effort devoted to devices realized on a $CuInSe_2$ single crystal apart from this first work, because of the difficulty in growing high-quality crystals. But, the aforementioned properties of $CuInSe_2$ channeled all the attention to thin-film solar cells because of their intrinsic advantages. The first thin-film $CuInSe_2$/CdS solar cell was fabricated by Kazmerski et al. in 1976 [8] by using films deposited by evaporation of $CuInSe_2$ powder in excess of Se vapor. This solar cell showed an efficiency of about 4-5%.

We had to wait until 1981 when, in the Boeing laboratories, the first high-efficiency all thin film solar cell based on the system *n*-ZnCdS/*p*-$CuInSe_2$ was realized with a conversion efficiency of about 9,4% and in 1985 they reached the efficiency of 11.4% [9].

Since the early 80's, ARCO Solar and Boeing have tackled the difficult issues involved with industrial production such as through put and yield. These efforts have led to many advancesin the technology of $CuInSe_2$ solar cells.

The two groups have characterized their R&D approaches in different ways. The diversity of the two approaches consists basically in the $CuInSe_2$(CISe) deposition methods, while the architecture of the device remains essentially the same.

The Boeing method includes the co-evaporation from separate sources of the single elements for CISe deposition. These films were deposited on alkali-free glass or ceramic covered by a thin layer of Mo, which acts as a positive electrode. The devices were finally completed by evaporating, on top of the CISe film, two layers of CdS (or ZnCdS), the first one was an intrinsic layer and the second one heavily doped with indium in order to ensure a best photo current collection.

http://dx.doi.org/10.5772/51684

The two methods, introduced by Boeing and ARCO Solar, still remain the most common techniques for producing high efficiency cells and modules. Boeing was focused on co-evaporation of individual elements from separate crucibles while ARCO Solar was more confident in a two-stage process in which a low-temperature deposition of Cuand In was followed by a heat treatmentat high temperature in $H_2Se$ ambient.

With the "Boeing" basic structure, in 1996 [10] was reached the fantastic result for an all thin film solar cell: a conversion efficiency of 17,7%! This improvement was obtained by using $CuGa_XIn_1$-$XSe_2$ as absorber layer. Effects of partial substitution of Ga for In appeared to be optimized for X=0,25. The band gap of the quaternary compound varies from 1,04 eV for X=0 to 1,7 eV for X=1; this means that the substitution of Ga for In causes an increase in open-circuit voltage, but a decrease in short-circuit current and fill factor and only for X=0,25 does the system reach the right equilibrium. Adjusting the Ga concentration profile into the absorber layer, in order to enhance the collection of the photo-generated carriers, it was possible to fabricate thin film solar cells based on the CdS/$CuGaInSe_2$ system with an efficiency of 18,8% in 1999 [11], of 19,2% in 2003 [12] and of 20.3% in 2011 [1]. This last result is the highest value for energy conversion efficiency in an all thin film photovoltaic device.

| cell | Energy conversion efficiency % | reference |
|---|---|---|
| n-CdS/p-$CuInSe_2$ single crystal (1974) | 12 | [6] |
| n-CdS/p-$CuGaSe_2$ single crystal (1977) | 7 | [7] |
| n-ZnCdS/p-$CuInSe_2$ all thin film (1976) | 4-5 | [8] |
| n-ZnCdS/p-$CuInSe_2$ all thin film (1985) | 11.9 | [9] |
| n-CdS/p $CuInGaSe_2$ all thin film (1996) | 17.7 | [10] |
| n-CdS/p-$CuInGaSe_2$ all thin film (1999) | 18.8 | [11] |
| n-CdS/p-$CuInGaSe_2$ all thin film (2003) | 19.2 | [12] |
| n-CdS/p-$CuInGaSe_2$ all thin film (2011) | 20.3 | [1] |

**Table 1.** Representative CuInSe2 and CuGaSe2 based solar cells.

Let's summarize the key enhancements to the method that gave the more efficient cells (co-evaporation-Boeing).

1. Soda lime glass replaced ceramic or borosilicate glass substrates. This change was made for the lower costs of soda lime glass and its good thermal expansion match with $CuInSe_2$. An increase in processes tolerance and device functioning were the result. It was soon clear that the better results obtained came primarily from the beneficial inter-diffusion of sodium from the glass [13].

2. The high thickness of the In-doped CdS or ZnCdS film was replaced by a thin un-doped CdS layer followed by a conducting Al-doped ZnO (ZAO) film. This was effective in

increasing the photocurrent having enlarged the spectral response in the blue region wavelengths [14].

3. The absorber energy gap was increased from 1.02 eV for $CuInSe_2$ to 1.1–1.2 eV for $Cu(In,Ga)Se_2$ by the partial substitution of In with Ga, leading to an important increase in efficiency [15].

4. Innovative absorber deposition processes were developed to obtain energy gap gradients improving the photovoltage and current collection [16, 17].

Several companies around the world are coming to the market with $Cu(In,Ga)Se_2$-based modules. The more advanced features are briefly shown in Table 2, where one can distinguish the two processes described above. One is the typical co-evaporation method of Shell Solar Industries, formerly Arco Solar and then Siemens Solar in California, Würth Solar and Solibro in Germany and Matsushita in Japan, with which these companies have announced modules efficiencies of around 12-13%. The selenization of metallic precursors in $H_2Se$ ambientis instead the technology used by Showa Shell that has announced module efficiency in excess of 14%.

| Producers | Prodn. capacity MW/Year (since) | Glass-size (m x m) | Efficiency % max./med. | On the market |
|---|---|---|---|---|
| | | CIGS | | |
| Bosch Solar CISTech (Johanna Solar, Ger.) | 30 (2008) | 0.5 x 1.2 | --/9.4 | No |
| Wuerth Solar, Ger. | 14.8 (2007) | 0.6 x 1.2 | <13/11.7 | Yes |
| Global Solar, USA | 4.2 (2006) | 1" wide metal sheet | 10/8 | Yes |
| ISET, USA | Pilot plant | 0.6 x 1.2 | 10 | Yes |
| MiaSolè, USA | 150 (2012) | 0.66 x 1.61 | 13 | Yes |
| Showa Shell, Japan | 20 (2007) | 0.6 x 1.2 | 14.2/11.8 | Yes |
| Honda Soltec, Japan | 27 (2007/2008) | 0.8 x 1.3 | 13/10 | Yes |
| Sulfur Cell, Ger. | 5 (2007/2008) | 0.65 x 1.25 | 8.2/7 | Yes |
| AVANCIS, Ger. | 20 (from 2008) | 0.65 x 1.6 | 13.1/12.2 | Yes |
| Hanergy China (Solibro, Ger.) | 25-30 (2009) | 0.65 x 1.2 | 12 | Yes |

**Table 2.** Some manufacturers of $CuInGaSe_2$ thin-film photovoltaic modules, and their current market condition.

In addition a Phoenix Solar Holdings Corp subsidiary company, EPV Solar Corp, formerly Energy Photovoltaics, Inc. is using its own in-line evaporation process, International Solar Electric Technology (ISET) is developing a particle-based precursor for selenization, while Global Solar Energy (GSE) and MiaSolè are pursuing a process for roll-to-roll co-evaporation onto a flexible substrate with final efficiencies of around 15.5%.

http://dx.doi.org/10.5772/51684

Despite these encouraging results and the efforts made to develop the manufacturing processes, there remains a large difference in efficiency between the laboratory-scale solar cells and mini-modules, and the best modules on the market. In part, this is due to the need to develop innovative equipment for large-area, high-throughput deposition required for manufacturing thin-film photovoltaic's. Presumably, this is because the material has only been studied for use in photovoltaic applications, and many of the advances in scientific understanding of materials and technologies have been purely empirical.

However, in recent years, many enhancements in the scientific knowledge of the materials and device have been made and this has also led to evident improvements in manufacturing technology.

## 3. The history of $CuInSe_2$ and Cu(In,Ga)$se_2$ at the ThiFiLab

The Thin Film Laboratory (ThiFiLab) of the Physics Department at the University of Parma-Italy, started to work on $CuInSe_2$ in 1986 with the aim of achieving high quality films suitable to realize an all thin film solar cell made entirely using only the sputtering technique [18-22]. The first approach was the sputtering deposition of $CuInSe_2$ starting directly from stoichiometric targets. At this stage, great care was placed on the preparation of the substrates. As substrates 1 inch square Corning glasses 7059 were used. Glasses were covered with a 4 μm thick layer of Al deposited by sputtering at a substrate temperature of 350°C. The Al layer obtained was crystalline with an average grain size of 100 μm and with the (111) plane uniquely oriented along the glass surface. Since Al is not a good ohmic contact for *p*-type $CuInSe_2$, the Al film was covered with either a 0.2 μm thick layer of Mo or a 0.5 μm layer of Au; both these films were deposited by sputtering. Au was deposited on Al at a substrate temperature higher than 500°C. In this way, Au reacts with Al forming the metallic compound $AuAl_2$. This compound exhibits the cubic structure with a lattice constant of about 6 Å which is closer, in respect to any other metal, (Mo has a lattice constant of 3.15 Å) to the lattice constant of $CuInSe_2$ (5.78 Å). Both Mo and $AuAl_2$ thin films, prepared as previously described, were used as substrates for the sputtering deposition of $CuInSe_2$.

The RF magnetron sputtering system was provided with three targets like Mo, $CuInSe_2$ and CdS and a rotatable heating-etching station whose temperature could be controlled up to 600°C. Mo and CdS targets were supplied by commercial suppliers while the $CuInSe_2$ target was prepared in the ThiFiLabby synthesis in a high pressure furnace. In this case the liquid encapsulation technique was used, with $B_2O_3$ acting as the encapsulant. The crucibles had a flat bottom whose diameter was equal to that of the target holder in the sputtering system. In order to avoid the reaction between In and Se at a temperature lower than the $B_2O_3$ melting point (450°C) a pre-reacted Cu-In alloy instead of the individual elements was used. The reaction of components and melting were carried out under a 50 atm $N_2$ pressure. Several $CuInSe_2$ targets with different Cu/In ratios and one with an excess of Se with respect to the metals have been investigated. The substrate temperature was varied between 300 and

550°C. It was found out that stoichiometry, crystallinity, carrier type and resistivity of $CuInSe_2$ films depended on several deposition parameters, like the Ar pressure, R.F. power, bias applied to the substrate, substrate temperature and type of substrate, whether glass, Mo or $AuAl_2$ (see figures 2-3).

Among these, the substrate temperature and the bias applied to the substrate seemed to be the most effective. Stoichiometric films with good crystallinity were generally grown at a substrate temperature of around 450°C, with the substrate bias kept at a minimum value (self-biased substrate). $CuInSe_2$/CdS solar cells were fabricated as depicted in figure 4.

Mo, $CuInSe_2$ and undoped CdS films were deposited in sequence in the same sputtering chamber without interrupting the vacuum [23, 24]. Mo and $CuInSe_2$ films were deposited at the same substrate temperature, between 400 and 500°C. In some cases, $CuInSe_2$ films were deposited on $AuAl_2$ covered substrates. The undoped CdS film was deposited at 200°C substrate temperature with an $H_2$ partial pressure in the sputtering chamber of about $1.5x10^{-4}$ mbar, that corresponds to 3% of the Ar+$H_2$ total pressure. These films exhibited resistivity in the range of $10^{-1}$ - 1 Ωcm and were highly transparent in the wavelength region between 1.6 μm and the absorption edge of CdS (0.52 μm).

After that, a mecanical scribing was done in order to obtain an active cell area of about 0.2 $cm^2$. The photovoltaic efficiency of such a cell was in the range of 5-8%. To achieve high efficiency cells it was necessary to use two $CuInSe_2$ layers, the first one Cu-rich and the second In-rich [25-27]. The low efficiency obtained with this technique was essentially due to the segregation of binary phases, like $Cu_2Se$ in the first layer.

In order to overcome the segregation of binary phases some alternative techniques were studied; among them the selenization of stacked elemental layers seemed to be one of the most effective since the technique is very promising for large-scale application.

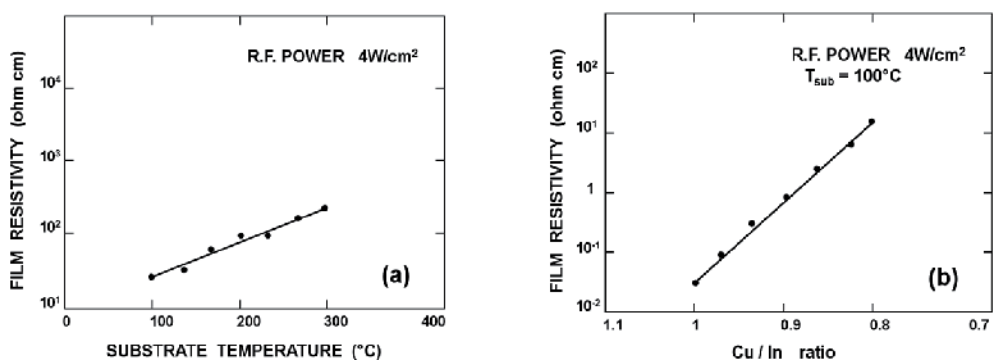


**Figure 2.** a) Resistivity of *p*-type $CuInSe_2$ films as a function of the substrate temperature. The Cu/In ratio in the target was 0.8 and no bias was applied to the substrate. (b) Resistivity of *p*-type $CuInSe_2$ films as a function of the Cu/In ratio in the target. The substrate temperature is 100°C and no bias was applied to the substrate. Redrawn *from "Proceedings of the 18 th IEEE Photovoltaic Specialists Conf., 1985, Las Vegas, Nevada, October 21-25. p. 1388-1392".*

http://dx.doi.org/10.5772/51684

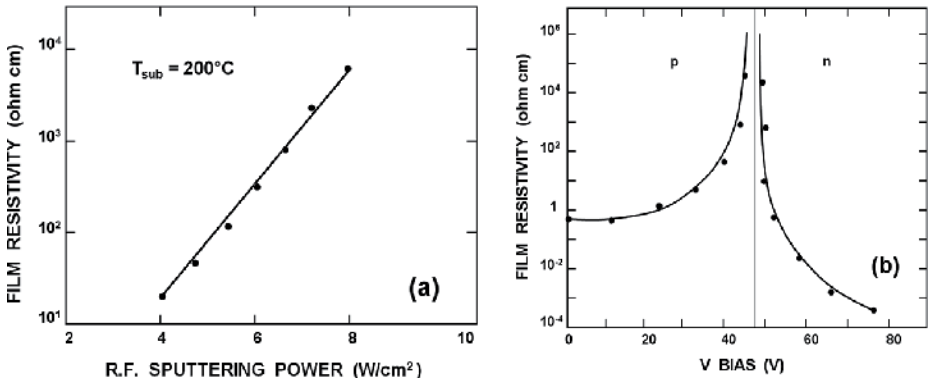


**Figure 3.** a) Resistivity of *p*-type $CuInSe_2$ films as a function of sputtering power. The Cu/In ratio in the target was 0.8 and the substrate temperature was 200°C. No bias was applied to the substrate. (b) Resistivity of both *p*- and *n*-type $CuInSe_2$ films as a function of the negative bias applied to the substrate. The Cu/In ratio in the target was 1 and the substrate temperature was kept at 250°C. Redrawn from *"Proceedings of the 18 th IEEE Photovoltaic Specialists Conf., 1985, Las Vegas, Nevada, October 21-25. p. 1388-1392"*.

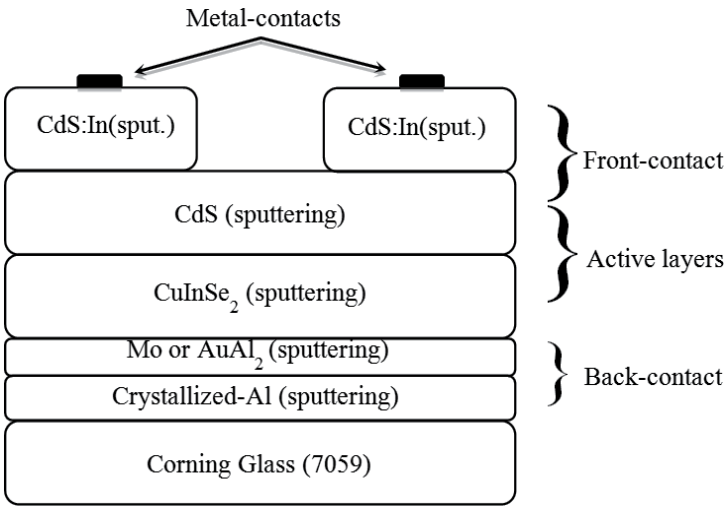


**Figure 4.** Structure of the all-sputtered thin film $CuInSe_2$ solar cell.

By using the same substrates described above, a 2500 Å thick Cu film and a 5600Å thick In film were deposited by sputtering on top of the Mo layer. The deposition of Cu and In elemental layers was done at several temperatures, ranging from 50 to 220°C. After the deposition of the elemental layers, the sample was set inside an evaporation chamber for the selenization. The Se-vapor was obtained from a graphite boat kept 5 cm apart from the substrate holder, at a substrate temperature of about 300°C. The Se-deposition rate, measured by a quartz crystal monitor, was on the order of 0.5-0.8 μm/sec. The substrate was indirectly heated up using the Joule-effect with a Mo thin sheet. In this way a substrate temperature of

400-500°C could be reached in less than one minute. One of the problems encountered with the selenization of elemental layers was the sticking of the formed $CuInSe_2$ film. If the In layer was deposited on top of Cu layer at a substrate temperature below 100°C the sticking was very poor. The best adhesion was obtained when the In layer was deposited at a substrate temperature close to its melting point. It seems that at this temperature Cu and In mix completely [28]. After the selenization process, the $CuInSe_2$ film was polycrystalline with a grain size larger than 1 micron and it was very well oriented along the (112) direction. The $CuInSe_2$/CdS solar cells were made following the method described above. The best cells prepared with this technique gave the following photovoltaic parameters: $V_{oc}$ = 380 mV, $J_{sc}$ = 39 mA/cm$^2$, f.f. = 0.61, $\eta$ = 9.1%

The conclusion of this work was that the selenization of elemental Cu-In layers seemed to be a very good technique to make $CuInSe_2$ films for the following three reasons:

**a.** it is a scalable technique.

**b.** it allows the formation of well-crystallized and single phase $CuInSe_2$ layers over large areas.

**c.** Se-vapor in the selenization process works as well as $H_2Se$.

It was evident that in order to improve the performance of the cells it was necessary to add Ga to the precursor. In this way a $CuIn_xGa_{1-x}Se_2$ film as the absorber material is obtained. Since the sputtering technique didn't allow Ga to be deposited directly, the deposition of the precursor was carried out by high vacuum evaporation assisted by an electron beam gun (E.B.G.).The Cu, Ga and In elemental layers were deposited by E.B.G. evaporation from a single rotatable crucible, in order to have a good uniformity on the substrate. First of all, 370 nm of In and 240 nm of Cu were deposited in sequence on top of a Mo covered glass substrate, which was kept at 120°C. Then the In-Cu bilayer was annealed at 290°C for 30-60 min in order to form the $Cu_{11}In_9$ phase. After the annealing, 120 nm of Ga were deposited at 240°C substrate temperature. At this temperature Ga reacts with the $Cu_{11}In_9$ phase forming the $CuGa_2$ phase and freeing a small amount of In. A substrate temperature of 240°C was chosen for the deposition of Ga since the $CuGa_2$ phase melts at 254°C. It had been confirmed by X-ray diffraction that the Cu-Ga-In film was made up of the $Cu_{11}In_9$ phase, the $CuGa_2$ phase and a small amount of In. This method for preparing the Cu-Ga-In elemental layers gives the maximum possible intermixing between the layers, without having melt droplets in the film. Since the addition of Ga, being a low-melting element, increases the amount of liquid present in the film at a given temperature, a new selenization process was implemented. A peculiarity of this process was the oscillation of the substrate temperature at the first stage of $CuGaInSe_2$ growth. The temperature oscillation seemed to be very effective in containing the surface tension of the liquid. At the beginning, the substrate temperature was raised up to 280°C in about 30 s and decreased to 200°C in about 3-4 min. During this first oscillation a small part of the film grew on the surface. This covering seemed to be sufficient to contain the surface tension during the second oscillation up to 450°C, which was done with a rise time of about 1 min and a cooling down time of about 6 min. During the second oscillation part of the film grew further covering the film with a solid one. Hence allowing a

http://dx.doi.org/10.5772/51684

third temperature oscillation and so on. It has been seen that the process depends on both the oscillation rise time, which should not be larger than 2 min for reaching a maximum temperature of 550°C and the cooling down time from 550°C to 200°C which should be between 6 to 9 min.

At this stage, the front-contact was also changed; 30-50 nm thick layer of intrinsic CdS at 220°C substrate temperature was deposited by sputtering on top of the $CuGa_{0.3}In_{0.7}Se_2$ films. The cell was completed with a 1-2 μm thick film of In-doped CdS or Al-doped ZnO, deposited by sputtering. On average, better results were obtained when soda lime glass was used as a substrate, indicating that the diffusion of Na atoms into the growing $CuGa_{0.3}In_{0.7}Se_2$ film during the selenization step, should play some role. These cells shown a maximum efficiency of 12.4% with an open-circuit voltage of 450 mV, a short-circuit current density of 40 $mA/cm^2$ and a fill factor of 0.69. No better efficiencies were achieved because this process doesn't allow a Ga concentration gradient to be obtained within the film thickness. Probably, if the junction was made with a thin layer of CdS obtained by chemical bath deposition, a larger efficiency could be achieved [29]. For this reason new type of precursors were tested, which allowed the concentration profile of Ga to be easily designed[30].

As it was the custom at that time, a substrate of l $inch^2$, 4mm thick soda-lime glass was used. The substrate was mounted in a sputtering chamber, where 4 targets namely Mo, $In_2Se_3$, Cu and a Cu-Ga alloy containing 50% at. ofGa and 50% at. of Cu were installed [31, 32]. Common commercial suppliers provided Mo, Cu and the Cu-Ga alloy, while the $In_2Se_3$ target was home-prepared, starting from the In and Se elements. In and Se elements were put in a suitable graphite container and brought to a temperature higher than the $In_2Se_3$ melting point (890°C) and then slowly cooled down to room temperature. This process was done in an oven where an inert gas such as $N_2$ was introduced at a pressure higher than 10 atmospheres in order to avoid the In or Se evaporation. The target was polycrystalline and exhibited a 99.9% density comparable with the bulk material.

This characteristic of the target is very important since, if a target prepared by "hot pressing" starting from $In_2Se_3$ powder was used one could have instabilities in the sputtering discharge produced by the high vapor pressure of Se.

Furthermore, if the cooling of the target is not very effective, some cracks at the edges of the target can form. On top of the soda-lime glass, 1 μm of Mo, 1.5 μm of $In_2Se_3$ and 0.2 μm of Cu were deposited in sequence at room temperature by sputtering. Mo and Cu were deposited by pulsed D.C. sputtering while, $In_2Se_3$ was deposited by R.F. sputtering.

The Mo-$In_2Se_3$-Cu stacked layers were brought to a temperature of 450°C where they were left to interact, respecting their phase diagram, for about 30 min. In this way a film of $CuInSe_2$ was formed. As it can be seen in figure 5(a), this layer contains a residual of the $Cu_{11}In_9$ and $In_2Se_3$ phases.

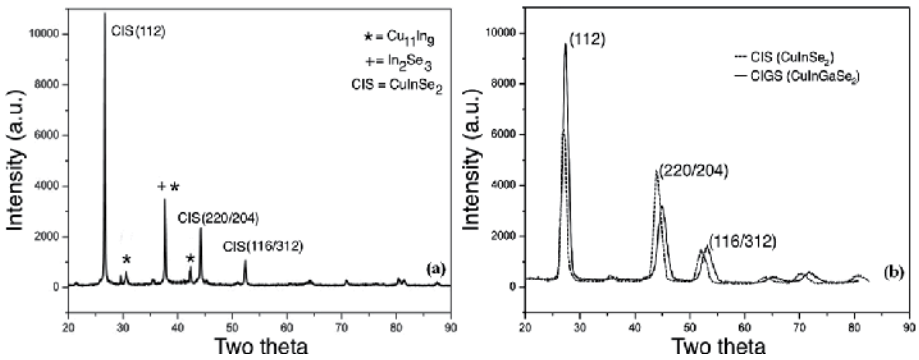


**Figure 5.** a) $CuInSe_2$ precursor X-Ray Diffraction spectrum. (b) Comparison between $CuInSe_2$ (dashed- line) and $CuInGaSe_2$ (solid-line) X-Ray Diffraction spectra.

In order to obtain the right $CuInSe_2$ film without any secondary phases, the precursor had to be selenized at a substrate temperature of 520-530°C. The selenization was done in the same way described before. Similar technology was also reported by other authors [33] but InSe instead of $In_2Se_3$ was used and it was deposited by high vacuum evaporation (HVE).

Furthermore, the selenization was started from room temperature up to 500°C and then no precursor was formed before selenization. In order to make the $Cu(In,Ga)Se_2$ film, the $CuInSe_2$ layer, obtained as described before, was covered by 80 nm of the Cu-Ga alloy (50%-50%) deposited by D.C. sputtering and this system was again selenized. The $Cu(In,Ga)Se_2$ film, formed in this way has a graded Ga content, that means it contains more Ga close to the surface than into the bulk. The $Cu(In,Ga)Se_2$, analyzed by X-rays, exhibits the peaks of $Cu(In,Ga)Se_2$ material as one can see from figure 5(b) where the diffraction peaks are shifted to higher angles with respect to $CuInSe_2$.

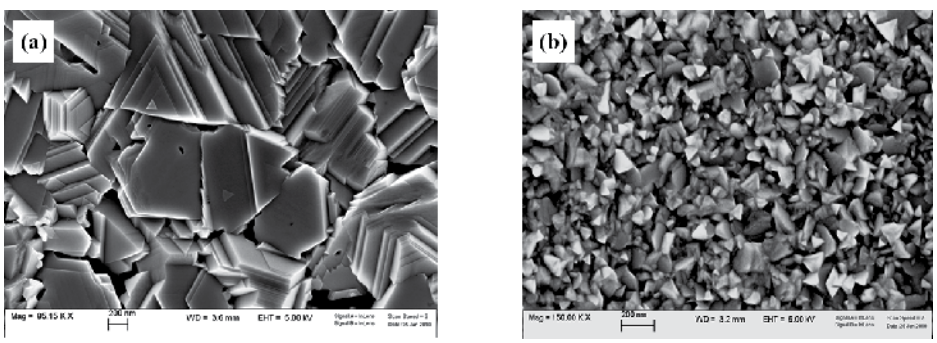


**Figure 6.** a) $CuInSe_2$ film surface morphology after selenization. (b) $CuInGaSe_2$ film surface morphology after selenization.

Figure 6(a) shows the morphology of the $CuInSe_2$ film while figure 6(b) displays the morphology of the $Cu(In,Ga)Se_2$ film referred to the two-steps process presented in figure 7. In

http://dx.doi.org/10.5772/51684

order to have a better control on the Ga concentration gradient of the $CuInGaSe_2$ film, the ThiFiLab developed an alternative way to prepare the precursor (see figure 7).

Once the $CuInSe_2$ precursor is obtained it is possible to follow two different pathways:

1. The process continues by depositing in sequence on top of the precursor, formed by $CuInSe_2$+$Cu_{11}In_9$ and $In_2Se_3$ as described before, a film of $Ga_2Se_3$ followed by a film of Cu at a substrate temperature of 400-450°C. This new precursor is then selenized in pure Se vapor and the Cu(In,Ga)$Se_2$ film is obtained.

2. The precursor is immediately selenized and on top of the so-obtained $CuInSe_2$ film, the same sequence of $Ga_2Se_3$ film followed by a Cu film is deposited at a substrate temperature of 400-450°C. This system is suitable for the selenization process and a film of Cu(In,Ga)$Se_2$ is made.

With this second method we have more freedom in varying the concentration profile of Ga in the final Cu(In,Ga)$Se_2$ film since the profile depends on the ratio between the $Ga_2Se_3$ and $CuInSe_2$ film thicknesses. In contrast, the first method is more convenient because it needs only one selenization step. In Table 3 the results of manufactured cells with both methods are summarized.

Great improvements have been made in finishing the cell, in fact Cu(In,Ga)$Se_2$/CdS solar cells were prepared as described above, by depositing in sequence on top of Cu(In,Ga)$Se_2$ layer, 60 nm of CdS(F) [34], 80 nm of pure ZnO and 1μm of ZnO doped with 2% atomic of Al.

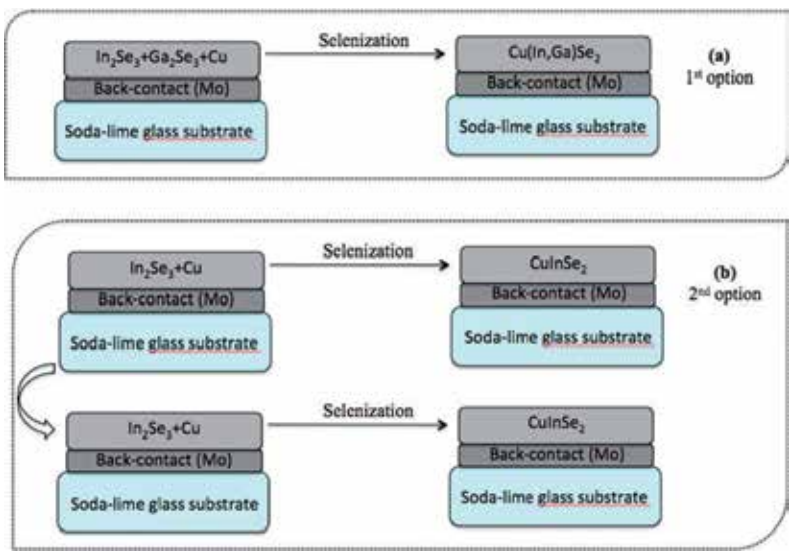


**Figure 7.** Representation of the two options developed in the THIFILAB, University of Parma-Italy to obtain high quality Cu(In,Ga)$Se_2$ absorber film. (a) single-step process. (b) double-step process. For both options all the layers are deposited by sputtering and selenization in pure Se atmosphere is made.

If one uses the sputtering technique for the deposition of CdS films, employed as the window material in $Cu(In,Ga)Se_2$ based solar cells, great results are not obtained and efficiencies converge to values not higher than 13% -14%. This result is due to the fact that these devices exhibit a too high diode reverse saturation current. One possible explanation is that the grain boundaries in the CdS film are active and can channel the diode reverse current.

| Absorber | Ga/In+Ga (%) | Voc (mV) | Jsc (mA/cm$^2$) | FF (%) | Efficiency (%) |
|---|---|---|---|---|---|
| $CuInSe_2$ | 0 | 410 | 39.8 | 70.20 | 11.45 |
| $Cu(In,Ga)Se_2$ | 20 | 531 | 34.8 | 71.60 | 13.23 |
| $Cu(In,Ga)Se_2$ | 20 | 578 | 35.2 | 71.08 | 14.46 |

**Table 3.** Photovoltaic parameters of the solar cells fabricated by sputtering and selenization in pure Se atmosphere.

It is possible to get over this problem by introducing in the sputtering chamber, during the CdS deposition, Argon containing 3% of $CHF_3$. This gas is decomposed and ionized in the sputtering discharge, freeing $F^-$ ions which, being strongly electronegative, are directed to the substrate that is the positive electrode; here two different events can happen:

1- the presence of energetic $F^-$ ions near the substrate favors the formation of a fluorine compound such as $CdF_2$ during the growth of the CdS film [34].

2- the $F^-$ ions, accelerated by the electric field present in the discharge, hit the film surface during the deposition with sufficient energy to sputter back the more weakly bonded Cd or S atoms.

This effect leaves a CdS film with high optical quality and structural properties. We can see in figure 8 that the CdS films deposited in Argon+$CHF_3$ have an energy gap greater than that of the films deposited in Argon alone. Better efficiencies (15%-18%) are routinely obtained if CdS(F) films are used. One can explain this fact by considering that CdS(F) may contain $CdF_2$ probably segregated in the grain boundaries and this can be useful to passivate them.

As an alternative to ZnO(Al), 0.5 μm of ITO doped with Zr was used. All the layers were deposited by sputtering. While CdS(F) and pure ZnO were deposited by R.F., ZnO(Al) and ITO(Zr) were deposited by pulsed D.C. sputtering. ITO doped with Zr has been used since it was discovered that for dielectric oxides, permittivity can be increased by the addition of higher-permittivity oxides such as $ZrO_2$ (or $HfO_2$). It is also known that the permittivity of dielectric oxides increases rapidly with even small additions of a higher-permittivity constituent and this is especially true for high-frequency permittivity $\varepsilon_\infty$. The increase in $\varepsilon_\infty$ as Zr is added can shift $\lambda_p$, which corresponds to the plasma resonance wavelength, to a longer wavelength and make it possible to improve NIR transmission significantly without altering the material parameters, like carrier concentration or mobility[35].

http://dx.doi.org/10.5772/51684

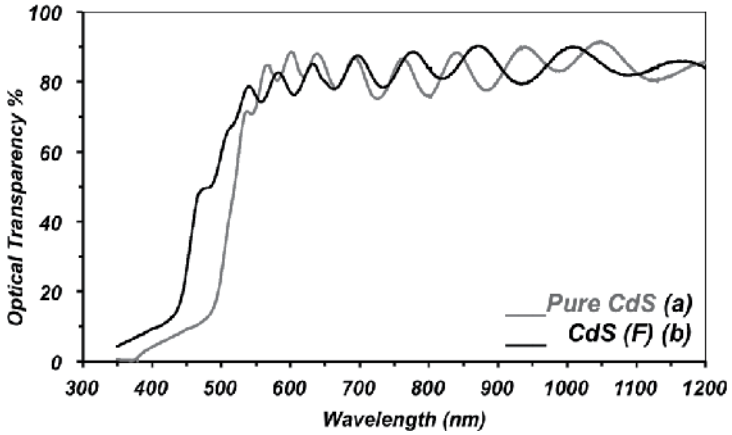


**Figure 8.** Transmission spectrum of an 80 nm thick sputtered CdS film: (a) deposited in pure Argon and (b) deposited in Argon+$CHF_3$. The shift of the absorption edge towards shorter wavelengths proves the beneficial effects of deposition in the presence of $CHF_3$.Redrawn from *"Proceedings of 3rdWorld Conference on Photovoltaic Energy Conversion*, 2003, Osaka, Japan, May18-21, Vol 1, 469 – 470.

In order to further improve the efficiency of the solar cells, the precursor was further modified by replacing $In_2Se_3$and $Ga_2Se_3$ with InSe and GaSe targets. The change in the starting selenides was especially effective as it resulted in the complete mixing of the materials, which formed the precursor. In fact, at a given temperature, InSe and GaSe were more reactive with Cu than their counter parts $In_2Se_3$ and $Ga_2Se_3$. So we came to the last version of the fabrication process for the CIGS-baseds olar cells developed so far at the ThiFiLab.

Thestarting systemwas the usualsputtering machinein which 4 targets namely Mo, InSe, GaSe and Cu were contained. While Mo and Cu were deposited by pulsed-D.C., InSe and GaSe were deposited by R.F. sputtering. The constructionof the solar cellbeganwith thedeposition of a Mo bi-layer at room temperature. The first Mo layer was quite thin, 30 nm and was deposited with an Ar flow of 45 sccm, which corresponds to apressureof 4.5x $10^{-3}$mbar. The Ar flow was then decreased to 15 sccm, which corresponds to apressureof 1.5x $10^{-3}$mbar.

Approximately 500 nm of Mo was deposited. The deposition of a bi-layer of Mo was necessary in order to have good adhesion of the Mo film to the substrate [36].

In order to get a good precursor, it was discovered that the sequence of InSe, GaSe and Cu as well as the substrate temperature at which they were deposited wasvery important. While Mo films had to be deposited at room temperature for sticking purposes, both InSe and GaSe layers were deposited at a high temperature (400°C) in order to avoid a Se-excess growth. The thickness of the InSe film was commonly 1.5 μm and that of GaSe was 0.5 μm. Cu was also deposited at asubstrate temperature of 400°C and its thickness was around 350 nm. All the layers mix during the deposition and don't require further annealing. An X-ray analysis shows that the precursor exhibits a mix of InSe, GaSe and $CuInSe_2$ phases (figure 9a), while, the selenized material shows two phases one which contains 30% of Ga and the other one which contains 60% of Ga(figure 9b).

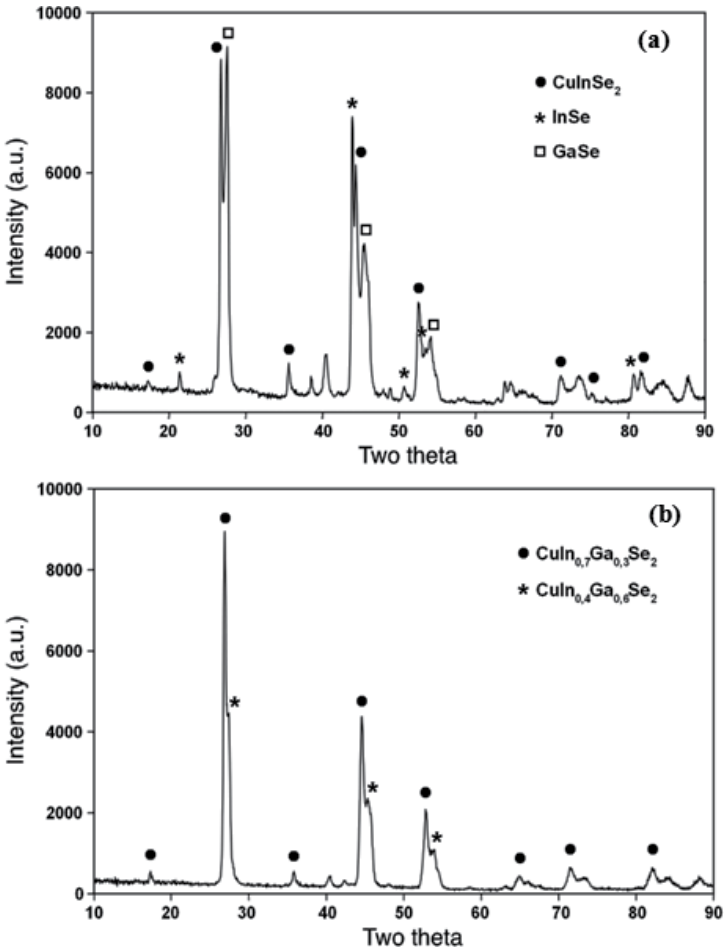


**Figure 9.** Cu(In,Ga)$Se_2$ precursor X-Ray Diffraction spectra (a) before and (b) after selenization.

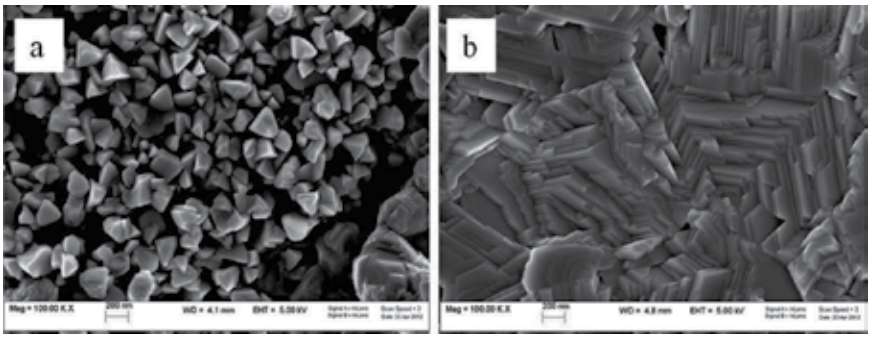


**Figure 10.** Electron microscope image of precursor (a) before and (b) after selenization.

http://dx.doi.org/10.5772/51684

The precursor is then selenized in a vacuum chamber where pure Se is evaporated from a graphite crucible. Selenization lasts approximately 7 minutes. The first 5 minutes are used to bring the substrate from room temperature to 530°C and the last 2 minutes are spent by leaving the substrate at 530°C. The morphology of the precursor before and after selenization is shown in figure 10.

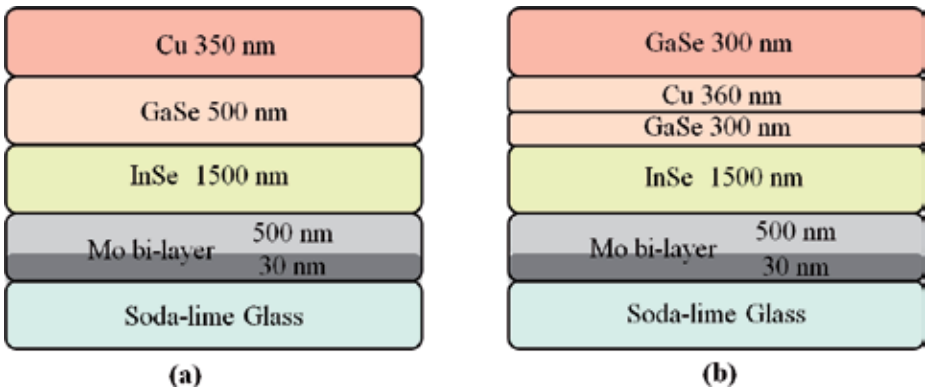


**Figure 11.** Preparation of the precursor. (a) Sequence of deposition for the InSe, GaSe and Cu layers; (b) the last new optimized sequence for the InSe, GaSe and Cu layers, which led to a high efficiency CIGS-based solar cell.

The cell was completed by depositing the CdS layer, the transparent electrode and the contact grid in the same way that was previously described.

Solar cells made in this way exhibit an efficiency of about 13% with an open circuit voltage ($V_{OC}$) that is never higher than 500 mV, a high short circuit current density ($J_{SC}$) on the order of 40 mA/cm$^2$ and a f.f. of 0.62-0.65.

The low open circuit voltage and f.f. are attributed to the fact that Ga, being less reactive than In, tends to diffuse to the bottom leaving the surface poor in Ga. This has been confirmed by doing a depth profile, in which one can see that most of Ga is confined to the bottom. At this point, in order to have more Ga close to the surface, a final change in the sequence of the layers had been performed and is highlighted in figure 11.

A GaSe thin layer is put on top of Cu and another layer of GaSe is put under Cu on top of InSe. The new precursor has been selenized in the same way as the old precursor. A depth profile made on this new absorber shows that there is more Ga close to the surface and that it decreases starting from the surface and increases again going deep into the sample (figure 12). The characteristics of the solar cells made with the new absorber exhibit a $V_{OC}$ close to 570 mV, a $J_{SC}$ of ~38 mA/cm$^2$ and f.f. of 0.74 with an efficiency of 16.2% (figure 13).

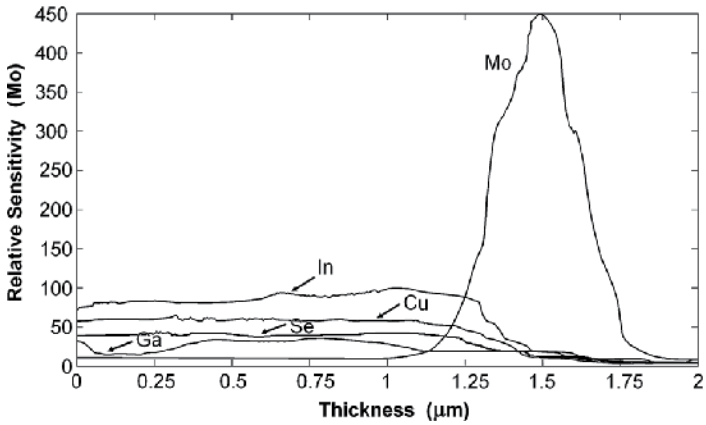


**Figure 12.** Sims depth profile of a CIGS film obtained starting from the new stratigraphy of the InSe/GaGe-based precursor. Note the trend of the Ga profile, which decreases starting from the surface and then re-increase approaching the back contact.

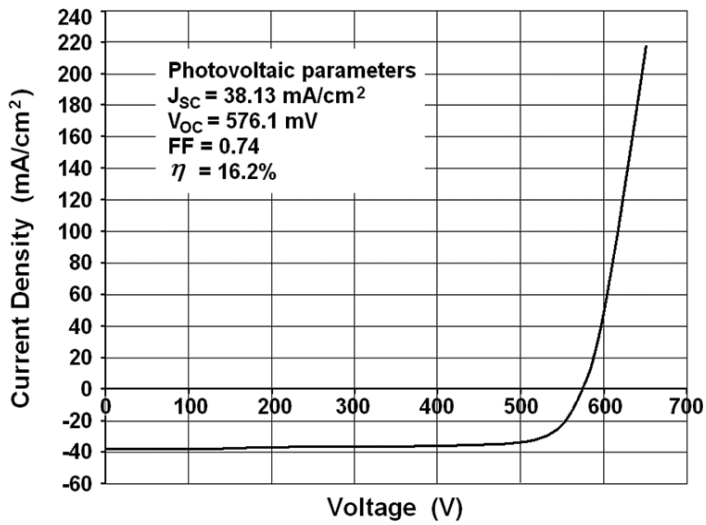


**Figure 13.** J-V characteristics of the Cu(In,Ga)$Se_2$ based solar cell made with the new precursor.

The process described above was also used to prepare Cu(In,Ga)$Se_2$/CdS solar cells directly on ceramic substrates (commercial tiles). This kind of ceramics is normally used in construction of buildings aimed to energy savings through the implementation of ventilated walls. However, the ceramic tile was modified in order to adapt its surface to become a good substrate for PV purpose. For this reason the surface of the tile was vitrified with the application of a special enamel. By checking in detail the composition and the constituent elements of this layer it has been possible to make the ceramic very similar, from the physico-chemi-

http://dx.doi.org/10.5772/51684

cal point of view, to the most common soda-lime glass. In fact, solar cells prepared on this ceramic substrate exhibit similar results to those obtained by using soda-lime glass as a substrate. (see figure 14 and table 4)

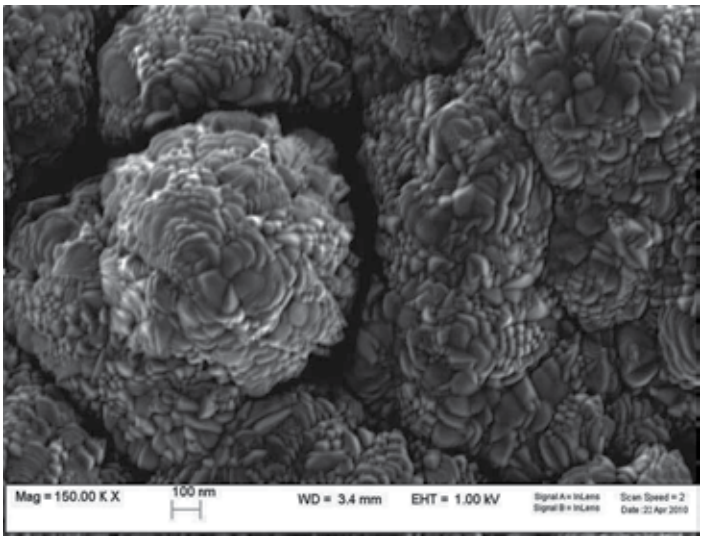


**Figure 14.** Scanning electron microscope photograph of the surface morphology of a CIGS film grown on an evolved ceramic tile.

| Absorber | Ga/In+Ga (%) | Voc (mV) | Jsc (mA/cm$^2$) | FF (%) | Efficiency (%) |
|---|---|---|---|---|---|
| *Cu(In,Ga)$Se_2$ | 10-15 | 531 | 34.8 | 71.60 | 13.23 |
| #Cu(In,Ga)$Se_2$ | 15-25 | 570 | 38 | 74 | 16.02 |
| ^Cu(In,Ga)$Se_2$ | 15-25 | 577 | 36.4 | 72 | 15.12 |

**Table 4.** Photovoltaic parameters of CIGS-based solar cells fabricated by using the last two different precursors both on soda-lime glass and commercial ceramic tile substrates.*the absorber layer is made starting with the $In_2Se_3$+$Ga_2Se_3$+Cu precursor and the cell is realized on SLG. # the absorber layer is made starting with the InSe+GaSe +Cu+GaSe precursor and the cell is realized on SLG.^the absorber layer is made starting with the InSe+GaSe+Cu+GaSe precursor and the cell is realized on commercial ceramic tile.

## 4. A future perspective: the $cu_2znsns_4$ system

Since it is necessary to develop non-Si-based solar cells due to a lack of highly pure Si sources, the PV world is oriented to develop new type of solar cell material that uses simple process and low-cost easily scalable techniques. Thin film polycrystalline solar cells have shown a remarkable growth in terms of efficiency, stability and scalability. CdTe and CuInGa$Se_2$ (CIGS) materials have demonstrated to be robust and reliable for delivering low cost

solar electricity. Because of direct band gap, which assures a high absorption coefficient, these devices use a very limited amount of material, which strongly reduces the production costs. However some issues on this are raised in particular the presence of rare and toxic elements that could impact on the perception of the population.

Indium and gallium for CIGS and tellurium for CdTe result to be rare materials that could limit the module production when we talk about Terawatts, if a proper recycling system is not set up [37].

Moreover, there is an old controversial discussion on the opportunity of using cadmium in photovoltaics; unfortunately this argument has been going above the scientific considerations and has been taken as an opportunity for crystalline silicon producer to limit the spreading of less expensive polycrystalline thin film devices [38].

As a matter of fact the introduction of cadmium in photovoltaic materials has been in the fabrication either of CdTe absorber material or of CdS buffer layer; in the first case there is mainly a problem or perception since CdTe is a secure and non toxic material, in the second case the amount of material is very little and encapsulated and the impact of cadmium in the overall environmental effect is minimal.

However, to overcome the environmental issues and most important to remove any doubt of massive production connected with material scarcity, in 1996 Katagiri et al. [39] have introduced a new device based on $Cu_2ZnSnS_4$ (CZTS) absorber layer; the structure was very similar to the CIGS standard structure having CdS as buffer layer, ZnO as front and Mo as back contact. The idea was not new since it has been introduced for the first time in 1988 from Ito and Nagazawa by making a heterojunction between CZTS and CTO (Cadmium Tin Oxide) [40]. The introduction of CZTS allows practically to substitute indium and gallium with zinc and tin which are pretty much available on the earth crust.

Furthermore, thin film photovoltaics is competing with other industries, which use similar elements such as In (flat panel) and Ga (optoelectronics). This issue together with the raw material availability mentioned above could affect the raw material prices. As already written the availability of In could limit the module production in the terawatt/year range [37].

The advantage of the kesterite materials (CZTS family) is that with similar material properties, similar preparation methods and same device structure as chalcopyrite solar cells, they are a real alternative to In-containing absorbers.

Generally for kesterites two kind of absorbers are considered: $Cu_2ZnSnS_4$ and $Cu_2ZnSnSe_4$, however their structure is pretty different since in the first case we have a real kesterite structure (space group I4) and in the second case a stannite structure is observed (space group I_42m).

So when it comes to a $Cu_2ZnSn(S,Se)_4$ absorber, which has also been employed, a polymorph structure has been observed. Polymorphism gives place to coexistence of different structure and it has been shown that stannite structure has lower binding energy and so lower stability. Stannite structure has lower band gaps and this could explain the lower open circuit voltages of these devices compared to the expected values. Band gap of the materials are

http://dx.doi.org/10.5772/51684

fluctuating depending on the different deposition methods and crystallization procedure; however most of band gaps for $Cu_2ZnSnS_4$ are around 1.5eV [41-46] while for $Cu_2ZnSnSe_4$ they stay around 1 eV. The main reason for the fluctuation of the band gaps is the very likely presence of secondary phases. As a matter of fact CZTS materials tend to produce many secondary phases, investigation on the phase diagram of this material shows that only in a very small region is possible to make single phase CZTS while a large variety of different secondary phases can easily be formed, such as ZnS(e), CuS(e), CuSnS(e). However the best solar cells show a Zn-rich and Cu-poor composition, which tendentially provides a ZnS(e) secondary phase. While ZnS(e), having a wide band gap and low conductivity, would not affect the open-circuit voltage, it could be responsible for the high series resistance observed in all solar cells [47,48].

The standard structure of the solar cells is very similar to the CIGS one, using ZnO doped with aluminum as front contact, CdS as buffer layer and Molibdenum as back contact. Friedlmeier et al. introduced this first design in 1997; they fabricated thin film solar cells by using a CZTS layer as the light absorber in contact with an n-CdS/ZnO window layer [47]. The best energy conversion efficiency produced by these cells was 2.3%. Later, Katagiri's group broke this record in 1999 producing a CZTS solar cell with 2.63% power conversion efficiency. In this cell, the CZTS film was deposited on a Mo coated soda lime glass (SLG) substrate [42]. By optimization of the sulfurization process, the efficiency of the solar cells was increased to 5.45% in 2003 [49], and then to 6.7% in 2008 [50].

Finally in 2010 Todorov reached 9.6% by inserting a selenization step [51], in 2011 the psychological limit of 10% has been overcome by Mitzi et al. by a non vacuum deposition method [52].

CZTS has been prepared already by a wide variety of deposition methods with different results, however what is surprisingly remarkable is that both vacuum and non vacuum techniques are very much in competition on the efficiency level. This is not the case for other polycrystalline thin films where generally the vacuum techniques are delivering higher performance. A large number of different vacuum deposition methods have been employed.

Vacuum-based fabrication techniques normally involve deposition of the constituent atoms of the CZTS compound on a substrate by sputtering or evaporation/coevaporation of the target sources under a certain pressure and temperature. These techniques have the advantage of easily controlling the chemical composition and phase profile in the thin films and normally have good reproducibility.

As mentioned before the first CZTS processing by Ito and Nakazawa was made by vacuum deposition, such as atomic beam sputtering in 1988. They were able to measure a band gap of 1.45 eV and the photovoltaic effect was proved by preparing an heterojunction with cadmium tin oxide (CTO) and a voltage of 165 mV was obtained [40].

After a long time in 1996 Katagiri made a complete photovoltaic cell with the following structure: ZnO:Al/CdS/CZTS/Mo/SLG. The absorber layer was deposited by electron beam gun followed by sulfurization; this process gave a power conversion efficiency of 0.66%. In 1997 Friedlmeier et al. at the university of Stuttgart deposited the CZTS absorber layer by coevaporation of the single constituents (using a similar method as the CIGS fabrication

process where the single elements or binary chalcogenides compounds are vacuum-deposited onto a heated substrate) obtaining a 2.3% efficiency cell. They also report, for the first time, that the electrical resistivity of the films can be improved considerably by treating the films with a KCN solution; this is still an important step of the fabrication process. Later on, Katagiri improved his deposition process by substituting Zn with ZnS in the e-beam sequence and improved the adhesion of the absorber to the molybdenum, increasing its efficiency up to 1.08%.

An approach based on one-step synthesis of CZTS thin films by simultaneous coevaporation of precursor sources Cu, Zn, Sn, S was reported by Tanaka et al. The grain size of the film depended on the substrate temperature. Larger grains were obtained at higher substrate temperature [52].

An integrated vacuum apparatus, which combined the RF sputtering technique with the sulfurization process was employed to reduce the effect of moisture from air ambient on the property of CZTS films. Target sources were based on ZnS, SnS and Cu. Both the quality and reproducibility of the CZTS films were significantly improved by this method and a 5.7% conversion efficiency with the CZTS-based thin film solar cells was achieved [53]. By eliminating the metal oxide impurity in the CZTS films using deionized water, the efficiency of the solar cells was further improved to 6.7% [49,54].

A lot of work has been recently presented by the IBM group; the research has been going on two different paths: vacuum and non vacuum deposition of CZTS.

For vacuum deposition a recent work from Wang et al. has been presented where the single elements are contemporarily evaporated on a SLG substrate by a rapid thermal deposition system. With an absorber thickness of only 1 micron and a few minutes annealing time the process is very promising for industrial application and has demonstrated a 6.8% conversion efficiency. High series resistance and a high charge recombination limit the efficiency [55].

Generally, if the composition of the precursor films is copper rich, it results in the formation of a $Cu_{2-x}$ S secondary phase, which can be removed by a post treating with KCN aqueous solution.

In metallic layer deposition it has been shown that the sequence of the different elements plays an important role in the crystallization of the absorber as shown with controversial results by Araki et al. [56] and Fernandes et al. [43] by pulsed laser deposition.

Another important effect is the known loss of Sn in CZTS during the annealing process. Above 350°C Sn tends to re-evaporate and stoichiometry is lost. Different corrections of this effect have been presented among which the addition of inert gas in the chamber during the annealing or addition of SnS in the precursor to compensate the loss.

Weber et al. studied the loss of Sn in CZTS during the annealing process. It was found that desorption of SnS from the CZTS at temperature above 350∘C led to the losses of Sn in vacuum. The decomposition process of CZTS could be reduced by addition of an inert gas in the chamber where the sintering was carried out [44]. Redinger et al. suggested to add extra SnS and S materials in the precursor to prevent the decomposition of CZTS at high temperature [45].

http://dx.doi.org/10.5772/51684

Non vacuum deposition methods are very attractive since they would allow a lower production cost since expensive vacuum machines and high energy evaporation system would be avoided.

Like CdTe and CIGS also CZTS has been prepared by non-vacuum alternative methods such as spray pyrolysis, electrochemical deposition, and spin coating of precursor solutions, but in this case with very nice performance [48].

One of the first non vacuum synthesis of CZTS thin films by spray pyrolysis of precursor solutions was introduced in 1997 by Nakayama and Ito. The layer was fabricated by preparing a mixture of water and ethanol with specific precursors such as CuCl, $ZnCl_2$, $SnCl_4$, and thiourea. With different precursors many other laboratories have studied this simple fabrication method, like Kumar et al. (high substrate temperature spray) [57] and Prabhakar et al. (ultrasonic spray) [58].

Spin-Coating of CZTS precursor solution is one of the most successful technique among the non vacuum methods but also among the vacuum ones. It is typically consisting in first the preparation of a precursor solution, then spin-coating the precursor solution on a SLG substrate and finally annealing the stacks in a controlled atmosphere to form the CZTS absorber.

Many different recipes have been presented from different researchers like Tanaka et al. [53], who presented an all-non vacuum deposited device. With a copper poor solution a 2.03% efficiency has been obtained. Other researcher like Pawar improved the crystallinity by the introduction of a complexing agent which increased inhomogeneity on the surface, later improved by sulfurization [59]. Fischereder et al. deposited CZTS films by spin coating a precursor solution consisting of metal salts of copper (I), tin (IV), and zinc (II) and thioacetamide in pyridine. They found out that the formation of CZTS compound occurred at temperature as low as 105°C in vacuum. The band gap energy of the films varied between from 1.41 to 1.81 eV by changing the annealing temperature point [60]. This is probably due to the coexistence of secondary phases in the film under low annealing temperature.Todorov et al. firstly presented best efficiency by preparing a CZTS solution based on hydrazine. The CZTS films were obtained by annealing the precursor films in sulfur or sulfur and selenium atmosphere at high temperature. The best cell efficiency was 9.66%, later improved by Mitzi et al. up to 10.1%. These devices use a hybrid absorber which is selenized and sulfurized as well. Measurements presented and comparison with a typical high efficiency CIGS solar cell shows that this high performing device still suffers from dominant interface recombination, short minority carrier lifetime, and high series resistance.

In conclusions, CZTS is a new material, which has in the last ten years seen a huge improvement; a lot has been done to study the physical properties and to control the stoichiometry, especially secondary phases that are still a strong limitation to high efficiency. High series resistance and short minority carrier lifetime generally reduce the current of these devices and the tendency to form a great numbers of detrimental defects decreases the open circuit voltage.

However efficiencies above 10% have been demonstrated, moreover these devices can be successfully prepared in a very large variety of deposition methods from vacuum growth

(coevaporation, sputtering, electron beam of precursors) to non-vacuum techniques among which the record cell has been obtained.

## 5. Conclusions

The need for more and more energy supplies due to increased demand from emerging countries such as India, China and Brazil and the contemporary necessity to preserve the environment, has increased interest in the development of new technologies that make use of solar energy.

In particular photovoltaic solar energy, the direct conversion of solar energy into electricity by means of semiconducting materials, has had very strong development in the last 20 years.

The most important parameter that characterizes a photovoltaic device is the ratio between its conversion efficiency and its cost. A value less than 0.5 $/Wp is considered competitive with the electricity obtained from fossil energy sources (Grid-parity). Although large progress in Cu(In,Ga)$Se_2$ solar cell scientific knowledge and process management has been accomplished, as evidenced by the high module and cell efficiencies fabricated by many groups, the range of deposition and device options that have been developed are not sufficient to ensure the achievement of this objective. In particular, for CIGS-based devices the question is: what is needed to be done to guarantee that Cu(In,Ga)$Se_2$ solar cell technology reaches its potential for large-scale production?

We could first respond by indicating how critical the need is for opportunities to develop new production technologies, including enhanced equipment for the deposition of the layers as well as production processes based on well-known engineering models. In addition a new second generation of production process-control tools will have to be worked out.

Improved equipment and very good diagnostic can be directly turned in to higher throughput, yield, and performance. This results in a better conversion efficiency-cost ratio.

In the ThiFiLab, considerable effort in the direction of simplifying the production process has been made and the achieved results suggest that we are closer to the development of a high-yield production line of low-cost highly efficient modules.

A second essential question could be: what might be the innovations that are needed for laying the groundwork for a new generation of thin-film Cu(InGa)$Se_2$-based solar cells?

A lot of R&D can be made by studying alternative substrates such as the ceramic tiles proposed by the ThiFiLab that directly allow the buildings integration of photovoltaics (BIPV).

Another step may be achieved by developing low-temperature manufacturing processes that allows the use of innovative substrates such as polymeric ribbons, which represents a basic passage towards the low-cost Roll-to-Roll (R2R) technology. Similarly, there may be significant cost and processing advantages to a cell structure that enables the use of a Cu(InGa)$Se_2$ layer much less than 1 μm.

http://dx.doi.org/10.5772/51684

R&D on Cu(In,Ga)$Se_2$ remains very attractive as well as promising through all of these challenges, aimed at improving the knowledge of both the material and the device, in addition to developing new production technologies and revolutionary innovations.

The great stability over time shown by the high-efficiency devices together with the great variability of material stoichiometry and manufacturing processes provide a great expectation that this material will give its contribution to energy demand at a competitive price while respecting the environment.

In this groove the research on kesterites is to be placed; these are relatively new materials for solar cell applications, and a lot of research remains to be done before the best components and processing methods are found. In particular, concerning $Cu_2ZnSnSe_4$ as PV material a bigeffort must be made in the knowledge related to the segregation of phases, which affectthe final functioning of the device. The structure of this cell, being similar to that normally used for CIGS solar cells, has already been well defined, but the deposition methods of the absorber layer are still subject of study. Despite this, with this material as absorber, solar cells with conversion efficiency greater than 10% have been realized.

## Author details

Alessio Bosio[1*], Daniele Menossi[1], Alessandro Romeo[2] and Nicola Romeo[1]

*Address all correspondence to: alessio.bosio@unipr.it

1 Physics Dept. University of Parma, Italy

2 Computer Science Dept.Universityof Verona, Italy

## References

[1] Jackson, P., Hariskos, D., Lotter, E., Paetel, S., Wuerz, R., Menner, R., Wischmann, W., & Powalla, M. (2011). Prog. Photovolt:. *Res. Appl*, 19, 894-897.

[2] Hahn, H., Frank, G., Klingler, W., Meyer, A. D., & Störger, G. (1953). *Z. Anorg. Allg. Chem.*, 271, 153-170.

[3] Shay, J., & Wernick, J. (1974). Ternary Chalcopyrite Semiconductors: Growth, Electronic Properties, and Application. Oxford, Pergamon Press.

[4] Tell, B., Shay, J., & Kasper, H. (1971). *Phys. Rev.*, B4, 4455-4459.

[5] Tell, B., Shay, J., & Kasper, H. (1972). *J. Appl. Phys.*, 43, 2469-2470.

[6] Wagner, S., Shay, J. L., Migliorato, P., & Kasper, H. M. (1974). *Appl. Phys. Lett.*, 25, 434.

[7] Romeo, N., Sberveglieri, G., Tarricone, L., & Paorici, C. (1977). *Appl. Phys. Lett.*, 30, 108.

[8] Kazmerski, L., White, F., & Morgan, G. (1976). *Appl. Phys. Lett.*, 29, 268-269.

[9] Devaney, W., Michelsen, R., & Chen, W. (1985). Paper presented at 18th IEEE Photovoltaic Specialists Conference. IEEE Publishing, NY, 173.

[10] Tuttle, I. R., Ward, J. S., Berens, T., Duda, A., Contreras, M. A., Ramanathan, K. R., Tennant, A. L., Keane, J., Cole, E. D., Emery, K., & Noufi, R. (1996). Proc. Materials Research Society,. San Francisco.

[11] Contreras, M. A., Egaas, B., Ramanathan, K., Hiltner, J., Swarzlander, A., Hasan, F., & Noufi, R. (1999). *Progr. Photovolt: Res. Appl.*, 7, 311.

[12] Ramanathan, K., Contreras, M. A., Perkins, C. L., Asher, S., Hasoon, F. S., Keane, J., Young, D., Romero, M., Metzger, W., Noufi, R., Ward, J., & Duda, A. (2003). *Progr. Photovolt: Res. Appl.*, 11, 225.

[13] Hedstroem, J., Olsen, H., Bodegard, M., Kyler, A., Stolto, L., Hariskos, D., Ruckh, M., & Schock, H. W. (1993). *Proc. 23rd IEEE Photovoltaic Specialist Conf.*, 364-371.

[14] Chen, W., Stewar, J. M., & Stanbery, B. J. (1987). *Proc. 19th IEEE Photovoltaic Specialist Conf.*, 1445-1447.

[15] Potter, R. (1986). *Sol. Cells*, 16, 521-527.

[16] Gabor, A. M., Tuttle, J. R., Bode, M. H., Franz, A., Tennant, A. L., Contreras, M. A., Noufi, R., Jansen, D. G., & Heramnn, A. M. (1996). *Sol. Energy Mater. Sol. Cells*, 4, 247-260.

[17] Tarrant, D., & Ermer, J. (1993). *Proc. 23rd IEEE Photovoltaic Specialist Conf.*, 372-375.

[18] Mickelsen, R. A., Chen, W. S., Hsiao, Y. R., & Lowe, V. (1984). *IEEE Trans. Electr. Devices*, 311984, 542.

[19] Noufi, R., Matson, R. J., Powell, R. C., & Herrington, C. (1986). *Solar Cells*, 16, 479.

[20] Birkmire, R. W., Dinetta, L. C., Lasswell, P. G., Meakin, J. D., & Phillips, J. E. (1986). *Solar Cells*, 16, 419.

[21] Potter, R. R. (1986). *Solar cells*, 16, 521.

[22] Piekoszewski, J., Loferski, J. J., Bealieu, R., Beall, J., Roessler, B., & Shewchun, J. (1980). *14th IEEE Photovoltaic Specilist' Conf. 98.*

[23] Romeo, N., Canevari, V., Sberveglieri, G., Bosio, A., & Zanotti, L. (1986). *Solar Cells*, 16, 155.

[24] Samaan, A. N., Abdul-Karim, N., Abdul-Hussein, N., Tomlinson, R. D., Hill, A. E., & Armour, D. G. (1980). *Jpn. J. Appl. Phys.*, 19-3.

[25] Stolt, L. (1993). *Photovoltaic Insider's Report,, XII-*, 6, 1-2.

[26] Noufi, R. (1994). *Photovoltaic Insidrr's Report*, *I-*, 31, 2-4.

[27] Basol, B. M., Kapur, V. J., & Halany, A. (1991). Proc 22th IEEE Photov. Spec. Conf IEEE-New York, ., 893.

[28] Binary alloy phase diagrams. (1986). *Park-OHIO: American Society for Metal*, 1.

[29] Lincot, D., Ortega-Borges, R., Vedel, J., Ruckh, M., Kessler, J., Velthaus, K. O., Hariskos, D., & Schock, H. W. (1992). *Proc. 11th E.C. Photov. Solar Energy conf., Harwood Academic Publ. Switzerland*, 870.

[30] Repins, I., Contreras, M. A., Egaas, B., De Hart, C., Scharf, J., Perkins, C. L., To, B., & Noufi, R. (2008). *Progress on Photovoltaic Research and Application,*, 16, 235-239.

[31] Marudachalan, M., Hichri, H., Klenk, R., Birkmire, R. W., Shafarman, W. N., & Schultz, J. M. (1995). *Appl. Phys. Letters,*, 67, 3978-3980.

[32] Nakada, T. N., & Kunioka, A. (1998). *Jap. J. Appl. Phys.*, 37, L1065-L1067.

[33] Zweigart, S., Walter, T., Koble, C., Sun, S. M., Ruhle, U., & Schock, H. W. (1994). *Proc. First World Conf. on Photovoltaic Energy Conversion*, 60-67.

[34] Romeo, N., Bosio, A., & Canevari, V. (2003). *Proc. of 3rd Worl Conf. On Photovoltaic Energy Conversion*, 1838-1840.

[35] Gessert, T. A., Yoshida, Y., Fesenmaier, C. C., & Coutts, T. J. (2009). *J. Appl. Phys.*, 105, 083547/-1-083547/-7.

[36] Edoff, M., Viard, N., Wätijen, T., Schleussener, S., Westin, P. O., & Leifer, K. (2009). *Proc. of the 24th Photovoltaic Solar Energy Conference, Munich*, 3037-3040.

[37] Fhtenakis, V. M. (2009). *Renewable and Sustainable Energy Reviews*, 13-2746.

[38] Fthenakis, V. M., Fuhrmann, M., Heiser, J., Lanzirotti, A., Fitts, J., & Wang, W. (2005). *Progress in Photovoltaics: Research and Application*, 13(8), 713.

[39] Katagiri, H., Sasaguchi, N., Hando, S., Hoshino, S., Ohashi, J., & Yokota, T. (1996). *Tech. Dig.Int. Photovoltaic Science and Engineering Conf.,Miyazaki*, 745.

[40] Ito, K., & Nakazawa, T. (1988). *Japanese Journal of Applied Physics*, 27(11), 2094-2097.

[41] Katagiri, H., Jimbo, K., Maw, W. S., Oishi, K., Yamazaki, M., Araki, H., & Takeuchi, A. (2009). *Thin Solid Films*, 517, 2455-2460.

[42] Araki, H., Mikaduki, A., Kubo, Y., Sato, T., Jimbo, K., Maw, W. S., Katagiri, H., Tamazaki, M., Oishi, K., & Taeuchi, A. (2008). *Thin Solid Films*, 517, 1457-1460.

[43] Fernandes, P. A., Salomè, P. M. P., & da Cunha, A. F. (2009). *Semiconductor Science and Technology*, 24, 105013-105019.

[44] Weber, A., Mainz, R., & Schock, H. W. (2010). *Journal of Applied Physics*, 107, 013516-013521.

[45] Redinger, A., Berg, D. M., Dale, P. J., & Siebentritt, S. (2011). *Journal of the American Chemical Society*, 133, 3320-3323.

[46] Hibberd, C. J., Chassaing, E., Liu, W., Mitzi, D. B., Lincot, D., & Tiwari, A. N. (2010). *Progress in Photovoltaics*, 18, 434-452.

[47] Friedlmeier, T. M., Wieser, N., Walter, T., Dittrich, H., & Schock, H. W. (1997). *Proc. 14th EuropeanConference of Photovoltaic Science and Engineering and Exhibition, Bedford, UK, 1242.*

[48] Katagiri, H., Saitoh, K., Washio, T., Shinohara, H., Kurumadani, T., & Miyajima., S. (2001). *Solar Energy Materials and Solar Cells*, 65, 141-148.

[49] Katagiri, H., Jimbo, K., Moriya, K., & Tsuchida, K. (2003). *Proc. World Conf. on Photovoltaic Energy Conversion, Osaka,2874*.

[50] Katagiri, H., Jimbo, K., Yamada, S., Kamimura, T., Maw, W. S., Fukano, T., Ito, T., & Motohiro, T. (2008). *Applied Physics Express*, 1, 041201-2.

[51] Todorov, K., Reuter, K. B., & Mitzi, D. B. (2010). *Advanced Materials*, 22, E156-E159.

[52] Mitzi, D., Gunawan, O., Todorov, T., Wang, K., & Guha, S. (2011). *Solar Energy Materials & Solar Cells*, 95, 1421-1436.

[53] Jimbo, K., Kimura, R., Kamimura, T., Yamada, S., Maw, W. S., Araki, H., Oishi, K., & Katagiri, H. (2007). *Thin Solid Films*, 515, 5997-5999.

[54] Tanaka, T., Nagatomo, T., Kawasaki, D., Nishio, M., Guo, Q., Wakahara, A., Yoshida, A., & Ogawa, H. (2005). *Journal of Physics and Chemistry of Solids*, 66, 1978-1981.

[55] Wang, K., Gunawan, O., Todorov, T., Shin, B., Chey, S. J., Bojarczuk, N. A., Mitzi, D., & Guha, S. (2010). *Applied Physics Letters*, 97, 143508-3.

[56] Araki, H., Mikaduki, A., Kubo, Y., Sato, T., Jimbo, K., Maw, W. S., Katagiri, H., Yamazaki, M., Oishi, K., & Takeuchi, A. (2008). *Thin Solid Films*, 517, 1457-1460.

[57] Kumar, Y., Kumar, B. K., Babu, G. S., Bhaskar, P. U., & Raja, V. S. (2009). *Physica Status Solidi A*, 206, 1525-1530.

[58] Prabhakar, T., & Nagaraju, J. (2010). *Proc. of the 35th IEEE Photovoltaic Specialists Conference*, 1964-1969.

[59] Pawar, B. S., Pawar, S. M., Shin, S. W., Choi, D. S., Park, C. J., Kolekar, S. S., & Kim, J. H. (2010). *Applied Surface Science*, 257, 1786-1791.

[60] Fischereder, A., Rath, T., Haas, W., Amenitsch, H., Albering, J., Meischler, D., Larissegger, S., Edler, M., Saf, R., Hofer, F., & Trimmel, G. (2010). *Chemistry of Materials*, 22, 399-3406.

Chapter 5

# $Cu_2ZnSnS_4$ Thin Film Solar Cells: Present Status and Future Prospects

Minlin Jiang and Xingzhong Yan

Additional information is available at the end of the chapter

http://dx.doi.org/10.5772/50702

## 1. Introduction

Pollution of the earth and shortage of energy sources have been the bottle-neck of survival and development for human beings since the start of the 21st century. Therefore, lowering energy consumption and protecting the environment have gradually gained attention from countries all over the world. In order to keep sustainable development, governments, research institutes, and industries have been working on the problems caused by the shortage of available energy sources. It is well known that the best way is to exploit renewable energy resources. Solar energy is considered to be the most economic and effective among all available renewable energy resources. Solar energy is inexhaustible and it has already been theoretically and experimentally proved that the earth would not be polluted at all if solar energy was utilized effectively.

To encourage and to promote the direct utilization of solar energy, developed countries have been legislating and deploying solar initiatives [1-3]. Joint Research Centre (Europe) predicted that energy directly harvested from sunlight would be 20% of total energy consumption in 2050, and this value could be over 50% in 2100 [4]. Solar energy will be widely utilized in industry, agriculture and daily life. Photovoltaic (PV) systems have recently attracted much attention due to their inherent advantages. Firstly, PV systems are capable of directly translating sunlight into electrical energy. The theoretical conversion efficiency of PV systems is relatively higher than other power generators. Secondly, PV systems do not necessarily contain movable parts. System wear induced by mechanical movement is avoided. Therefore, PV systems can work continuously free from maintenance longer than other power generation technologies.

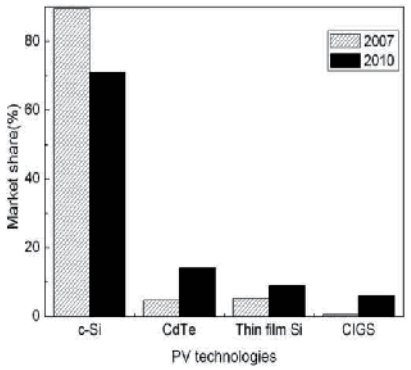


**Figure 1.** Market share of different PV technology [8].

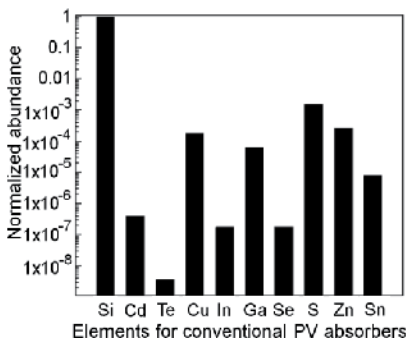


**Figure 2.** Normalized abundance of elements for conventional PV absorbers.

It was reported by Solarbuzz that 16.3 GW PV modules had been shipped to customers in 2010 with the lion's share going to crystalline silicon (c-Si) technology (71%) [5]. Due to high cost and energy consumption input in manufacturing c-Si PV of modules, market share of the c-Si technology has been dropping while thin film PV technologies have been increasing rapidly [6, 7]. There are three main thin film PV technologies, CdTe, $CuInxGa_{1-x}S(Se)_2$ (CIGS), and thin film Si, which has gained 14%, 9%, and 6% of PV market share in 2010, respectively (Fig.1) [8]. Nevertheless, Si thin film solar cell (TFSC) has been relatively underdeveloped due to low efficiency and instability from the Staebler–Wronski effect. For the other two thin film technologies, there are restriction on the usage of heavy metals such as cadmium, the limitation in supplies for indium and tellurium, and the wide fluctuation in prices of indium and tellurium. These render the combined production capacity of the existing CdTe and CIGS technologies at a small scale lower than 100 GW per year. This is only a small fraction of energy consumption in 2050 which is expected to be 27 TW [4, 9].

Recently, quaternary compound $Cu_2ZnSnS_4$ (CZTS) has been intensively examined as an alternative PV material due to its similarity in material properties with CIGS and the relative abundance of raw materials (Fig. 2). CZTS is a compound semiconductor of $(I)_2(II)(IV)(VI)_4$.

http://dx.doi.org/10.5772/50702

With a high absorption coefficient (> $10^4$ $cm^{-1}$) and a desirable bandgap (~1.45 eV), CZTS thin film has been considered an excellent PV material. Theoretical calculations have shown that conversion efficiency as high as 32% was possible for CZTS TFSCs with a CZTS layer of several micrometers. Wadia et al. also calculated the minimum cost of raw materials for the existing PV technologies and the emerging PV technologies [10]. Part of the results is shown in Fig. 3. The cost of raw material for CZTS PV technology is much lower than that of the three existing thin film PV technologies.

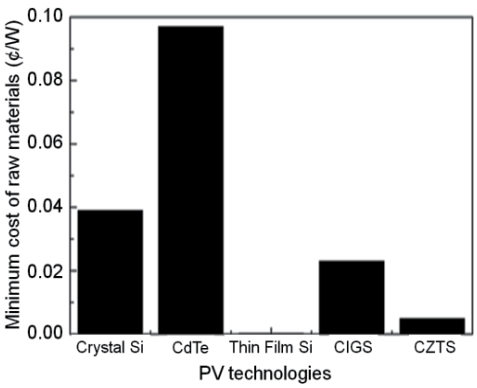


**Figure 3.** Minimum cost of raw materials for different PV technology [10].

Significant progress on this relatively new research area has been achieved in last five years. Champion efficiency of CZTS thin film solar cell (TFSC) has reached 8.4 % and an efficiency of 6.21 % has been demonstrated for CZTS sub-module with an area of 22.6 $cm^2$. However, these efficiencies are still much lower than those of CIGS PV devices. This chapter reviews the present status of various CZTS TFSC technologies with special emphasis on properties of CZTS thin films deposited by different methods. New results generated by solution-based processing have been reported, and the methodologies to make CZTS photovoltaic technology more marketable are also proposed and discussed. Based on the information reported and our experiences gained on the research and development of CIGS and CZTS solar cells, the challenges and perspectives of CZTS TFSCs have been addressed.

## 2. General properties of CZTS thin film

In 1967, CZTS single crystal was synthesized and analyzed [11]. However, it had not gained intensive interest from academies and industries until 2007 when solar power was heavily subsidized by governments and Si-based PV technologies encountered a skyrocketing price of highly pure polycrystalline silicon. Thus far, structural, optical, and electrical properties of CZTS thin film have been intensively investigated.

### 2.1. Crystal structure

CZTS thin films are usually in a polycrystalline form consisting of kesterite crystal structures. Kesterite CZTS single crystal was first synthesized by Nitsche et al. using the chemical vapor transport method [11]. X-ray diffraction (XRD) results showed that this synthesized CZTS had sphalerite-like crystal structure with c/a being close to 2 (a=5.43 Å, c=10.83 Å). In 1974, detailed lattice data of a CZTS single crystal were reported by Schäfer and Nitsche (Table 1) [12]. Thereafter, this data was frequently referenced to determine CZTS phase in literatures. In 2011, Lu et al. claimed that wurtzite CZTS nanocrystals were synthesized through a hot injection method [13]. The experimental XRD patterns were indexed to a simulated crystal structure with a wurtzite phase (Table 2).

| $d$ (Å) | $I/I_0$ (%) | ($hkl$) | $2\theta$ (degree) |
|---|---|---|---|
| 5.421 | 1 | 002 | 16.338 |
| 4.869 | 6 | 101 | 18.205 |
| 3.847 | 2 | 110 | 23.101 |
| 3.126 | 100 | 112 | 28.530 |
| 3.008 | 2 | 103 | 29.675 |
| 2.713 | 9 | 200 | 32.989 |
| 2.426 | 1 | 202 | 37.025 |
| 2.368 | 3 | 211 | 37.966 |
| 2.212 | 1 | 114 | 40.758 |
| 2.013 | 2 | 105 | 44.996 |
| 1.919 | 90 | 220 | 47.331 |
| 1.636 | 25 | 312 | 56.177 |
| 1.618 | 3 | 303 | 56.858 |
| 1.565 | 10 | 224 | 58.969 |
| 1.45 | 1 | 314 | 64.177 |
| 1.356 | 2 | 008 | 69.229 |
| 1.245 | 10 | 332 | 76.442 |

**Table 1.** Lattice data of the kesterite CZTS single crystal [12].

Notes: $d$ indicates the distance between two neighbor parallel planes, $I/I_0$ is the relative peak intensity, ($hkl$) are Miller indexes, and $2\theta$ is the twice of Bragg diffraction angle.

Kesterite CZTS has highly similar crystal structure with chalcopyrite CIGS where half of indium and (or) gallium is replaced by zinc and the other half by tin (Fig. 4(a)). Similar to ZnO or ZnS, the anions and cations in kesterite CZTS crystal are located in a tetrahedral bonding envi-

http://dx.doi.org/10.5772/50702

ronment with a stacking model which is similar to zincblende (Fig. 4(c)) [14]. The other important structure for CZTS crystal is a stannite structure (Fig. 4(d)) [14]. The difference between kesterite CZTS crystal and stannite CZTS crystal lies in a different order in the cation sub-lattice. In kesterite CZTS, cation layers of CuSn, CuZn, CuSn, and CuZn alternate at z = 0, 1/2, 1/2, and 3/4, respectively; while in stannite structures, ZnSn layers alternate with $Cu_2$ layers. The wurtzite structure can be formed by replacing Zn (II) with Cu (I), Zn (II) and Sn (IV) in wurtzite ZnS with each sulfur atom equally coordinating with two Cu (I), one Zn (II), and one Sn (IV) (Fig. 4(b)) [13]. First-principle calculations by Chen et al. indicated that the kesterite structure had a lower energy and should be more stable than the stannite structure [15]. Most of CZTS samples crystallized in the kesterite structure as predicted theoretically. XRD results showed that diffraction peaks of (112), (200), (220/204), and (312/116) with a preferred orientation along (112) were commonly observed [16-19]. Peaks of (002), (008), (101), (103), (105), (110), (211), (213), (224), and (332) were also demonstrated in the XRD spectra [20- 24].

| Experimental *d* (Å) | Calculated *d* (Å) | (*hkl*) | Experimental 2*θ* (degree) |
|---|---|---|---|
| 3.339 | 3.324 | 100 | 26.70 |
| 3.175 | 3.169 | 002 | 28.10 |
| 2.954 | 2.944 | 101 | 30.26 |
| 2.299 | 2.294 | 102 | 39.19 |
| 1.921 | 1.919 | 110 | 47.32 |
| 1.783 | 1.783 | 103 | 51.23 |

**Table 2.** Lattice data of the wurtzite CZTS crystal [13].

### 2.2. Optical properties

The optical bandgap of stoichiometric kesterite-CZTS was theoretically determined to be 1.50 eV [15]. Experimental results demonstrated that bandgap of CZTS thin film deposited using different method varied from 1.4 eV to 1.5 eV [16, 19, 20, 25, 26]. It is commonly recognized that CZTS thin film has an absorption coefficient as high as $10^4$ $cm^{-1}$. Sol-gel derived CZTS thin film from our group confirmed that the absorption coefficient is higher than $10^4$ $cm^{-1}$ in the photon energy range greater than 1.2 eV (Fig. 5) [27].

Raman spectrum is a powerful characterization method to reveal Raman shift peaks in CZTS especially for the peaks associated with secondary phases such as $Cu_xS$, ZnS, $Sn_xS$, $Cu_2SnS_3$, and $Cu_3SnS_4$. The universally acknowledged peak is 338 $cm^{-1}$ [28]. However, peaks at 96 $cm^{-1}$, 166 $cm^{-1}$, 250 $cm^{-1}$, 251 $cm^{-1}$, 287 $cm^{-1}$, 288 $cm^{-1}$, 289 $cm^{-1}$, 337 $cm^{-1}$, 338 $cm^{-1}$, 352 $cm^{-1}$, 370 $cm^{-1}$, 372 $cm^{-1}$ have also been observed and assigned to CZTS [16, 29-32].

To study the recombination mechanisms, low temperature photoluminescence spectra were recorded from CZTS thin films. Several groups observed a broad peak centering at around 1.24 eV, which was attributed to the typical donor-acceptor pair transition involving tail states created by potentials fluctuations [33-35]. It is claimed that the presence of potential

fluctuations indicates CZTS is strongly compensated [33]. Time-resolved PL data illustrated that lifetime of free carriers in CZTS thin film was lower than 1 ns [36].

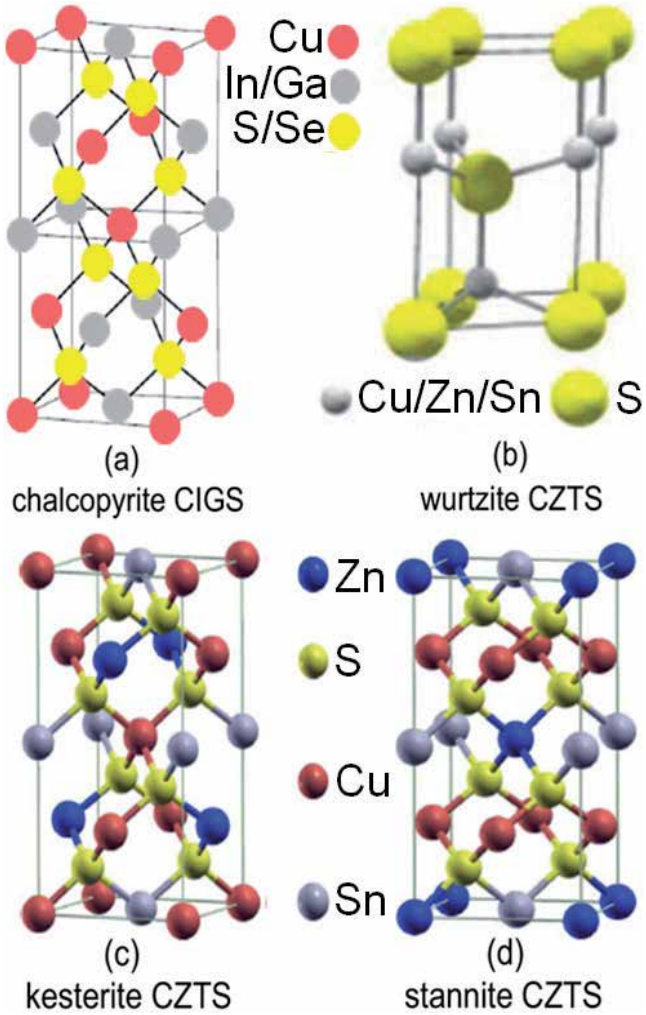


**Figure 4.** Crystal structures of CIGS and CZTS [13, 14].

### 2.3. Electrical properties

In contrast with silicon, where either atoms of phosphorus or atoms of boron are intentionally introduced for producing n-type and p-type semiconductors, respectively, CZTS is self-doped through a formation of intrinsic defects including vacancies ($V_{Cu}$, $V_{Zn}$, $V_{Sn}$, and $V_S$), antisite defects ($Cu_{Zn}$, $Zn_{Cu}$, $Cu_{Sn}$, $Sn_{Cu}$, $Zn_{Sn}$, and $Sn_{Zn}$), and interstitial defects ($Cu_i$, $Zn_i$, and $Sn_i$). These defects could form during growth of CZTS thin film. Chen et al. systematically studied the defect properties of CZTS using first-principle calculations [37]. It was found

http://dx.doi.org/10.5772/50702

that the formation energy of acceptor defects was lower than that of donor defects, which makes n-type doping very difficult in CZTS [37]. The commonly observed p-type conductivity of CZTS thin films comes mainly from the $Cu_{Zn}$ antisite defect, partly explaining why CZTS thin films must be Cu-poor and Zinc-rich to successfully fabricate CZTS solar cells.

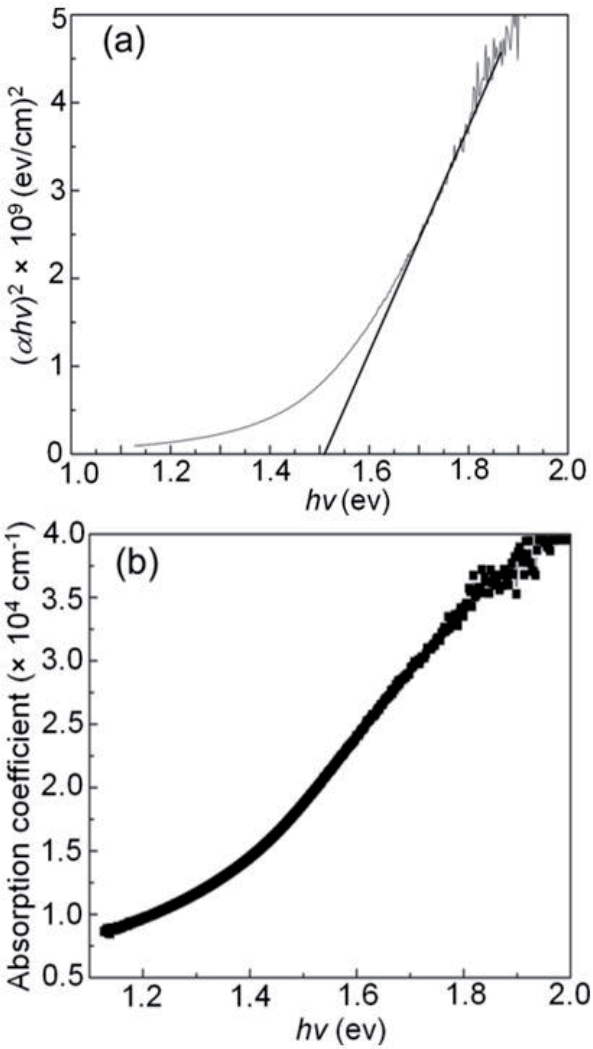


**Figure 5.** a) Typical bandgap and (b) absorption coefficients of a CZTS thin film [27].

Reported resistivity of CZTS thin films was significantly different [38-40]. The most suitable value for CZTS thin film should range from $10^{-3}\Omega$•cm to $10^{-1}\Omega$•cm according to published data for CZTS solar cells [25]. The hole concentration was reported to vary from $10^{16}cm^{-3}$ to $10^{18}cm^{-3}$ [41-43], although extremely high and extremely low concentration were also report-

ed [44, 45]. Hall effect measurement results showed that hole mobility of CZTS changed from lower than 0.1 to as high as 30 $cm^2 \bullet V^{-1} \bullet s^{-1}$, while most published values were in the range of 1 to 10 $cm^2 \bullet V^{-1} \bullet s^{-1}$ [40, 44-47]. The lower mobility indicates that the optimized thickness of absorber layer in CZTS TFSCs cannot be as large as that for CIGS TFSCs.

## 3. CZTS thin film solar cell

We would like to first introduce the basic definitions which are very important parameters when evaluating a solar cell. The solar cell can be basically taken as a battery in a simple electrical circuit (Fig. 6 (a)). Without sunlight shining on solar cell, it can do nothing. However, the solar cell will work as a battery if it is activated by light (Fig. 6 (b)). Electrical potential difference will be developed between its two ends and electrical current can flow through the solar cell. The potential difference derived when the resistance of the load is infinite is defined as open circuit voltage, $V_{OC}$. Correspondingly, the electrical current flowing in the circuit when the resistance of the load is zero is defined as short circuit current, $J_{SC}$. Shown in Fig. 6 (c) is a typical *I-V* relationship curve of the illuminated solar cell when the load resistance changes from zero to infinite. The delivered power by the solar cell, *P*, is given by

$$P = I \times V \tag{1}$$

The typical *P-V* relationship curve is also shown in Fig. 6 (c). *P* reaches a maximum value at certain condition under which the solar cell will deliver the highest power to the external load. This condition is defined as maximum power point and the maximum power is denoted as $P_m$. The corresponding voltage and current is denoted as $V_m$ and $I_m$, respectively. Another important parameter to evaluate a solar cell is fill factor, *FF*, which is defined as

$$FF = \frac{I_{\mathrm{m}} \times V_{\mathrm{m}}}{I_{\mathrm{SC}} \times V_{\mathrm{OC}}} \tag{2}$$

The most important parameter for a solar cell is conversion efficiency, $\eta$, which describes the solar cell's ability to translate solar energy into electrical energy. The conversion efficiency is given by

$$\eta = \frac{P_{\mathrm{m}}}{P_{\mathrm{L}}} \tag{3}$$

where $P_L$ is the power of the simulated light.

Parameters such as $J_{SC}$, $V_{OC}$, *FF*, and $\eta$ are key performance characteristics of a solar cell. These parameters are light-dependent and environment-dependent, which means that the values of these parameters of a specific solar cell will change if the solar cell is illuminated with different light intensity. Worldwide recognized characterization condition for solar cells is the

http://dx.doi.org/10.5772/50702

Standard Test Condition (STC) which stipulates that a solar cell should be tested at 25℃ under Air Mass 1.5 spectrum illumination with an incident power density of 100 mW/cm$^2$.

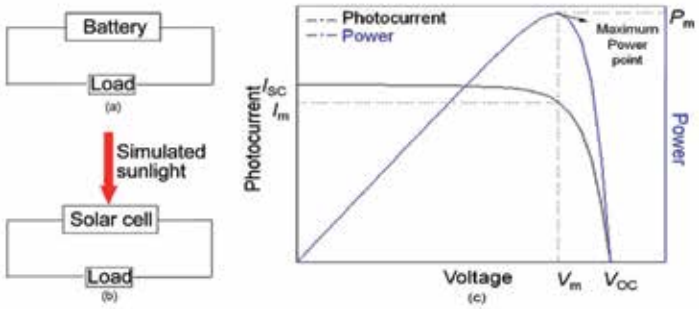


**Figure 6.** a) Schematic basic electrical circuit, (b) schematic basic operating circuit of solar cell, (c) typical I-V curve of a solar cell.

### 3.1. Basic structure and fabrication procedures

The schematic structure of CZTS solar cell is shown in Fig.7. Molybdenum thin film with thickness of 500~700 nm is sputtering-deposited on glass substrate as back contact because Mo is stable in harsh reactive conditions such as sulfur-containing vapor and high temperature. The absorber layer, p-type CZTS thin film with thickness ranging from 1.0 to 2.0 μm is then coated on Mo thin film. To form p-n junction with the p-type CZTS, 50~100 nm n-type CdS thin film is deposited on the absorber layer usually by chemical bath deposition. The surface of CZTS thin film is too rough to be fully covered by CdS thin film, leading to shortage between front contact and back contact. To prevent leakage, 50~90 nm intrinsic ZnO (i-ZnO) thin film is usually sputtering-coated on CdS before 500~1000 nm transparent conducting oxide (TCO) thin film is deposited by sputtering as the front contact layer of the cell. Finally, to electrically measure the *I-V* property of CZTS solar cell, Ni/Al grid is separately deposited on both TCO and Mo layer.

### 3.2. Deposition techniques of CZTS thin films

The first $(I)_2(II)(IV)(VI)_4$ solar cell was developed in 1977 by Wagner and Bridenbaugh. A n-type CdS thin film was evaporation-coated on vapor transportation-grown $Cu_2CdSnS_4$ single crystal substrate to form the p-n junction [48]. This device showed a short-circuit current density of 7.9 mA/cm$^2$, an open-circuit voltage of 0.5 V, and a conversion efficiency of 1.6%. The authors pointed out that a large series resistance limited the performance. In 1988, a heterojunction solar cell with an open circuit voltage of 165 mV was achieved by depositing cadmium tin oxide on CZTS thin film [40]. In 1997, the first CZTS TFSC with efficiency of 0.66% was realized by Katagiri using electron beam deposition followed by sulfurization [49]. The highest efficiency of 8.4% for CZTS TFSC and 6.21% for sub-module has been achieved by IBM and by Solar Frontier, respectively [36, 50].

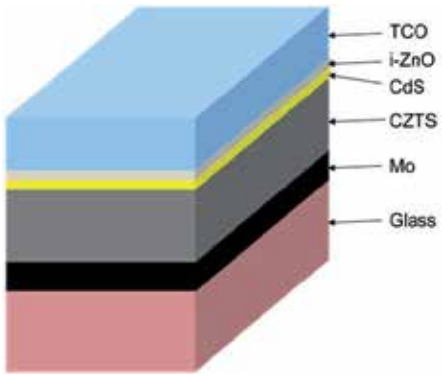


**Figure 7.** Schematic structure of typical CZTS solar cell.

Shown in Fig.8 are conversion efficiencies for CZTS solar cells obtained by different methods. Evaporation and sputtering have been intensively employed for the deposition of CZTS thin film both because the properties of CZTS thin film are more readily controlled using these two methods and because great success has been achieved experimentally and commercially for CIGS solar cells manufactured using evaporation and sputtering.

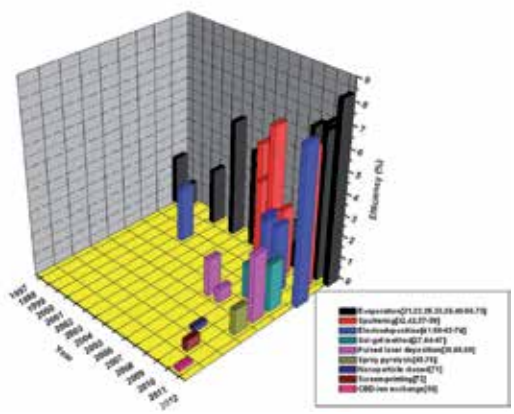

**Figure 8.** Conversion efficiencies obtained for CZTS solar cells by different methods.

The highest efficiencies achieved by the specific methods shown in Fig. 8 are listed in Table 3. Many technologies have been explored for fabricating CZTS TFSCs, as discussed in detail in the following paragraphs. Similar to the CIGS solar cells, whose highest efficiency was obtained by evaporation deposition [75], the highest efficiency of CZTS solar cell was also attained by evaporation deposition [36]. Conversion efficiency of 10.1% by IBM and 7.23% by Guo et al. have been realized for $Cu_2ZnSn(S,Se)_4$ (CZTSSe) solar cells made using solution-based method and nanoparticle-based method, respectively [76,77]. However, both cas-

es modified the composition of CZTS thin films through introduction of selenium, which is a rare element in the earth crust.

| Method | Precursor | Efficiency (%) | Year | Reference |
|---|---|---|---|---|
| Evaporation | Cu, Zn, Sn, S | 8.4 | 2011 | [73] |
| Sputtering | Cu, SnS, ZnS | 6.77 | 2008 | [59] |
| Electrodeposition | Cu(II) ion, Zn(II) ion, Sn(IV) ion | 7.3 | 2012 | [74] |
| Sol gel-based method | Copper (II) acetate monohydrate<br>zinc (II) acetate dehydrate<br>tin (II) chloride dehydrate | 2.23 | 2011 | [66] |
| Pulsed laser deposition | in-house fabricated CZTS pellet | 3.14 | 2011 | [69] |
| Spray pyrolysis | not available | 1.15 | 2011 | [70] |
| NP-based method | Copper(II) acetylacetonate, zinc acetate,<br>tin(II) chloride dehydrate, elemental sulfur | 0.23 | 2009 | [71] |
| Screen-printing | CZTS microparticle | 0.49 | 2010 | [72] |
| CBD-ion exchange | tin chloride dehydrate, zinc acetate dehydrate,<br>aqueous $Cu^{2+}$ | 0.16 | 2011 | [16] |

**Table 3.** Highest efficiency achieved for CZTS solar cell by different method.

### *3.3.1. Evaporation*

Evaporation is a well-known technique in the development of thin film solar cells. In 1997, Katagiri et al. reported electron beam evaporation-deposited CZTS precursor films followed by sulfurization [49]. Solar cell with an efficiency of 0.66% was obtained. In this work, Zn, Sn and Cu layers were sequentially deposited on Mo-coated soda lime glass substrates which were heated up to 150 ℃. The targeted composition ratio was decided by the thickness of metallic layers. Annealing at 500 ℃ in the atmosphere of $N_2$ + $H_2S$ (5%) was then employed to transform Cu/Sn/Zn stacked layers into a CZTS thin film. Finally, chemical bath deposition was employed to deposit n-type CdS thin film on the p-type CZTS to form a p-n junction. As a result, the open-circuit voltage was significantly enhanced in comparison to the previously reported value [40].

Similar deposition procedures were performed by the same group in 2001 with a replacement of Zn metal source by ZnS [25]. Also, the annealing temperature was increased to 550 ℃. CZTS thin films with thickness of 0.95 μm, 1.34 μm, and 1.63 μm were deposited on Mo-coated SLG substrates, respectively. The *J-V* results demonstrated that the short-circuit current density and the fill factor of these cells drastically decreased with the increase of thickness of CZTS thin film (Table 4). The authors concluded that the extremely high series resistance of CZTS absorber layer was attributed to the significant degradation encountered in the CZTS solar cells. Similar dependence of performance on the thickness of CZTS ab-

sorber layer was demonstrated in 2010 by Wang et al. (Table 4) [56]. Capacitance-voltage measurement results showed that the density of uncompensated charge in the CZTS layer was to be $5\times10^{16}$ $cm^{-3}$ at 27 ℃, which indicates that part of the high series resistance comes from the bulk CZTS absorber layer. Evaluation of the dependence of $R_s$ on temperature from dark *J-V* curve provides insight on another potential source for the series resistance (Fig. 9). The strong dependence indicates a back-contact blocking (Schottky) barrier exists at the interface between CZTS and Mo, leading to the suppression of holes transporting across the interface to Mo.

| R & D group | Thickness (nm) | $J_{SC}$ (mA/cm$^2$) | $V_{OC}$ (mV) | *FF* (%) | $\eta$ (%) |
|---|---|---|---|---|---|
| Katagiri et al. | 950 | 7.01 | 415 | 50.3 | 1.46 |
| | 1340 | 3.41 | 425 | 26.5 | 0.384 |
| | 1630 | 1.53 | 525 | 26.6 | 0.214 |
| Wang et al. | 650 | 17.8 | 587 | 65 | 6.81 |
| | 660 | 20.4 | 620 | 52 | 6.63 |
| | 900 | 18.3 | 640 | 38 | 4.40 |
| | 1200 | 14.4 | 608 | 28 | 2.44 |

**Table 4.** Comparison of *I-V* properties of CZTS TFSCs with different thickness of absorber layer [25, 56].

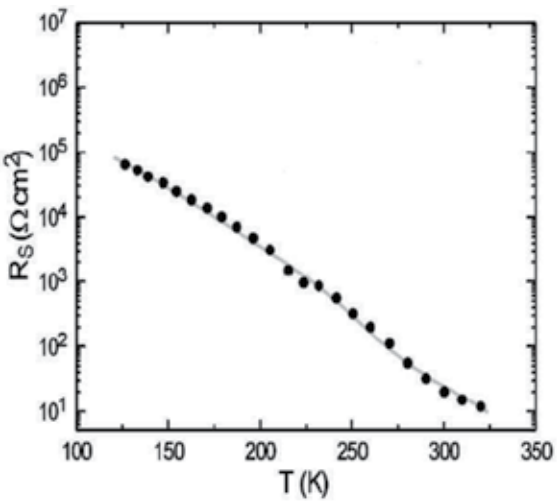


**Figure 9.** The dependence of $R_s$ on temperature [56].

The large dependence of physical properties of CIGS thin film on the ratio of Cu/(In+Ga) suggests that it is necessary to investigate the effects of Cu/(Zn+Sn) ratio on the properties of CZTS films to further the understanding of CZTS solar cells [78]. In 2010, Tanaka et at. em-

http://dx.doi.org/10.5772/50702

ployed evaporation method to fabricate CZTS samples with constant Zn/Sn and S/metal ratios of 1.1 and 0.93 and with Cu/(Zn+Sn) ratio varying from 0.82 to 1.06 [79]. All samples were determined to be kesterite structure. XRD data showed that FWHM of the diffraction peak of (112) plane became narrower, and the $I_{(112)}/I_0$ increased with increasing Cu/(Zn+Sn) ratio. This indicated that the increasing of Cu/(Zn+Sn) ratio helped improve the crystallinity of CZTS films (Fig. 10 (a)). Surface SEM images of the CZTS films demonstrated that the grain size also increased with increasing Cu/(Zn+Sn) ratio (Fig. 10 (b)), suggesting deposition process containing Cu-rich condition could be developed for growing high-quality CZTS thin films. The champion CIGS solar cell was fabricated using three-stage co-evaporation method where CIGS thin film was changed to Cu-rich in the second stage from Cu-poor in the first stage. In the last stage, the Cu source was blocked and Ga, In, and Se were simultaneously deposited to restore the Cu-poor state. Similar procedures have yet to be proved effective for CZTS solar cells.

Na incorporation into the CIGS polycrystalline thin film is a necessary process to fabricate CIGS modules with high efficiency. The enhancement of efficiency largely comes from higher open-circuit voltage, improvement of fill factor, increasing of p-type conductivity as well as improvement of crystallinity of (112)-oriented CIGS films [80-82]. Na incorporation was performed for evaporated-CZTS solar cell by Katagiri et al. using $Na_2S$ as Na source [54]. It was found that the efficiency was enhanced from 4.25% to 5.45%. This enhancement is mainly due to the increase of short-circuit current density which increased significantly from 10.3 $mA/cm^2$ to 15.5 $mA/cm^2$. The open-circuit voltage and fill factor were slightly lower than the CZTS solar cells without Na incorporation. While why the efficiency was improved was not mentioned in the paper, it can be assumed that Na incorporation can improve the quality of CZTS thin film at different mechanism compared with CIGS thin film. The effects of Na incorporation for improving the quality of CZTS thin film has been addressed by Jampana et al. [83]. CZTS thin films were deposited on soda-lime glass (SLG) and low-alkaline glass (LAG). An increase in grain size and an improvement of morphology were obviously demonstrated in CZTS thin films deposited on SLG (Fig. 11 (a) and Fig. 11 (b)). However, our experiment results indicated that no significant difference could be detected from CZTS thin films deposited on SLG and low-alkaline glass (Fig. 11 (c) and Fig. 11 (d)). The wide variation among effects of sodium incorporation on CZTS thin films possibly partly arises from the difference of deposition methods. The other explanation could be tracked to the lack of precision by only changing substrate type. More experiments have to be carried out on sodium-free substrate by exactly controlling the doping amount of sodium before sodium incorporation can be effectively employed to improve the performance of CZTS PV devices.

In 2011, IBM reported a champion efficiency of 8.4% was achieved for CZTS solar cell which was grown on Mo-coated SLG substrates by thermal evaporation using elemental Cu, Zn, Sn, and S as sources [36]. A cracker, which can increase the reactivity of S, was applied to S vapor. The employment of cracker probably helped improve the efficiency.

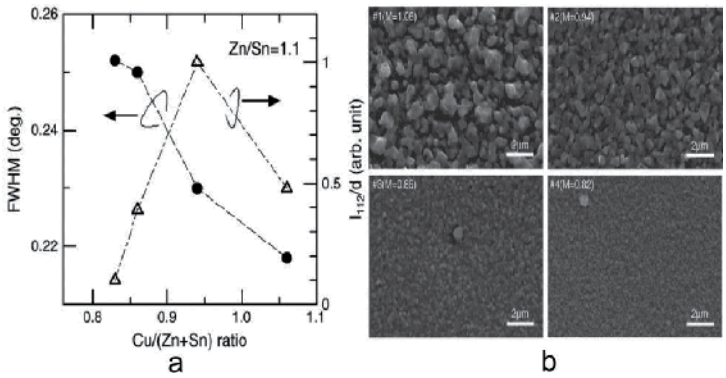


**Figure 10.** a) FWHM of the (112) diffraction peak and normalized (112) diffraction intensity of CZTS films ($I_{112}/d$) as a function of Cu/(Zn+Sn) ratio, (b) SEM surface images of CZTS films with different Cu/(Zn+Sn) ratios [79].

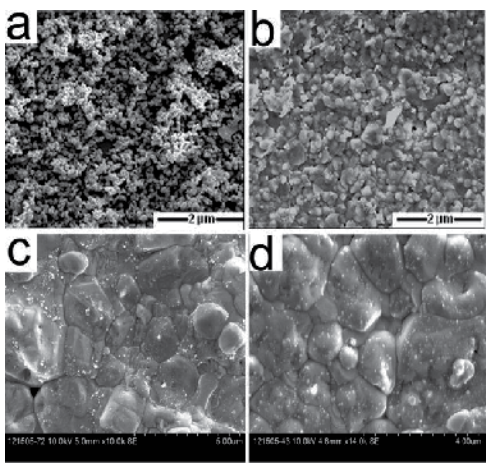


**Figure 11.** SEM surface images of CZTS thin films deposited on different substrates: (a) LAG, (b) SLG, (c) LAG, (d) SLG. [(a) and (b) were reported by Jampana et al. [83] (c) and (d) are results from our group].

All the reports showed that the conventional evaporation method is efficient for the development of CZTS TFSCs. However, non-uniformity caused by splash encountered in the evaporation of copper will significantly deteriorate the performance of CZTS module as does in the fabrication of CIGS module (Unpublished data). The fact that the commercial production capacity of CIGS solar modules by evaporation is far lower than that by sputtering is a perfect suggestion for CZTS solar industries [84]. More stable and controllable sputtering method is more readily applied to mass production of CZTS solar modules.

### *3.3.2. Sputtering*

In 1988, Ito analyzed the electrical and optical properties of CZTS thin film which was deposited on slide glass substrate by atom beam sputtering [40]. The deposited CZTS thin film

http://dx.doi.org/10.5772/50702

was (112)-oriented and polycrystalline. The grain size increased when CZTS thin film was deposited at higher temperature because the mobility of sputtered particles was higher on the substrate surface (Fig. 12(a)). Its resistivity decreased from $4x10^4$ Ω•cm to 1.3 Ω•cm with the increase of deposition temperature (Fig. 12(b)). Hall-effect measurement estimated that CZTS thin film had mobility lower than 0.1 $cm^2 \bullet V^{-1} \bullet s^{-1}$ and the carrier concentration was higher than $5\times10^{19}$ $cm^{-3}$. This CZTS thin film was considered optically desirable for the absorber layer of solar cell because the deposited CZTS thin film had an absorption coefficient larger than $1.2\times10^4$ $cm^{-1}$ and a direct bandgap of 1.45 eV.

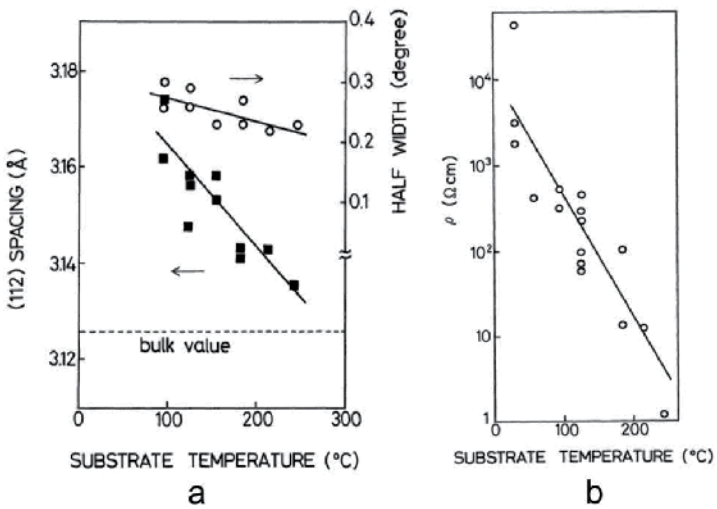


**Figure 12.** a) (112) plane spacing (■) and FWHM of the (112) peak (○) of CZTS, (b) the correlation between resistivity (ρ) of CZTS and substrate temperature [40].

In 2003, Seol et al. deposited CZTS films using RF-magnetron sputtering system and quaternary CZTS target (composed of finely mixed $Cu_2S$, ZnS and $Sn_s2$ at ratio of 2:1.5:1) followed by annealing in the atmosphere of Ar+S (g) [85]. The effects of sputtering power and annealing temperature on the properties of CZTS thin films were checked. It was found that the atomic ratio of the thin films obtained between 50 W and 100 W was appropriate. However, the Cu content of CZTS thin films was significantly decreased while the Sn content was rapidly increased with a power above 100 W. The authors suggested that the plasma density caused the abrupt changes of the Cu and Sn contents. CZTS thin films annealed at above 250 ℃ were (112)-oriented and other major diffraction peaks were assigned to (200), (220), and (312) planes. As annealing temperature increased, the intensity of the (112) peak was stronger.

In 2005, hybrid sputtering was employed by Tanaka et al. to prepare CZTS thin films [44]. The hybrid sputtering system was constructed in a deposition chamber with two effusion cells for Zn and S and two sputtering sources for Cu and Sn. CZTS thin films were fabricated by sequential deposition of Sn, Zn, and Cu followed by annealing in S vapor. The substrate temperature was varied between 300 ℃ and 500 ℃. The film thickness decreased with

increasing of substrate temperature. This was probably caused by the decrease of the sticking coefficient and/or by the increase of density due to crystallization at high temperature. CZTS thin films remained stoichiometric when the substrate temperature was elevated to up to 400 ℃. However, the composition of the thin films became Zn-poor at the substrate temperature above 450 ℃. At higher temperature, the vapor pressure of Zn is higher, leading to loss of Zn. It was proposed that Zn loss at higher substrate temperature could be prevented by using binary compound ZnS instead of Zn or by introducing S vapor during the deposition of Zn to form zinc sulfide on the surface of precursor.

CZTS precursor films are generally taken out of the deposition chamber and exposed to the atmosphere before sulfurization is performed to grow CZTS polycrystalline thin films. Moisture can be adsorbed on the surface of CZTS precursor films which is thereof oxidized during annealing at high temperature. Thus, in-line sulfurization should be capable of avoiding the problem. Jimbo et al. carried out this process with sputtered CZTS precursor films to curb the oxidization [57]. Targets of Cu, ZnS and SnS were simultaneously sputtered by RF sources. The finished precursor was automatically transferred to the annealing chamber without being exposed to atmosphere and annealed at 580 ℃ for 3 h in an atmosphere of $N_2$+$H_2S$ (20%). Measurement data showed that annealed CZTS thin film had the thickness of 2.5 μm and bandgap of 1.45 eV. The film was copper-poor and slightly zinc-rich and sulfur-rich (Cu/Zn+Sn: 0.87, Zn/Sn: 1.15, S/metals: 1.17). The sample had an open circuit voltage of 662 mV, a short circuit current of 15.7 mA/cm$^2$, a fill factor of 55%, a conversion efficiency of 5.74%. The improved efficiency was attributed to the in-line annealing process and better CZTS morphology achieved.

| | $J_{SC}$ (mA/cm$^2$) | $V_{OC}$ (mV) | *FF* (%) | $R_S$ (Ω•cm$^2$) | $R_{Sh}$ (Ω•cm$^2$) | $\eta$ (%) |
|---|---|---|---|---|---|---|
| Before DI-water soaking | 15.7 | 662 | 55 | 9.04 | 612 | 5.74 |
| After DI-water soaking | 17.9 | 610 | 62 | 4.25 | 370 | 6.77 |

**Table 5.** Comparison of *J-V* properties of CZTS solar cells treated with and without deionized-water soaking [57, 59].

In 2008, the champion efficiency for CZTS solar cell was achieved by Katagiri's group through preferential etching technique where the CZTS absorber layer on the Mo-coated SLG substrate was soaked in deionized water (DI-water) for 10 min before the CdS buffer layer was grown on the CZTS absorber layer using chemical bath deposition method [59]. The comparison of *J-V* properties was listed in Table 5. As we can see, DI-water soaking treatment CZTS absorber layer was very effective to improve the efficiency. The effect of the DI-water soaking on the oxygen distribution in CZTS thin film was studied by electron probe X-ray micro analysis (EPMA). Areas with higher concentration of oxygen are scattered in the CZTS layer before the soaking treatment (Fig. 13(a)). In contrast, the concentration of oxygen in the CZTS layer after the soaking treatment is lower than the measurement limit of the EPMA instrument (Fig. 13(b)). The authors suggested that oxygen removed was in the form of metal oxide because metal oxide nanoparticles are easy to dissolve in water. The removal of these metal oxide nanoparticles by DI-water is beneficial to improve the per-

http://dx.doi.org/10.5772/50702

formance of CZTS solar cell. On the one hand, more sunlight will be absorbed by CZTS, resulting in higher $J_{SC}$ because free carriers will not be generated in the metal oxides as effectively as CZTS. On the other hand, the contact area between CdS buffer layer and CZTS absorber layer will be increased after the removal of metal oxide nanoparticles, leading to lower series resistance of CZTS PV device.

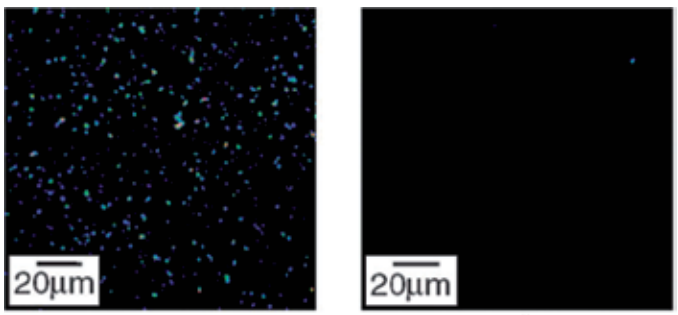


**Figure 13.** Distributions of oxygen in the CZTS layer before (a) and after (b) DI-water soaking for 4 h (bright areas are higher concentration areas of oxygen) [58].

As introduced above, the material properties of CZTS thin films and the performance of CZTS TFSCs are not only highly dependent on the deposition techniques but also dependent on how the sputtering target is made and what it is made of. The cooperation between PV device researchers and sputtering target vendors has to be intensified to make full use of their respective experiences and therefore to expedite the development of CZTS PV technology.

### *3.3.3. Pulsed laser deposition (PLD)*

So far, laser has only successfully been applied to formation of interconnection paths between individual cells in series-connected solar modules such as a-Si, CdTe, and CIGS. In 2007, Moriya et al. deposited CZTS thin films on Mo-coated soda lime glass (SLG) substrate at room temperature using KrF excimer laser for ablating sintered CZTS pellets [68]. Annealing at 500 ℃ in $N_2$ was carried out for growing CZTS crystals. The CZTS TFSCs showed an open-circuit voltage of 546 mV, a short-circuit current of 6.78 mA/cm$^2$, a fill factor of 48% and a conversion efficiency of 1.74%.

In 2010, Pawar et al. investigated the effect of incident energy density of laser on the structural, morphological and optical properties of CZTS thin films using similar PLD method as reported previously [68, 86]. Laser incident energy density was changed from 1.0 J/cm$^2$ to 3.0 J/cm$^2$. XRD results indicated that the crystallinity of the as-deposited CZTS thin films was improved with the increase of laser incident density up to 2.5 J/cm$^2$. However, the film was slightly degraded when the laser energy density was further increased to 3.0 J/cm$^2$ due to the large plasma density and high kinetic energy induced by too intense laser. SEM surface images of the annealed CZTS thin films showed the average grain size increased, and these films be-

came relatively more uniform as the laser incident energy was increased from 1.0 to 2.5 J/cm$^2$. The bandgap decreased with the increase of laser incident energy up to 2.5 J/cm$^2$ as well.

The efficiency of CZTS solar cell fabricated by PLD was further improved to 3.14% in 2011 [69]. CZTS pellets were made from $Cu_2S$, ZnS, and $SnS_2$ mixed powders (molar ration of 1:1:1) which were synthesized by solid state reaction method. CZTS thin films were then deposited by PLD method in high vacuum using the CZTS pellets as source. These films were further annealed under $N_2$ (95%) + $H_2S$ (5%) atmosphere at 400 ℃ for 1 h. The best CZTS solar cell reported in this work had a $V_{OC}$ of 651 mV, an $I_{SC}$ of 8.76 mA/cm$^2$, and a *FF* of 55%.

*3.3.4. Non-vacuum processes*

Cost-effectiveness is the core of the development of any new technology. Total abandonment of vacuum facilities in the manufacture of PV systems is the best way to further lower the cost of PV modules. Several non-vacuum methods have been successfully employed in the development of CZTS TFSCs.

*3.3.4.1. Electrodeposition*

The first CZTS solar cell deposited using electrodeposition was achieved by Scragg et al. [41]. In this method, copper chloride, tin chloride and zinc chloride were separately dissolved in a mixture solution containing NaOH and sorbitol. Metal layers were potentiostatically deposited at room temperature in the order Cu, Sn, Zn using a conventional 3-electrode electrochemical cell with a platinum counter electrode and Ag/AgCl reference electrode. The electroplated metallic films and sulfur powder were loaded into a graphite container, which was inserted into a furnace tube. CZTS thin films were then synthesized at 550 ℃ by the sulfurization of the electroplated metallic films. The fabricated solar cell demonstrated an efficiency of 0.8% with an open circuit voltage of 295 mV, a short circuit current density of 8.7 mA/cm$^2$, and a fill factor of 32%.

The crystallization and sulfurization processes of the elecrodeposited CZTS precursor films were investigated by Schurr et al. using angle-dispersive time-resolved XRD measurements [87]. Two different types of precursor films with copper-rich and copper-poor ratios in the as-deposited films were checked. It was found that the kesterite crystallization was completed by the solid state reaction of $Cu_2SnS_3$ and ZnS in both cases. However, in-situ XRD data showed reaction path for the formation of $Cu_2SnS_3$ depended on the metal ratios in the as-deposited films. The reaction schemes were derived from time-resolved XRD results and shown below. The reactions can be described below.

For copper-rich samples,

$$2Cu_3Sn + 7S \rightarrow 3Cu_2 - xS + 2SnS_2; \quad (4)$$

$$2CuZn + 3S \rightarrow Cu_{2-x}S + 2ZnS; \quad (5)$$

http://dx.doi.org/10.5772/50702

$$Cu_{2-x}S + SnS_2 \rightarrow Cu_2SnS_3; \quad (6)$$

$$Cu_2SnS_3 + ZnS \rightarrow Cu_2ZnSnS_4; \quad (7)$$

For copper-poor samples,

$$Cu_6Sn_5 + S \rightarrow SnS_2 + Cu_{2-x}S + Cu_3Sn; \quad (8)$$

$$2Cu_2S + SnS_2 + 2S \rightarrow Cu_4SnS_6; \quad (9)$$

$$Cu_4SnS_6 \rightarrow 2Cu_{2-x}S + SnS_2(melted) + 2S; \quad (10)$$

$$Cu_{2-x}S + SnS_2(melted) \rightarrow Cu_2SnS_3; \quad (11)$$

$$Cu_2SnS_3 + ZnS \rightarrow Cu_2ZnSnS_4; \quad (12)$$

These reactions also indicate how the sulfurization and crystallization are completed in CZTS precursor films deposited using vacuum-based technologies since these methods usually involve similar precursors.

In 2009, Ennaoui et al. achieved an efficiency of 3.4% using electrodeposited copper-poor CZTS thin film as absorber layer [61]. The formation of the binary sulfides and the thereof resulted liquid phase could contribute to the enhancement of kesterite crystal growth.

In 2012, electrodeposited CZTS solar cell with an efficiency of 7.3% was fabricated by Deligianni et al. using a three-step method [74]. Firstly, metal stacks of either Cu/Zn/Sn or Cu/Sn/Zn were electrodeposited. Secondly, low temperature annealing at 210–350 °C in $N_2$ was employed to produce homogeneous (Cu, Zn) and (Cu, Sn) alloys. Lastly, these well-mixed CuZn and CuSn alloys were annealed at 550 –590 °C in sulfur vapor for 5 to 15 min. A single highly crystalline CZTS phase was achieved. This is so far the record efficiency for electrodeposited CZTS solar devices.

*3.3.4.2. Sol-gel method*

CZTS precursor sol-gel was made by dissolving copper (II) acetate monohydrate, zinc (II) acetate dehydrate and tin (II) chloride dehydrate in mixture solution of 2-methoxyethanol (2-metho), deionized water and binder and then spin-coated on Mo-coated soda lime glass substrates followed by drying at 300 ℃ on a hot plate [67]. The coating and drying process were repeated several times. Lastly, the precursors were annealed at 500 ℃ in an atmosphere of $N_2$ +$H_2S$ (5%). The CdS layer was grown on CZTS thin film by the chemical bath deposition (CBD) method. The CdS thickness was optimized by changing deposition time from 5 to 25 minutes. It was found that sample with CdS thin film deposited for 23 minutes showed the best conversion efficiency ($J_{SC}$=6.70 mA/cm$^2$, $V_{OC}$=554 mV, *FF*=43.4%, $\eta$=1.61%).

Tanaka et al. fabricated a CZTS solar cell with all semiconductor layers being coated by non-vacuum deposition techniques [66]. The ZnO:Al window layer and the CZTS absorber layer were deposited using sol-gel method. CdS buffer layer was coated by chemical bath deposition method. CZTS precursor thin films were coated using sol–gel solution of Cu, Zn, and Sn ions. Sulfurization was employed at 500 ℃ under a mixture atmosphere of $H_2S$ and $N_2$ with $H_2S$ concentration changing from 3% to 20%. CZTS thin film prepared with a $H_2S$ concentration of 3% had grains with size of 1 μm. The best solar cell, which was obtained from a sample sulfurized at a $H_2S$ concentration of 3%, demonstrated a conversion efficiency of 2.23%. This is so far the highest efficiency for sol-gel method deposited CZTS solar cells.

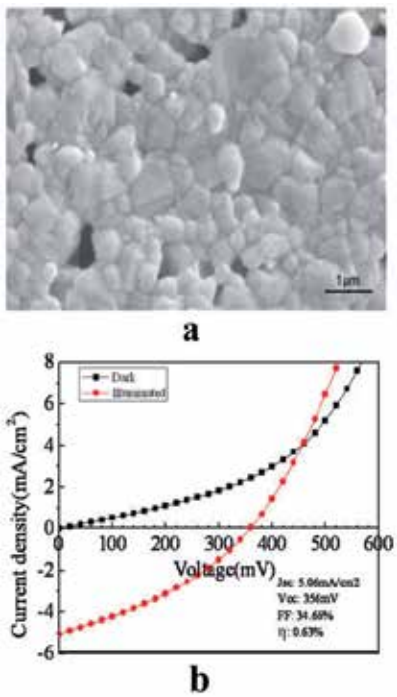


**Figure 14.** a) SEM surface image of CZTS thin film, (b) typical J-V curve of CZTS TFSC deposited by sol-gel method [27].

We have deposited CZTS thin films by employing sol-gel method [26]. The deposited CZTS thin film consisted of large densely packed grains with size of more than 400 nm (Fig. 14(a)) and had an optical bandgap of 1.51 eV. The compositional ratios could be optimized through modification of the composition of CZTS sol-gel precursor and annealing processes. An efficiency of 0.63% has been demonstrated (Fig. 14(b)). The relatively low efficiency resulted from the low $V_{OC}$ and *FF* which was caused by the cracks and penetrating pores generated during the annealing process. With this ongoing project, we have already improved FF by 19% using ~ 450 nm thick CZTS film by controlling the deposition process, leading to significant improvement of morphology (Fig. 15). A multiple layer deposition process successfully blocked the penetrating pores.

http://dx.doi.org/10.5772/50702

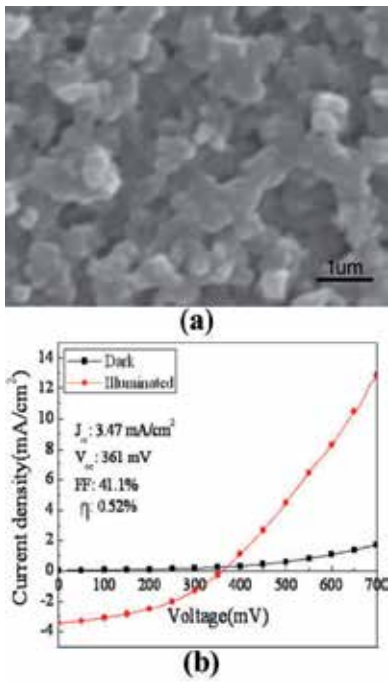


**Figure 15.** a) SEM surface image and (b) J-V property of CZTS TFSC with improved morphology.

*3.3.4.3. Nanoparticle-based method*

Hot-injection method is usually employed to synthesize CZTS nanoparticles [88, 89]. In a typical synthesis, copper salt, zinc salt, and tin salt are dissolved in oleylamine. The mixture solution is heated to 130 ℃ under inert atmosphere. The temperature is then raised to 225 ℃ where mixture solution of sulfur and oleylamine is injected. The mixture is then cooled to 80 ℃. Organic solvents such as toluene and isopropanol are added into the reaction mixture where CZTS nanoparticles are collected using centrifuge. Steinhagen et al. fabricated a CZTS PV device by dispersing CZTS nanoparticles in toluene (20 mg/mL) and spray coating the CZTS layer on CdS/ZnO-coated indium tin oxide (ITO) glass [71]. A typical CZTS solar cell showed an open-circuit voltage of 321 mV, a short-circuit current density of 1.95 mA/cm$^2$, a fill factor of 37%, and a conversion efficiency of 0.23%.

High quality CZTS nanocrystals with well controlled size, shape, and chemical composition have been successfully synthesized [90-93]. Nevertheless, to what extent these properties will affect CZTS TFSCs has rarely been addressed and needs to be further explored. Annealing procedure has to be applied to CZTS nanocrystals to grow polycrystalline CZTS thin films. Cracking and material loss encountered in other methods must be prevented to achieve CZTS polycrystalline thin film with high semiconductor quality. For more details, we recommend the recently published review paper by Lin et al. about nanoparticle-based method for CZTS TFSCs [94].

*3.3.4.4. Screen-printing*

Zhou et al. produced CZTS ink by dispersing CZTS microparticles in mixture solution of isopropanol and ethyl cellulose [72]. CZTS thin film with thickness of about 3 μm was screen printed on Mo-coated glass substrate and then was dried naturally. Organic materials were removed using a hot roll at 195 ℃. I-V measurement of a typical CZTS solar cell showed the feasibility of this method to be used to make CZTS solar cell ($J_{SC}$=4.76 mA/cm$^2$, $V_{OC}$=386 mV, $FF$=0.27, $\eta$=0.49%). The authors speculated that the comparatively low efficiency could attribute to internal deficiencies in the screen-printed CZTS solar cells, such as high contact resistance between CZTS paste and Mo conductive layer and small amount of residual oxide in the precipitate.

Screen-printing technology has been successfully applied on Si wafer-based PV technologies, which partly contributed to rapid decrease of the price of Si wafer-based PV modules. However, screen-printing process is widely employed to prepare the front and back metal contacts. The p-n junction formed using screen-printing method has yet to be proved to be successful due to non-uniformity generated in the screen-printed film and carbon-based solvents employed in the preparation of paste. Considering the high sensitivity of CZTS thin film to composition variation, it will be more difficult to achieve desirable CZTS absorber layer using screen-printing technology.

The demonstrated performance of CZTS TFSCs by these methods is lower than those by vacuum-based method. However, non-vacuum-based techniques such as nanoparticle-based method and sol-gel method are promising because of simplicity and versatility associated with these methods.

## 4. Prospects

The efficiency of CZTS solar cell has been significantly improved since 2000. Due to know-how gained from the research on CIGS solar module, an efficiency of 6.21% has been realized for CZTS solar module with an aperture area of 22.6 cm$^2$ [50]. Collaboration to market CZTS PV technology has been laid ground among semiconductor industry and photovoltaic industry giants [95, 96]. However, a number of technical issues must be addressed and corresponding solutions are provided before CZTS PV technology becomes marketable.

### 4.1. Defect engineering

*4.1.1. Defect control*

Defect states in quaternary compounds such as CIGS and CZTS thin films are very complicated. As introduced above, vacancies such as $V_{Cu}$, $V_{Zn}$, $V_{Sn}$, and $V_S$, antiesite defects such as $Cu_{Zn}$, $Zn_{Cu}$, $Cu_{Sn}$, $Sn_{Cu}$, $Zn_{Sn}$, and $Sn_{Zn}$, intrinsic defects such as $Cu_i$, $Zn_i$, and $Sn_i$ are possible to form during deposition of CZTS thin film. The formation energy of acceptor defects was lower than that of donor defects, which makes p-type self-doping comparably easy in CZTS. The commonly observed p-type conductivity of CZTS thin films mainly arises from the $Cu_{Zn}$ antisite defect. Successfully fabricated CZTS solar cells are usually Cu-poor and Zinc-rich.

http://dx.doi.org/10.5772/50702

On the one hand, the conductivity of CZTS thin film derived from intrinsic defects helps to minimize extrinsic defects which have a high density in highly phosphor-doped Si to form emitter which is usually called as dead region because most of photon-excited free carriers recombine at defect states. On the other hand, the electrical properties of CZTS thin film are extremely difficult to be precisely controlled. As far as composition concerned, the transition region from being highly efficient to being dead is very narrow as is CIGS thin film solar cell. Defect engineering such as Na incorporation and Sb doping have been successfully employed for CIGS thin film to extend the region and henceforth improve the efficiency. Similar experiments could benefit CZTS solar cell as well because CZTS has a lot in common with CIGS. Most researchers have been dedicating their efforts in developing novel deposition methods for CZTS thin film. The research focus will soon be turned to defect engineering once the newly developed deposition methods gain maturity.

*4.1.2. Pure CZTS phase generation and secondary phase detection*

The investigation on the phase equilibrium in the $Cu_2S$-ZnS-$SnS_2$ system showed that single-phase CZTS crystals can only be grown in a very narrow region (Fig. 16) [97]. To form pure CZTS phase is a challenge. Secondary phases such as ternary and quaternary compounds are much easier to form than CZTS. Therefore, it is quite challenging to deposit CZTS thin film without significant presence of secondary phases. Time-resolved XRD measurements clearly illustrated that the crystallization of kesterite CZTS was completed by the solid state reaction of $Cu_2SnS_3$ and ZnS whatever the precursor was [85]. The formation of binary and ternary secondary phases including $Zn_xS$, $Cu_xS$, $Sn_xS$, and $Cu_xSnS_y$ are often observed during and after the growth of CZTS crystals.

Highly performed CZTS solar cells are slightly Zn-rich and Cu-poor. However, secondary phases such as ZnS and $Cu_2SnS_3$ are readily to be formed during thin-film growth in a Zn-rich regime. Inhomogeneity due to the presence of these secondary phases was assumed to contribute to the comparatively low efficiencies. Detection of secondary phases will guide how to improve the growth method for CZTS thin film. Nevertheless, it is commonly recognized that detecting secondary phases using only XRD in CZTS is not as easy as in CIGS because kesterite CZTS shares multiple peaks with cubic ZnS and $Cu_2SnS_3$ (Fig. 17). Raman spectroscopy is often combined with XRD results to characterize CZTS thin films [30, 32].

Hartman et al. developed a technique defined as extended X-ray absorption fine structure (EXAFS) which is sensitive to local chemical environment and able to determine the quantity of ZnS phase in CZTS films by detecting differences in the second-nearest neighbor shell of the Zn atoms [98]. The results so far are promising. Significant differences in EXAFS spectra with varying amounts of Zn and Cu in the CZTS films have been observed. Further work is required to quantify the amount of secondary ZnS phase in EXAFS spectra and to enable EXAFS technique to be confidently employed in characterizing CZTS thin film.

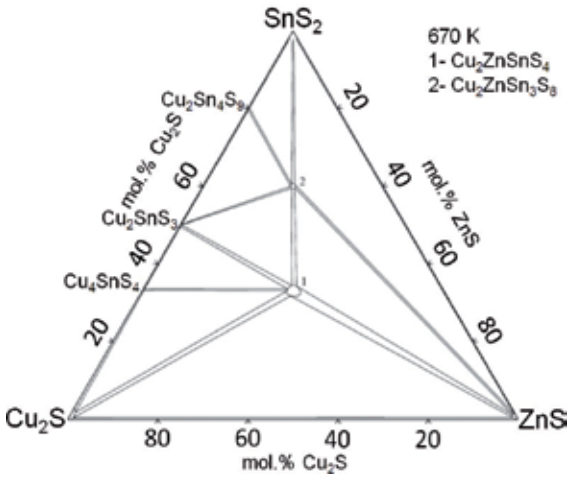


**Figure 16.** Phase diagram of $SnS_2$-$Cu_2S$-ZnS system [97].

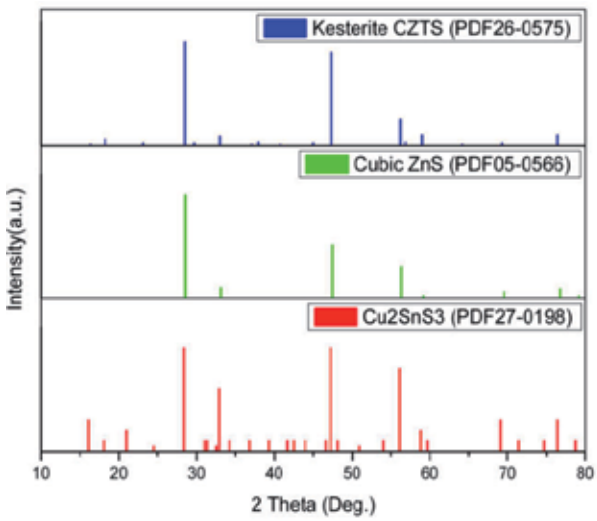


**Figure 17.** Comparison of XRD peaks of CZTS, ZnS, and $Cu_2SnS_3$.

### 4.2. Bandgap engineering

Bandgap tuning has been widely and successfully employed in fabrication of CIGS TFSCs. Techniques such as substitution of In by Ga and replacement of Se by S can precisely control the bandgap of CIGS thin film [99-102]. The performance of CIGS TFSCs was significantly improved not only because gradient bandgap was introduced into the absorber layer but also because the conduction band offset (CBO) between buffer layer and CIGS absorber layer was optimized through tuning the conduction band of CIGS thin film [103,105]. This pro-

http://dx.doi.org/10.5772/50702

vides CZTS TFSC researchers with another powerful technology to improve the efficiency of CZTS TFSC.

Theoretical calculation and experimental results demonstrated that the bandgap of CZTS nanocrystal could also be controlled through incorporation of Se [105]. Zhang et al. analyzed experimentally and theoretically the effects of Se incorporation on the bandgap of CZTS nanocrystal. It was found that band gap of CZTS nanocrystal demonstrated a parabolic nature. The bandgap firstly decreased with the increase of Se/(S + Se) ratio and then increased with the increase of Se/(S + Se) ratio when the ratio was higher than 0.55 (Fig 18). The variation range of optical band gap for CZTS nanocrystal is from 1.28 eV to 1.5 eV.

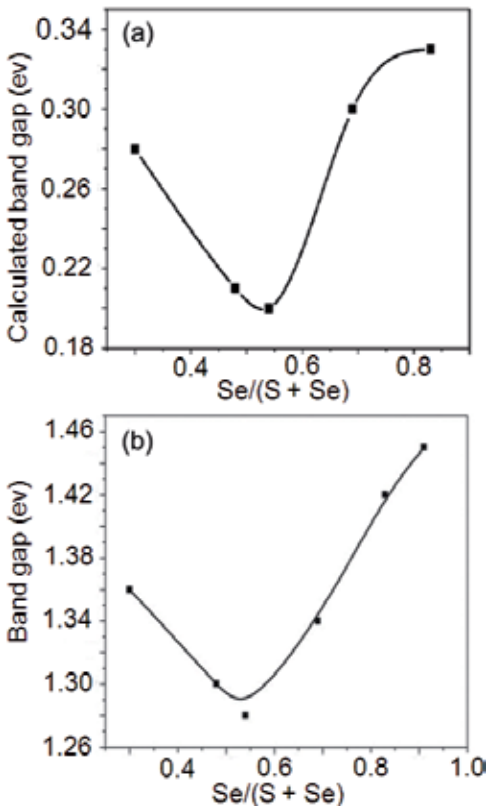


**Figure 18.** The dependence of bandgap of $Cu_2ZnSnS_{4x}Se_{4(1-x)}$ nanocrystals on the ratio of Se/(Se+S): (a) theoretical results, (b) experimental results [105].

The control of bandgap of CZTS nanocrystal was also realized by Agrawal et al. [106]. $GeCl_4$ was added into the reaction solution to partly replace tin (IV) acetylacetonate dichloride. TEM images and XRD data indicated that the $Cu_2ZnSn_{1-x}Ge_xS_4$ (CZTGS) nanocrystals varying in size from 5 to 30 nm were successfully produced. UV-Vis results for CZTGS nanocrystals indicated that the bandgap of CZTGS nanocrystals increased with the increase of Ge/(Sn +Ge) ratio (Fig. 19). CZTGS TFSCs with comparatively high efficiency have been fabricated

after selenization. The highest efficiency for CZTGS TFSCs was achieved from the cell with a Ge/(Sn+Ge) ratio of 6.8% (Table 6). This efficiency is slightly lower but comparable to that of CZTGS TFSC without Ge incorporation.

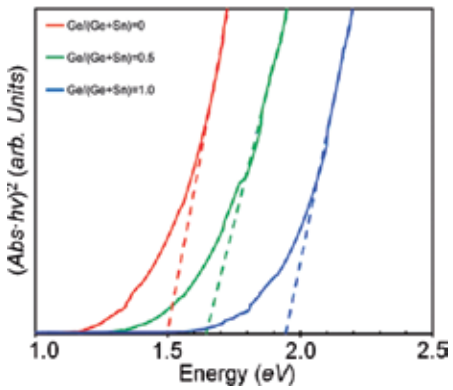


**Figure 19.** Absorbance of CZTGS nanocrystals with different ratio of Ge/(Ge+Sn) [106].

| | Ge/(Ge+Sn)=0 | Ge/(Ge+Sn)=0.7 | Ge/(Ge+Sn)=1.0 |
|---|---|---|---|
| $J_{SC}$ (mA/cm$^2$) | 31.2 | 21.5 | 4.7 |
| $V_{OC}$ (mV) | 430 | 640 | 320 |
| *FF* (%) | 54 | 49 | 33.7 |
| $R_S$ (Ω) | 4.9 | 9.1 | 30.5 |
| $R_{Sh}$ (Ω) | 850 | 460 | 269 |
| $\eta$ (%) | 7.2 | 6.8 | 0.51 |

**Table 6.** J-V properties of CZTGS TFSC with different ratio of Ge/(Ge+Sn) [106].

The widening effect of bandgap through Ge incorporation and the narrowing effect of bandgap through Se incorporation facilitate the design of high efficiency CZTS TFSC based on multi-junction (Fig. 20). Interfacial recombination caused by crystal mismatch will be minimized due to the high similarity of crystal structures among these materials.

### 4.3. Toxic element-free

Toxic chemicals are widely and heavily consumed in the manufacturing process of PV industry. The environmental damage could be minimized if the wastes were well treated because they are usually confined in a certain area. Nevertheless, toxic elements contained in PV modules have potential to polluting the earth because a large amount of PV modules are required to be installed in the desert and on residential roofs to power households. Lives

could be lost due to the emission of toxins during fire. Toxic element-free PV technologies will be more preferred when solar electricity is selected to be main power source.

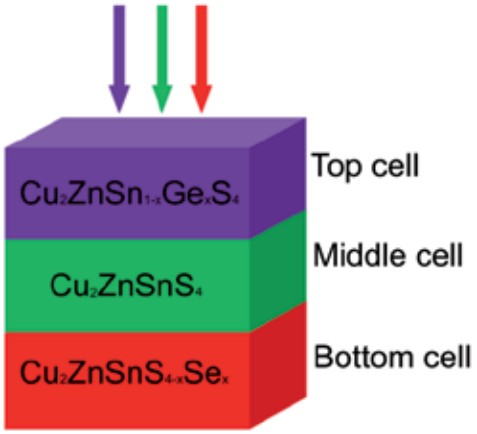


**Figure 20.** Proposed multi-junction CZTS solar cell.

*4.3.1. Selenium-free*

Selenium compounds such as hydrogen selenide are extremely toxic while selenium itself is not highly toxic. Selenization and sulfurization are often employed to CZTS precursors to grow high quality CZTS thin films. The efficiency of CZTS solar cell is lower than that of CZTSSe solar cell which is incorporated with selenization (Table 7) [36]. The authors concluded that the comparatively low efficiency associated with CZTS and CZTSSe solar cells were caused by the extremely low lifetime because a typical lifetime of a high quality CIGS device is beyond 50 ns. The differences of $J_{SC}$ and $V_{OC}$ were mainly due to the difference of optical bandgap. The difference between the efficiencies of CZTS and CZTSSe PV devices was probably from the difference of bandgap which attributed to unfavourable band alignments with the CdS emitter layer, leading to higher series resistance.

| | Thin film | | Solar cell | | | | |
|---|---|---|---|---|---|---|---|
| | Bandgap (eV) | Lifetime (ns) | $J_{SC}$ (mA/cm$^2$) | $V_{OC}$ (mV) | *FF* (%) | $\eta$ (%) | $R_S$ (Ω•cm$^2$) |
| CZTS | 1.45 | 0.78 | 21.0 | 614 | 55.3 | 7.13 | 7.4 |
| CZTSSe | 1.17 | 0.50 | 29.5 | 422 | 60.0 | 7.51 | 1.5 |

**Table 7.** Comparison of properties of CZTS and CZTSSe TFSCs [36].

For solution-based CZTS solar cells, selenium incorporation plays an even greater role in improving the efficiency of CZTS solar cell. Firstly, Se has higher reactivity than S. Metals in

CZTS precursors will more readily react with Se to produce metal selenides and consequently to grow CZTSSe thin films. Phase separation in sulfurized CZTS thin film is more common than that in selenized CZTS thin film. Secondly, CZTS thin film is usually deposited at so high a temperature that cracks are highly possible to be generated due to volume contraction caused by evaporation of metal sulfides and excess sulphur [107]. Displacement of S with Se during selenization can prevent crack forming because the aomic radius of selenium is larger than that of sulfur

However, knowledge achieved from fabrication of CIGS solar cell can shed light on how to make selenium-free CZTS solar cell with high efficiency. It was reported that CIGS solar cell showed higher efficiency when deposited under heat-cracked selenium vapor because cracked selenium vapor is more reactive than selenium vapor without cracking treatment which mainly consists of $Se_8$ [108]. Cracking treatment for sulfur vapor has been first employed to fabricate CZTS solar cell by IBM [36]. Treatment details were not available. It would be a feasible method to improve the quality of CZTS thin film in that sulfur vapor is mainly composed of $S_8$ which has lower reactivity than S as does $Se_8$ than Se. Moreover, CIGS solar cell with high efficiency has been successfully fabricated by ISET who synthesized copper oxide, indium oxide, and gallium oxide nanoparticles as precursors [109]. Similar technology can be developed to deposit CZTS thin film. Synthesis of nanoparticles of copper oxide, zinc oxide, and tin oxide has been widely reported in literatures. Volume contraction will be minimized if sulfurization is employed to CZTS precursors containing these metal oxide nanoparticles because the atomic radius of S is larger than that of O as is Se larger than S. It was found that zinc oxide was easily turned into zinc sulfide after being annealed in a mixture atmosphere of hydrogen sulfide, hydrogen, and nitrogen [110]. Similar methods have yet proved to be possible to produce copper sulfide and tin sulfide. It would be a novel technology to fabricate selenium-free CZTS solar cell with high efficiency once the methods are available.

*4.3.2. Cadmium-free*

CdS thin film is commonly incorporated in CZTS PV device as buffer layer to form p-n junction with p-type CZTS absorber layer. However, the environmental risk brought by the implementation of CdS is nontrivial when CZTS PV technology is widely employed, not to mention the marketing problem caused by legal regulations of Cd in electrical or electronic equipment in different countries [111, 112]. Free carriers excited by photons with energy ranging from 2.3 eV to 3.6 eV are lost in CdS thin film. The elimination or replacement of CdS thin film has potential of increasing photocurrent generated in this energy region, and therefore improving the cell efficiency.

So far, Cd-free CZTS solar cells have been reported by just a few groups [50, 70, 113]. The buffer layers employed and *J-V* properties are summarized in Table 8. Solar Frontier has successfully fabricated a Cd-free CZTS sub-module [50]. The Zn-based buffer layer was deposited by chemical bath deposition on CZTS thin film coated by sulfurization of an evaporated stacking precursor. It was interesting that the efficiency of the Zn-based buffer sub-module was higher than that of the Cd-based buffer sub-module even if the Zn-based buffer

cell fabricated with same batch of CZTS had lower efficiency than the Cd-based buffer cell. The authors attributed the enhancement of efficiency to the higher transparency and improvement of shunt resistance, resulting in higher external quantum efficiency, *EQE*, higher $J_{SC}$ and higher $V_{OC}$.

| Buffer layer | $J_{SC}$ (mA/cm$^2$) | $V_{OC}$ (mV) | *FF* (%) | $\eta$ (%) | Aperture area (cm$^2$) | Year | Reference |
|---|---|---|---|---|---|---|---|
| ZnS | 8 | 410 | 35.5 | 1.16 | unavailable | 2011 | [69] |
| ZnS(O,H) | 15.77 | 618 | 59.8 | 5.82 | 0.54 | 2011 | [97] |
| Cd-free sub-module | 10.30 | 631 | 30.7 | 2.01 | 21.8 | 2011 | [49] |

**Table 8.** *J-V* properties of Cd-free CZTS PV devices.

Excitingly, our tests demonstrated that the efficiency of Cd-free CIGS solar cell had been significantly improved to be over that of Cd-based CIGS solar cell through modifying the composition of CIGS absorber (unpublished data). Similar results (Table 9) have also been observed for CZTS solar cell [50]. The efficiency decreased with the decrease of the ration of Zn to Sn for Cd-based CZTS solar cell. However, the contrary was true for Cd-free CZTS solar cell. The champion efficiency of 5.82% for Cd-free CZTS solar cell was obtained at a Zn/Sn ratio of 1.02. Efforts have to be focused on not only the successful deposition of Cd-free buffer layer but also the optimization of the whole PV device [114].

| Zn/Sn | Power conversion efficiency (%) | |
|---|---|---|
| | Cd-based | Cd-free |
| 0.99 | 4.24 | 4.33 |
| 1.24 | 5.09 | 3.69 |
| 1.50 | 6.08 | 3.00 |

**Table 9.** Efficiencies of Cd-based and Cd-free CZTS PV devices depend on the ratio of Zn to Sn [50]

### 4.4. Nanostructured CZTS solar cell

Nanostructured PV devices have gained tremendous interest since the advent of dye-sensitized solar cell [115-117]. Organic semiconductors have absorption coefficients as high as $10^5$ $cm^{-1}$ but exciton diffusion length as low as tens of nanometers. Nanostructure provides excitons with high possibility to be dissociated before they recombine [118]. Furthermore, efficient light trapping associated with nanostructure reduces the amount of deposited absorber materials [119]. Also, nanostructures are compatible with printing PV technology based on nanoparticles, leading to reduction of processing costs and energy pay-back time of solar cells.

Nanostructured CZTS solar cell has not been reported although ZnO nanorod coated on ITO has been successfully applied to CIGS solar cells [120]. The efficiency was improved for

nanostructured CIGS solar cell compared to planar one. However, the efficiencies are much lower than those of conventional CIGS solar cells fabricated on Mo-coated glass. It was assumed that organic materials contained in the CIGS precursors sprayed on ZnO nanorods could not be totally eliminated, leading to degradation of CIGS thin film. Moreover, the annealing temperature cannot be as high as that employed in the fabrication of conventional CIGS solar cells because ITO thin film will be damaged under S or Se vapor, leading to poorer crystal qualities of CIGS thin film.

Therefore, we propose a nanostructured CZTS PV device based on Mo nanorods and sol-gel derived CZTS thin film (Fig. 21). Mo thin film and Mo nanorods are sequentially deposited on glass [Fig. 21(a)]. CZTS sol-gel precursor is then spin-coated on Mo nanorods [Fig. 21(b)]. Annealing at high temperature is employed to grow CZTS polycrystalline thin film. Lastly, CdS, i-ZnO, and TCO are sequentially coated on CZTS polycrystalline thin film [Fig. 21(c) and Fig. 21(d)]. The advantages of nanostructure and conventional CZTS will be integrated in a single PV device.

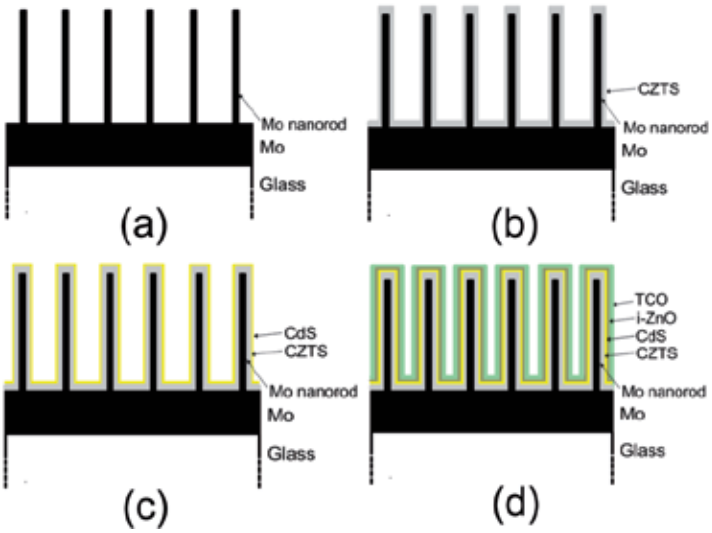


**Figure 21.** Proposed nanostructured CZTS PV device.

## 5. Remarks and conclusions

The tremendous progresses recently achieved on CZTS have demonstrated the potential of fabricating high-performance and cost-effective PV devices with low environmental pollution. Both vacuum-based and non-vacuum-based methods have been successfully explored to fabricate CZTS solar cells. Among vacuum-based methods, evaporation and sputtering are appropriate deposition techniques in terms of efficiencies. Non-vacuum-based techni-

ques including nanoparticle-based and sol-gel methods are also promising because of simplicity. To further improve the performance of CZTS solar cells, intensive efforts should be committed to the development of the approaches for forming pure CZTS phase and the detection techniques of secondary phases formed during the deposition of the CZTS thin film. Also, research efforts need to be focused on cadmium-free and selenium-free CZTS PV technologies. Further improvement can be expected in that know-how of CIGS PV technology and related nanotechnology is readily transferred to the research of CZTS PV technology due to great similarity between these two materials. A maturated CZTS PV technology is expected for the TFSC family in a near future.

## Acknowledgements

We acknowledge the financial support from the NASA through Contract NNX09AU83A.

## Author details

Minlin Jiang and Xingzhong Yan

*Address all correspondence to: xingzhong.yan@sdstate.edu

Department of Electrical Engineering and Computer Science, South Dakota State University, SD, 57007, USA

## References

[1] Husser, P., Watt, G., & Kaizuka, I. *Proceedings 17 17th International PVSEC 2007*, 1110-1113.

[2] Honda, J. *Proceedings 17 17th International PVSEC 2007*, 114.

[3] Wortmann, D. *Proceedings 17th International PVSEC 2007*, 120.

[4] European commissions. http://ec.europa.eu/dgs/jrc/index.cfm.

[5] Solarbuzz. http://www.solarbuzz.com/news/NewsNACO1205.htm.

[6] Von, Roedern. B., Zweibel, K., & Ullal, H. S. *Proceedings 31 31st PVSC 2005*, 183-188.

[7] Komoto, K., Uchida, H., Ito, M., Kurokawa, K., & Inaba, A. *Proceedings 23rd European Photovoltaic Solar Energy Conference and Exhibition 2008*, 3833-3835.

[8] Aydil, E.S. http://www1.umn.edu/iree/e3/archive/archive_2010/E3_Aydil.pdf.

[9] Green, M. A. *Prog. Photo volt.Res. Appl.*, 17-347.

[10] Wadia, C., Alivisatos, A. P., & Kammen, D. *Environ. Sci. Technol. 2009*, 43, 2072-2077.

[11] Nische, R., Sargent, D. F., & Wild, P. J. *Cryst. Growth 1967*, 1, 52-53.

[12] Schäfer, W., & Nitsche, R. *Mat. Res. Bull. 1974*, 9, 645-654.

[13] Lu, X., Zhuang, Z., Peng, Q., & Li, Y. *Chem. Comm.*, 47-3141.

[14] Paier, J., Asahi, R., Nagoya, A., & Kresse, G. *Phys. Rev. B. 2009*, 115-126.

[15] Chen, S., Gong, X. G., Walsh, A., & Wei, S. (2009). *Appl. Phys.Lett*, 041-903.

[16] Wangperawong, A., King, J. S., Herron, S. M., Tran, B. P., Pangan-Okimoto, K., & Bent, S. F. *Thin Solid Films 2011*, 519, 2488-2492.

[17] Zhang, X., Shi, X., Ye, W., Ma, C., & Wang, C. *Appl. Phys. A 2009*, 94-381.

[18] Pawar, S. M., Pawar, B. S., Moholkar, A. V., Choi, D. S., Yun, J. H., Moon, J. H., Kolekar, S. S., & Kim, J. H. *Electrochim Acta.*, 55-4057.

[19] Zhou, Y., Zhou, W., Du, Y., Li, M., Wu, S., & Mater, Lett. (20116). 65-1535.

[20] Araki, H., Kubo, Y., Jimbo, K., Maw, W. S., Katagiri, H., Yamazaki, M., Oishi, K., & Takeuchi, A. *Phys. Status. Solidi 2009*, 6, 1266-1268.

[21] Araki, H., Mikaduki, A., Kubo, Y., Sato, T., Jimbo, K., Maw, W. S., Katagiri, H., Yamazaki, M., Oishi, K., & Takeuchi, A. *Thin Solid Films 2008*, 517, 1457-1460.

[22] Araki, H., Kubo, Y., Mikaduki, A., Jimbo, K., Maw, W. S., & Katagiri, H. *Sol. Energy. Mater Sol. Cells 2009*, 93, 996-999.

[23] Katagiri, H., Ishigaki, N., Ishida, T., Saito, K., & Jpn, J. *Appl. Phys. 2001*, 40, 500-504.

[24] Cao, M., & Shen, Y. J. *Cryst. Growth 2011.*, 318, 1117-1120.

[25] Katagiri, H., Saitoh, K., Washio, T., Shinohara, H., Kurumadani, T., & Miyajima, S. *Sol. Energy. Mater Sol. Cells 2001.*, 65, 141-148.

[26] Jiang, M., Dhakal, R., Li, Y., Thapaliya, P., & Yan, X. *Proceedings 37 37th IEEE PVSC2011 (Seattle, USA)*.

[27] Jiang, M., Li, Y., Dhakal, R., Thapaliya, P., Mastro, M., Caldwell, J. D., Kub, F., & Yan, X. J. *Photon Energy 2011.*, 1, 019501.

[28] Wang, X., Sun, Z., Shao, C., Boye, D. M., & Zhao, J. *Nanotechnology 2011*, 22, 245605.

[29] Fontané, X., Calvo-Barrio, L., Izquierdo-Roca, V., Saucedo, E., Pérez-Rodriguez, A., Morante, J. R., Berg, D. M., Dale, P. J., & Siebentritt, S. *Appl. Phys. Lett. 2011.*, 98, 181905.

[30] Yoo, H., & Kim, J. *Thin Solid Films*, 518-6567.

[31] Wang, K., Shin, B., Reuter, K. B., Todorov, T., & Mitzi, D. B. *Appl. Phys. Lett. 2011.*, 98, 051912.

[32] Chalapathy, R. B. V., Lee, C., & Ahn, B. T. *Proceedings 37th IEEE PVSC 2011 (Seattle, USA)*.

[33] Unold, T., Kretzschmar, S., Just, J., Zander, O., Schubert, B., Marsen, B., & Schock, H. *Proceedings 37th IEEE PVSC 2011 (Seattle, USA)*.

[34] Miyamoto, Y., Tanaka, K., Oonuki, M., Moritake, N., Uchiki, H., & Jpn, J. *Appl. Phys.*, 47, 596-597.

[35] Leitão, J. P., Santos, N. M., Fernandes, P. A., Salomé, P. M. P., da, Cunha. A. F., González, J. C., & Matinaga, F. M. *Thin Solid Films 2011.*, 519, 7390-7393.

[36] Shin, B., Wang, K., Gunawan, O., Reuter, K. B., Chey, S. J., Bojarczuk, N. A., Todorov, T., Mitzi, D. B., & Guha, S. *Proceedings 37th IEEE PVSC2011 (Seattle, USA)*.

[37] Chen, S., Yang, J., Gong, X., Walsh, A., & Wei, S. *Phys. Rev. B. 2010*, 245204.

[38] Moriya, K., Tanaka, K., & Uchiki, H. *Jpn. J. Appl. Phys. 2008*, 47, 602-604.

[39] Jun, Z., & Xi, S. *Sci. China. Ser-TechE. Sci. 2009.*, 52, 269-272.

[40] Ito, K., & Nakazawa, T. *Jpn. J. Appl. Phys. 1988.*, 27, 2094-2097.

[41] Scragg, J. J., Dale, P. J., Peter, L. M., Zoppi, G., & Forbes, I. Phys. Stat. Sol. B. 2008 , 245, 1772-1778.

[42] Fernandes, P. A., Salomé, P. M. P., da Cunha, A. F., & Schubert, B. Thin Solid Films 2011. , 519, 7382-7385.

[43] Liu, F., Zhang, K., Lai, Y., Li, J., Zhang, Z., & Liu, Y. *Electrochem-StateSolid.Lett. 2011*, H379-H381.

[44] Tanaka, T., Nagatomo, T., Kawasaki, D., Nishio, M., Guo, Q., Wakahara, A., Yoshida, A., & Ogawa, H. J. *Phys. Chem. Solids 2005.*, 66, 1978-1981.

[45] Rajeshmon, V. G., Kartha, C. S., Vijayakumar, K. P., Sanjeeviraja, C., Abe, T., & Kashiwaba, Y. *Sol. Energy. 2011.*, 85, 249-255.

[46] Liu, F., Li, Y., Zhang, K., Wang, , Yan, C., Lai, Y., Zhang, Z., Li, J., & Liu, Y. *Sol. Energy. Mater Sol. Cells 2010*, 94, 2431-2434.

[47] Chan, C. P., Lam, H., & Surya, C. *Sol., Energy. Mater Sol. Cells 2010.*, 94, 207-211.

[48] Wagner, S., & Bridenbaugh, P. M. J. *Cryst. Growth. 1977.*, 39, 151-159.

[49] Katagiri, H., Sasaguchi, N., Hando, S., Hoshino, S., Ohashi, J., & Yokota, T. *Sol. Energy. Mater. Sol. Cells 1997.*, 49, 407-414.

[50] Hiroi, H., Sakai, N., & Sugimoto, H. *Proceedings 37th IEEE PVSC 2011 (Seattle, USA)*.

[51] Kobayashi, T., Jimbo, K., Tsuchida, K., Shinoda, S., Oyanagi, T., & Katagiri, H. *Jpn. J. Appl. Phys. 2005.*, 44, 783-787.

[52] Schubert, B., Marsen, B., Cinque, S., Unold, T., Klenk, R., Schorr, S., & Schock, H. *Prog. Photovolt. Res. Appl. 2011.*, 19, 93-96.

[53] Weber, A., Krauth, H., Perlt, S., Schubert, B., Kötschau, I., Schorr, S., & Schock, H. W. *Thin Solid Films 2009.*, 2524-2526.

[54] Katagiri, H., Jimbo, K., Moriya, K., & Tsuchida, K. *Proceedings 3rd World Conference on Photovoltaic Energy Conversion 2003.*, 3, 2874-2879.

[55] Redinger, A., Berg, D. M., Dale, P. J., & Siebentritt, S. J. *Am. Chem. Soc. 2011.*, 133, 3320-3323.

[56] Wang, K., Gunawan, O., Todorov, T., Shin, B., Chey, S. J., Bojarczuk, N. A., Mitzi, D., & Guha, S. *Appl. Phys. Lett. 2010.*, 143508.

[57] Jimbo, K., Kimura, R., Kamimura, T., Yamada, S., Maw, W. S., Araki, H., Oishi, K., & Katagiri, H. *Thin Solid Films 2007.*, 515, 5997-5999.

[58] Katagiri, H., & Jimbo, K. *Proceedings 37th IEEE PVSC 2011 (Seattle, USA).*

[59] Katagiri, H., Jimbo, K., Yamada, S., Kamimura, T., Maw, W. S., Fukano, T., Ito, T., & Motohiro, T. *Appl. Phys. Express 2008.*, 041201.

[60] Scragg, J. J., Berg, D. M., & Dale, P. J. J. *Electroanal Chem. 2010.*, 646, 52-59.

[61] Ennaoui, A., Lux-Steiner, M., Weber, A., Abou-Ras, D., Kötschau, I., Schock, H., , W., Schurr, R., Hölzing, A., Jost, S., Hock, R., Vo, T., Schulze, J., & Kirbs, A. *Thin Solid Films*, 517, 2511-2514.

[62] Araki, H., Kubo, Y., Jimbo, K., Maw, W. S., Katagiri, H., Yamazaki, M., Oishi, K., & Takeuchi, A. *Phys. Status. Solidi 2009*, 96, 1266-1268.

[63] Araki, H., Kubo, Y., Mikaduki, A., Jimbo, K., Maw, W. S., Katagiri, H., Yamazaki, M., Oishi, K., & Takeuchi, A. *Sol. Energy. Mater Sol. Cells 2009.*, 996-999.

[64] Tanaka, K., Fukui, Y., Moritake, N., & Uchiki, H. *Sol. Energy. Mater. Sol. Cells 2011*, 95, 838-842.

[65] Tanaka, K., Oonuki, M., Moritake, N., & Uchiki, H. *Sol. Energy. Mater Sol. Cells 2009*, 93, 583-587.

[66] Maeda, K., Tanaka, K., Fukui, Y., & Uchiki, H. *Sol. Energy. Mater Sol. Cells 2011.*, 95, 2855-2860.

[67] Moritake, N., Fukui, Y., Oonuki, M., Tanaka, K., & Uchiki, H. *Phys. Status. Solidi 2009*, 1233-1236.

[68] Moriya, K., Tanaka, K., & Uchiki, H. *Jpn. J. Appl. Phys. 2007*, 46, 5780-5781.

[69] Moholkar, A. V., Shinde, S. S., Babar, A. R., Sim, K., Lee, H., Rajpure, K. Y., Patil, P. S., Bhosale, C. H., & Kim, J. H. J. *Alloys Compd. 2011.*, 509, 7439-7446.

[70] Prabhakar, T., & Nagaraju, J. *Proceedings 37th IEEE PVSC 2011 (Seattle, USA).*

[71] Steinhagen, C., Panthani, M. G., Akhavan, V., Goodfellow, B., Koo, B., & Korgel, B. A. J. *Am. Chem. 2009.*, 12554-12555.

[72] Zhou, Z., Wang, Y., Xu, D., & Zhang, Y. *Sol. Energy. Mater Sol. Cells 2010.*, 94, 2042-2045.

[73] Shin, B., Gunawan, O., Zhu, Y., Bojarczuk, N. A., Chey, S. J., Guha, S., & Prog, Photovolt. *Res.Appl. 2011.*, DOI:10.1002/pip.1174.

[74] Ahmed, S., Reuter, K. B., Gunawan, O., Guo, L., Romankiw, L. T., & Deligianni, H. *Adv. Energy. Mater 2012.*, 2, 253-259.

[75] Repins, I., Contreras, M. A., Egaas, B., De Hart, C., Scharf, J., Perkins, C. L., To, B., & Noufi, R. *Prog. Photovolt. Res. Appl. 2008.*, 16, 235-239.

[76] Barkhouse, D. A. R., Gunawan, O., Gokmen, T., Todorov, T. K., & Mitzi, D. B. *Prog. Photovolt. Res. Appl. 2012.*, 20, 6-11.

[77] Guo, Q., Ford, G. M., Yang, W., Walker, B. C., Stach, E. A., Hillhouse, H. W., & Agrawal, R. J. *Am. Chem. Soc. 2010.*, 13, 17384-17386.

[78] Han, S., Hasoon, , S., F., Al-Thani, H. A., Hermann, A. M., & Levi, D. H. J. *Phys. Chem. Solids 2005.*, 66, 1895-1898.

[79] Tanaka, T., Yoshida, A., Saiki, D., Saito, K., Guo, Q., Nishio, M., & Yamaguchi, T. *Thin Solid Films 2010.*, S29-S33.

[80] Caballero, R., Kaufmann, C. A., Eisenbarth, T., Cancela, M., Hesse, R., Unold, T., Eicke, A., Klenk, R., & Schock, H. W. *Thin Solid Films 2009.*, 517, 2187-2190.

[81] Rudmann, D., Bilger, G., Kaelin, M., Haug, F. J., Zogg, H., & Tiwari, A. N. *Thin Solid Films 2001.*, 431-432, 37-40.

[82] Ye, S., Tan, X., Jiang, M., Fan, B., Tang, K., & Zhuang, S. *Appl. Opt. 2010.*, 49, 1662-1665.

[83] Prabhakar, T., & Jampana, N. *Sol. Energy. Mater. Sol. Cells. 2011.*, 95, 1001-1004.

[84] Waldau, A. J. *Sol. Energy. Mater. Sol. Cells 2011.*, 95, 1509-1517.

[85] Seol, J., Lee, S., Lee, J., Nam, H., & Kim, K. *Sol. Energy. Mater Sol. Cells 2003.*, 75, 155-162.

[86] Pawar, S. M., Moholkar, A. V., Kim, I. K., Shin, S. W., Moon, J. H., Rhee, J. I., & Kim, J. H. Curr. Appl. Phys. 2010. , 10, 565-569.

[87] Schurr, R., Hölzing, A., Jost, S., Hock, R., Vo, T., Schulze, J., Kirbs, A., Ennaoui, A., LuxSteiner, M., Weber, A., Kötschau, I., & Schock, H.W. Thin Solid Films 2009. , 517, 2465-2468.

[88] Riha, S. C., Parkinson, B. A., & Prieto, A. L. J. *Am. Chem. Soc. 2009.*, 12054-12055.

[89] Guo, Q., Hillhouse, H. W., & Agrawal, R. J. *Am. Chem. Soc. 2009.*, 131, 11672-11673.

[90] Kameyama, T., Osaki, K. T., Okazaki, Shibayama. T., Kudo, A., Kuwabatade, S., & Torimoto, T. J. *Mater Chem. 2010.*, 20, 5319-5324.

[91] Zhou, Y., Zhou, W., Li, M., Du, Y., & Wu, S. J. *Phys. Chem. C. 2011.*, 115, 19632-19639.

[92] Ching, J. Y., Gillorin, A., Zaberca, O., Balocchi, A., & Marie, X. *Chem. Commun. 2011.*, 47, 5229-5231.

[93] Shi, L., Pei, C., Xu, Y., & Li, Q. J. *Am. Chem. Soc. 2011.*, 133, 10328-10331.

[94] Wang, J., Xin, X., & Lin, Z. Nanoscale, 2011. , 3, 3040.

[95] PV magazine. http://www.pv-magazine.com/news/details/beitrag/solar-frontier-and-ibm-to-develop-czts-cell-100001390/.

[96] Business insider. http://www.businessinsider.com/delsolar-and-ibm-to-jointly-develop-czts-solar-cell-technology-20109.

[97] Oleksyuk, I. D., Dudchar, I. V., & Piskach, L. V. J. *Alloys Compd. 2004.*, 368, 135-143.

[98] Hartman, K., Newman, B. K., Johnson, J. L., Du, H., Fernandes, P. A., Chawla, V., Bolin, T., Clemens, B. M., da, Cunha. A. F., Teeter, G., Scarpulla, M. A., & Buonassisi, T. *Proceedings 37th IEEE PVSC 2011 (Seattle, USA).*

[99] Lundberg, O., Edoff, M., & Stolt, L. Thin Solid Films 2005. , 480-481, 520-525.

[100] Sakurai, K., Scheer, R., Nakamura, S., Kimura, Y., Baba, T., Kaufmann, C. A., Neisser, A., Ishizuka, S., Yamada, A., Matsubara, K., Iwata, K., Fons, P., Nakanishi, H., & Niki, S. *Sol. Energy. Mater Sol. Cells 2006.*, 90, 3377-3384.

[101] Jung, S., Ahn, S., Yun, J., Gwak, J., Kim, D., & Yoon, K. *Current Appl. Phys. 2010*, 10, 990-996.

[102] Li, W., Sun, Y., Liu, W., & Zhou, L. *Sol. Energy. 2006*, 80, 191-195.

[103] Nakada, T., Hongo, M., & Hayashi, E. Thin Solid Films 2003. , 431-432, 242-248.

[104] Minemoto, T., Hashimoto, Y., Kolahi, W., Satoh, T., Negami, T., Takakura, H., & Hamakawa, Y. *Sol. Energy. Mater Sol. Cells 2003.*, 75, 121-126.

[105] Wei, H., Ye, Z., Li, M., Su, Y., Yang, Z., & Zhang, Y. *Cryst. Eng. Comm. 2011.*, 13, 2222.

[106] Ford, G. M., Guo, Q., Agrawal, R., & Hillhouse, H. W. *Chem. Mater. 2011.*, 23, 2626-2629.

[107] Todorov, T., Mitzi, D. B., & Eur, J. *Inorg. Chem. 2010.*, 17, 17-28.

[108] Kawamura, M., Fujita, T., Yamada, A., & Konagai, M. J. *Cryst. Growth. 2009.*, 311, 753-756.

[109] International Solar Electric Technology. http://isetinc.com/technology-overview.php.

[110] Zhang, R., Wang, B., Wan, D., & Wei, L. *Opt. Mater. 2004.*, 27, 423-419.

[111] Hynes, K. M., & Newham, J. *Proceedings 16th European Photovoltaic Solar Energy Conference 2000*, 2297.

[112] Directive 2002/96/EC. *27 the European parliament and of the council of 27 January 2003 on waste electrical and electronic equipment (WEEE), Official Journal of the European Union (2003) L37/24.*

[113] Sakai, N., Hiroi, H., & Sugimoto, H. *Proceedings 37th IEEE PVSC 2011 (Seattle, USA).*

[114] Jiang, M., Tang, K., & Yan, X. J. *Photon Energy 2012 in progress.*

[115] Yang, H., Song, Q., Lu, Z., Guo, C., Gong, C., Hu, W., & Li, C. Energy Environ. Sci. 2000. , 3, 1580-1586.

[116] Wang, L. *Energy Environ. Sci. 2009.*, 2, 944-955.

[117] Muduli, S., Game, O., Dhas, V., Yengantiwar, A., & Ogale, S. B. *Energy Environ. Sci. 2011.*, 4, 2835-2839.

[118] Li, Y., Yan, M., Jiang, M., Dhakal, R., Thapaliya, P. S., & Yan, X. J. *Photon Energy 2011.*, 1, 011115.

[119] Kuang, Y., van der Werf, K.H.M., Houweling, Z. S., & Schropp, R. E. I. Appl. Phys. Lett. 2011. , 113111.

[120] Krunks, M., Katerski, A., Dedova, T., Acik, I. O., & Mere, A. Sol. Energy. Mater Sol. Cells 2008. , 92, 1016-1019.

Chapter 6

# Thin Film Solar Cells Using Earth-Abundant Materials

Parag S. Vasekar and Tara P. Dhakal

Additional information is available at the end of the chapter

http://dx.doi.org/10.5772/51734

## 1. Introduction

In a p-n junction photovoltaic (PV) cell, a photon of light produces an electron hole pair if the energy of the photon is at least equal to the band gap of the material constituting the p-n junction. The electrons and holes first diffuse toward the respective edge of the depletion region, and then drift across the junction due to the built-in potential and are collected at the electrodes. Thus, materials with long minority carrier life times and high carrier mobilities are desired for high efficiency. Because electrons have higher mobility than the holes, a p-type semiconductor is used as light absorber in a p-n junction solar cell.

The theoretical efficiency limit for an ideal homo-junction solar cell as calculated by Loferski [1] is 23%, and this maximum efficiency falls in the vicinity of the absorbers with band gap energy of 1.5 eV. A more justifiable theoretical efficiency limit that used atomic processes was put forward by Shockley and Queisser [2] later in the sixties. According to this theoretical efficiency limit, also known as the Shockley-Queisser limit, a maximum efficiency of 30% for a band gap of 1.1 eV is possible (assuming only radiative recombination) if exposed to the sunlight of global air mass 1.5.

The most recent data published in *Progress in Photovoltaics* [3] depict an efficiency of 25% for a crystalline silicon (Si) solar cell measured under the global AM 1.5 spectrum at 25°C. This value of efficiency approaches the theoretical value set by Shockley-Queisser limit. However, coupled with its low absorption cross section and high synthesis and processing cost, this first generation crystalline Si- solar cell doesn't show promise for a low cost, thin film PV device.

For thin film technologies, amorphous silicon-hydrogen alloy (a-Si) solar cells have exhibited efficiencies in the 10-12% range [4] and are fabricated with low cost technology. However, degradation of the performance over time is a major issue associated with the a-Si solar cells. Recently, metal induced crystallization of a-Si is used to make thin film polycrystalline Si-solar cell at relatively low temperature in an effort to reduce the processing cost [5], but fabrication

of these devices is combined with high temperature chemical vapor deposition, which makes it incompatible with roll-to-roll processing. Other emerging second generation solar cells are thin film chalcogenides like CIGS ($CuInGaSe_2$) and CdTe, which show terrestrial cell efficiency of 20.3% and 16.5% respectively [6,7]. The scarcity, cost and toxicity associated with In, Ga, and Cd elements present in these cells limit their sustainability in the future.

Thus wide spread applications of solar cells will require dramatic decrease in cost through the use of non-toxic, inexpensive, and earth-abundant materials. The drawbacks in the present PV materials motivate us to look for alternatives. Due to the low absorption cross section, crystalline silicon requires thick layers, which will increase costs. Amorphous silicon (a-Si) has a higher absorption cross section and low processing cost compared to its crystalline counterpart, but it has stability problems. GaAs based solar cells have high efficiency, but the arsenic toxicity and the substrate cost limit their use. CIGS thin film solar cells show promise if the scarce and costly indium and gallium could be replaced by other elements. The quaternary compound semiconductor CZTS ($Cu_2ZnSnS_4$) [8] possesses promising characteristic optical properties; band-gap energy of about 1.5 eV and large absorption coefficient in the order of $10^4$ $cm^{-1}$. The highly efficient CdTe solar cell is promising, but has obstacles such as cadmium toxicity, tellurium scarcity, and cost. While the results of research and commercialization of crystalline Si, GaAs, CIGS, CdTe, etc. cells are commendable, a search for alternative materials is indispensable and necessary to achieve low cost, light weight, and low toxicity arrays.

| Property | CZTS | $Zn_3P_2$ | $FeS_2$ |
|---|---|---|---|
| Band gap | 1.5 eV [10] | 1.5 eV [11] | 0.95 eV [12] |
| Absorption Coeff. | ~ $10^4$ $cm^{-1}$ [10] | ~ $10^4$ $cm^{-1}$ [13] | 3.3 x $10^5$ $cm^{-1}$ [12] |
| Electron diff. length | n/a† | 4 to 10 μm [11] | 0.13 to 1 μm [12] |
| Dark resistivity (ρ) | 1 to 39 x$10^3$ Ω.cm [14] | 2.5 x $10^3$ Ω.cm [15] | 1.43 Ω.cm [16] |
| Carrier mobility (μ) | 30 $cm^2$/Vs [10] | 450 $cm^2$/Vs [17] | 200 to 300 $cm^2$/Vs [12] |

**Table 1.** Figure of Merits of CZTS, $Zn_3P_2$ and $FeS_2$ toward a PV cell compiled from the literature. †Although the exact value of the electron diffusion length of CZTS is not available, the quantum efficiency (QE) spectra suggest a relatively lower carrier diffusion length for this material.

In a recent study [9], a number of promising solar cell materials including CZTS, $Zn_3P_2$, and $FeS_2$ etc. were identified as materials with low extraction cost. It is estimated that the cost of material extraction for CZTS, $Zn_3P_2$ and $FeS_2$ is around 0.005 cents/W, 0.0007 cents/W and 0.000002 cents/W respectively. More encouraging is the fact that the constituent materials of these absorbers are abundant in the earth's crust. The light absorption cross sections for CZTS, $Zn_3P_2$ and $FeS_2$ are all greater than $10^4$ $cm^{-1}$ (Table 1), thus making thin film devices practical. The band gaps are also in the optimum range for efficient photo-energy conversion. These three contenders will be discussed mainly in this review with some discussion on other earth-abundant candidates such as tin sulfide (SnS).

http://dx.doi.org/10.5772/51734

## 2. Copper zinc tin sulfide

### 2.1. Introduction

Thin film solar cells based on $Cu(In,Ga)(S,Se)_2$ and CdTe have demonstrated significant improvement in the last few years, and they are also being transferred to production levels [18,19]. Out of these two technologies, CIGS based solar cells are the most efficient ones at the laboratory level and have demonstrated efficiencies in the range of 20% [6]. However, both CIGS and CdTe based thin film solar cells are hindered by potential environmental hazard issues [20] and scarcity issues associated with the constituent elements: mainly Te, In, Ga, and to some extent, Se [20,21]. Recent research trends are moving towards finding alternatives based on earth-abundant and non-toxic elements. An alternative material $Cu(Zn,Sn)(S,Se)_2$ is being explored these days by the thin film photovoltaics community which contains earth-abundant materials like Zn and Sn. CZTS structure can be derived from $CuInS_2$ chalcopyrite structure by replacing one-half of the constituent indium atoms by zinc and other half by tin. The resulting bandgap varies in the range of 0.8 eV for a selenide structure to 1.5 eV for a sulfide structure [22]. Copper-Zinc-Tin Sulfide or $Cu_2ZnSnS_4$ (CZTS) has a nearly ideal direct bandgap (1.5 eV) to absorb the most of the visible solar spectrum as well as a high absorption coefficient ($10^4$ $cm^{-1}$). CZTS film contains neither rare metals nor toxic materials, and combined with the cadmium-free buffer layer, we can expect solar cells with complete non-toxicity.

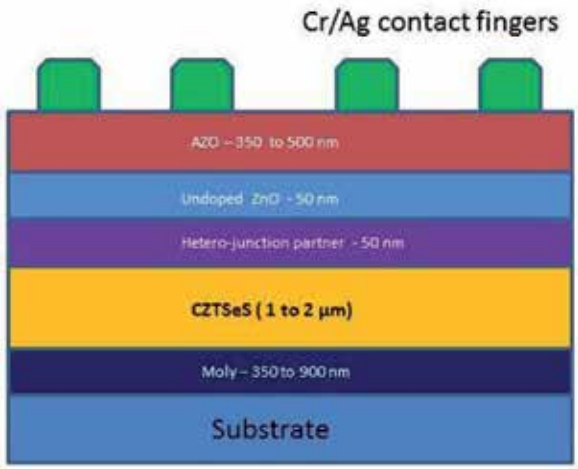


**Figure 1.** Schematic of the complete CZTSeS solar cell.

Several preparation methods have been reported in literature for preparation of CZTS solar cells [23]. These are physical vapor methods such as sulfurization of e-beam evaporated metallic layers and sputtered layers [24,25], RF magnetron sputtering [26], co-evaporation [27], hybrid sputtering [28]. Chemical methods involve sulfurization of electrochemically deposited metallic precursors [29], photochemical deposition [30], sol-gel sulfurization

methods [31], sol-gel spin-coated deposition [32] and spray pyrolysis [33,34]. In addition, there are syntheses based on solution methods [35,36].

Ever since Nakazawa reported the photovoltaic effect in a heterodiode of CZTS in 1988 [37], research in CZTS field has come a long way. The current highest efficiency for solution-processed CZTSeS based solar cells is 10.1% [38]. The efficiency for pure CZTS based solar cells that use the vacuum based approach is reported to be 8.4% [39]. The Schematic of a CZTSeS solar cell is as shown in Fig.1.

### 2.2. Crystal Structure

CIGSeS based films are mostly crystallized with a chalcopyrite structure [40], while CZTSeS based films exhibit either a Kesterite type of crystal structure or Stannite structure [41]. Because XRD peaks for Kesterite structure are similar to Stannite structure, it is difficult to distinguish between them unless other measurement techniques, such as neutron diffraction or Raman spectroscopy, are also employed. All three crystal structures are shown in Fig. 2 in order to understand the similarity and difference between them. It is also quite likely that both Kesterite and Stannite structures co-exist simultaneously because there is not much of energy difference for these structures to achieve/attain a stable state [41].

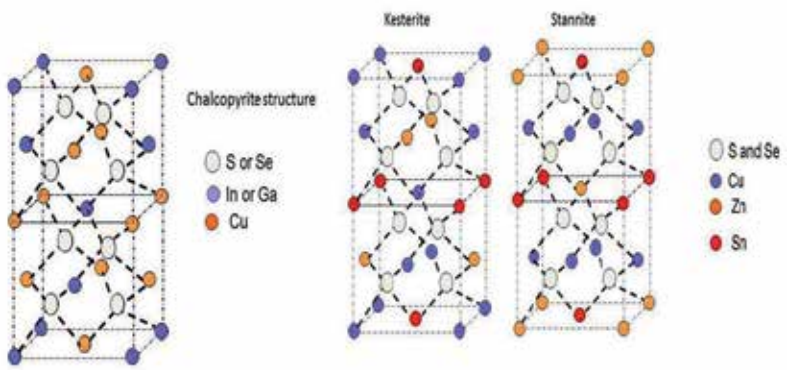


**Figure 2.** Chalcopyrite, Kesterite and Stannite crystal structures.

### 2.3. Electronic properties

The band-gap is the most important property of a photovoltaic material and near-optimum band-gap value around 1.5 eV is supposed to be ideal for effective photon absorption and photo-generation. CZTSe phase has a band-gap of 0.8 eV, while CZTS phase has a band-gap value of 1.5 eV [22]. The band-gap can be engineered between these two values by adding sulfur to CZTSe phase. The doping behavior in Kesterite is also controlled by intrinsic doping similar to their chalcopyrite counterparts. The p-type behavior of CZTSeS phase is controlled by $Cu_{Zn}$ or $Cu_{Sn}$ antisite donor defects, or this may also result due to direct creation of copper vacancy and compensation for $Zn_{Cu}$ antisite and the S vacancy [41].

http://dx.doi.org/10.5772/51734

## 2.4. Phase stability

Similar to CIGSeS thin films, CZTSeS phase also has a narrow region of phase stability in which the device quality phase can be synthesized without any adverse effect of secondary phases. In fact, the phase stability region is even narrower as compared to chalcopyrites, thus making single phase device quality CZTSeS synthesis more difficult [42]. Solid state CZTS can also be synthesized through reactions between ZnS, $Cu_2S$,and $SnS_2$. As can be seen in the phase diagram in Fig. 3, there is very narrow region where CZTS is stable and secondary phases are very easy to form. Copper-poor and zinc-rich composition has been found to be ideal so far to obtain efficient devices from CZTS films [8].

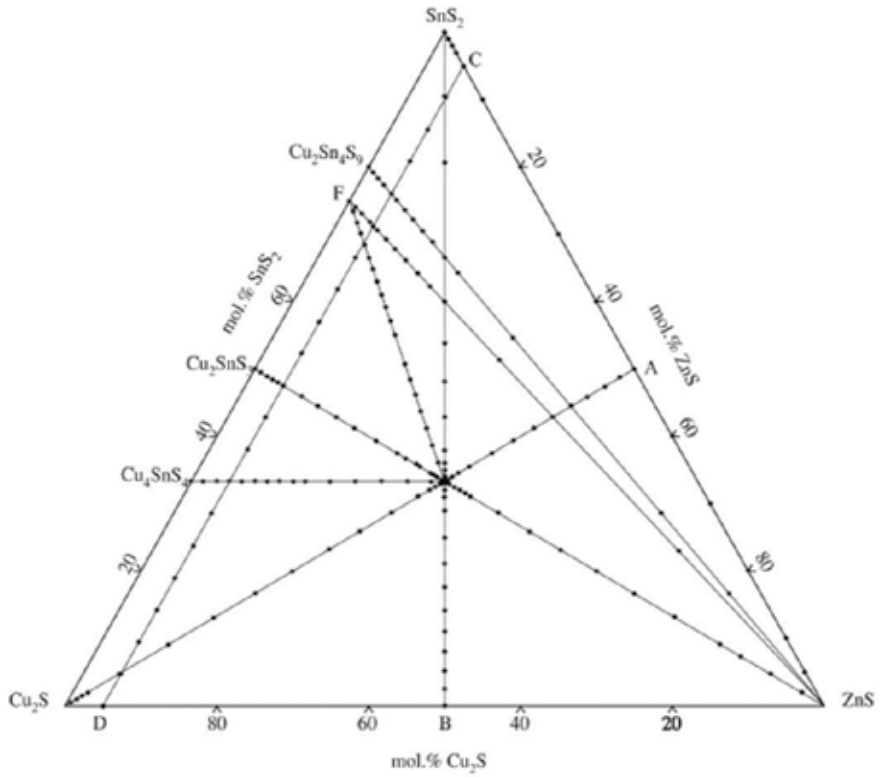


**Figure 3.** Ternary phase diagram of the $Cu_2S$-ZnS-$SnS_2$ system. (Reprinted from [42] with permission from Elsevier).

## 2.5. Synthesis techniques

### *2.5.1. Vacuum based approaches ( sputtering/evaporation)*

The synthesis techniques are both vacuum-based processes and non-vacuum based processes. Dr. Katagiri's group has pioneered vacuum-based approaches [8,22,24,43]. Their first report on E-B evaporated precursors followed by sulfurization yielded an efficiency of 0.66% [24]. With modification of fabrication process, the conversion efficiency was

gradually increased in their successive reports. It was observed that longer time and temperature cycles were detrimental for the performance of the CZTS films: hence, by adjusting the time and temperature cycles, Katagiri et al reported an efficiency of 2.62% in their next report [14]. After overcoming the problem of residual gases in the sulfurization chamber, the efficiency number rose to 5.45% [44].

This group has also contributed towards sputtered CZTS films followed by sulfurization [43] and reported an efficiency of 6.7%. They observed that soaking the CZTS layer on the Mo coated sodalime glass in deionized water leads to significant improvement in the device performance. Recently, they also reported 6.48% efficiency using CZTS compound target and a simple single sputtering step [45].

In 2010, IBM group reported an efficiency of 6.8% by using co-evaporated film of Cu, Zn, Sn and S sources followed by reactive annealing [46]. The best efficiency so far for pure sulfide phase CZTS is 8.4% [39], as noted in the IBM group report for evaporated CZTS films. Also, they recently reported an efficiency for pure selenide phase using co-evaporation is 8.9% [47]. An NREL group reports the best efficiency for pure selenide phase CZTSe as 9.15% [48]. The highest reported efficiency using vacuum based techniques is 9.3% [49], which is for mixed CZTSeS phase using co-sputtering of compound targets followed by annealing at a higher temperature. This report is by an industrial research group ( AQT Solar ).

Some other notable recent reports on vacuum based approaches are as follows:

1. In the quest to obtain Cd-free devices, the researchers at Solar Frontier, Japan recently demonstrated an efficiency of 6.3% for In-based hetero-junction partners and 5.8% for Zn-based hetero-junction partners [50].

2. The same group in Japan reports > 8% efficiency on CZTS sub-module [51]. Another interesting and note-worthy contribution here is that the absorber thickness is reported to be just 600 nm.

3. Salomé et al demonstrate that incorporation of $H_2$ is beneficial for preventing Zn loss during the sulfurization [52].

4. Shin et al mention that stacking of precursors has a role in getting single-phase final CZTS compound and reducing the secondary phases [53].

5. Chalapathy and co-workers demonstrate an efficiency of 4.59% using ZnSn (60:40at%) alloy target [54].

*2.5.2. Electrodeposition*

Electro-deposition is of particular interest for the thin film photovoltaics community due to the advantages it offers: low cost, environment friendly, large area deposition, room temperature growth, and less or almost no wastage of materials. CIGS technology based on electrodeposition has already been commercialized [55]. There are numerous reports on electrodeposition of CZTS as well [29,56,57]. Most of the reported efficiencies are in the range of 3% to 4% for electro-deposited CZTS films [57-59].

Some other notable recent reports on electro-deposited CZTS films are as follows:

1. Li et al recently demonstrated 1.7% efficiency in CZTSe films prepared by co-electro-deposition [60].

2. Mali et al used a successive ionic layer adsorption and reaction (SILAR) method for CZTS films. In this method, a substrate is immersed into separately placed cations and anions. This particular electro-chemical method is used for making uniform and large area thin films [61].

*2.5.3. Spray pyrolysis*

Spray pyrolysis is a versatile as well as a low-cost technique that has been used to deposit semiconductor films. In this process, a thin film is deposited by spraying a solution on a hot surface. The constituents react to form a chemical compound. The chemical reactants are selected such that the products other than the desired compound are volatile at the temperature of deposition [62]. There have been early reports of sprayed CZTS films [33].

Some other notable recent reports on sprayed CZTS films are as follows:

1. Prabhakar et al prepared CZTS films using ultrasonic spray pyrolysis and observed that sodium plays an important role in CZTS films as well [63]. This observation similar to CIGS films and the role of sodium in CIGS films is well known. The authors observed that sodium enhanced (112) orientation and grain size of the CZTS films also increased the hole carrier concentration.

2. In another report, authors prepared CZTS films using two different tin precursors: stannous as well as stannic chloride [64]. They observed that crystallinity and grain size as well as carrier concentration and mobility values were better for films prepared using stannic chloride.

*2.5.4. Solution based methods*

Direct liquid deposition or 'ink' based approaches are attractive due to their compatibility with high volume manufacturing techniques such as printing. It is a low-cost scalable route for the thin film solar technology. One of the popular approaches is to prepare precursors using sol-gel method, then sulfurize it, and deposit on substrate using spin-coating [65]. The micro-particles of CZTS have also been prepared using ball milling, sintering type of processes and later screen printed on flexible substrates [66]. There are various other reports using colloidal nanoparticles [67], Photochemical deposition [30] etc.

The researchers at IBM in their recent publication have reported the highest record efficiency by any process so far for CZTSeS as 10.1% [38]. The J-V curve of this record sample and cross-sectin of the CZTSeS film is as shown in Fig. 4. Here metal chalcogenides were dissolved in hydrazine solution and later spin-coated on glass-substrates followed by a heat-treatment at 540°C.

Some other notable recent reports on solution/ink based CZTS films are as follows:

1. Using band-gap engineering with Germanium, researchers at Purdue University have achieved an efficiency of 8.4%. They have utilized nanoparticles of CZTSeS on Moly-coated glass substrates [68].
2. The researchers at DuPont have demonstrated an efficiency of 8.5% [69]. They use binary and ternary chalcogenide nanocrystals produced by simple colloidal syntheses.

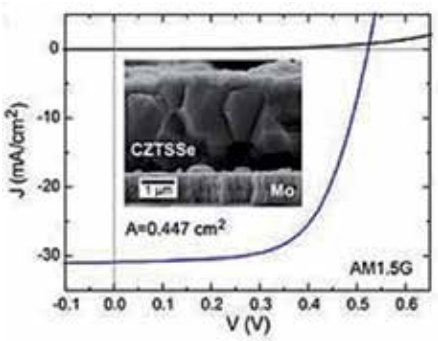


**Figure 4.** J–V characteristics of the record 10.1% sample at AM1.5G simulated illumination along-with CZTSSe film cross-section (Reprinted from[38] with permission from John Wiley and Sons).

### 2.6. Current status

The laboratory level efficiencies are more than 10% [38] and there are some recent reports of sub-module efficiencies of more than 8% [51]. However, the technology still needs to go a long way before it can be commercialized. The complex phase diagram and material properties impose most of the challenges. Also, the narrow stoichiometry window for a stable CZTS phase requires a robust control on composition. The processing window is even narrower compared to their CIGS counterparts. The volatile nature of some components, such as tin sulfide and zinc, impedes further challenges for traditional vacuum-based processing approaches which require high sulfurization/selenization temperatures after precursor deposition. The secondary phases formed are difficult to detect with conventional techniques such as XRD due to the overlapping peaks with pure CZTS phase. The interface properties with hetero-junction partners need to be studied well. However, the initial results in last few years look quite promising.

## 3. Zinc phosphide ($Zn_3P_2$)

### 3.1. Introduction

With rise in the prices and non-abundance of the materials such as indium and gallium current research trends in thin film solar cells have been moving toward development of earth-abundant solar cell materials that can be synthesized using low-cost processes. Also, zinc-based hetero-junction partners are preferred over toxic cadmium based compounds such as Cadmium sulfide [70]. Zinc phosphide ($Zn_3P_2$) is an important optoelectronic material,

which also has applications in lithium ion batteries [71]. It is an important semiconductor from the II-V group, and is used for optoelectronic applications [13,72-74]. Zinc phosphide exhibits favorable optoelectronic properties, such as direct bandgap of 1.5 eV, which corresponds to the optimum solar energy conversion range [74-77]. Zinc phosphide has a large optical absorption coefficient of $>10^4$ $cm^{-1}$, hence it can be positively used as a p-type absorber [78]. Also, due to its long minority diffusion length of ~10 μm, high current collection efficiency can be yielded. Zinc, as well as phosphorous, is abundant in the earth's crust. This makes their cost-effective development quite feasible when it comes to large scale production [73,79]. Zinc phosphide is a tetragonal p-type low cost material with lattice constants of a = b =8.097 Å and c=11.45 Å [17] and has all the right characteristics for photo conversion. $Zn_3P_2$ is synthesized most of times with a p-type conductivity [80].

### 3.2. Early efforts

Thin film solar cell devices using $Zn_3P_2$ have been fabricated using Schottky contacts, p-n semiconductor hetero-junctions [81] or liquid contacts [82]. Zinc phosphide was explored extensively in the early eighties and nineties [11,78,80,83,84]. With a Schottky diode, an efficiency as high as 6% was demonstrated [78]. Zinc phosphide homo-junctions have been difficult to make. However, even a zinc phosphide hetero-junction solar cell has not been successful with an efficiency range around 2% [11,85,86].

The researchers at the Institute of Energy Conversion were leaders in the early eighties in exploring $Zn_3P_2$ [78,80,83,87,88]. They demonstrated the effect of Mg doping and also fabricated Schottky barrier solar cells [78,88]. They also successfully made hetero-junction solar cells using ZnO as a hetero-junction partner [11].

Another interesting study is by Misiewicz et al [89]. They made various metal contacts (Au, Ag, Sb, Al, Mg) with $Zn_3P_2$ and measured current-voltage characteristics. It was observed that Ag and Sb made the best ohmic contacts, while Au, Mg and Al exhibited rectifying properties. Mg was found to be the most useful for making Schottky barriers.

### 3.3. Synthesis technqiues

Some of the synthesis techniques to grow $Zn_3P_2$ are summarized below :

#### *3.3.1. Vapor transport*

Catalano et al [90] report synthesis of $Zn_3P_2$ by vapor transport using perforated capsule technique. Crystals were grown in silica tubes placed mid-way in a capsule immediately ahead of $Zn_3P_2$ charge. When heated at a high temperature (900°C), effusion of zinc and phospherous out of the inner growth capsule resulted in the condensation of $Zn_3P_2$ on the walls of outer tube's cooler portion.A similar vapor transport technique has been reported by Wang et al [91] for growing single crystal $Zn_3P_2$.

#### *3.3.2. Evaporation*

Deiss et al report synthesis of $Zn_3P_2$ thin film by direct evaporation of $Zn_3P_2$ on glass substrates in a vacuum chamber at 750°C [92]. The films deposited on a cold substrate were re-

ported as amorphous, while the films deposited on a heated sunstrate (>300°C) were reported as crystalline. In a similar technique, Murali et al report that films grown with source-substrate distance < 3 cm were crystalline in nature [93].

*3.3.3. Metal organic chemical vapor deposition (MOCVD)*

Kakishita et al report a low-pressure MOCVD system with dimethylzinc (DMZ) and diluted phosphine ($PH_3$) as reactant gas [72]. Phosphine was cracked at 800°C and $Zn_3P_2$ films were grown on ZnSe single crystal substrates at a growth temperature of 290-410°C. Hermann et al report use of diethlzinc (DEZ) as a zinc precursor [15].

*3.3.4. Electrodeposition*

Soliman et al [94] report electrodepositon of $Zn_3P_2$ with $SnO_2$ coated glass as working electrode and the aqueous solution containing different concentrations of both $ZnCl_2$, $ZnSO_4$ and $Na_2PO_3$. The pH was adjusted at 2.5 by adding $H_2SO_4$. It was observed that $Zn_3P_2$was obtained, and the degree of crystallinity increased with higher Zn/P molar ratio. There is a recent report similar to that of Soliman et al, reporting electrodeposition of $Zn_3P_2$ [95].

*3.3.5. Chemical reflux technique*

Recently our group has successfully synthesized $Zn_3P_2$ using chemical reflux technique [96,97]. The zinc-coated glass substrate is placed on the top of a fritted glass, which is sorrounded by trioctylphosphine (TOP) liquid. The entire vessel is heated while vapors of TOP are refluxed back to the bottom of the glass vessel by a condenser connected at the top of the vessel. The glass vessel is heated to 350°C for two to four hours, and then slowly cooled to room temperature. It was observed that zinc phosphide can be successfully synthesized using this simple chemical route in both nano-wire and thin film forms depending on the exposure mechanism of the phosphorous precursor with the zinc-deposited substrates.

### 3.4. Current status

Recently Kimball et al have studied the effect of magnesium doping on $Zn_3P_2$ thin films [98,99]. Our group has recently demonstrated that zinc phosphide can be successfully synthesized in both nano-wire and thin film forms [96,97]. Efforts are ongoing to improve the photovoltaic properties using various hetero-junction partner options.

## 4. Iron disulfide ( $FeS_2$)

### 4.1. Introduction

Pyrite ($FeS_2$) is a non-toxic material and is abundant on earth, and has a potential to be an inexpensive and sustainable alternative for achieving low-cost and high-efficiency solar cells due both to its environmental compatibility and its optimal optical properties for efficient energy conversion. Its energy band gap of 0.95 eV and optical absorption coefficient of the

order of $10^5$ $cm^{-1}$ are in the optimal range for efficient conversion of sunlight into electricity [12,100]. A saturation current of 40 to 50 mA/$cm^2$ for a thickness between 0.2 μm to 1 μm is possible for pyrite [101]. In addition, a carrier mobility of 200 $cm^2$/Vs and sufficiently high minority carrier lifetimes makes pyrite highly favorable for photovoltaic application [102]. It has been calculated that theoretical conversion efficiency close to 30% is possible because its band gap is quite close to silicon.

Iron pyrite, like other metal chalcogenides, received considerable attention after the photoelectrochemical solar cells using $FeS_2$ single crystal electrodes in contact with iodide/tri-iodide ($I^-/I_3^-$) redox electrolyte exhibited a quantum efficiency close to 100% across a n-$FeS_2$/($I^-/I_3^-$) interface [103-105]. However, a solar conversion efficiency of this photochemical cell was only 2.8% when illuminated under AM 1.5. The open circuit voltage ($V_{oc}$) was 187 mV. This value of $V_{oc}$ is lower than the theoretical value of about 500 mV [106]. The low photopotential is attributed to the strong pinning of the Fermi level caused by surface states [105] as well as bulk defects caused by the sulphur deficiency [107].

It should be noted that numerous iron sulphides exist in nature with unique properties depending on different iron (Fe) and sulphur (S) stoichiometric ratios and different crystal structures. Thus creating a phase pure iron pyrite is a challenge. Orthorhombic marcasite $FeS_2$ and hexagonal troilite FeS are both common iron sulfur phases, but because they have much smaller band gaps (0.34 eV for marcasite and 0.04 eV for troilite), even trace amounts would significantly diminish the photovoltaic properties of the pyrite [108]. So, examining the preparation of pyrite by using various techniques is important.

### 4.2. Synthesis techniques

Some of the experimental techniques used to grow pyrite are summarized below:

#### *4.2.1. Chemical vapor transport (CVT)*

This technique involves high crystal growth with halogens, such as $Br_2$ and $Cl_2$, and polycrystalline $FeS_2$ sealed in an ampoule [109]. This process produced cubic crystals with (111) and (100) faces up to 5 mm edge length. However, the growth process was too long (10 days) and was performed at high temperature (~1000°C). At elevated temperatures, segregation of sulphur and iron species is unavoidable.

#### *4.2.2. Metal organic chemical vapor depositon (MOCVD)*

Iron source, such as iron penta-carbonyl [Fe $(CO)_5$], and sulphur sources such as sulphur and $H_2S$ gas, are used in this technique [102]. The advantage of this technique is that the growth temperature is low (150°C) and the growth process is fast.

#### *4.2.3. Spray pyrolysis*

Chemical spray pyrolysis is used to grow $FeS_2$ using thiourea and $FeCl_2$ [110]. Chlorine contamination, slow growth, non-uniformity, reduced repeatability are some issues associated with this technique.

*4.2.4. Chemical methods*

A recent synthesis approach to grow a single phase $FeS_2$ nanoparticle is carried out by different groups using hydrothermal process [108,111]. Wadia and his group show single phase growth of $FeS_2$ nanoparticles. On the other hand, colloidal $FeS_2$ nano-crystal ink by using a hot-injection method has been synthesized by many groups [112-116]. These processes are encouraging in that these are low temperature processes and variation in particle sizes allows the manipulation of band gap, which will help to absorb a broader spectrum of sunlight. To translate these nanocrystals into a form of a compact thin film layer is a challenge [113,116,117].

*4.2.5. Sulfurization of iron oxides*

Sulphurization of iron oxides ($Fe_3O_4$ or $Fe_2O_3$) is predicted by Gibbs free energy phase diagram to give $FeS_2$ films [118]. Smestad et. al, sulphurized $Fe_3O_4$ or $Fe_2O_3$ using gaseous sulphur at 350°C. However, they didn't observe a good photovoltaic behavior from the photochemical cells made by using the $FeS_2$ films grown this way. One of the main reasons attributed to the poor photocurrent and voltage is the presence of micro-pinholes, which led to a short circuit in the photogenerated current and effectively shunted the pyrite cell. Recently, defect-free pyrite thin films were synthesized from iron oxide by using non-toxic and a more controllable organic precursor such as Di-tert butyl disulfide (TBDS) [119].

*4.2.6. Sulfurization of iron*

It is also claimed by another group that iron oxide route is not necessary to grow pyrite [12]. They used iron film and sulphurized it under nitrogen flux. But their films had a presence of an amorphous phase, which caused an indirect transion at 1.31 eV incompatible with the strong absorption of $FeS_2$

**4.3. Issues to be addressed for an optimal $FeS_2$ cell**

Low open circuit ($V_{oc}$) in pyrite solar cell is attributed to sulphur deficiency among other reasons [120]. A correlation between S deficiency and the transport parameters of pyrite was found, indicating that high quality intrinsic material can be prepared when the S/Fe ratio is close to the stoichiometric value of 2 [121]. In addition to the intrinsic material property, a device design would also affect $V_{oc}$.

*4.3.1. Influence of cell design on $V_{oc}$*

The electrical and optical properties of $FeS_2$ are promising for an efficient photovoltaic action, but the conversion efficiency of the $FeS_2$ cell is not impressive: 1% with Schottky type solar cells [101] and 2.8% with photochemical cells. Cells fabricated with Schottky contacts exhibited short circuit currents ($J_{sc}$) below 10 mA/cm$^2$ and open circuit voltages ($V_{oc}$) below 20 mV. However, quantum efficiencies of 90% and above and high photo-current density observed in the latter type of the cell indicate the potential of an efficient pyrite based solar cell. The reason for the low efficiency was due to low open circuit volt-

age of about 200 mV. The interfacial chemistry of the p-n junction plays a role in dictating the open circuit voltage. A solar cell structure with a wide band gap window layer, such as ZnS, may improve the open circuit voltage.

*4.3.2. Stoichiometry of $FeS_2$*

The ratio of Fe and S is extremely important to obtain a defect-free $FeS_2$ phase. It is necessary that the homogeneity range should be within 1%. It was shown in pyrite grown by MOCVD that whenever a stoichiometry is such that the composition of S is less than 2, a phase mixture of pyrite and pyrrhotite (FeS) existed. The band gap of pyrrhotite phase is 0.04 eV, which greatly diminishes the photovoltaic action. Thus reaffirmation of the pyrite stoichiometry is important.

*4.3.3. Influence of doping on $V_{oc}$*

A recent work on simulation of p-n type $FeS_2$ homo-junction diffusion limited solar cells showed that efficiencies around 20% are possible [101] by assuming that at low doping density Shockley–Read–Hall (SRH) recombination [122,123] limits the carrier life time, or in other words, the cell efficiency. Altermatt et. al [101] simulated a case where the carrier life time (t) limits only $V_{oc}$, e.g. a cell with d = 1 μm and t = 100 ns. The optimally obtainable photocurrent in pyrite under AM 1.5G illumination is about 50 mA/cm$^2$. The achievable efficiency level then was 18.5% (13.5%) in a highly (lowly) doped cell. There is trade-off between the carrier life time and open circuit voltage. For a high density of carriers, the voltage across the junction increases, which may create a higher $V_{oc}$ provided the recombination of the generated carriers is prevented. This is possible with the low carrier density (thus low dopant induced defects) case where the carrier life time is longer. Thus a subtle balance between $V_{oc}$ and excess carrier life time should be sought by carefully choosing the right dopant density. It was observed in Cobalt doped $FeS_2$ that by manipulating the carrier concentration, the grain barrier height can be changed, which in turn will change the photo-voltage [124].

*4.3.4. Fermi level pinning at the surface*

Low photo-voltage in a pyrite solar cell is dependent upon its surface structure. Ultraviolet photoemission spectroscopy (UPS) measurements carried out in Cobalt doped $FeS_2$ showed that the Fermi level at the surface is pinned [125], implying high density of surface. Thus controlling the dopant density with a high level of precision is critical. In a situation where surface defects are unavoidable, application of a resistive thin layer, such as n-type i-ZnO, could be helpful.

**4.4. Recent progress in $FeS_2$ solar cell device**

Recently Ganta et. al fabricated solid state based $FeS_2$ thin film solar cell using CdS as an n-type layer [116]. The super-strate type cell structure was glass/FTO/CdS/$FeS_2$/Ag/Cr. $FeS_2$ layer was formed by drop casting the $FeS_2$ nanoparticle ink directly onto the CdS layer at room temperature. The efficiency for CdS/$FeS_2$ cell was 0.03%. The low efficiency was due to

the low short-circuit current. The open-circuit voltage was high, which is large compared to a previously reported value of 200 mV [106].

Although the circuit current was low at 0.01 mA/cm$^2$, an open-circuit voltage of 565 mV was observed. Residual organic components present in the nanoparticle-film could be a reason for low short-circuit current. A compact film with the organic residues removed can be expected to improve the short-circuit current and the cell efficiency.

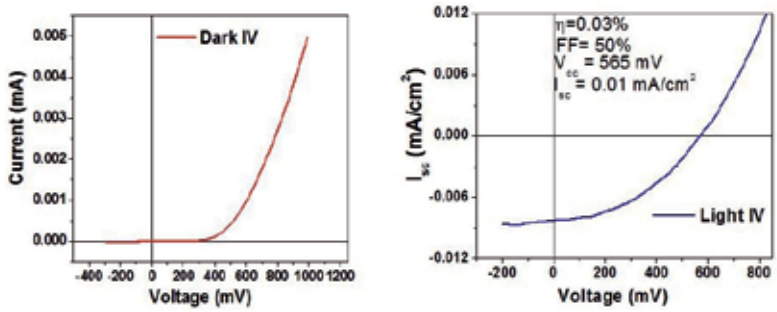


**Figure 5.** Dark and light I-Vcurves of the $FeS_2$ super-strate solar cell.

## 5. Other earth-abundant candidates

In a recent study, a number of materials were screened based on their abundance and non-toxicity, and semiconducting compounds composed of these identified materials were listed [126]. The authors found that even if binary compounds are focused, there are a good number of alternatives. Once semiconducting properties such as ideal band-gap and minority carrier diffusion length are considered, the next step is the processing capability. Obtaining the right phase without any defects is crucial. The next step is to identify ideal hetero-juction partner with right band-alignment as well as chemical and mechanical compatibility. Several other earth-abundant candidates are being researched these days.

Tin Sulfide (SnS) is metal chalcogenide semiconductor material from the IV-VI group. It has a near optimum direct bandgap of ~ 1.3 eV [127] and also a good absorption co-efficient ($10^5$ cm $^{-1}$) [128]. Elements such as tin and sulfur are abundantly available. Tin sulfide has been synthesized using a variety of techniques such as sputtering [127], evaporation [129], electrodeposition [130] as well as chemical routes [131]. The highest reported efficiency to date is 1.3% [132].

$Cu_2FeSnS_4$ (CFTS) with Stannite structure can also be a viable alternative and there are some recent reports of growing CFTS nanocrystals [133,134]. The bandgap of CFTS was found to be ~ 1.28 eV with p-type conductivity [134].

In a recent study, Fernandes et al identified ternary sulfides $Cu_2SnS_3$ and $Cu_3SnS_4$ as good alternatives [135]. The estimated bandgap values are between 1 to 1.6 eV and absorption coefficient $10^4$ cm$^{-1}$.

$Cu_2S$ is another interesting material that was extensively researched in the eighties. However, performance degradation due to copper diffusion led this technology to be abandoned. $Cu_2S$ has a bandgap of 1.2 eV [136]. The highest reported efficiency was 9.1% [137]. Recently this material has again received attention and innovative approaches, such as nanocrystals, are being implemented to overcome the issues encountered in the past [138].

## 6. Conclusion

One of the important p-type absorber CZTSe(S) has reached a laboratory level efficiency of more than 10% and has matured to a stage where it can be seriously considered for commercialization. Complex phase diagram and narrow stoichilometry window for CZTS remains a challenge; in addition, interface properties with suitable hetero-junction partners need to be understood better. However, despite these challenges, CZTS is the most promising material synthesized using earth-abundant constituents. Other materials discussed in detail in this review are $Zn_3P_2$ and $FeS_2$. These two materials also show considerable promise, despite their current low lab-level efficiency values. Apart from these, there are several other promosing materials synthesized using earth-abundant constutuents, such as SnS, CFTS and $Cu_2SnS_3$, and these potentially can be used in solar cells due to their photovoltaic properties.

## Author details

Parag S. Vasekar* and Tara P. Dhakal

*Address all correspondence to: psvasekar@yahoo.com, tpdhakal@gmail.com

Center for Autonomous Solar Power, Binghamton University, Binghamton, NY, USA

## References

[1] Loferski, J. J. J. (1956). Theoretical Considerations Governing the Choice of the Optimum Semiconductor for Photovoltaic Solar Energy Conversion. *J Appl Phys*, 27, 777.

[2] Shockley, W.W. (1961). Detailed Balance Limit of Efficiency of p-n Junction Solar Cells. *J Appl Phys*, 32, 510.

[3] Green, M. A., Emery, K., Hishikawa, Y., Warta, W., & Dunlop, E. D. (2011). Solar cell efficiency tables (Version 38). *Prog Photovoltaics Res Appl*, 19, 565-72.

[4] Guha, S.S. (1986). Enhancement of open circuit voltage in high efficiency amorphous silicon alloy solar cells. *Appl Phys Lett*, 49, 218.

[5] Gordon, I., Carnel, L., Van Gestel, D., Beaucarne, G., & Poortmans, J. (2007). Efficient thin-film polycrystalline-silicon solar cells based on aluminum- induced crystallization and thermal CVD. *Prog Photovoltaics Res Appl*, 15, 575-86.

[6] Jackson, P., Hariskos, D., Lotter, E., Paetel, S., Wuerz, R., Menner, R., et al. (2011). New world record efficiency for Cu(In,Ga)$Se_2$ thin-film solar cells beyond 20%. *Prog Photovoltaics Res Appl*, 19, 894-7.

[7] Wu, X. X. (2004). High-efficiency polycrystalline CdTe thin-film solar cells. *Solar Energy*, 77, 803-14.

[8] Katagiri, H., Jimbo, K., Maw, W. S., Oishi, K., Yamazaki, M., Araki, H., et al. (2009). Development of CZTS-based thin film solar cells. *Thin Solid Films*, 517, 2455-60.

[9] Wadia, C. C. (2009). Materials Availability Expands the Opportunity for Large-Scale Photovoltaics Deployment. *Environ Sci Technol*, 43, 2072-7.

[10] Liu, F., Li, Y., Zhang, K., Wang, B., Yan, C., Lai, Y., et al. (2010). In situ growth of $Cu_2ZnSnS_4$ thin films by reactive magnetron co-sputtering. *Solar Energy Mater Solar Cells*, 94, 2431-4.

[11] Nayar, P. P. S. (1981). Zinc phosphide-zinc oxide heterojunction solar cells. *Appl Phys Lett*, 39, 105.

[12] Rezig, B., Dahman, H., & Kenzari, M. (1992). Iron pyrite $FeS_2$ for flexible solar cells. *Renewable Energy*, 2, 125-8.

[13] Babu, V. S., Vaya, P. R., & Sobhanadri, J. (1988). Optical absorption and photoconductivity studies on $Zn_3P_2$ thin films grown by hot wall deposition. *Solar Energy Materials*, 18, 65-73.

[14] Katagiri, H. H. (2001). Development of thin film solar cell based on $Cu_2ZnSnS_4$ thin films. *Solar Energy Mater Solar Cells*, 65, 141-8.

[15] Hermann, A. M., Madan, A., Wanlass, M. W., Badri, V., Ahrenkiel, R., Morrison, S., et al. (2004). MOCVD growth and properties of $Zn_3 P_2$ and $Cd_3P_2$ films for thermal photovoltaic applications. *Solar Energy Mater Solar Cells*, 82, 241-52.

[16] Morsli, M. M. (1995). Electrical Properties of a Synthetic Pyrite FeS Non Stoichiometric Crystal. *Journal de physique.I : JP*, 5, 699-705.

[17] Sudhakar, S.S. (2008). Influence of cooling rate on the liquid-phase epitaxial growth of $Zn_3 P_2$ . *J Cryst Growth*, 310, 2707-11.

[18] Dhere, N. G. (2007). Toward GW/year of CIGS production within the next decade. *Solar Energy Materials and Solar Cells*, 91, 1376-82.

[19] Dhere, N. G. (2011). Scale-up issues of CIGS thin film PV modules. *Solar Energy Mater Solar Cells*, 95, 277-80.

[20] Green, M. M. A. (2006). Consolidation of thin-film photovoltaic technology: the coming decade of opportunity. *Progress in photovoltaics*, 14, 383-92.

[21] Anderson, B. A., Azar, C., Holmberg, J., & Karlsson, S. (1998). Material constraints for thin-film solar cells. *Energy*, 23, 407-11.

[22] Katagiri, H. (2005). $Cu_2ZnSnS_4$ thin film solar cells. *Thin Solid Films*, 480, 426.

[23] Fischereder, A. A. (2010). Investigation of Cu ZnSnS Formation from Metal Salts and Thioacetamide. *Chemistry of materials*, 22, 3399-406.

[24] Katagiri, H., Sasaguchi, N., Hando, S., Hoshino, S., Ohashi, J., & Yokota, T. (1997). Preparation and evaluation of $Cu_2ZnSnS_4$ thin films by sulfurization of E---B evaporated precursors. *Solar Energy Mater Solar Cells*, 49, 407-14.

[25] Araki, H. (2008). Preparation of $Cu_2ZnSnS_4$ thin films by sulfurization of stacked metallic layers. *Thin Solid Films*, 517, 1457.

[26] Seol, J., Lee, S., Lee, J., Nam, H., & Kim, K. (2003). Electrical and optical properties of $Cu_2ZnSnS_4$ thin films prepared by rf magnetron sputtering process. *Solar Energy Mater Solar Cells*, 75, 155-62.

[27] Tanaka, T., Kawasaki, D., Nishio, M., Guo, Q., & Ogawa, H. (2006). Fabrication of $Cu_2ZnSnS_4$ thin films by co-evaporation. *physica status solidi (c)*, 3, 2844-7.

[28] Tanaka, T., Nagatomo, T., Kawasaki, D., Nishio, M., Guo, Q., Wakahara, A., et al. (2005). Preparation of $Cu_2ZnSnS_4$ thin films by hybrid sputtering. *Journal of Physics and Chemistry of Solids*, 66, 1978-81.

[29] Araki, H., Kubo, Y., Mikaduki, A., Jimbo, K., Maw, W. S., Katagiri, H., et al. (2009). Preparation of $Cu_2ZnSnS_4$ thin films by sulfurizing electroplated precursors. *Solar Energy Mater Solar Cells*, 93, 996-9.

[30] Moriya, K., Watabe, J., Tanaka, K., & Uchiki, H. (2006). Characterization of $Cu_2ZnSnS_4$ thin films prepared by photo-chemical deposition. *physica status solidi (c)*, 3, 2848-52.

[31] Tanaka, K., Oonuki, M., Moritake, N., & Uchiki, H. (2009). $Cu_2ZnSnS_4$ thin film solar cells prepared by non-vacuum processing. *Solar Energy Mater Solar Cells*, 93, 583-7.

[32] Yeh, M. M. Y. (2009). Influences of synthesizing temperatures on the properties of $Cu_2ZnSnS_4$ prepared by sol-gel spin-coated deposition. *J Sol Gel Sci Technol*, 52, 65-8.

[33] Nakayama, N., & Ito, K. (1996). Sprayed films of stannite $Cu_2ZnSnS_4$ . *Appl Surf Sci*, 92, 171-5.

[34] Kamoun, N., Bouzouita, H., & Rezig, B. (2007). Fabrication and characterization of $Cu_2ZnSnS_4$ thin films deposited by spray pyrolysis technique. *Thin Solid Films*, 515, 5949-52.

[35] Riha, S. C., Parkinson, B. A., & Prieto, A. L. (2009). Solution-Based Synthesis and Characterization of $Cu_2ZnSnS_4$ Nanocrystals. *J Am Chem Soc*, 131, 12054-5.

[36] Todorov, T. K., Reuter, K. B., & Mitzi, D. B. (2010). High-Efficiency Solar Cell with Earth-Abundant Liquid-Processed Absorber. *Adv Mater*, 22, E 156-9.

[37] K. Ito, T.N. (1988). Electrical and optical properties of stannite-type quaternary semiconductor thin films. *Japanese journal of Applied Physics*.

[38] Barkhouse, D. A. R., Gunawan, O., Gokmen, T., Todorov, T., & Mitzi, D. (2012). Device characteristics of a 10.1% hydrazine-processed $Cu_2ZnSn(Se,S)_4$ solar cell Characteristics of a 10.1% efficient kesterite solar cell. *Progress in photovoltaics*, 20, 6-11.

[39] Shin, B., Gunawan, O., Zhu, Y., Bojarczuk, N. A., Chey, S. J., & Guha, S. (2011). Thin film solar cell with 8.4% power conversion efficiency using an earth-abundant $Cu_2ZnSnS_4$ absorber. *Prog Photovoltaics Res Appl:n/a,n/a*.

[40] Stanbery, B. B. J. (2002). Copper Indium Selenides and Related Materials for Photovoltaic Devices. *Critical reviews in solid state and materials sciences*, 27, 73-117.

[41] Siebentritt, S. S. (2012). Kesterites-a challenging material for solar cells Kesterites-a challenging material for solar cells. *Progress in photovoltaics:n,a-n/a*.

[42] Olekseyuk, I. D. (2004). Phase equilibria in the $Cu_2S$-ZnS-$SnS_2$ system. *J Alloys Compounds*, 368, 135-43.

[43] Katagiri, H. (2008). Enhanced conversion efficiencies of $Cu_2ZnSnSP4$based thin film solar cells by using preferential etching technique. *Applied physics express*, 1.

[44] Katagiri, H., Jimbo, K., Moriya, K., & Tsuchida, K. (2003). Solar cell without environmental pollution by using CZTS thin film. *Photovoltaic Energy Conversion, Proceedings of 3rd World Conference on*, 3, 2874-2879.

[45] Katagiri, H., & Jimbo, K. (2011). Development of rare metal-free CZTS-based thin film solar cells. *Photovoltaic Specialists Conference (PVSC), 37th IEEE*, 003516-21.

[46] Wang, K., Gunawan, O., Todorov, T., Shin, B., Chey, S. J., Bojarczuk, N. A., et al. (2010). Thermally evaporated $Cu_2ZnSnS_4$ solar cells. *Appl Phys Lett*, 97, 143508.

[47] Shin, B., Zhu, Y., Bojarczuk, N. A., Chey, S. J., & Guha, S. (2012). High efficiency $Cu_2ZnSnSe_4$ solar cells with a TiN diffusion barrier on the molybdenum bottom contact. *38th IEEE Photovoltaic Specialists Conference (PVSC)*.

[48] Repins, I., Beall, C., Vora, N., De Hart, C., Kuciauskas, D., Dippo, P., et al. (2012). Co-evaporated $Cu_2ZnSnSe_4$ films and devices. *Solar Energy Mater Solar Cells*, 101, 154-9.

[49] Chawla, V., & Clemens, B. (2012). Effect of Composition on High Efficiency CZTSSe Devices Fabricated Using Co-sputtering of Compound Targets. *38th IEEE Photovoltaic Specialists Conference (PVSC)*.

[50] Hiroi, H., Sakai, N., Muraoka, S., Katou, T., & Sugimoto, H. (2012). Development of High Efficiency $Cu_2ZnSnS_4$ Submodule with Cd-Free Buffer Layer. *38th IEEE Photovoltaic Specialists Conference (PVSC)*.

[51] Sugimoto, H., Hiroi, H., Sakai, N., Muraoka, S., & Katou, T. (2012). Over 8% Efficiency $Cu_2ZnSnS_4$ Submodules with Ultra-Thin Absorber. *38th IEEE Photovoltaic Specialists Conference (PVSC)*.

[52] Salomé, P. M. P., Malaquias, J., Fernandes, P., Ferreira, M., Leitao, J., Cunha, A., et al. (2011). The influence of hydrogen in the incorporation of Zn during the growth of $Cu_2ZnSnS_4$ thin films. *Solar Energy Mater Solar Cells*, 95(12), 3482-9.

[53] Shin, S. W., Pawar, S., Park, C., Yun, J., Moon, J., Kim, J., et al. (2011). Studies on $Cu_2ZnSnS_4$ (CZTS) absorber layer using different stacking orders in precursor thin films. *Solar Energy Mater Solar Cells*, 95(12), 3202-6.

[54] Chalapathy, R. B. V., Jung, G. S., & Ahn, B. T. (2011). Fabrication of $Cu_2ZnSnS_4$ films by sulfurization of Cu/ZnSn/Cu precursor layers in sulfur atmosphere for solar cells. *Solar Energy Mater Solar Cells*, 95(12), 3216-21.

[55] Aksu, S., Pethe, S., Kleiman-Shwarsctein, A., Kundu, S., & Pinarbasi, M. (2012). Recent Advances in Electroplating Based CIGS Solar Cell Fabrication. *38th IEEE Photovoltaic Specialists Conference (PVSC)*.

[56] Scragg, J. J., Dale, P. J., Peter, L. M., Zoppi, G., & Forbes, I. (2008). New routes to sustainable photovoltaics: evaluation of $Cu_2ZnSnS_4$ as an alternative absorber material. *physica status solidi (b)*, 245, 1772-8.

[57] Scragg, J. J., Berg, D. M., & Dale, P. J. (2010 ). A 3.2% efficient Kesterite device from electrodeposited stacked elemental layers. *J Electroanal Chem*, 646, 52-9.

[58] Ennaoui, A. (2009). $Cu_2ZnSnS_4$ thin film solar cells from electroplated precursors: Novel low-cost perspective. *Thin Solid Films*, 517, 2511.

[59] Araki, H., Kubo, Y., Jimbo, K., Maw, W., Katagiri, H., Yamazaki, M., et al. (2009). Preparation of $Cu_2ZnSnS_4$ thin films by sulfurization of co-electroplated Cu-Zn-Sn precursors. *physica status solidi (c)*, 6, 1266-8.

[60] Li, J., Wei, T., Liu, M., Jiang, W., & Zhu, G. C. (2012). The $Cu_2ZnSnSe_4$ thin films solar cells synthesized by electrodeposition route. *Appl Surf Sci*, 258, 6261-5.

[61] Mali, S. S., Shinde, P. S., Betty, C. A., Bhosale, P. N., Oh, Y. W., & Patil, P. S. (2012). Synthesis and characterization of $Cu_2ZnSnS_4$ thin films by SILAR method. *Journal of Physics and Chemistry of Solids*, 73, 735-40.

[62] Mooney, J. J. B. (1982). Spray Pyrolysis Processing. *Annual review of materials science*, 12, 81-101.

[63] Prabhakar, T., & Jampana, N. (2011). Effect of sodium diffusion on the structural and electrical properties of $Cu_2ZnSnS_4$ thin films. *Solar Energy Mater Solar Cells*, 95, 1001-4.

[64] Rajeshmon, V. G., Kartha, C. S., Vijayakumar, K. P., Sanjeeviraja, C., Abe, T., & Kashiwaba, Y. (2011). Role of precursor solution in controlling the opto-electronic properties of spray pyrolysed $Cu_2ZnSnS_4$ thin films. *Solar Energy*, 85, 249-55.

[65] Tanaka, K., Moritake, N., & Uchiki, H. (2007). Preparation of thin films by sulfurizing sol-gel deposited precursors. *Solar Energy Mater Solar Cells*, 91, 1199-201.

[66] Zhou, Z., Wang, Y., Xu, D., & Zhang, Y. (2010). Fabrication of $Cu_2ZnSnS_4$ screen printed layers for solar cells. *Solar Energy Mater Solar Cells*, 94, 2042-5.

[67] Chory, C., Zutz, F., Witt, F., Borchert, H., & Parisi, J. (2010). Synthesis and characterization of $Cu_2ZnSnS_4$ . *physica status solidi (c)*, 7, 1486-8.

[68] Guo, Q., Ford, G. M., Yang, W., Hages, C. J., Hillhouse, H. W., & Agrawal, R. (2012). Enhancing the performance of CZTSSe solar cells with Ge alloying. *Solar Energy Mater Solar Cells*, 105, 132-6.

[69] Guo, Q., Cao, Y., Caspar, J., Farneth, W., Ionkin, A., Johnson, L., et al. (2012). A Simple Solution-based Route to High-Efficiency CZTSSe Thin-film Solar Cells. *38th IEEE Photovoltaic Specialists Conference (PVSC)*.

[70] Kumar, B., Vasekar, P. S., Pethe, S., Dhere, N. G., & Galymzhan, T. (2009). ZnxCd1-xS as a heterojunction partner for CuIn1-xGaxS2 thin film solar cells. *Thin Solid Films*, 517, 2295-9.

[71] Shen, G., Chen, P., Bando, Y., Golberg, D., & Zhou, C. (2008). Single-Crystalline and Twinned $Zn_3P_2$ Nanowires: Synthesis, Characterization, and Electronic Properties. *The Journal of Physical Chemistry C*, 112, 16405-10.

[72] Kakishita, K., Aihara, K., & Suda, T. (1994). $Zn_3P_2$ photovoltaic film growth for $Zn_3P_2$/ ZnSe solar cell. *Solar Energy Mater Solar Cells*, 35, 333-40.

[73] Misiewicz, J., Bryja, L., Jezierski, K., Szatkowski, J., Mirowska, N., Gumienny, Z., et al. (1994). $Zn_3P_2$ new material for optoelectronic devices. *Microelectron J*, 25, 23-28.

[74] Lousa, A., Bertrán, E., Varela, M., & Morenza, J. L. (1985). Deposition of $Zn_3P_2$ thin films by coevaporation. *Solar Energy Materials*, 12, 51-6.

[75] Sathyamoorthy, R., Sharmila, C., Natarajan, K., & Velumani, S. Influence of annealing on structural and optical properties of $Zn_3P_2$ thin films. *Mater Charact*, 58, 745-9.

[76] Murali, K. R., & Rao, D. R. (1981). Optical band gap of [alpha]- $Zn_3P_2$ . *Thin Solid Films*, 86, 283-6.

[77] Long, J. (1983). The Growth of $Zn_3P_2$ by Metalorganic Chemical Vapor Deposition. *J Electrochem Soc*, 130, 725-8.

[78] Bhushan, M. M., & Catalano, A. (1981). Polycrystalline $Zn_3P_2$ Schottky barrier solar cells. *Appl Phys Lett*, 38, 39-41.

[79] Kakishita, K. (1994). Zinc phosphide epitaxial growth by photo-MOCVD. *Appl Surf Sci*, 79, 281.

[80] Catalano, A. (1980). Defect dominated conductivity in $Zn_3P_2$ . *The Journal of physics and chemistry of solids*, 41, 635.

[81] Casey, M. S., Fahrenbruch, A. L., & Bube, R. H. (1987). Properties of zinc-phosphide junctions and interfaces. *Journal of Applied Physics*, 61, 2941-6.

[82] Bhushan, M., Turner, J. A., & Parkinson, B. A. (1986). Photoelectrochemical Investigation of $Zn_3P_2$ . *J Electrochem Soc*, 133, 536-9.

[83] Bhushan, M. M. (1982). Schottky solar cells on thin polycrystalline $Zn_3P_2$ films. *Appl Phys Lett*, 40, 51.

[84] Wyeth, N. C., & Catalano, A. (1979). Spectral response measurements of minority-carrier diffusion length in $Zn_3P_2$ . *Journal of Applied Physics*, 50, 1403-7.

[85] Ginting, M. M., & Leslie, J. (1989). Preparation and electrical properties of heterojunctions of ZnO on $Zn_3P_2$ and CdTe. *Can J Phys*, 67, 448-55.

[86] Suda, T., Suzuki, M., & Kurita, S. (1983). Polycrystalline $Zn_3P_2$ Indium-Tin Oxide Solar Cells. *Jpn J Appl Phys*, 22, L656-8.

[87] Catalano, A. A. (1980). Evidence of p/n homojunction formation in $Zn_3P_2$ . *Appl Phys Lett*, 37, 567.

[88] Bhushan, M. M. (1982). Mg diffused zinc phosphide n/p junctions. *J Appl Phys*, 53, 514.

[89] Misiewicz, J., Szatkowski, J., Mirowska, N., Jezierski, K., & Gumienny, Z. (1986). Solar energy conversion in metal- $Zn_3P_2$ contacts. *Acta Physica Polonica*, A69, 1131-5.

[90] Catalano, A. A. (1980). The growth of large $Zn_3P_2$ crystals by vapor transport. *J Cryst Growth*, 49, 681-6.

[91] Wang, Faa-Ching, Bube, R. H., Feigelson, R. S., & Route, R. K. (1981). Single crystal growth of $Zn_3P_2$ . *J Cryst Growth*, 55, 268-72.

[92] Deiss, J. J. L. (1988). Amorphous thin films of $Zn_3P_2$ . *Phys Scripta*, 37, 587-92.

[93] Murali, K. R. (1987). Properties of $Zn_3P_2$ films grown by close space evaporation. Materials science & engineering. *A, Structural materials : properties, microstructure and processing*, 92, 193.

[94] Soliman, M., Kashyout, A. B., Osman, M., & El-Gamal, M. (2005). Electrochemical deposition of $Zn_3P_2$ thin film semiconductors on tin oxide substrates. *Renewable Energy*, 30, 1819-29.

[95] Nose, Y. Y. (2012). Electrochemical Deposition of $Zn_3P_2$ Thin Film Semiconductors Based on Potential-pH Diagram of the Zn-P-$H_2O$ System. *J Electrochem Soc*, 159, D181.

[96] Vasekar, P. S., Adusumilli, S. P., Vanhart, D., Dhakal, T., & Desu, S. (2012). Development of zinc phosphide as a p-type absorber. *Photovoltaic Specialists Conference (PVSC), 38th IEEE*.

[97] Adusumilli, S. P., Vasekar, P. S., Vanhart, D., Dhakal, T., Westgate, C. R., & Desu, S. (2011). Development of zinc phosphide as an absorber using chemical reflux technique. *MRS conference proceedings, Spring*.

[98] Kimball, G. M., Müller, A., Lewis, N. S., & Atwater, H. A. (2009). Photoluminescence-based measurements of the energy gap and diffusion length of $Zn_3P_2$. *Appl Phys Lett*, 95, 112103.

[99] Kimball, G. M., Lewis, N. S., & Atwater, H. A. (2010). Mg doping and alloying in $Zn_3P_2$ heterojunction solar cells. *Photovoltaic Specialists Conference (PVSC), 35th IEEE*, 001039-43.

[100] Wilcoxon, J. P., Newcomer, P. P., & Samara, G. A. (1996). Strong quantum confinement effects in semiconductors: $FeS_2$ nanoclusters. *Solid State Commun*, 98, 581-5.

[101] Altermatt, P. P., Kiesewetter, T., Ellmer, K., & Tributsch, H. (2002). Specifying targets of future research in photovoltaic devices containing pyrite ($FeS_2$) by numerical modelling. *Solar Energy Mater Solar Cells*, 71, 181-95.

[102] Chatzitheodorou, G. G. (1986). Thin photoactive $FeS_2$ (pyrite) films. *Mater Res Bull*, 21, 1481-7.

[103] Ennaoui, A. A. (1985). Photoactive Synthetic Polycrystalline Pyrite ($FeS_2$). *J Electrochem Soc*, 132, 1579.

[104] Ennaoui, A. (1993). Iron disulfide for solar energy conversion. *Solar Energy Mater Solar Cells*, 29, 289.

[105] Ennaoui, A., Fiechter, S., Smestad, G., & Tributsch, H. (1990). Preparation of iron disulphide and its use for solar energy conversion. *Proceedings of 1st World Renewable Energy Congress*, 458-64.

[106] Dahman, H. H. (1996). Iron pyrite films prepared by sulfur vapor transport. *Thin Solid Films*, 280, 56-60.

[107] Fiechter, S. (1992). The microstructure and stoichiometry of pyrite. *J Mater Res*, 7.

[108] Wadia, C. C. (2009). Surfactant-Assisted Hydrothermal Synthesis of Single phase Pyrite FeS Nanocrystals. *Chemistry of materials*, 21, 2568-70.

[109] Kunst, M., & Tributsch, H. (1984). Surface microwave conductivity spectroscopy. A new experimental tool. *Chemical Physics Letters*, 105, 123-6.

[110] Smestad, G., Da Silva, A., Tributsch, H., Fiechter, S., Kunst, M., Meziani, N., et al. (1989). Formation of semiconducting iron pyrite by spray pyrolysis. *Solar Energy Materials*, 18, 299-313.

[111] Wu, R., Zheng, Y. F., Zhang, X. G., Sun, Y. F., Xu, J. B., & Jian, J. K. (2004). Hydrothermal synthesis and crystal structure of pyrite. *J Cryst Growth*, 266, 523-7.

[112] Joo, J. J. (2003). Generalized and Facile Synthesis of Semiconducting Metal Sulfide Nanocrystals. *J Am Chem Soc*, 125, 11100-5.

[113] Lin, Y. Y. Y. (2009). Extended red light harvesting in a poly(P3-hexylthiophene)/iron disulfide nanocrystal hybrid solar cell. *Nanotechnology*, 20, 405207.

[114] Bi, Y. Y. (2011). Air Stable, Photosensitive, Phase Pure Iron Pyrite Nanocrystal Thin Films for Photovoltaic Application. *Nano letters*, 11, 4953-7.

[115] Puthussery, J. J. (2010). Colloidal Iron Pyrite (FeS ) Nanocrystal Inks for Thin-Film Photovoltaics. *J Am Chem Soc*, 101222110759049.

[116] Ganta, L., Dhakal, T., Rajendran, S., & Westgate, C. R. (2012). Synthesis of $FeS_2$ nanocrystals for ink-based solar cells. *MRS Online Proceedings Library*, 1447.

[117] Dhakal, T., Ganta, L., Vanhart, D., & Westgate, C. R. (2012). Annealing of $FeS_2$ Nanocrystal Thin Film. *38th IEEE Photovoltaic Specialists Conference (PVSC)*.

[118] Smestad, G., Ennaoui, A., Fiechter, S., Tributsch, H., Hofmann, W. K., Birkholz, M., et al. (1990). Photoactive thin film semiconducting iron pyrite prepared by sulfurization of iron oxides. *Solar Energy Materials*, 20, 149-65.

[119] Adusumilli, S. P., & Dhakal, T. (2012). Synthesis of Iron Pyrite Film through Low Temperature Atmospheric Pressure Chemical Vapor Deposition. *MRS conference proceedings, Spring*.

[120] Alonso-Vante, N., Chatzitheodorou, G., Fiechter, S., Mgoduka, N., Poulios, I., & Tributsch, H. (1988). Interfacial behavior of hydrogen-treated sulphur deficient pyrite ($FeS_{2-x}$). *Solar Energy Materials*, 18, 9-21.

[121] Schieck, R. R. (1990). Electrical properties of natural and synthetic pyrite ($FeS_2$) crystals. *J Mater Res*, 5, 1567-72.

[122] Hall, R. R. N. (1952). Electron-Hole Recombination in Germanium. *Physical review*, 87, 387.

[123] Shockley, W. W. (1952). Statistics of the Recombinations of Holes and Electrons. *Physical review*, 87, 835-42.

[124] Oertel, J., Ellmer, K., Bohne, W., Röhrich, J., & Tributsch, H. (1999). Growth of n-type polycrystalline pyrite ($FeS_2$) films by metalorganic chemical vapour deposition and their electrical characterization. *J Cryst Growth*, 198-199, Part 2, 1205-10.

[125] Ellmer, K., & Tributsch, H. (2000). Iron disulphide (pyrite) as photovoltaic material: problems and opportunities. *Proceedings of the 12th Workshop on Quantum Solar Energy Conversion*.

[126] Alharbi, F., Bass, J., Salhi, A., Alyamani, A., Kim, H., & Miller, R. (2011). Abundant non-toxic materials for thin film solar cells: Alternative to conventional materials. *Renewable Energy*, 36(10), 2753-8.

[127] Ramakrishna Reddy, K. T., Purandhara Reddy, P., Datta, P. K., & Miles, R. W. (2002). Formation of polycrystalline SnS layers by a two-step process. *Thin Solid Films*, 403-404, 116-9.

[128] Devika, M., Reddy, N., & Gunasekhar, K. (2011). Structural, electrical, and optical properties of as-grown and heat treated ultra-thin SnS films. *Thin Solid Films*, 520(1), 628-32.

[129] Devika, M., Reddy, N., Ramesh, K., Gunasekhar, K., Gopal, E., & Reddy, K. T. R. (2006). Influence of annealing on physical properties of evaporated SnS films. *Semiconductor science and technology*, 21, 1125-31.

[130] Gunasekaran, M. M. (2007). Photovoltaic cells based on pulsed electrochemically deposited SnS and photochemically deposited CdS and $Cd_{1-x}Zn_xS$. *Solar Energy Mater Solar Cells*, 91, 774-8.

[131] Avellaneda, D., Nair, M. T. S., & Nair, P. K. (2009). Photovoltaic structures using chemically deposited tin sulfide thin films. *Thin Solid Films*, 517, 2500-2.

[132] Ramakrishna Reddy, K. T., Koteswara Reddy, N., & Miles, R. W. (2006). Photovoltaic properties of SnS based solar cells. *Solar Energy Mater Solar Cells*, 90, 3041-6.

[133] Li, L., Liu, X., Huang, J., Cao, M., Chen, S., Shen, Y., et al. (2012). Solution-based synthesis and characterization of $Cu_2FeSnS_4$ nanocrystals. *Mater Chem Phys*, 133, 688-91.

[134] Yan, C., Huang, C., Yang, J., Liu, F., Liu, J., Lai, Y., et al. (2012). Synthesis and characterizations of quaternary $Cu_2FeSnS_4$ nanocrystals. *Chem Commun*, 48, 2603-5.

[135] Fernandes, P. P. A. (2010). A study of ternary $Cu_2SnS_3$ and $Cu_3SnS_4$ thin films prepared by sulfurizing stacked metal precursors. *Journal of physics.D, Applied physics*, 43, 215403.

[136] Liu, G. G., Schulmeyer, T., Brötz, J., Klein, A., & Jaegermann, W. (2003). Interface properties and band alignment of $Cu_2S$/CdS thin film solar cells. *Thin Solid Films*, 431-432, 477-82.

[137] Bragagnolo, J. A., Barnett, A., Phillips, J., Hall, R., & Rothwarf, A. (1980). The design and fabrication of thin-film CdS/$Cu_2S$ cells of 9.15-percent conversion efficiency. *IEEE Trans Electron Devices*, 27, 645-51.

[138] Wu, Y. Y., Wadia, C., Ma, W., Sadtler, B., & Alivisatos, A. P. (2008). Synthesis and Photovoltaic Application of Copper(I) Sulfide Nanocrystals. *Nano letters*, 8, 2551-5.

Chapter 7

# Enhancing the Light Harvesting Capacity of the Photoanode Films in Dye-Sensitized Solar Cells

Xiang-Dong Gao, Xiao-Min Li and Xiao-Yan Gan

Additional information is available at the end of the chapter

http://dx.doi.org/10.5772/51633

## 1. Introduction

Dye-sensitized solar cell (DSC) has been receiving continuous academic and industrial attention as a potential low-cost, clean, and renewable energy source, since its inception in 1985 (Desilvestro et al., 1988; Regan et al., 1991; Gao et al., 2008; Hagfeldt et al., 2010; Yella et al., 2011). The DSC is the only photovoltaic device that uses molecules to absorb photons and converts them to electric charges without the need of intermolecular transport of electronic excitation. It is also the only photovoltaic device that separates two functions of light harvesting and charge-carrier transport, mimicking the photosynthesis found in green leaves. The primary photon-to-electron conversion process in DSC occurs at the oxide/dye/electrolyte interface, functioning at a molecular and nano scale. There exist many complicated optical, electrical, and chemical processes during the light-to-electric conversion process in DSC, including the light absorption of dye molecules (producing electrons and leaving the dyes in their oxidized states), the electron injection from dyes to the conduction band of semiconductor (e.g., $TiO_2$), the percolation of electrons through the mesoporous semiconductor network toward the bottom electrode, the recombination of photo-excited electrons in the porous electrode with either oxidized dyes or acceptors in the electrolyte, and the regeneration of dye molecules by iodides in the electrolyte etc. For an efficient DSC device, while above processes should be kept in a complicated and delicate balance, the high light-harvesting, the rapid electron transport, and the minimum electron-hole recombination are essential. In special, the light-harvesting efficiency of the photoanode is the most important and indispensable factor for the high-efficiency DSC, which is mainly related to the molar extinction coefficient of the sensitizer, the dye-loading capacity of the porous electrode, and the optical path of the incident light in the electrode.

At present, the record efficiency of DSC has reached 12.03% (Yella et al., 2011) after the first breakthrough of M. Grätzel in 1991 and through the continuous efforts of the scientists for more than 20 years. With an aim to further improve the conversion efficiency of DSC to 15% or higher, recently, intensive efforts have been directed to enhance the functions of the major components in DSC, focusing on mainly three aspects, i.e., the ordered nanoporous electrode, the novel organic or quantum-dot sensitizer, and the new redox electrolyte system (Hagfeldt et al., 2010; Tetreault et al., 2012). During this journey toward high-efficiency DSC, the light-harvesting capacity of the photoanode is expected to play a critical and indispensable role by spanning the mesoporous electrodes utilizing varied nano/meso materials and the sensitizers with high molar extinction coefficient or quantum dots, and by connecting the optical functions of the photoanode with its electrical response together.

There are mainly two components concerning the light-harvesting property of DSC, the dye and the mesoporous electrode which supports the sensitizer. While the development of the novel sensitizers with higher molar extinction coefficient and better response to near-infrared wavelength has been long studied since the first breakthrough of DSC in 1991 (Nazeeruddin et al., 2001; Grtäzel et al., 2009; Yum et al., 2011), the significance of the light scattering and/or reflection of the mesoporous electrode on the light-harvesting properties is only recognized in recent years. Accompanying the rapid advance of the ordered or hybrid photoanode materials, novel semiconductor nanostructures or new concepts are widely used to construct new type photoanodes, including the plenary optical waveguide nanowire enhancing the multiple internal reflections (Wei et al., 2010), the plasmonic core-shell metal-insulator nanoparticles enhancing the near-infrared absorption (Brown et al., 2011), the dual-function mesoporous $TiO_2$ structures increasing both the dye-loading and the optical scattering effects (Koo et al, 2008; Huang et al., 2010), and so on. In view of the wide coverage of the optical and photoelectrical nanostructures involved in these studies and their rapid progresses, it is great valuable to make a comprehensive and in-depth review on the current status of the light-harvesting capacities of the photoanode in DSC.

The chapter will start with a brief description of the basic concept of the light-harvesting efficiency (LHE), and then give a review on five typical branches representing the significant advances in this area, including

1. the mesoporous photoanodes with high surface area,
2. the hierarchically nanostructured photoanodes,
3. the dual-function scattering layer on the top of nanocrystalline (nc) electrode,
4. the plasmonic photoanodes, and
5. the photonic crystal photoanode and others.

The basic principles of these novel nanostructures/ methods enhancing the light-harvesting capacity of DSC, together with their mutual effects on the electrical and photoelectrochemical properties of the nanoporous electrode, will be discussed in detail. Based on the in-depth analysis of literature and the authors' experience, a perspective will be presented, shedding a light on the research road in near future.

http://dx.doi.org/10.5772/51633

## 2. The Light Harvesting Efficiency (LHE)

The typical DSC device is a sandwich type electrochemical cell, as seen from Figure 1, with the dye molecules absorbing the incident sunlight, and the framework of $TiO_2$ mesoporous electrode transporting the photo-excited electrons generated from dye molecules to the bottom electrode. Therefore, the semiconductor porous electrode, or the photoanode film, is the kernel component in DSC, undertaking two major functions: supporting dye molecules, and transporting photo-excited electrons. To harvest the sunlight as far as possible, the photoanode film has to possess a high internal surface area, to guarantee the massive uptake of dye molecules. The cell performance of DSC, that is, the solar-to-electric conversion efficiency, is determined by the short-circuit photocurrent ($J_{sc}$), open-circuit photovoltage ($V_{oc}$), and fill factor (*FF*) under a definite intensity of light such as the AM 1.5 solar spectrum. $J_{sc}$, the critical parameter affecting the power conversion efficiency (PCE) of DSC most, can be increased by raising the light-harvesting efficiency (LHE), which is defined by Equation 1,

$$\mathrm{LHE}\,(\lambda) = 1 - 10^{-\Gamma\sigma(\lambda)} \tag{1}$$

where Γ is the number of moles of sensitizer per square centimeter of projected surface area of the film, and σ is the absorption cross section in units of $cm^2$/mol obtained from the decadic extinction coefficient (units of $M^{-1}$ $cm^{-1}$) by multiplication with 1000 $cm^3$/L (Nazeeruddin et al., 1993). The LHE is directly determined by the surface concentration of the dyes in the film, and the molar extinction coefficient of dye. The LHE, together with the quantum yield of charge injection ($\varphi_{inj}$) and the efficiency of collecting the injected charge at the back contact ($\eta_c$), determines the incident monochromatic photon-to-current conversion efficiency (IPCE), defined as the number of electrons generated by light in the external circuit divided by the number of incident photons (Equation 2).

$$\mathrm{IPCE}\,(\lambda) = \mathrm{LHE}\,(\lambda)\varphi_{\mathrm{inj}}\eta_{\mathrm{c}} \tag{2}$$

Previous studies proved that $\varphi_{inj}$ is a wavelength independent parameter, and almost all of photons absorbed by the sensitizer are quantitatively converted to the conduction band electrons (Nazeeruddin et al., 1993). Meanwhile, the time-resolved laser photolysis experiments showed that the injected electrons can percolate without significant loss through the network of interconnected particles present in the nc-$TiO_2$ film, and the back reaction is relatively slow, indicating that the majority of the injected charges is able to reach the back contact, and the influence of $\eta_c$ on IPCE is minor (Regan et al., 1990). So the wavelength-depedent LHE has predominant effects on the IPCE and the PCE of DSC.

In essence, the LHE of DSC is the electrical response of the photovoltaic device to the solar spectrum projected on earth. It is predominantly related to there factors, the wavelength dependent light-absorbing capacity of the dye molecules, the quantity of the dye molecules adsorbed on the porous electrode, and the optical path of the incident light traveled in the

electrode (determining the collision numbers of the light with the dye molecules). As a wavelength-dependent parameter, the LHE is usually evaluated by the IPCE spectrum. Figure 2 gives the IPCE spectrum of a typical DSC with nc-$TiO_2$ electrode, N719 dye and $I_2/I_3^-$ electrolyte system, and its comparison with the standard solar irradiation spectrum (ASTM G173). To characterize the response of DSC to the solar irradiation, the IPCE spectrum can be divided into four wavelength zones, i.e., the strong absorption zone between 500-550 nm, two moderate absorption zones between 400-500 nm and 550-700 nm, and the weak absorption zone above 700 nm. While the broadband or near-infrared absorption sensitizers are devised to harvest the sun light beyond 700 nm, the modulation of the optical path of the incident light by introducing scattering or reflection is mostly used to improve the light harvesting in two moderate absorption zones. From the viewpoint of the photoanode film (i.e., the porous electrode), there are several measures to improve the LHE, including

1. increasing the internal surface area of the electrode, which has the potential to improve the dye-loading capacity of the photoanode over a specific film thickness and area;
2. increasing the optical path of the incident light in the electrode, by introducing scattering centers in the bulk film, by introducing the scattering layer on the top of nanocrystalline electrode, and by constructing hierarchical structures possessing strong light scattering effects; and
3. enhancing the absorption of dye molecules by introducing plasmonic metal-semiconductor structures.

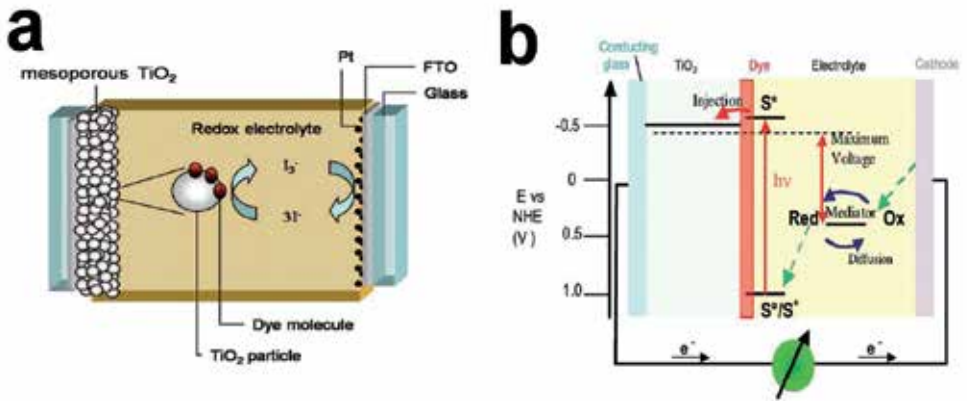


**Figure 1.** a) Schematic illustration of dye-sensitized solar cells (Hagfeldt, et al., 2010). b) Working principle of a typical DSC employing an iodide/triiodide-based redox electrolyte and N719 as a sensitizer (Grätzel, 2009).

In current days, the nanocrystallite electrode is confronting the maximum photocurrent theoretically achievable with the Ru-based sensitizers (e.g. N719 dye), and the quest for the novel nanostructured photoanode has becoming prosperous (Zhang et al., 2011; Tetreault et al., 2012). Among numerous innovative nanostructured photoanodes, a considerable amount of studies are directed to improve the LHE of the photoanode, in view of the moderate surface

http://dx.doi.org/10.5772/51633

area, the moderate electron transporting property of nc-$TiO_2$ electrode, and the intrinsically low-surface-area nature of the traditional submicron scattering layer. In the following sections, we will introduce five typical research branches in this area, to provide readers with a comprehensive and in-depth overview on the development of the LHE studies in DSC.

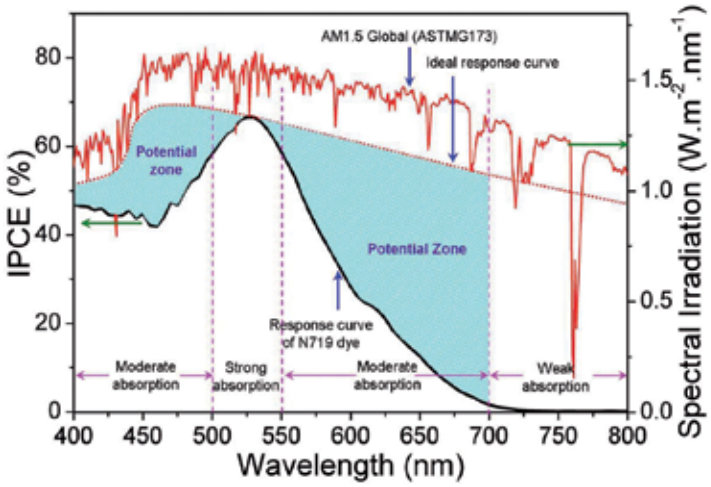


**Figure 2.** The light-harvesting capacity of N719 sensitized nc-$TiO_2$ photoanode in DSC and its comparison with AM 1.5 Global solar spectrum.

## 3. Mesoporous photoanodes with high surface area

It is essential for the photoanode in DSC to possess a high internal surface area, to adsorb sensitizer as much as possible. Typically, the hydrothermal nc-$TiO_2$ with the particle size of 15-30 nm is used to fabricate the porous electrode, which usually exhibits the BET surface area of 50-100 $m^2/g$. While these nanocrystallite photoanodes perform fairly well and occupy the highland of DSC with the best efficiency, their moderate dye-loading capacity motivate researchers to seek other materials with higher surface area. In fact, there are several materials which do possess much higher surface area than nc-$TiO_2$ electrode, such as the mesoporous materials, aerogel, and metal-organic framework (MOF), whose surface area usually range from several hundred to three thousand $m^2/g$. It is greatly intriguing to construct photoanodes using these high-surface-area materials, which is expected to remarkably improve the dye-loading capacity of the photoanode and the PCE of DSC in case a good charge transport can be maintained in these mesoporous structures. Up to date, mesoporous $TiO_2$ in the form of powder, sphere, bead, or film, and aerogel have been used to synthesize the photoanode, which usually exhibited the surface area of 100-1100 $m^2/g$. Here we present some typical mesoporous photoanodes prepared by the high-surface-area $TiO_2$ mesostructures and $TiO_2$ aerogel.

Mesoporous powders possessing a large volume of mesopores and irregular micron/ submicron secondary particles are the mostly-used materials in constructing the mesoporous photoanodes. The template methods are the common strategy to prepare these mesoporous powders. For example, T. K. Yun et al. prepared two different mesoporous $TiO_2$ powders, using a soft template of tri-block copolymer and a hard template of mesoporous ZnO/ $Zn(OH)_2$-composite, respectively (Yun et al., 2011). Both mesoporous $TiO_2$ possessed the same high surface area (BET ~210 $m^2/g$) but with different pore sizes of 6.8 (for soft template) and 3.0 nm (for hard template). Different photovoltaic performances were observed. While the photoanode using the mesoporous $TiO_2$ having larger pores showed the PCE of 6.71%, higher than P25 $TiO_2$ nanopowders based photoanode ($\eta$= 5.62%), only half the performance (3.05%) was observed for the mesoporous $TiO_2$ having small pores. The work indicated that, a suitable selection of the pore sizes was important for mesoporous materials used in DSC, and a too small pore size would inhibit the diffusion of dye molecules through the pores, thus greatly reducing the uptake of the dye molecules.

Beside the template method, the external fields such as the microwave irradiation can also be very useful in synthesizing mesoporous $TiO_2$ powders. C. H. Huang et al. reported the rapid synthesis of mesoporous $TiO_2$ via a microwave-assisted hydrothermal route using water-soluble titanium citrate complexes as the precursor, and obtained $TiO_2$ powders showed the surface area of 217–323 $m^2/g$, and the pore diameter of 5.8–6.9 nm (Huang et al., 2011). The photoanode based on this mesoporous $TiO_2$ exhibited the highest conversion efficiency of 7.1% (active area: 0.25 $cm^2$). Also, the cell exhibited good long-term stability, and the PCE of a 1 $cm^2$ device decreased merely from 4.8% to 4.3% after being stored for more than 490 h.

For most photoanodes using the high-surface-area mesoporous materials, it is required to prepare the mesoporous powders first, and the final electrode is obtained via the doctor-blade method using the mesoporous paste prepared from the mesoporous powders. This is a relatively complicated process. In contrast, W. Chen et al. developed a facile one-step preparation of crack-free thick ordered mesoporous $TiO_2$ films, via the combination of ''doctor blade'' technique and the evaporation induced self-assembly method (Chen et al., 2007). By employing the as-synthesized mesoporous film (7 μm in thickness) as the photoanode, a PCE of 6.53% was obtained at 30 $mW/cm^2$ light intensity, illustrating the potential of this simple strategy in constructing powerful DSC devices.

While the mesoporous materials of pure $TiO_2$ give a promising potential to improve the LHE, the introduction of other oxides (e.g., $Al_2O_3$, $SiO_2$) in the mesoporous structure of $TiO_2$ opens an alternative route to enhance the LHE of DSC. As an example, J. Y. Kim et al. prepared highly ordered mesoporous $Al_2O_3/TiO_2$ via a sol-gel reaction and evaporation-induced self-assembly route using Pluronic P123 as the structure-modifying reagent (Kim et al., 2011). Obtained mesoporous powders possessed an average pore size of 6.33-6.58 nm, and BET surface area of 181-212 $m^2/g$, and the content of $Al_2O_3$ had significant effects on the BET surface area. The thin $Al_2O_3$ layer was located mostly on the surface of mesopore (as seen in X-ray photoelectron spectroscopy (XPS) spectra in Figure 4c), blocking the charge recombination during the photon-to-electron conversion process. The photoanode based on the mesoporous $Al_2O_3/TiO_2$ (1 mol % $Al_2O_3$) exhibited ~10% efficiency improvement com-

http://dx.doi.org/10.5772/51633

pared to the pure mesoporous $TiO_2$ electrode ($\eta$ increasing from 5.88% to 6.50%). Though the authors didn't compare their results with traditional nanocrystalline counterpart, the much higher surface area of the mesoporous electrode than P25 $TiO_2$ may possibly lead to higher dye-loading quantity, and corresponding higher light-harvesting capacity. Also, the introduction of $Al_2O_3$ barrier layer in mesoporous $TiO_2$ illustrated a viable and versatile route to further improve the functions of the mesoporous photoanodes.

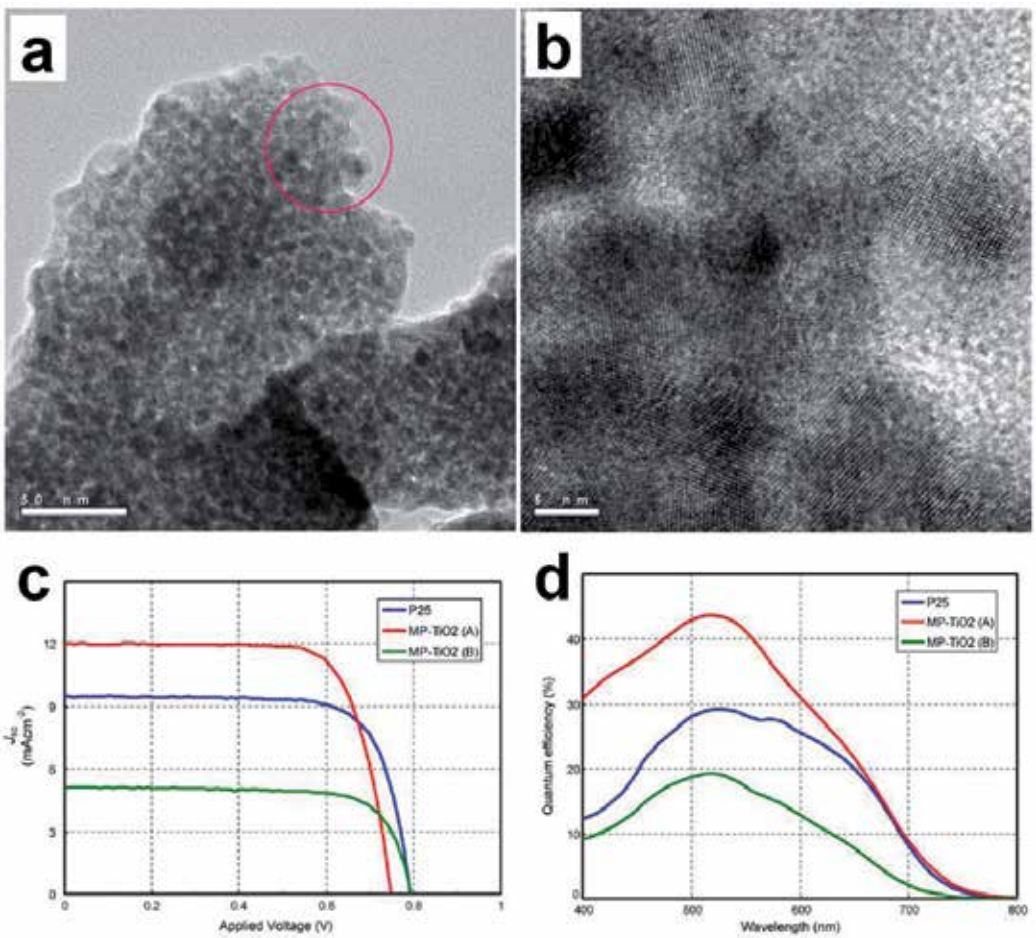


**Figure 3.** TEM image of mesoporous $TiO_2$ with a) low and b) high magnifications. c) *J*-V curves and d) IPCE spectra of DSCs prepared from P25 and mesoporous $TiO_2$ with $TiCl_4$ post-treatment. (Yun et al., 2011).

Though above mesoporous powders with irregular secondary particles are promising in improving the dye-loading capacity of the photoanode, it is usually difficult for them to obtain high quality electrodes with good transparency, due to the poor workability of the paste produced from the irregular micron/submicron particles. Therefore, it is intriguing to prepare mesoporous $TiO_2$ with regular secondary particles, e.g., $TiO_2$ mesoporous spheres.

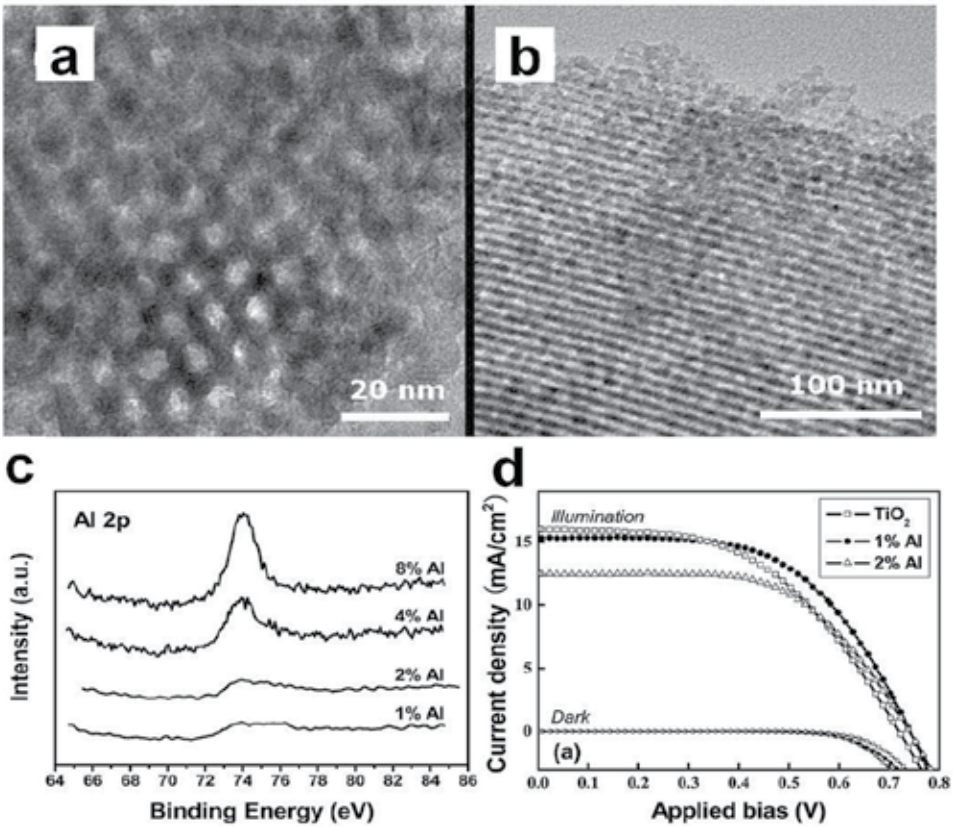


**Figure 4.** a-b) TEM images of mesoporous $TiO_2$, illustrating the ordered mesopores. c) XPS spectra of mesoporous $Al_2O_3$/$TiO_2$ with various levels of Al calcined at 525°C. d) *J*-V curves in the illuminated and dark states of pure mesoporous $TiO_2$, 1 and 2 mol% $Al_2O_3$/$TiO_2$ (light intensity: 100 mW/cm$^2$; AM 1.5 filter; illumination area: 0.25 cm$^2$). (Kim et al., 2010).

D. Chen et al. did a good job on this area, and synthesized uniform, crystalline, and mesoporous $TiO_2$ beads in size of ~800 nm through a combination of sol-gel and solvothermal processes, which exhibited the surface area of 108.0 m$^2$/g and tunable pore sizes (pore diameter: 14.0 ~ 22.6 nm) (Chen et al., 2009). Due to the submicrometer-sized particle diameter and the high specific surface area, the mesoporous $TiO_2$ beads enhanced the LHE without sacrificing the accessible surface for dye loading, thereby increasing the PCE compared to P25 nanoparticles. The photoanode based on these mesoporous $TiO_2$ beads exhibited an overall light conversion efficiency of 7.20% ($V_{oc}$ = 0.777 V, $J_{sc}$ = 12.79 mA/cm$^2$, *FF* = 0.72), significantly higher than that derived from standard Degussa P25 $TiO_2$ electrode with similar thickness (5.66%).

In a further study, the group selected Ru(II)-based dye C101 and C106 to match with the mesoporous $TiO_2$ beads, and realized an overall PCE of greater than 10% ($\eta$=10.7%) using a single screen-printed $TiO_2$ layer cell construction (without an additional scattering layer). Hence, a delicate modulation of the micron/submicron size/ shape of mesoporous materials, and a careful selection of the dye to match the dye's photon-absorption characteristics with

http://dx.doi.org/10.5772/51633

the light scattering properties of the mesoporous materials, are important to improve the LHE and PCE of DSC (Sauvage et al., 2010).

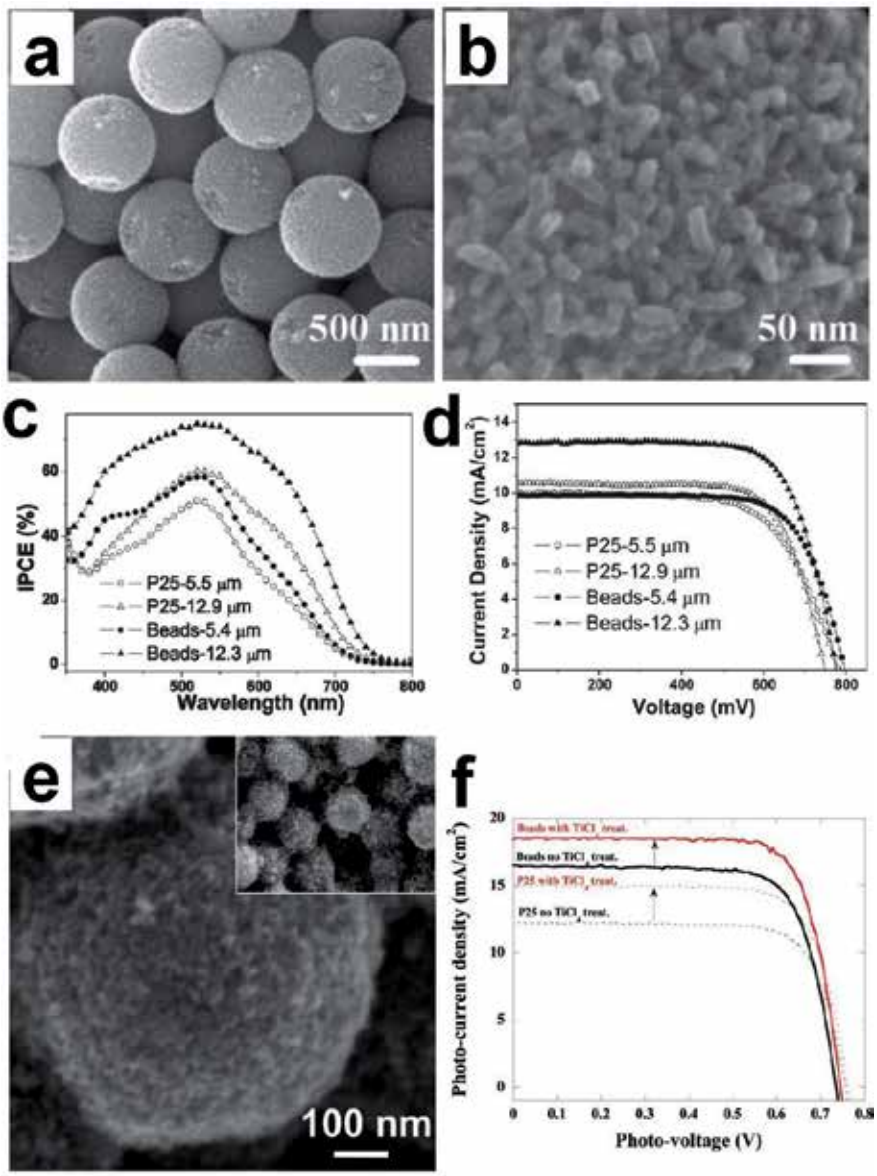


**Figure 5.** a-b) SEM images of the calcined mesoporous $TiO_2$ beads obtained after a solvothermal process with no ammonia for a) and 1.0 mL ammonia for b). c) IPCE curves and d) *J*-*V* curves of the $TiO_2$ electrodes prepared from P25 NPs and mesoporous $TiO_2$ beads with two film thicknesses. (Chen et al., 2009) e) SEM image of the screen-printed film composed of $TiO_2$ porous beads; f) *J*-*V* curves recorded at 100 mW/cm$^2$ of the 12 um thick film composed of P25 particles (dashed) or $TiO_2$ beads (solid) sensitized with the C101 dye without (in black color) and with $TiCl_4$ post-treatment (in red color). (Sauvage et al., 2010).

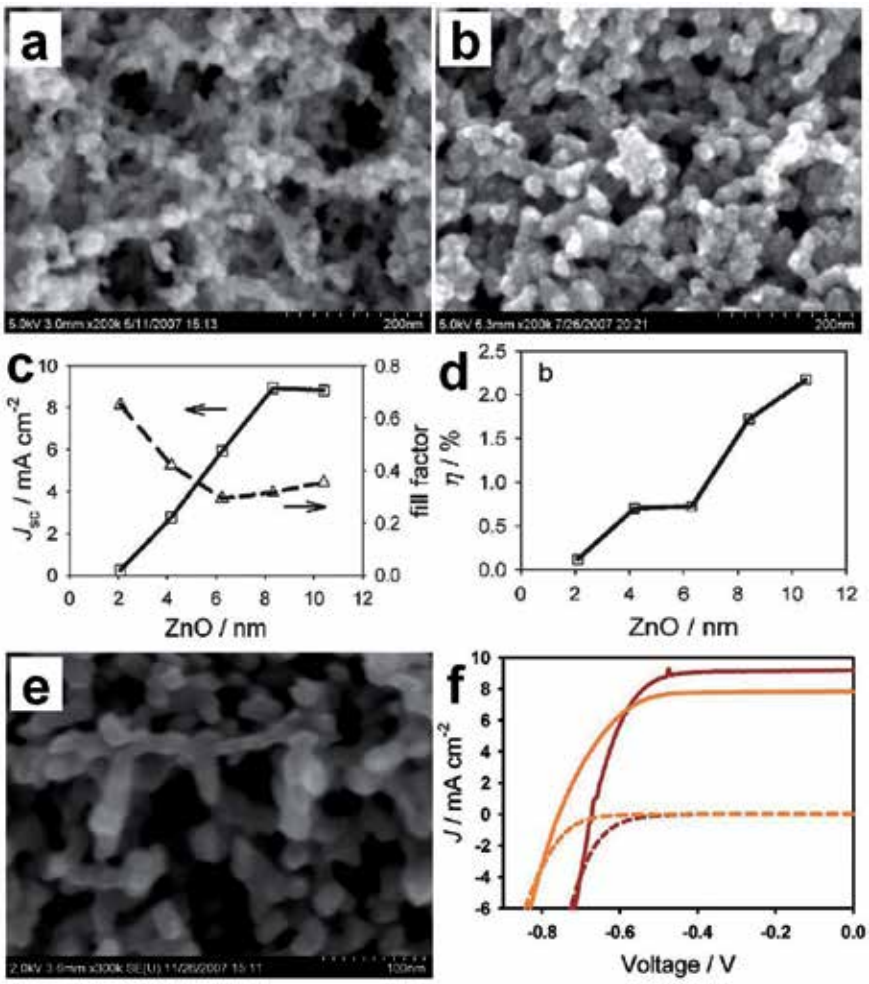


**Figure 6.** a-b) SEM images of aerogel frameworks coated with a) 4.4 and b) 8.4 nm ZnO. c-d) Plots of c) $J_{sc}$, *FF* and d) efficiency ($\eta$) as a function of thickness of ZnO deposited on aerogel frameworks. (Hamann et al., 2008a) e) SEM image of a ~30 μm thick aerogel film coated with 9.6 nm $TiO_2$. f) *J*-V curves for aerogel electrodes coated with 12 nm $TiO_2$ (Red) and $TiO_2$ nanoparticle (orange) in the dark (dasked lines) and under AM 1.5 illumination (solid). (Hamann et al., 2008b).

Among various mesoporous materials, aerogel is distinguished from others by its high surface area (100-1600 $m^2/g$) and light weight (0.003-0.5 $g/cm^3$) (Hüsing et al., 1998). The application of aerogel in the photoanode of DSC was pioneered by J. J. Pietron and J. T. Hamann in 2007-2008. The former work prepared the aerogel photoanode by the direct doctor-blading of the crushed $TiO_2$ aerogel particles, and demonstrated the IPCE of ~85% in the 500-600 nm range and ~52% at 700 nm for N719 sensitized photoanode (Pietron et al., 2007). Hamann et al. prepared $SiO_2$ aerogel film first via the supercritical drying process, and then coated ZnO or $TiO_2$ thin layer with controllable thickness via the atomic layer deposition (ALD) method (Hamann et al., 2008a, 2008b). They realized the aerogel based DSC devices with the efficiency of 2.4% (for ZnO cell) and 4.3% (for $TiO_2$ cell). Al-

http://dx.doi.org/10.5772/51633

so, the authors investigated systematically the effects of ZnO thickness on $SiO_2$ aerogel template on the photovoltaic performance, and found a nearly linear relationship between the key photovoltaic index and the thickness of ZnO layer (Figure 6c,d), with the optimal ZnO thickness of 10.5 nm. These results indicated that, on one hand, the aerogel film in combination of ALD or other physical or chemical deposition processes was a powerful candidate to prepare mesoporous photoanode with controllable microstructures. On the other, the use of the dangerous supercritical drying process in the synthesis of aerogel, together with the expensive and complicated ALD process involved in the preparation of $ZnO/TiO_2$ layer, limited the popularization of this method greatly. There were very few studies on the aerogel photoanodes in recent five years.

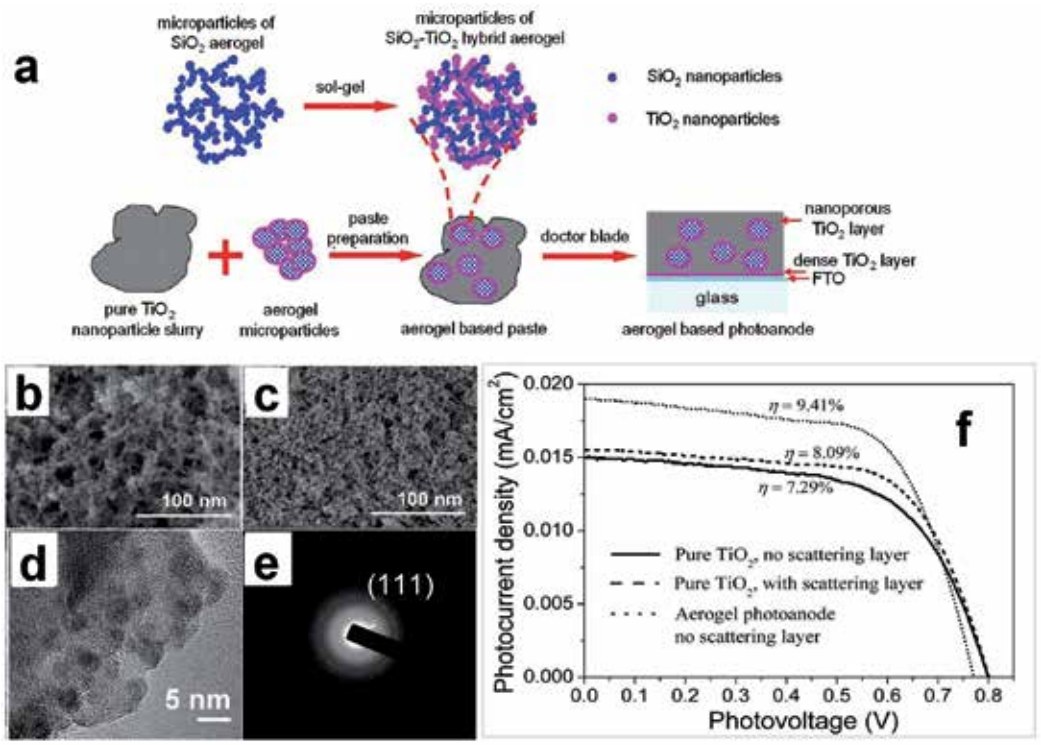


**Figure 7.** a) Schematic of the preparation of $SiO_2$-$TiO_2$ hybrid aerogel and aerogel based photoanode. SEM image of b) $SiO_2$ and c) $SiO_2$-$TiO_2$ hybrid aerogel (packing density: 0.037 and 0.125 g/cm$^3$). d) TEM image and e) SAED pattern of $SiO_2$-$TiO_2$ hybrid aerogel. f) *J*-V curves of DSC based on pure $TiO_2$ photoanode with and without scattering layer and aerogel modified photoanode. (Gao et al., 2012).

To crack above problems, X. D. Gao et al. developed a low-cost sol-gel and ambient-drying route to fabricate $SiO_2$-$TiO_2$ hybrid aerogels, which possessed a very high surface area of 500-1170 m$^2$/g, and incorporated them into nc-$TiO_2$ electrode, obtaining the aerogel hybrid photoanodes (Gao, et al., 2012). These hybrid photoanodes yielded significantly higher photocurrent densities than nc-$TiO_2$ photoanodes due to the increased dye-loading

capacity and the enhanced visible scattering effect, showing the highest efficiency of 9.41% at optimal condition, 16% higher than the $TiCl_4$-treated $TiO_2$ photoanode modified with a conventional scattering layer. This work indicated that, the hybrid photoanodes integrating both the high-surface-area mesoporous materials and nc-$TiO_2$ represented a powerful and viable route toward high-efficiency DSCs.

In brief, current studies on the mesoporous photoanodes built up by the high-surface-area mesoporous materials have unambiguously proved that, the application of high-surface-area powders/beads/aerogel in the photoanode can effectively increase the dye-loaing capacity and the light scattering of the electrode, and correspondingly improve the LHE of DSC in most cases. The preparation of mesoporous materials with regular and uniform size/shape in micron/submicron scale, and their integration with nc-$TiO_2$ or other nanostructures, seem feasible to achieve high conversion efficiency. A remaining problem in these high-surface-area mesoporous materials is the inferior electron-transporting property, intrinsically originating from their lower particle coordination number than the common nc-$TiO_2$ porous electrode. A possible solution may be the development of hybrid electrodes by incorporating metal, carbon nanotube, or graphene etc into the mesoporous structures. A mesoporous material possessing both high surface area and good conductivity is by all means necessary for highly efficient DSCs.

## 4. Hierarchical photoanodes

Hierarchical nanostructures, those with different morphology at different length scale and usurally characterized by the high surface area, are intresting candidates for efficienct photoanodes in DSC. This special class of nanostrcutures is spurred at the low surface area and consequently the low PCE of nanowire based photoandes, and have receivd wide-spread and intensive studies in recent years. Hierarchical ZnO and $TiO_2$ in the form of grass, forest, popborn ball, and tube etc. have been developed, and a wide range of chemical and physical methods have been used to prepare the hierarchical structures, including the hydrothermal synthesis, sol-gel, chemical bath deposition, pulsed laser deposition, photolithography, and so on. Due to the huge literature in this field, here we merely present some representive results in recent three years.

ZnO nanowire array may be the piorneer in the nanostructured photoanode since the outstanding work of M. Law et al. (Law et al., 2005). However, the PCE of nanowire based photoanode was low (mostly 1%-3% for a long time) mainly due to its low surface area. So the development of hierarchical ZnO and their application in DSC are wide-spread recently. As an example, Xu et al. reported a two-step synthesis process to produce hierarchical ZnO nanoarchitectures (Figure 8a,b), in which ZnO nanosheet arrays were first prepared by the pyrolysis of the precursor $Zn_5(OH)_8Cl_2$ electrodeposited on conductive glass substrates, and then dense ZnO nanowires were grown on the surfaces of the primary ZnO nanosheets by the chemical bath deposition method (Xu et al., 2010). Due to the better dye loading through the increased internal surface area and the higher light scattering behavior through extend-

http://dx.doi.org/10.5772/51633

ing the optical path length within the photoanode, the DSC based on the hierarchical ZnO nanowire-nanosheet architectures showed a PCE of 4.8%, nearly twice as high as that of DSC constructed using a photoanode of bare ZnO nanosheet array.

Apart from these hierarchical structures with relatively simple structures, several groups developed ZnO or $TiO_2$ forest (Figure 8c,d), more complicated hierarchical structures. F. Sauvage et al. prepared the hierarchical assemblies of nanocrystalline particles of anatase $TiO_2$ (Sauvage et al., 2010), by a pulsed laser deposition method, via the fine modulation of the plasma expansion dynamics by means of a reactive atmosphere during the ablation process. In combination with the high molar extinction coefficient heteroleptic C101 dye, the authors achieved 3.1% power conversion efficiency for 2 um thick films and 5.0% for films 7 um thick, demonstrating the great potential of the physical vapor deposition method in growing hierarchical nanostructured photoanodes with high conversion efficiency.

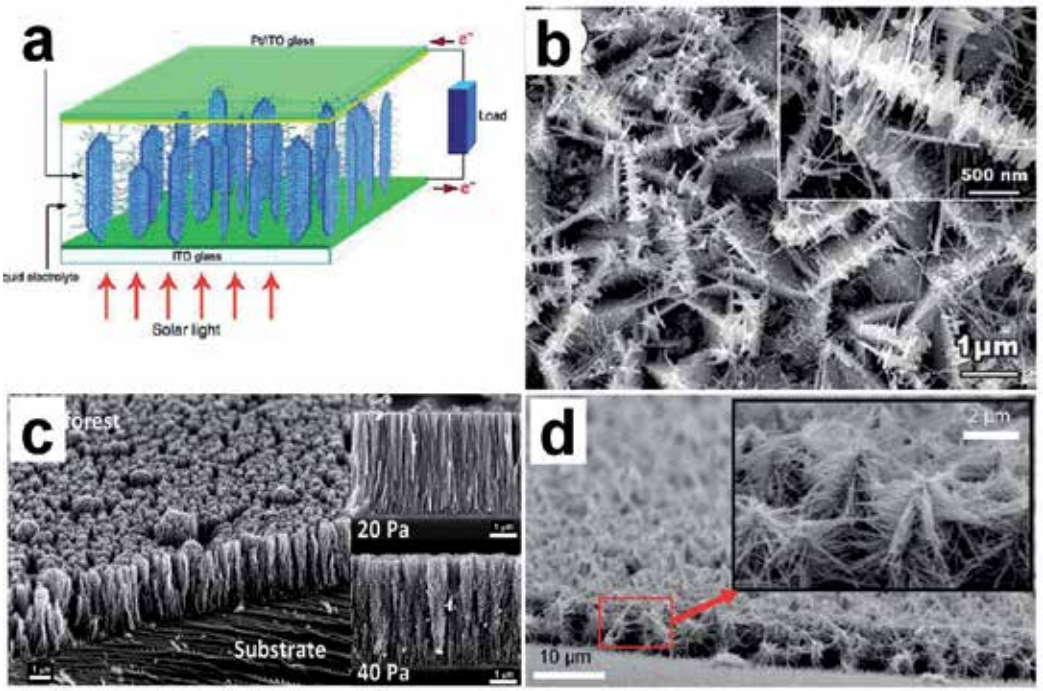


**Figure 8.** a) Schematic of ZnO hierarchical nanostructures derived from ZnO nanosheet arrays and b) top-view SEM image of ZnO nanowire-nanosheet architectures obtained by aqueous chemical growth after 4 h. The inset of b) corresponds to the magnified image. (Xu et al., 2010) c) $TiO_2$ forest-like films grown by pulsed laser deposition: (left) overview of a film deposited at 40 Pa; (right) cross sections of films deposited at 20 and 40 Pa. (Sauvage et al., 2010) d) SEM image of ZnO nanowire nanoforest (tilted view). (Ko et al., 2011).

Meanwhile, using the traditional hydrothermal method integrating with the simple selective hierarchical growth sequence, S. Ko et al. demonstrated ZnO nanoforest photoanode with high density, long branched treelike multigeneration hierarchical crystalline ZnO nanowires (Figure 8d) (Ko et al., 2011). The DSC exhibited almost 5 times higher than the efficiency of

DSCs constructed by upstanding ZnO nanowires (2.63% v.s. 0.45%). The enhanced surface area for higher dye loading and light harvesting, and the reduced charge recombination by providing direct conduction pathways along the crystalline ZnO "nanotree" multi generation branches, were responsible for the efficiency improvement.

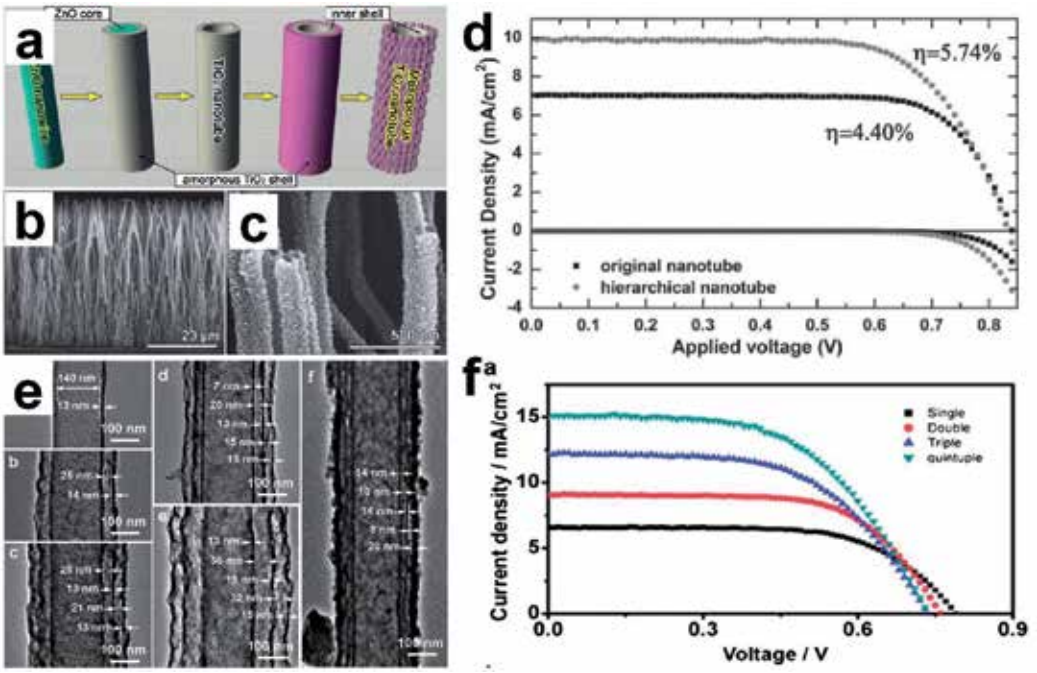


**Figure 9.** a) Schematic of the preparation of hierarchical $TiO_2$ NTA: beginning with a ZnO nanowire and followed by multiple procedures of $TiO_2$ coating, ZnO core removal, subsequent $TiO_2$ coating, and hierarchical derivation to a double-shell architecture. b) cross-section SEM image of $TiO_2$ nanotube array with 41 um thickness and c) magnified SEM image of hierarchical $TiO_2$ nanotube. d) *J–V* curves of the nanotube DSCs prepared with 20-μm thick nanotube arrays with the original and hierarchical structure. (Zhuge et al., 2011) e) TEM images of triple-shelled $TiO_2$ NTs with different structural features. f) J–V curves of DSCs based on multi-sheel $TiO_2$ nanotube electrodes. (Qiu et al., 2012).

Nanotube array (NTA) is another type of hierarchical structures receiving great attention, which is developed on the basis of nanowire in view of its much higher surface area than nanowire. Currently, the hierarchical $TiO_2$ NTA has becoming an intensive research branch. Different from the traditional synthesis of $TiO_2$ nanotube via the anodic oxidation, F. Zhuge et al. reported the synthesis of vertically aligned $TiO_2$ NTAs (up to 40 um) on FTO by using ZnO nanowire array as the hard template, and demonstrated the hierarchical derivation for effective surface area enhancement in DSCs (Figure 9 a-c) (Zhuge et a., 2011). The distinctive double-shell structure of the nanotube provided both the high surface area and the high electron-transport path, showing the overall conversion efficiency of 5.7%, 50% higher than the original nanotube (Figure 8d). In a further work, the group updated their multi-shell fabrication technology via ZnO nanowire template, and successfully obtained coaxial multi-shelled $TiO_2$ NTA with controllable shell numbers and shell thickness (Figure 9e) (Qiu et al.,

http://dx.doi.org/10.5772/51633

2012). Exhibiting the BET surface area of 119-331 $m^2/g$, DSC devices based on these multi-shelled NTA exhibited the highest efficiency of 6.2%, higher than that based on the single-layer $TiO_2$ nanotube array (3.35%) at similar experimental parameters (Figure 9f).

Apart from the hierarchical nanowire/nanotube array, there are also a few studies which modulate the pores in the photoanode to realize the hierarchical structures. C. Y. Cho et al. reported an interesting method to generate hierarchical electrodes consisting of meso- and macroscale pores (Cho et al., 2011). Mesoscale colloidal particles and lithographically patterned macropores were used as the dual templates, with the colloidal particles assembled within the macropores. An infiltration of $TiO_2$ into the template and subsequent removal of the template produced hierarchical $TiO_2$ electrodes for DSC (Figure 10a). While the holographic lithography defined the macroporous networks, the colloidal crystal templates provided three-dimensionally organized mesoscale pores with a uniform size distribution (Figure 10 b-e). Owing to the strong scattering and the suppression of charge recombination in the hierarchical $TiO_2$ electrodes, the photovoltaic performance of the cell was comparable with nc-$TiO_2$ electrodes, showing a maximum efficiency of 5.0% with 50 nm pores and 6 μm thickness.

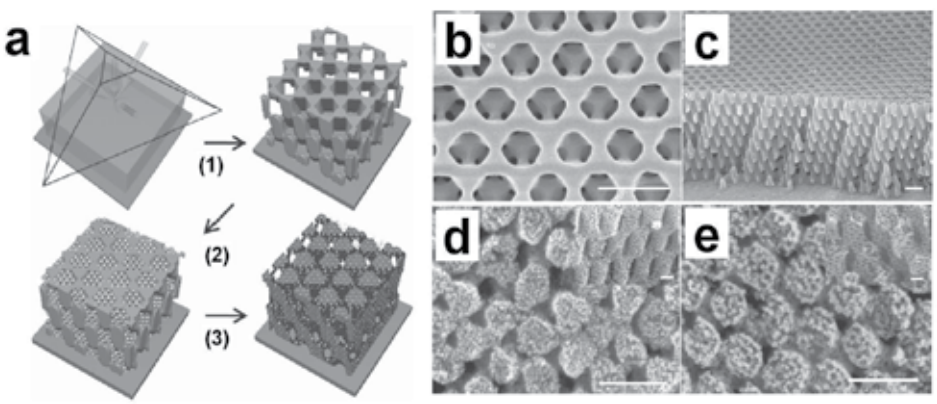


**Figure 10.** a) Schematic of the preparation of hierarchical $TiO_2$ electrode via double template method. (1) Formation of four-beam interference and the fabrication of the macroporous SU-8 structures. (2) Filling of the holographic patterns with mesoscale colloidal particles, and (3) Coating of precursors and removal of dual templates. SEM image of b) the surface and c) the cross-section of the macroporous SU-8 surface. SEM image of the hierarchical porous $TiO_2$ electrode from dual templates of SU-8 filled with colloidal particles with diameters of d) 60 nm and e) 110 nm. Scale bar: 1 μ m. (Cho et al., 2011).

In general, the hierarchical photoanodes, though possessing obviously higher internal surface area than the nanowire/nanotube/nanoplate counterparts and higher conductivity than nc-$TiO_2$ electrode, haven't show a predominant advantage over other materials up to now. The PCE of most photoanodes based on the hierarchical structures is still much lower than the state-of-the-art performance of nc-$TiO_2$ electrode. A possible vent for the hierarchical photoanodes may be the further increase of its internal surface area while maintaining its high electron-transporting nature. Also the combination of the hierarchical structures with the mesoporous material is a meaningful and feasible strategy.

## 5. Scattering layers on nc-$TiO_2$ electrode

The photoanode of DSC is traditionally composed of nc-$TiO_2$ film, which is basically transparent for visible light (Rayleigh scattering, mainly), resulting in a considerable part of light shone on the DSC transmitting through the $TiO_2$ layer without interacting with the sensitizer. To overcome this problem, scattering layers with different structures, including scattering centers and upper scattering layers, have been employed. The theoretical studies since 1998, and subsequent substantial experimental studies on scattering layers based on the submicron particles of $TiO_2$, $ZrO_2$, ZnO, nanowire, hierarchical structures, mesoporous spheres, photonic crystals, and upper-conversion materials, comprise a vivid picture about the research activities in this area. By briefing some important advances, we describe here some novel scattering layers developed in recent years.

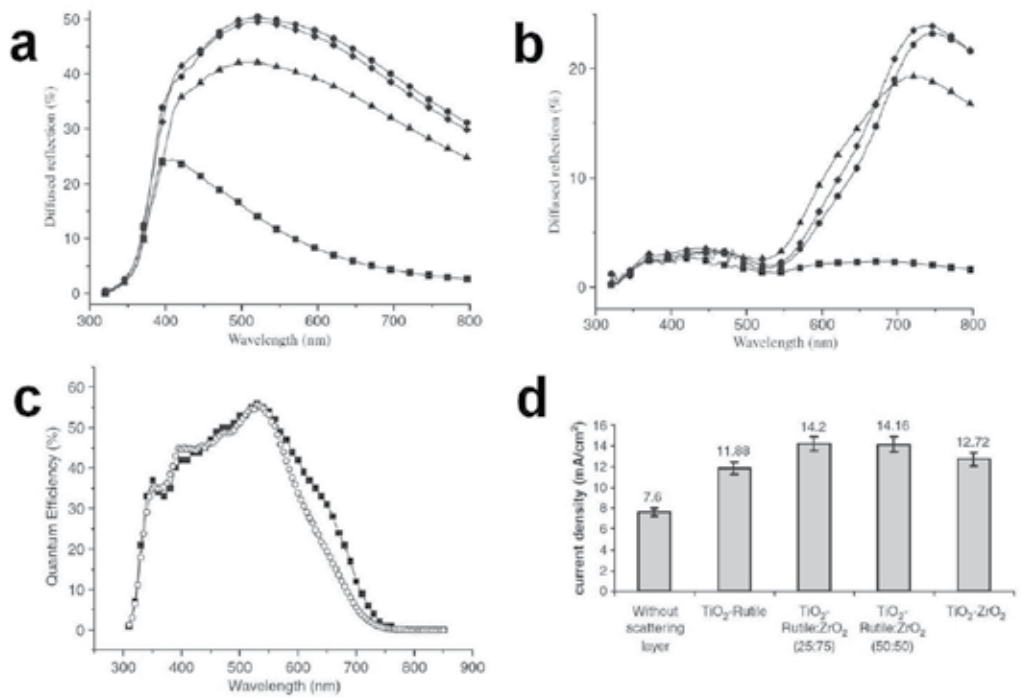


**Figure 11.** a-b) Diffused reflection spectra of a) undyed and b) sensitized $TiO_2$ layer without scattering layer (■), with the scattering layers of $TiO_2$-Rutile (▲), $ZrO_2$ (●) and 25:75 mixture of $TiO_2$-Rutile and $ZrO_2$ (◆). c) IPCE curves for devices with $TiO_2$ electrode with (■) and without (○) a scattering layer, the scattering layer being 25:75 mixture of $TiO_2$-Rutile and $ZrO_2$. d) Current densities obtained from devices with 4 mm thin layer of $TiO_2$ with and without scattering layers. The thickness of the scattering layers is ~6 um for all samples. (Hore et al., 2006).

In 1998, J. Ferber et al. started from Mie theory, and calculated the multiple scattering in $TiO_2$ electrodes using a numerical solution of the radiative transfer equation (Ferber et al., 1998). These calculations predicted that, a suitable mixture of small particles (20 nm), which

http://dx.doi.org/10.5772/51633

resulted in a large effective surface, and of large particles (250-300 nm), which were effective light scatterers, had the potential to enhance the solar absorption significantly.

In 2006, S. Hore et al. reported systematically the effects of $TiO_2/ZrO_2$ scattering layer on the photovoltaic performances (Hore et al., 2006). Different scattering layers composed of commercial $TiO_2$-Rutile (Bayer Germany) and $ZrO_2$ (TOSOH Corporation, Tokyo, Japan) with varied proportion were examined, providing an in-depth understanding on the functions of the top scattering layer. DSC device with an area of 2.5 $cm^2$ exhibited the PCE of 6.8% using an only 4 μm layer of $TiO_2$ electrode together with an optimal scattering layer, illustrating the potential of a suitable scattering layer on both the improvement of the efficiency and the reduction of the cost by using less sensitizer.

Very recently, F. E. Galvez et al. reported an integral optical and electrical theoretical analysis on the effects of the different design of the diffuse light scattering on the performance of DSCs (Galvez et al., 2012). Based on a Monte Carlo approach, they introduced the light harvesting efficiency and the electron generation function extracted from optical numerical calculations in a standard electron diffusion model, to obtain the steady-state characteristics of the different configurations considered (Figure 12). They proposed that the diffuse scattering layers acting as the back reflector provided the largest achievable light harvesting efficiencies, which determined an optimum overall performance, for electron diffusion lengths longer than the electrode thickness. When the electron diffusion length was shorter than the electrode thickness, the embedding of the diffuse scattering particles in the nanocrystalline paste yielded a better output even when the light harvesting was not optimal. These results can provide helpful guidance for us to design and prepare the scattering structure of the photoanode.

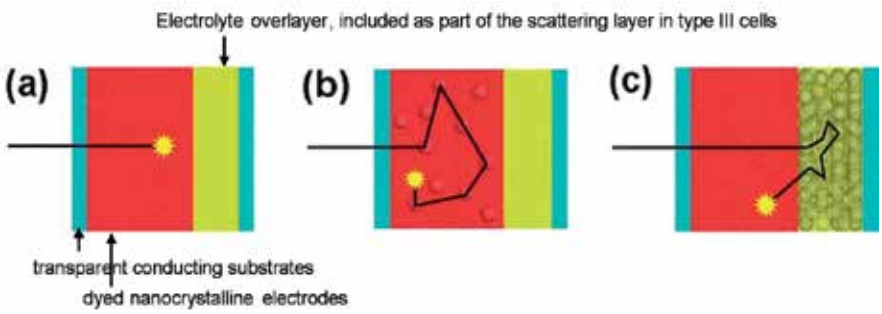


**Figure 12.** Simulated trajectories of a photon absorbed by a) standard semi-transparent cell, b) cell with an electrode embedding diffuse scattering particles, and c) cell made of a semi-transparent electrode coupled to a diffuse scattering layer, illustrating the different series of scattering events that yield longer optical paths and thus enhance the probability of absorption in each type of modified cell under consideration. (Galvez et al., 2012).

In recent years, with the rapid development of nanostructured photoanodes, various nanostructures have been used as the top scattering layer of nc-$TiO_2$ electrode or the novel photoanodes based on nanowire/ nanotube arrays etc. For example, K Fan et al. applied $TiO_2$ fusiform nanorods (diameter: 20-80 nm, length: 200-400 nm) as the scattering layer of P25-based electrode (Figure 13), and observed 66.5% improvement in the efficiency with lower

resistance and longer electron lifetimes as compared to the bare P25-based solar cell (Fan et al., 2011). The reduced charge recombination and the sufficient scattering effect of the nanorods in the film electrode were responsible for this improvement.

Koo H. J. et al. prepared nano-embossed hollow spherical (NeHS) $TiO_2$ particles and investigated their photovoltaic property in DSC as the bifunctional scattering layer (Koo et al., 2008). The walls of the obtained hollow spheres were composed of nanocrystalline anatase $TiO_2$ particles with mesoporous structure (Figure 14 a-c), which endowed them 5 times higher dye-loading capacity (N719 dye: up to $5.0\times10^{-5}$ mol/g) than that of the normally used 400 nm-diameter scattering particles with flat surfaces. The NeHS particles scattered incoming light effectively as confirmed by the reflectance spectroscopy (Figure 14 d,e). When the NeHS $TiO_2$ particles were used as the secondary scattering layer in DSC, a substantial improvement in the efficiency has been achieved, with the highest conversion efficiency of 10.34%. Huang F et al. used the submicrometer-sized mesoporous $TiO_2$ beads as the dual function scattering layer for the nanocrystalline electrode, and observed similar results, demonstrating that the dual-function scattering layer represented a powerful alternative for the traditional large-particle scattering layer for high-efficiency DSCs (Huang et al., 2010).

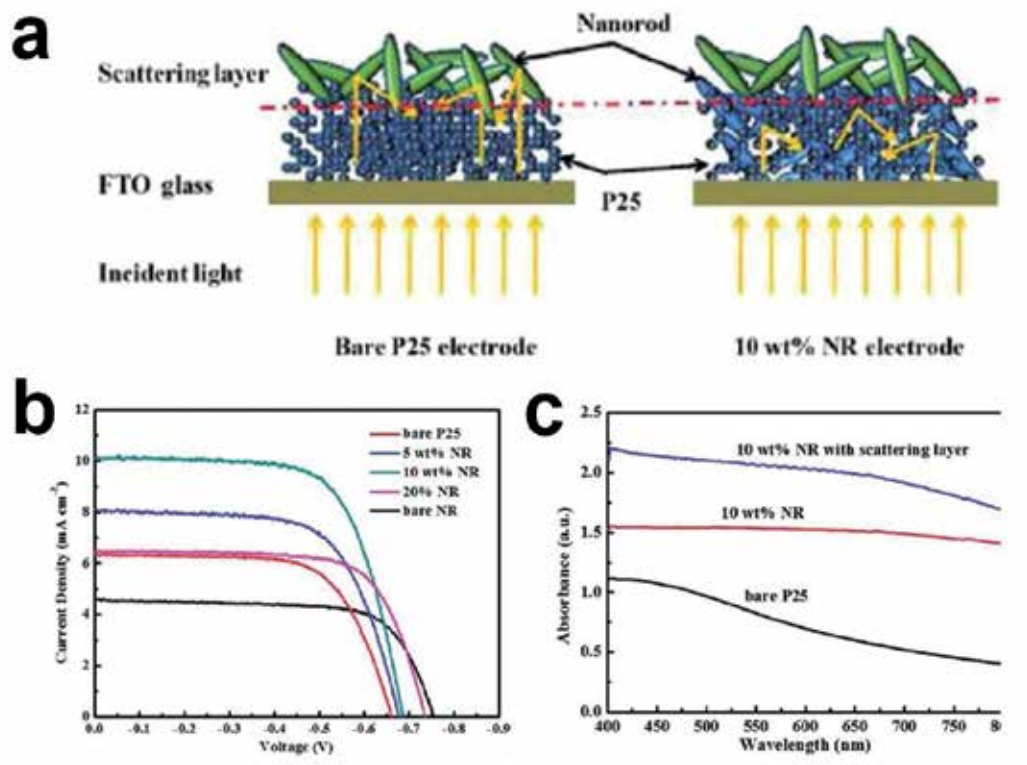


**Figure 13.** a) Schematic of the photoanodes with nanorod scattering layer. b) *J*-V curves of DSCs, and c) UV-VIS spectra of bare P25 film, and with different nanorod scattering layer. (Fan et al., 2011).

http://dx.doi.org/10.5772/51633

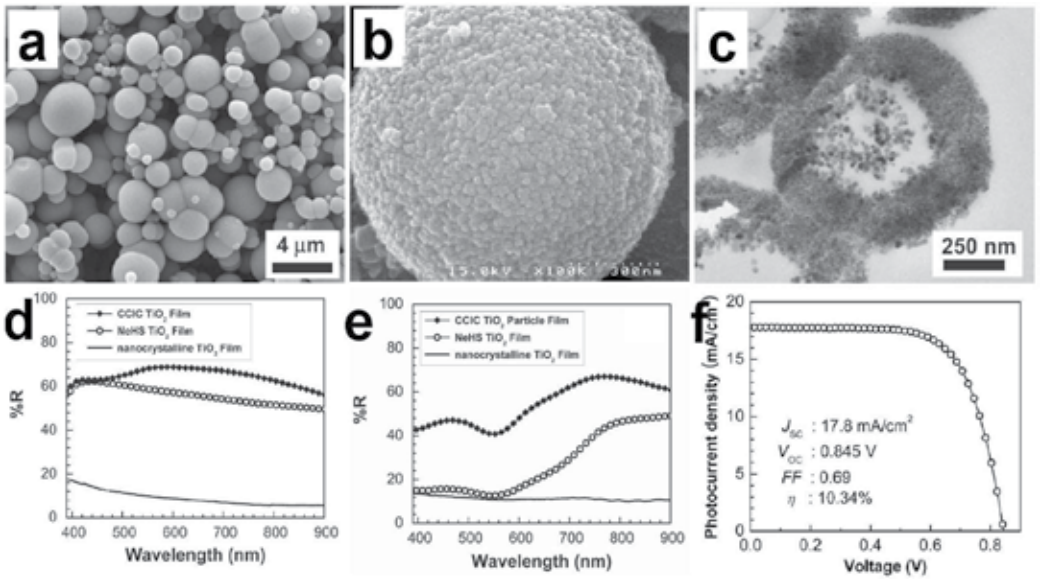


**Figure 14.** SEM image of a) the as-synthesized nano-emboded hollow sphere (NeHS) $TiO_2$ particles, b) high-magnification image for NeHS $TiO_2$ calcined at 450 °C. c) TEM image of a sliced NeHS $TiO_2$ particle. d-e) Diffused reflectance spectra of the nanocrystalline, CCIC, and NeHS $TiO_2$ particulate films d) without and e) with adsorbed N-719 dye. f) *J*-*V* curve of a DSC based on NeSH $TiO_2$ particulate film as an overlayer on a nanocrystalline $TiO_2$ film under AM 1.5G-one sun light intensity. (Koo et al., 2008).

Below we gave two examples which used the nanostructured scattering layer on the electrodes based on nanowire array or nanofibers. Shao et al. demonstrated an interesting double layer photoanode, with the bottom layer of $TiO_2$ nanorod array providing direct conduction pathway for photo-generated electrons, and the upper layer of micro-flowers built up by $TiO_2$ nanobelt, increasing the light harvesting ability as the scattering part (Shao et al., 2011). The cell based on this hierarchical anatase $TiO_2$ exhibited a conversion efficiency of 5.53%, superior than commercial $TiO_2$ (P25). The much higher optical reflectance of the hierarchical structures than the nanorod array and nanoparticle films (Figure 15) proved that this morphology was beneficial to the light-scattering capacity of the photoanode.

Yang et al. reported an innovative bilayer $TiO_2$ nanofiber photoanode, which combined both smaller (60 nm) and larger (100 nm) diameter $TiO_2$ nanofibers fabricated by electrospinning (Yang et al., 2011). The smaller diameter nanofiber (SNF) layer with a high surface-to-volume ratio was used to adsorb sufficiently dye molecules and directly transport electrons released from excited dyes. The bigger-diameter nanofi ber (BNF) layer worked as light scattering, adsorbed sufficient dye molecules for energy harvest, and provided higher pore volume in BNF to facilitate electrolyte diffusion for regenerating sensitized dye molecules in the photoanode. Therefore, this bilayer composite nanostructure photoanode offered excellent dye-loading, lightharvesting, and electron-transport properties. The PCE of DSC was improved from 7.14% for the single-layer to 8.40% for the bilayer of $TiO_2$ nanofiber photoanode, representing an increase of 17%.

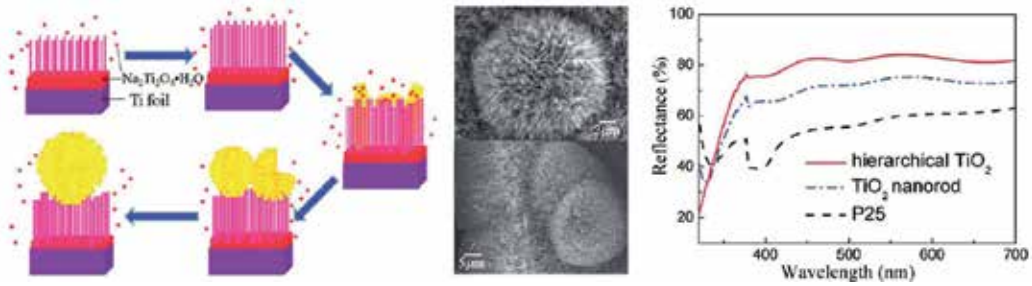


**Figure 15.** Schematic of $TiO_2$ nanorod array-micro flower hierarchical photoanode, SEM images of the photoanode at surface and cross section, and reflectance spectra of three kinds of $TiO_2$ photoanode on FTO substrate. (Shao et al., 2011).

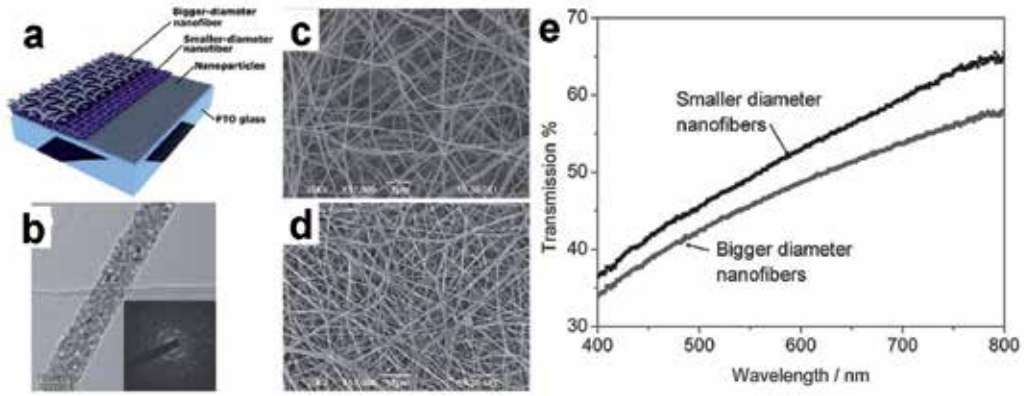


**Figure 16.** a) Schematic of the photoanode based on bi-layer electronspinned $TiO_2$ nanofibers. b) TEM image of smaller nanofiber and corresponding SAED pattern. c-d) SEM images of c) smaller and d) bigger nanofibers. e) UV-VIS transmission spectra of smaller diameter and bigger-diameter nanofiber photoanode with the same thickness (Yang et al., 2011).

As the conclusion of this section, we introduce a special scattering layer using up-converting materials. G. B. Shan et al. utilized the hexagonal nanoplatelets of β-$NaYF_4$:$Er^{3+}$/$Yb^{3+}$, a typical up-conversion phosphor owing to $Er^{3+}$ doping with $Yb^{3+}$ codopant assisting in the energy transfer process, as the second layer on nc-$TiO_2$ electrode (Figure 17) (Shan et al., 2011). Approximately 10% enhancements of photocurrent and overall DSC efficiency were achieved by the addition of the external layer, which exhibits two functions of light reflecting and near-infrared (NIR) light harvesting. Though the overall PCE of the cell and the improvement were moderate, the work opened a new opportunity to use some advanced functional materials to enhance the light-harvesting functions of DSC.

In summary, a wide variety of nanostructures including submicron particles, nanowires, nanofibers, mesoporous beads, spheres, nanopalletes etc have been used as the top scattering layer of DSC, which are proved to be very effective in improving the LHE and PCE of DSC, especially for the dual-function materials possessing both high surface area and large-

http://dx.doi.org/10.5772/51633

particle size. At the same time, the application of multiple function materials such as the up-converting nanopalletes in the scattering layer sheds a new light for further development.

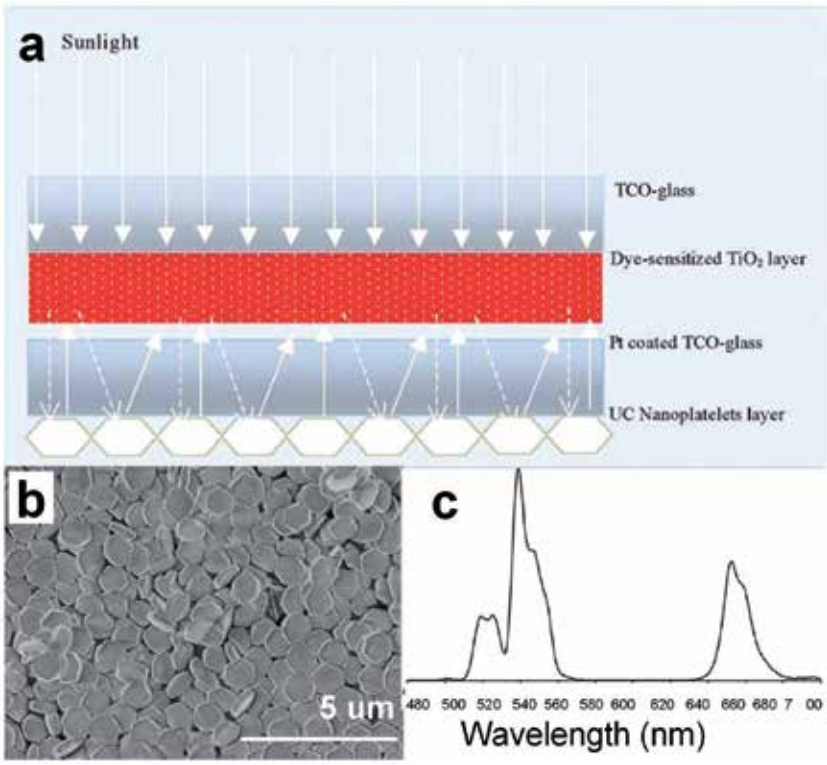


**Figure 17.** a) Schematic of the DSC device consisting of one internal $TiO_2$ transparent layer plus an external rear layer of β-$NaYF_4$:$Er^{3+}$/$Yb^{3+}$ nanoplatelets. b) SEM image and c) up-conversion fluorescence spectrum of the β-$NaYF_4$:$Er^{3+}$/$Yb^{3+}$ nanoplatelets. (Shan et al., 2011).

## 6. Plasmonic DSCs

Localized surface plasmon resonance (LSPR) behavior is an intriguing characteristic of metal nanoparticles (NPs), which is generated by the resonance between electric fields of electromagnetic waves and free electrons in metal NPs. The use of plasmonic effects has been proposed as a promising pathway to increase the light absorption in active layers of solar cells, and has been demonstrated on several thin-film solar-cell materials such as amorphous silicon, gallium arsenide, polymers, and DSC. Previous studies on the plasmonic solar cells with thin active layers have proved the beneficial functions of the LSPR on the photocurrent density through such following channels:

**1.** excitation of localized surface plasmon resonances of metallic NPs;

2. scattering of light by metallic NPs into dielectric-like waveguide modes of the solar cell;
3. coupling to propagating surface plasmon polariton (SPP) modes (Ding et al., 2011).

This has established a solid foundation for the rapid development of plasmonic DSCs in recent years.

The mostly-used metal NPs in the plasmonic DSCs are Ag and Au. While earlier studies have found the corrosion of metal particle in the electrolyte or the undesired introduction of electron-hole recombination by the plasmonic particles, it has become a common practice to protect the Ag or Au NPs by a thin $TiO_2$ or $SiO_2$ layer. Coupled with the standard thick nc-$TiO_2$ electrode, these plasmonic photoanodes performed fairly well compared with the control samples.

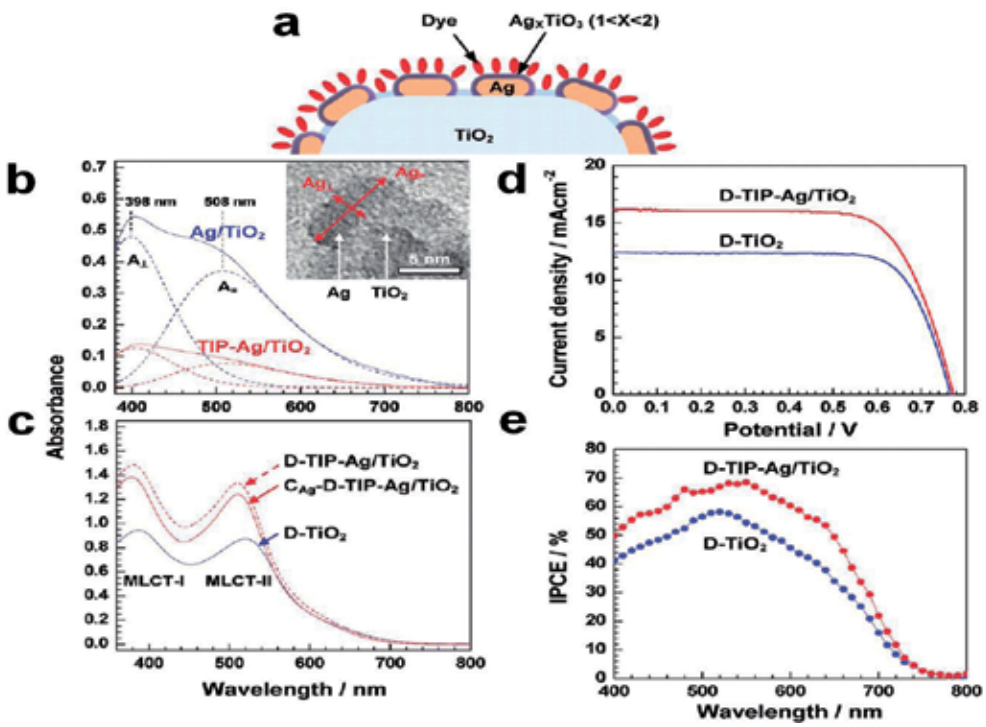


**Figure 18.** a) Schematic of Ag NPs deposited on $TiO_2$ NPs. b) Plasmonic absorption spectra of Ag NPs in Ag/$TiO_2$ (blue solid curve) and TIP-Ag/$TiO_2$ (red solid curve). Each spectrum is decomposed into two absorption peaks depending upon the geometry of Ag NPs. The inset shows a TEM image of the side view of Ag NP on $TiO_2$. $Ag_\perp$ and $Ag_=$ indicate the direction in the geometry of Ag NP. c) UV-VIS absorption spectra of D-$TiO_2$, D-TIP-Ag/$TiO_2$, and $C_{Ag}$-D-TIP-Ag/$TiO_2$. d) *J*-V and e) IPCE curves of D-$TiO_2$ and D-TIP-Ag/$TiO_2$ photoanodes. TIP-Ag: $TiO_2$ coated Ag NPs; D-$TiO_2$: N719 dye sensitized $TiO_2$ electrode; $C_{Ag}$-D-TIP-Ag/$TiO_2$: the extinction spectrum after removing the contributions of Ag NPs from the spectrum of D-TIP-Ag/$TiO_2$. (Jeong et al., 2011).

N. C. Jeong et al. provided a detail examination on the effects of the protection of Ag NPs on the LSPR and the cell performance (Jeong et al., 2011). They deposited Ag NPs on $TiO_2$ framework via the photo-reduction of $Ag^+$ from dissolved $AgNO_3$, and protected them by

http://dx.doi.org/10.5772/51633

a thin $TiO_2$ layer by refluxing Ag-$TiO_2$ electrode in isopropyl alcohol and subsequent annealing at 370°C. The electrode incorporating the protected silver NPs (Ag-$TiO_2$) showed enhanced extinction of a subsequently adsorbed dye (the ruthenium-containing molecule, N719), realizing an overall conversion efficiency of 8.9% and 25% improvement over the performance of otherwise identical solar cells incorporating silver NPs lacking protection (Figure 18). Roughly half the improvement could be traced to the increased dye loading by the photoanodes following silver incorporation, with the remaining improvement coming from the localized surface plasmon resonance (LSPR) enhancement of the effective absorption of N719 dye molecules.

J. Qi et al. coated $TiO_2$ thin layer (~2 nm) on Ag NPs and incorporated this Ag@$TiO_2$ nanostructures into the $TiO_2$ photoanode (Qi et al, 2011), which can easily transferred the carriers to surrounding $TiO_2$ NPs in contact with the shell, while providing a good protection for the metal NPs. By utilizing Ag@$TiO_2$ core-shell nanostructures, the optical absorption of dye molecules in solution and in thin film was enhanced by the strong localized electric field generated by LSPs (Figire 19 a,b). By incorporating Ag@$TiO_2$ NPs, the PCE of DSCs with very thin photoanodes (1.5 μm) was increased from 3.1%to 4.4%, and a small amount of Ag@$TiO_2$ NPs (0.1 wt%) improved efficiency from 7.8% to 9.0% while decreasing the photoanode thickness by 25% for improved electron collection (Figure 19c,d).

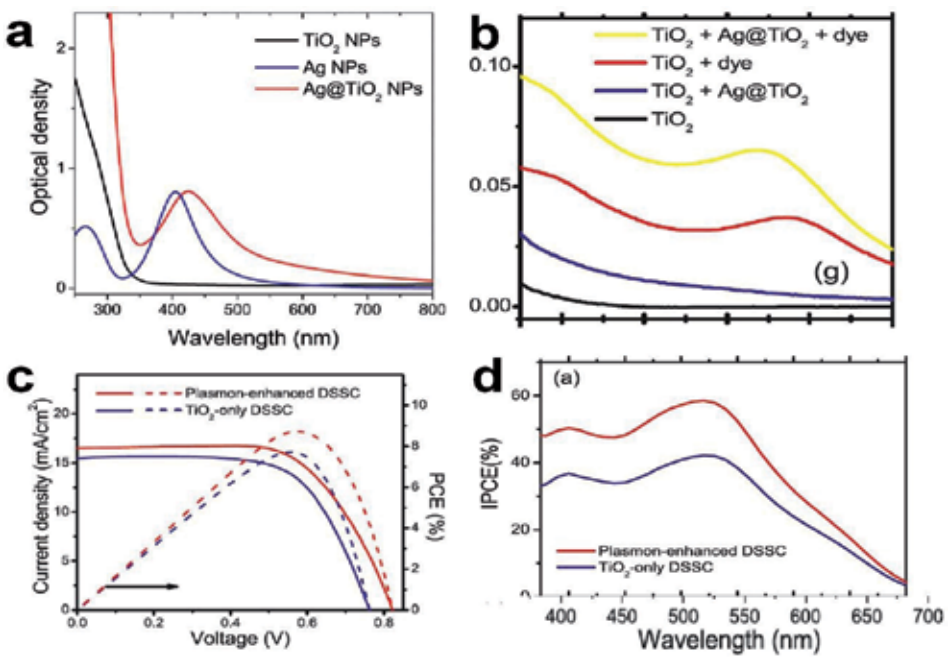


**Figure 19.** a) Absorption spectra of Ag NPs solutions stabilized by PVP, $TiO_2$ NPs, and Ag@$TiO_2$ NPs. b) Absorption spectra of Ag@$TiO_2$ NPs, dye, and their mixtures in $TiO_2$ film. c) *J*-*V* curves of plasmonic DSC (Ag/$TiO_2$ = 0.1 wt %, $\eta$ = 9.0%, *FF* = 67%, 15 μm) and $TiO_2$-only DSC ($\eta$ = 7.8%, *FF* = 66%, 20 μm). d) IPCE spectra of the DSCs with and without Ag@$TiO_2$. (Qi et al, 2011).

M. D. Brown et al. integrated Au NPs, which exhibited intense absorption due to the surface plasmon resonance in the visible band, into both the liquid and solid state DSCs (Brown et al., 2011). They successfully overcame the detrimental effects of the incorporating "bare" metal NPs into the bulk DSCs, by coating the Au NPs with a thin shell of silica, which could sustain the sintering process of the $TiO_2$ with negligible influence to the optical properties, resist the corrosion from the iodide/triiodie electrolyte, and enhance the photocurrent generation and solar cell performance as a result of light harvesting by the metal NPs. With a significant increase in the shortcircuit photocurren, the best solid state plasmonic cell sensitized with Z709 exhibited a PCE of 4.0% (Figure 20). The readily tunable optical properties of metallic NPs, through the use of structures such as nanobars, nanostars, or other complex shapes, provided extensive scope for further work to fully optimize the technology.

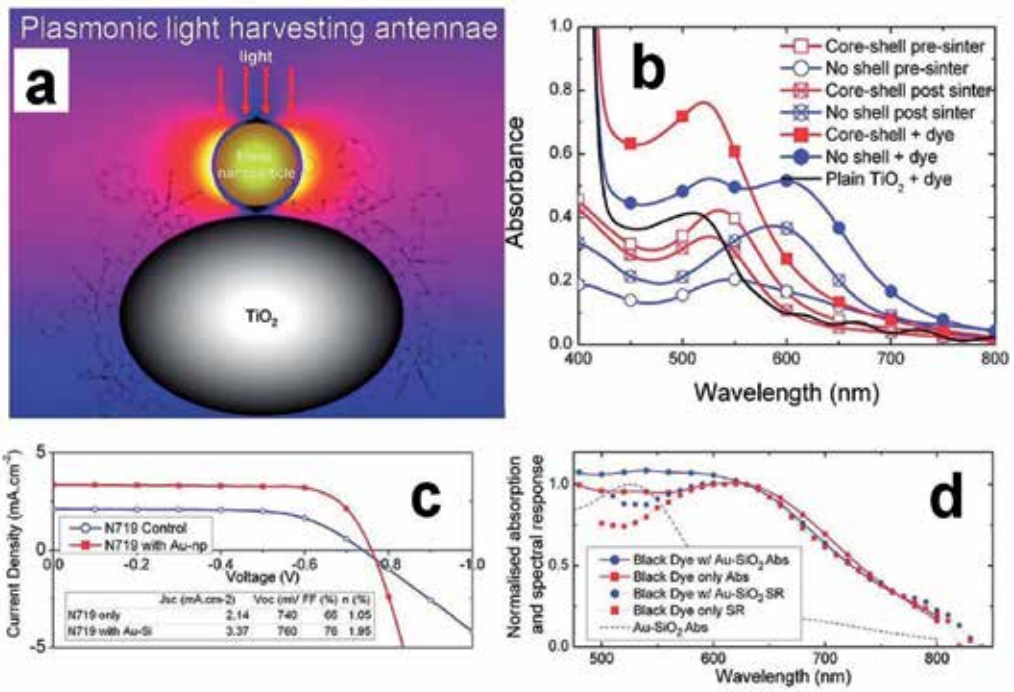


**Figure 20.** a) Schematic of plasmonic Au-$TiO_2$ structures. b) Absorption spectra of thin films (~1 μm) processed with nc-$TiO_2$ paste at different fabrication stages, including directly after doctor blade coating (pre-sinter), after two sintering cycles at 500°C and a $TiCl_4$ treatment (post-sinter), with final sensitization of Z907 (dye), $TiO_2$ paste incorporating bare Au NPs, Au-$SiO_2$ core shell NPs, and nc-$TiO_2$ film sensitized with Z907. c) *J*-V curves of liquid DSC (N719 sensitization, 1.1 μm thickness), with and without Au-$SiO_2$ core (15 nm)-shell (3 nm) nanoparticles. d) Normalized absorption (as 1-transmission-reflection) and spectral response of liquid DSCs. (Brown et al., 2011).

H. Choi et al. investigated the effects of the oxide capping layer of Au nanoparticles on the performance of plasmonic DSCs (Choi et al., 2012). By employing $SiO_2$- and $TiO_2$-capped Au NPs, they improved the cell efficiency from 9.3% for an N719 sensitized device to 10.2% upon incorporation of 0.7% Au@$SiO_2$ and to 9.8% upon loading of 0.7% Au@$TiO_2$ NPs. The

http://dx.doi.org/10.5772/51633

plasmonic effect was observed in Au@$SiO_2$ incorporated DSC, which produced higher photocurrent (Figure 21). However, in Au@$TiO_2$ incorporated DSC, Au NPs underwent charge equilibration with $TiO_2$ NPs and shifted the apparent Fermi level of the composite to more negative potentials, which resulted in a higher photovoltage. These observations opened up new opportunities to introduce both these paradigms and to synergetically enhance the photocurrent and photovoltage of DSC.

In brief, the plasmonic photoanodes are still a newly-emerged research area in DSC, spanning a wide range of materials (metal, semiconductor) and optical and electrochemical phenomena (localized surface plasmon resonance, scattering, electron-hole recombination). It is currently the main task for scientists to seek a suitable plasmonic structures (metal-oxide core-shell structures) and effective strategies to incorporate them into the nanocrystalline or nanostructured electrodes. While at present the nanoparticles of Au and Ag have been attempted to produce plasmonic DSC, further efforts may be extended to other metals (Ti, Zn, etc.) or morphologies with complex structures of metals (cubic, hexagonal, star-form etc.). Also, in-depth explorations on the mechanism of the plasmonic resonance embedded in the nanoporous electrode, and their detail influences on the photo-to-electric conversion process, are very useful to promote the development of this intriguing area.

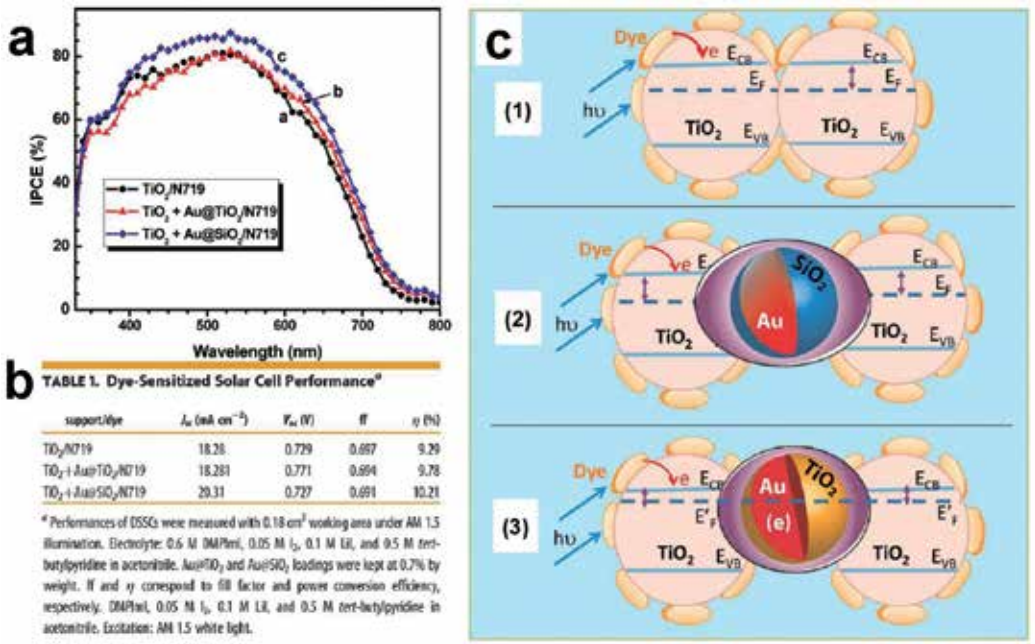


**Figure 21.** a) IPCE spectra of DSC employing N719 adsorbed onto $TiO_2$, $TiO_2$/Au@$TiO_2$, and $TiO_2$/Au@$SiO_2$ as photoanodes. The loading of core-shell particles is maintained at 0.7%. b) Photovoltaic performance of DSCs. c) Electron equilibration and its influence on the apparent Fermi level (EF): (1) dye $TiO_2$, (2) dye $TiO_2$/Au@-$SiO_2$, and (3) dye $TiO_2$/Au@$TiO_2$. LSP influence is seen in both (2) and (3), and shift in Fermi level as a result of electron accumulation in the metal core is seen in only (3). (Choi et al., 2012).

## 7. Photonic crystals based photoanodes and more

Photonic crystals (PCs) are materials that exhibit periodicities in their refractive index on the order of the wavelength of light, and thus provide many interesting possibilities for "photon management" (John, 1987). PC layers can be coupled to the charge-generating layer of DSC, and increase the LHE via such following mechanisms,

1. photon localization and enhanced red light absorption near the edges of the photonic bandgap,
2. light reflection within the photonic bandgap at various angles, and
3. formation of photon resonance modes within the dye-sensitized layer (Yip et al., 2010).

Compared with the traditional scattering techniques using geometrical optic-based elements (incoherent scattering layers, or high-reflectivity metallic mirrors), the application of PCs can obtain a more significant improvement on the LHE via the delicate control of the reflected, diffracted, or refracted light passing through the cell, apart from the apparent advantage in obtaining the transparent and colorful DSC rather than the opaque ones. The major limitation for the incorporation of PCs (especially the self-assembled 3D PCs) into DSC is the incompatibility between the fabrication routes for the photonic structures and the photoanode. So in the current stage, the preparation technology of PCs and their coupling to nc-$TiO_2$ layer represent the emphasis of many studies. In this section, we give several examples of PC layer in DSC with distinctive features in their structure.

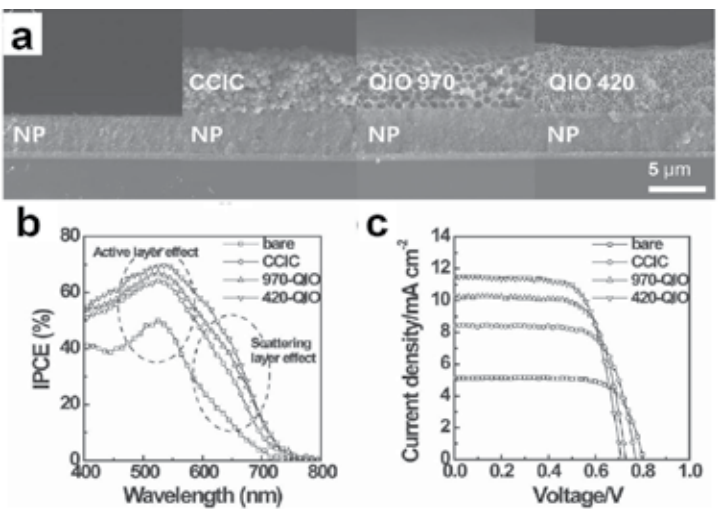


**Figure 22.** a) Cross-sectional SEM images of the photoelectrodes of nc-$TiO_2$ and with different scattering layers. b) IPCE spectra and c) *J–V* curves of the DSCs employing different scattering layers. (Han et al., 2011).

S. Han et al. fabricated quasi-inverse opal (QIO) layers with imperfect periodicity of hollows and applied them as the new scattering layer in DSC (Han et al., 2011). The porous QIO lay-

http://dx.doi.org/10.5772/51633

ers composed of highly crystalline anatase $TiO_2$ nanocrystals exhibited good dye-adsorptive properties and effective light-scattering properties over the wavelength range of 600–750 nm. The photocurrent of DSC based on the 420 nm-QIO layer was higher than the commercial scattering layer-based DSSC, achieving an efficiency of 5.7% (Figure 22).

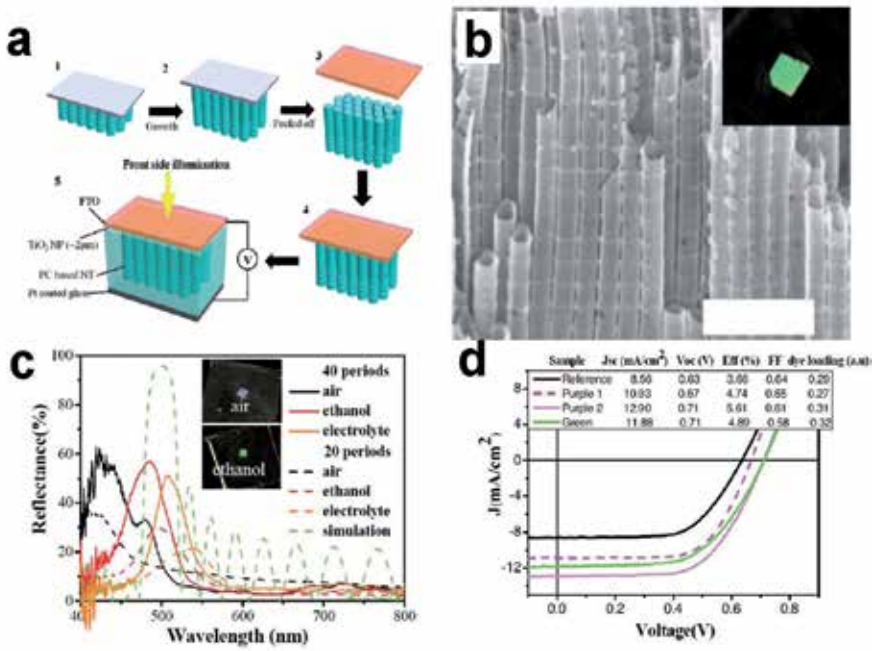


**Figure 23.** a) Schematic of the cell fabrication process. 1) Formation of PC layer. 2) Formation of NT layer. 3) Detachment of bi-layer from substrate. 4) Gluing to FTO by $TiO_2$ NPs. 5) Assembly of DSC. b) Cross-section SEM image of the PC layer. Scale bar:1 μ m. c) Reflectance of PC layers with 20 and 40 periods (lattice constant ~ 150 nm). Insets: photographs of the samples (with 20 periods) in air and infiltrated with ethanol. The green curves are simulated results with lattice constants of 150 and 190 nm for purple and green samples. d) *J*-V curves under AM 1.5 solar light illumination. The axial lattice parameters in the PC layer of the purple and green cells are ~ 150 and ~ 190 nm, and the numbers of periods are 30 and 20, respectively. Purple 1 and purple 2 are similar cells with a slight difference in dye loading. (Yip et al., 2012).

To solve a series of problems related to the PC coupled DSCs, including the poor physical contact between the PC layer and the $TiO_2$ absorbing layer, and the poor charge transport due to the nonconductive nature of PC, etc., C. T. Yip et al. developed a seamless PC-$TiO_2$ nanotube assembly (Yip et al., 2012), where the $TiO_2$ nanotube (NT) layer was fabricated by normal electrochemical anodization and the $TiO_2$ PC layer was obtained by a periodic current pulse anodization (Figure 23). Corresponding DSCs showed a 50% efficiency improvement compared with the cells without a PC layer, due to the enhanced light harvesting of the DSCs in the spectral range corresponding to the photonic bandgap of the PC and a longer wavelength range.

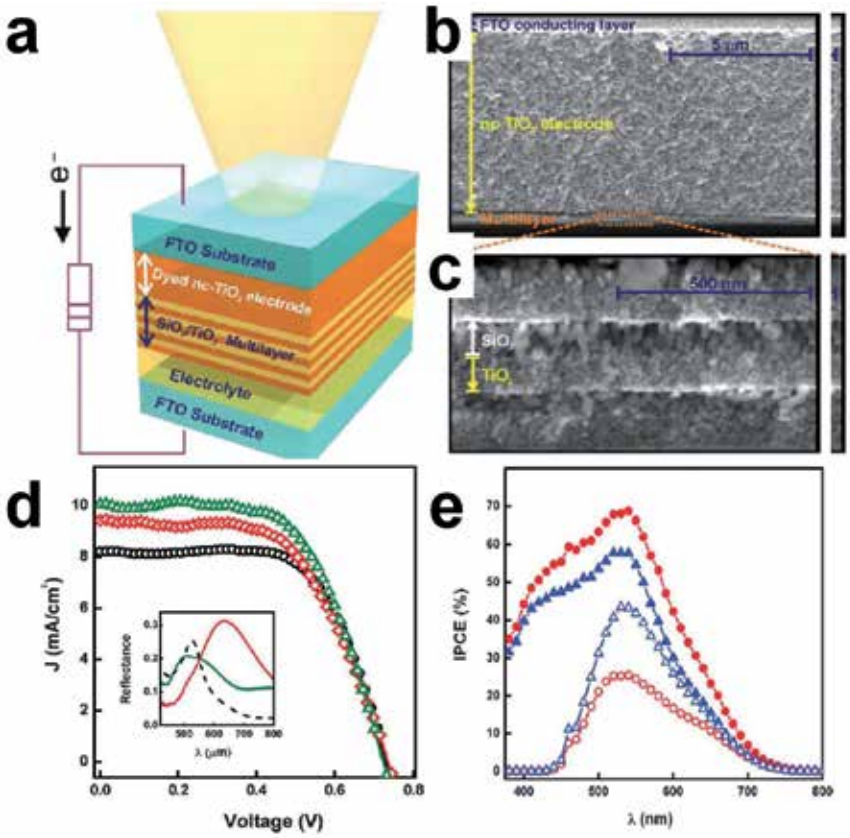


**Figure 24.** a) Scheme of DSC based on the 1D PC exposed to frontal illumination. b) Cross-section SEM image of nc-$TiO_2$ electrode, onto which a $TiO_2$–$SiO_2$ NP multilayer is deposited. c) Magnified view of the $SiO_2$ and $TiO_2$ layers composing the 1D PC. d) *J*–V curves of nc-$TiO_2$ electrode (7.5 mm thick) coupled to different 1D PCs under one-sun illumination. The lattice parameters are 120±10 nm (open green triangles), and 160±10nm (open red diamonds). Reference cell with the same nc-$TiO_2$ electrode is plotted as the open black circle line. Inset: reflectance spectra of the PC-based cell together with the absorption spectrum of the ruthenium dye. e) IPCE spectra for a DSC containing a 7.5 mm thick dye-sensitized $TiO_2$ electrode (solid blue triangles) and for the same electrode coupled to a PC of parameters 120±10nm (solid red circles), measured under frontal illumination and rear illumination (open blue triangles and open red circles, respectively). (Colodrero et al., 2009).

S. Colodrero, et al. couped a porous and highly reflecting 1D photonic crystal into a nc-$TiO_2$ electrode, by the deposition of alternate layers of NPs of different compositions by spin-coating (Colodrero et al., 2009). While the porous mesostructure allowed the electrolyte to flow through it and soak the electrode without interfering with the charge transport through the cell, the PC layer with a thickness of just half a micrometer efficiently localized the incident light within the nc-dyed $TiO_2$ electrode in a targeted wavelength range (Figure 24). Consequently, the average PCEs were improved to between 15 and 30% of the reference value attained for standard electrodes, while the open-circuit voltage and the transparency of the cell remained intact, contrary to what happened when the scattering layers were employed to improve the light harvesting.

http://dx.doi.org/10.5772/51633

Apart from the intensive studies on the PCs based DSC, other optical elements such as planar waveguide were also explored to enhance the LHE of DSC. Typically, Z. L. Wang's group demonstrated a novel three-dimensional DSC by integrating planar optical waveguide and nanowires (NWs) (Wei et al., 2010). The ZnO NWs were grown normally to the quartz slide, and the 3D cell was constructed by alternatively stacking a slide and a planar electrode. While the slide served as a planar waveguide for light propagation, the 3D structure effectively increased the light absorbing surface area due to internal multiple reflections without increasing the electron path length to the collecting electrode. Obtained 3D DSCs exhibited a significant improvement in energy conversion efficiency by a factor of 5.8 compared to the planar illumination case.

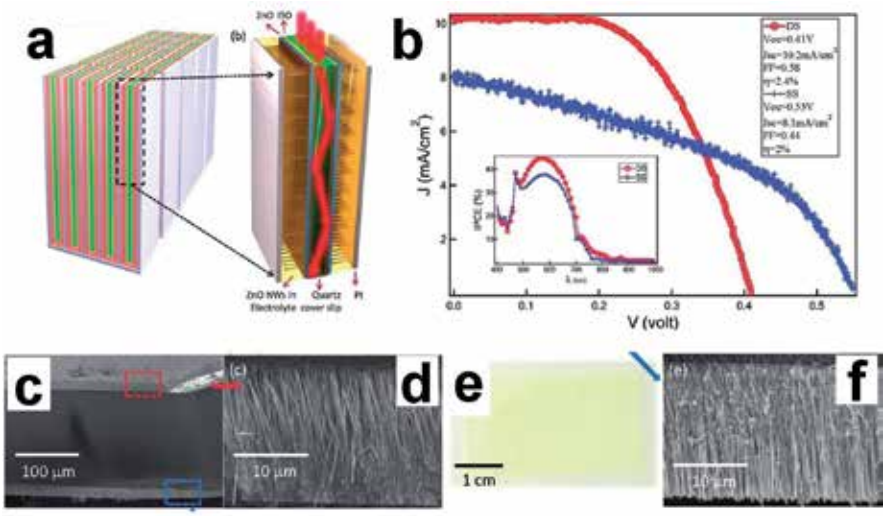


**Figure 25.** a) Schematic architecture of large scale 3D DSSC. The waveguide-NW 3D unit cells are plugged into the counter electrode housing and then sealed and fully packaged. b) *J*-V curves of DSCs under one full sun illumination for the parallell to the waveguide surface (PS) configuration. Inset: typical IPCE curves measured for single-side (SS) and double-side (DS) coated DSCs in the PS case. c) Low-magnification SEM image of a quartz slide with uniformly grown ZnO NWs on DS surfaces. d, f) High-magnification SEM images showing the densely packed ZnO NWs on top and bottom surfaces of the slide, respectively. e) Image of a slide coated with grown ZnO nanowire arrays. (Wei et al., 2010).

In summary, the optical elements such as the photonic crystals and the planar waveguide can provide exciting perspective to deliberately modulate the optical path of the incident lights and to significantly enhance the LHE of DSC. However, the ultimate PCE of corresponding DSCs is still far lower than that of nc-$TiO_2$ counterpart. How to tackle with the preparation problems related to the PC layers, and to avoid the possible adverse effects of the PC layers on the dye-loading and charge-transporting properties of the original electrode, are the kernel issues which should be solved in near future.

## 8. Conclusion

In conclusion, the light-harvesting efficiency (LHE) of the photoanode film has determinative effects on the power conversion efficiency of DSC. The deliberate modulations of the internal surface area of the nanoporous electrode and the optical path of the incident light are currently the main pathway to enhance the LHE of DSC. A wide range of novel materials or techniques have been utilized to improve the LHE of the electrode, including the high-surface area mesoporous nanostructures or aerogel, scattering-enhanced hierarchical nanostructures, up-conversion materials, plasmonic core-shell structures, and photonic crystals etc. However, while most of reported work realized obvious enhancement on one or more specific capacities of DSC, such as the dye-loading properties, optical scattering, or improved harvesting of near-infrared light, very few study can demonstrate high device performance comparable with the state-of-the-art nc-$TiO_2$ cell. The intrinsically different particle size, microstructures, preparation strategy of these novel materials from the traditional nc-$TiO_2$ electrode will inevitably result in significant changes in the microstructure or the optical/ electrical properties of the photoanode, which may greatly impair the final performance of the device. How to balance the advantageous and disadvantageous factors involved in these new-type photoanodes, and realize the solid improvement of the overall performance of DSC, are the emphasis of the scientists in near future. After all, the photoanodes based these novel materials or structures are still in an infant stage, containing infinite possibilities to improve or even revolutionize the basic principle and performance of the traditional DSC. We believe, via the intensive and extensive efforts of the scientist all over the world and through the collaborative studies among different areas spanning from material, chemistry to physics, the new-type photoanodes will certainly usher a brilliant future.

## Acknowledgements

This work is supported by the 973-project (Grant no. 2009CB623304) of Ministry of Science and Technology of China and the Basic Research Program (Grant no. 51072214, 51002174) of National Natural Science Foundation of China.

## Author details

Xiang-Dong Gao*, Xiao-Min Li and Xiao-Yan Gan

*Address all correspondence to: xdgao@mail.sic.ac.cn

State Key Lab of High Performance Ceramics and Superfine Microstructures, Shanghai Institute of Ceramics, Chinese Academy of Sciences, Shanghai, P. R. China

## References

[1] Brown, M. D., Suteewong, T., Kumar, R. S. S., Innocenzo, V. D., Petrozza, A., Lee, M. M., Wiesner, U., & Snaith, H. J. (2011). Plasmonic Dye-Sensitized Solar Cells Using Core–Shell Metal–Insulator Nanoparticles. *Nano Lett.*, 11(2), 438-445.

[2] Chen, W., Sun, X., Cai, Q., Weng, D., & Li, H. (2007). Facile Synthesis of Thick Ordered Mesoporous $TiO_2$ Film for Dye-Sensitized Solar Cell Use. *Electrochem. Comm.*, 9(3), 382-385.

[3] Chen, D, Huang, F, Cheng, Y. B., & Caruso, R. A. (2009). Mesoporous Anatase $TiO_2$ Beads with High Surface Areas and Controllable Pore Sizes: A Superior Candidate for High-Performance Dye-Sensitized Solar Cells. *Adv. Mater.*, 21(20), 2206-2210.

[4] Cho, C. Y., & Moon, J. H. (2011). Hierarchically Porous $TiO_2$ Electrodes Fabricated by Dual Templating Methods for Dye-Sensitized Solar Cells. *Adv. Mater.*, 23(26), 2971-2975.

[5] Choi, H., Chen, W. T., & Kamat, P. V. (2012). Know Thy Nano Neighbor. Plasmonic versus Electron Charging Effects of Metal Nanoparticles in Dye-Sensitized Solar Cells. *ACS Nano*, 6(5), 4418-4427.

[6] Colodrero, S., Mihi, A., Haggman, L., Ocana, M., Boschloo, G., Hagfeldt, A., & Miguez, H. (2009). Porous One-Dimensional Photonic Crystals Improve the Power-Conversion Efficiency of Dye-Sensitized Solar Cells. *Adv. Mater.*, 21(7), 764-770.

[7] Desilvestro, J., Grätzel, M., Kavan, L., Moser, J. E., & Augustynski, J. (1988). Highly Efficient Sensitization of Titanium Dioxide. *J. Am. Chem. Soc.*, 107(10), 2988-2990.

[8] Ding, I. K., Zhu, J., Cai, W., Moon, S. J., Cai, N., Wang, P., Zakeeruddin, S. M., Grätzel, M., Brongersma, M. L., Cui, Y., & Mc Gehee, M. D. (2011). Plasmonic Dye-Sensitized Solar Cells. *Adv. Energy Mater.*, 1(1), 52-57.

[9] Fan, K., Zhang, W., Peng, T., Chen, J., & Yang, F. (2011). Application of $TiO_2$ Fusiform Nanorods for Dye-Sensitized Solar Cells with Significantly Improved Efficiency. *J. Phys. Chem. C*, 115(34), 17213-17219.

[10] Ferber, J., & Luther, J. (1998). Computer Simulations of Light Scattering and Absorption in Dye-Sensitized Solar Cells. *Sol. Energy Mater. Sol. Cells*, 54(1-4), 265-275.

[11] Gaĺvez, F. E., Kemppainen, E., Míguez, H., & Halme, J. (2012). Effect of Diffuse Light Scattering Designs on the Efficiency of Dye Solar Cells: An Integral Optical and Electrical Description. *J. Phys. Chem. C*, 116(21), 11426-11433.

[12] Gao, X. D., Li, X. M., Gan, X. Y., Wu, Y. Q., Zheng, R. K., Wang, C. L., Gu, Z. Y., & He, P. (2012). Aerogel Based $SiO_2$-$TiO_2$ Hybrid Photoanodes for Enhanced Light Harvesting in Dye-Sensitized Solar Cells. *J. Mater. Chem.*, 22(36), 18930-18938.

[13] Gao, F., Wang, Y., Shi, D., Zhang, J., Wang, M. K., Jing, X. Y., Humphry-Baker, R., Wang, P., Zakeeruddin, S. M., & Grätzel, M. (2008). Enhance the Optical Absorptivity

of Nanocrystalline $TiO_2$ Film with High Molar Extinction Coefficient Ruthenium Sensitizers for High Performance Dye-Sensitized Solar Cells. *J. Am. Chem. Soc.*, 130(32), 10720-10728.

[14] Gratzel, M. (2009). Recent Advances in Sensitized Mesoscopic Solar Cells. *Acc. Chem. Res.*, 42(11), 1788-1798.

[15] Hagfeldt, A., Boschloo, G., Sun, L., Kloo, L., & Pettersson, H. (2010). Dye-Sensitized Solar Cells. *Chem. Rev.*, 110(11), 6595-6663.

[16] Hamann, T. W., Martinson, A. B. F., Elam, J. W., Pellin, M. J., & Hupp, J. T. (2008a). Aerogel Templated ZnO Dye-Sensitized Solar Cells. *Adv. Mater.*, 20(8), 1560-1564.

[17] Hamann, T. W., Martinson, A. B. F., Elam, J. W., Pellin, M. J., & Hupp, J. T. (2008b). Atomic Layer Deposition of $TiO_2$ on Aerogel Templates: New Photoanodes for Dye-Sensitized Solar Cells. *J. Phys. Chem. C*, 112(27), 10303-10307.

[18] Han, S. H., Lee, S., Shin, H., & Jung, H. S. (2011). Quasi-Inverse Opal Layer Based on Highly Crystalline $TiO_2$ Nanoparticles: A New Light-Scattering Layer in Dye-Sensitized Solar Cells. *Adv. Energy Mater.*, 1(4), 546-550.

[19] Hore, S., Vetter, C., Kern, R., Smit, H., & Hinsch, A. (2006). Influence of Scattering Layers on Efficiency of Dye-Sensitized Solar Cells. *Sol. Energy Mater. Sol. Cells*, 90(9), 1176-1188.

[20] Huang, F., Chen, D., Zhang, X. L., Caruso, R. A., & Cheng, Y. B. (2010). Dual-Function Scattering Layer of Submicrometer-Sized Mesoporous $TiO_2$ Beads for High-Efficiency Dye-Sensitized Solar Cells. *Adv. Funct. Mater.*, 20(8), 1301-1305.

[21] Huang, C. H., Yang, Y. T., & Doong, R. A. (2011). Microwave-Assisted Hydrothermal Synthesis of Mesoporous Anatase $TiO_2$ via Sol-Gel Process for Dye-Sensitized Solar Cells. *Microporous Meseporous Mater.*, 142(2-3), 473-480.

[22] Hüsing, N., & Schubert, U. (1998). Aerogels-Airy Materials: Chemistry, Structure, and Properties. *Angew. Chem. Int. Ed.*, 37(1-2), 22-45.

[23] Jeong, N. C., Prasittichai, C., & Hupp, J. T. (2011). Photocurrent Enhancement by Surface Plasmon Resonance of Silver Nanoparticles in Highly Porous Dye-Sensitized Solar Cells. *Langmuir*, 27(23), 14609-14614.

[24] Kim, J. Y., Kang, S. H., Kim, H. S., & Sung, Y. E. (2010). Preparation of Highly Ordered Mesoporous $Al_2O_3/TiO_2$ and Its Application in Dye-Sensitized Solar Cells. *Langmuir*, 26(4), 2864-2870.

[25] Ko, S. H., Lee, D., Kang, H. W., Nam, K. H., Yeo, J. Y., Hong, S. J., Grigoropoulos, C. P., & Sung, H. J. (2011). Nanoforest of Hydrothermally Grown Hierarchical ZnO Nanowires for a High Efficiency Dye-Sensitized Solar Cell. *Nano Lett.*, 11(2), 666-671.

[26] Koo, H. J., Kim, Y. J., Lee, Y. H., Lee, W. I., Kim, K., & Park, N. G. (2008). Nano-embossed Hollow Spherical $TiO_2$ as Bifunctional Material for High-Efficiency Dye-Sensitized Solar Cells. *Adv. Mater.*, 20(1), 195-199.

[27] Law, M., Greene, L. E., Johnson, J. C., Saykally, R., & Yang, P. (2005). Nanowire dye-sensitized solar cells. *Nature Materials*, 4(6), 455-459.

[28] Nazeeruddin, M. K., Kay, A., Rodicio, I., Humphry-Baker, R., Mueller, E., Liska, P., Vlachopoulos, N., & Grätzel, M. (1993). Conversion of Light to Electricity by Cis-X2bis(2,2′-bipyridyl-4,4′-dicarboxylate)ruthenium(II) Charge-Transfer Sensitizers (X = $Cl^-$, $Br^-$, $I^-$, $CN^-$, and $SCN^-$) on Nanocrystalline Titanium Dioxide Electrodes. *J. Am. Chem. Soc.*, 115(14), 6382-6390.

[29] Nazeeruddin, M. K., Pechy, P., Renouard, T., Zakeeruddin, S. M., Humphry-Baker, R., Comte, P., Liska, P., Cevey, L., Costa, E., Shklover, V., Spiccia, L., Deacon, G. B., Bignozzi, C. A., & Grätzel, M. (2001). Engineering of Efficient Panchromatic Sensitizers for Nanocrystalline $TiO_2$-Based Solar Cells. *J. Am. Chem. Soc.*, 123(8), 1613-1624.

[30] Regan, B. O., Moser, J., Anderson, M., & Grätzel, M. (1990). Vectorial Electron Injection into Transparent Semiconductor Membranes and Electric Field Effects on the Dynamics of Light-Induced Charge Separation. *J. Phys. Chem.*, 94(24), 8720-8726.

[31] Pietron, J. J., Stux, A. M., Compton, R. S., & Rolison, D. R. (2007). Dye-Sensitized Titania Aerogels as Photovoltaic Electrodes for Electrochemical Solar Cells. *Sol. Energy Mater. Sol. Cells*, 91(12), 1066-1074.

[32] Qi, J., Dang, X., Hammond, P. T., & Belcher, A. M. (2011). Highly Efficient Plasmon-Enhanced Dye-Sensitized Solar Cells through Metal@Oxide Core-Shell Nanostructure. *ACS Nano*, 5(9), 7108-7116.

[33] Qiu, J., Zhuge, F., Li, X., Gao, X., Gan, X., Li, L., Weng, B., Shi, Z., & Hwang, Y. H. (2012). Coaxial multi-shelled $TiO_2$ nanotube arrays for dye sensitized solar cells. J. Mater. Chem. , 22(8), 3549-3554.

[34] Regan, B. O., Moser, J., Anderson, M., & Grätzel, M. (1990). Vectorial Electron Injection into Transparent Semiconductor Membranes and Electric Field Effects on the Dynamics of Light-Induced Charge Separation. *J. Phys. Chem.*, 94(24), 8720-8726.

[35] Regan, B. O., & Grätzel, M. (1991). A Low-Cost, High-Efficiency Solar Cell Based on Dye-Sensitized Colloidal $TiO_2$ Films. *Nature*, 353(6346), 737-740.

[36] Sauvage, F., Chen, D., Comte, P., Huang, F., Heiniger, L. P., Cheng, Y. B., Caruso, R. A., & Gratzel, M. (2010a). Dye-Sensitized Solar Cells Employing a Single Film of Mesoporous $TiO_2$ Beads Achieve Power Conversion Efficiencies Over 10%. *ACS Nano*, 4(8), 4420-4425.

[37] Sauvage, F., Fonzo, F. D., Bassi, A. L., Casari, C. S., Russo, V., Divitini, G., Ducati, C., Bottani, C. E., Comte, P., & Graetzel, M. (2010b). Hierarchical $TiO_2$ Photoanode for Dye-Sensitized Solar Cells. *Nano Lett.*, 10(7), 2562-2567.

[38] Shan, G. B., Assaaoudi, H., & Demopoulos, G. P. (2011). Enhanced Performance of Dye-Sensitized Solar Cells by Utilizationofan External, Bifunctional Layer Consisting of Uniform β-$NaYF_4$:$Er^{3+}$/$Yb^{3+}$ Nanoplatelets. *ACS Appl. Mater. Interfaces*, 3(9), 3239-3243.

[39] Shao, F, Sun, J, Gao, L, Yang, S, & Luo, J. (2011). Template-Free Synthesis of Hierarchical $TiO_2$ Structures and Their Application in Dye-Sensitized Solar Cells. *ACS Appl. Mater. Interfaces*, 3(6), 2148-2153.

[40] Tetreault, N., & Grätzel, M. (2012). Novel Nanostructures for Next Generation Dye-Sensitized Solar Cells. *Energy Environ. Sci.*, 9(5), 8506-8516.

[41] Wei, Y, Xu, C, Xu, S, Li, C, Wu, W, & Wang, Z. L. (2010). Planar Waveguide−Nanowire Integrated Three-Dimensional Dye-Sensitized Solar Cells. *Nano Lett.*, 10(6), 2092-2096.

[42] Xu, F., Dai, M., Lu, Y., & Sun, L. (2010). Hierarchical ZnO Nanowire-Nanosheet Architectures for High Power Conversion Efficiency in Dye-Sensitized Solar Cells. *J. Phys. Chem. C*, 114(6), 2776-2782.

[43] Yella, A., Lee, H. W., Tsao, H. N., Yi, C., Chandiran, A. K., Nazeeruddin, M. K., Diau, E. W., Diau, G., Yeh, C. Y., Zakeeruddin, S. M., & Grätzel, M. (2011). Porphyrin-Sensitized Solar Cells with Cobalt (II/III)-Based Redox Electrolyte Exceed 12 Percent Efficiency. *Science*, 334(6056), 629-634.

[44] Yang, L., & Leung, W. W. F. (2011). Application of a Bilayer $TiO_2$ Nanofiber Photoanode for Optimization of Dye-Sensitized Solar Cells. *Adv. Mater.*, 23(39), 4559-4562.

[45] Yip, C. T., Huang, H., Zhou, L., Xie, K., Wang, Y., Feng, T., Li, J., & Tam, W. Y. (2012). Direct and Seamless Coupling of $TiO_2$ Nanotube Photonic Crystal to Dye-Sensitized Solar Cell: A Single-Step Approach. *Adv. Mater.*, 23(47), 5624-5628.

[46] Yum, J. H., Baranoff, E., Wenger, S., Nazeeruddin, M. K., & Grätzel, M. (2011). Panchromatic Engineering for Dye-Sensitized Solar Cells. *Energy Environ. Sci.*, 4(3), 842-857.

[47] Yun, T. K., Park, S. S., Kim, D., Hwang, Y. K., Huh, S., Bae, J. Y., & Won, Y. S. (2011). Pore-Size Effect on Photovoltaic Performance of Dye-Sensitized Solar Cells Composed of Mesoporous Anatase-Titania. *J. Power Sources*, 196(7), 3678-3682.

[48] Zhang, Q., & Cao, G. Z. (2011). Nanostructured photoelectrodes for dye-sensitized solar cells. *Nano Today*, 6(1), 91-109.

[49] Zhuge, F., Qiu, J., Li, X., Gao, X., Gan, X., & Yu, W. (2011). Toward Hierarchical $TiO_2$ nanotube Arrays for Efficient Dye-Sensitized Solar Cells. *Adv. Mater.*, 23(11), 1330-1334.

Chapter 8

# Metal Oxide Nanomaterials, Conducting Polymers and Their Nanocomposites for Solar Energy

Sadia Ameen, M. Shaheer Akhtar, Minwu Song and Hyung Shik Shin

Additional information is available at the end of the chapter

http://dx.doi.org/10.5772/51432

## 1. Introduction

The increasing concern on energy and the global warming due to the depletion of fossil fuel demands to search the alternative renewable energy resources for covering the energy crisis in the coming decade. A very popular renewable source called photovoltaic device is anticipated to solve energy problem, which converts directly the solar energy from sun to the electricity energy. Recently, dye sensitized solar cells (DSSCs) are widely used as promising photovoltaic device owing to its important properties like high solar to electricity energy conversion efficiency, low production cost, ease of fabrication and vast varieties of various semiconducting materials. DSSC is composed of few micrometer-thick nanocrystalline semiconducting oxides thin film combined with monolayer of charge-transfer dye as a photoanode, a redox electrolyte and a platinum metal electrode as counter electrode. In principle, upon illumination, the electron injection to conduction band of semiconductor takes place by the absorption of photons from dye molecules and the redox electrolyte regenerates the oxidized dye by the transportation of charges or ions. These days, the photovoltaic devices are facing inherent drawbacks such as leakage and evaporation problem that limits its practical application. In this regards, efforts are being done to overcome the leakage and evaporation of liquid electrolyte with solid or gel electrolytes such as room temperature molten salts (RTMSs), p-type semiconductor, conducting organic polymers and polymer gel electrolytes. Furthermore, the choice of catalytic in counter component of DSSCs is crucial to improve the reduction rate of $I_3^-$ to $I^-$ in the redox electrolyte. In general, the conducting glass electrode without any catalytic materials such as metals, conducting polymers etc shows very low electrocatalytic activity towards the iodide couple electrolyte due to overvoltage and high energy loss. It has been realized that the low resistance and high electrocatalytic materials

might deliver the better catalyst to avoid the overvoltage and energy loss for the high reduction of $I_3^-$ in redox electrolyte.

The semiconducting nanomaterials based thin film electrodes with high surface area are of great significance for acquiring the high amount dye adsorption which leads to the higher light harvesting efficiency and photocurrent density. Various metal oxides semiconductors such as $TiO_2$, ZnO and $SnO_2$ have shown good optical and electronic properties and are accepted as the effective photoanode materials for DSSCs. Additionally, the morphology and sizes of metal oxides semiconducting materials, particularly one dimensional (1D) nanostructures like nanorods (NRs), nanowires (NWs) and nanotubes (NTs) based electrodes have shown increased electron transfer during the operation of DSSCs owing to their high surface to volume ratio and arrangements. Until now, the photoanodes with $TiO_2$, $SnO_2$/ZnO, $Nb_2O_5$ and ZnO nanomaterials have presented the maximum solar to electricity energy conversion efficiencies of ~11.2%, ~8%, ~2% and ~5% respectively.

On the other hand, the conducting polymers are regarded as promising semiconducting materials due to distinguishable electrical properties, mechanical flexibility, and the relative ease of processing. The conductive polymers such as polypyrrole, poly (3, 4-ethylenedioxy-thiophene) and polyaniline (PANI) are frequently used in DSSC as hole transport materials, electron acceptor and electrocatalytic materials for tri-iodide reduction in redox electrolyte. Among them, PANI is an excellent host for the trapping of semiconducting nanomaterials and conducts the electric charges through the polymeric chain due to extended $\pi$-electron conjugation. The conducting polymers and dye sensitized metal oxides are good electron donors upon the photo-excitation during the operation of DSSCs.

In this chapter, we have briefly discussed the different conducting polymers, metal oxides and their application for the performance of DSSCs. The chapter includes the brief literature surveys, properties and photovoltaic properties of various metal oxides nanomaterials, nanofillers in polymer electrolytes and the conducting polymers. Additionally, the latest research advancements are surveyed for the development of efficient conducting polymers as p-type semiconducting nanomaterials for counter electrode materials and efficient nanofillers in the solid polymers of DSSCs. Moreover, the doping and the utilization of $TiO_2$ and ZnO nanomaterials for the performance of DSSCs have been discussed in details. It has been seen that the preparation methods, doping, morphologies, and the sizes of conducting polymers and metal oxides have shown the considerable impact on the electrical properties of the nanomaterials and performances of DSSCs. The study also demonstrates the enhanced properties of inorganic metal oxides like ZnO and $TiO_2$ with different sizes and morphologies for achieving the efficient photovoltaic properties of DSSCs such as $J_{SC}$, $V_{OC}$, FF and conversion efficiency.

## 2. Types of conducting polymers

The conducting polymers are composed of $\pi$-conjugated polymeric chain and are known as "synthetic metals" [1-2]. These extended $\pi$-conjugated systems of conducting polymers have

http://dx.doi.org/10.5772/51432

alternating single and double bonds along the polymeric chain [3]. The conducting polymers display the overlapping of molecular orbital to allow the formation of delocalized molecular wave functions and secondly these molecular orbital must be partially filled so that there is a free movement of electrons in the polymeric structure. The presence of unusual electronic properties such as electrical conductivity, low ionization potential and high electron affinity are associated with the π-electron backbone of the conjugated polymers. These are promising candidates for electronics applications, and offer possible replacements of the conventional metals and inorganic semiconductors [4-5]. The electrical conductivity of the conducting polymers could be altered upon partial oxidation or reduction by a commonly referred process called 'doping'. The electrical conductivity of these polymers could be changed from insulating to metallic by chemical or electrochemical doping and they could be used to produce electronic devices. These polymers have the electrical properties like that of metals, and have attractive characteristics of organic polymers such as light weight, resistance to corrosion, flexibility and lower cost. Additionally, these polymers could be tailor-made to the requirements of the application through modifications in the polymer structure by varying the functional groups in the organic moiety. The commercial applications of conducting polymers are in thin film transistor, batteries, antistatic coatings, electromagnetic shielding, artificial muscles, light-emitting diodes, gas and bio-sensors [6], fuel and solar cells, fillers [7] and corrosion protective coatings [8]. The conducting polymers are easy to synthesize through chemical or electrochemical processes, and their molecular chain structure could be modified conveniently by the copolymerization or structural derivations. Typically, the conducting polymers are of several types as listed below:

### 2.1. Polypyrrole (PPy)

Polypyrrole (PPy) is a versatile polymer of significant properties like redox activity [9] ion-exchange, ion discrimination capacities [10], electrochromic effects, charge/discharge processes [11] and exhibits strong absorptive properties towards gases [12], catalytic activity [13] and corrosion protection properties [14]. It is one of the important conducting polymers due to its good electrochemical reversibility between its conducting and insulating states and the ease of preparation through chemical or electrochemical routes [15].

### 2.2. Poly phenylenes) (PP)

Poly phenylene (PP) is one of the most unusual electro conducting polymers due to the extended planar conjugated π-system, along with high strength and high heat resistance [16]. The most widely used method of PP production is benzene oxidation with a Friedel-Crafts catalyst (the Kovacic method) [17], which yield a polycrystalline powder. Besides, electrochemical polymerization is also a method for PP synthesis, but the molecular weight of the polymer is limited due to its insolubility and chemical defect [18].

### 2.3. Polyacetylene (PA)

Polyacetylene (PA) is the polymer of highest conductivity as compared to those of conventional metals. PA has the simplest structure of the linear chains of C-H units with alternating single

and double bonds [19]. Moreover, the existence of the two hydrogen atoms in its repeat unit offers ample opportunity to decorate the backbone with pendants which perturbs the electronic conjugation and influences the molecular alignment of the polymeric chain. Significantly, the proper structural design might tune the backbone-pendant interplay into harmony and synergy, generating new substituted PAs with novel functionalities [20].

### 2.4. Polyazule (PAz)

The electron-donor and electron-acceptor character of polyazulene (PAz) has been explained by the electron-donor effect of the seven-membered ring toward the five-membered ring. The five-membered ring carries a partial negative charge and the seven-membered ring of azulene carries a partial positive charge. The polymers and its derivatives show high electrical conductivity almost similar as polythiophene, polypyrrole and polyaniline [21].

### 2.5. Polyindole (PIN)

Polyindol (PIN) is an electroactive polymer which could be obtained by the anodic oxidation of indole in various electrolytes. It is reported that the conductivity of PIN is lower than that of PPy and PANI but its thermal stability is better with respect to PANI and PPy. PIN, a macromolecular compound, is a good candidate for applications in various areas, such as electronics, electrocatalysis, and active materials for anodes of batteries, anticorrosion coatings and pharmacology.

### 2.6. Polycarbazole (PCz)

Polycarbazole (PCz) among conducting polymers, is attributed with good electroactivity, and useful thermal, electrical and photophysical properties [22]. However, π-π electron system along its backbone imparts rigidity to the polymer and therefore, makes it infusible and poorly processable. The increasing interest in PCz is towards its role as a hole-transport material and an efficient photoluminescence unit [23]. Derivatives of carbazole are easily prepared by the substitution at -N atom and thus, the solubility and functionality of the resulting polymers could be improved. More importantly, the substituted groups might influence the effective conjugation length which is promising materials in making the emitting light in devices.

### 2.7. Polyaniline (PANI)

Polyaniline (PANI) exhibits the high stability, conductivity and low cost [24-25]. PANI basically undergoes oxidative polymerization in the presence of a protonic acid. Protonation induces an insulator-to-conductor transition, while the number of π-electrons in the chain remains constant. The oxidation and reduction takes place on this –NH– group, and various forms are obtained due to the number of imine and amine segments on the PANI chain. Other substituted aniline like *N*-benzenesulfaniline [26], o-, p- and m-toluidine, o-chloroaniline [27], o-, m- and p-halogenated anilines [28] and 1-Napthylamine are also the subject of current studies and could be used for the semiconducting polymers based electronic applications.

http://dx.doi.org/10.5772/51432

Out of several conducting polymers, the interest of researchers in PANI could possibly be linked to the numerous applications that exist for the electronic conducting polymers and also aniline is cheap product and also a very stable material. On the other hand, the nanocomposites of conducting polymers with inorganic semiconducting nanomaterials show the improved mechanical, electrical and thermal properties due to the combined effects of both the semiconducting nanomaterials and conducting polymers. In particular, PANI nanocomposites display applications on a large scale for various electrochemical, electrorheological and in the electronic fields such as batteries, sensors, controlling systems and organic displays [29]. The nanocomposites of PANI with cadmium sulphide has been discussed in the next section of the chapter

## 3. Nanocomposites of conducting polymers

### 3.1. Nanocomposites of PANI and cadmium sulphide

Cadmium Sulphide (CdS) is a semiconductor with a direct band gap of ~2.42 eV which displays superior optical, photophysical and photochemical properties [30]. The nanocomposites of CdS and PANI have presented the effective electrode materials for many electrochemical, photoelectrochemical, sensing and electrochromic devices [31]. The nanocomposites are anticipated as effective and promising electrode materials in many electrochemical devices. Xi et al studied the influence of optical and absorption properties of CdS by the incorporation of CdS into PANI matrix [32]. R. Seoudi et al studied the dependence of structural, vibrational spectroscopy and optical properties on the particle sizes of PANI/CdS nanocomposites [33]. B.T. Raut et al reported the novel method of fabrication of PANI/CdS nanocomposites and studied the structural, morphological and optoelectronic properties [34]. In this regards, Ameen et al has reported a simple solution method to synthesize the CdS decorated PANI nanorods (NRs) and studied the electrochemical impedance properties of the nanocomposites [35].

The synthesized PANI NRs exhibit the entangled network with diameter of ~40-50 nm and length of several hundred nanometers, as shown in Fig. 1 (a). The uniform decoration and the thicknesses of CdS-PANI NRs increase gradually with the increase of $CdCl_2$ concentration. After sensitization with the highest concentration of $CdCl_2$ (0.1 M), the surface of PANI NRs (Fig. 1(b)) is completely decorated by CdS nanoparticles which results in the enhanced diameter of ~60-70 nm. The TEM characterization (Fig. 1 (c and d)) clearly justifies the decoration of CdS nanomaterials on the surface of PANI NRs and shows the increased thickness of PANI NRs with the average diameter of ~60-70 nm due to the decoration of CdS nanoparticles with highest concentration of $CdCl_2$ (0.1 M). From the EDS studies, the overall CdS contents have been estimated as 0.34, 0.53 and 1.08 wt% in the synthesized CdS-PANI NRs with $CdCl_2$ concentrations of 0.01 M, 0.05 M and 0.1 M respectively.

The Raman bands at ~1175 $cm^{-1}$, ~1507 $cm^{-1}$, ~1595 $cm^{-1}$ are observed in all the samples of CdS-PANI NRs (Fig. 2), corresponding to the C-H bending vibration of the semi quinonoid rings (cation-radical segments), N-H deformation vibration associated with the semiquinonoid structures and C=C stretching vibration in the quinonoid ring respectively [36]. PANI NRs show a relatively high band at ~1368 $cm^{-1}$ in the spectrum which provides the information of

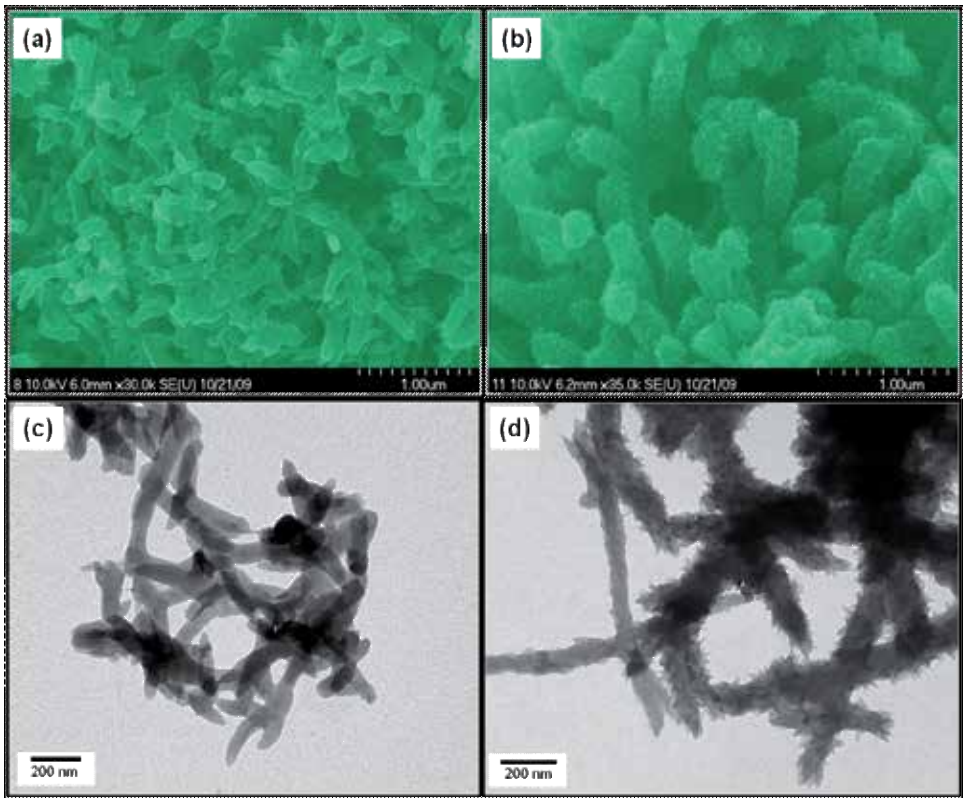


**Figure 1.** FESEM (a, b) and TEM (c, d) images of synthesized PANI NRs and CdS-PANI NRs. Reprinted with permission from [Ameen S., 2012], Chem. Eng. J. 181 (2012) 806 ©2012, Elsevier Ltd.

the C-$N^{+\bullet}$ vibration of delocalized polaronic structures [37]. The absence of this band in CdS-PANI NRs might due to the efficient interaction of imine (-NH) group of PANI with CdS nanomaterials.

The UV-Vis absorption spectra of the PANI NRs and CdS-PANI NRs are depicted in Fig. 3(a). In PANI NRs, the broad absorption bands at ~617 nm is related to n-π* transition, and the absorption peak at ~268 nm and ~327 nm arises due to π-π* transition within the benzenoid segment which is associated to the extent of conjugation between adjacent phenyl rings in the PANI [38]. On comparison to PANI NRs, the red shifting are seen and absorption bands move to higher wavelength of ~279 nm, ~338 nm and ~630 nm respectively in CdS-PANI NRs due to the sensitization of CdS nanomaterials with PANI NRs. The red shift of absorption bands with high intensities reveals that PANI NRs might form a partial bond with CdS nanoparticles. The room temperature photoluminescence (PL) spectra (Fig. 3(b)) of PANI NRs and CdS-PANI NRs exhibit a single large amplitude band in the blue green region which originated due to the π–π* transition of the benzenoid unit of PANI [39]. The sensitization of PANI NRs with the highest concentration of $CdCl_2$ (0.1 M) causes a significant red shift from ~421 nm to ~438 nm as compared to the PANI NRs which might occur by the chemical interaction between -

http://dx.doi.org/10.5772/51432

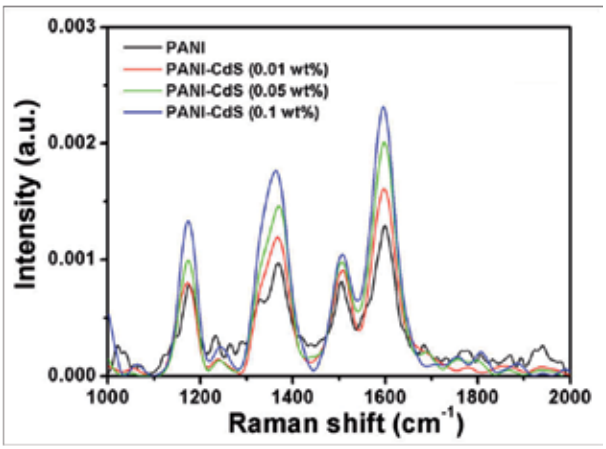


**Figure 2.** Raman Spectra of PANI NRs and CdS-PANI NRs. Reprinted with permission from [Ameen S., 2012], Chem. Eng. J.181 (2012) 806 ©2012, Elsevier Ltd.

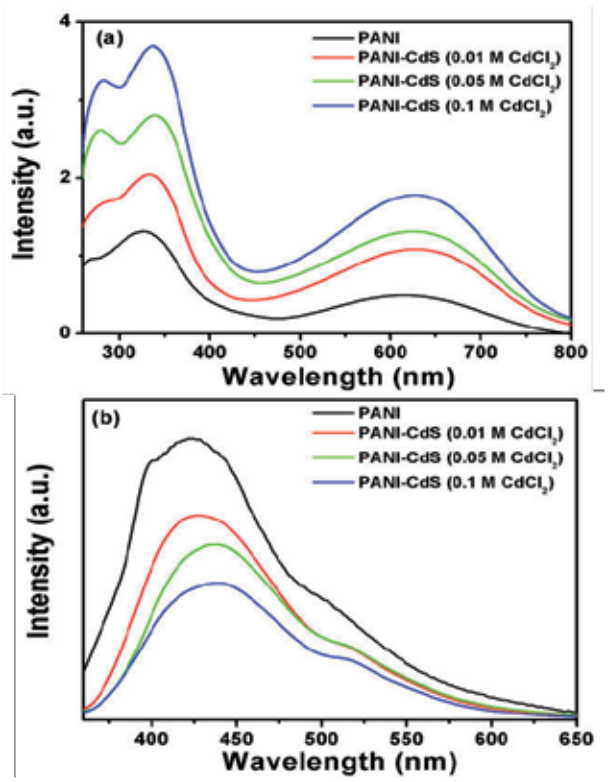


**Figure 3.** UV-vis absorption spectra (a) and photoluminescence spectra (b) of PANI NRs and CdS-PANI NRs. Reprinted with permission from [Ameen S., 2012], Chem. Eng. J.181 (2012) 806 ©2012, Elsevier Ltd.

NH groups of the PANI chains and surface of CdS. The CdS-PANI NRs sensitized with 0.1 M $CdCl_2$, shows the lowest PL intensity and the highest peak shift, suggesting the large π–π* transition of the benzenoid unit and the strong chemical interaction between -NH groups of the PANI chains and surface of CdS.

The X-rays Photoelectron Spectroscopy (XPS) has studied to examine the interaction between CdS nanoparticles and the PANI NRs, as shown in Fig. 4. The C 1s XPS spectrum (Fig. 4 (a)) of CdS-PANI NRs shows the center peak at ~284.0 eV with five resolved peaks at the binding energies spanning the range from ~288 to ~283 eV. The strong peak at ~ 283.4 eV represents the carbon (C) of benzonoid ring in which a combination of protonation of imine and amine sites are formed via shake-up processes [40]. The next three resolved peaks at ~284.8 eV, ~285.7 eV and ~286.8 eV confirm the origin of the neutral C-C/C-H bond-PANI backbone, C-$N^+$/C=$N^+$ bond and C=O/C-O bond (might occur due to the absorption of moisture on the CdS-PANI), respectively [41]. The resolved peaks at ~287.8 eV assigns to the π-π* bonding in a long-range order with a polymer chain shake-up satellite structure and coincides with the doped states. On comparison with typical PANI peak [42], C 1s peak has shifted backwardly, suggesting that C toms of PANI is interacted with other materials (CdS, $TiO_2$ etc.) or impurities [43]. The O 1s XPS spectrum (Fig. 4(c)) exhibits the center peak at ~530.1 eV with three resolved peaks

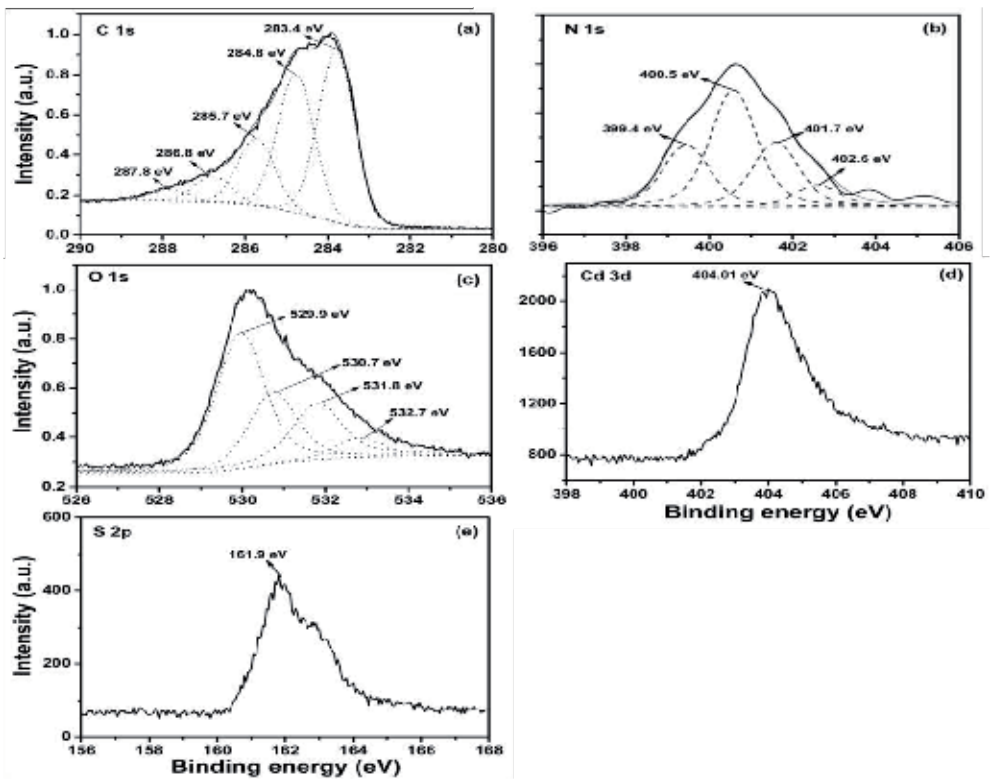


**Figure 4.** (a) C 1s, (b) N 1s, (c) O 1s, (d) Cd 3d and (e) S 2p XPS spectra of CdS-PANI NRs. Reprinted with permission from [Ameen S., 2012], Chem. Eng. J.181 (2012) 806© 2012, Elsevier Ltd.

http://dx.doi.org/10.5772/51432

at ~530.7, ~531.8 and ~532.7 eV, suggesting the absorption of moisture and some oxygen impurities on the surface of CdS-PANI NRs during the synthesis. In N 1s XPS spectra (Fig. 4(b)), the main center peak with binding energy at ~400.5 eV and a resolved peak with lower binding energy at ~399.4 eV attribute to nitrogen atom originated from benzenoid diamine and quinoid di-imine nitrogen of PANI respectively. The other binding energies of ~401.7 and ~402.6 eV are ascribed to the positively charged nitrogens i.e. oxidized amine ( $N^+$) and protonated imine ( $N^+$) respectively [44]. The positive shifting is seen in the binding energies at ~401.7 eV and ~402.6 eV as compared with N 1s spectrum of pristine PANI indicating the involvement of positively charged nitrogen or protonated nitrogen for the partial bonding between PANI and CdS. Furthermore, the singlet peak at ~404.01 eV observes in Cd 3d XPS (Fig. 4(d)) spectrum, corresponding to Cd $3d_{5/2}$ and the typical peak of $Cd^{+2}$ atoms in CdS [45]. Fig. 4(e) presents the S 2p XPS spectrum of CdS-PANI NRs and observed one distinct peak of $S2p_{3/2}$ at ~161.9 eV, corresponds to $S^{-2}$ of CdS nanoparticles. This suggests the interaction and bonding between CdS nanomaterials and PANI molecules. Thus, it is concluded that the PANI and CdS nanomaterials are partially interacted and bonded by two charged nitrogen species ($N^+$ and $N^+$) of PANI with CdS nanomaterials.

Fig. 5 shows the Nyquist plot of EIS measurement for PANI NRs and CdS-PANI NRs electrodes in the electrolyte (LiI, $I_2$ and $LiClO_4$ in ethanol) at a frequency range from 100 kHz to 1 Hz. The almost same $R_S$ (electrolyte resistance) with a depressed semi circle in the high frequency region is observed for the all the samples. The presence of depressed semi circle plot is ascribed to the parallel combination of the charge transfer resistance ($R_{CT}$) of the electrochemical reaction and the double layer capacitance ($C_{dl}$) of the PANI film/electrolyte interface [46] has been removed. As shown in Fig. 5, the PANI NRs electrode displays large $R_{CT}$ value of ~17 kΩ. The $R_{CT}$ values drastically decreases by the incremental addition of $CdCl_2$ in PANI NRs, and the order of $R_{CT}$ values are measured as 8.4 kΩ ($CdCl_2$ (0.01 M)-PANI NRs) < 5.7 kΩ ($CdCl_2$ (0.05 M)-PANI NRs) < 4.08 kΩ ($CdCl_2$ (0.10 M)-PANI NRs). Usually, the electrode with large $R_{CT}$ leads the slow charge transfer rate of the electrochemical system [46]. It could be seen that the highest $R_{CT}$ value of PANI NRs electrode might result the low charge transfer rate to the electrochemical system. Moreover, the CdS decorated PANI NRs electrode with 0.01 M $CdCl_2$ presents lowest $R_{CT}$ value which delivers the higher charge transfer rate. The variation in charge transfer resistance ($R_{CT}$) after the CdS sensitization by different concentrations of $CdCl_2$ might attribute to the changes in the NRs structure. Considerably, the direct band gap of CdS nanoparticles might also affect which improve the electronic state like polarons and bipolarons of PANI for the high charge carriers and enhance the charge transfer. Therefore, the CdS-PANI NRs is potential and cost effective electrode materials for the fabrication of efficient electrochemical (sensor, field emission transistor), photoelectrochemical and photovoltaic devices.

## 4. Basic structure and kinetics of DSSCs

Last few decades, considerable researches on DSSCs have extensively explored in terms of both fundamental and applied viewpoints. The basic components of DSSCs involves the

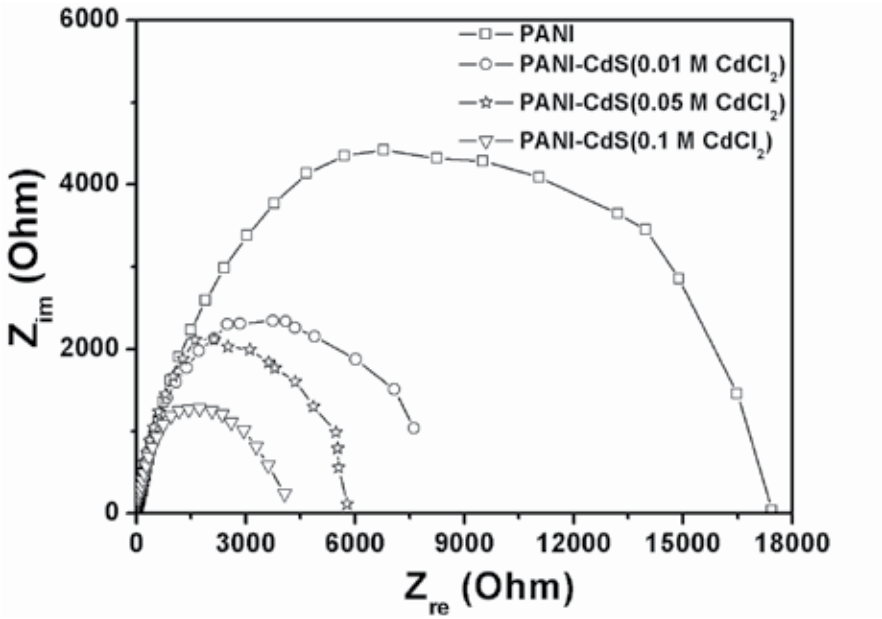


**Figure 5.** Nyquist plots of PANI NRs and CdS–PANI NRs at a frequency range from 100 kHz to 1 Hz. Reprinted with permission from [Ameen S., 2012], Chem. Eng. J.181 (2012) 806 ©2012, Elsevier Ltd.

conducting fluorine doped tin oxide (FTO) glass, sensitized dye, titania nanoparticles, electrolyte and Pt deposited FTO glass. The working principle of DSSC, involves the adsorption of photons by dye molecules upon light illumination and the injection of electrons from their excited states into the conduction band of the $TiO_2$ nanoparticles. During the entire process, the oxidized dye molecules are recharged by a redox electrolyte, which transports the positive charges by diffusion to a Pt counter electrode. The low absorption coefficient of a dye monolayer is compensated by the mesoporous structure of the $TiO_2$ film, which leads to a strong increase in the number of $TiO_2$/dye/electrolyte interfaces through which photons pass, thus increases the absorption probability. The following steps are in photoelectric chemical mechanism process of DSSC:

**i.** $TiO_2|D + h\nu \rightarrow TiO_2|D^*$ Excitation

**ii.** $TiO_2|D^* \rightarrow TiO_2|D^+ + \bar{e}$ (cb) Injection

**iii.** $TiO_2|2D^+ + 3I^- \rightarrow TiO_2|2S + I_3^-$ Regeneration

**iv.** $I_3^- + 2\,\bar{e}$ (Pt) $\rightarrow 3I^-$ Reduction

**v.** $I_3^- + 2\,\bar{e}$ (cb) $\rightarrow 3I^-$ Recaption (dark reaction)

**vi.** $TiO_2|S^+ + \bar{e}$ (cb) $\rightarrow TiO_2|S$ Recombination (dark reaction)

For the efficient working of DSSCs, the rate of re-reduction of the oxidized dye must be higher than the rate of back reaction of the injected electrons with the dye as well as the rate of reaction of injected electrons with the electron acceptor in the electrolyte. The kinetics of the reaction

http://dx.doi.org/10.5772/51432

at the counter electrode and mesoscopic semiconductor materials with an enormous internal surface area to absorb more incident light via dye as sensitizers determines the fast regeneration of charge mediator performance [47]. Apart from this, the other significant parameters which influence the performance of DSSCs are the mesoporous morphology with high surface area of semiconducting electrode to allow absorption of a larger amount of dye and the efficient charge carriers transport at the interface of photoanode and counter electrode by the semiconducting electrode. Moreover, the oxidized dye should be reduced to its ground state rapidly, after the injection of photoexcited electron from dye into the conduction band of semiconducting electrode. Furthermore, the semiconducting electrode must be able to permit the fast diffusion of charge carriers (higher conductivity) and produces good interfacial contact with the porous nanocrystalline layer and the counter electrode, the long-term stability, including chemical, thermal, optical, electrochemical, and interfacial stability of the electrolyte, which does not cause the desorption and degradation of the dye from the oxide surface and lastly, the optimized concentration of $I^-/I_3^-$ which could reduce the visible light absorption by the dye, and the efficient reaction of $I_3^-$ ions with the injected electrons to increase the dark current.

## 5. DSSCs based on conducting polymers

### 5.1. PANI as hole transport materials for DSSCs

The DSSCs and polymer solar cell have been exploring the new approaches in the design of both active materials and device architectures [48]. J. Wagner et al reported the new carbazole-based polymers for DSSCs with hole-conducting polymer [49]. N. Kudo et al fabricated the organic-inorganic hybrid solar cells based on conducting polymer and $SnO_2$ nanoparticles which were chemically modified with a fullerene derivative [50]. S. Woo et al reported the hybrid solar cells with conducting polymers and vertically aligned silicon nanowire arrays and studied the effects of silicon conductivity [51]. F. Tan et al synthesized PANI films by electrodepostied methods and applied as anode buffer layers in solar cells [52]. M. Y. Chang et al fabricated the polymer solar cells by incorporating one-dimensional polyaniline nanotubes [53]. T. H. Lim et al utilized PANI for a flexible organic solar cells anode [54]. H. Bejbouji et al reported PANI as a hole injection layer on organic photovoltaic cells [55]. S. Zhu et al synthesized the hybrid structure of PANI/ZnO nanograss for the application in dye-sensitized solar cell1 [56]. PANI is also known as large band gap hole transporting material (HMTs) which could easily deposit as thin film on several substrates. In this regards, Ameen et al has reported the application of PANI as photoelectrode using N710 and Z907 as sensitizers for the performance of DSSCs [57].

The morphologies of ZnO nanoparticles, PANI/N719/ZnO and PANI/Z907/ZnO thin films exhibit well crystalline ZnO nanoparticles of size ~30-40 nm. The size of ZnO nanoparticles increases by ~10-15 nm from their original particle sizes after the plasma enhanced chemical vapor deposition (PECVD) polymerization of PANI molecule on dye (N719 and Z907) sensitized ZnO nanoparticulate thin film. PANI/Z907/ZnO thin film displays uniform covering

or coating of PANI, indicating the well penetration of PANI on the surface of Z907/ZnO nanoparticulate thin film. The arrangement of ZnO/PANI nanoparticles are more pronounced for PANI/Z907/ZnO thin films might due to the substantive interaction and the incorporation of Z907 into ZnO nanoparticulate thin film which might allow the uniform deposition and well penetration of PANI through PECVD process. Likewise, the TEM images of ZnO nanoparticles and PANI/Z907/ZnO thin film electrode, again confirm the enhancement in the size of ZnO nanoparticles after PECVD polymerization of PANI. Significantly, after PECVD deposition of PANI, the aggregation of nanoparticles enhances the size of ZnO nanoparticles [57].

UV-Vis spectroscopy is investigated to describe the optical properties of PANI and PANI/ZnO thin film. The PECVD polymerized PANI exhibits the characteristic absorption bands at ~273 nm and ~345 nm which are ascribed to $\pi$–$\pi^*$ transitions. However, the broad band at ~611 nm is referred to $n$-$\pi^*$ transitions which provides the information of the polarons formation into the conducting PANI. The UV-visible spectrum of PANI/ZnO thin film shows the clear red shifts with the absorption bands at ~299 nm and ~628 nm from ~273 and ~611 nm, indicating the interference in the absorption bands of PANI by ZnO nanoparticles. These shifts in the peaks are usually associated to the interactions between ZnO and PANI in PANI-ZnO thin film which might due to the existence of partial hydrogen bonding between NH (PANI)..O–Zn (metal oxide) [58].

The room temperature PL spectra of PECVD polymerized PANI shows two absorption bands in blue-green region at ~438 nm and ~642 nm. The significant higher absorption wavelength shift at ~452 nm with slightly decreased peak intensity is observed in the PANI/ZnO thin film. The considerable changes in the PL emission peak might arise due to the effective interaction between imine (-NH) of PANI and hydroxyl (-OH) group of ZnO nanoparicles in PECVD polymerized PANI-ZnO thin film [57].

The current density-voltage (J-V) characteristics at one sun light illumination (100 mW/cm$^2$, 1.5AM) have been carried out to evaluate the performances of solar cell fabricated with PANI/N719/ZnO and PANI/Z907/ZnO thin film electrode. The measurements of $V_{OC}$, $J_{SC}$, FF and overall solar-to-electrical energy conversion efficiency are obtained from the J-V characteristics of both the DSSCs. The PANI/N719/ZnO electrode based DSSC exhibits low solar-to-electricity conversion efficiency of ~0.6%, with $J_{SC}$ of ~2.80 mA/cm$^2$, $V_{OC}$ ~0.432 V and FF ~0.51, whereas, PANI/Z907/ZnO electrode based DSSC executes the greater overall solar-to-electricity conversion efficiency of ~1.31% with $V_{OC}$ of $J_{SC}$ ~4.56 mA/cm$^2$, ~0.521 V, and FF ~0.55. On comparison with PANI/N719/ZnO electrode, DSSC with PANI/Z907/ZnO electrode attains considerably improved the solar-to-electricity conversion efficiency by ~53% along with other parameters of J-V characteristics. The enhanced performances and $J_{SC}$ might attribute to the fast movements of photon generated electrons at the interface of the PANI/ZnO and the nature of Ru dye (Z907) with long chain alkyl group at pyridine rings. Moreover, as seen in FESEM results, the high penetration of the hole conductor (PANI) into the pores of Z907 sensitized ZnO thin film might execute reasonably fast charge injection and electron transfer at the interface of PANI and ZnO layer to Pt layer of electrode. Thus, the choice of dye is crucial to obtain the high performance DSSC with PECVD polymerized PANI/ZnO electrodes. In other

http://dx.doi.org/10.5772/51432

previous report, Ameen et al showed the effects of PANI on $TiO_2$ as an effective photoelectrode for the performance of DSSCs [59].

A schematic energy level diagram for the device FTO/$TiO_2$/Dye/PANI/Pt is shown in Fig. 6 (a). The diagram, in accordance with step (1) indicates that the electrons from the dye, upon illumination, jumps from the HOMO level to the LUMO level and thus, as per step (2), these electrons are transferred from the conduction band (C.B) to the valence band (V.B) of $TiO_2$. The step (3) shows the transfer of electrons from V.B to the HOMO of PANI. As indicated by step (4), further transfer of electrons could be preceded through two different possible ways. Firstly, the electron could move either through the LUMO of PANI, followed by step (5) or then may jump to the LUMO of the dye and finally move onwards by repeating the step (2). Secondly, electrons, from step (3), could also jump to the HOMO of dye and would move ahead by following the same step (1), leading to the transfer of electrons to the entire cell. During the entire cycle, the recovery of the holes is accomplished at the counter electrode. Additionally, Fig. 6(b) depicts that PANI participates in the light absorption through the effective injection of electrons from its LUMO to the C.B of $TiO_2$. Therefore, the proposed mechanism presents that FTO/$TiO_2$/Dye/PANI/Pt system might deliver the high transportation of charge carriers during the operation of device under the illumination.

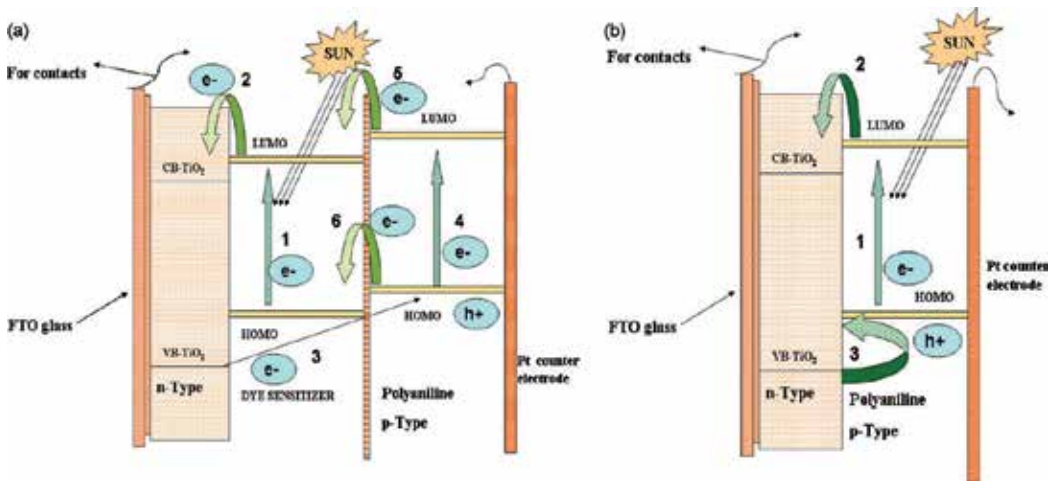


**Figure 6.** An overview of the energy level diagram of the fabricated devices (a) FTO/$TiO_2$/Dye/PANI/Pt (b) FTO/$TiO_2$// PANI/Pt. Reprinted with permission from [Ameen S., 2009], J. Alloys comp. 487 (2009) 382.© 2011, Elsevier Ltd.

To elucidate the charge transfer properties of $TiO_2$/PANI electrodes, an electrical impedance spectroscopy (EIS) measurement is used. According to the diffusion recombination model proposed by Bisquert [60], an equivalent circuit representing device is illustrated [(Inset of Fig. 7 (a)]. Equivalent circuit is composed of the series resistance ($R_S$), the charge transfer resistance at the junction of $TiO_2$ and PANI layer in $TiO_2$/PANI or $TiO_2$/Dye/PANI electrodes ($R_{CT}$), the charge transfer resistance at the interface of $TiO_2$/PANI or $TiO_2$/Dye/PANI and TCO ($R_{P/TCO}$), the capacitance of accumulation (of $e^-$) layer of the $TiO_2$ ($C_{acc}$), and space charge

capacitance ($C_{SC}$) [61]. The values of real impedance ($Z_{re}$) are used to estimate the values of $R_{P/TCO}$ and $R_{CT}$ at different frequencies. Fig. 7 (a, b) exhibits the Nyquist curve of cell fabricated with $TiO_2$/PANI and $TiO_2$/Dye/PANI electrodes. A very high $R_{P/TCO}$ of 52.4Ω and $R_{CT}$ of 3700 Ω observed for $TiO_2$/PANI electrodes based cells, which are estimated from Fig. 7(a). Comparatively, $TiO_2$/Dye/PANI based device (Fig.7 (b)) shows the low $R_{P/TCO}$ (35.8 Ω) and $R_{CT}$ (81.9 Ω) due to the influence of dye layer which is placed between the $TiO_2$ and PANI layer of the electrode. It is reported that a small $R_{CT}$ of the device suggests the fast electron transfer, while a large $R_{CT}$ indicates the slow charge transfer at the junction of inorganic and organic layer [62]. In our case, it is found that the value of $R_{CT}$ in $TiO_2$/Dye/PANI based device is very low as compared to the $R_{CT}$ of $TiO_2$/PANI based device. Therefore, it explains the high electron transfer at the junction of $TiO_2$ and PANI in $TiO_2$/Dye/PANI based device, resulting in the high photocurrent density and overall conversion efficiency, which are in the excellent agreement with the J-V curve results of the devices. The impedance results clearly indicate that the high photocurrent density, high overall conversion efficiency and low $R_{CT}$ are resulted from the uniform distribution of PANI molecules on the mesoporous surface of $TiO_2$ electrode. Therefore, the lower $R_{CT}$ and $R_{P/TCO}$ in $TiO_2$/Dye/PANI based device reveals that the dye and PANI layers on the surface of $TiO_2$ electrode play an important role in the charge transfer at hole conductor (PANI)-dye absorbed $TiO_2$ region, which results the high $J_{SC}$, FF, and conversion efficiency than that of $TiO_2$/PANI electrode based cells.

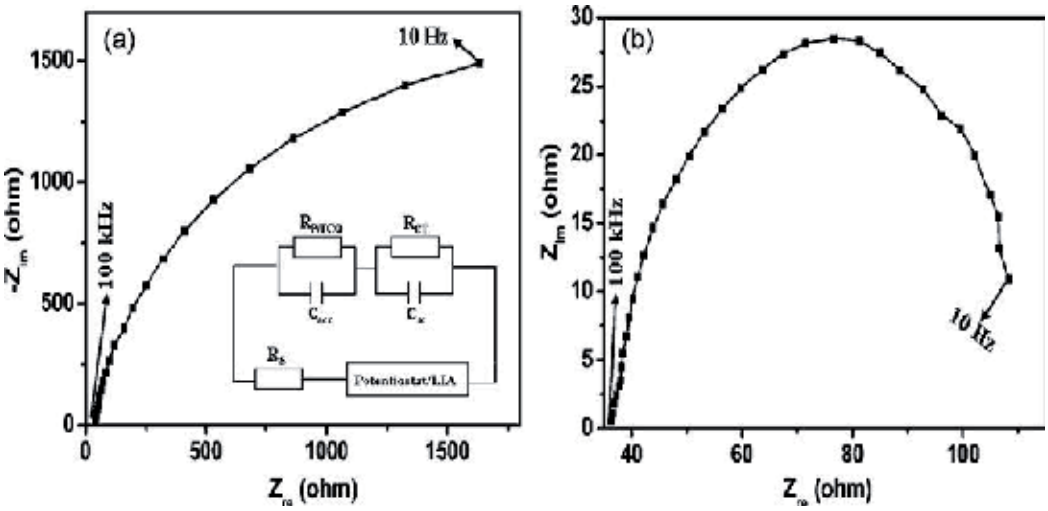


**Figure 7.** AC impedance of (a) FTO/$TiO_2$/PANI/Pt and (b) $TiO_2$/Dye/PANI thin film electrode based DSSCs at the frequency range from 10 Hz to 100 kHz. Inset shows the equivalent circuit model of the device. Reprinted with permission from [Ameen S., 2009], J. Alloys comp. 487 (2009) 382. ©2011, Elsevier Ltd.

The J-V performance of solar cell FTO/$TiO_2$/Dye/PANI/Pt and FTO/$TiO_2$/PANI/Pt are shown in Fig. 8 (a, b) under 100 mW/cm$^2$ light intensity. On comparison with $TiO_2$/PANI, the solar cell based on $TiO_2$/Dye/PANI electrode executes great improvement in the overall conversion efficiency with the incorporation of dye layer on $TiO_2$/PANI electrode. The conversion

http://dx.doi.org/10.5772/51432

efficiency of the solar cell drastically increases from ~0.005% to ~0.68%. It is noteworthy that the photovoltaic properties such as $V_{OC}$, $J_{SC}$ and FF of the DSSCs enhance dramatically as compared to $TiO_2$/PANI electrode based DSSC. The high $J_{SC}$ is imputed to the high electrical conductivity of PANI/$TiO_2$ thin film. The enhancement in JV parameters are resulted from the formation of $TiO_2$/PANI thin film, where the photon generated electrons could freely travel at the interface of PANI and $TiO_2$ without decay, and dissociate into free charge carriers effectively. Moreover, the pore filling extent of the hole conductor into the dye-sensitized $TiO_2$ film, and the electric contact of the hole conductor are the two important factors to determine the photovoltaic behaviors of device. The advanced $TiO_2$/Dye/PANI electrode executes reasonably fast charge injection and transfer of electron at the interface of hole conductor (PANI) and Pt layer of electrode.

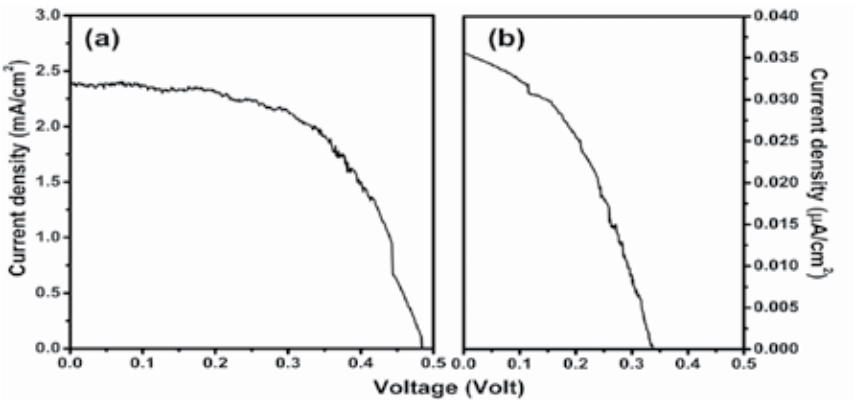


**Figure 8.** J–V curve of fabricated solar cell (a) FTO/$TiO_2$/Dye/PANI/Pt (b) FTO/$TiO_2$//PANI/Pt. Reprinted with permission from [Ameen S., 2009], J. Alloys comp. 487 (2009) 382 ©2011, Elsevier Ltd.

### 5.2. PANI as counter electrodes for DSSCs

The counter electrode in DSSCs is responsible for the electrocatalytic reduction of $I_3^-$ ions. Until now, Pt counter electrode shows the high electrocatalytic activity for $I_3^-$ ions reduction, high conductivity, and stability. Pt is one of the most expensive components in DSSCs. Therefore, the development of counter electrodes with alternative materials is expected to reduce production costs of DSSCs. Several varieties of materials such as carbon nanotubes, activated carbon, graphite, and conducting polymers are employed as active catalysts for counter electrodes. In this regards, M. H. Yeh et al reported the conducting polymer-based counter electrode for a quantum-dot-sensitized solar cell (QDSSC) with a polysulfide electrolyte [63]. K. M. Lee et al fabricated the DSSC based on poly (3, 4-alkylenedioxythiophene) as counter electrode [64]. In another report, K. M. Lee et al exhibited the effects of mesoscopic poly (3, 4-ethylenedioxythiophene) films as counter electrodes for DSSCs [65]. W. Maiaugree et al optimized the $TiO_2$ nanoparticle mixed PEDOT-PSS counter electrodes for high efficiency of DSSCs [66]. J. Chen et al reported polyaniline nanofiber-carbon film as flexible counter electrodes in platinum-free dye-sensitized solar cells [67]. Q. Li et al fabricated the microporous

polyaniline thin film as counter electrode for DSSCs [68]. J. Zhang et al applied the nanostructured PANI thin film as counter electrode for DSSCs and investigated the electrochemical formation mechanism [69]. Furthermore, G. Wang et al synthesized PANI-graphene hybrids thin film and utilized as a counter electrode in DSSCs [70]. Tai et al prepared the highly uniform and transparent PANI counter electrodes by a facile in situ polymerization method for the DSSCs [71]. In this regards, Ameen et al performed the doping of PANI with sulfamic acid (SFA) and applied as counter electrode for the efficient performance of DSSCs [72].

Fig. 9(a) shows the J-V curve of the DSSCs fabricated with the counter electrodes made of PANI NFs and SFA-doped PANI NFs under dark and light intensity of 100 mW/cm$^2$ (1.5AM). DSSCs fabricated with SFA-doped PANI NFs counter electrode achieve high conversion efficiency (η) of ~5.5% with $J_{SC}$ of ~13.6 mA/cm$^2$, $V_{OC}$ of ~0.74 V, and FF of ~0.53. Significantly, the conversion efficiency increases from ~4.0% to ~5.5% after SFA doping into the PANI NFs. DSSC fabricated with SFA-doped PANI NFs counter electrode has appreciably improved the conversion efficiency and $J_{SC}$ by ~27% and ~20% than that of DSSC fabricated with PANI NFs counter electrode. These improvements are resulted from the higher electrocatalytic activity of SFA-

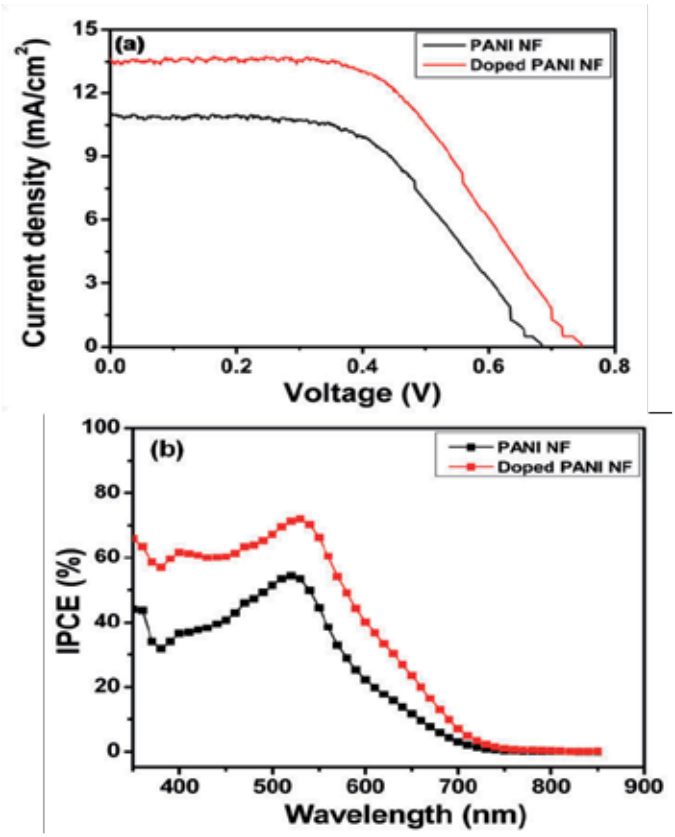


**Figure 9.** J-V curve (a) and IPCE curves (b) of a fabricated solar cell of PANI NFs and SFA doped PANI NFs as counter electrodes. Reprinted with permission from [Ameen S., 2010], J. Phys. Chem. C 114 (2010) 4760. ©2010, American Chemical Society.

http://dx.doi.org/10.5772/51432

doped PANI NFs, which serves a good path for the charge transport of $I^-/I_3^-$ redox. Therefore, the superior photovoltaic properties such as η, $J_{SC}$, and $V_{OC}$ of the cell are attributed to the sufficiently high conductivity and electrocatalytic activity of doped PANI NFs, which alleviates the reduction of $I_3^-$ at the thin SFA-doped PANI NFs layers. Fig. 9(b) presents the IPCE curves of DSSCs fabricated with PANI NFs and SFA-doped PANI NFs counter electrodes. DSSCs fabricated with PANI NFs counter electrode exhibits the low IPCE of ~54% in the absorption range of 400-650 nm. The IPCE value is prominently increased by ~70% with the SFA doped PANI NFs counter electrode-based DSSCs. It is noteworthy that the IPCE of the device is considerably enhanced by ~24% upon SFA doping on PANI NFs-based counter electrodes. The enhanced IPCE results are consistent with high electrical conductivity [73] and the electrocatalytic activity of the SFA-doped PANI NFs electrode. Thus, SFA doping significantly enhances the electrical conductivity and increases the higher reduction of $I_3^-$ to $I^-$ in the electrolyte at the interface of PANI NFs layer and electrolyte.

### 5.3. Other ions doped PANI counter electrode based DSSCs

Z. Li et al recently studied on the in situ electropolymerized-PANI thin film of thickness ~5–20 μm, deposited on FTO glass. The PANI thin films were doped by various counter ions like $SO_2^{-4}$, $ClO^{-4}$, $BF^{-4}$, $Cl^-$, p-toluenesulfonate ($TsO^-$), etc. Different doping counter ions showed different impact on the morphology, electrochemical activity of the electropolymerized-PANI thin film. The electropolymerized-PANI doped by $SO_2^{-4}$ anion (PANI-$SO_4$) film was much porous morphology with pore size diameter of several micrometers and possessed the higher reduction current for the reduction of $I_3^-$ and a low charge transfer resistance of 1.3 $\Omega cm^2$ as compared with Pt as counter electrode (CE). Dye-sensitized solar cell (DSSC) with PANI-$SO_4$ as CE was assembled, and the device under full sunlight illumination (100mW$cm^{-2}$, AM 1.5 G) showed ~5.6% photovoltaic conversion efficiency, which was comparable to ~6.0% of that with Pt CE under the same experimental condition. The electropolymerized-PANI doped with $SO_2^{-4}$ ion with a porous and homogeneously structure was a promising candidate which showed the high performance of DSSC. On the other hand, PANI-$BF_4$ and PANI-Cl was porous and fibrillar thin film which exhibited the modest efficiency of ~3.9% and ~2.6%. On the other hand, PANI-$ClO_4$ and PANI-TsO showed the very low performance of DSSC ca. <1%, and the $R_{CT}$ was greatly increased accordingly to over 100 $\Omega cm^2$ [74].

## 6. DSSCs based on metal oxide semiconductors

In DSSCs, the choice of semiconductor is governed by the conduction band energy and density of states, which facilitate the charge separation and minimize the recombination. Secondly, the high surface area and morphology of semiconductors is important to maximize the light absorption by the dye molecules while maintaining the good electrical connectivity with the substrate [75]. The semiconducting metal oxides such as titania ($TiO_2$), zinc oxide (ZnO), and tin oxide ($SnO_2$) have shown good optical and electronic properties and are accepted as the effective photoelectrode materials for DSSCs. To improve the light harvesting efficiency, the metal oxide nanostructures must possess a high surface-to-volume ratio for high absorption of dye molecules. Particularly in DSSCs, the porous nature of nanocrystalline $TiO_2$ films

provides the large surface for dye-molecule adsorption and therefore, the suitable energy levels at the semiconductor-dye interface (the position of the conduction band of $TiO_2$ being lower than the excited-state energy level of the dye) allow for the effective injection of electrons from the dye molecules to the semiconductor. Compared with other photovoltaic materials, anatase phase $TiO_2$ is outstanding for its stability and wide band gap and, thus, widely used in the devices [76]. On the other hand, ZnO nanomaterials are chosen as an alternative material to $TiO_2$ photoanodes due to their wide band gap with higher electronic mobility, which would be favorable for the efficient electron transport, with reduced recombination loss in DSSCs. Studies have already been reported on the use of ZnO material photoanodes for the application in DSSCs. Although the conversion efficiencies of ZnO (0.4-5.8%) is comparably lower than $TiO_2$ (~11%), ZnO is still a distinguished alternative to $TiO_2$ due to its ease of crystallization and anisotropic growth. In this part of the chapter, the $TiO_2$ and ZnO have been briefly summarized for the application for DSSCs.

### 6.1. DSSCs Based on $TiO_2$ Photoanode

Due to versatile and the exotic properties, $TiO_2$ nanomaterials are so far used in many technological applications as a photocatalyst, photovoltaic material, gas sensor, optical coating, structural ceramic, electrical circuit varistor, biocompatible material for bone implants, and spacer material for magnetic spin valve systems etc [77]. The dimensionality of $TiO_2$ at the nanoscale level is the crucial characteristic for determining the physiological and electrical properties. In recent years, one dimensional (1D) $TiO_2$ nanomaterials like NRs, NWs and NTs display significantly larger surface areas as compared to bulk materials, which deliver unique chemical and the physical properties [78] and contribute towards the electrical and photoelectrochemical applications [79]. The 1D $TiO_2$ such as NRs and NTs have shown the reduced recombination rate for the excited electron-hole pair and display unique optical and the electric properties [80]. Particularly, the vertically grown $TiO_2$ NRs allow shorter and the uninterrupted electrical pathways for the photogenerated carriers and improves the charge separation and charge transport properties in many photoelectrochemical devices like dye sensitized solar cells (DSSCs) [81]. As compared to $TiO_2$ nanoparticles, it is expected that the highly oriented $TiO_2$ NRs could be the potential electrode and photocatalyst material for several photoelectrochemical applications. S. Ameen et al reported the $TiO_2$ nanorods (NRs) based photoanode for the fabrication of DSSCs [82].

The morphology of the $TiO_2$ NR thin films deposited on FTO substrates by the hydrothermal process with variations of the ethanol/DI water precursor solution is shown in FESEM images (Fig. 10). With an ethanol/DI water ratio of 0:100 v/v as the precursor solution, the distorted hexagonal $TiO_2$ NRs (Fig. 10 (a, b)) of average diameter ~100-200 nm and length of 3.0 mm are obtained. However, the round headed $TiO_2$ NRs with ethanol/DI water (50: 50 v/v) as the precursor solution (Fig. 10 (c, d)) is formed. The highly ordered tetragonal $TiO_2$ NRs have grown on the FTO substrate with the precursor solution of ethanol/DI water (80: 20 v/v) as seen in Fig. 10 (e, f). The grown $TiO_2$ NRs possess the average lengths of 2-4 mm and diameters of ~50–70 nm respectively. The high amount of ethanol in the precursor solution is crucial to achieve the highly ordered nanorods.

http://dx.doi.org/10.5772/51432

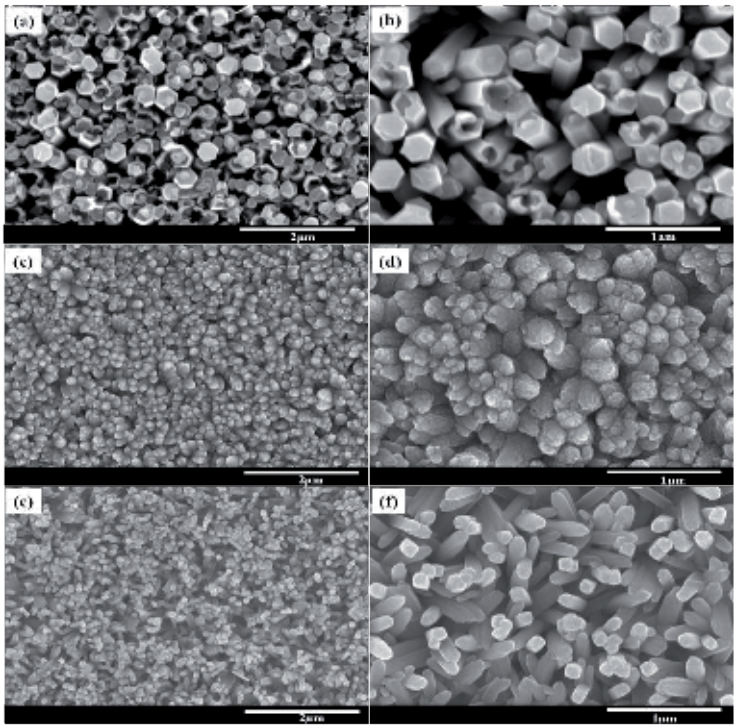


**Figure 10.** Low and high resolution FESEM images of the $TiO_2$ NR thin films obtained with the precursor solutions of ethanol/DI water with ratios of (a, b) 0 : 100 v/v, (c, d) 50 : 50 v/v and (e, f) 80 : 20 v/v. Reprinted with permission from [Ameen S., 2012], RSC Adv. 2 (2012) 4807 ©2012, RSC Publications Ltd.

Fig. 11 shows the transmission electron microscopy (TEM), high resolution (HR) TEM and the selected area electron patterns (SAED) of the grown $TiO_2$ NR coated FTO substrate. Similar to the FESEM results, the highly ordered tetrgonal $TiO_2$ NRs from the precursor solution of ethanol/DI water (80:20v/v) solvent comprises the average length of 2-4 mm and the diameter of 50-70 nm, as shown in Fig. 11 (a). Each NR is made of a bundle of the densely packed nanofibers (NFs) with an average fibril's diameter of ~5 nm. The corresponding SAED pattern (Fig. 11 (b)) displays the clear phases, suggesting the high crystal quality with the single crystalline fibrils derived from $TiO_2$ NRs along the [001] direction. However, the HRTEM image (Fig. 11 (c)) shows the well-resolved lattice fringes of the grown $TiO_2$ NRs and estimates an average interplanar distance of 0.35 nm between the two fringes, which reveals the typical interplanar distance of anatase $TiO_2$ [83]. On the other side, the width and length of distorted hexagonal $TiO_2$ NRs are respectively observed as ~200 nm and ~3.2 mm, as seen in Fig. 11(d).

The XRD patterns (Fig. 12) of grown $TiO_2$ NRs from both precursor solutions exhibit the anatase phase with the peaks at 25.1°, 37.9°, 48.1°, 53.8° and 55.1°, which correspond to typical anatase $TiO_2$ materials and indexes at JCPDS no. 89-4203. However, the diffraction peaks of the FTO substrate are also observed at 33.8°, 35.7° and 52.8° (JCPDS no. 88-0287). On comparison with the distorted hexagonal $TiO_2$ NRs, the intensities of XRD diffraction peaks have slightly changed, which might indicate the high crystalline nature of the highly ordered tetragonal $TiO_2$ NRs.

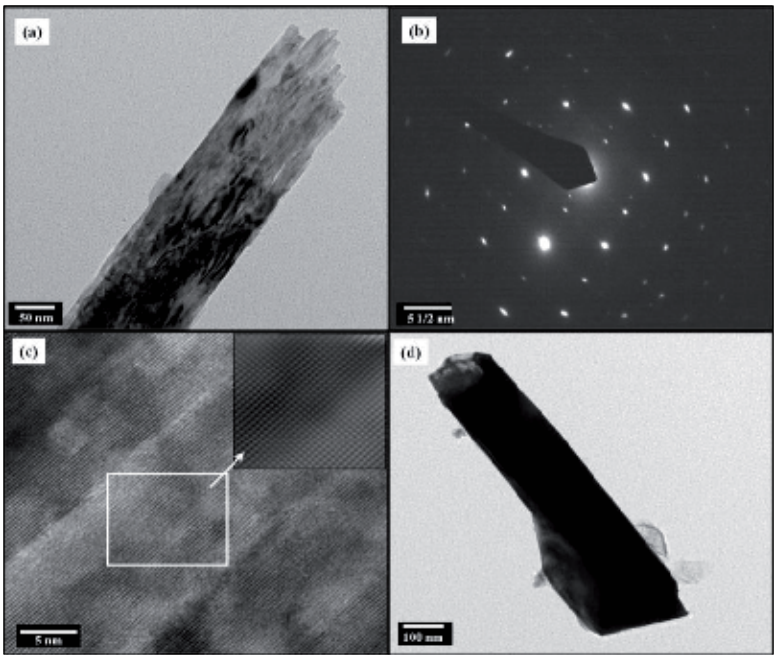


**Figure 11.** TEM image of (a) highly ordered tetragonal $TiO_2$ NRs, (b) SAED patterns, (c) HRTEM image and (d) TEM image of grown hexagonal distorted $TiO_2$ NRs. Reprinted with permission from [Ameen S., 2012], ], RSC Adv. 2 (2012) 4807 ©2012, RSC Publications Ltd.

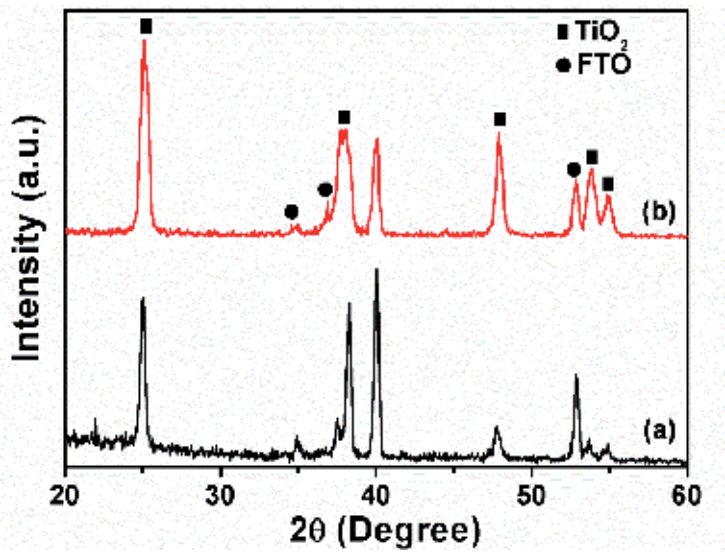


**Figure 12.** XRD patterns of (a) the distorted hexagonal $TiO_2$ NRs and (b) the highly ordered tetragonal $TiO_2$ NR thin film. Reprinted with permission from [Ameen S., 2012], RSC Adv. 2 (2012) 4807 ©2012, RSC Publications Ltd.

http://dx.doi.org/10.5772/51432

The J-V characteristics (Fig. 13 (A)) have been performed to elucidate the performance of the DSSCs fabricated with the photoanodes of grown $TiO_2$ NRs and are measured under a light intensity of 100 mW $cm^{-2}$ (1.5 AM). DSSC fabricated with the distorted hexagonal $TiO_2$ NRs photoanode shows a relatively low solar efficiency of ~1.08%, with a low $J_{SC}$ of ~4.48 mA $cm^{-2}$, $V_{OC}$ ~0.571 V and FF of ~0.42. However, DSSCs fabricated with the highly ordered tetragonal $TiO_2$ NRs photoanode achieves an appreciably improved overall conversion efficiency of ~3.2% with a high $J_{SC}$ of ~8.7 mA $cm^{-2}$, $V_{OC}$ of ~0.67 V, and FF of ~0.54. As compared to the distorted hexagonal $TiO_2$ NRs photoanode based DSSC, the photovoltaic performance, $J_{SC}$, $V_{OC}$ and FF are significantly enhanced by ~ 67%, ~48%, ~15% and ~22% respectively. It is seen that the size of the NRs also plays an important role for achieving the high photocurrent density and performance of the device. It is known that the high photovoltaic performance and photocurrent density are related to high light harvesting through the highly uniform and high surface to volume ratio of the photoanode materials [84]. In general, the $TiO_2$ thin film electrodes with larger particles have the smaller surface area and produce moderate contact points between nanoparticles at the interface of the sintered nanoparticles and the conducting substrate, leading to the lower availability of the active surface for dye adsorption, which perhaps decreases the amount of light absorbed and generates the large number of electrons and holes. Whereas, the $TiO_2$ thin film with smaller particles acquires the larger surface area and higher number of contact points of the sintered colloidal particles present at the interface of the nanoparticles and the conducting substrate, which gives rise to larger dye adsorption and higher light harvesting efficiency [85]. In this case, the distorted hexagonal $TiO_2$ NRs consist of larger diameters and lengths as compared to the highly ordered $TiO_2$ NRs, as shown in the FESEM images. It is believed that the smaller diameters of the NRs might generate the high light harvesting efficiency, which might lead to the high photocurrent density and the conversion efficiency. From the UV-Vis spectra (Fig. 13 (B)) of the dye desorption from dye absorbed $TiO_2$ NRs photoanodes in NaOH solution, the photoanode of highly ordered tetragonal $TiO_2$ NRs attains the higher dye loading than the photoanode of the distorted hexagonal $TiO_2$ NRs. Herein, the enhanced photovoltaic performance and $J_{SC}$ are related to the highly ordered NRs morphology, high dye loading and improved light harvesting efficiency through the high surface area of the film. Besides these, the unique ordered morphology of the NRs might retard the recombination rate and contribute to longer electron lifetimes [86], resulting in the increased $V_{OC}$ and FF of device.

The IPCE (Fig. 14) of DSSCs fabricated with highly ordered tetragonal $TiO_2$ NRs and distorted hexagonal $TiO_2$ NRs photoanodes have shown the broad the absorption edge of visible spectrum from 400-800 nm. The highly ordered tetragonal $TiO_2$ NRs photoanode based DSSC exhibits the maximum IPCE of ~31.5% at the highest absorption edge of ~528 nm, whereas ~17.9% IPCE at ~528 nm is achieved by the distorted hexagonal $TiO_2$ NRs photoanode based DSSC. The highly ordered tetragonal $TiO_2$ NRs photoanode based DSSC considerably improves IPCE by approximately two times to DSSC with distorted hexagonal $TiO_2$ NRs photoanode, which is attributed to the high dye loading of the photoanode, resulting in the high light harvesting efficiency and the electron injection from dye to CB of $TiO_2$. Thus, the highly ordered tetragonal $TiO_2$ NRs photoanode with enhanced dye loading, light harvesting and IPCE, have resulted to increased $J_{SC}$, $V_{OC}$ and the photovoltaic performance for DSSC.

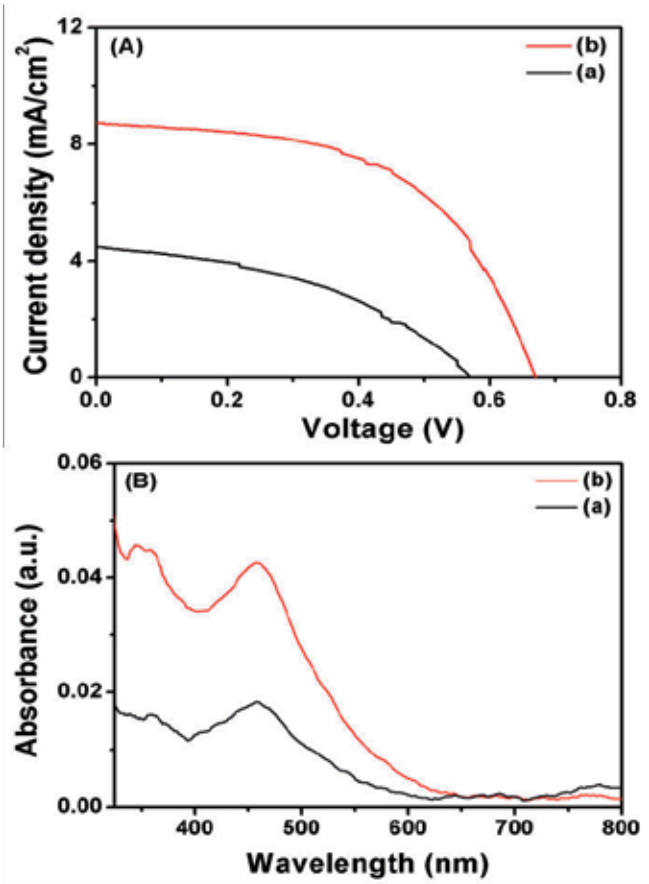


**Figure 13.** (A) J-V curve of the DSSC fabricated with (a) distorted hexagonal $TiO_2$ NRs and (b) highly ordered tetragonal $TiO_2$ NRs. (B) UV-Vis spectroscopy of desorbed dye from (a) distorted hexagonal $TiO_2$ NRs and (b) highly ordered tetragonal $TiO_2$ NRs. Reprinted with permission from [Ameen S., 2012] ], RSC Adv. 2 (2012) 4807©2012, RSC Publications Ltd.

### 6.2. DSSCs based ZnO photoanode

Another metal oxide nanomaterials such as ZnO nanomaterials, are recently dealing with the versatile applications in various fields such as field-effect transistors, lasers, photodiodes, sensors and photovoltaics owing to their unique photoelectric properties, optical transparency, electric conductivity and piezoelectricity properties [87]. Importantly, ZnO nanomaterials possess similar wide band gap (~3.37 eV) with large exciton binding energy (~60 meV) and higher electron mobility [88]. Moreover, ZnO nanomaterials with different nanostructures have presented the versatile properties like higher surface-to-volume ratio, chemical stability, high exciton binding energy, and moderate charge transport capability [89] and therefore, it becomes one of the promising alternatives of nanocrystalline $TiO_2$ photoanode in DSSCs and hybrid solar devices. To control the parameters like morphology, physical and the crystalline properties of ZnO nanomaterials, the performance of DSSCs could be accelerated [90]. So far, the different morphologies of ZnO nanostructures such as nanorods [91], nanotetrapods,

http://dx.doi.org/10.5772/51432

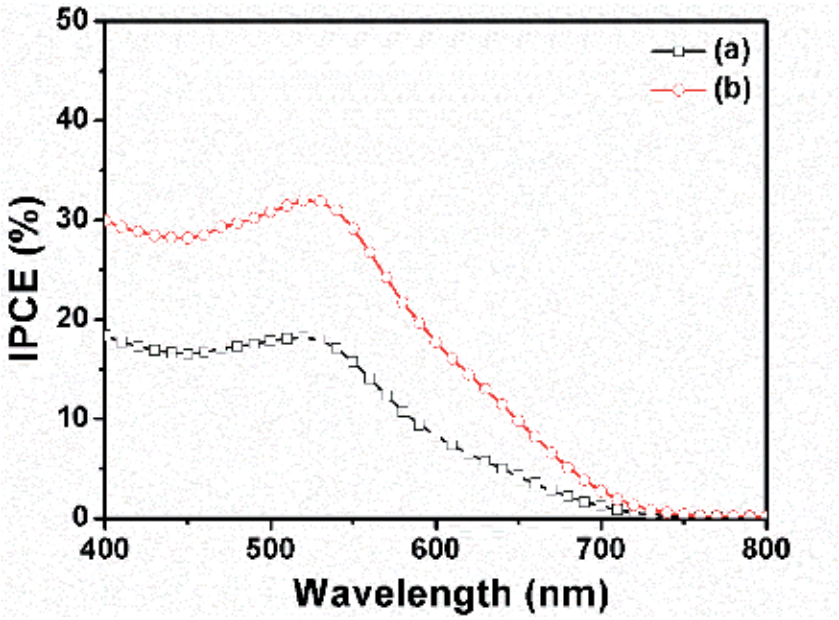


**Figure 14.** IPCE curve of the DSSC fabricated with (a) the distorted hexagonal $TiO_2$ NR photoanode and (b) the highly ordered tetragonal $TiO_2$ NR photoanode. Reprinted with permission from [Ameen S., 2012], RSC Adv. 2 (2012) 4807©2012, RSC Publications Ltd.

nanosheet [92] and nanobelts based photoanodes have been studied for the fabrication of efficient DSSCs [93] and achieved encouraging results. Law et al. firstly designed ZnO NW arrays to increase the electron diffusion length, and applied as photoelectrodes for the fabrication of DSSCs [94]. The grown ZnO NW array films exhibited relatively good resistivity values that ranged from 0.3 to 2.0 Ωcm for individual NWs and a mobility of 1-5 $cm^2 V^{-1}s^{-1}$. The overall conversion efficiencies of ~1.2-1.5% were obtained by DSSCs fabricated with ZnO NW arrays with $J_{SC}$ of ~5.3-5.85 $mA/cm^2$, $V_{OC}$ of ~0.610-0.710 V, and FF of ~0.36-0.38. Another

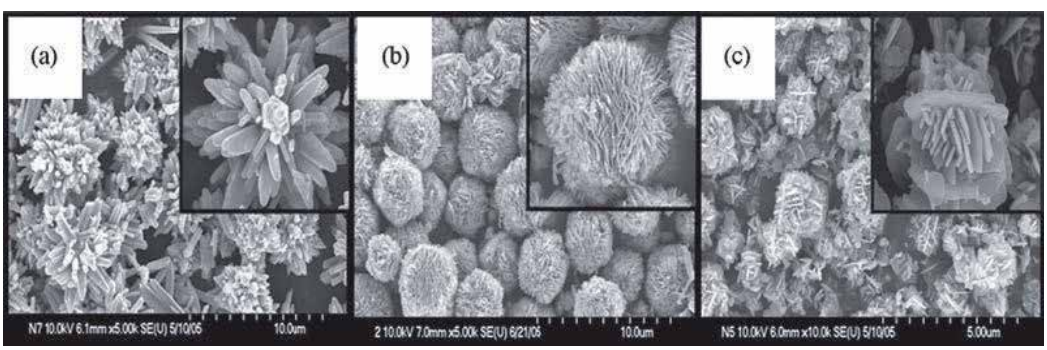


**Figure 15.** FE-SEM images of (a) ZnO–NH3, (b) ZnO-citric, and (c) ZnO-oxalic materials prepared by hydrothermal method. Inset shows the high magnification FE-SEM images of (a), (b), and (c). Reprinted with permission from [Akhtar., 2008], Electrochim. Acta 53(2008)7869.© 2008, Elsevier Ltd.

group synthesized ZnO NWs by the use of ammonium hydroxide for changing the super saturation degree of Zn precursors in solution process [95]. The length-to-diameter aspect ratio of the individual NWs was easily controlled by changing the concentration of ammonium hydroxide. The fabricated DSSCs exhibited remarkably high conversion efficiency of ~1.7%, which was much higher than DSSC with ZnO NR arrays [96]. Jiang et al. fabricated the flexible DSSCs with a highly bendable ZnO NWs film on PET/ITO substrate which was prepared by a low-temperature hydrothermal growth at 85°C [97]. The fabricated composite films obtained by immersing the ZnO NPs powder in a methanolic solution of 2% titanium isopropoxide and 0.02 M acetic acid was treated with heat, which favored a good attachment of NPs onto the NW surfaces [97]. Here, the achieved conversion efficiency of the fabricated DSSCs was less as compared to DSSCs based on NPs. Recently, Akhtar et al. demonstrated that the performance of DSSCs effectively altered by varying the morphologies of ZnO nanomaterials. They reported the morphology of ZnO nanomaterials through a hydrothermal process using Zinc acetate, NaOH and different capping agents, as shown in Fig 15. The photoanode was prepared by spreading the ZnO paste on an FTO substrate by a doctor blade technique for the fabrication of DSSCs [98], and they obtained non-uniform surface of film. Unfortunately, the DSSCs with ZnO NRs photoanode presented a very low conversion efficiency of ~0.3% with a high FF of ~0.54 (Fig 16), which might attribute to the low dye absorption on the surface of ZnO NRs due to the less uniformity of the thin film with low surface-to-volume ratio (Fig 17). Furthermore, a flower-like structure consisted of NRs/NWs could deliver a larger surface area and a direct pathway for electron transport with the channels arisen from the branched to NR/NW backbone. Recently, hydrothermally grown ZnO nanoflower films accomplished an improved overall conversion efficiency of ~1.9%, with a high $J_{SC}$ of ~5.5 mA/cm$^2$ and an FF of ~0.53 [99]. These parameters are higher than NR arrays film-based DSSCs of the conversion efficiency ~1.0%, $J_{SC}$ ~4.5 mA/cm$^2$, and FF ~0.36. Recently, S. Ameen et al reported the nanospikes decorated ZnO sheets thin film as photoanode for the performance of DSSCs [100].

The FESEM image (Fig. 18) shows dense and uniform deposition of the nanospikes decorated ZnO sheets morphology on the FTO substrate. Each nanospikes decorated ZnO sheets is comprised of a sheet with the average thickness of ~50-60 nm and the aligned nanospikes with the average diameter of ~80-100 nm and length of ~150-200 nm. Interestingly, the nanospikes are consisted of the bundles of small nanorods. The nanospikes are aligned either on one side or other side of ZnO sheet, but in some cases, these nanospikes are found on the both sides of ZnO sheets.

Similarly, TEM images (Fig. 19(a)) present the nanospikes with nanosheets in which nanospikes decorated on both the sides of ZnO sheet. The average thickness of the sheet is ~50-60 nm and the decorated nanospikes possess the average diameter of ~30 nm (single rods) and the length of ~150-200 nm. From the HRTEM image (Fig. 19 (b)), the well-resolved lattice reveals that the grown ZnO nanomaterials exhibit the good crystallinity. The inter-planar spacing of ~0.52 nm is observed which is consistent to the lattice constant in the reference (JCPDS No. 36-1451) for ZnO nanomaterials. This inter-planar spacing value of the lattice fringes correspond to the [0001] crystal plane of the wurtzite ZnO confirms that the grown ZnO nanomaterials are almost defect free [100]. Moreover, the corresponding selected area electron diffraction (SAED) also indicates the typical wurtzite single crystalline structure and the ZnO nanomaterials are grown along caxis direction [0001].

http://dx.doi.org/10.5772/51432

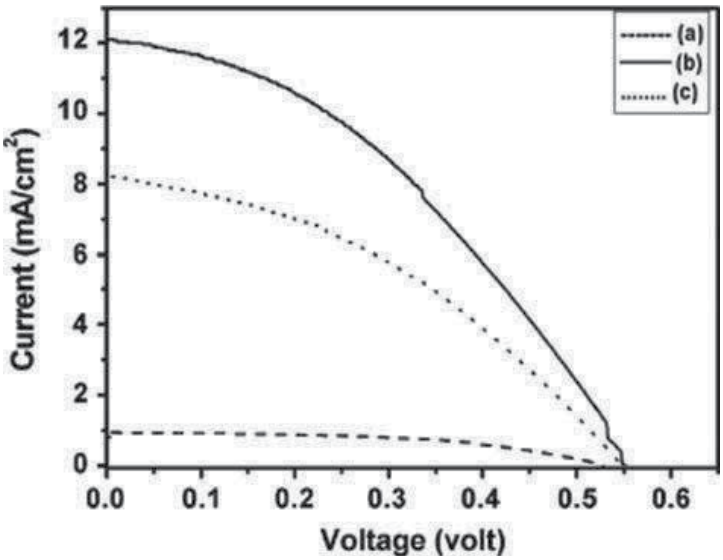


**Figure 16.** Current–voltage curve of DSSC fabricated with (a) ZnO–$NH_3$, (b) ZnO-citric, and (c) ZnO-oxalic at 1.5 AM. Reprinted with permission from [Akhtar., 2008], Electrochim. Acta 53, (2008) 7869.© 2008, Elsevier Ltd.

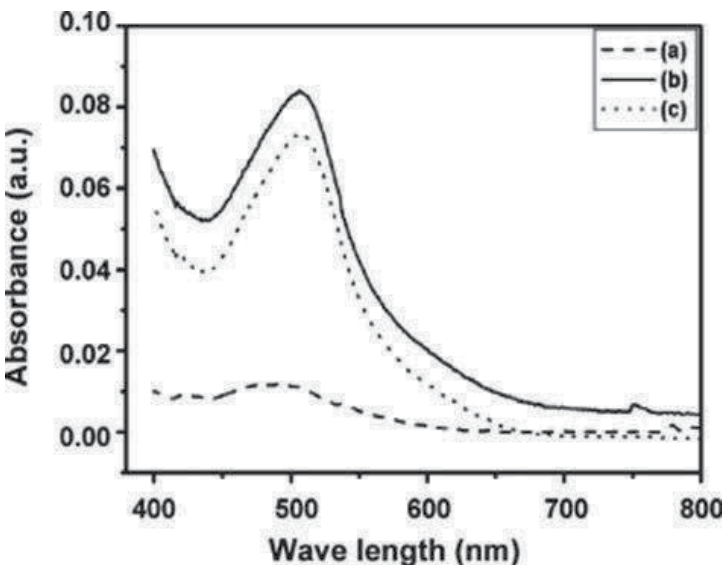


**Figure 17.** UV-vis absorption of dye (N-719) extracted with 2 M NaOH from the electrodes of (a) ZnO–$NH_3$, (b) ZnO-citric, and (c) ZnO-oxalic. Reprinted with permission from [Akhtar., 2008], Electrochim. Acta 53 (2008) 7869.© 2008, Elsevier Ltd.

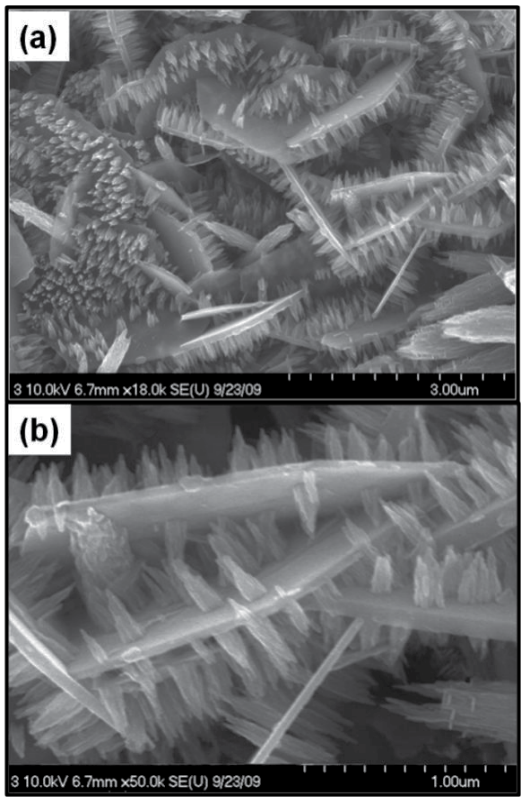


**Figure 18.** FESEM images of nanospikes decorated ZnO sheets (a) at low magnification and (b) at high magnification. [Ameen S., 2012], Chem. Eng. J. 195 (2012) 307©2012. Elsevier Ltd.

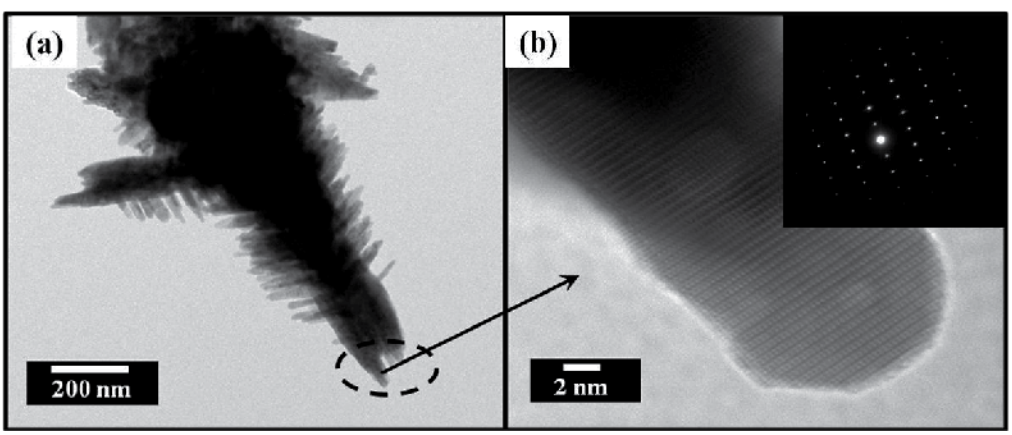


**Figure 19.** TEM image (a) and HR-TEM image (b) of grown nanospikes decorated ZnO sheets. Inset shows the corresponding SAED patterns of grown nanospikes decorated ZnO sheets. Reprinted with permission from [Ameen S., 2012], Chem. Eng. J. 195 (2012) 307 ©2012, Elsevier Ltd.

http://dx.doi.org/10.5772/51432

XRD patterns (Fig. 20 (a)) of the nanospikes decorated ZnO sheets obtain all the diffraction peaks appeared at 32.3° (100), 35.2° (002), 36.8° (101), 48.2° (102), 57.2° (110), 63.5° (103) and 66.2° (200) which are well matched with the JCPDS card No.36-1451. It confirms that the ZnO nanomaterials possess the hexagonal wurtzite phase with the lattice parameters: a-3.246 and c-5.206 Å. The intensity of (101) diffraction peak is much higher compared to other peaks, indicating the preferential growth direction due to the instability of polar (101) plane [101]. A single narrow absorption peak is observed near the UV region at ~376 nm in the UV-Vis absorbance spectrum of nanospikes decorated ZnO sheets structures (Fig. 20 (b)), corresponds to the characteristic band of the wurtzite hexagonal structure in bulk ZnO [102]. Moreover, the single peak suggests purity of the grown nanospikes decorated sheets morphology.

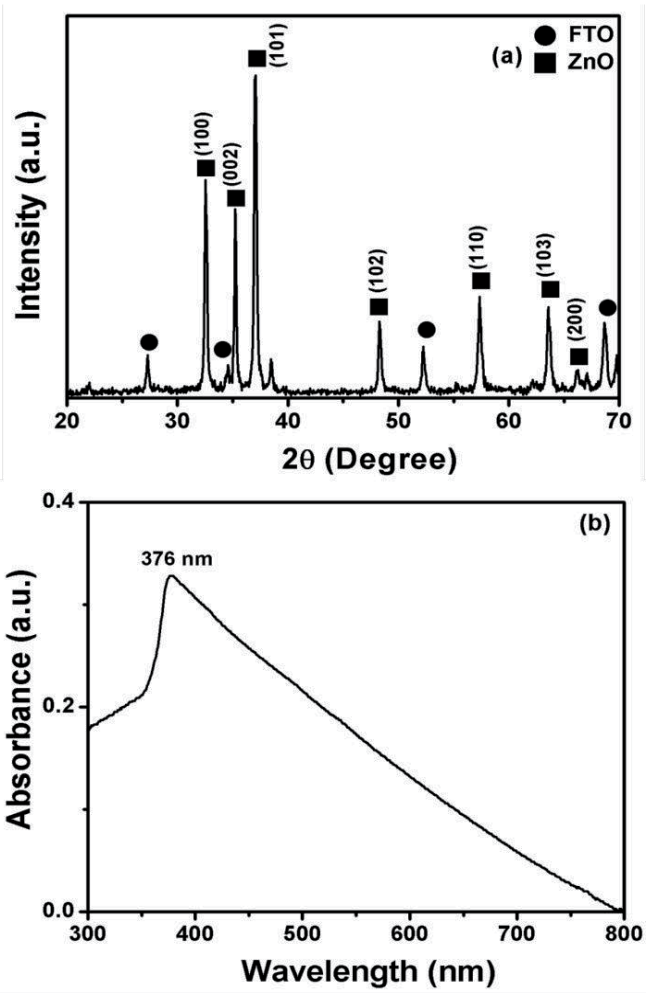


**Figure 20.** XRD patterns (a) and UV-Vis spectra (b) of nanospikes decorated ZnO sheets. Reprinted with permission from [Ameen S., 2012], Chem. Eng. J. 195 (2012) 307©2012, Elsevier Ltd.

The survey XPS spectrum (Fig. 21 (a)) of grown nanospikes decorated ZnO sheets shows the three strong binding energies of Zn $2p_{3/2}$, Zn $2p_{1/2}$ and O 1s along with small C 1s binding energy. The other binding energies peaks are not detected, indicating the presence of Zn and O without other impurities. However, the C1s binding energy at ~ 284.6 eV is usually used as calibration for other binding energies in the spectrum to avoid the specimen charging [103]. The Zn 2p spectrum of the doublet peaks with the binding energies of ~1021 eV and ~1045 eV are shown Fig 21(b), corresponding to Zn $2p_{3/2}$ and Zn $2p_{1/2}$ in better symmetry, respectively. These binding energies and the difference between two binding energies to ~24 eV are attributed to the typical lattice Zinc in ZnO [104]. The peak at ~1021 eV is associated with the $Zn^{2+}$ in ZnO wurzite structure [105]. Moreover, Zn 2p binding energy and the binding energy difference values confirm that Zn atoms are in +2 oxidation state in ZnO. The deconvolution of O 1s XPS spectrum (Fig. 21(c)) exhibits the main peak at ~528.3 eV along with three resolved peaks at ~529.2 eV, ~530.1 eV and ~531.1 eV. The higher and lower binding energy component at ~528.3 eV and ~529.2 eV are attributed to $O_2^-$ ions on the wurtzite structure of the hexagonal $Zn^{2+}$ ions [106]. Every $O_2^-$ ions are surrounded by Zn atoms with the full appreciation of nearest neighbor $O_2^-$ ions. The other binding energies at ~530.1 eV and ~531.1 eV are ascribed to few oxygen deficiency or oxygen vacancies within the ZnO materials. Therefore, highest binding energy of Zn 2p and O 1s spectra are associated with $Zn^{2+}$ and $O_2^-$ ions which form Zn-O bonds in ZnO crystals.

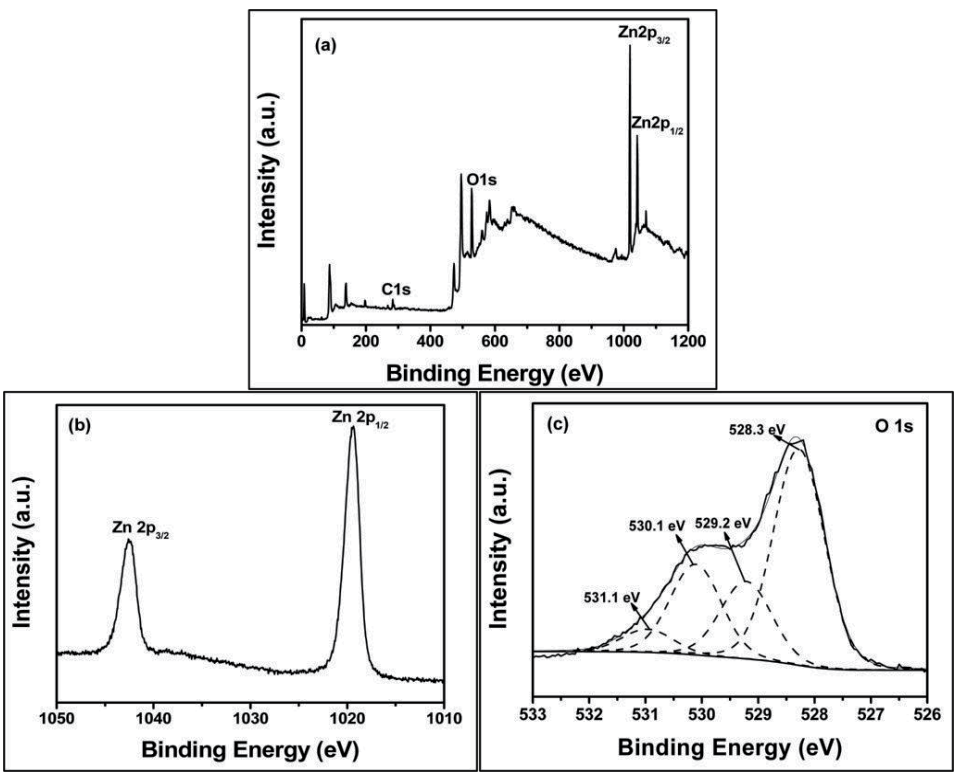


**Figure 21.** Survey (a), Zn 2p (b) and O 1s (c) XPS spectra of nanospikes decorated ZnO sheets. Reprinted with permission from [Ameen S., 2012], Chem. Eng. J. 195 (2012) 307 ©2012, Elsevier Ltd.

http://dx.doi.org/10.5772/51432

The J-V curve (Fig. 22(a)) of DSSC fabricated with nanospikes decorated ZnO sheets photoanodes is demonstrated under the light intensity of 100 mW/cm$^2$ (1.5 AM). The fabricated DSSC with the photoanode of nanospikes decorated ZnO sheets has achieved the overall conversion efficiency of ~2.51% with the reasonably high $J_{SC}$ of ~6.07 mA/cm$^2$, $V_{OC}$ of ~0.68 V and FF of ~0.60. The relatively high $J_{SC}$ is associated to high dye absorption through nanospikes decorated ZnO sheets morphology, resulting from the high amount of dye absorption (2.05 x10$^{-7}$ mol/cm$^2$) which is calculated by area integration of the maximum absorbance in the UV-Vis spectrum of desorbed dye from the photoanode (as shown in inset of Fig. 22(a)). The unique morphology of the prepared nanospikes decorated ZnO sheets might pronounce the charge collection and transfer properties of electrode due to the presence of standing spikes on the ZnO sheets [107]. The improved $V_{OC}$ and FF of DSSC might attribute to the reduced charge recombination and the series resistance by the photoanode of nanospikes decorated ZnO sheets. As compared to the reported DSSCs based on ZnO nanostructures photoanodes, the nanospikes decorated ZnO sheets photoanode based DSSC shows the significantly higher conversion efficiency and $J_{SC}$ [108]. It has been estimated that the conversion efficiency and $J_{SC}$ are enhanced by ~40% and ~25% as compared to reported values. In this case, the sheets morphology of ZnO display highly uniform and the standing nanospikes might considerably

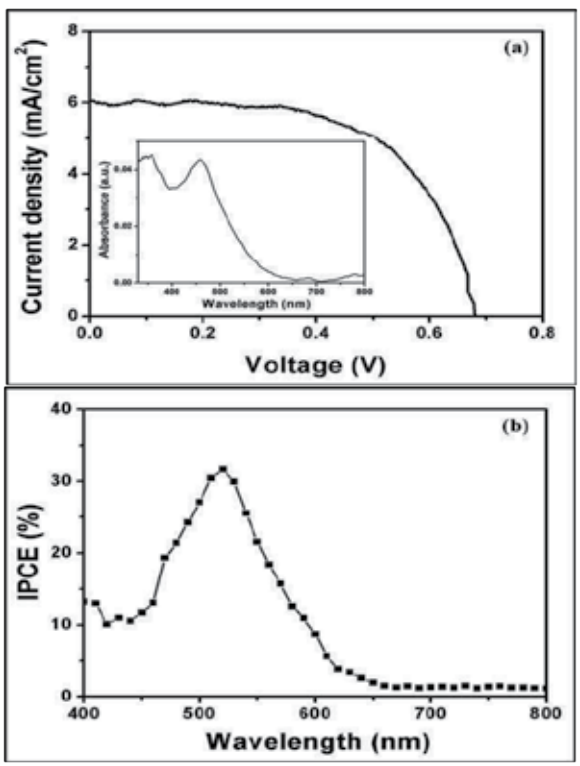


**Figure 22.** J-V curve (a) and IPCE (b) curve of the DSSC fabricated with nanospikes decorated ZnO sheets photoanode. Inset (a) shows the UV-Vis spectrum of desorbed dye from the nanospikes decorated ZnO sheets photoanode. Reprinted with permission from [Ameen S., 2012], Chem. Eng. J. 195 (2012) 307 ©2012, Elsevier Ltd.

facilitates the electrons transfer at the interface of the conduction and the electrolyte layer. The fabricated DSSC with photoanode of nanospikes decorated ZnO sheets attains the moderate IPCE of ~31.8%, as shown in Fig. 22 (b), which is probably originated from the larger amount of dye-loading through large surface area of sheet and the standing spikes of photoanode. Moreover, the presence of nanospikes on ZnO sheets might efficiently enhance the electron transport and reduces the recombination rate to high IPCE and $J_{SC}$ value 109].

## 7. Doping of ZnO for improved electrical and photovoltaic properties

One of the modifications is still in the developing stage called doping of ZnO nanomaterials by metals like F, Cu, Ag, Ga, Al, In, Sn and Sb which usually tailors the chemical, conductive and the electrical properties of ZnO nanomaterials [110]. The metal doping is an effective procedure to modify the grain size, orientation and the conductivity and could greatly influence the crystalline, optical and the electrical properties of the ZnO nanostructures. Among various metal doping, Sn-ion is recently known as promising dopant to ZnO nanomaterials for enhancing the electrical and optical properties [111]. Tsay et al. [112] prepared the Sn doped ZnO thin films coated glass substrates and investigated the effects of Sn doping on the crystallinity, microstructures and the optical properties of ZnO thin film. Several reports are available on the preparation of the Sn doped ZnO thin films and the effects of Sn doping on grain size, vibrational structure, optical and the structural properties of ZnO thin film substrates [113]. Ameen et al recently reported the doping of ZnO nanostructures with Sn ion by simple hydrothermal process for the fabrication of DSSC [114].

### 7.1. Sn doped ZnO nanostructures for solar cell performance

The synthesized ZnO and Sn-ZnO nanostructures are morphologically characterized by the FESEM images, as shown in Fig. 23. The ZnO nanostructure shows the irregular, non-uniform and highly aggregated nanoparticles with the average size of range ~150–200 nm. After Sn-ion doping, the ZnO nanostructures have dramatically arranged into the spindle shaped morphology and each Sn-ZnO spindle comprises of small aggregated nanoparticles with average size of 350 ±50 nm.

Fig. 24 (a, b) shows the high resolution TEM images of Sn-ZnO nanostructures which are completely consistent with FESEM observations. The aggregated ZnO nanoparticles arranged spindle shaped morphology is observed with some black spots or particles, clearly indicating the presence of the Sn-ions. The HR-TEM image of Sn-ZnO displays dark spots on the fringes which are expressed by the circles in Fig. 24(c). The morphological changes in Sn-ZnO nanostructures might due to the substantive influence of Sn-ion into ZnO nanostructures. The EDS spectrum (Fig. 24 (d)) obtains two high intense peaks (Zn & O) and single small peak (C) along with Sn peaks, again confirming the Sn-ion doping into the ZnO nanostructures.

From the UV-DRS spectra of ZnO and Sn-ZnO nanostructures (Fig. 25), the broad intense absorption edge from ~400 nm to lower wavelengths region is assigned to the charge-transfer process from the valence band to conduction band of ZnO [115]. After Sn-ion doping, the

http://dx.doi.org/10.5772/51432

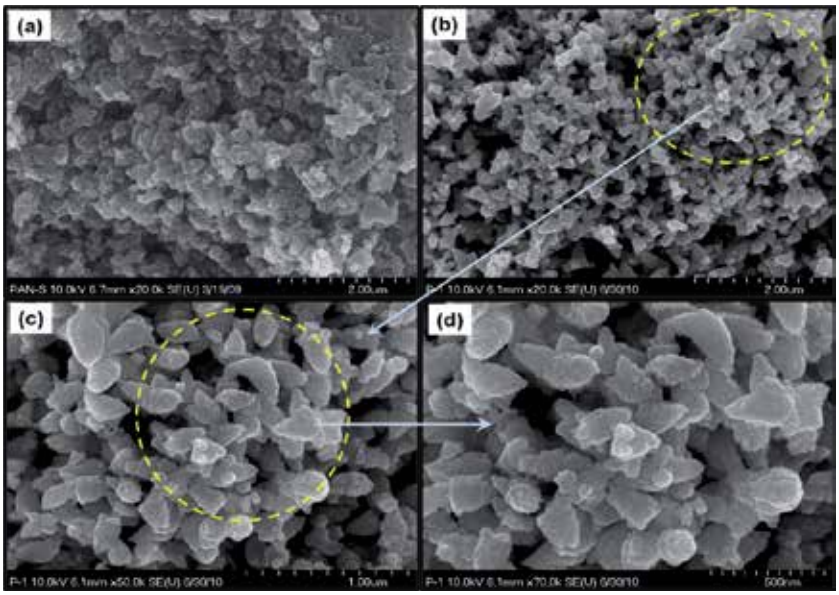


**Figure 23.** FESEM images of ZnO (a) and Sn-ZnO (b) nanostructures at low resolution, and FESEM images of Sn-ZnO nanostructures at high resolution (c and d). Reprinted with permission from [Ameen S., 2012], Chem. Eng. J. 187 (2012) 351 ©2012, Elsevier Ltd.

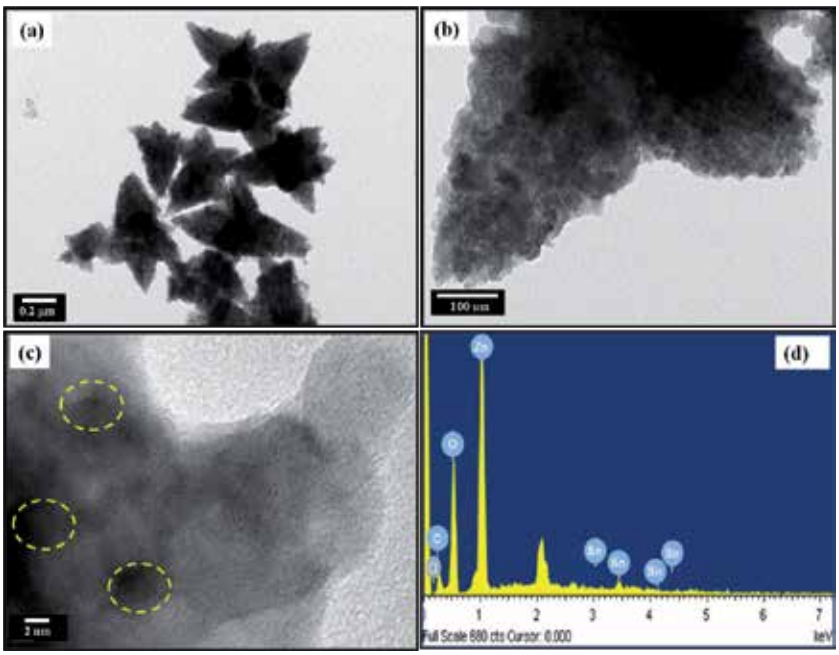


**Figure 24.** TEM images of Sn-ZnO nanostructures at low resolution (a and b), HRTEM image (c), and EDS spectrum of Sn-ZnO nanostructures (d). Reprinted with permission from [Ameen S., 2012], Chem. Eng. J. 187 (2012) 351 ©2012, Elsevier Ltd.

absorption wavelength of ZnO has significantly shifted from ~389 nm to ~406 nm and its band gap has changed from ~3.18 eV to ~3.05 eV. It has arisen due to the presence of interstitially embedded Sn-ion into ZnO nanomaterials. This small variation in band gaps again confirms the Sn-ion doping into ZnO nanomaterials.

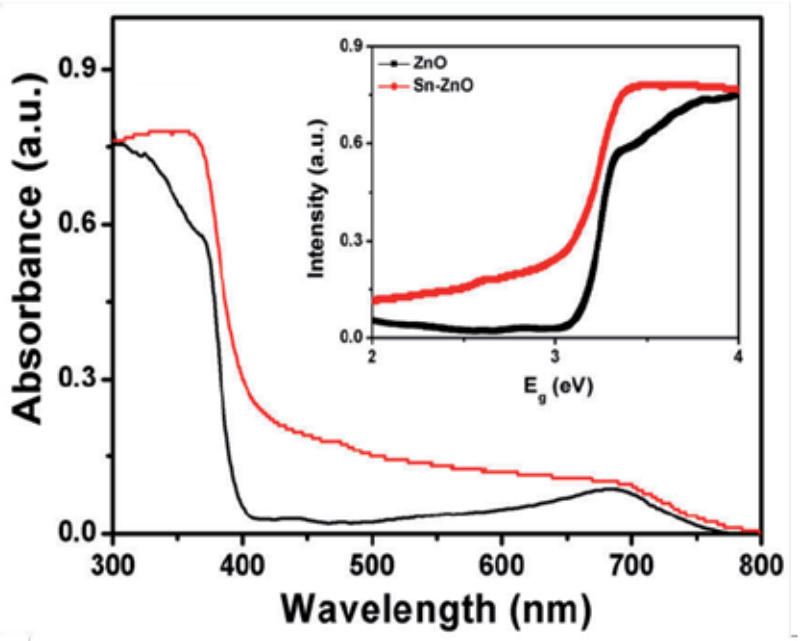


**Figure 25.** UV-DRS spectra of ZnO and Sn-ZnO nanostructures. Reprinted with permission from [Ameen S., 2012], Chem. Eng. J. 187 (2012) 351 ©2012, Elsevier Ltd.

The XPS survey (Fig. 26 (a)) spectrum displays all Zn 2p, O 1s and Sn 3d binding energy peaks with very small C 1s binding energy. Sn-ZnO nanomaterials show the doublet binding energies at ~1022.1 eV and ~1046.1 eV in Zn 2p XPS spectra (Fig. 26 (b)) which correspond to Zn $2p_{3/2}$ and Zn $2p_{1/2}$ respectively. The energy difference between doublet binding energies is calculated to ~24 eV, which is in excellent agreement with the standard value of ~22.97 eV. The deconvoluted O 1s XPS presents the four binding energies peaks at ~533.6 eV, ~532.4 eV, ~530.8 eV and ~529.1 eV, as shown in Fig. 26 (c). The highest binding energy at ~533.6 eV is originated from the oxygen atoms chemisorbed at the surface of synthesized materials [116]. The binding energy at ~532.4 e V is ascribed to $O_2^-$ ions (surface hydroxyl (OH) group) on the synthesized Sn-ZnO (in the oxygen deficient region) and the lowest binding energy at ~529.1 eV is attributed to $O_2^-$ ions in the Zn-O structures The binding energy at ~530.8 eV is attributed to oxidized metal ions in the synthesized Sn-ZnO such as, O-Sn and O-Zn in the ZnO lattice. Sn 3d spectra (Fig. 26 (d)) presents the doublet binding energies at ~487.2 eV and ~496.7 eV, correspond to Sn $3d_{5/2}$ and Sn $3d_{3/2}$ respectively. The appearance of these peaks indicates the incorporation of Sn dopant in the form of O-Sn in the ZnO lattice [117], as deduced by O 1s XPS results. Moreover, the energy gap of ~9.5 eV is

http://dx.doi.org/10.5772/51432

observed between these two peaks which resembles to the reported value [118]. It is observed that since no diffraction peaks corresponding to the SnO and $SnO_2$ are observed in the XRD spectra therefore, the O-Sn bonding could be considered as the substitutional doping of Sn-ions into the ZnO lattice.

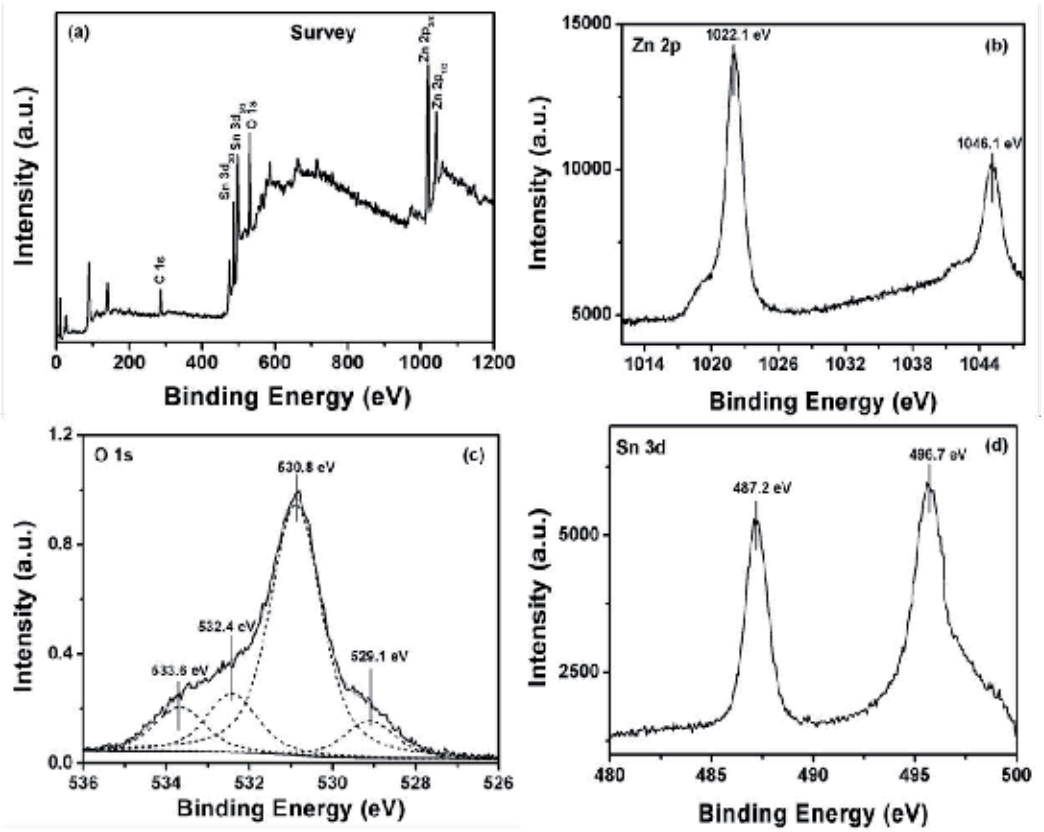


**Figure 26.** Survey (a), Zn 2p (b), O 1s (c), and Sn 3d (d) XPS spectra of Sn-ZnO nanostructures. Reprinted with permission from [Ameen S., 2012], Chem. Eng. J. 187 (2012) 351. ©2012, Elsevier Ltd.

DSSC fabricated (Fig. 27) with Sn-ZnO photoanode depicts reasonably high solar-to -electricity conversion efficiency of ~1.82% with $J_{SC}$ of 5.1 mA/cm$^2$, $V_{OC}$ of 0.786 V and FF of 0.45. While, DSSC with ZnO photoanode shows relatively low conversion efficiency of ~1.49% with $J_{SC}$ of ~4.05 mA/cm$^2$, $V_{OC}$ (~0.761 V) and FF of ~0.48. Noticeably, the conversion efficiency and $J_{SC}$ are considerably enhanced by ~20% and ~21% respectively after Sn-ion doping into ZnO nanostructures. Moreover, it could be explained that Sn-ZnO nanostructures might due to the increase of high charge collection and the transfer of electrons at the interface of Sn-ZnO and the electrolyte layer. The dopants like Sn, is known to enhance the electrons transport capacity and electron mobility of ZnO nanomaterials [119]. Moreover, the Sn-ion doping into ZnO nanostructures might increase the specific surface area by lowering the particle size and

arranging into spindle shaped morphology, which might contribute to high dye absorption. The increased photocurrent density and the improved photovoltaic performance might also result from high dye absorption and the improved electron transport by Sn-ZnO nanostructures, leading the enhancement in light harvesting efficiency and photo-excited electron transportation under sun light. Therefore, the arrangement of ZnO nanoparticles into Sn-ZnO spindle shaped, and good optical properties of Sn-ZnO are crucial to improve the conversion efficiency and the photocurrent density of the fabricated DSSCs.

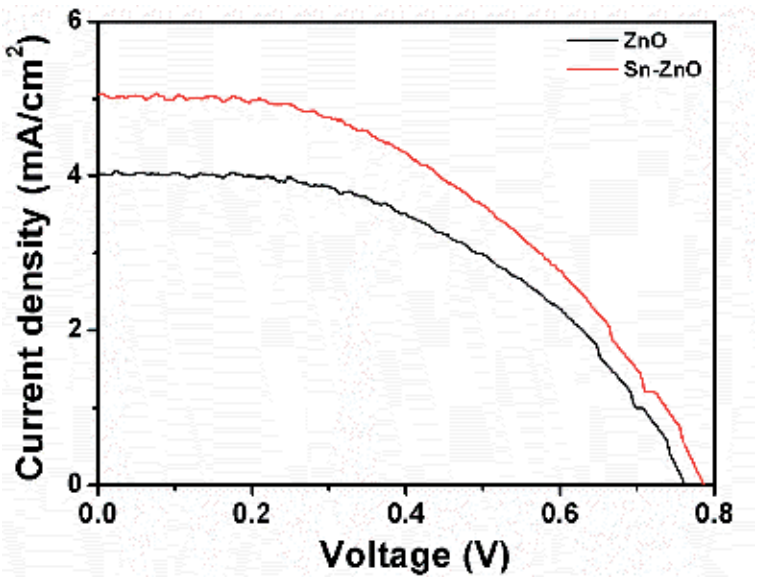


**Figure 27.** J-V curve of the DSSC fabricated with ZnO and Sn-ZnO nanostructures based photoanodes. Reprinted with permission from [Ameen S., 2012], Chem. Eng. J. 187 (2012) 351. ©2012, Elsevier Ltd.

### 7.2. Ga doped ZnO nanostructures with improved electrical properties

ZnO nanomaterials along with conjugated polymers like PANI, PPy and poly (3-alkylthiophene) comports the high quality organic/inorganic Schottky diodes [120]. Recently, ZnO-PANI films sandwiched between indium tin oxide (ITO) and a Pt electrode have displayed the linear I-V behavior [121]. The effects of Ga ion doping on ZnO NPs have been studied by Ameen et al on the basis of optical and electrical properties of the fabricated heterostructure devices [122]. The morphology of the synthesized ZnO and Ga-ZnO NPs were studied by FESEM and TEM analysis, as shown in Fig. 28 (a-d). The synthesized ZnO NPs obtain an average diameter of ~20–25 nm. After Ga ion doping, the average diameter increases to ~30–35 nm by the agglomeration of NPs due to entrapping and the substantive influence of Ga ion with ZnO NPs.

The optical properties of ZnO and Ga-doped ZnO NPs were studied by the UV-Vis spectra, as shown in Fig. 29 (a, b). ZnO and Ga-doped ZnO NPs present the absorption in the UV region with strong absorption peak at ~370 nm and ~378 nm respectively, corresponding to the

http://dx.doi.org/10.5772/51432

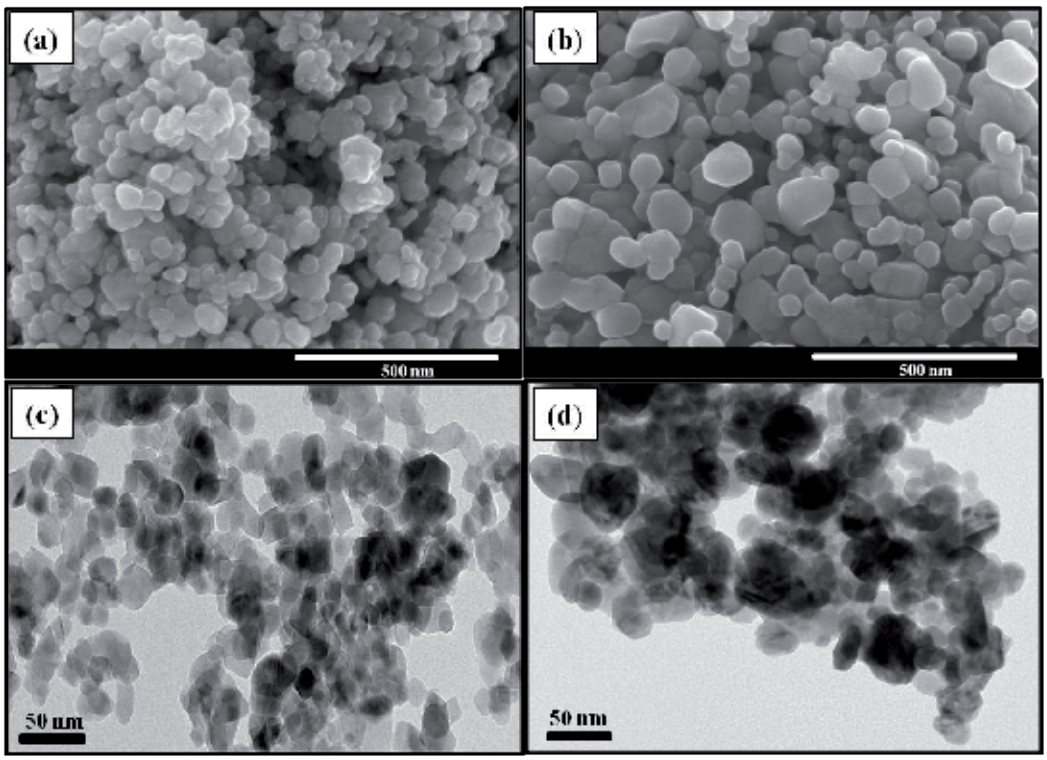


**Figure 28.** FESEM (a, b) and TEM (c, d) images of ZnO NPs and Ga-ZnO NPs. Reprinted with permission from [Ameen S., 2011], Microchim. Acta 172 (2011) 471. © 2012, Springerlink Ltd.

characteristic band of wurtzite hexagonal ZnO nanomaterials [123]. A considerable red shift from ~370 nm to ~378 nm after Ga ion doping is seen in the absorption peak of Ga-ZnO NPs and results that the band gap of ZnO NPs has changed from ~3.4 eV to ~3.26 eV due to the presence of interstitially embedded Ga ion on the surface of ZnO NPs. Thus, the small variation in band gaps again confirms the Ga doping on the surface of ZnO NPs.

Fig. 30 shows the XPS of PANI/Ga-ZnO thin film electrodes. The Carbon (C 1s), oxygen (O 1s), nitrogen (N 1s) and Zinc (Zn 2p) peaks at ~284.4 eV, ~529.8 eV, ~400.9 eV and ~1019.4/1042.5 eV are taken to investigate the interaction between PANI and Ga-ZnO NPs. The deconvoluted C 1s peak at ~284.4 eV presents four resolved peaks at ~289.1, ~286.8, ~285.7 eV and ~284.9 eV (Fig. 30 (a)) and are ascribed to C = O/C–O bond, C–$N^+$/C = $N^+$ bond, neutral C–C/C–H bond of PANI backbone and C of the benzonoid ring showing a combination of protonation of imine and amine sites via shake-up processes [124]. Figure 30(b) shows the four O 1s XPS resolved peaks of PANI/Ga-ZnO thin film. The main peak at ~529.8 eV confirms the nature of oxygen atom originated from metal oxide [125] i.e. the oxide of ZnO NPs. Zn 2p XPS of PANI/Ga-ZnO thin film typically exhibits the doublet peaks at ~1019.4 eV/1042.5 eV (Fig. 30 d), suggests that Zn atoms are linked with oxide bond in Ga doped ZnO NPs. Moreover, Fig. 30(e) shows the Ga 2p peak at ~1116.2 eV which confirms the doping of ZnO with the $Ga^{+2}$ oxidation state [126].

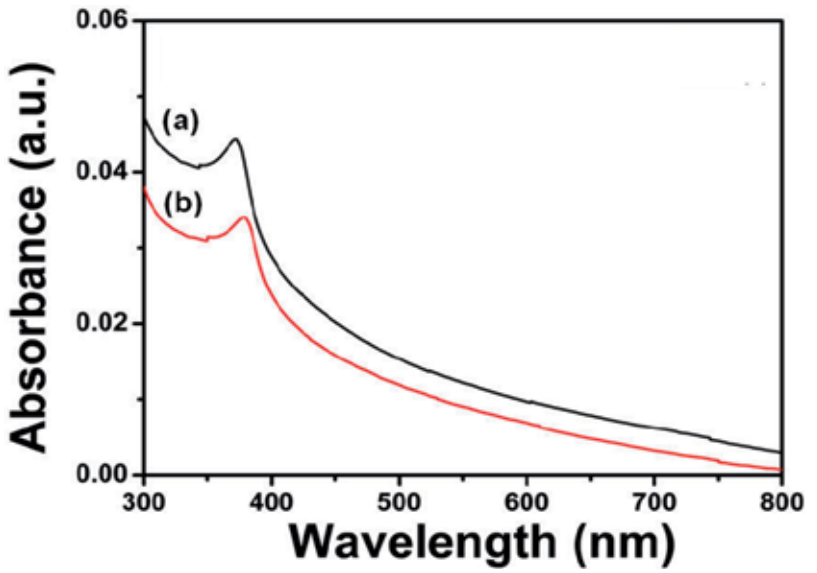


**Figure 29.** UV-Vis spectra of ZnO (a) and Ga-ZnO NPs (b). Reprinted with permission from [Ameen S., 2011], Microchim Acta 172 (2011) 471© 2012, Springerlink Ltd

N 1s XPS spectrum of PANI/Ga-ZnO thin film (Fig. 30(c)) exhibits the bonding between imine group of PANI and Ga-ZnO. The centered peak at ~400.9 eV ascribes quinoid di-imine nitrogen of PANI [127]. The main peak at ~400.9 eV is resolved into four hide peaks at ~400.5, ~401.3, ~401.9 and ~402.8 eV which correspond to benzenoid di-amine nitrogen, quinoid di-imine nitrogen, positively charged nitrogen ($-N^+$) and the protonated imine ($=N^+$) respectively. It is known that the protonation of PANI produces electronic defects such as polarons or bipolarons which might form by the addition of protons to the neutral polymer chain. In this case, positively shifted binding energy at ~401.9 and ~402.8 eV might exhibit the participation of protonated N atom for the bond formation between PANI and Ga-ZnO. These two charged nitrogen species ($-N^+$ and $=N^+$) are originated from these defect states [128] and are observed in N 1s results of PANI/Ga-ZnO thin film. In conclusion, the PANI and Ga-ZnO are interacted to each other by the formation of partial hydrogen bonding between two charged nitrogen species ($-N^+$ and $=N^+$) of PANI and surface hydroxyl of Ga-ZnO.

The I-V characteristics of Pt/PANI/ZnO and Pt/PANI/Ga-ZnO heterostructure devices are obtained at 298 K with applied voltage from −1 V to +1 V, shown in Fig. 31. Both the devices display non-linear and rectifying behavior of I–V curves due to the existence of Schottky barrier via a Schottky contact at the interfaces of Pt layer and PANI-ZnO thin film layer. Pt/PANI/ZnO device shows almost Ohmic or very weak rectifying behavior (Fig. 31(a)) that attains very low turn-on voltage (~0.0005 V) with least current (~0.002 mA). Similarly, in forward bias, a breakdown voltage (~0.05 V) and high leakage current (~0.015 mA) indicate poor I-V characteristics of Pt/PANI/ZnO device. Whereas, Pt/PANI/Ga-ZnO device (Fig. 31 (b)) presents

http://dx.doi.org/10.5772/51432

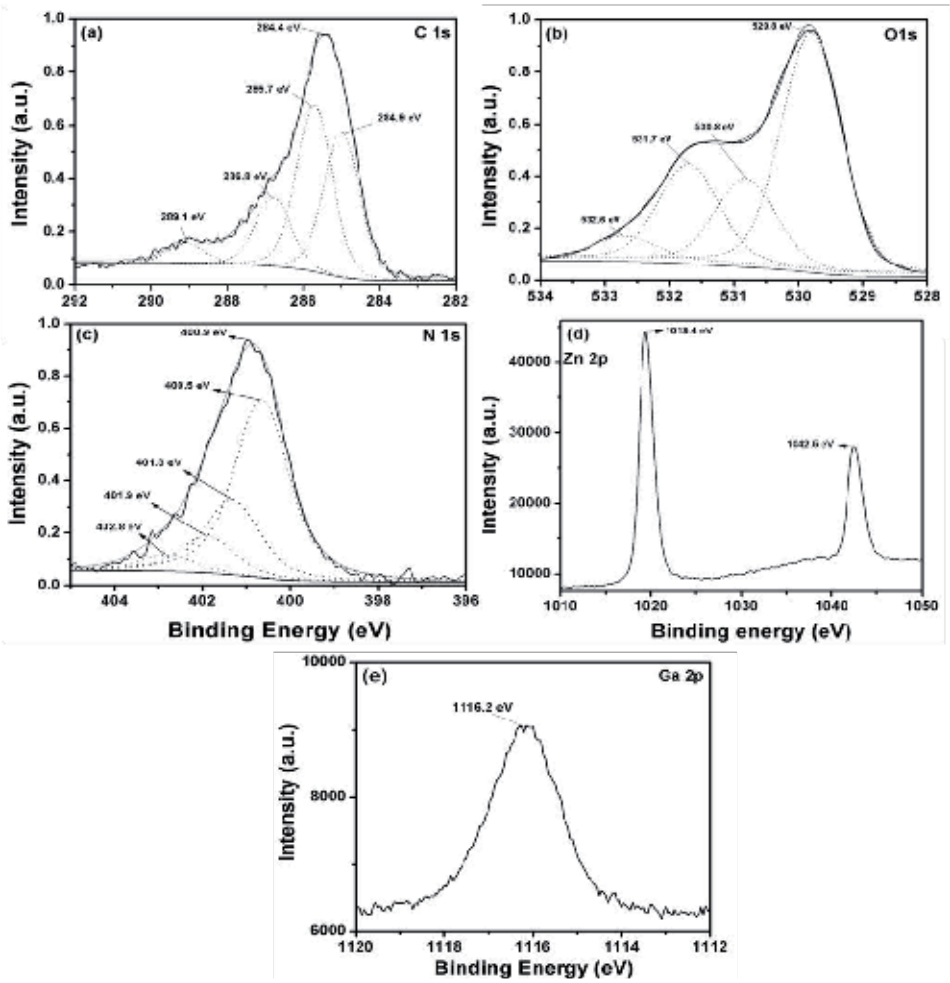


**Figure 30.** (a) C 1 s, (b) O 1 s, (c) N 1 s, (d) Zn 2p and (e) Ga 2p XPS spectra of PANI/Ga-ZnO thin film electrode. Reprinted with permission from [Ameen S., 2011], Microchim. Acta 172 (2011) 471©2012, Springerlink Ltd.

rectifying behavior of lower turn on voltage (~0.4 V) with least current (~0.09 mA) and breakdown voltage (~0.56 V) with high leakage current (~0.5 mA). The I-V properties of Pt/PANI/Ga-ZnO device are considerably better than the data reported elsewhere on PANI/ZnO and PANI based heterostructure devices [129]. Herein, the Ga ion doping to ZnO NPs might generate high density of minority charge carriers and the efficient charge movement at the junction of PANI and Ga-ZnO interfaces, resulting in the high leakage current with moderate turn on and breakdown voltage [130]. Additionally, the improved I-V properties might result from the molecular geometry of PANI chains and the increased electronic conduction by Ga ions in ZnO NPs which likely generate the hopping effect.

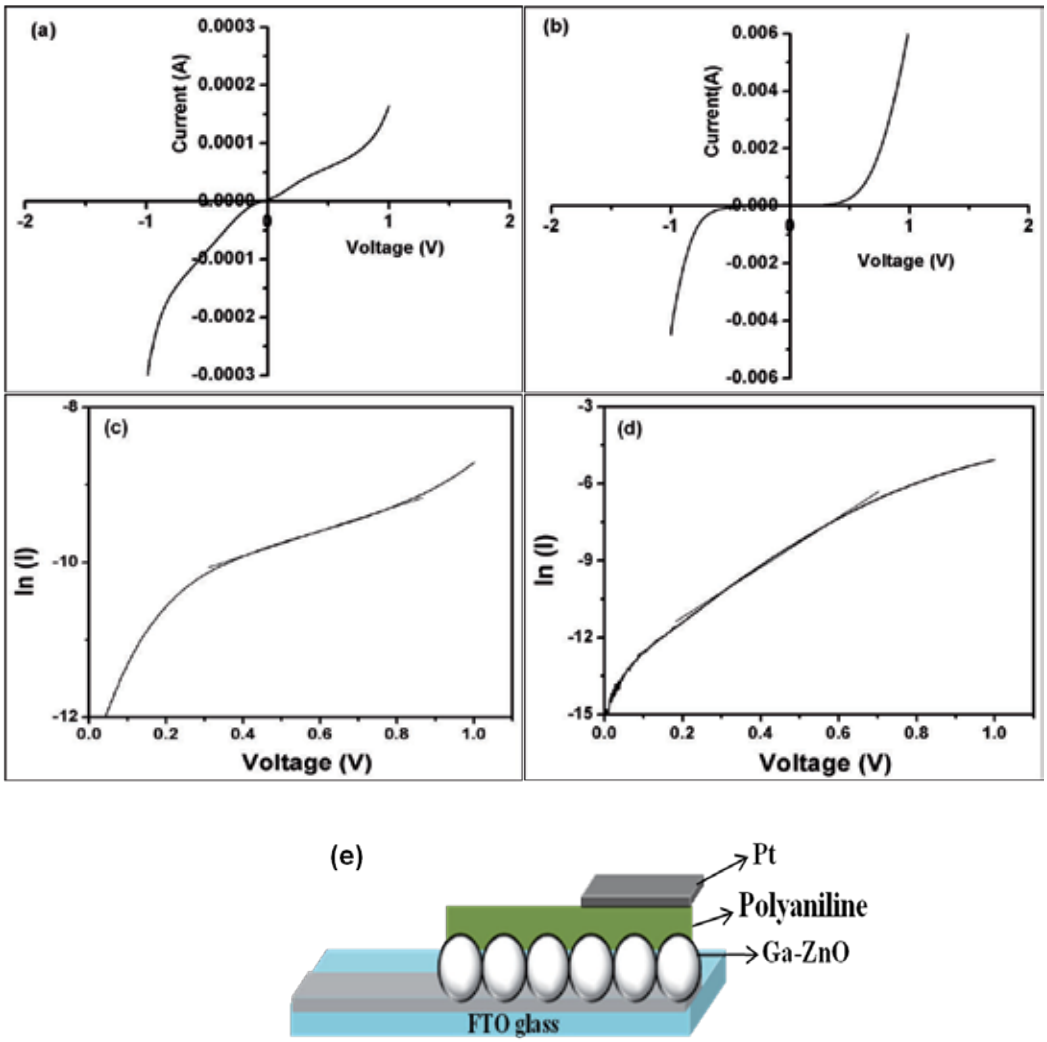


**Figure 31.** I-V characteristics of (a) Pt/PANI/ZnO (b) Pt/PANI/Ga- ZnO heterostructure device. ln(I) versus (V) plots of (c) Pt/PANI/ZnO and (d) Pt/PANI/Ga-ZnO heterostructure devices. (e) the schematic of Pt/PANI/Ga-ZnO heterostructure device. Reprinted with permission from [Ameen S., 2011], Microchim. Acta 172 (2011) 471©2012, Springerlink Ltd.

## 8. Metal oxides as nanofillers in polymer electrolytes

The inorganic semiconductor especially metal oxides nanomaterials as nanofillers are conceived to improve the mechanical, thermal, interfacial, and ionic conductivity properties of the polymer electrolytes, which could effectively utilize for high performance solid-state DSSCs. In general, the introduction of inorganic NPs in the polymer alters the conduction mechanisms,

http://dx.doi.org/10.5772/51432

which assigns to the ions conduction. In 1998, Croce et al. [131] studied the enhancement of the ionic conductivity of polymer electrolytes by the addition of $TiO_2$ and other NPs. Later, a ternary component polymer-gel electrolyte with $TiO_2$ NPs was prepared by Kang et al and explicated that these NPs led to a light-scattering effect [132]. The fabricated DSSC with the ternary component polymer electrolyte showed a high overall conversion efficiency of ~7.2% under 100 mW/cm$^2$. Falaras et al [133] developed the polymer composite electrolyte by the addition of commercial $TiO_2$ nanoparticles (NPs, P25, Degussa) consisted of polyethylene oxide (PEO), LiI, and $I_2$. The addition of $TiO_2$ NPs considerably prevented the re-crystallization and decreased the degree of crystallinity of PEO due to their large surface area. The differential scanning calorimetry (DSC) studies revealed that the introduction of $TiO_2$ NPs caused a significant increase in the glass transition temperature of PEO, which indicated the incorporation of the polymer to the inorganic oxide fillers. The fabricated DSSCs with $TiO_2$-PEO nanocomposite electrolyte achieved a reasonably high overall conversion efficiency of ~4.2% with a $J_{SC}$ of ~7.2 mA/cm$^2$, $V_{OC}$ ~0.664 V, and FF ~0.58 at ~65.6 mW/cm$^2$ [134]. Additionally, other research groups have also used $TiO_2$ NPs as nanofillers and explained the effects of nanofillers on different polymer electrolytes. Recently, Akhtar et al [135] reported a composite electrolyte of polyethylene glycol methyl ether (PEGME) and $TiO_2$ NPs and demonstrated the heat treatment effects on the properties of PEGME-$TiO_2$ composite electrolyte. It was found that the heat treatment was an essential step to improve morphology, amorphicity, and ionic conductivity of PEGME-$TiO_2$ composite electrolytes. From AFM images (Fig. 32), $TiO_2$ particles with ~20-30 nm size are well distributed on the PEGME matrix in the case of PEGME-$TiO_2$ composite film (Fig. 32(a). However, $TiO_2$ particles are aggregated and become a bigger size (40-60 nm) on the polymer matrix in PEGME-$TiO_2$/80$^o$C (Fig. 32 (b)). From the film roughness analysis (Fig. 32 (c, d)), it is observed that the surface roughness of the PEGME-$TiO_2$/80$^o$C and PEGME-$TiO_2$ composites are estimated to be about ~23.1 nm and ~18.5 nm for the root mean square roughness ($R_{rms}$), and ~12 nm and 8~.8 nm for the average surface roughness ($R_a$), respectively. Generally, it has been well known that the low surface roughness of the polymer composite film is ascribed to the high-crystallized surface of thr composite materials. Therefore, the crystallinity of PEGME-$TiO_2$/80$^o$C might lower than PEGME-$TiO_2$ because the former exhibits the higher $R_{rms}$ and $R_a$ value than later composite film. Consistently, the 3D AFM images (Fig. 32 (d)) of PEGME-$TiO_2$/80$^o$C exhibit a highly rough surface morphology with non-uniformly distributed $TiO_2$ particles into the PEGME matrix, while a highly uniform and less rough surface is observed in PEGME-$TiO_2$ composite film before heating (Fig. 32 (c)). This rough morphology of PEGME-$TiO_2$/80$^o$C might create free spaces and voids in which the $I^-/I_3^-$ ions could easily migrate, which suggest the PEGME-$TiO_2$/80$^o$C as excellent electrolyte materials. With the improved morphology of PEGME-$TiO_2$ composite, the electrolyte shows the high ionic conductivity of ~1.9 mS/cm as compared to the PEGME acid (1.2 mS/cm) and PEGME-$TiO_2$ (0.92 mS/cm) which results from the enhanced morphological properties in terms of high roughness and amorphicity after heating of PEGME-$TiO_2$. The Raman spectra (Fig. 33) of the PEGME-acid, PEGME-$TiO_2$, and PEGME-$TiO_2$/80$^o$C composite electrolytes exhibit a significant peak at the range of 110-115 cm$^{-1}$, which is ascribed to the symmetric stretch of $I_3^-$ species in redox electrolytes [136]. The heat treatment on PEGME-$TiO_2$ drastically increased the strong Raman peak, indicating a significant increase in the amount of $I_3^-$ species in redox

electrolytes. It might attribute to the increased bond strength between PEGME and $TiO_2$ and high roughness of the composite materials, which might help to absorb a large amount of the iodide couple as compared to PEGME-acid and PEGME-$TiO_2$ composite electrolytes. The increased intensity of peak suggests that a large amount of $I_3^-$ species is formed in the PEGME-$TiO_2$/80°C composite electrolyte upon heat treatment. In general, the diffusional $I^-/I_3^-$ ions migration in the redox electrolyte is responsible for the ionic conductivity of electrolyte, which causes electron exchange between ions by electronic conduction process [137]. The electronic conduction in redox electrolyte depends on the formation of $I_3^-$ ions. Raman results show the proportional relation between the ionic conductivity and concentration of $I_3^-$ species of the composite electrolytes, which is directly related to relative intensity of Raman peak. The enhanced ionic conductivity of PEGME-$TiO_2$/80°C composite electrolyte might associate with the formation of high $I_3^-$ species in redox electrolyte. However, low ionic conductivity in PEGME-acid and PEGME-$TiO_2$ composite electrolyte results from the low relative intensity of the Raman peak and less formation of $I_3^-$ species in redox electrolyte. Therefore, a heat treatment step plays an essential role to prepare the improved composite electrolyte with enhanced ionic conductivity. DSSC fabricated with PEGME-$TiO_2$/80°C composite electrolyte shows the maximum overall conversion efficiency of ~3.1% with a $J_{SC}$ of ~8.9 mA/cm$^2$, $V_{OC}$ of ~0.625 volt, and FF of ~56.2%. The conversion efficiency and $J_{SC}$ of DSSCs with PEGME-$TiO_2$/80°C composite electrolytes is higher than those of fabricated with PEGME-acid (~1.3%) and PEGME-$TiO_2$ (~2.4%) electrolytes. This could be expected from the enhanced ionic conductivity and enlargement of the amorphous phase of the polymer upon heat treatment. The heat treatment on PEGME-$TiO_2$ composites enhances the ionic conductivity and cross-linking properties of composite electrolyte, which are essential factors to achieve the high current density and high PV performance. Furthermore, Akhtar et al [138] investigated the effect of titania nanotubes (NTs) as nanofillers on the properties of PEG-based electrolytes and fabricated solid-state DSSCs. PEG-TiNT electrolytes with 10% of TiNTs exhibit the high penetration and complete filling into the pores of the $TiO_2$ film, as shown in Fig. 34. The XPS studies (Fig. 35) were carried out to elucidate the strong interaction between PEG and TiNTs. PEG-TiNT10 electrolyte shows the highest interaction between the titanium atoms of the NTs and the polymer network as compared to those of other PEG-TiNTs electrolytes. This results to the decrease in the crystallinity degree of the polymer after introduction of the NTs which achieves the highest ionic conductivity of ~$2.4\times10^{-3}$ S/cm. DSSC fabricated with PEG-TiNT composite electrolyte (Fig. 36) exhibits the maximum overall conversion efficiency of ~4.4% with $J_{SC}$ of ~9.4 mA/cm$^2$, $V_{OC}$ of ~0.73 V, and FF of ~0.65 under 100 mW/cm$^2$ irradiation. No significant decrease of the conversion efficiency for 30 days was observed in DSSCs fabricated with PEG-TiNT10 (inset of Fig. 36), indicating the high stability of the composite electrolytes. The lower current density in PEG-TiNT20 is due to its lower ion conductivity, lower penetration, and weak interaction between PEG to TiNTs. It is proved that the better penetration into the pores of the $TiO_2$ layer was obtained at a ratio of TiNT and PEG in the composite electrolyte (PEG-TiNT10). Thus, due to the better interfacial contact between the electrolyte and $TiO_2$ layer, high ion conductivity is obtained, which enhances the photocurrent density. Moreover, the PEG-TiNT composite electrolytes might facilitate the movement of electrons in the redox ($I^-/I_3^-$) couple due to the fast electron transfer characteristics of NTs with less grain-boundary,

http://dx.doi.org/10.5772/51432

in comparison to NPs. The other metal oxide nanomaterials, such as ZnO, $SiO_2$ and $Al_2O_3$, have been introduced as nanofillers to different polymer electrolytes [139]. Caruso et al. prepared the polymer composite electrolyte with the composition of PEO-poly (vinylidenefluoride) (PVDF) and $SiO_2$ NPs and applied as a solid electrolyte for solid-state DSSCs [140]. These kinds of solid state electrolytes presented high viscosity to the solid state electrolyte with $TiO_2$-based polymer composites. They used a vacuum technique for introducing the composite polymer electrolytes into the dye-sensitized $TiO_2$ electrode which showed that the vacuum method exhibited a better performance than those prepared via the conventional drop casting method. This approach improved the fulfilling of the photoelectrode with a solid electrolyte by vacuum technique, but the optimization of the electrolyte composition is still an important issue. In this regards, Xia et al utilized ZnO NPs as nanofillers for preparing the composite polymeric electrolyte of poly (ethylene glycol methyl ether) (PEGME) [141]. The PEGME was first grafted onto the surface of ZnO NPs through covalent bond formation by a chemical process. The solid composite electrolyte consisted of KI and $I_2$ dissolved in PEGME and ~24 wt% of the polymer-grafted ZnO NPs. The obtained prepared electrolyte showed that the ionic conductivity increased as the salt concentration increased and reached a maximum value of ~$3.3\times10^{-4}$ S/cm and then decreased, acting as a classical polymer electrolyte system. DSSC fabricated with polymer-grafted NPs electrolyte presented the lower conversion efficiency of ~3.1% compared to that of DSSC with a liquid electrolyte (~4.0%). After the addition of polymer-grafted ZnO NPs in liquid electrolyte, the $V_{OC}$ of DSSC increased by ~0.13 V while the $J_{SC}$ decreased, this was probably due to the high viscosity of the gel electrolyte. Another report addressed the new polymer electrolyte system of $Al_2O_3$ NPs with different sizes and a PVDF derivative and polyacrylonitrile in an ionic-liquid-based electrolyte [142]. The diffusion coefficient of $I_3^-$ ions altered by the addition $Al_2O_3$ NPs. The variation in sizes of $Al_2O_3$ NPs greatly influenced the charge transfer rate at the electrolyte and semiconducting layer interfaces. In this report, the imidazolium cations might adsorb on the NP surface, which might help in the charge transfer at counter and anions $I^-/I_3^-$ gather around them. Some researchers have recently used clay-like NPs as nanofillers in the polymer electrolytes and applied to the DSSCs [143]. Nogueira et al. [144] examined the incorporation of a montmorillonite (MMT) derivative to a polymer electrolyte based on a poly-(ethylene oxide) copolymer, the plasticizer GBL, and Li $I/I_2$. The improved ionic conductivity of the composite electrolyte attributed to the large number of charge carriers introduced into the complex after the addition of the clay. The addition of 5 wt % MMT promoted the increase in the mechanical stability of the nanocomposite polymer electrolyte film, resulted in the lower deformation as compared to the film without any clay. From their observations, it was found that the addition of MMT clay to the plasticized polymer electrolyte not only increased the ionic conductivity but also improved the solidification of the electrolyte. These improvements led to the mechanical stability of the polymer composite films and the stability of DSSCs as well. DSSCs fabricated with the nanocomposites polymer electrolyte showed reasonable conversion efficiencies of ~1.6% and ~3.2% at 100 mW/cm$^2$ and 10 mW/cm$^2$, respectively. The device presented very poor FF values of ~0.40 at 100 mW/cm$^2$, which was attributed to the low penetration of the composite electrolyte into the pores of the $TiO_2$ film. The MMT clay as nanofillers was also used by Lin et al. They prepared the nano-composites of poly (nisopropylacrylamide) with MMT clay to a liquid electrolyte system as a

gelator and applied as solid polymer electrolyte. The poly (nisopropylacrylamide)-MMT electrolyte-based DSSC achieved a relatively high conversion efficiency of ~5.4% with a $J_{SC}$ of ~12.6 mA/cm$^2$, $V_{OC}$ of ~0.73 V, and FF of ~0.59, whereas the DSSC prepared with the electrolyte gelled with the pure polymer presented lower photovoltaic parameters of $J_{SC}$ (~7.28 mA/cm$^2$), $V_{OC}$ (~0.72 V), FF (0.60), and conversion efficiency (~3.2%) at 100 mW/cm$^2$. From the electrochemical impedance spectroscopy, a considerable decrease in impedance values was observed by DSSC fabricated with nanocomposite-gelled electrolyte. The impedance at the electrolyte/dye-coated $TiO_2$ interface, and the Nernstian diffusion within the electrolytes were decreased, resulted in the high photocurrent density leading to the high performance of DSSCs. They also investigated the molar conductivity of the nanocomposite-gelled electrolytes to explain the high ionic conductivity and improved electrochemical behavior of electrolyte.

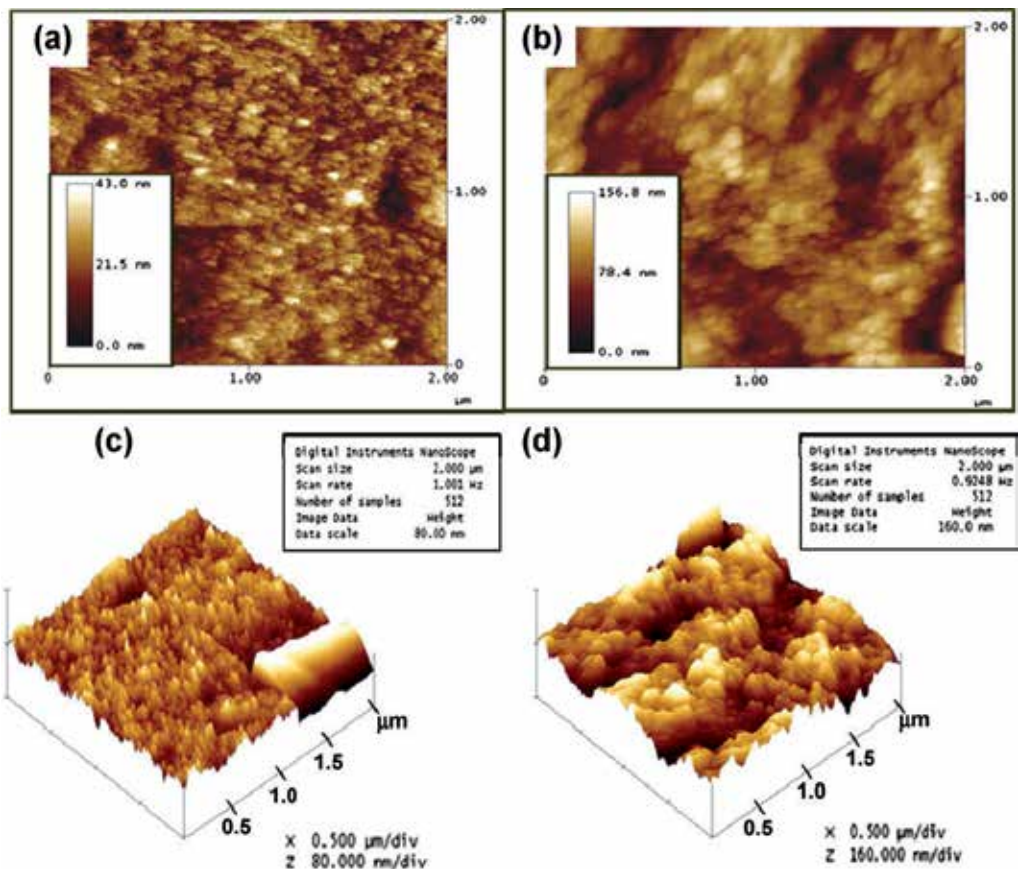


**Figure 32.** Topographic and three-dimensional AFM images of (a), (c) PEGME-$TiO_2$ and (b), (d) PEGME$TiO_2$/80C. Reprinted with permission from [Akhtar, 2011], Mater. Chem. Phys. 127 (2011) 479.© 2011, Elsevier Ltd.

http://dx.doi.org/10.5772/51432

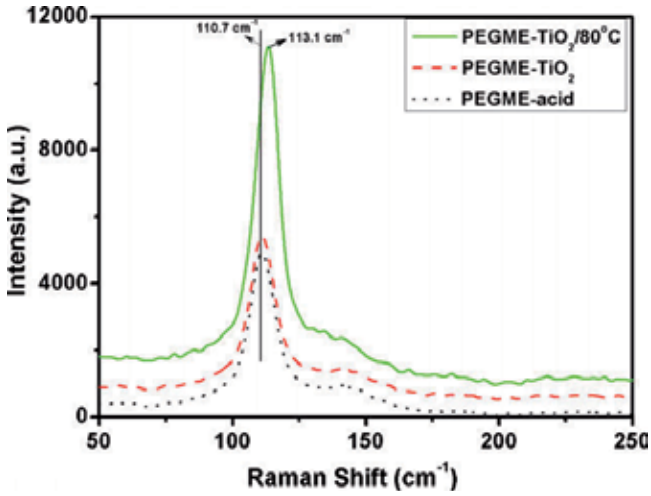


**Figure 33.** Raman spectra of PEGME-acid, PEGME–$TiO_2$ and PEGME–$TiO_2$/80 ∘C composite electrolytes. Reprinted with permission from [Akhtar., 2011], Mater. Chem. Phys. 127 (2011) 479. © 2011, Elsevier Ltd.

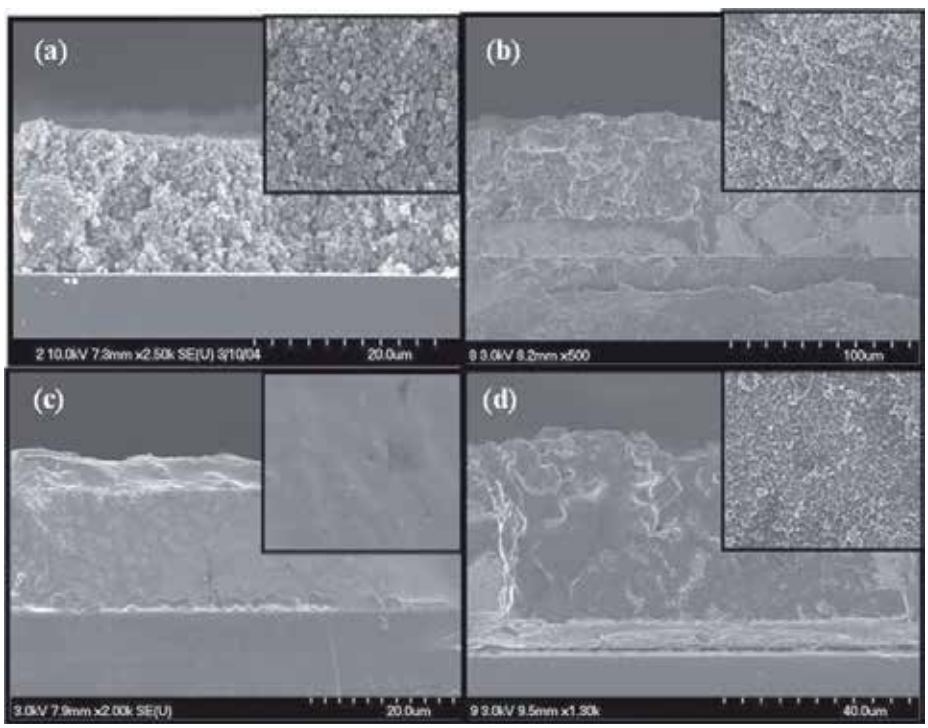


**Figure 34.** Cross-section and top view (inset) FE-SEM images of the TiO2 thin film (a) before electrolyte filling and after introducing composite electrolytes of (b) PEG-TiNT5, (c) PEG-TiNT10, and (d) PEG-TiNT20. Reprinted with permission from [Akhtar., 2007], Electrochem. Commun. 9 (2007) 2833.© 2007, Elsevier Ltd.

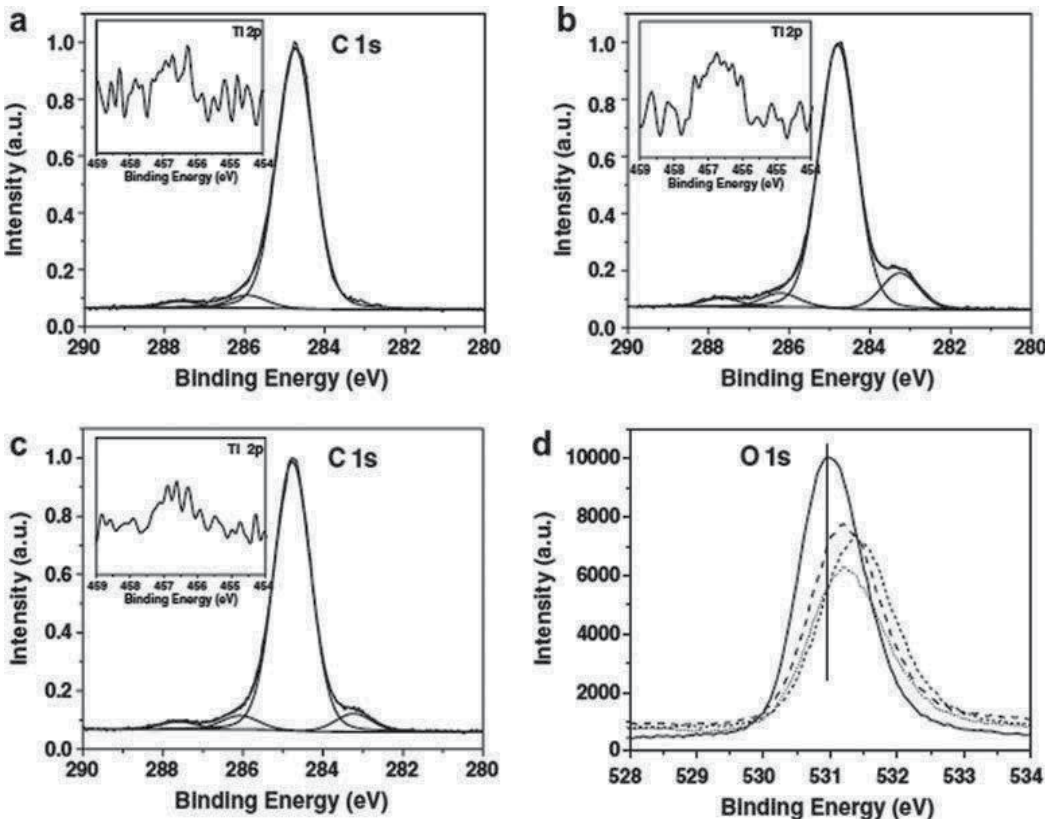


**Figure 35.** XPS spectra of the composite electrolytes. (a) PEG-TiNT5, (b) PEG-TiNT10, (c) PEG-TiNT20, and (d) O 1 s of PEG (—), PEG-TiNT5 (- - - -) PEG-TiNT10 (…..) and PEG-TiNT20 (-.-.-). Reprinted with permission from [Akhtar., 2007], Electrochem. Commun. 9 (2007) 2833.© 2007, Elsevier Ltd.

http://dx.doi.org/10.5772/51432

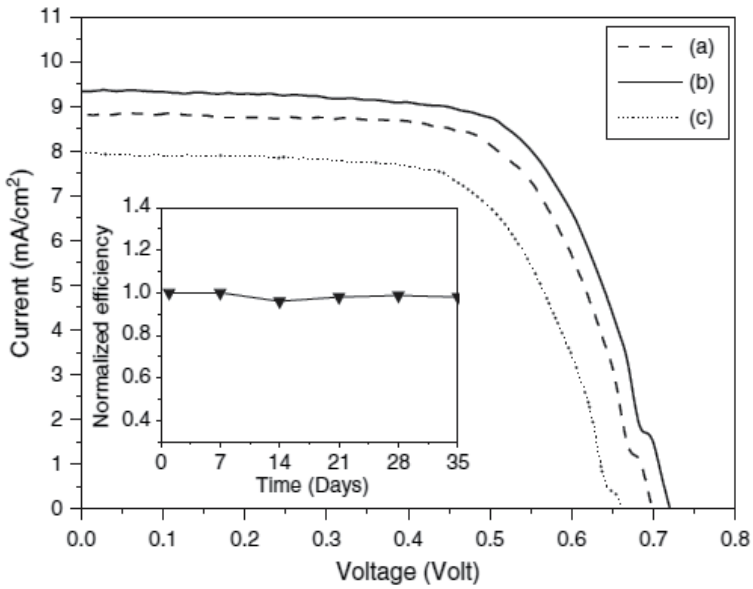


**Figure 36.** Current–voltage characteristics of DSSC fabricated with composite electrolytes of (a) PEG-TiNT5, (b) PEG-TiNT10, and (c) PEG-TiNT20. Inset shows the stability test of DSSC fabricated with composite electrolyte of PEG-TiNT10. Reprinted with permission from [Akhtar, 2007], Electrochem. Commun. 9 (2007) 2833.© 2007, Elsevier Ltd.

## 9. Conclusions

In summary, the morphological, structural, crystalline, optical, electrical and photovoltaic properties of conducting polymers, nanocomposites of conducting polymer/inorganic nanomaterials and semiconducting metal oxides have been discussed. The PANI nanocomposites with semiconducting materials have shown the improved penetration and optoelectronic properties, and applied for the electrical and electronic application such as diodes and solar cells. Here, the uniform distribution of CdS nanomaterials effectively improves the electronic state of PANI like polarons and bipolarons for the high charge carriers and enhances the charge transfer. The unique conducting polymers, particularly PANI nanomaterials have been used as hole transporting material and as counter electrodes for the applications of DSSCs. The metal oxide semiconducting nanomaterials, particularly $TiO_2$ and ZnO nanomaterials, in terms of morphology, surface properties, dye absorption and application in DSSCs are extensively summarized. Various morphologies of metal oxides nanostructures greatly affect the performances of dye absorption, electrical, electrochemical, and photovoltaic devices. The metal oxides semiconducting nanomaterials with different morphologies and sizes enhance the surface-to-volume ratio and produce the highly advanced photoanodes for the efficient DSSCs. The morphologies of metal oxides semiconducting considerably influence the dye absorption, light harvesting and results in increased electron transfer and reduce the recom-

bination rate during the operation of DSSCs. The photovoltaic properties such as $J_{SC}$, $V_{OC}$, FF, and conversion efficiency have significantly improved by altering the sizes and shapes of the metal oxides semiconductors. The chapter also summarizes the use of various metal oxide semiconducting nanomaterials as nanofillers in polymer electrolytes and describes their effect on the properties of polymer electrolytes and the performances of DSSCs. The introduction of metal oxide semiconducting nanomaterials into the polymer matrix has significantly improved the amorphicity, mechanical, thermal and ionic conductivity of polymer electrolytes. The chapter includes some of the polymer composite electrolytes and their photovoltaic properties for DSSCs.

## Author details

Sadia Ameen[1], M. Shaheer Akhtar[2], Minwu Song[1] and Hyung Shik Shin[1]

1 Energy Materials & Surface Science Laboratory, Solar Energy Research Center, School of Chemical Engineering, Chonbuk National University, Jeonju, Republic of Korea

2 New and Renewable Energy Material Development Center (NewREC), Chonbuk National University, Jeonbuk, Republic of Korea

## References

[1] Shirakawa H. The discovery of polyacetylene film: the dawning of an era of conducting polymers. Angewandte Chemie International Edition 2001;40:2575–2580.

[2] MacDiarmid AG. Synthetic metals: a novel role for organic polymers. Angewandte Chemie International Edition 2001; 40:2581–2590.

[3] Gerard M, Chaubey A, Malhotra BD. Biosens. Application of conducting polymers to biosensors. Biosensors and Bioelectronics 2002;17:345-359.

[4] Friend RH, Gymer RW, Holmes AB, Burroughes JH, Marks RN, Taliani C, Bradley DD C, Santos DA, Brédas JL, Lögdlund M, Salaneck WR. Electroluminescence in conjugated polymers. Nature 1999; 397:121-128.

[5] Sirringhaus H, Tessler N, Friend RH. Integrated Optoelectronic Devices based on. Conjugated Polymers. Science 1998; 280:1741-1744.

[6] Morrin A, Wilbeer F, Ngamna O, Moulton SE, Killard AJ, Wallace GG, Novel biosensor fabrication methodology based on processable conducting polyaniline nanoparticles. Electrochemistry Communication 2005; 7:317-322.

[7] Jang J, Bae J, Lee K. Synthesis and characterization of polyaniline nanorods as curing agent and nanofiller for epoxy matrix composite, Polymer 2005;46:3677-3684.

[8] Plesu N, Ilia G, Pascariu A, Vlase G. Preparation, degradation of polyaniline doped with organic phosphorus acids and corrosion essays of poly aniline-acrylic blends. Synthetic Metals 2006; 156:230-238.

[9] Han DH, Lee HJ, Park SM. Electrochemistry of conductive polymers XXXV: Electrical and morphological characteristics of polypyrrole films prepared in aqueous media studied by current sensing atomic force microscopy. Electrochimica Acta 2005;50:3085-3092.

[10] Johanson U, Marandi A, Tamm T, Tamm J. Comparative study of the behavior of anions in polypyrrole films. Electrochimica Acta 2005;50:1523-1528.

[11] Krivan E, Peintler G, Visy C. Matrix rank analysis of spectral studies on the electropolymerisation and discharge process of conducting polypyrrole/dodecyl sulfate films. Electrochimica Acta 2005;50:1529-1535.

[12] Chehimi MM, Abel ML, Perruchot C, Delamar M, Lascelles SF, Armes SP. The determination of the surface energy of conducting polymers by inverse gas chromatography at infinite dilution. Synthetic Metals 1999;104:51-59.

[13] Khomenko VG, Barsukov VZ, Katashinskii AS. The catalytic activity of conducting polymers toward oxygen reduction. Electrochimica Acta 2005;50:1675-1683.

[14] Hien NTL, Garcia B, Pailleret A, Deslouis C. Role of doping ions in the corrosion protection of iron by polypyrrole films. Electrochimica Acta 2005;50:1747-1755.

[15] Liu L, Zhao Y, Zhou Q, Xu H, Zhao C, Jiang Z. Nano-polypyrrole supercapacitor arrays prepared by layer-by-layer assembling method in anodic aluminum oxide templates. Journal of Solid State Electrochemistry 2007;11:32-37.

[16] Krivoshei IV, Skorobogatov VM. "Polyacetylene and Polyarylenes; Polymer Monographs." Vol. 10,Gordon and Breach Science Publishers, Philadelphia, PA, 1991

[17] Kovacic P, Jones MB. Dehydro coupling of aromatic nuclei by catalyst-oxidant systems: poly(p-phenylene). Chemical Reviews 1987;87:357-379.

[18] Shi G, Xue G, Li C, Jin S, Yu B. Uniaxial oriented poly(p-phenylene) fibrils and films. Macromolecules 1994;27:3678-3679.

[19] Roth S, Bleier H. Solitons in polyacetylene. Advances in Physics1987;36:385-462.

[20] Jacky JWY, Tang BZ. Functional polyacetylenes. Account of Chemical Research 2005;38:745-754.

[21] Asato AE, Liu RSH, Rao VP, Cai YM. Azulene-Containing Donor-Acceptor Compounds as Second-Order Nonlinear Chromophores. Tetrahedron Letters 1996;37:419-422.

[22] Taudi H, Bernede JC, Valle D, Bonnet MAA, Morsli M. Influence of the electrochemical conditions on the properties of polymerized carbazole. Journal of Materials Science 2001;36:631-634.

[23] Baba A, Onishi K, Knoll W, Advincula RC. Investigating Work Function Tunable Hole-Injection/Transport Layers of Electrodeposited Polycarbazole Network Thin Films. Journal of Physical Chemistry B 2004;108:18949-18955.

[24] Pud AA. Stability and degradation of conducting polymers in electrochemical systems. Synthetic Metals 1994;66(1):1–18.

[25] Min G. Conducting polymers and their applications in the film industry: polyaniline polyimide blended films. Synthetic Metals 1999;102(1–3):1163–1166.

[26] Davies JE, Less RJ, May I, Rawson JM. Isolation of the first diselenadiazolyl complex, $Pd_3[PhCNSeSeN]_2[PPh_3]_4$ 2PhMe New J. Chem. 1998;22:763-765

[27] Hahiwara T, Demura T, Iwata K. Synthesis and properties of electrically conducting polymers from aromatic amines. Synthetic Metals 1987;18:317-322.

[28] Snauwaert P, Lazzaroni R, Riga J, Verbist JJ. Electronic structure of polyaniline and substituted derivatives. Synthetic Metals 1987; 18:335-340.

[29] Cho MS, Cho YH, Choi HJ, Jhon MS. Synthesis and electrorheological characteristics of polyaniline-coated poly(methyl methacrylate) microsphere: Size effect. Langmuir 2003;19:5875-5881.

[30] Jindal Z, Verma NK. Electrochemical template–assisted fabrication of CdS micro/nanostructures. Physica E 2009;41:1752–1756.

[31] Soudi R, Kamal M, Shabaka AA, Abdelrazek EM, Eisa W. Synthesis, characterization and spectroscopic studies of CdS/polyaniline core/shell nanocomposites. Synthetic Metals 2010;160:479–484.

[32] Xi Y, Zhou J, Guo H, Cai C, Lin Z. Enhanced photoluminescence in core-sheath CdS–PANI coaxial nanocables: a charge transfer mechanism. Chemical Physics Letters 2005;412:60-63.

[33] Seoudi R, Shabaka AA., Kamal M, Abdelrazek EM, Eisa H. Dependence of structural, vibrational spectroscopy and optical properties on the particle sizes of CdS/polyaniline core/shell nanocomposites. Journal of Molecular Structure 2012;10(13):156-162.

[34] Raut BT, Chougule MA, Sen S, Pawar RC, Lee CS, Patil VB. Novel method of fabrication of polyaniline–CdS nanocomposites: Structural, morphological and optoelectronic properties. Ceramics International 2012;38:3999-4007.

[35] Ameen S, Akhtar MS, Kim YS, Shin HS. Synthesis and electrochemical impedance properties of CdS nanoparticles decorated polyaniline nanorods. Chemical Engineering Journal 2012;181–182:806–812.

[36] Boyer MI, Quillard S, Louarn G, Froyer G, Lefrant S. Vibrational study of the $FeCl_3$-doped dimer of polyaniline; a good model compound of emeraldine salt. Journal of Physical Chemistry B 2000;104:8952–896.

[37] Mazeikiene R, Statino A, Kuodis Z, Niaura G, Malinauskas A. In situ Raman spectroelectrochemical study of self-doped polyaniline degradation kinetics. Electrochemistry Communications 2006;8:1082–1086.

[38] Khiew PS. Huang NM, Radiman S, Ahmad MS. Synthesis and characterization of conducting polyaniline-coated cadmium sulphide nanocomposites in reverse microemulsion. Materials Letters 2004;58:516–521.

[39] Shimano JY, MacDiarmid AG. Polyaniline, a dynamic block copolymer: key to attaining its intrinsic conductivity. Synthetic Metals 2001;123:251–262.

[40] Monkman AP, Stevens GC, Bloor D. X-ray photoelectron spectroscopic investigations of the chain structure and doping mechanisms in polyaniline. Journal of Physics D: Applied Physics 1991;24:738–743.

[41] Wu MS, Wen TC, Gopalan A. Electrochemical copolymerization of diphenylamine and anthranilic acid with various feed ratios. Journal of the Electrochemical Society 2001;148:D65–D73.

[42] Ameen S, Akhtar MS., Kim YS, Yang OB, Shin HS. Electrical and structural characterization of plasma polymerized polyaniline/$TiO_2$ heterostructure diode: a comparative study of single and bilayer $TiO_2$ thin film electrode. Journal of Nanoscience and Nanotechnology 2011;11:3306–3313.

[43] Glidle A, Swann MJ, Hadyoon CS, Cui L, Davis J, Ryder KS, Cooper JM. XPS assaying of electrodeposited copolymer composition to optimise sensor materials. Journal of Electron Spectroscopy and Related Phenomena 121 (2001) 131–148.

[44] Suzer S, Birer O, Sevil UA, Guven O. XPS investigations on conducting polymers. Turkish Journal of Chemistry 1998;22:59–65.

[45] Duran JDG, Guindo MC, Delgado AV, Caballero FG. Surface chemical analysis and electrokinetic properties of synthetic spherical mixed zinc–cadmium sulfides, Journal of Colloids and Interface Science 1997;193:223–233.

[46] Fiordiponti P, Pistoia G. An impedance study of polyaniline films in aqueous and organic solutions. Electrochimica Acta 1989;34:215–221. (b) Vorotyntsev MA, Badiali JP, Inzelt G. Electrochemical impedance spectroscopy of thin films with two mobile charge carriers: effects of the interfacial charging. Journal of Electroanalytical Chemistry 1999;472:7–19.

[47] Hagfeldt A, Gratzel M. Light-Induced Redox Reactions in Nanocrystalline Systems. Chemical Reviews 1995;95:49-68.

[48] Cheng YJ, Yang SH, Hsu CS. Synthesis of conjugated polymers for organic solar cell applications, Chemical Reviews 2009;109:5868–5923.

[49] Jaglarz J, Wagner T, Cisowski J, Sanetra J. Ellipsometric studies of carbazole-containing polymer layers. Optical Materials, 2007;29:908-912.

[50] Kudo N, Shimazaki Y, Ohkita H, Ohoka M, Ito S. Organicinorganic hybrid solar cells based on conducting polymer and $SnO_2$ nanoparticles chemically modified with a fullerene derivative. Solar Energy Materials Solar Cells 2007;91:1243-1247.

[51] Woo S, Jeong JH, Lyu HK, Jeong S, Sim JH, Kim WH, Han YS, Kim Y. Hybrid solar cells with conducting polymers and vertically aligned silicon nanowire arrays: The effect of silicon conductivity. Physica B: Condensed Matter 2012;407:3059-3062.

[52] Tan F, Qu S, Wu J, Wang Z, Jin L, Bi Y, Cao J, Liu K, Zhang J. Wang Z., Electrodepostied polyaniline films decorated with nano-islands: Characterization and application as anode buffer layers in solar cells. Solar Energy Materials Solar Cells 2011;95:440-445.

[53] Chang MY, Wu CS, Chen YF, Hsieh BZ, Huang WY, Ho KS, Hsieh TH, Han YK. Polymer solar cells incorporating one-dimensional polyaniline nanotubes. Organic Electronics 2008; 9:1136-1139.

[54] Lim TH, Oh KW, Kim SH. Self-assembly supramolecules to enhance electrical conductivity of polyaniline for a flexible organic solar cells anode. Solar Energy Materials Solar Cells 2012;101:232-240.

[55] Bejbouji H, Vignau LL, Miane J, Dang MT, Oualim EM, Harmouchi M, Mouhsen A. Polyaniline as a hole injection layer on organic photovoltaic cells. Solar Energy Materials Solar Cells. 2010;94:176-181.

[56] Zhu S., Wei W., Chen X., Jiang M., Zhou Z. Hybrid structure of polyaniline/ZnO nanograss and its application in dye-sensitized solar cell with performance improvement. Journal of Solid State Chemistry 2012;190:174-179.

[57] Ameen S, Akhtar MS, Song M, Kim YS, Shin HS. Plasma Deposited Polyaniline on Ruthenium Dye Sensitized Zno Thin Film for Dye Sensitized Solar Cell. Advanced Science Letters 2012: doi:10.1166/asl.2012.3305.

[58] Malherbe R, Martinez J, Reguera E, Navarro E. Journal of Materials Science 1992;28:274.

[59] Ameen S, Akhtar MS, Kim G-S, Kim YS, Yang O-B, Shin HS. Plasma-enhanced polymerized aniline/$TiO_2$ dye-sensitized solar cells. Journal of Alloys and Compounds 2009;487:382–386.

[60] Bisquert J. Theory of the Impedance of Electron Diffusion and Recombination in a Thin Layer. Journal of Physical Chemistry B 2002;106:325-333.

[61] J.R. Macdonald, Impedance Spectroscopy, John Wiley & Sons, New York, 1987.

[62] Brad AJ, Faulkner LR. Electrochemical Methods: Fundamentals and Applications, John Wiley & Sons, New York, 1980, p. 350.

[63] Yeh MH, Lee CP, Chou CY, Lin LY, Wei HY, Chu CW, Vittal R, Ho KC. Conducting polymer-based counter electrode for a quantum-dot-sensitized solar cell (QDSSC) with a polysulfide electrolyte. Electrochimica Acta, 2011;57:277-284.

[64] ] Lee KM, Chen PY, Hsu CY, Huang JH, Ho WH, Chen HC, Ho KC. A high-performance counter electrode based on poly(3,4-alkylenedioxythiophene) for dye-sensitized solar cells. Journal of Power Sources. 2009;188:313-318.

[65] Lee KM, Chiu WH, Wei HY, Hu CW, Suryanarayanan V, Hsieh WF, Ho KC. Effects of mesoscopic poly(3,4-ethylenedioxythiophene) films as counter electrodes for dye-sensitized solar cells. Thin Solid Films, 2010;518:1716-1721

[66] Maiaugree W, Pimanpang S, Towannang M, Saekow S, Jarernboon W, Amornkitbamrung V. Optimization of $TiO_2$ nanoparticle mixed PEDOT–PSS counter electrodes for high efficiency dye sensitized solar cell. Journal of Non-Crystalline Solids 2012; In Press: doi:10.1016/j.jnoncrysol.2011.12.104.

[67] Chen J, Li B, Zheng J, Zhao J, Jing H, Zhu Z. Polyaniline nanofiber/carbon film as flexible counter electrodes in platinum-free dye-sensitized solar cells. Electrochimica Acta 2011; 56:4624-4630.

[68] Li Q, Wu J, Tang Q, Lan Z, Li P, Lin J, Fan L. Application of microporous polyaniline counter electrode for dye-sensitized solar cells. Electrochemistry Communications 2008; 10:1299-1302.

[69] Zhang J, Hreid T, Li X, Guo W, Wang L, Shi X, Su H, Yuan Z. Nanostructured polyaniline counter electrode for dye-sensitised solar cells: Fabrication and investigation of its electrochemical formation mechanism. Electrochimica Acta, 2010;55:3664-3668.

[70] Wang G, Xing W, Zhuo S. The production of polyaniline/graphene hybrids for use as a counter electrode in dye-sensitized solar cells. Electrochimica Acta 2012;66:151-157.

[71] Tai Q, Chen B, Guo F, Xu S, Hu H, Sebo B, Zhao XZ. In situ prepared transparent polyaniline electrode and its application in bifacial dye-sensitized solar cells. ACS Nano 2011; 24;5(5):3795-9.

[72] Ameen S, Akhtar MS, Kim YS, Yang OB, Shin HS. Sulfamic Acid-Doped Polyaniline Nanofibers Thin Film-Based Counter Electrode: Application in Dye-Sensitized Solar Cells. Journal of Physical Chemistry C 2010;114:4760–4764.

[73] Nazeeruddin, MK, Kay A, Rodicio I, Humphry-Baker R, Muller E, Liska P, lachopoulosn N, Gratzel M. Conversion of light to electricity by cis-X2bis(2,2'-bipyridyl-4,4'-dicarboxylate)ruthenium(II) charge-transfer sensitizers (X = $Cl^-$, $Br^-$, $I^-$, $CN^-$, and $SCN^-$) on nanocrystalline titanium dioxide electrodes. Journal of the American Chemical Society 1993;115:6382–6390.

[74] Li Z, Ye B, Hu X, Ma X, Zhang X, Deng Y. Facile Electropolymerized-PANI as counter electrode for low cost dye-sensitized solar cells. Electrochemistry Communications 2009;11:1768-1771.

[75] Graetzel M. Photoelectrochemical cells. Nature 2011;414:338-344.

[76] Kawai T, Takahashi H, Matsushima Y, Ogata T, Unuma H. Evaluation of Photocatalytic Activity of $TiO_2$ Thin Films by Spin-Trap ESR Spectroscopy. Science of Advanced Materials, 2010; 2:74-78.

[77] Thomas J, Kumar KP, Mathew S. Enhancement of Sunlight Photocatalysis of Nano $TiO_2$ by Ag Nanoparticles Stabilized with D-Glucosamine. Science of Advanced Materials 2011;3:59-65.

[78] Lee SM, Cho SN, Cheon S. Anisotropic Shape Control of Colloidal Inorganic Nanocrystals. Advanced Materials 2003;15:441-444.

[79] Hyam RS, Bhosale RK, Lee W, Han SH, Hannoyer B, Ogale SB. Room Temperature Synthesis of Rutile $TiO_2$ Hierarchical Nanoneedle Flower Morphology for Dye Sensitized Solar Cell. Journal of Nanoscience and Nanotechnology 2010;10:5894-5898.

[80] Du G, Wan B, Guo Z, Shen J, Li Y, Liu H. Effect of Annealing on Electrochemical Performance of Anodized TiO2 Nanotubes for Lithium Ion Batteries. Advanced Science Letters, 2011;4:469-473.

[81] Mor GK, Shankar K, Paulose M, Varghese PK, Grimes CA. Use of Highly-Ordered $TiO_2$ Nanotube Arrays in Dye-Sensitized Solar Cells. Nano Letters, 2006;6:215-218.

[82] Ameen S, Akhtar MS, Kim YS, Shin HS. Controlled synthesis and photoelectrochemical properties of highly ordered $TiO_2$ nanorods. RSC Advances, 2012;2:4807–4813

[83] Shin K, Seok SI, Im SH, Park JH. CdS or CdSe decorated $TiO_2$ nanotube arrays from spray pyrolysis deposition: use in photoelectrochemical cells. Chemical Communication, 2010;46:2385-2387.

[84] Du PA, Chen HH, Lu YC. Dye sensitized solar cells using well-aligned zinc oxide nanotip arrays. Applied Physics Letters 2006;89:253513-253615.

[85] Gregg BA. Interfacial processes in the dye-sensitized solar cell. Coordination Chemistry Reviews 2004;248:1215-1224.

[86] Lee S, Cho IS, Lee JH, Kim HD, Kim DW, Kim JY, Shin H, Lee JK, Jung HS, Park NG, Kim K, Ko MJ, Hong KS. Two-Step Sol–Gel Method-Based $TiO_2$ Nanoparticles with Uniform Morphology and Size for Efficient Photo-Energy Conversion Devices. Chemistry of Materials, 2010;22:1958-1965.

[87] Chakravarty R, Periasamym C. Effect of aluminium doping on structural and optoelectronic properties of sol-gel derived nanocrystalline ZnO thin film. Science of Advanced Materials 2011;3:276–283.

[88] Chao CH, Chan CH, Huang JJ, Chang LS, Shih HC. Manipulated the band gap of 1D ZnO nano-rods array with controlled solution concentration and its application for DSSCs. Current Applied Physics 2011;11:S136–S139

[89] Mohanta SK, Kim DC, Kong BH, Cho HK, Liu W, Tripathy S. Optical Properties of ZnO Nanorods and Hybrid Structures Grown on p-type GaN/Sapphire and Silicon-on-

Insulator Substrates. Science of Advanced Materials 2010;2:64-68. (b) Zhang H, Du N, Chen B, Li D, Yang D. Carbon Nanotube-ZnO Nanosphere Heterostructures: Low-Temperature Chemical Reaction Synthesis, Photoluminescence, and Their Application for Room Temperature $NH_3$ Gas Sensor. Science of Advanced Materials 2009;1:13-17.

[90] Akhtar MS, Khan MA, Jeon MS, Yang OB. Controlled synthesis of various ZnO nanostructured materials by capping agents-assisted hydrothermal method for dye-sensitized solar cells. Electrochimica Acta 2008;53:7869–7874.

[91] Tseng YK, Hsu HC, Hsieh WF, Liu KS, Chen IC. Two-step oxygen injection process for growing ZnO nanorods. Journal of Materials Research 2003;18:2837–2844.

[92] Yu WD, Li XM, Gao XD, Self-catalytic synthesis and photoluminescence of ZnO nanostructures on ZnO nanocrystal substrates, Applied Physics Letters 2004;84:2651–2658.

[93] Uthirakumar P, Kang JH, Senthilarasu S, Hong CH. The different types of ZnO materials on the performance of dye-sensitized solar cells, Physica E 2011;43:1746–1751.

[94] Greene LE, Yuhas BD, Law M, Zitoun D, Yang PD. Solution-Grown Zinc Oxide Nanowires. Inorganic Chemistry 2006;45:7535-7543.

[95] Han H, Bach U, Cheng YB, Caruso RA. Increased nanopore filling: Effect on monolithic all-solid-state dye-sensitized solar cells. Applied Physics Letters 2007;90:213510-213512.

[96] Gao YF, Nagai M, Chang TC, Shyue JJ. Solution-Derived ZnO Nanowire Array Film as Photoelectrode in Dye-Sensitized Solar Cells. Crystal Growth and Design 2007;7:2467-2471.

[97] Jiang CY, Sun XW, Tan KW, Lo GQ, Kyaw AKK, Kwong DL. High-bendability flexible dye-sensitized solar cell with a nanoparticle-modified ZnO-nanowire electrode. Applied Physics Letters 2008;92:143101-143103.

[98] Akhtar MS, Khan MA, Jeon MS, Yang OB. Controlled synthesis of various ZnO nanostructured materials by capping agents-assisted hydrothermal method for dye-sensitized solar cells. Electrochimica Acta 2008;53:7869-7874.

[99] Umar A, Al-Hajry A, Hahn YB, Kim DH. Rapid synthesis and dye-sensitized solar cell applications of hexagonal-shaped ZnO nanorods. Electrochimica Acta 2009;54:5358-5362.

[100] Ameen S, Akhtar MS, Shin HS. Growth and characterization of nanospikes decorated ZnO sheets and their solar cell application. Chemical Engineering Journal 2012;195-196:307–313.

[101] Umar A, Kim SH, Kim JH, Al-Hajry A, Hahn YB. Temperature-dependant non-catalytic growth of ultraviolet-emitting ZnO nanostructures on silicon substrate by thermal evaporation process. Journal of Alloys and Compounds 2008;463:516–521.

[102] Laudise RA, Kolb ED, Caporason AJ. Hydrothermal growth of large sound crystals of zinc oxide. Journal of the American Ceramic Society 1964;47:9–12.

[103] Ameen S, Akhtar MS., Kim YS, Yang OB, Shin HS. Influence of seed layer treatment on low temperature grown ZnO nanotubes: performances in dye sensitized solar cells, Electrochimica Acta 2011;56:1111–1116.

[104] Wagner CD, Riggs WM, Davis LE, Moulder JF, Muilenberg GE. Handbook of X-ray Photoelectron Spectroscopy, Perkin Elmer, Eden Prairie, 1979.

[105] Leunga CY, Djurisic AB, Leung YH, Ding L, Yang CL, Ge WK. Influence of the carrier gas on the luminescence of ZnO tetrapod nanowires, Journal of Crystal Growth 2006;290:131–136.

[106] Fan JCC, Goodenough JB. X-ray photoemission spectroscopy studies of Sn doped indium-oxide films, Journal of Applied Physics 1977;48:3524–3531.

[107] Martinson ABF, Elam JW, Hupp JT, Pellin MJ. ZnO nanotube based dyesensitized solar cells Nano. Letters 2007;7:2183–2187.

[108] Umar A, Singh P, Al-Ghamdi AA, Al-Heniti S. Direct growth of ZnO nanosheets on FTO substrate for dye-sensitized solar cells applications, Journal of Nanoscience and Nanotechnology 2010;10:6666–6671.

[109] Al-Hajry A, Umar A, Hahn YB, Kim DH. Growth, properties and dyesensitized solar cells–applications of ZnO nanorods grown by lowtemperature solution process. Superlattice Microstructures 2009;45:529–534.

[110] Ilican S, Caglar Y, Caglar M, Yakuphanoglu F. Structural, optical and electrical properties of F-doped ZnO nanorod semiconductor thin films deposited by solgel process. Applied Surface Science 2008;255:2353–2359.

[111] Peiteado M, Iglesias Y, Fernandez JF, De Frutos J, Caballero AC. Microstructural development of tin-doped ZnO bulk ceramics. Materials Chemistry and Physics 2007;101:1–6.

[112] Tsay CY, Cheng HC, Tung YT, Tuan WH, Lin CK. Effect of Sn-doped on microstructural and optical properties of ZnO thin films deposited by sol-gel method. Thin Solid Films 2008;517:1032–1036.

[113] Yung KC, Liem H, Choy HS, 185002 enhanced redshift of the optical band gap in Sn-doped ZnO free standing films using the sol–gel method. Journal of Physics D: Applied Physics 2009;42:15002-15006.

[114] Ameen S, Akhtar MS, Seo HK, Kim YS, Shin HS. Influence of Sn doping on ZnO nanostructures from nanoparticles to spindle shape and their photoelectrochemical properties for dye sensitized solar cells. Chemical Engineering Journal 2012;187: 351–356

[115] Exarhos GJ, Sharma SK. Influence of processing variables on the structure and properties of ZnO films. Thin Solid Films 1995;270:27–32.

[116] Yang J, Lee J, Im K, Lim S, Influence of Sn-doping in hydrothermal methods on the optical property of the ZnO nanorods. Physica E 2009;42:51–56.

[117] Sheini FJ, More MA, Jadkar SR, Patil KR, Pillai VK, Joag DS. Observation of photoconductivity in Sn-doped ZnO nanowires and their photoenhanced field emission behavior. Journal of Physical Chemistry C 2010;114:3843–3849.

[118] Dolbec R, ElKhakani MA, Serventi AM, Jacques RGS. Influence of the nanostructural characteristics on the gas sensing properties of pulsed laser deposited tin oxide thin films. Sensors and Actuators B 2003;93:566–571.

[119] Ye N, Qi J, Qi Z, Zhang X, Yang Y, Liu J, Zhang Y. Improvement of the performance of dye-sensitized solar cells using Sn-doped ZnO nanoparticles. Journal of Power Sources 2010;195:5806–5809.

[120] Kim MH, Suh M, Gowrishankar V, McGehee MD, Kwon YU. Confinement Effects of P3HT in Nanochannels and Their Implications for Bulk Heterojunction Solar Cells. Journal of Nanoscience and Nanotechnology 2010;10:279–284.

[121] Mridha S, Basak D. ZnO/polyaniline based inorganic/organic hybrid structure: Electrical and photoconductivity properties. Applied Physics Letters 2008;92:142111–142113

[122] Ameen S, Akhtar MS, Kim YS, Yang OB, Shin HS. Polyaniline/Ga doped ZnO Heterostructure Device via Plasma Enhanced Polymerization. Microchim Acta 2011;172:471–478.

[123] Umar A, Al-Hajry A, Hahn YB, Kim DH. Rapid synthesis and dye-sensitized solar cell applications of hexagonal-shaped ZnO nanorods. Electrochimica Acta 2009;54:5358–5362.

[124] Monkman AP, Stevens GC, Bloor D. X-ray photoelectron spectroscopic investigations of the chain structure and doping mechanisms in polyaniline. Journal of Physics D: Applied Physics 1991;24:738-741.

[125] Barr TL. Recent advances in x-ray photoelectron spectroscopy studies of oxides. Journal of Vacuum Science & Technology A 1991;93:179-185.

[126] Sans JA, Segura A, Royo JFS, Barber V, Fenollosa MAH, Marí B. Correlation between optical and transport properties of Ga doped ZnO thin films prepared by pulsed laser deposition. Superlattice Microstructures 2006;39:282–290.

[127] Chen Y, Kang ET, Neon KG, Lim SL, Ma ZH, Tan KL. Intrinsic redox states of polyaniline studied by high-resolution X ray photoelectron spectroscopy. Colloid and Polymer Science 2001;279:73–76.

[128] Kang ET, Neoh KG, Tan KL. Polyaniline: A polymer with many interesting intrinsic redox states. Progress in Polymer Science 1998;23:277–324.

[129] Mridha S, Basak D. ZnO/polyaniline based inorganic/organic hybrid structure: Electrical and photoconductivity properties. Appl. Phys. Lett. 2008;92:142111–142113.

[130] Ameen S, Akhtar MS, Ansari SG, Yang OB, Shin HS. Electrophoretically deposited polyaniline/ZnO nanoparticles for p–n heterostructure diodes. Superlattice and Microstructures 2009;46:872–880.

[131] Croce F, Appetechi GB, Persi L, Scrosati B. Nanocomposite polymer electrolytes for lithium batteries. Nature (London) 1998;394: 456-458.

[132] Kang MS, Ahnand KS, Lee JW. Quasi-solid-state dye-sensitized solar cells employing ternary component polymer-gel electrolytes. Journal of Power Sources 2008;180:896-901.

[133] Katsaros G, Stergiopoulos T, Arabatzis IM, Papadokostaki KG, Falaras P. A solvent-free composite polymer/inorganic oxide electrolyte for high efficiency solid-state dye-sensitized solar cells. Journal of Photochemistry and Photobiology A 2002;149:191-198.

[134] Stergiopoulos T, Arabatzis IM, Katsaros G, Falaras P. Binary Polyethylene Oxide/ Titania Solid-State Redox Electrolyte for Highly Efficient Nanocrystalline $TiO_2$ Photoelectrochemical Cells. Nano Letters 2002;2:1259-1261.

[135] Akhtar MS, Park JG, Kim UY, Yang OB. Composite electrolytes of polyethylene glycol methyl ether and $TiO_2$ for dye-sensitized solar cells—Effect of heat treatment. Materials Chemistry and Physics 2011;127:479-483.

[136] Tadayyoni MA, Gao P, Weaver MJ. Application of surface-enhanced Raman spectroscopy to mechanistic electrochemistry: Oxidation of iodide at gold electrodes. Journal of Electroanalytical Chemistry 1986;198:125-136.

[137] Kubo W, Murakoshi K, Kitamura T, Yoshida S, Haruki M, Hanabusa K, Shirai H, Wada Y, Yanagida S. Quasi-Solid-State Dye-Sensitized $TiO_2$ Solar Cells: Effective Charge Transport in Mesoporous Space Filled with Gel Electrolytes Containing Iodide and Iodine. Journal of Physical Chemistry B 2001;105:12809- 12815.

[138] Akhtar MS, Chun J M, Yang OB. Advanced composite gel electrolytes prepared with titania nanotube fillers in polyethylene glycol for the solid-state dye-sensitized solar cell. Electrochemistry Communications 2007;9:2833-2837.

[139] Zhang J, Han H, Wu S, Xu S, Yang Y, Zhou C, Zhao X. Conductive carbon nanoparticles hybrid PEO/P(VDF-HFP)/$SiO_2$ nanocomposite polymer electrolyte type dye sensitized solar cells. Solid State Ionics 2007;178:1595-1601.

[140] Han H, Bach U, Cheng YB. Caruso R A. Increased nanopore filling: Effect on monolithic all-solid-state dye-sensitized solar cells. Applied Physics Letters 2007;90:213510-213412.

[141] Zhang X, Yang H, Xiong HM, Li FY, Xia YY. A quasi-solid-state dye-sensitized solar cell based on the stable polymer-grafted nanoparticle composite electrolyte. Journal of Power Sources 2006;160:1451-1455.

[142] Nazmutdinova G, Sensfuss S, Schrödner M, Hinsch A, Sastrawan R, Gerhard., Himmler S, Wasserscheid P. Quasi-solid state polymer electrolytes for dye-sensitized solar cells:

Effect of the electrolyte components variation on the triiodide ion diffusion properties and charge-transfer resistance at platinum electrode. Solid State Ionics 2006;177:3141-3146.

[143] Tu CW, Liu KY, Chien AT, Yen MH, Weng TH, Ho KC, Lin KF. Enhancement of photocurrent of polymer-gelled dye-sensitized solar cell by incorporation of exfoliated montmorillonite nanoplatelets. Journal of Polymer Science A: Polymer Chemistry 2008;46:47- 53.

[144] Ito BI, de Freitas JN, De Paoli MA, Nogueira AF. Application of a Composite Polymer Electrolyte Based on Montmorillonite in Dye Sensitized Solar Cells. Journal of Brazilian Chemical Society 2008:19:688-696.

Chapter 9

# Investigation of Organic Bulk Heterojunction Solar Cells from Optical Aspect

Chunfu Zhang, Yue Hao, Dazheng Chen,
Zhizhe Wang and Zhenhua Lin

Additional information is available at the end of the chapter

http://dx.doi.org/10.5772/52819

## 1. Introduction

Low in cost, light in weight and flexible in mechanics, the solution-processed organic solar cells have aroused worldwide interest and have been the promising alternative to the traditional silicon-based solar cells [1-4]. However, they are still not available for the commercialization due to their low power conversion efficiency (PCE). Therefore, many research works have focused on the employing of new materials and device structures to improve the device performance. The milestone is the introduction and application of the bulk heterojunction structure consisting of an interpenetrating network of electron donor and acceptor materials [5]. By using this structure, the conventional organic solar cell (OSC) with poly(3-hexylthiophene)/[6,6]-phenyl C61-butyric acid methyl ester (P3HT:PCBM) blend shows a superior performance. Recently, the inverted organic solar cell (IOSC, in which the polarities of the two electrodes are exchanged) has also been introduced as the possible candidate for OSC to remedy the low air stability of OSC [6]. Both OSC and IOSC are now attracting the research interest. However, most of the previous works are mainly done for OSC or IOSC separately, and almost no researches are reported about the systemic comparison between OSC and IOSC for their different performances besides the air stability. Since the reported PCE of IOSC is relatively lower than that of OSC in many researches, one may doubt that which structure is better, the conventional one or the inverted one? As a result, one section of this chapter aims to investigate the performance differences of OSC and IOSC.

Although PCE of the standalone organic solar cell (including OSC and IOSC) is improved continuously with the research development, some bottlenecks still seem to appear because of the drawbacks coming from the molecular and macromolecular materials: First, the organic solar cell is dominated by the excitonic effect, the relatively short lifetime and the low

charge mobility, and these factors limit the maximum thickness of the active layer for light absorption. Second, most organic semiconducting materials show discrete absorption behaviour and cover only a fraction of the solar spectrum, leading to inefficient light harvest. To overcome these drawbacks, the realization of the tandem structure based on complementary thin absorber materials provides a reasonable solution to the above obstacles. As a promising concept to achieve high PCE, the tandem solar cell can reduce the loss via subbandgap transmission of photons, the major loss mechanism in solar cells [7]. For an ideal tandem solar cell, it requires current matching of the subcells, a lossless recombination contact and a complementary absorption of the subcells. Among them, current matching of the subcells is a leading design criterion for improving the tandem device performance. Then, the organic tandem solar cell optimization by considering the current matching is also involved in this chapter.

As is well known, the working principle of organic photovoltaic devices can be simply described as a process of "light in- current out". This process consists of seven parts:

**1.** in-coupling of photon,

**2.** photon absorption,

**3.** exciton formation,

**4.** exciton migration,

**5.** exciton dissociation,

**6.** charge transport, and

**7.** charge collection at the electrodes.

The first two parts are the optical mechanisms of the device and the other parts constitute the electrical aspect. The optical aspect plays a significant role because more incident photons and absorbed photons are the baseline for the better device performance. It has been reported that the internal quantum efficiency (IQE) of organic bulk heterojunction solar cells can reach 100% [8]. Thus the external quantum efficiency (EQE) can be approximately described as the product of IQE and the ratio of the number of absorbed photons in active layer to the number of incoming photons. As a result, the optimization of organic solar cells from the optical aspect is seriously important. This is why we investigate the device performance of standalone and tandem organic solar cells mainly from the optical aspect in this work.

The contents of this chapter are arranged as the following: Section 2 investigates the performance of the standalone conventional and inverted organic solar cells, especially the performance differences between the two types of devices. Section 3 discusses the optimization of the organic tandem solar cell from the optical aspect by considering the current matching. At last, a short conclusion is given in Section 4.

http://dx.doi.org/10.5772/52819

## 2. Invetigation of Standalone Organic Solar Cells

### 2.1. Methology

In order to investigate the standalone organic solar cell, we have performed optical simulations based on the Transfer Matrix Formalism with two subsets of 2×2 matrices (layer matrix and interface matrix), which was firstly introduced into organic solar cells by Pettersson et al [9] and now has been used widely. In this method, the cell is treated as a one-dimensional stack of homogeneous and isotropic layers with flat interfaces, and the number of photons absorbed in the active layer is obtained by calculating the time average of the energy dissipated per second in it. The detailed calculation processes are not presented here since the transfer matrix method is widely applied [10].

In the calculation, we assume that one absorbed photon produces one exciton in the active layer and one exciton divides into two free charges (one electron and one hole), and one electron (or hole) is collected by cathode (or anode). As a result, the number of photons absorbed in the active layer can be used as the substitute for the maximum possible short circuit current density and the EQE can be simplified as the ratio of the number of photons absorbed in the active layer to the number of incident photons.

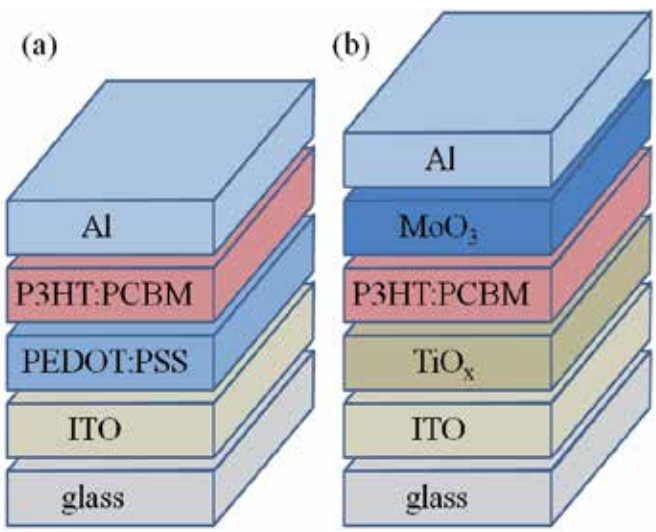


**Figure 1.** Schematic illustration of the conventional organic solar cell (OSC) with a structure of ITO/PEDOT:PSS/P3HT:PCBM/Al (a), and the inverted organic solar cell (IOSC) with a structure of ITO/$TiO_x$/P3HT:PCBM/$MoO_3$/Al (b). For OSC, the layers of ITO/PEDOT:PSS act as anode and Al acts as cathode, however for ISOC, the layers of $TiO_x$/ITO and Al play the roles of cathode and anode, respectively. Meanwhile, the layers of $TiO_x$ and $MoO_3$ are chosen for electron and hole transport layers. The P3HT:PCBM (1:1) is the active layer and the incident light enters devices from glass in both structures.

In this optical model, the layer of P3TH:PCBM is chosen as the active layer. OSC has the structure of ITO (150 nm)/PEDOT:PSS(50 nm)/P3HT:PCBM(x nm)/Al(100 nm) and ISOC has

the structure of ITO(150 nm)/$TiO_x$ (10 nm)/P3HT:PCBM(x nm)/$MoO_3$ (10 nm)/Al (100 nm), as shown in Fig.1. The optical constants of P3HT:PCBM, PEDOT:PSS, ITO, $TiO_x$, $MoO_3$, ZnO and Al are obtained from literatures [11-13].

It should be noted that, the reflection of the glass substrate is taken into account to revise the initial intensity of optical electric field at glass/ITO interface and can be described as

$$|E_{0g}|^2 = \frac{1-R^*}{n_g(1-RR^*)}|E_0|^2 \tag{1}$$

where R* represents the reflectance of air/glass interface, R the reflectance for the stack structure, $n_g$ the refraction coefficient of glass and $|E_0|^2$ (modulus squared of the optical electric filed) the initial intensity of optical electric field when light arrives at air/glass interface.

To calculate the number of absorbed photons (or excitons) in the active layer, the energy flow dissipation per second for single wavelength in active layer, Q is given as

$$Q = \frac{1}{2}c\varepsilon_0\alpha n|E|^2 \tag{2}$$

where c is the speed of light, $\varepsilon_0$ the permittivity of vacuum, $\alpha$ the absorption coefficient, n the real index of refraction, and $|E|^2$ the total optical electric field intensity in the multilayer stack at single wavelength. Then the number of photons absorbed in the active layer can be expressed as

$$N = \int_{\lambda=300nm}^{800nm} Q(\lambda)\frac{\lambda}{hc}d\lambda \tag{3}$$

where N represents the number of photons absorbed in the active layer, $hc/\lambda$ the photon energy at a specified wavelength $\lambda$, h the Planck constant and c the speed of light. The devices are illuminated with AM 1.5G solar spectra.

## 2.2 Results and discussion

The number of photons absorbed in the active layer as a function of the active layer thickness is obtained for OSC and IOSC, as well the EQE as a function of the wavelength or the active layer thickness. The optical modulation effect is investigated by inserting a ZnO layer between P3HT: PCBM and Al for OSC, and changing the thickness of $MoO_3$ layer for ISOC, respectively.

http://dx.doi.org/10.5772/52819

*Comparison of photons absorbed in the active layer*

The results of the number of photons absorbed in the active layer as a function of the active layer thickness for OSC are shown in Fig. 2(a). It is clear that the number of absorbed photons increases with the active layer thickness and one can see a notable behavior of oscillation which is due to the optical interference effect induced by the incident light and the reflected light from the mirror metal electrode. The inserting of a ZnO layer leads to the shift of interference maxima to lower thicknesses and the remarkable increase of absorbed photons especially for the relatively thin active layer. However, the insertion of a ZnO layer makes no improvement near the active layer thicknesses where the interference maxima are obtained. This variation of the number of absorbed photons with the active layer thickness is the same as that of maximum possible short circuit current density in other researches [14].

For IOSC, Fig. 2(b) shows the same tendency as OSC. It is obvious that the influence of optical modulation effect is more slightly when the active layer is relatively thick (about 150 nm). Comparing OSC with IOSC, as shown in Fig. 2 (c), it is clear that the number of absorbed photons in IOSC is larger at any active layer thicknesses except for the thicknesses around which the interference maxima of OSC are obtained. In other words, for most active layer thicknesses, the light absorption in IOSC is more effective, hence the larger contribution to photocurrent. It has been reported that the refractive index of $TiO_x$ is very similar to that of PEDOT:PSS, therefore the light loss induced by the reflection at the ITO/$TiO_x$ interface and that at the ITO/PEDOT:PSS interface is nearly equivalent. However, light absorption loss in the TiOx layer is smaller than that in the PEDOT:PSS layer [15].In addition, the layer of $MoO_3$ in IOSC can act as an optical spacer layer. As a result, one can say the better light absorption in IOSC is attributed to the nearly equal amount of entering light and the smaller absorption loss in $TiO_x$ layer, as well as the optical modulation effect caused by $MoO_3$ layer. Although IOSC shows a better performance than OSC at most of the active layer thicknesses, it is noted that the performance of IOSC is slightly lower than that of OSC around the interference peaks as shown in Fig. 2(c). One possible reason is the parasitic absorption in the $MoO_3$ layer, because not only the the optical modulation effect but also the absorption loss could be caused by the $MoO_3$ layer, which produces a tradeoff.

To well understand the difference between OSC and IOSC, the distribution of optical electric field is investigated at different active layer thicknesses. According to the absorption coefficient of P3HT:PCBM calculated by $\alpha=4\pi k/\lambda$, the maximum absorption coefficient is obtained at the incident light wavelength of around 512 nm, which agrees to the range of maximum absorption coefficient from 500 nm to 550 nm for P3HT:PCBM active material. As a result, the incident light of 512 nm is chosen to calculate the optical electric field distribution. The distributions of normalized modulus squared optical electric field at three different active layer thicknesses (45, 85, and 150 nm) for OSC and IOSC are shown in Fig. 3. The thickness of $TiO_x$ is specified as 50 nm to make the active layer region at same position in Fig. 3 for a clear comparison since its thickness has no significant influence on the photons absorbed in the active layer. Fig. 3(a) and (c) illustrate that the area below the curve of IOSC is larger than that below the curve of OSC for both thin and thick devices, which is consistent with the more absorbed photons in IOSC. And from Fig. 3(b), the opposite result can be seen when the

active layer is 85 nm where the interference maximum of OSC is obtained, which agrees to the situation in Fig. 2(c). The similar results will also be shown in next part where the different performances of EQE for OSC and IOSC are discussed.

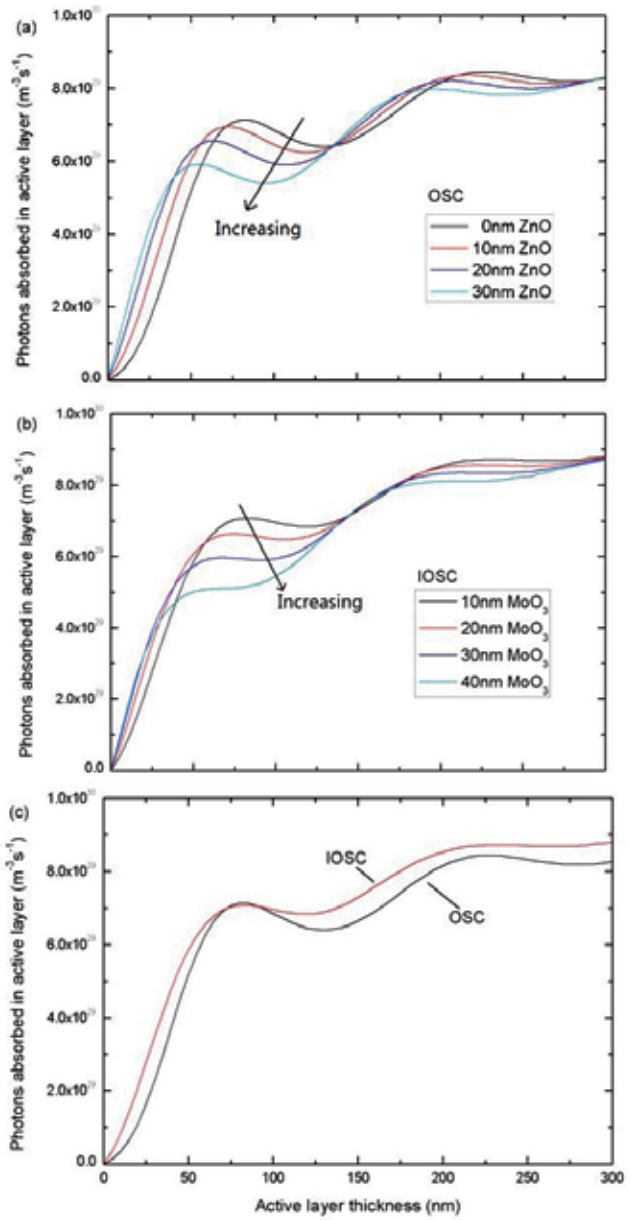


**Figure 2.** Number of photons absorbed in the active layer versus the active layer thickness with various thicknesses of the optical spacer layer. (a) OSC with the ZnO layer thickness ranging from 0 to 30 nm. (b) IOSC with the $MoO_3$ layer

http://dx.doi.org/10.5772/52819

thickness ranging from 10 to 40 nm. (c) Comparison of the number of photons absorbed in active layer of OSC and ISOC as a function of the active layer thickness. In this case, no ZnO layer is inserted in OSC and the thickness of $MoO_3$ is specified as 10 nm for ISOC.

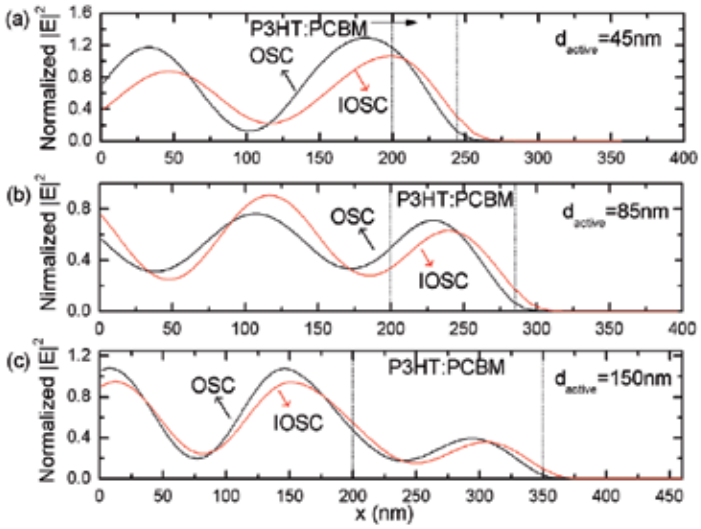


**Figure 3.** Normalized optical electric field distribution varies with the distance from glass/ITO interface for OSC (black) and IOSC (red) devices. The incident light wavelength is specified as 512 nm. The active layer thicknesses are 45 nm (a), 85 nm (b), and 150 nm (c), respectively.

*Comparison of EQE*

The EQE as a function of incident light wavelength for OSC and IOSC is shown in Fig. 4, and the thicknesses of the active layer are specified as 40, 80, 160 and 220 nm. For OSC in Fig. 4(a), the EQE trends to increase with the thickness of the P3HT:PCBM layer in the range of wavelength from 450 to 650 nm. It should be noted that, the lower EQE at 160 nm than 80 nm can be explained by the fact that 80 nm is closed to the thickness where the first interference maximum of OSC is obtained (Fig. 2(c)). At the same time, the wavelength range possessing higher EQE is also expanded especially at the wavelength near 600 nm, where the shoulders are generally changed into peaks with the increasing of the active layer thickness. Of course, for the light over 650 nm, it prefers thicker active layer to achieve better absorption of light, and for the light near 400 nm, the variation of EQE with the active layer thickness displays a behavior of increase and decrease in turn. The similar results can be obtained from Fig.4 (b) for IOSC. For the thicker active layer beyond 220 nm, the same simulation results can be obtained (not presented here) and the results are agreed to the measured EQE of OSC and IOSC with 250 nm thick active layer. In short, the thick active layer brings higher EQE for both OSC and IOSC, and the main absorption range from 400 to 650 nm can be observed from Fig. 4.

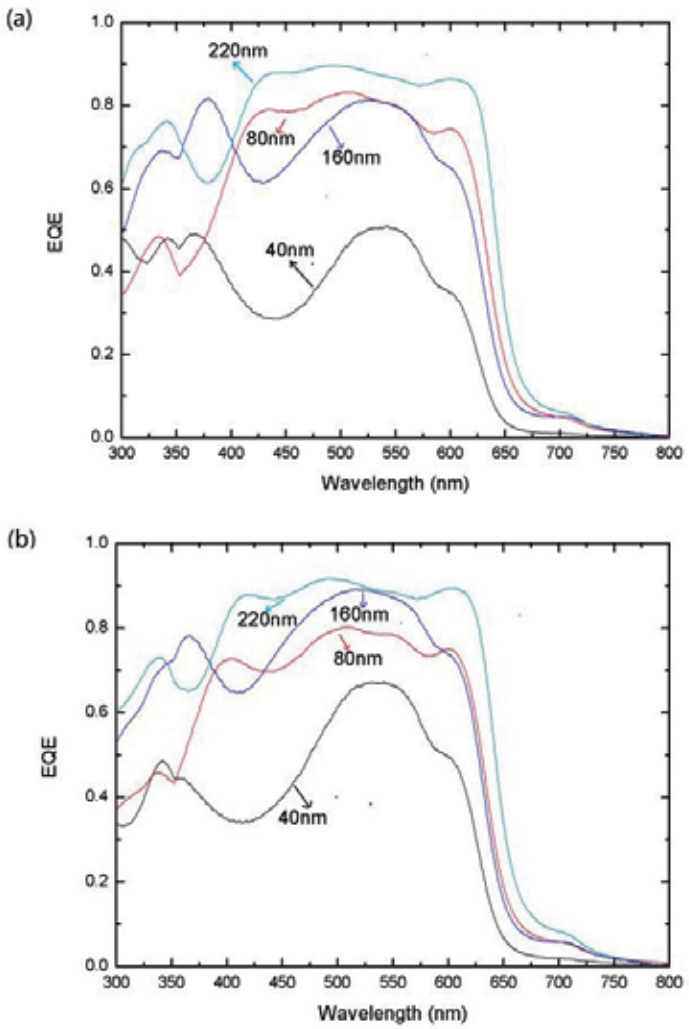


**Figure 4.** EQE vs. wavelength for OSC (a) and IOSC (b) with four different thicknesses of active layer: 40 nm(black), 80 nm(red), 160 nm(blue), and 220 nm(green), respectively.

The comparison of EQE varying with the wavelength for OSC and IOSC is presented in Fig. 5. It is evident that IOSC with 40 and 160 nm active layer has better performance in EQE in the main absorption range. However, for the 80 and 220 nm active layer, the EQE of OSC is closed to or even higher than that of IOSC, which is due to the fact that these two thicknesses nearly equal the thicknesses where the interference maxima of OSC are obtained. In other words, IOSC is super to OSC in EQE in the main absorption range for both thin and thick active layers except for thicknesses around which the interference maxima of OSC are obtained, which agrees to the analysis of the number of photons absorbed in active layer in Fig. 2. Hence the explanation is the same for this result.

http://dx.doi.org/10.5772/52819

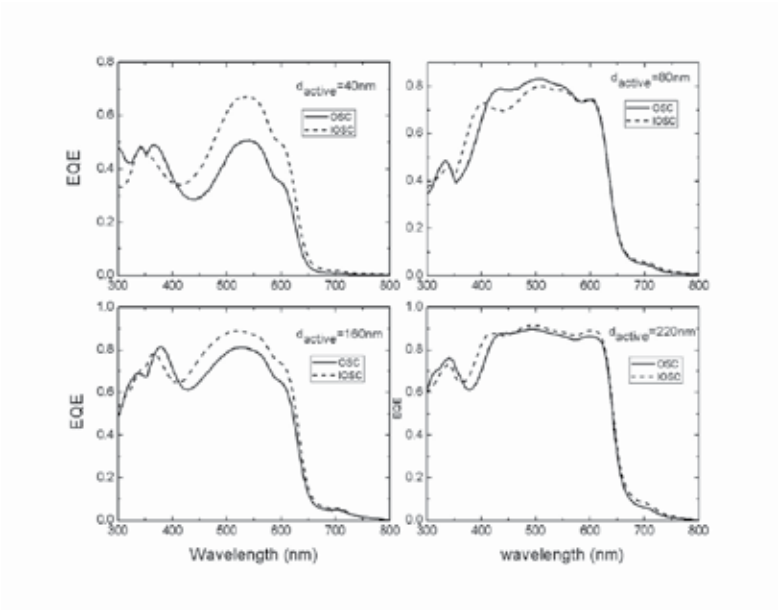


**Figure 5.** Comparison of EQE as a function of wavelength for OSC (solid line) and IOSC (dash line) with four different active layer thicknesses: 40 nm, 80 nm, 160 nm, and 220 nm.

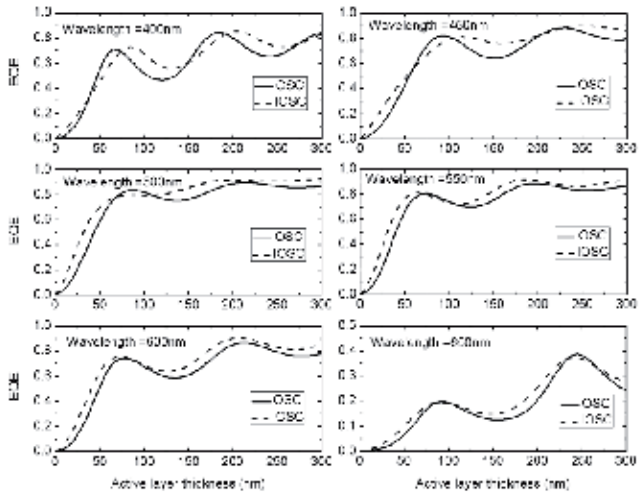


**Figure 6.** Comparison of EQE as a function of the active layer thickness for OSC (solid line) and IOSC (dash line) with six wavelengths of incident light: 400 nm, 450 nm, 500 nm, 550 nm, 600 nm, and 650 nm.

| Light wavelength (nm) | | 400 | 450 | 500 | 550 | 600 | 650 |
|---|---|---|---|---|---|---|---|
| **OSC** | Position (nm) | 65 | 95 | 85 | 75 | 75 | 90 |
| | EQE | 0.7100 | 0.8252 | 0.8363 | 0.8060 | 0.7437 | 0.1975 |
| **IOSC** | Position (nm) | 85 | 115 | 85 | 65 | 75 | 90 |
| | EQE | 0.7306 | 0.8150 | 0.7987 | 0.8109 | 0.7574 | 0.1952 |

**Table 1.** The positions and amplitudes of the first maximum EQE of OSC and IOSC at different wavelengths. The positions correspond to the active layer thickness and OSC behaves slighter thickness oscillation behavior than IOSC.

To verify the above conclusion, the EQE as a function of the active layer thickness at different wavelengths of incident light is investigated. For the EQE of OSC and IOSC depicted in Fig. 6, a remarkable increase and oscillation behavior with the increase of the active layer thickness can be observed. From Fig. 6, a conclusion may be obtained that IOSC performs better than OSC at any thickness of active layer for the light ranging from 400 to 650 nm. However, at the active layer thicknesses around which the interference maxima of OSC are obtained, the EQE of OSC is close to or even higher than that of IOSC. To well investigate the difference between OSC and IOSC, the positions and amplitudes of the first maximum EQE at different wavelengths are shown in Table 1. The clear oscillation behavior of the positions and amplitudes of the maximum EQE can be seen for both OSC and IOSC, and OSC exhibits more slight thickness oscillation behavior than IOSC. It is evident that the slight oscillation of maxima at single wavelength is beneficial to the final maximum in the range including all wavelengths. Therefore, the results from Table 1 can also be used to explain the results shown in Fig. 2(c) and Fig. 5.

In summary, from pure optical aspect, OSC and IOSC have the same tendency in the number of photons absorbed in the active layer, EQE, and the optical electric field distribution as well as the similar influence of optical modulation effect. However, IOSC performs better than OSC except for the case wherein the interference maxima of OSC are obtained, which is due to the better light absorption of ISOC possible absorption loss caused by MoO3 layer.

## 3. Investigation of the Organic Tandem Solar Cell

Although PCE of the organic solar cell is improved continuously, there are still some drawbacks for standalone devices: First, the organic solar cell is dominated by the excitonic effect, the relatively short lifetime and the low charge mobility. All of these limit the maximum thickness of the active layer for light absorption. Second, most organic semiconducting materials show discrete absorption behavior and cover only a fraction of the solar spectrum, leading to inefficient light harvest. The realization of the organic tandem solar cell based on complementary thin absorber materials provides a reasonable solution to improve device performance further.

In the existing views, matching the photocurrents of the subcells leads to the maximum PCE in the corresponding tandem cell, making it a crucial design criterion for optimum perform-

http://dx.doi.org/10.5772/52819

ance. Then to achieve a better device performance, the tandem cell should be optimized by considering current matching.

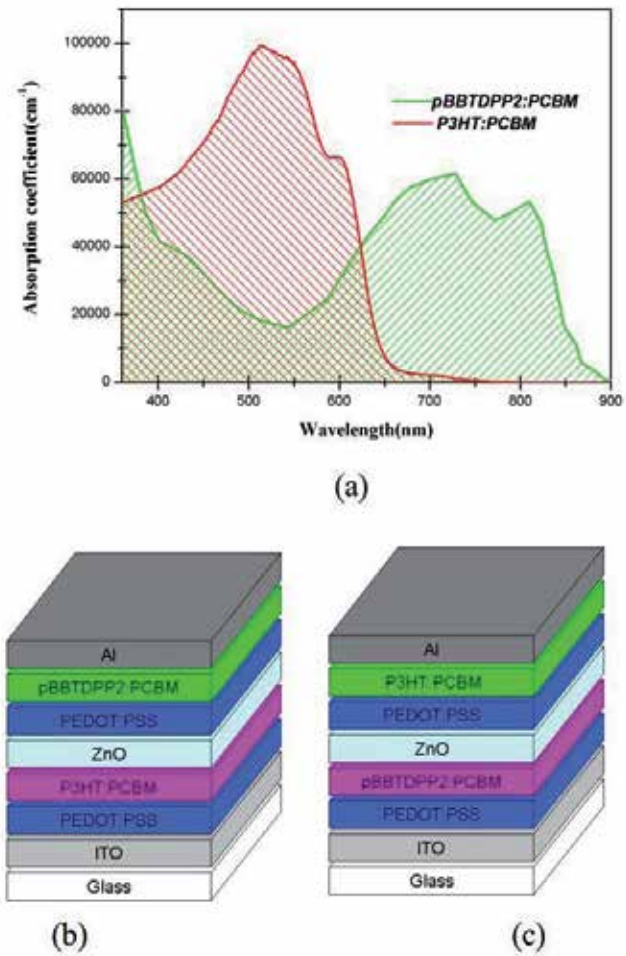


**Figure 7.** a) Absorption coefficients of both individual active layers. b) Normal and c) Reversed device structure.

As discussed in previous section, P3HT has been widely used as the donor conjugated polymer in the quest for high-efficiency bulk heterojunction organic solar cells. Its combination with PCBM as the acceptor is a standard active layer of organic solar cells based on polymer, whereas the low-energy onset of the absorption of this combination at about 650 nm limits the number of photons absorbed in the active layer. Recently, a very promising organic material has been reported and applied [16], namely poly[3,6-bis-(40-dodecyl-[2,20] bithiophenyl-5-yl)-2,5-bis-(2-ethyl-hexyl)-2,5-dihydropyrrolo[3,4-]pyrrole-1,4-dione] (pBBTDPP2). This new polymer combines electron-rich quaterthiophene (BBT) segments with electron-poor diketo pyrrolo-pyrrole (DPP) units to lower the optical bandgap to 1.4 eV in thin films. The onset of

the absorption of the blend of pBBTDPP2 and PCBM is significantly shifted to 860 nm with o-dichlorobenzene as solvent. Thus, a series connected tandem solar cell based on P3HT:PCBM and pBBTDPP2:PCBM almost covers the whole UV and visible parts of the solar spectrum, making it attractive (see Fig. 7 (a)). It is necessary to carefully optimize the thicknesses of the front and back cells for different layer sequences to deeply exploit the opportunity provided by this tandem solar cell. Therefore, detailed optical simulations of tandem cells based on P3HT:PCBM and pBBTDPP2:PCBM have been carried out in this chapter.

### 3.1. Methodology

As in previous section, the calculation is still based on the Transfer Matrix Formalism. The basic structure of the tandem solar cell is shown in Fig. 7(b). On top of the glass, a 100 nm indium-tin-oxide (ITO) layer is used as the anode, followed by a 50 nm layer of PEDOT:PSS and a front active layer with variable thicknesses. The recombination contact consists of a 30 nm ZnO layer and a 15 nm PEDOT:PSS layer, followed by a back active layer with variable thicknesses. Finally, 100 nm Al is deposited to realize the cathode. In conventional tandem solar cells, materials mainly absorbing light of shorter wavelengths act as the front active layer to provide a window for the back cell while materials mostly absorbing light of longer wavelengths work as the back active layer. Thus the device with P3HT:PCBM in the front cell and pBBTDPP2:PCBM in the back cell is defined as“Normal Tandem Solar Cell” or “NTSC”, the device with pBBTDPP2:PCBM in the front cell and P3HT:PCBM in the back cell as “Reverse Tandem Solar Cell” or “RTSC”.

Before starting our work, three assumptions should be stated. First, an electron-hole pair is generated in the solar cell with every photon absorbed. Second, Ohmic losses in the recombination contact and the spacer are negligible. In consequence, the open circuit voltage of the tandem solar cell is a summation of those of both subcells. Thus, the performance of the tandem solar cell is mainly determined by its short circuit current density ($J_{SC}$). Three, the glass substrate is thicker than the coherence length of light, so optical interference in it can be neglected.

The optical parameters (n and k) of P3HT:PCBM (1:1 in weight), pBBTDPP2:PCBM (1:2 in weight), ITO, ZnO, PEDOT:PSS and Al used in this work are obtained from literatures [11, 14, 17, 18].

Considering current matching, we optimize the thicknesses of the front and back cells for NTSC and RTSC respectively. All the calculations are carried out under AM 1.5G radiation.

### 3.2. Results and discussion

According to the existing views, the optimized PCE can be obtained when the photocurrents of the subcells are matched. Thus, we vary the thicknesses of both the front ($d_{front}$ between 10 and 250 nm) and back ($d_{back}$ between 10 and 200 nm) active layers to investigate $J_{SC}$ of both subcells.

http://dx.doi.org/10.5772/52819

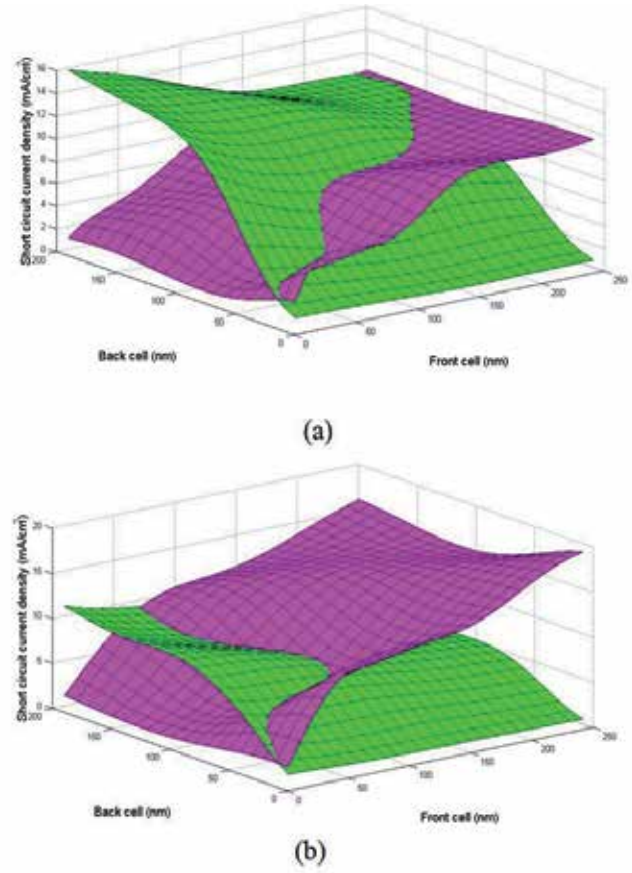


**Figure 8.** a) and b) 3D plots of $J_{SC(front)}$ (magenta) and $J_{SC(back)}$ (green) versus $d_{front}$ and $d_{back}$ for NTSC and RTSC.

Such a result of the calculation is plotted in Figs. 8 (a) and (b) for NTSC and RTSC separately. $J_{SC}$ for the front ($J_{SC(front)}$) and back ($J_{SC(back)}$) cells are shown in the three-dimensional (3D) space as surfaces, magenta and green, respectively. Figures 9 (a) and (b) display the same results as Figs. 8 (a) and (b) respectively, but in a two-dimensional format. In NTSC, the front cell may provide up to a $J_{SC}$ of 11.22 mA/cm$^2$ when $d_{back}$=10 nm. Whereas when $d_{back}$ increases up to 200 nm, $J_{SC(front)}$ can decrease down to 10.30 mA/cm$^2$. Because the front cell is much far from the mirror Al electrode, $J_{SC(front)}$ scarcely shows any interference oscillation in the variation range of $d_{back}$. Thus, this 8% loss is $J_{SC(front)}$ not induced by the interference effect but the reduction of the amount of light reflected from the Al surface (and arriving at the front cell a second time) as the thickness of the back cell increases. The variation of $J_{SC(back)}$ is more strongly affected by $d_{front}$ than vice versa. While for $d_{front}$=10 nm, $J_{SC(back)}$ goes up to 15.76 mA/cm$^2$. However, when $d_{front}$=250 nm, $J_{SC(back)}$ reduces to 10.29 mA/cm$^2$. This is obviously caused by the absorption spectra overlap of the two active layer materials (see Fig. 7(a)), which reduces photons arriving at the back cell. Because the back cell is much nearer to the Al electrode than the front cell, the interference behavior of $J_{SC(back)}$ is very obvious as

shown in Fig. 9(a). Because of the same reason, the same tendency can be observed in RTSC (see Figs. 8(b) and 9(b)). In RTSC, while for $d_{back}$=10 and 200 nm, $J_{SC(front)}$ goes up to 18.93 and 16.04 mA/cm$^2$, respectively. With the increase of $d_{front}$ from 10 to 250 nm, $J_{SC(back)}$ decreases from 10.97 to 5.53 mA/cm$^2$. A obvious increase of $J_{SC}$ of pBBTDPP2:PCBM layer and a strong decrease of $J_{SC}$ of P3HT:PCBM layer can be observed in RTSC, compared with NTSC. This is caused by the absorption difference of two blends. As shown in Fig. 7(a), the spectral range of pBBTDPP2:PCBM is much wider than that of P3HT:PCBM (the former absorbs photons in the nearly entire wavelength range discussed while the latter hardly absorbs photons of wavelengths beyond 650 nm). Therefore, when acting as the front active layer, pBBTDPP2:PCBM hinders the harvest of photons in P3HT:PCBM more strongly than that in P3HT:PCBM with pBBTDPP2:PCBM as the back active layer.

| NTSC | | | | RTSC | | | | difference |
|---|---|---|---|---|---|---|---|---|
| $d_{front}$ | $d_{back}$ | $J_{sc(front)}$ | $J_{sc(back)}$ | $d_{front}$ | $d_{back}$ | $J_{sc(front)}$ | $J_{sc(back)}$ | Δ |
| 6 | 10 | 1.00 | 0.89 | 7 | 10 | 1.06 | 1.09 | -0.20 |
| 8 | 20 | 1.55 | 1.55 | 11 | 20 | 2.17 | 2.09 | -0.53 |
| 15 | 30 | 2.64 | 2.57 | 15 | 30 | 3.18 | 3.29 | -0.71 |
| 58 | 40 | 3.28 | 3.26 | 21 | 40 | 4.26 | 4.35 | -1.09 |
| 73 | 50 | 4.20 | 4.14 | 32 | 50 | 5.25 | 5.17 | -1.04 |
| 80 | 60 | 5.21 | 5.22 | 66 | 60 | 6.05 | 6.06 | -0.84 |
| 87 | 70 | 6.32 | 6.35 | 102 | 70 | 6.75 | 6.73 | -0.37 |
| 99 | 80 | 7.49 | 7.46 | 109 | 80 | 7.12 | 7.12 | 0.34 |
| 173 | 90 | 8.76 | 8.77 | 110 | 90 | 7.42 | 7.38 | 1.39 |
| 191 | 100 | 9.28 | 9.29 | 107 | 100 | 7.54 | 7.53 | 1.76 |
| 201 | 110 | 9.55 | 9.57 | 102 | 110 | 7.59 | 7.59 | 1.98 |
| 210 | 120 | 9.72 | 9.70 | 96 | 120 | 7.62 | 7.58 | 2.12 |
| 218 | 130 | 9.81 | 9.80 | 89 | 130 | 7.58 | 7.57 | 2.24 |
| 228 | 140 | 9.93 | 9.92 | 82 | 140 | 7.54 | 7.60 | 2.32 |
| 238 | 150 | 10.09 | 10.09 | 77 | 150 | 7.73 | 7.70 | 2.39 |
| 245 | 160 | 10.24 | 10.23 | 72 | 160 | 7.86 | 7.92 | 2.30 |
| 247 | 170 | 10.29 | 10.29 | 70 | 170 | 8.26 | 8.21 | 2.08 |
| 246 | 180 | 10.28 | 10.28 | 68 | 180 | 8.51 | 8.57 | 1.71 |
| 245 | 190 | 10.25 | 10.25 | 69 | 190 | 8.90 | 8.90 | 1.34 |
| 244 | 200 | 10.21 | 10.20 | 72 | 200 | 9.18 | 9.16 | 1.04 |

**Table 2.** Current matching points for NTSC and RTSC, corresponding to the black dots of the bold lines in Figs. 9 (a) and (b) respectively. Corresponding $J_{SC(front)}$, $J_{SC(back)}$, $d_{back}$ and $d_{front}$ are all displayed here. The differences between matching $J_{SC}$ of NTSC and RTSC displayed in the same row are shown in the last column (Δ). d is in nm and $J_{SC}$ is in mA/cm$^2$ here.

The bold lines in Figs. 9 (a) and (b) represent the intersection between both surfaces in the corresponding 3D plots, namely, current matching points of the subcells, which correspond

http://dx.doi.org/10.5772/52819

to the optimized thicknesses of the active layers. Seen from Figs. 9(a) and (b), it is obvious that a single value for $d_{front}$ can have more than one counterpart $d_{back}$ along the bold line for RTSC while there is only one counterpart $d_{back}$ for NTSC. This interesting thing leads us to list the optimized active layer thicknesses in Table 2 for NTSC and RTSC, respectively. It can be observed from Table 2 that RTSC shows its superiority in matching $J_{SC}$ when the active layers of both subcells are relatively thin. We note that RTSC can provides a larger matching $J_{SC}$ with a smaller $d_{front}$ when the device is relatively thin ($d_{back}$ is usually less than 100 nm). But NTSC is better as the thicknesses of both active layers increase, in agreement with the general view presented.

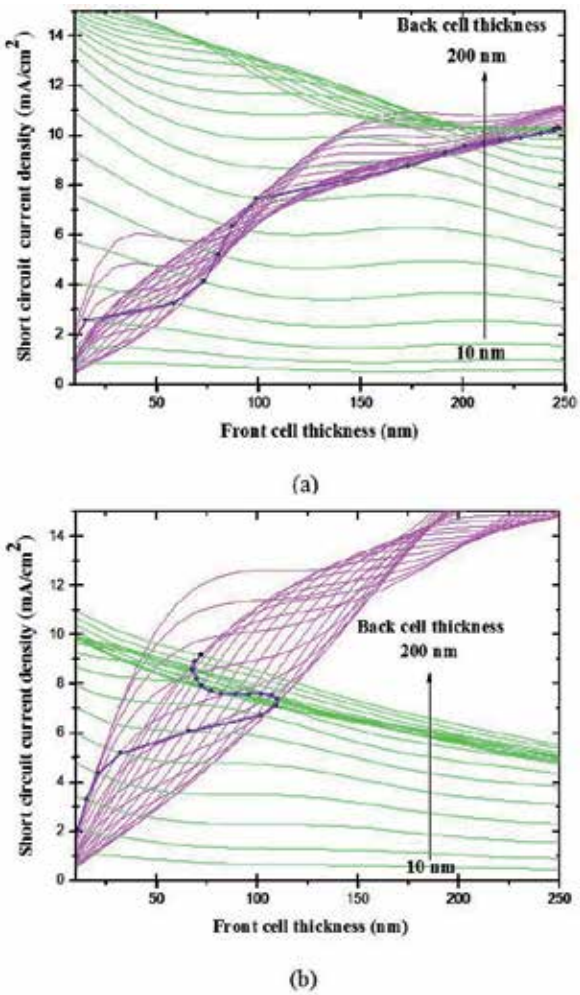


**Figure 9.** a) and b) Different viewing angle of the 3D plots shown in Figs. 8 (a) and (b), respectively. Every magenta or green line indicates $J_{SC(front)}$ or $J_{SC(back)}$ versus $d_{front}$ with the fixed $d_{back}$. $d_{back}$ is ranging from 10 to 200 nm in a uniform step of 10 nm (see the arrow).

In order to well understand this amazing phenomenon, optical electric field distributions of tandem solar cells should be taken into account. Four current matching points listed in Table 2 are used here: a 58-40-nm NTSC, a 21-40-nm RTSC, a 238-150-nm NTSC and a 77-150-nm RTSC. The reason why we choose these points is that the matching $J_{SC}$ differences between the corresponding NTSC and RTSC reach the maxima in positive and negative, respectively (see $\Delta$, the last column in Table 2). The distributions of normalized modulus squared of optical electric filed $|E|^2$ for the above tandem solar cells are calculated and shown in Fig. 10 (the shadow area indicates the active layers of the front (left) and back (right) cells). As shown in Fig. 7(a), 512 and 600 nm are around the peak and shoulder of the absorption spectrum of P3HT:PCBM respectively while 727 and 809 nm are around two absorption maxima of pBBTDPP2:PCBM. Thus, the cases for wavelengths of 512, 600, 727 and 809 nm are discussed here. By observing optical electric filed distributions of a 58-40 nm NTSC and a 21-40-nm RTSC (both active layers are relatively thin) as shown in Figs. 10 (a) and (b), it is very clear that RTSC has a better optical electric filed distribution in both active layers although it has a smaller $d_{front}$, in accordance with the values of $J_{SC}$ shown in Table 2. It can be explained by the properties of the materials and device structures. As shown in Figs. 10 (a) and (b), no matter with which structure, the peaks of optical electric field for light of wavelengths of 727 and 809 nm are usually near or in the front active layer. Since pBBTDPP2:PCBM mainly absorbs light of longer wavelengths and P3HT:PCBM absorbs light of shorter wavelengths, RTSC (place pBBTDPP2:PCBM in the front and P3HT:PCBM in the back) has a better performance when the active layers are thin. However, things become different when the device becomes thicker and thicker. For a very thick RTSC, the first interference peaks for wavelengths of 727 and 809 nm begin to leave the front active layer and then the pBBTDPP2:PCBM subcell is no longer an effective device. At the same time, owing to the much wider spectral range of pBBTDPP2:PCBM, it hinders the harvest of photons in P3HT:PCBM with pBBTDPP2:PCBM as the front active layer. Thus, when the active layers become thicker ($d_{back}$ is usually over 100 nm), RTSC only allows a smaller matching $J_{SC}$ with a smaller $d_{front}$ compared with NTSC and NTSC shows its superiority. This is in good agreement with the results in Table 2.

In conclusion, it is observed that RTSC takes over the lead in matching $J_{SC}$ when the active layers are relatively thin; but NTSC allows a larger matching $J_{SC}$ as the active layers are relatively thick. The similar results are also found in the tandem solar cell based on P3HT:$PC_{70}$BM and PCPDTBT:$PC_{60}$BM [19]. The results are very interesting since we can choose the thinner RTSC to achieve matching $J_{SC}$, which can alleviate the carrier transport problem and save the material cost.

http://dx.doi.org/10.5772/52819

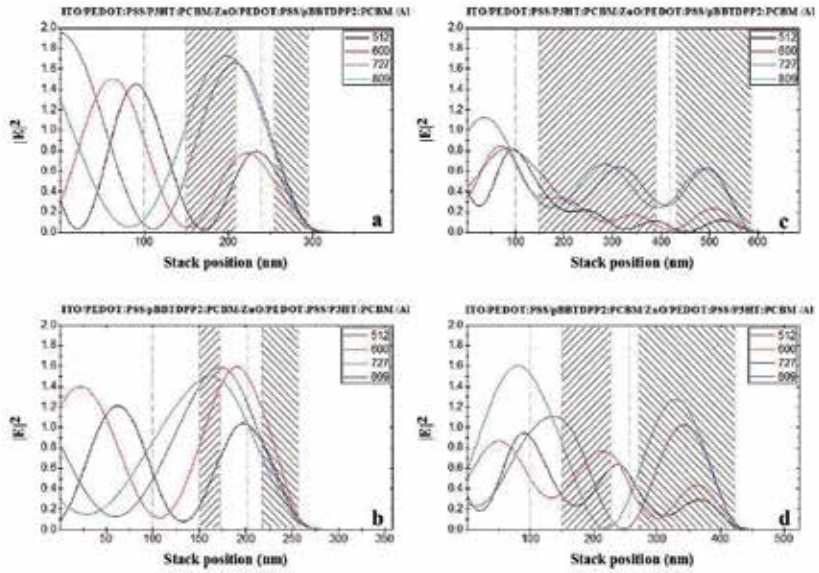


**Figure 10.** Calculated distributions of normalized modulus squared of optical electric field |E|2 inside a a) 58-40-nm NTSC b) 21-40-nm RTSC c) 238-150-nm NTSC d) 77-150-nm RTSC for four wavelengths of 512, 600, 727 and 809 nm.

## 4. Conclusion

The application of the bulk heterojunction structure consisting of an interpenetrating network of electron donor and acceptor materials greatly improves the standalone organic solar cells. Now there are mainly two types of standalone organic solar cells: OSC and IOSC. IOSC is introduced as the possible candidate for OSC to remedy the low air stability of OSC. However, most of the previous works reported that PCE of IOSC is relatively lower than that of OSC. As a result, the performance differences of OSC and IOSC are discussed in this work. It is concluded that in the optical aspect, OSC and IOSC have the same tendency in the number of photons absorbed in the active layer, EQE, and the optical electric field distribution as well as the similar influence of optical modulation effect. Normally, IOSC performs better due to the better light absorption of IOSC because the absorption loss in $TiO_x$ layer for IOSC is smaller than that in PEDOT:PSS layer for OSC and the hole transporting layer ($MoO_3$ layer in this work) can play the role of optical layer. However, around the interference maxima of OSC, OSC shows better performance because the optical electric field has been optimized under this condition and there is no room for further improvement.

Although PCE of the standalone organic solar cell is improved continuously, there are still some drawbacks for this type of devices: First, the organic solar cell is dominated by the excitonic effect, the relatively short lifetime and the low carrier mobility. And these limit the maximum thickness of the active layer for light absorption. Second, most organic semiconducting materials show discrete absorption behavior and cover only a fraction of the solar

spectrum, leading to inefficient light harvest. The realization of organic tandem solar cells based on complementary thin absorber materials provides a reasonable solution to improve PCE further. In a tandem cell, to achieve the maximum PCE, it is necessary to ensure current matching of both subcells, which leads to detailed optical simulations in this work. At first, active layer thicknesses of the tandem cell are optimized by considering current matching for normal and reverse structures (see Fig. 7), respectively. Owing to the different spectral ranges of two blend materials (P3HT:PCBM and pBBTDPP2:PCBM) and device structures, it is noted that the reverse tandem cell allows a larger matching $J_{SC}$ when the total device is relatively thin. When the thicknesses of the active layers increase, the normal tandem solar cell begins to present its superiority in the performance. This makes senses in the aspect of application that we can choose a thinner reverse tandem cell to achieve $J_{SC}$ needed in some cases, which saves cost and increases the profit to an extent.

## Acknowledgements

The work is supported by National Natural Science Foundation of China (61106063) and the Fundamental Research Funds for the Central Universities (K50511250003).

## Author details

Chunfu Zhang[1*], Yue Hao[1*], Dazheng Chen[1], Zhizhe Wang[1*] and Zhenhua Lin[2]

*Address all correspondence to: cfzhang@xidian.edu.cn

1 School Of Microelectronics, Xidian University, China

2 ECE, National University of Singapore, Singapore

## References

[1] Brabec, C. J., Sariciftci, N. S., & Hummelen, J. C. (2001). Plastic solar cells. *Adv. Funct. Mater*, 11(1), 15-26.

[2] Huynh, W. U., Dittmer, J. J., & Alivisatos, A. P. (2002). Hybrid nanorod-polymer solar cells. *Science*, 295(5564), 425-427.

[3] Kim, Y., Lee, K., Coates, N. E., Moses, D., Nguyen, T. Q., Dante, M., & Heeger, A. J. (2007). Efficient tandem polymer solar cells fabricated by all-solution processing. *Science*, 317(5835), 222-225.

[4] Zhang, C. F., Hao, Y., Tong, S. W., Lin, Z. H., Feng, Q., Kang, E. T., & Zhu, C. X. (2011). Effects of cathode confinement on the performance of polymer/fullerene photovoltaic cells in the thermal treatment. *IEEE Trans. Electron Devices*, 58(3), 835-842.

[5] Yu, G., Gao, J., Hummelen, J. C., Wudl, F., & Heeger, A. J. (1995). Polymer photovoltaic cells: enhanced efficiencies via a network of internal donor-acceptor heterojunctions. *Science*, 270(5243), 1789-1791.

[6] Pacios, R., Chatten, A. J., Kawano, K., Durrant, J. R., Bradley, D. D. C., & Nelson, J. (2006). Effects of photo-oxidation on the performance of poly [2-methoxy-5-(3′,7′-dimethyloctyloxy)-1, 4-phenylene vinylene]:[6,6]-phenyl C61-butyric acid methyl ester solar cells. *Adv. Funct. Mater*, 16(10), 2117-2126.

[7] Gregg, B. A., & Hanna, M. C. (2003). Comparing organic to inorganic photovoltaic cells: Theory, experiment, and simulation. *J. Appl. Phys*, 93(6), 3605-3614.

[8] Park, S. H., Roy, A., Beaupre, S., Cho, S., Coates, N., Moon, J. S., Moses, D., Leclerc, M., Lee, K., & Heeger, A. J. (2009). Bulk Heterojunction Solar Cells With Internal Quantum Efficiency Approaching 100%. *Nature Photonics*, 3, 297-303.

[9] Pettersson, L. A. A., Roman, L. S., & Inganas, O. (1999). Modeling photocurrent action spectra of photovoltaic devices based on organic thin films. *J. Appl. Phys*, 86(1), 487-496.

[10] Zhang, C. F., You, H. L., Hao, Y., Lin, Z., & H. and, Zhu. C. X. (2011). Effects of Optical Interference and Annealing on the Performance of Polymer/Fullerene Bulk Heterojunction Solar Cells. *In: Leonid A. Kosyachenko (Ed.) Solar Cells- New Aspects and Solutions, Rijeka: InTech*, 1-26.

[11] Burkhard, G. F., Hoke, E. T., & Mc Gehee, M. D. (2010). Accounting for interference, scattering, and electrode absorption to make accurate internal quantum efficiency measurements in organic and other thin solar cells. *Adv. Mater*, 22(30), 3293-3297.

[12] Hadipour, A., Cheyns, D., Heremans, P., & Rand, B. P. (2011). Electrode considerations for the optical enhancement of organic bulk heterojunction solar cells. *Adv. Energy Mater*, 1(5), 930-935.

[13] Yoshikawa, H., & Adachi, S. (1997). Optical constants of ZnO. *Jpn. J. Appl. Phys*, 36(10), 6237-6243.

[14] Gilot, J., Barbu, I., Wienk, M., & Janssena, R. A. J. (2007). The use of ZnO as optical spacer in polymer solar cells: Theoretical and experimental study. *Appl. Phys. Lett*, 91(11), 113520-1-113520-3.

[15] Ameri, T., Dennler, G., Waldauf, C., Denk, P., Forberich, K., Scharber, M. C., & Hingerl, K. (2010). Realization, characterization, and optical modeling of inverted bulk-heterojunction organic solar cells. *J. Appl. Phys.*, 103(8), 084506-1-084506-6.

[16] Gilot, J., Wienk, M. M., & Janssen, R. A. J. (2010). Optimizing Polymer Tandem Solar Cells. *Adv. Mater*, 22(8), E67-E71.

[17] Ng, A., Li, C. H., Fung, M. K., Djurišić, A. B., Zapien, J. A., Chan, W. K., Cheung, K. Y., Wong, W., & , Y. (2010). Accurate Determination of the Index of Refraction of Polymer Blend Films by Spectroscopic Ellipsometry. *J. Phys. Chem. C*, 114(35), 15094-15101.

[18] Rakić, A. D. (1995). Algorithm for the determination of intrinsic optical constants of metal films: application to aluminum. *Applied Optics*, 34(22), 4755-4767.

[19] Dennler, G., Forberich, K., Ameri, T., Waldauf, C., Denk, P., Brabec, C. J., Hingerl, K., & Heeger, A. J. (2007). Design of efficient organic tandem cells: On the interplay between molecular absorption and layer sequence. *J. Appl.Phys*, 102(12), 123109-1-123109-6.

Chapter 10

# GaAsN Grown by Chemical Beam Epitaxy for Solar Cell Application

Kazuma Ikeda, Han Xiuxun, Bouzazi Boussairi and Yoshio Ohshita

Additional information is available at the end of the chapter

http://dx.doi.org/10.5772/51885

## 1. Introduction

InGaAsN is a candidate material to realize the ultrahigh efficiency lattice-matched multi-junction solar cell. This material has the 1eV band gap energy and same lattice constant as GaAs or Ge substrate by controlling the In and N compositions to be 9% and 3%, respectively [1, 2]. So far, the highest conversion efficiency of the lattice-matched multi-junction solar cell is 43.5% at 418-suns which was achieved by the 3-junction solar cell, GaInP/GaAs/GaInNAs [3]. By realizing the 4-junction device, InGaP/InGaAs/InGaAsN/Ge, the efficiency is expected to be 41% at 1-sun under the AM1.5G spectrum and 51% at 500-suns under the AM1.5D spectrum [4]. In order to achieve the expected super high efficiency, the short circuit current, $J_{sc}$, under a GaAs filter has to be 17 mA/cm$^2$ at 1-sun under AM0 conditions. However, the highest $J_{sc}$ under that condition has been 10.9mA/cm$^2$. This corresponds to the 6.2% conversion efficiency and $J_{sc}$=26.0 mA/cm$^2$ without GaAs filters at 1-sun under AM1.5 [5]. The diffusion length of the minority carrier in this case is supposed to be much shorter than 1 μm which is required to achieve the ultrahigh efficiency. Therefore, the mobility and lifetime of the minority carrier should be improved.

The large miscibility gap is a particular characteristic of (In)GaAsN. It means that the phase separation easily occurs in the near equilibrium condition. It is caused by the large difference between the atomic radii of As and N [6]. Because of this property, homogeneous alloys are difficult to be obtained. Various growth techniques have been tried to avoid the phase separation and obtain good alloys: the plasma-assisted molecular beam epitaxy (MBE) [7], solid source MBE with a radio frequency (RF) nitrogen plasma source [8], metal organic vapor phase epitaxy (MOVPE) [9], metalorganic MBE [10-13], and chemical beam epitaxy (CBE) [14].

The chemical reactions at the surface of the substrates are expected to occur in the far-from-equilibrium states in those methods.

The electrical properties of (In)GaAsN has been reported to be drastically deteriorated by increasing the N composition [15]. The Hall hole mobility of p-GaAsN as a function of the N composition is shown in Figure 1 [15, 16]. It seems that the hole mobility is largely determined by the amount of N atoms and independent of the growth methods. This indicates that the N atoms contribute to the formation of dominant scattering centers. The electrical deterioration has been considered to be caused by the inhomogeneity of the N distribution. Therefore, it may be possible to improve the electrical property by controlling the growth process. In this work, CBE technique was used for the growth of GaAsN. This method has been developed in our group and shown the improvement in the electrical properties [18, 19].

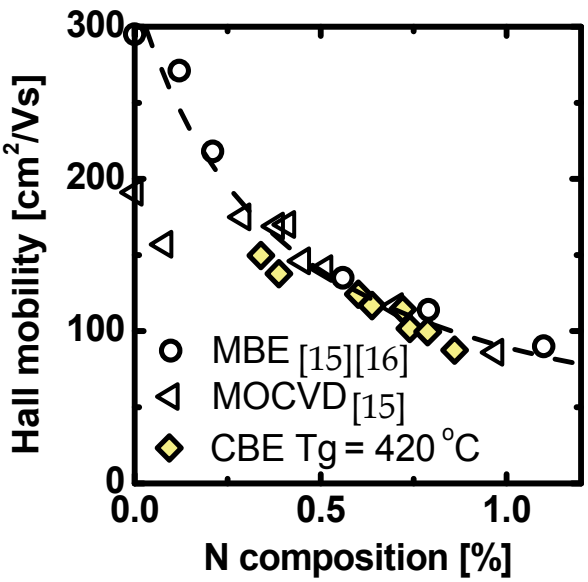


**Figure 1.** The N composition dependence of the hall mobility of p-GaAsN. The dashed line is a guide for the eye.

In this chapter, the improvement of the carrier mobility and minority carrier lifetime in GaAsN grown by CBE is described. The effects of the growth rate and substrate orientation on these electrical properties are discussed.

## 2. Chemical beam epitaxy

### 2.1. Growth procedure of chemical beam epitaxy

The CBE technique has both natures of the metal organic chemical vapor deposition (MOCVD) and molecular beam epitaxy (MBE): metal organic gas sources and low pressure growth [19].

http://dx.doi.org/10.5772/51885

In addition, the growth temperature is lower than the other methods. The low temperature is expected to be advantageous to obtain a non-equilibrium condition and homogeneous distribution of N in As sites. The growth condition of the CBE technique is shown in Table 1. The semi-insulating GaAs(001) oriented in 2° towards [010] was used as the substrate. The growth pressure is around $10^{-2}$ Pa or below, therefore the mean free path of the source gas molecules is in the order of $10^{-1}$ m. Triethylgallium [TEGa, Ga(C2H5)3], and monomethylhydrazine [MMHy, (CH3)N2H3], were used as the sources of Ga, and N. Trisdimethylaminoarsenic [TDMAAs, As(N(CH3)2)3] was used as the As source instead of $As_2$ obtained by cracking $As_2H_4$. Typical flow rates of TEGa, TDMAAs, and MMHy were 0.1, 1.0, and 9.0 sccm, respectively. The substrate was annealed in the chamber at a temperature of 500 °C for 5 minutes with supplying TDMAAs to remove the oxidized layer on the surface. Then, GaAsN thin film was grown by supplying TEGa and MMHy. The growth temperature was 340 to 460 °C. The growth time was 30 minutes.

| **Substrate** | | | **Semi-insulating GaAs(001) with 2° offcut toward [010]** | |
|---|---|---|---|---|
| Growth pressure | | | $2\times10^{-2}$ Pa | |
| Source | Flow rate (sccm) | Ga | TEGa [$Ga(C_2H_5)_3$] | 0.02 - 0.1 |
| | | As | TDMAAs [$As(N(CH_3)_2)_3$] | 1.0 |
| | | N | MMHy [$(CH_3)N_2H_3$] | 9.0 |
| Post annealing | | | 5 min. at 500 ℃ | |
| Growth temperature (℃) | | | 340 ~ 480 | |
| Growth time (min.) | | | 30 | |

**Table 1.** The growth condition of the CBE technique.

The N composition was estimated from the lattice constant of GaAsN(004) determined by X-ray diffraction (XRD). Here, elastic distortion and Vegard's law were assumed [20]. The growth rate was determined by the film thickness estimated from the interference fringe peaks in an XRD curve and growth time, or the Dektak surface profilometer in the case that no fringe peaks appeared. The crystal quality of the films was evaluated by the full width at half maximum (FWHM) of the rocking curve of a GaAsN(004) peak.

### 2.2. Growth of GaAsN thin films

The growth temperature dependences of the growth rates are shown in Figure 2. The growth temperature can be divided into three regions. In the lower temperature region (340 – 390 °C), the growth rate increases with increasing temperature. In the middle temperature region (390 – 445 °C), the growth rate decreases with increasing temperature. In the higher temperature region (445 – 480 °C), the growth rate slightly changes. The relationship between the TEGa flow rate and growth rate in each growth temperature region is shown in Figure 3. The growth temperatures of 360, 420, and 480 °C in Figure 3 belong to the low, middle, and high growth temperature regions, respectively. Here, the TDMAAs flow rate was 1.0 sccm and MMHy flow rate was 9.0 sccm. In the case that the growth temperature was 360 °C (in the low temperature

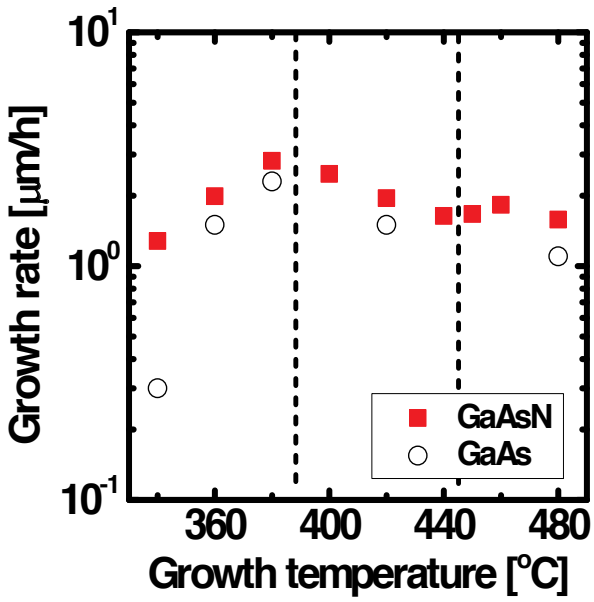


**Figure 2.** The dependence of the growth rate on the growth temperature of GaAs and GaAsN thin films.

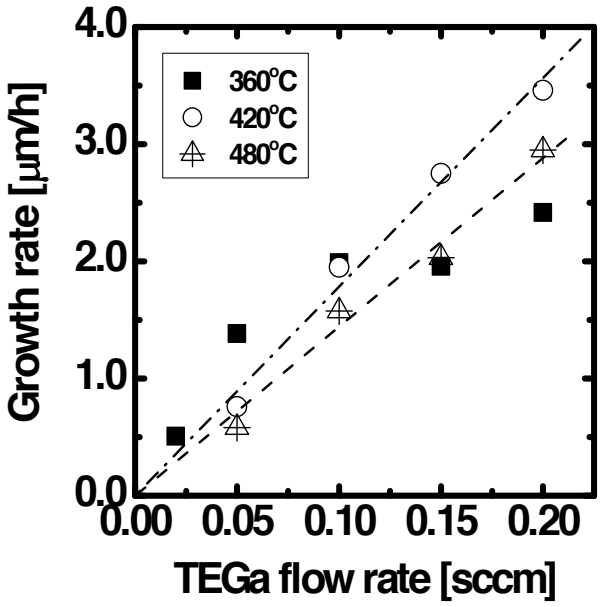


**Figure 3.** The dependence of TEGa flow rate on the growth rate of GaAsN thin films.

region), the growth rate saturated above the TEGa flow rate of 0.1 sccm. It indicates that the factor that determines the growth rate changed from the TEGa supply to another process such

http://dx.doi.org/10.5772/51885

as the decomposition rate of TEGa on the surface. At higher growth temperatures (in the middle and high temperature regions), the growth rate linearly increased as increasing TEGa flow rate, which indicates that the TEGa supply was dominant to determine the growth rate.

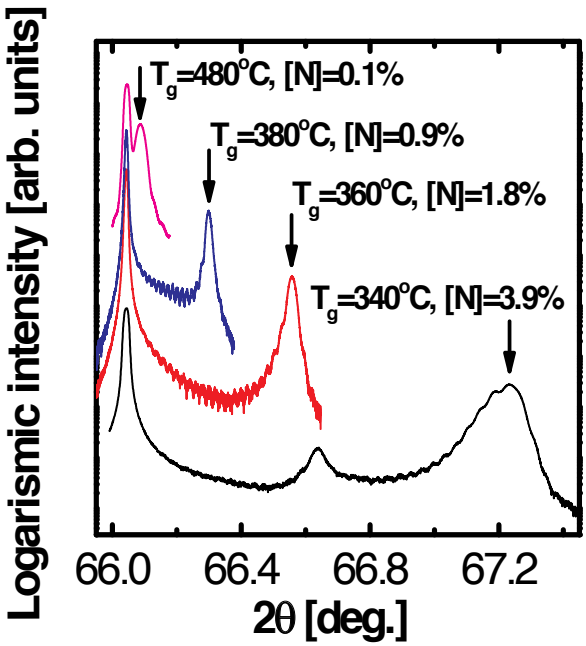


**Figure 4.** The XRD rocking curves of the GaAsN thin films grown by CBE. The corresponding growth temperature and N composition of each sample is also shown

The XRD rocking curves of GaAsN(004) are shown in Figure 4. The GaAsN films were grown at the temperatures of 340, 360, 380, and 480 °C. There are interference fringes in the rocking curves of the last three films, which suggest the uniformity of the lattice constant with flat interface. On the other hand, there is no fringe in the rocking curve of the film grown at 340 °C, indicating a poor quality of the crystal. The N compositions estimated from the XRD measurements monotonically decreased by increasing the growth temperatures as shown in Figure 5. This is the same tendency as those in the temperature dependence of the growth rate. In the middle region of the growth temperature (390 – 445 °C), the decrement of the N composition is relatively small compared to those in the lower (340 – 390 °C) and higher (445 – 480 °C) regions.

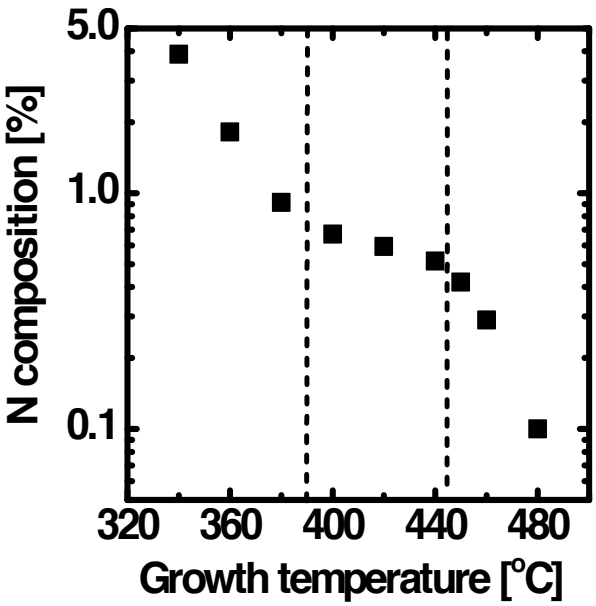


**Figure 5.** The dependence of growth temperature on the N composition in GaAsN thin films.

### 2.3. Crystal quality of GaAsN grown by CBE

The FWHM's of measured samples divided by the theoretical calculations of GaAsN(004) peaks are shown in Figure 6. To remove the contribution of the film thickness, those were normalized by using the Schereer's equation. When the film was grown above 360 °C, the ratios are almost 1.0, which indicates good crystal quality. On the other hand, the large ratio of the film grown at 340 °C means poor quality of the crystal, corresponding to no fringe in XRD spectra. This deterioration of the crystal quality possibly occurred due to the incorporation of a large amount of impurities, such as hydrogen and carbon.

The dependence of the N composition on the growth temperature as shown in Figure 5 can be explained qualitatively as follows. A rapid decrease in the N composition with increasing the growth temperature in the low growth temperature region is due to both the increases in the growth rate and desorption rate of N species at the growing surface. Here, we assume that the amount of N species supplied to the growing surface is independent of growth temperatures. Then, the higher growth rate caused the decrement of the N source supply per unit layer growth, since the N source flow rate was constant in every growth conditions. In the middle growth temperature region, the decrement of the growth rate as increasing the growth temperature would enhance the N source supply per unit layer growth. However, the N composition did not increase. It indicates that the desorption rate of N species prevailed in the middle growth temperature region to reduce the N composition as the growth temperature increased. In the high growth temperature region, the N composition again markedly decreases with increasing the growth temperature. The fact that the growth rate remains almost

http://dx.doi.org/10.5772/51885

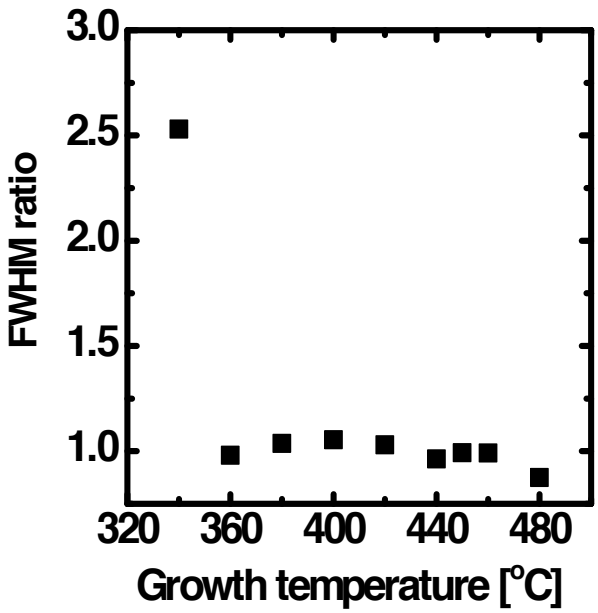


**Figure 6.** The ratio of FWHM obtained from the measured samples and theoretical calculation at each growth temperature.

constant in that region as shown in Figure 2 indicates that the increased desorption rate of N species are dominant to determine the N composition. Although these three dependences were also observed in the CBE-grown GaAsN with the atomic N source [14], the slope of XRD rocking curves in each region is steeper in our result. This is considered to mainly come from the difference in desorption rate between the N sources on the growing surface. To further understand the N incorporation mechanism in CBE with compound N sources, such as MMHy, it is necessary to consider the desorption rate of N species.

## 3. Hole mobilities

### 3.1. Hall hole mobility

The hole mobility in p-GaAsN films grown by CBE, MBE, and MOCVD is shown in Figure 7 as a function of N composition [16, 21]. Those grown by the CBE in our group were obtained by Van der Pauw method. The dashed line represents the mobility obtained theoretically by considering the alloy and phonon scatterings. The hole mobility monotonically decreases as increasing the N composition and they are smaller than the theoretical values. The deviation of the mobility from the ideal value is at the same level despite the different impurity concentrations [16, 21]. This indicates that some N-related defects are generated due to the N incorporation, which determine the hole mobility at the room temperature. To evaluate the number of N-related defects, the temperature dependence (77-400K) of the hole mobility was

obtained as shown in Figure 8. The result suggests that there are several different scattering mechanisms. To determine the amount of the N-related scattering centers, we analyzed this temperature dependence. Here, ionized impurity scattering, alloy scattering, phonon scattering, and N-related carrier scattering were considered [22, 23]. The inverse of the mobility limited by the N-related carrier scattering $1/\mu_N$, which is proportional to the density of N-related scattering centers, was determined by excluding the contributions of the mobility limited by ionized impurity ($\mu_{II}$), alloy scattering ($\mu_{AL}$), and phonon scattering ($\mu_{PN}$) from the measured mobility ($\mu_{exp}$), as follows:

$$\frac{1}{\mu_N} = \frac{1}{\mu_{\exp}} - \frac{1}{\mu_{II}} - \frac{1}{\mu_{AL}} - \frac{1}{\mu_{PN}}. \tag{1}$$

Here, $1/\mu_{PN}$ is the sum of the contributions from the acoustical phonon ($\mu_{AC}$), polar optical phonon ($\mu_{PO}$), and non-polar optical phonon scattering ($\mu_{NPO}$) as

$$\frac{1}{\mu_{PN}} = \frac{1}{\mu_{AC}} + \frac{1}{\mu_{PO}} + \frac{1}{\mu_{NPO}}. \tag{2}$$

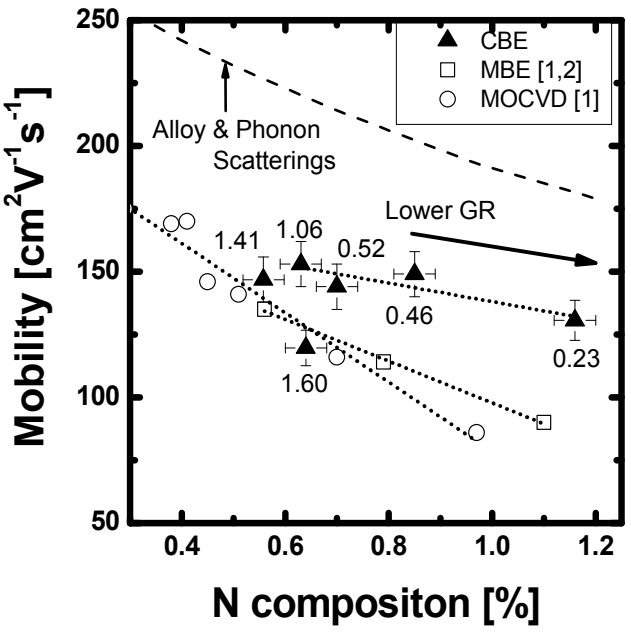


**Figure 7.** Hole mobility at room temperature in p-GaAsN films grown by CBE, MBE, and MOCVD as a function of N composition. The mobility is the value at room temperature. The dashed line represents the estimated mobility limited by the alloy and phonon scatterings. In the case of CBE, the growth rate (GR) is shown in the unit of μm/h. The dotted lines are a guide for the eye.

http://dx.doi.org/10.5772/51885

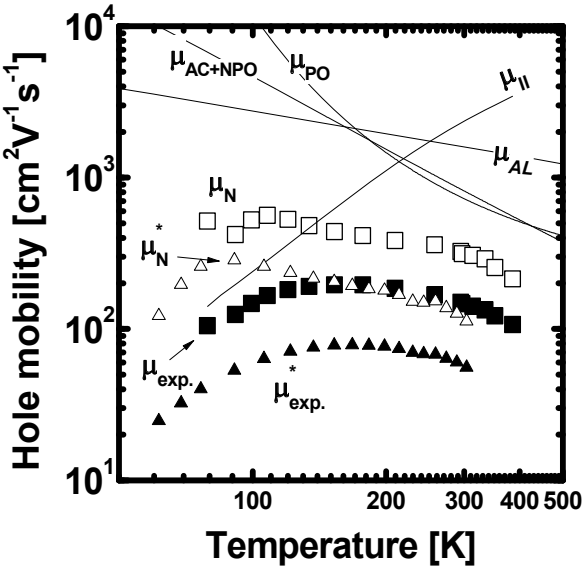


**Figure 8.** Temperature dependence of the hole mobility of p-GaAsN films with N composition of approximately 0.34% ($\mu_{exp.}$) and its components denoted in eq. (1). The contribution from N-related scattering centers ($\mu_N$) is obtained by using eq. (1). The mobility with N composition of approximately 0.79% ($\mu^*_{exp.}$) and contribution from the N-related scattering centers ($\mu^*_N$) are also shown.

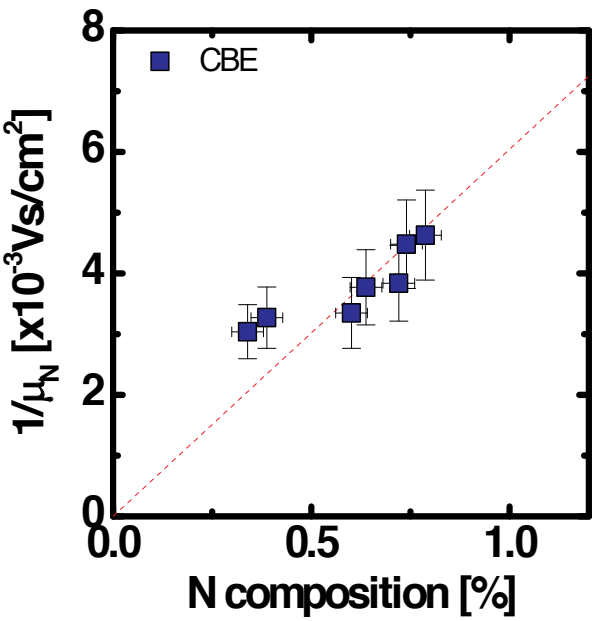


**Figure 9.** $1/\mu_N$ at each N composition in p-GaAsN films.

The expressions of each component of the mobility are described, for example, in ref. [16].

The relationship between $1/\mu_N$ and N composition is shown in Figure 9. The inverse of the mobility limited by the N-related carrier scattering center ($1/\mu_N$) was determined, which is proportional to the amount of N-related scattering centers. Independent of growth technique, the number of N related scattering centers ($1/\mu_\infty$ ) increases as N composition increases.

### 3.2. Improvement of mobility by controlling the growth rate

The above result suggested that the number of N-related defects may be determined by the N concentration of the GaAsN independent of the growth technique. However, here we show the increase of the mobility by controlling the growth rate in CBE. The hole mobility at room temperature and the N composition in p-GaAsN films as a function of growth rate are shown in Figure 10. The higher mobilities are obtained by decreasing the growth rate. Generally, the hole mobility is decreased by the increase in the N composition owing to the alloy scattering. To discuss the reason for the increase in the hole mobility, the relationship between the $1/\mu_N$ and N composition are shown in Figure 11. When the growth rate is higher than 1.41 μm/h, there is no improvement of the mobility. By decreasing the growth rate lower than 1.04 μm/h, the $1/\mu_N$ (the number of the N-related defects) remains almost constant despite the increase in the N composition. $(\mu_N [N])^{-1}$ as a function of the growth rate is shown in Figure 12. This is a relative amount of the N-related scattering centers to the total amount of N atoms. $(\mu_N [N])^{-1}$ is decreased by decreasing the growth rate monotonically. Then, the controlling growth rate in CBE is effective to suppress the formation of N-related scattering centers and to improve the mobility, especially for a higher N composition.

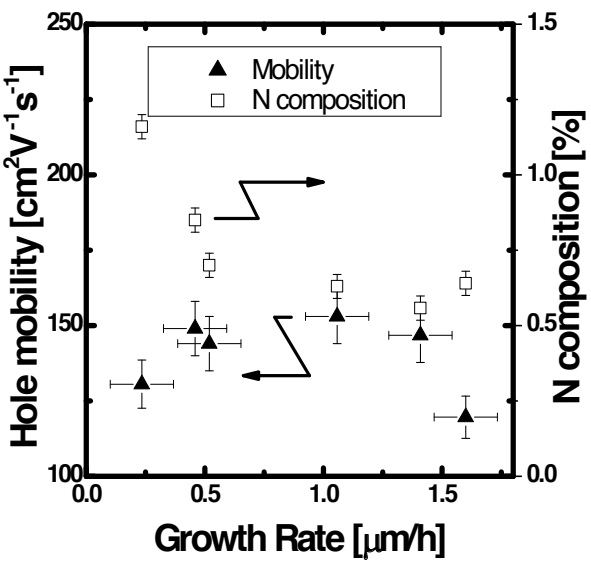


**Figure 10.** Hole mobility at room temperature and N composition in p-GaAsN films as a function of growth rate.

http://dx.doi.org/10.5772/51885

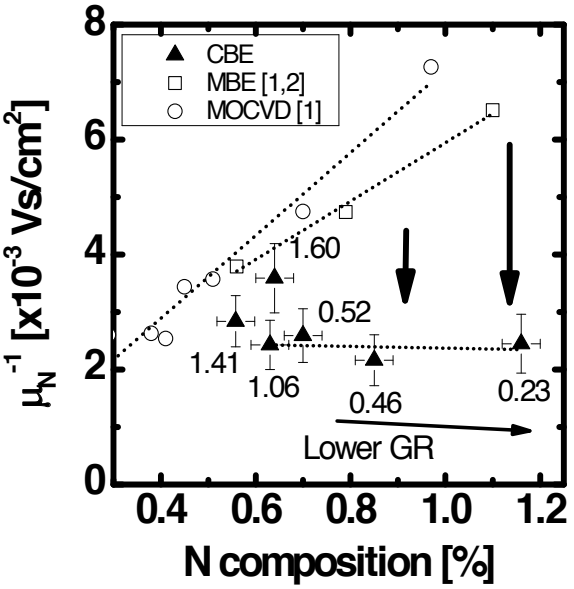


**Figure 11.** μN-1 at room temperature as a function of N composition in p-GaAsN films. $\mu_N^{-1}$ is proportional to the amount of N-ralated scattering centers. In the case of CBE, the growth rate (GR) is shown in the unit of μm/h. The dotted lines are a guide for the eye.

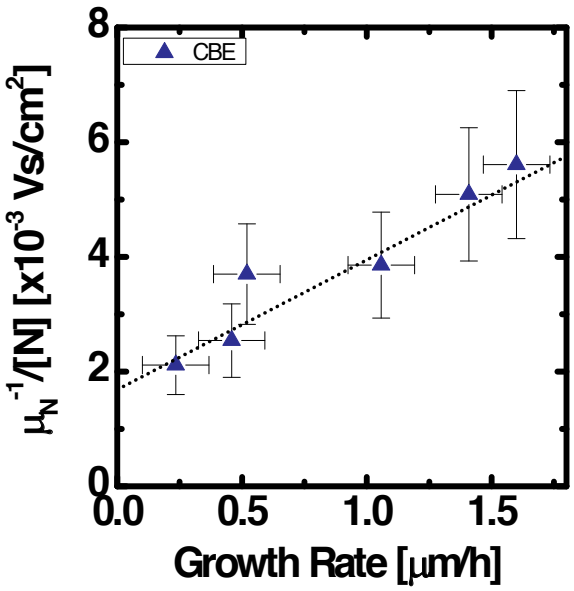


**Figure 12.** $(\mu_N\ [N])^{-1}$ as a function of growth rate of p-GaAsN films. $(\mu_N\ [N])^{-1}$ is the relative amount of the N-related scattering centers to the total amount of N atoms. The dotted line is a guide for the eye.

We inferred two reasons for the reduction of the amount of N-related scattering centers by decreasing the growth rate: i) The amount of N adsorbed species which are desorbed from a terrace increases by decreasing the growth rate. We expect that the N adsorbed species adsorbed from a terrace is a cause of N-related scattering centers. The desorption from a terrace is expected to be more frequent than that from a step, since the number of connected bonds of N adsorbed species to the growing surface is smaller at terrace than at step; ii) The decrease in the growth rate increases the diffusion length of N adsorbed species on the growing surface. A large diffusion length is expected to increase the probability of a N adsorbed species to come over a step. Therefore, the probability of a N adsorbed species adsorbed at a step increases. Then, i) and ii) are expected to be advantageous for the improvement of the carrier mobility and lifetime.

## 4. Mobility contributed from N-related scattering center

### 4.1. Minority-carrier lifetime

#### *4.1.1. Improvement of minority carrier lifetime by controlling growth rate*

As the control of the growth rate improved the mobility, here we show that the decreasing the TEGa flow rate improves the minority carrier lifetime.. The minority-carrier lifetime at room temperature was obtained by time-resolved photoluminescence (TR-PL). A titanium sapphire pulse laser was used for the carrier excitation. The excitation power, wavelength, pulse width, and recurrence frequency were 900 mW, 800 nm, ~100 fs, and 80 MHz, respectively. To evaluate the minority carrier lifetime of p-GaAsN, the structure of GaAs buffer layer (500 nm)/ p-GaAsN layer (140~950 nm)/GaAs cap layer (30 nm) was adopted. The cap layer reduced the surface recombination. The PL lifetime ($\tau_{PL}$) was obtained by PL decay curves. $\tau_{PL}$ consists of minority-carrier lifetimes in the bulk of the p-GaAsN layer ($\tau_B$) and at GaAs/GaAsN interfaces ($\tau_S$). The contribution of $\tau_S$ to $\tau_{PL}$ changes as a function of the p-GaAsN layer thickness (d)16) as follows:

$$\frac{1}{\tau_{PL}} = \frac{1}{\tau_B} + \frac{1}{\tau_S} = \frac{1}{\tau_B} + \frac{2S}{d}. \tag{3}$$

Here, S is the GaAs/GaAsN interface recombination velocity. PL lifetime as a function of GaAsN layer thickness was obtained and $\tau_B$ was determined by eq. (3). The amount of nonradiative recombination centers were estimated qualitatively based on eq. (4),

$$N_{NR} \propto \frac{1}{\tau_{NR}} = \frac{1}{\tau_B} - \frac{1}{\tau_R}, \tag{4}$$

http://dx.doi.org/10.5772/51885

| GR (μm/h) | [N] (%) | $\tau_B$ (ns) | $\tau_R$ (ns) | $\tau_{NR}$ (ns) |
|---|---|---|---|---|
| 2 | 0.6 | $3.2 \times 10^{-1}$ | $8.0 \times 10^{1}$ ($p = 1 \times 10^{17}$ cm$^{-3}$) | $3.2 \times 10^{-1}$ |
| 0.4 | 0.8 | $9.0 \times 10^{-1}$ | $1.7 \times 10^{2}$ ($p = 5 \times 10^{16}$ cm$^{-3}$) | $9.0 \times 10^{-1}$ |

**Table 2.** Summary of growth rate (GR), N composition ([N]), minority-carrier lifetime in the bulk of p-GaAsN ($\tau_B$), and radiative, nonradiative recombination lifetime ($\tau_R$, $\tau_{NR}$). $\tau_B$ was estimated by the PL lifetime dependence on the thickness of the p-GaAsN layer. $\tau_R$ was determined by using the hole concentration (p). $\tau_{NR}$ is obtained by using eq. (3).

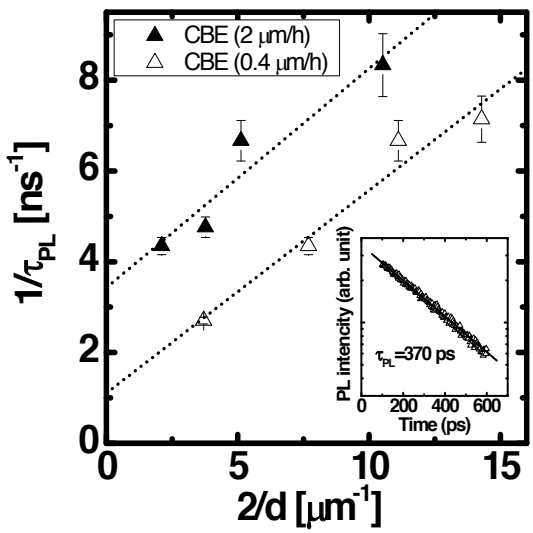


**Figure 13.** Fitting results of PL lifetime ($\tau_{PL}$) dependence on GaAsN layer thickness (d). The inserted figure shows a typical PL decay curve at room temperature, which is for the sample with GaAsN layer thickness of approximately 500 nm grown at a growth rate of 0.4 μm/h.

where NNR is the density of the nonradiative recombination centers, and $\tau_{NR}$ and $\tau_R$ are the nonradiative and radiative recombination lifetimes, respectively. $\tau_R$ was determined by the hole concentration (p) theoretically.

The decay of PL intensity was shown in Figure 13. The following equation

$$I_{PL}(t) = I_0 \exp\left(-\frac{t}{\tau}\right). \tag{5}$$

explains well about the PL decay curve. Here, $I_{PL}(t)$ is the PL intensity at the time t, and $I_0$ is the PL intensity at t = 0, just after the carriers are excited. The lifetime τ obtained by eq. (5) is the PL lifetime ($\tau_{PL}$) in eq. (3). To estimate the minority-carrier lifetime in the bulk of the p-

GaAsN layer ($\tau_B$), $\tau_{PL}$ dependence on GaAsN layer thickness (d) was obtained (Figure 13). When the growth rate was 2 μm/h, $\tau_B$ was 3.2 x $10^{-1}$ ns ([N] = 0.6%). By decreasing the growth rate to 0.4 μm/h, $\tau_B$ was increased to 9.0 x $10^{-1}$ ns ([N] = 0.8%) despite the increase in the N composition. Therefore, decreasing the growth rate in CBE is effective to improve $\tau_B$. Further, the improvement is more effective when the N composition is higher.

The density of the nonradiative recombination centers determines the nonradiative recombination lifetime ($\tau_{NR}$). To discuss the amount of nonradiative recombination centers, $\tau_{NR}$ is estimated by eq. (4). The recombination lifetime ($\tau_R$) depends on the hole concentration (p), as follows:

$$\tau_R = \frac{1}{Bp}. \tag{6}$$

Here, B is the radiative recombination probability,

$$B = 0.58 \times 10^{-12} \sqrt{\varepsilon} \left( \frac{1}{m_p^* + m_n^*} \right)^{1.5} \times \left( 1 + \frac{1}{m_p^*} + \frac{1}{m_n^*} \right) \left( \frac{300}{T} \right)^{1.5} {E_g}^2, \tag{7}$$

where ε is the dielectric constant, $m_p$* and $m_n$* are the hole and electron effective masses, respectively, in units of the free electron mass, T is the temperature, and $E_g$ is the band gap. For the p-GaAsN layers discussed here, B calculated by eq. (7) was 1.2 x 10-10 cm3/s. When the growth rate was 2 μm/h, the carrier concentration was 1 x 1017 cm-3. By decreasing the growth rate to 0.4 μm/h, it was decreased to 5 x 1016 cm-3. From eqs. (4) and (6), $\tau_{NR}$ and $\tau_R$ were obtained to be $\tau_{NR}$ = 3.2 x 10-1 ns and $\tau_R$ = 8.0 x 101 ns for the growth rate of 2 μm/h, and $\tau_{NR}$ = 9.0 x 10-1 ns and $\tau_R$ = 1.7 x 102 ns for the growth rate of 0.4 μm/h. These results are summarized in Table 2. Since $\tau_{NR}$ is much smaller than $\tau_R$, $\tau_B$ is mainly determined by $\tau_{NR}$. Therefore, the improvement of $\tau_B$ is mainly due to the increase in $\tau_{NR}$. These results suggest that decreasing the growth rate in CBE is effective to suppress the formation of nonradiative recombination centers and to improve the carrier lifetime. Then, CBE is highly expected to realize the minority-carrier lifetime of more than 1 ns and the diffusion length of more than 1 μm with the target value of the N composition (3%).

### 4.2. Improvement of minority carrier lifetime by controlling substrate orientation

The effect of the surface orientation on the minority carrier lifetime is studied. GaAsN films were grown on GaAs(311)A, (311)B, and (100) substrates. The (311) surface consists of (111) and (100) components. The surface configurations of the (311)A and (311)B surfaces are shown in Figure 14. On the (311)A surface, a Ga atom connects to three As atoms, while an As atom

http://dx.doi.org/10.5772/51885

connects to two Ga atoms. The same bond configuration holds for the (311)B surface by exchanging Ga and As atoms.

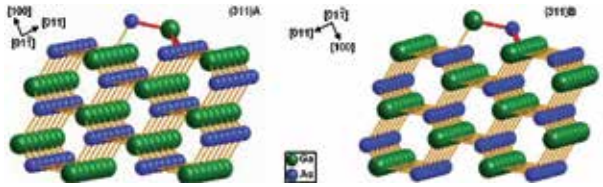

**Figure 14.** The surface structures of GaAs(311)A (left figure) and (311)B (right figure) substrates. Green balls are Ga atoms, blue balls are As atoms, and yellow and red sticks are Ga-As bonds.

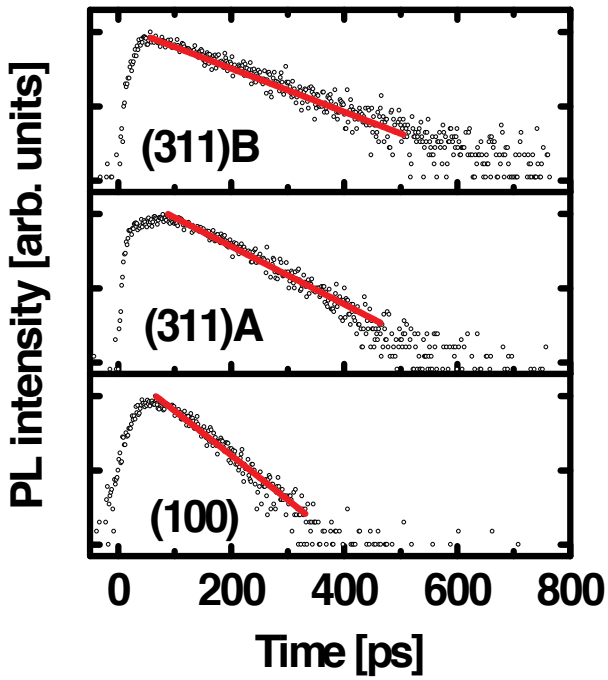


**Figure 15.** Typical PL decay curves at 4.5K of GaAsN with different growth orientations. The growth temperature was 440 ℃.

The results of the TR-PL measurements at 4.5K of GaAsN films with each growth orientation are shown in Figure 15. The PL lifetime is estimated by approximating the decay curve of the PL intensity as a straight line. The film with (311)B orientation has a longer PL lifetime, which indicates the longer minority carrier lifetime. The PL spectra at 4.5K of as-grown films with various substrate orientations are shown in Figure 16(a). The growth temperature was 440 ℃. There are two GaAsN-related peaks denoted as BE (near-band edge) and DL (deep levels) and

one GaAs-related peaks in the spectra. The GaAsN-related peaks are in the range of 1.25 – 1.40 eV and 1.1 – 1.2 eV which are caused by BE and DL emissions, respectively. To understand the orientation-dependent photoluminescence of GaAsN films, the ratio of the integrated intensities of DL to BE ($P_{DL}/P_{BE}$) were calculated. The $P_{DL}/P_{BE}$ ratio of the film grown on (311)A had the lowest value at any growth temperatures as shown in Figure 16 (b). The film grown on (311)A has almost the same N composition as that of (100). Therefore, N composition is not related to the difference in the integrated intensity ratios. This result indicates that the high-index substrate surfaces contribute to reduce defects and composition fluctuations in the epilayers [24]. On the other hand, in contrast to the continuous increase in total emission intensities of (3 1 1)B sample, a decreasing tendency with a rise in growth temperature was recorded for (3 1 1)A.

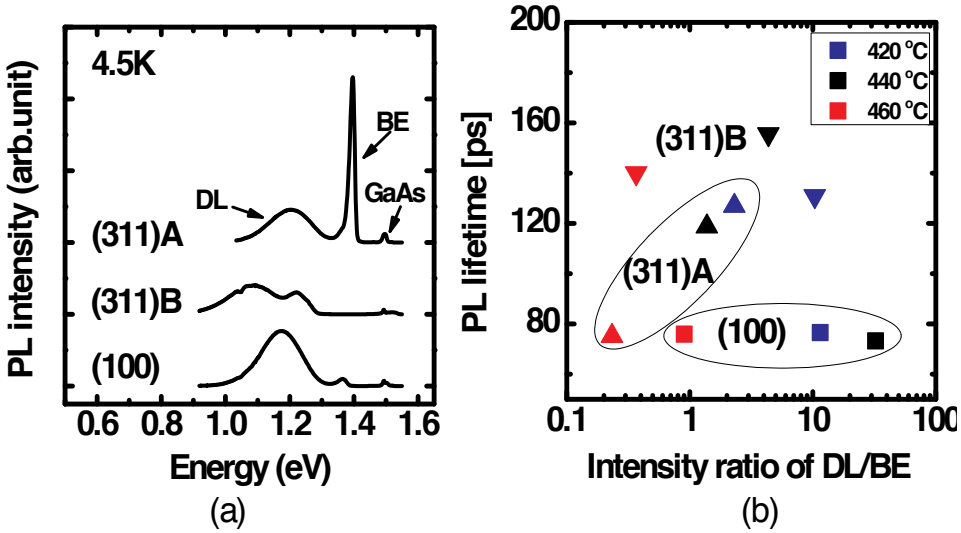


**Figure 16.** (a) PL spectra at 4.5K of as-grown films with different substrate orientations. The growth temperature was 440 ℃. (b) Growth-temperature dependences of N composition in GaAsN layers on (3 1 1)A/B and (1 0 0) substrates.

## 5. Lattice defects in GaAsN grown by CBE

GaInAsN suffers from three main N-related problems: (i) the shortening lifetime of minority carriers, (ii) the lowering of their mobility, and (iii) the increase of carrier concentration with increasing N concentration in the alloy [25-27]. Indeed, the incorporation of a small atomic fraction of N in the lattice of GaAs gives rise to the formation of high density acceptor states, recombination centers, and scattering levels [28]. It is; therefore, clear that the degradation of electrical properties of GaAsN may be attributed only to the formation of lattice defects. These defects were expected to be formed during growth owing to the smaller atomic size of N than of As, as well as, to the large gap miscibility between GaAs and GaN. For that, extensive works

http://dx.doi.org/10.5772/51885

on the distribution of lattice defects in the forbidden gap of Ga(In)AsN and their effects on their electrical properties were published during the last decade. Indeed, the summary of experimental results reported by Geisz and Friedman provides a basic knowledge of these defects [4]. Furthermore, undoped Ga(In)AsN alloys grown by chemical compound sources present a high density of residual impurities [29]. This property is a hindrance to a flexible design of Ga(In)AsN based solar cell and reduces the lifetime of minority carriers. Despite the very interesting results about the distribution of lattice defects in GaAsN, the main causes of short diffusion length of minority carriers and high background doping are still elusive. In this section of the chapter, we summarize the distribution of energy states in the forbidden gap of GaAsN grown by CBE, which was obtained using deep level transient spectroscopy and some related methods. Furthermore, we report the relationship of some defects and the poor electrical properties of the alloy, as well as, our recent results to decrease their impacts. All GaAsN samples were grown by CBE on GaAs (100) 2° off toward (110) substrate, under a growth temperature and a pressure of 420-460 °C and $2 \times 10^{-2}$ Pa, respectively. TEGa, TDMAAs, and MMHy were used as Ga, As, and N chemical compound sources, respectively. $SiH_4$ was used as n-type doping source, whereas undoped films are p-type. The detail of growth conditions using CBE can be found elsewhere [30-33]. The N concentration in each sample were evaluated from the Bragg angles of the GaAs and GaAsN reflection obtained by high resolution X-ray diffraction (HRXRD) method. The Schottky and ohmic contacts were evaporated through metal masks at a vacuum pressure of $10^{-4}$ Pa. The free donor and acceptor concentrations were calculated by the fitting of the Mott-Schottky plot using the capacitance-voltage method. DLTS spectra were collected using a BIO-RAD digital DLTS system (DL8000). The activation energies Ea [Ev + ET (eV)] for hole traps and Ea [EC - ET (eV)] for electron trap were determined from the slope of the Arrhenius plot of the DLTS signals, whereas the capture cross sections n/p (cm2) were evaluated from the intercept values [34]. Illustrated in Figure 17 (a) is the distribution of energy states in the forbidden gap of GaAsN0.005 grown by CBE. The main electron and hole traps in GaAsN were recorded by DLTS method and shown in Figure 17 (b) and (c). For electrons traps, two peaks (E1) and (E2) were observed in as grown film around 150 and 300 K, respectively. After rapid thermal annealing, E2 disappears completely and a new electron trap (E3) appears at 200 K. Compared with the electron traps in N-free GaAs, only E1 appears after the introduction of a small amount of N. Therefore, we have strongly suggested that E2 and E3 could be considered as native defects in GaAs. Based on the classification of electron traps in GaAs by Maunitton et al., E2 and E3 were considered to be EL2 (+/0) and EL5, respectively [35]. On the other hand, three hole traps, labeled H0, H2, and H5 were commonly observed in the DLTS spectrum of Figure 17 (c). Compared with the hole traps in N-free GaAs, we could only attribute H5 to the double donor state of EL2 with the charge state (+/++) [36], however, H2 and H0 appear to be newly observed. The hole trap H0 was confirmed to be a radiative recombination center using single and double carrier pulse DLTS method [30]. Since, our interest is only on the N-related defects which could be correlated with the poor electrical properties and the high carrier density in the alloy, we will focus only on the electron trap E1 and the hole trap H2, which were confirmed to be the main cause of the shortening of minority carrier lifetime and the high background doping in GaAsN films,

respectively. The properties of these two defects are summarized respectively in the two next sub-sections.

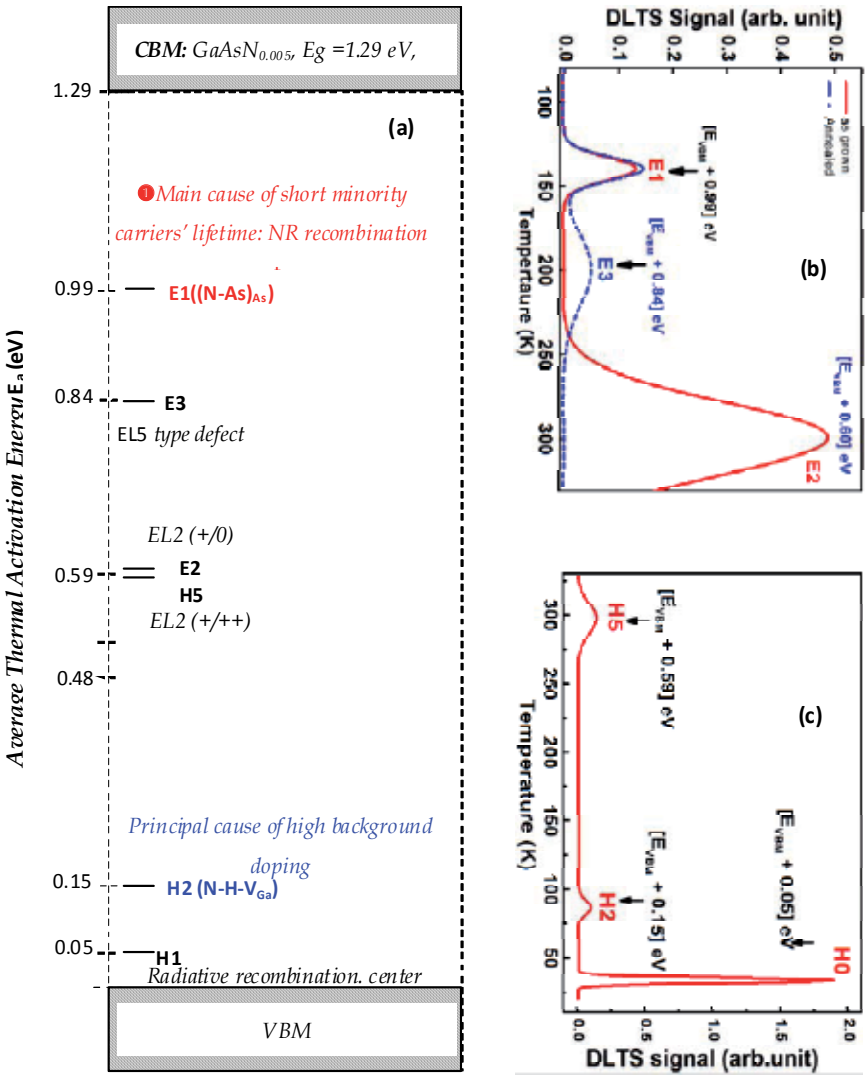


**Figure 17.** (left) Distribution of lattice defects in GaAsN grown by CBE for a N concentration of 0.5%, DLTS spectra for (a) as grown and annealed GaAs, (b) as grown GaAsN, (c) annealed GaAsN, (d) Arrhenius plot for electron traps, (e) DLTS spectrum for hole traps in GaAsN, and (f) Arrhenius plot for hole traps.

### 5.1. N-related non radiative recombination center

The electron trap E1 was confirmed to be related to the N atom, since its density increases with increasing the N concentration in GaAsN films [31]. Furthermore, it was not

http://dx.doi.org/10.5772/51885

observed in N-free GaAs [31]. The activation energy of E1 was found to vary between 0.3 and 0.4 eV below the conduction band minimum (CBM) [31-33]. This variation in energy level was explained by the effect of the electrical field on the thermal emission of carriers from E1, since the carrier concentration in GaAsN was not identical in all studied samples [4]. In addition, E1 was not only observed in CBE grown GaAsN but also in the DLTS spectra of MOCVD and MBE grown GaAsN and InGaAsN [37, 38]. Moreover, E1 approximately exhibited similar density and tendency with varying the N concentration, despite the quite difference in residual carrier densities between the three growth methods [31, 38, 39]. This result implies that the possible structure of E1 is independent of impurities. The thermal capture cross section of E1 is too large compared with that of native defects in GaAs. For that, it was found that the DLTS peak height of E1 saturates promptly with increasing the time of injection of electrons through the filling pulse parameter [33]. In view of the effective role of E1 in the degradation of electrical properties of GaAsN, we were able to provide evidence that E1 trap plays a major role in the degradation of minority carrier lifetime and acts as a recombination center [33]. For this, we carried out an experiment based on minority carrier capture at majority carrier trap by double carrier pulse DLTS method [30]. In this experiment, E1 was filled with majority carriers during the first pulse, so that E1 centers are occupied with electrons. Then, a forward bias minority carrier injection of short duration was applied in order to introduce capture of minority carriers. When the junction returned of quiescent reverse bias, E1 centers that remained occupied with majority carriers were emptied by thermal emission. The amplitude of this thermal emission provides a measure of the number of carriers that were trapped by E1 and not filled with minority carriers at the end of the injection pulse. A decrease of E1 peak height was observed and confirmed with varying the rate of injection through the duration and the voltage of the second pulse [33]. This result, indeed, indicates that E1 is a recombination center [33]. After this step, it was essential to identify the nature of this recombination mechanism. For that, the temperature dependence of the capture cross section of E1 ($\sigma_{E1}$( was investigated. As known in DLTS measurements, varying the emission rate window shifts the peak of the defect and the capture cross section may change. From the Arrhenius plots of each emission rate, we established the relationship between $\sigma_{E1}$ and the reciprocal temperature [33]. Absolutely, the recombination process through E1 was confirmed to be nonradiative, since $\sigma_{E1}$ presents a thermal activation energy of 0.13 eV [33]. Furthermore, $\sigma_{E1}$ was evaluated at room temperature to around $10^{-13}$ $cm^2$ [33]. This result proves that E1 is an active recombination center. In addition, this recombination activity may rises with increasing N in the film, since the activation energy of E1, comes closer to the midgap, following the decrease of the conduction band minimum. The recombination mechanism through E1 was quantified by evaluating the lifetime of electrons from the conduction band the energy level of the electron trap in the forbidden gap of the alloy. Using the SRH model for generationrecombination, the lifetime of electrons from the CBM to E1 was calculated to 0.2 ns [33-39]. This value was experimentally verified by time-resolved photoluminescence measurements. We, therefore, suggest that E1 is the main cause of short minority carrier lifetime in GaAsN alloys.

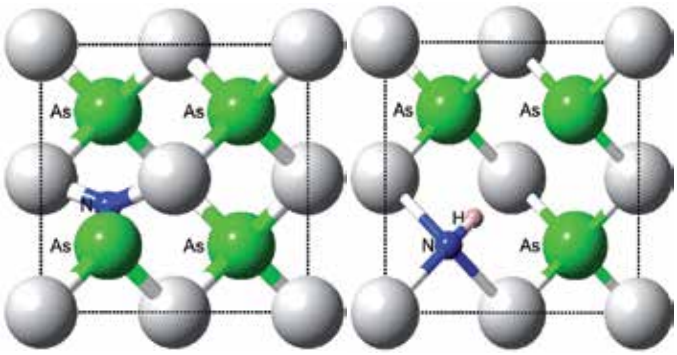


**Figure 18.** The split intestinal $(N\text{-}As)_{As}$ (left) and $N\text{-}H\text{-}V_{Ga}$ (right) as a possible origins of E1 and H2, respectively.

To understand the formation process of E1 and limit its effect, it was necessary to investigate its origin. First, it was mentioned above that E1 is independent of impurities, such as H, O, and C. Furthermore, E1 was observed in undoped p-type (minority carrier trap), n-type, and Si-doped GaAsN films, which exclude the doping atom from its origin. Therefore, E1 was tentatively suggested to be sensitive only to the host atoms (N, As, and Ga). In addition, using the isothermal capacitance transient method, the density profiling of E1 was found to be quasi-uniform distributed GaAsN [31]. This result indicates that the formation of E1 starts and goes on with the growth process. An obvious reason of this behavior is the compensation for the tensile strain, which could be caused by the small atomic size of N compared with that of As. Theoretically, the split interstitials $(N\text{-}As)_{As}$ and $(N\text{-}N)_{As}$ were expected to form two electron traps at 0.4 and 0.6 eV below the CBM of GaAsN, respectively [40]. These two defects were qualified to be energetically favorable on the growth surface [40]. As the N-dependence of the density of E1 did not show a straight line and since the total N concentration in the film could not be obtained using HRXRD measurements, we have proceed to investigate the relationship between the density of E1 and the flux of the As source. Indeed, we found that the density of E1 shows a peaking behavior with increasing TDMAAs [41]. This result implies that the formation of E1 is sensitive to both N and As atoms. However, this relationship could not be quantified since the atomic fractions between As and N in GaAsN films are quite different [41]. As shown in Figure 18, the split interstitial $(N\text{-}As)_{As}$ is, therefore, expected to be the possible origin for E1. However, more experiments are required to clarify the formation process of this recombination center and to limit its density.

### 5.2. N-related acceptor like state in GaAsN

The high background doping in undoped GaAsN films is a serious problem for solar cell design and fabrication. A small atomic fraction of N changes the conductivity in the film from n-type in GaAs to p-type. Obviously, the formation of N-related acceptors with high density is the main reason of donor compensation. Indeed, two acceptor levels, A1 and A2, were confirmed using Hall Effect measurements [42]. Their thermal activation energies were evaluated to $E_{A1} = 130 \pm 20$ meV and $E_{A2} = 55 \pm 10$ meV, respectively. On another hand, the ionized acceptor density $N_A$,

http://dx.doi.org/10.5772/51885

obtained using capacitance voltage (C-V) method, showed a linear dependence with N concentration in undoped films grown under a Ga flow rate of TEGa = 0.1 sccm [32]. This indicates that $N_A$ depends strongly on a N-related acceptor [32]. However, this linear dependence tends to saturate when TEGa is reduced, even the N concentration is enhanced [32]. The reason of this saturation was clarified using SIMS measurements, where the concentration of H impurity decreases slightly with decreasing TEGa [32]. Hence, this result implies that $N_A$ depends strongly to N and H atomic concentrations in the film. To identify this N-H related acceptor level, we carried out C-V measurements in the temperature range 20 - 330 K in order to get the temperature dependence of $N_A$. A sigmoid increase of $N_A$ was observed between 70 and 100 K [32]. Its amplitude showed a strong dependence with N concentration [32]. It approximately reflects the relationship between $N_A$ and N concentration at room temperature [39]. This result indicates that the sigmoid increase of $N_A$ between 70 and 100 K is owing to the thermal ionization of a N-related acceptor-like state, which thermal ionization energy can be estimated to be between 0.1 and 0.2 eV. Furthermore, as given in Figure 17 (c), the hole trap H2 was observed in the temperature range of sigmoid increase of $N_A$. The activation of H2 is within the expected range of the N-related acceptor state and it is in conformity with theoretical calculation [32, 44]. Furthermore the density of H2 was found to be in linear dependence with N concentration in the samples grown under TEGa = 0.1 sccm. Hence, H2 is suggested to be the main acceptor state which governs the tendency of $N_A$ and it is the cause of the increase of junction capacitance in the temperature range 70 to 100 K. The origin of H2 was investigated using the results of carrier concentration and the density of residual impurities in undoped GaAsN grown by CBE under various Ga flow rates, obtained using Hall Effect, FT-IR, and SIMS [32, 42]. From SIMS measurements, which were carried out on GaAsN grown under different TEGa flow rates, it was found that $N_A$ depends on the atomic concentrations of N and H [32, 42]. In addition, using FTIR measurements, a linear relationship was established between the concentration of N-H complexes and N concentration [29]. Therefore, H2 was strongly suggested to be an acceptor state and its origin is related to the N-H bond. However, the slope of the linear relationship between $N_A$ and the concentration of N-H complexes showed an increase with increasing the growth temperature ($T_G \in [400, 430]$ C) [29]. This indeed indicates that the N-H complexes could be accompanied with another defect, which binding energy was evaluated to 2.5 eV [29]. On another hand, using theoretical calculation, the formation energy of $(N\text{-}H\text{-}V_{Ga})^{-2}$ was found to be lower than $(N\text{-}V_{Ga})^{-3}$, $(H\text{-}V_{Ga})^{-2}$, and isolated $V_{Ga}^{-3}$ [43]. These results may expect $V_{Ga}$ as a possible origin of the unknown intrinsic defect. These predictions were experimentally supported using positron annihilation spectroscopy results [44]. Therefore, H2 may have $N\text{-}H\text{-}V_{Ga}$ as a possible structure as shown in Figure 18.

## 6. Conclusion

InGaAsN is a candidate material to realize the ultrahigh efficiency multi-junction solar cell. The efficiency of the 4-junction solar cell, InGaP/InGaAs/InGaAsN/Ge, is expected to be 41% under 1-sun (AM0) and 52% under 500-sun (AM1.5). In order to achieve the expected super high efficiency, the electrical property of the InGaAsN should be improved. In this paper, we have shown the following results:

1. The CBE method was developed for the growth of GaAsN films. The growth temperature region was divided into three parts. In the middle growth temperature region (390 – 445 °C), the higher N composition without broadening of the XRD rocking curve width was obtained. In this temperature region, a typical characteristics in the growth process is that the amount of the N incorporation into crystal at the surface is not only dominated by the growth rate but also the desorption rate of N species at the surface.

2. Decreasing the growth rate was effective to improve the hole mobility and minority-carrier lifetime in p-GaAsN films grown by the chemical beam epitaxy (CBE). The mobility was increased from 120 to 150 $cm^2V^{-1}s^{-1}$ for the N composition of 0.6%. Based on the temperature dependence of the mobility, $\mu_N$, which was inversely proportional to the amount of N-related scattering centers, was estimated. By decreasing the growth rate, $\mu_N^{-1}$ was reduced especially when the N composition was higher. The result indicates the improved mobility by decreasing the N-related scattering centers. The minority-carrier lifetime in the bulk of p-GaAsN films, $\tau_B$, estimated by PL decay curves was improved from $3.2\times10^{-1}$ ([N] = 0.6%) to $9.0\times10^{-1}$ ns ([N] = 0.8%) despite the higher N composition. The bulk minority-carrier lifetime $\tau_B$ was mainly determined by the nonradiative recombination lifetime ($\tau_{NR}$). This means that the nonradiative recombination centers were reduced by decreasing the growth rate, which resulted in the improvement of $\tau_B$.

3. The electron lifetime of p-GaAsN was also improved by controlling the GaAs substrate orientations. The investigation of the effects from GaAs substrate surface orientation and polarity indicates that N incorporation can be enhanced on the (3 1 1)B plane but reduced on (3 1 1)A compared with (1 0 0), where the three dangling bond sites on the (3 1 1) growing surface are considered to play the dominant role. The examination of intensity ratio between emissions from band edge and deep levels evidenced the improved luminescence efficiency of GaAsN layers on (3 1 1) substrates with both polarity. In response to variations in the growth temperature and the postgrowth annealing, optical behavior shows strong dependence on the epitaxial orientation, as illustrated by the relative intensity and low-energy tail of the band-edge emission. (3 1 1)B is distinguished to be the potential substrate to achieve efficient N incorporation.

4. The electron trap E1 located at 0.99 eV above VBM is a dominant non radiative recombination center. The formation of E1 is sensitive to both the amounts of N and As atoms. A possible structure of this defect is $(N\text{-}As)_{As}$. The hole trap H2 located at 0.15 eV above VBM is suggested to be the main acceptor state. The origin of H2 is related to the N-H bond. A possible structure is $N\text{-}H\text{-}V_{Ga}$.

## Author details

Kazuma Ikeda, Han Xiuxun, Bouzazi Boussairi and Yoshio Ohshita

Toyota Technological Institute, Japan

## References

[1] Kondow M, Uomi K., Niwa A, Kitatani T, Watahiki S, Yazawa Y, GaInNAs: A novel material for long-wavelength-range laser diodes with excellent high-temperature performance. Japanese Journal of Applied Physics 1996; 35 1273–1275. DOI: 10.1109/2944.640627.

[2] Bellaiche L. Band gaps of lattice-matched (Ga,In)(As,N) alloys. Applied Physics Letters 1999; 75 2578-2580. DOI: 10.1063/1.125083.

[3] Green MA, Emery K, Hishikawa Y, Warta W, Dunlop ED. Solar cell efficiency tables (version 39). Progress in Photovoltaics: Research and Applications 2012;20 12-20. DOI: 10.1002/pip.

[4] Geisz JF, Friedman DJ. III–N–V semiconductors for solar photovoltaic applications. Semiconductor Science and Technology 2002; 17 769–777.

[5] Dimroth F, Baur C, Bett A, Volz K, Stolz W. Comparison of dilute nitride growth on a single-and 8×4-inch multiwafer MOVPE system for solar cell applications. Journal of Crystal Growth 2004;272 726–731. DOI: 10.1016/j.jcrysgro.2004.08.038.

[6] Neugebauer J, Van de Walle CG. Electronic structure and phase stability of $GaAs_{1-x}N_x$ alloys. Physical Review B 1995;51 10568–10571. DOI: 10.1103/PhysRevB.51.10568.

[7] Pan Z, Li LH, Zhang W, Lin YW, Wu RH. Kinetic modeling of N incorporation in GaInNAs growth by plasma-assisted molecular-beam epitaxy. Applied Physics Letters 2000;77 214-216. DOI: 10.1063/1.126928.

[8] Zhongzhe S, Fatt YS, Chuin YK, Khai LW, Weijun F, Shanzhong W, Khee NT. Incorporation of N into GaAsN under N overpressure and underpressure conditions. Journal of Applied Physics 2003; 94 1069-1073. DOI: 10.1063/1.1582554.

[9] Ougazzaden A, Bellego YL, Rao EVK, Juhel M, Leprince L, Patriarche G. Metal organic vapor phase epitaxy growth of GaAsN on GaAs using dimethylhydrazine and tertiarybutylarsine. Applied Physics Letters 1997;70(21) 2861-2863. DOI: 10.1063/1.119025.

[10] Dumont H, Auvray L, Monteil L, Bouix J. Analysis of nitrogen incorporation mechanisms in GaAs1−xNx/GaAs epilayers grown by MOVPE. Materials Science and Engineering: B 2001;84(3) 258-264. DOI: 10.1016/S0921-5107(01)00639-0.

[11] Kurtz S, Reedy R, Keyes B, Barber GD, Geisz JF, Friedman DJ, McMahon WE, Olson JM. Evaluation of NF3 versus dimethylhydrazine as N sources for GaAsN. Journal of Crystal Growth 2002;234 323-326. DOI: 10.1016/S0022-0248(01)01712-2.

[12] Jin C, Nikishin SA, Kuchinskii VI, Temkin H, Holtz M. Metalorganic molecular beam epitaxy of (In)GaAsN with dimethylhydrazine. Journal of Applied Physics 2002;91 56-64. DOI: 10.1063/1.1419206.

[13] Uesugi K, Suemune I. Metalorganic molecular beam epitaxy of GaNAs alloys on (0 0 1)GaAs. Journal of Crystal Growth 1998;189–190 490-495. DOI: 10.1016/S0022-0248(98)00337-6.

[14] Sun Y, Yamamori M, Egawa T, Ishikawa H. Incorporation of N into GaAsN under N overpressure and underpressure conditions. Japanese Journal of Applied Physics 2004;43 2409-2413. DOI: 10.1143/JJAP.43.2409.

[15] Ptak AJ, Johnston SW, Kurtz S, Friedman DJ, Metzger WK. A comparison of MBE- and MOCVD-grown GaInNAs. Journal of Crystal Growth 2003;251 392-398. DOI: 10.1016/S0022-0248(02)02201-7.

[16] Matsuura T, Miyamoto T, Makino S, Ohta M, Matsui Y, Koyama F. p-Type Doping Characteristics of GaInNAs:Be Grown by Solid Source Molecular Beam Epitaxy. Japanese Journal of Applied Physics 2004;43 L433-L435. DOI: 10.1143/JJAP.43.L433.

[17] Fahy S, O'Reilly EP. Intrinsic limits on electron mobility in dilute nitride semiconductors. Applied Physics Letters 2003;83 3731-3733. DOI: 10.1063/1.1622444.

[18] Yamaguchi M, Warabisako T, Sugiura H. Chemical beam epitaxy as a breakthrough technology for photovoltaic solar energy applications. Journal of Crystal Growth 1994;136 29-36. DOI: 10.1016/0022-0248(94)90379-4.

[19] Lee HS, Nishimura K, Yagi Y, Tachibana M, Ekins-Daukes NJ, Ohshita Y, Kojima N, Yamaguchi M. Chemical beam epitaxy of InGaAsN films for multi-junction tandem solar cells. Journal of Crystal Growth 2005; 275 e1127-e1130. DOI: 10.1016/j.jcrysgro.2004.11.200.

[20] Tsang WT, From Chemical Vapor Epitaxy to Chemical Beam Epitaxy. Journal of Crystal Growth 1989;95 121-131. DOI: 10.1016/0022-0248(89)90364-3.

[21] Uesugi K, Morooka N, Suemune I. Reexamination of N composition dependence of coherently grown GaNAs band gap energy with high-resolution x-ray diffraction mapping measurements. Applied Physics Letters 1999;74 1254-1256. DOI: 10.1063/1.123516.

[22] Wiley JD., Mobility of Holes in III-V Compounds. In: Willardson RK, Beer AC. (ed.) Semiconductors and Semimetals. New York: Academic Press; 1975;10 p. 91-174.

[23] Nag BR. Electron Transport in Compound Semiconductors. Berlin Heidelberg: Springer-Verlag; 1980.

[24] Moto A, Takahashi M, Takahashi S. Effect of Substrate Orientation on Photoluminescence of GaNAs. Japanese Journal of Applied Physics 2000 39;1267-1269.

[25] Buyanova IA., Chens WM. Physics and Applications of Dilute Nitrides, New York: Taylor & Francis Books Inc.; 2004.

[26] Henini M. Dilute Nitrides, Oxford: Elsevier; 2005.

[27] Shan W, Walukiewicz W, Ager J, Haller EE, Geisz JF, Friedman DJ, Olson JM, Kurtz SR. Physical Review Letters 1999;82 1221-1224.

[28] Kurtz SR, Meyers D, Olson JM, Conference Record of the Twenty-Sixth IEEE: conference proceedings, September 29-October 3, 1997, Anaheim Marriott, California, USA. 26th IEEE Photovoltaic Specialists Conference; 1997.

[29] Nishimura K, Suzuki H, Saito K, Ohshita Y, Kojima N, Yamaguchi M. Electrical properties of GaAsN film grown by chemical beam epitaxy. Physica B: Condensed Matter 2007;401 343-346. DOI: 10.1016/j.physb.2007.08.183.

[30] Bouzazi B, Suzuki H, Kojima N, Ohshita Y, Yamaguchi M, A recombination center in p-type GaAsN grown by chemical beam epitaxy. Solar Energy Materials and Solar Cells 2011; 95 281-283. DOI: 10.1016/j.solmat.2010.04.047.

[31] Bouzazi B, Suzuki H, Kojima N, Ohshita Y, Yamaguchi M. Nitrogen Related Electron Trap with High Capture Cross Section in n-Type GaAsN Grown by Chemical Beam Epitaxy. Applied Physics Express 2010;3 0510021. DOI: 10.1143/APEX.3.051002.

[32] Bouzazi B, Suzuki H, Kojima N, Ohshita Y, Yamaguchi M. Nitrogen-Related Recombination Center in GaAsN Grown by Chemical Beam Epitaxy. Japanese Journal of Applied Physics 2010;49 051001. DOI: 10.1143/JJAP.49.051001.

[33] Bouzazi B, Suzuki H, Kojima N, Ohshita Y, Yamaguchi M. Double carriers pulse DLTS for the characterization of electron-hole recombination process in GaAsN grown by chemical beam epitaxy. Physica B: Condensed Matter 2011;406 1070-1075. DOI: 10.1016/j.physb.2010.11.086.

[34] Lang DV. Deep-level transient spectroscopy: A new method to characterize traps in semiconductors. Journal of Applied Physics 1974;45 3023-3032. DOI: 10.1063/1.1663719.

[35] Martin GM, Mitonneau A, Mircea A. Electron traps in bulk and epitaxial GaAs crystals. Electronics Letters 1977;13 191-193. DOI: 10.1049/el:19770140.

[36] Bouzazi B, Nishimura K, Suzuki H, Kojima N, Ohshita Y, Yamaguchi M. Properties of Chemical Beam Epitaxy grown $GaAs_{0.995}N_{0.005}$ homo-junction solar cell. Current Applied Physics 2010;10 S188-S190. DOI: 10.1016/j.cap.2009.11.020.

[37] Johnston SW, Kurtz SR. Comparison of a dominant electron trap in n-type and p-type GaNAs using deep-level transient spectroscopy. Journal of Vacuum Science and Technology A 2006;24 1252-1257. DOI: 10.1116/1.2167081.

[38] Krispin P, Gambin V, Harris JS, Ploog KH. Nitrogen-related electron traps in Ga(As,N) layers (<3%N). Journal of Applied Physics 2003;93 6095-6099. DOI: 10.1063/1.1568523.

[39] Shockley W, Read WT. Statistics of the Recombinations of Holes and Electrons. Physical Review 1952;87 835. DOI: 10.1103/PhysRev.87.835.

[40] Zhang SB, Wei SH. Nitrogen Solubility and Induced Defect Complexes in Epitaxial GaAs:N. Physical Review Letters 2001;86 1789.

[41] Bouzazi B, Lee JH, Suzuki H, Kojima N, Ohshita Y, Yamaguchi M. Origin Investigation of a Nitrogen-Related Recombination Center in GaAsN Grown by Chemical Beam Epitaxy. Japanese Journal of Applied Physics 2011;50 051001.

[42] Saito K, Nishimura K, Suzuki H, Kojima N, Ohshita Y, Yamaguchi M. Hydrogen reduction in GaAsN thin films by flow rate modulated chemical beam epitaxy. Thin Solid Films 2008;516 3517-3520. DOI: 10.1016/j.tsf.2007.08.022.

[43] Janotti A, Wei SH, Zhang SB, S. Kurtz, Van de Walle CG. Interactions between nitrogen, hydrogen, and gallium vacancies in $GaAs_{1-x}N_x$ alloys. Physical Review B 2003;67 161201. DOI: 10.1103/PhysRevB.67.161201.

[44] Toivonen J, Hakkarainen T, Sopanen M, Lipsanen H, Oila J, Saarinen K. Observation of defect complexes containing Ga vacancies in GaAsN. Applied Physics Letters 2003;82 40-42. DOI: 10.1063/1.1533843.

Chapter 11

# Solar Cell Efficiency vs. Module Power Output: Simulation of a Solar Cell in a CPV Module

Egbert Rodríguez Messmer

Additional information is available at the end of the chapter

http://dx.doi.org/10.5772/52707

## 1. Introduction

In the past few years Concentrating Photovoltaics (CPV) has moved from R&D and pilot projects (typically installations below 500 kilowatts) to multi-megawatt power plants. The starting point of the commercial deployment of this technology was in 2006 when the Institute for Concentration Photovoltaic Systems (ISFOC) purchased several CPV power plants of different technologies and provider that were installed in Puertollano (Spain). Each supplier provided a power plant that had a size between 200kW and 500kW. These power plants are operating since 2008 and the results are very promising [1]. After these first installations several MW-size power plants have been installed ([2], [3] and [4]), and the first multi-megawatt CPV power plants are under construction, like a 150MW power plant that Soitec is developing for the San Diego Gas & Electric in California [5], demonstrating here with that CPV technology can be a cost efficient alternative to conventional silicon-based flat-plate photovoltaic (PV) plants in areas of high direct solar irradiation.

A CPV module consists typically of a high-efficient solar cell and a concentrator that concentrates light and that can be made out of a mirror, a parabolic dish or lenses. These modules are then mounted on a 2-axis tracking system to make sure that the module is always perpendicular to the sun, so that the light spot reaches the active area of the solar cell. A CPV system is therefore more complex than a conventional PV system, and, in order to be commercially competitive with standard systems, it is important to control its cost figure. When making a cost analysis of a CPV system, from manufacturing of solar cells to a finished installation [6], the cost figure is given in terms of a monetary unit per Watt (€/W or $/W). This cost figure should be kept as low as possible, and can be done either for a complete installation including all the costs relative to the deployment of the system or it can be done partly, considering only the module or the module and tracking system.There are two possibilities

to reduce the value of this cost figure, which are either reducing the cost of the system, which is typically done reducing the cost of the raw materials or optimizing production processes, or by increasing the output power of the CPV module, which can be achieved by reducing possible sources of losses inside a module (these can be optical, electrical o thermal).The advantage of increasing the output power of a module is that this has an important impact to other related costs, since also the manufacturing and installation costs are reduced due to the need of fewer modules or even trackers for a CPV power plant of a given size.

The output power of a CPV module can be optimized by reducing the internal losses that appear in the module design. Therefore a good match of the materials from which a module is made should be aimed. The need of a good match is especially true for the interaction between the solar cell and the optical system, where the solar cell can be adapted in size, light spectrum, concentration ratio and interface to the optical system. In practice it is very difficult to achieve good matching of different materials, since the different parts of a CPV module are made by different manufacturers. These might have different interests as compared to a system developer, so that a compromise is needed. In order to keep the manufacturing cost of the CPV module low, all elements of the module should be standardized, but, on the other hand, CPV module manufacturer want to have components that are customized to their own module design to maximise their output power. Some CPV module manufacturer use parabolic dishes to concentrate light, while others use lenses, and also the concentration ratio at which the modules work differ from manufacturer to manufacturer. This means that from a technological point of view, a CPV module manufacturer desires to have components that are customized to its own system.

To go more into detail in this issue of matching of materials inside a CPV module, and to analyse its effect on module performance, the interface between solar cell and optical system of the module is analysed in this chapter. A solar cell can be designed to have either a maximum efficiency when it is measured as a stand-alone device (having air as the surrounding medium) or to have maximum efficiency when it is surrounded in any other optical medium that is used inside the CPV module (e.g. glass or an optical encapsulant). This fact has an important impact technically and commercially. The solar cell efficiency is usually defined when it is measured in air, and should for commercial purpose be designed to have maximum efficiency under these conditions. On the other hand, if the solar cell is going to be operated embedded in an encapsulant and a lens, the CPV manufacturer should choose a solar cell that is designed for this operating condition, even though the solar cell will have less efficiency when measured at air. In summary, it is important to consider a CPV module as one system during its development, and not composed of independent components that have to be developed independently.

In order to explain better how the embedding medium affects the solar cell performance and to quantify this effect, a series of simulations has been done with a simulation program that has been developed by Isofotón in collaboration with the University of Granada (Spain). This program is called ISOSIM and is able to simulate the performance of a multijunction solar cell, including its anti-reflection coating (ARC) and taking into consideration the concentration and the medium in which the solar cell is used (e.g. air or an optical gel to couple

http://dx.doi.org/10.5772/52707

the light from the lens to the solar cell). It is also possible to add optical layers on top of the solar cell structure and simulating thereby a CPV module.

For the sake of simplicity, in this chapter it has been considered a double junction solar cell that is operating at a temperature of 320K (50ºC). The obtained results give a qualitative indication on the effect of different parameters, but quantitatively the effects that are described in this chapter will exceeded at real operating conditions. On one hand the solar cells that are used are triple-junction cells and also the operating temperature is usually higher. It is estimated that when adapting the solar cell to an optical system instead of using a standard solar cell, an increase of output power of up to 10% can be achieved.

## 2. Outline of experimental work

In this Chapter, first, the capabilities and performance of the simulation program are explained, followed by several studies that show which factors affect the performance of a solar cell outside and inside of a CPV module.

The first study shows that the performance of a solar cell does not depend only on the material and thickness of the AR- coating layer(s), but also on the refractive index of the surrounding medium in which this solar cell is measured or operated. A solar cell does not have the same efficiency when it is operated in air (refractive index of 1) or when it is operated in a medium of refractive index of e.g. 1.5, (if the solar cell is covered by glass).

Afterwards the performance of the solar cell in air and when it is assembled in a CPV module will be compared. It has been analyzed the current matching of the double-junction solar cell, varying the thickness of the base of the top cell, and it has been identified the limiting subcell (either top-cell or bottom-cell), which is attributed to be due to different spectral losses (absorption or reflection) in the materials and interfaces of the elements of the system.

In the last part a practical example is given, in which the power output of a CPV module is quantified when it is assembled either with a double-junction solar cell that has been optimized having air as the interface or a solar cell that is optimized to the CPV module. It shows that even if the variation in efficiency of the solar cell is little, the difference in output power can be significant. This chapter summarizes previous work that has been done with the ISOSIM package ([7], [8] and [9]).

## 3. ISOSIM software and experimental parameters

There are currently several approaches and solutions proposed from module manufacturer and system integrator that develop CPV modules. On the market are currently several techniques to concentrate the light, since many companies have developed their own proprietary technological solution. The type of concentrator can be either based on mirrors, dishes, or lenses, and using only primary optics or also secondary and even tertiary optics. In order

to maximize the output power of a module, solar cells have to be optimized for each optical system. The problem that arises is that a solar cell that has been optimized for a given optical system does not necessarily have an optimum performance also in another optical system. It is also difficult for a solar cell manufacturer to predict how a solar cell will perform inside a given module type. To take into consideration various types of concentrator technology, and to be able to analyze also a stand-alone solar cell, the simulation software is organized in layers, in which each layer represents a material with its own material properties and function. In this manner it is possible to simulate any type of CPV module and at any operating condition (temperature, concentration ratio).

The software used for the simulations has been specifically designed for the analysis of multijunction solar cells in order to get a tool to aid the design of solar cells and concentrator PV systems. This software, that is called *ISOSIM*, is capable of modelling the performance from stand-alone single junction solar cells up to the performance of multijunction solar cells inside a CPV module under real operating conditions. The simulation program solves the Poisson and continuity equations by using a procedure optimized for multilayer structures. It includes the radiative interband, Shockley-Read-Hall and Auger recombination mechanisms, and computes the generation function of electron-hole pairs from the optical parameters of the cell materials. The dependence of these optical parameters on the photon energy has been included, taking into account the doping level and its effect on bandgap narrowing. The software uses the Rakic model for the calculation of the complex dielectric function, absorption coefficient, extinction and refraction index calculation, with the Gaussian broadening proposed by Kim. Additionally, several effects are included in the software, such as indirect transition contributions, the shift in the optical band gap due to doping, and free-carrier absorption, among others. The material parameters of several anti-reflection coatings were obtained either empirically by ellipsometry measurements or extracting them from the SOPRA database of refractive indexes [10].

The program also takes into consideration the optical medium that surrounds the solar cell, which can be either air which represents the case of a stand-alone solar cell that is measured, or any other medium, representing the case of a solar cell that is mounted in a CPV module (e.g. epoxies, solar glasses, optical gel). Apart of that, also the illumination spectra (space, terrestrial or any customized spectra), the concentration of the light source and the temperature of the solar cell can be modified for simulations. It is therefore possible to simulate the whole system, considering solar cell, lenses, optical gels that are used to couple optical components, possible air gaps between lenses inside the module, concentration ratio and operating temperature. It is therefore possible to estimate the total loss of a system if e.g. a wrong choice of materials or of its process parameters has been chosen for the manufacturing of a CPV module.

For the simulations in this chapter, I-V curves and spectral response of a stand-alone solar cell are obtained by simulating a typical solar cell structure. If not otherwise specified, the structure used for the studies in this chapter (Figure 1.) see is a dual-junction GaInP/GaAs solar cell with the two photovoltaic junctions connected by a GaAs tunnel junction, and the antireflection coating consisting of a double layer of $TiO_2$ and $Al_2O_3$ [11]. Light concentration

http://dx.doi.org/10.5772/52707

and operating temperature were fixed at 1000 suns and 320 K, respectively. It has been used the AM1.5D spectrum and has also been assumed a shadowing loss of the solar cell of 2% due to the area below the grid. Some of the parameters of the materials that are used for simulations show high dispersion. For instance, the band-gap of GaInP depends on the ordering level, and could vary from 1.66 eV for a fully ordered lattice to 2.01 eV for a totally disordered one. For the simulations presented in this article, we assumed that the band-gap of GaInP is 1.9 eV at 300K. In a previous paper in which we presented this software, it has been shown that the results of the simulations obtained by the ISOSIM software match reasonably well with experimentally observed results [7].

| Contact layer GaAs 0.2µm n=6e18 $cm^{-3}$ | | Antireflection (AR) coating | |
|---|---|---|---|
| Window | AlInP | 0.025µm | n=4e17 $cm^{-3}$ |
| Emitter | GaInP | 0.1µm | n=2e18 $cm^{-3}$ |
| Base | GaInP | 1µm | p=1.5e17 $cm^{-3}$ |
| BSF | GaInP | 0.06µm | p=3e18 $cm^{-3}$ |
| TJ | GaAs | 11nm | p=1e19 $cm^{-3}$ |
| TJ | GaAs | 11nm | n=1e19 $cm^{-3}$ |
| Window | GaInP | 0.1µm | n=1e18 $cm^{-3}$ |
| Emitter | GaAs | 0.1µm | n=1e18 $cm^{-3}$ |
| Base | GaAs | 3.5µm | p=8e16 $cm^{-3}$ |
| BSF | GaInP | 0.07µm | p=3e17 $cm^{-3}$ |
| Buffer | GaAs | 0.2µm | p=3e17 $cm^{-3}$ |
| Substrate | GaAs | | p-type |

**Figure 1.** Structure of the double junction solar cell used for the analysis in this chapter. The layers in light blue are the ones corresponding to the top-cell, the grey ones to the tunnel junction and the green ones to the bottom cell [12].

| | | |
|---|---|---|
| Coverglass | n=1.5 | D=4mm |
| Encapsulant | n=1.5 | D=1mm |
| Primary lens | n=1.5 | D=4mm |
| Air gap | n=1 | D=10mm |
| Secondary lens | n=1.5 | D=4mm |
| Encapsulant | n=1.5 | D=1mm |
| Solar Cell with AR coating | | |

**Figure 2.** Schematic representation of the layer sequence that light has to pass through until it reaches the solar cell. It represents a CPV module that is made out of a primary and secondary lens.

The structure of the ISOSIM simulation program makes it possible to add several layers and their parameters (thickness, doping level and gradient, doping type, composition, recombination velocity, recombination time constant, refractive index). It is also needed to specify the function of each layer, like e.g. *optical layer* for the window layer of the solar cell or the layers that represent the optical system (e.g. lenses, encapsulating material, air gaps between materials, cover glass). For running a simulation, the parameters that are specified are concentration ratio (in suns), solar cell operating temperature, shadowing loss, series resistance of the contact layer and refractive index of the medium that surrounds the solar (e.g. n=1 if the simulation should be done considering that the solar cell is measured in air). This high degree in flexibility makes it possible to simulate almost any type of multijuncion solar cells and any type of CPV module.

For the simulations presented in this chapter, three different type of simulations were made, a solar cell that is in air (refractive index is 1), a solar cell that is surrounded by a medium with refractive index equal to 1.5 (e.g. glass) and a solar cell that is mounted in a CPV module that is made of a cover glass, primary and secondary lenses, encapsulating materials, and an air gap between primary and secondary lens. A schematic description is shown in Figure 2.

In order to show the usefulness of the simulation software for the prediction of the behavior of solar cells under real operating conditions (i.e. under light concentration and at temperatures higher than room temperature), several figures are shown (Figure 3. to Figure 7.). These simulations can be of interest to extrapolate the measured parameter at room temperature to real operating conditions. The two parameters that affect mostly the solar cell performance when it is mounted in a CPV module are the operating temperature and the optical coupling of the sunlight to the solar cell. Even if the short-circuit current $I_{sc}$ increases slightly with increasing temperature (Figure 3.), the predominant effect is the decreases of

http://dx.doi.org/10.5772/52707

the open-circuit voltage $V_{oc}$ (Figure 4.) and the fill-factor FF (Figure 5.), reducing the solar cell efficiency (Figure 6.) and thereby also the output power of a module. Figure 7 shows the efficiency of the solar cell when the concentration is increased. The temperature is set to 320K. It shows the typical shape of this type of curves, although the maximum in efficiency is in our simulation at a concentration of around 2000 suns, which is higher than typical values observed experimentally [13]. More details about the performance of the ISOSIM software, as well as the discussion of the figures shown here can be found elsewhere [7].

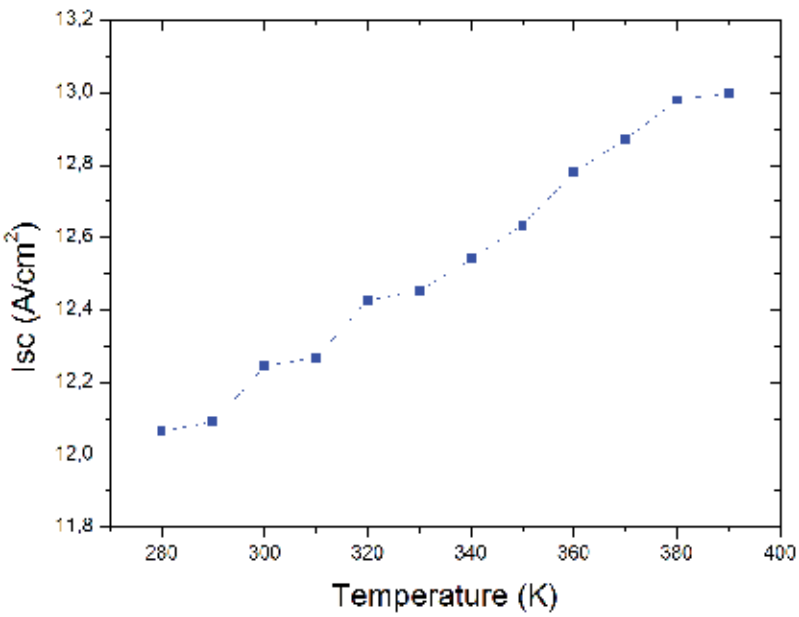


**Figure 3.** Simulation of the short-circuit current density ($I_{sc}$) of a double-junction solar cell as a function of temperature at a concentration of 1000 suns.

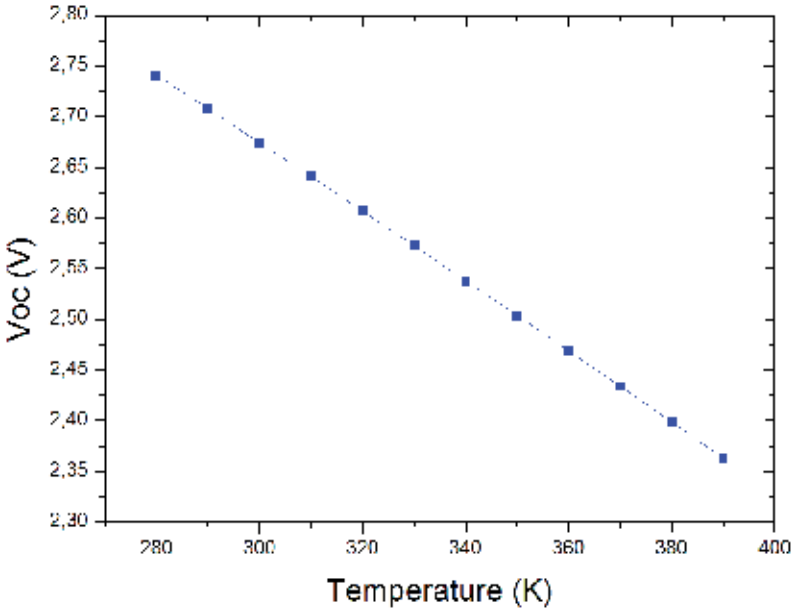


**Figure 4.** Simulation of the open-circuit Voltage ($V_{oc}$) of a double-junction solar cell as a function of temperature at a concentration of 1000 suns.

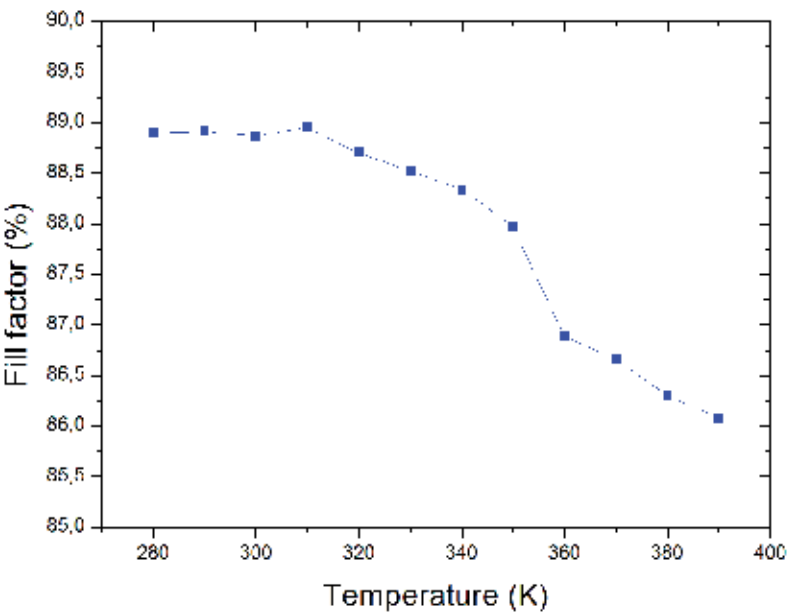


**Figure 5.** Simulation of the fill factor (FF) of a double-junction solar cell as a function of temperature at a concentration of 1000 suns.

http://dx.doi.org/10.5772/52707

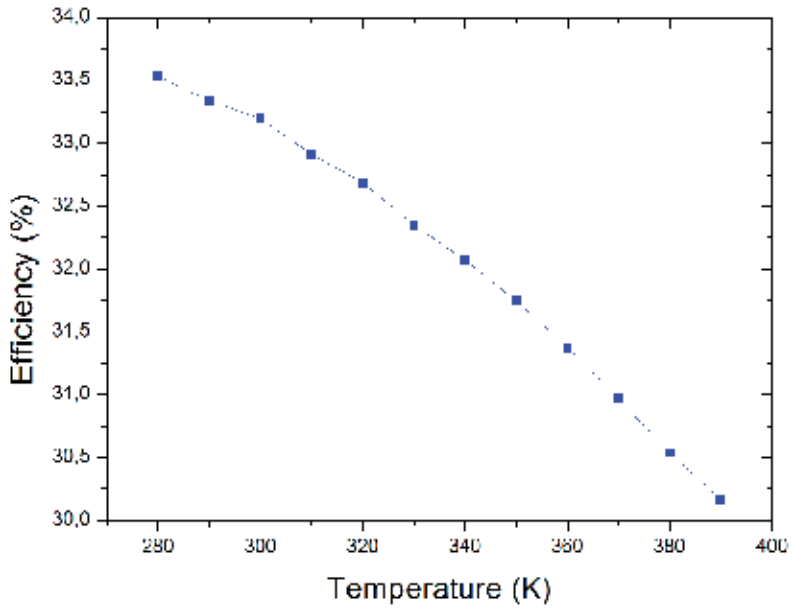


**Figure 6.** Simulation of the efficiency of a double-junction solar cell as a function of temperature at a concentration of 1000 suns.

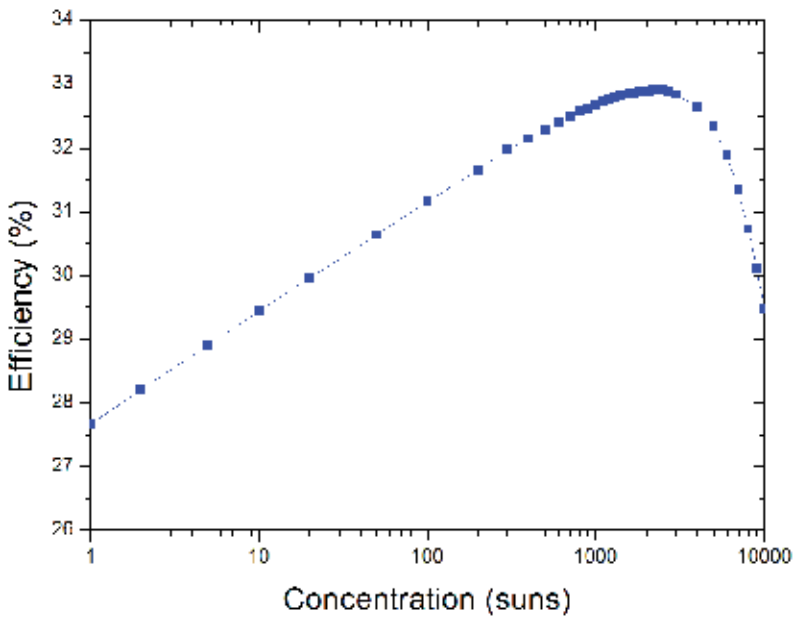


**Figure 7.** Simulation of the solar cell efficiency of a double-junction solar cell as a function of light concentration at a temperature of 320 K.

## 4. Effect of the surrounding medium on solar cell efficiency

There are currently several techniques used to concentrate light inside a CPV module. They can be made of primary and secondary lenses, as in the case of the examples given in this chapter, of only a primary lens or a (parabolic) mirror. To avoid losses due to changes in the refraction index, encapsulating materials might be used when using a secondary lens. The refraction index of this type of gels can be chosen to achieve the highest efficiency in the module. In all cases sunlight has to be properly guided and matched from air through several materials of different refractive index to the solar cell until if finally reaches each single junction of a multijunction solar cell, where the light is recombined. This leads to the question on how much is the output power of the CPV module affected due to the optical system. To analyze this issue, several simulations are made on a double-junction solar cell as the one described earlier.

The obtained results can be extrapolated to a triple-junction solar cell, at least qualitatively, since the third junction (typically made out of a germanium p-n junction) generates much more current than either the 1st or 2nd junction, and it does therefore not limit the multijunction solar cell. Figure 8 shows the simulated I-V curves of a triple-junction solar cell and all of its subcells, the bottom cell (typically a Ge cell, red curve), the middle cell (typically an InGaAs cell, green curve), the top cell (typical an InGaP cell, blue curve) and the resulting I-V curve of the triple junction solar cell (grey curve). This figure shows a triple-junction cell in which the top cell is the limiting subcell and also that the Ge junction generates much more current than any of the other two.

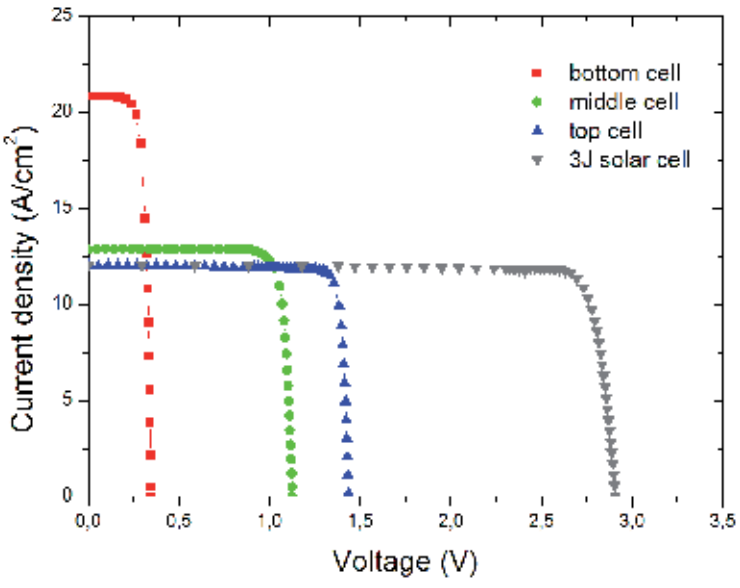


**Figure 8.** I-V curves of a triple-junction solar cell. There are given the three I-V curves of the subcells (top-cell, middle-cell and bottom cell) and the resulting I-V curve of the resulting 3J cell.

http://dx.doi.org/10.5772/52707

The efficiency of a double-junction solar cell with two different ARC layers, either a double layer of $TiO_2/Al_2O_3$ or a single layer of $Si_3N_4$ is analysed. The refractive index of the surrounding medium has been increased from 1 (air) to 1.5 (e.g. glass). The result of the simulated efficiency is shown in Figure 9 for a given thickness of the ARC layer. If the solar cell would be operated in air (n=1) the best choice would be to use a $TiO_2/Al_2O_3$ double layer and the solar cell would have an efficiency of 31.14%. But, if the solar cell would be operated in a medium with a refractive index higher than 1, e.g. 1.5, a $Si_3N_4$ single layer would be a better choice, yielding an efficiency of 31.87%. It can also be observed that if the solar cell has been optimized for being measured in air (ARC double layer of $TiO_2/Al_2O_3$), the efficiency of the system is reduced by around 1% when it is being operated in a medium with a refractive index of 1.5. On the other hand, a solar cell that has an ARC layer that is optimized to a medium with n=1.5, has a lower efficiency when measured at air. In the case that the solar cell is operated in a medium of n=1.5 and a wrong antireflection coating has been chosen (in this example $TiO_2/Al_2O_3$ instead of $Si_3N_4$), the solar cell would have an efficiency of 30.16% instead of 31.87%, having a loss in efficiency of 1.71%. It should be remembered that these values depend very much on the material and thickness of the ARC layer, and each system configuration has to be analysed separately.

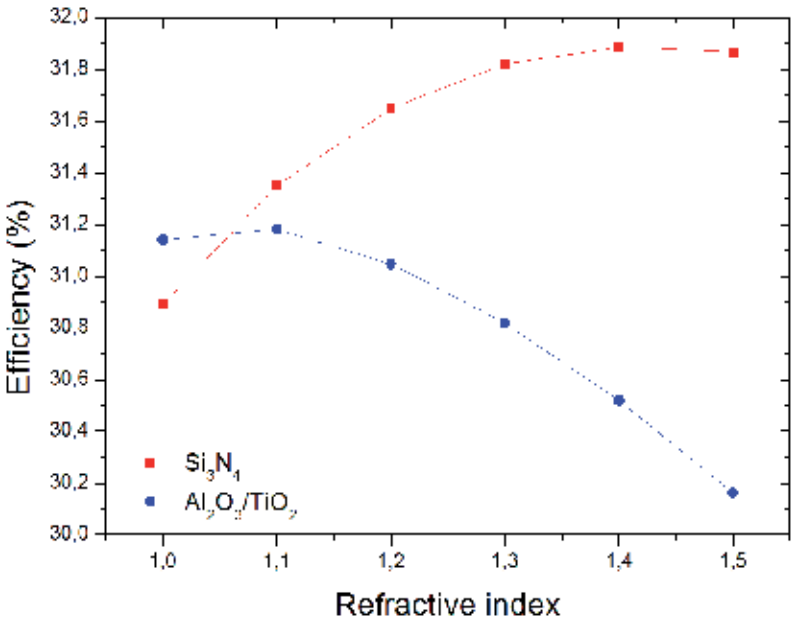


**Figure 9.** Solar cell efficiency as a function of the refractive index of the surrounding medium, for two alternatives of anti-reflection coatings.

This is a simplified example of how important the condition in which the solar cell operates is. If the solar cell would be encapsulated in a medium with a refractive index of 1.5, the situation would be as described above. In reality CPV modules are in general much more com-

plex, and even more layers might interfere with the sun rays on its way to the solar cell. This means, on one hand, that if the solar cell is optimized to be operating in air, the expected decrease in efficiency when operating in the CPV module might be even higher than in the previous simulations. On the other hand, if the complexity of the module increases, it is also much more difficult to optimize a solar cell to be operating in that specific CPV module. In any case, according to these simulations, it is strongly recommended not to develop separately the solar cell and the optics of the CPV module, rather than optimizing the system as one unit.

## 5. Effect of AR coating material on solar cell efficiency

Anti-reflection coatings are needed to match the refractive index of the solar cell window layer to the surrounding medium, increasing thereby the amount of light that penetrates into the photovoltaic structure [11]. These must be carefully designed to have the highest transmission and the broadest bandwidth. The tuning of these could yield by multijunction solar cells to different limiting cell configurations, since different spectral parts of the sunlight are absorbed or reflected differently during operation. For this reason, our software is capable to handle spectral responses of complete systems and with different irradiation spectra.

In this section the design of the AR coating is analysed. With a correct design of the AR coating, the solar cell can be adapted to the surrounding medium, reducing losses due to unwanted reflections. It is possible to increase the final efficiency of the cell, increasing it up to around 30% of its initial value in a cell/air interface. As this medium is fully dependent on the system design (epoxy, air, lens, potting, etc.), the AR coating should be designed taking into consideration the design of the CPV module. We performed some simulations with several materials that are typically used as AR coating in optoelectronic devices. These are aluminum oxide ($Al_2O_3$), titanium dioxide ($TiO_2$), silicon nitride ($Si_3N_4$), and magnesium difluoride ($MgF_2$). The result for a double-junction solar cell is shown in Figure 10.

This figure shows that there is a strong dependence of the efficiency of a solar cell on the material of the antireflection coating and on its thickness. The efficiency can therefore be maximised e.g. when it is measured in air. Whenever we change the medium from air to a different higher refractive index medium (glass, epoxy, lens, potting, etc.), results vary. Figure 11 shows simulations for the same solar cell as in Figure 10 but considering that the solar cell is mounted in a CPV module. This means that the optical system has a big influence in modifying the spectral performance of the CPV system.

Comparing Figure 10 and Figure 11 we see that the behaviour of the efficiency against AR coating thickness differ if the solar cell is either measured on air or mounted inside a CPV module. It is observed e.g. that an efficiency of 29% of a standalone solar cell with an approximately 80 nm thick $MgF_2$ AR coating layer, has only 24% efficiency when this solar cell is mounted in the CPV module.

http://dx.doi.org/10.5772/52707

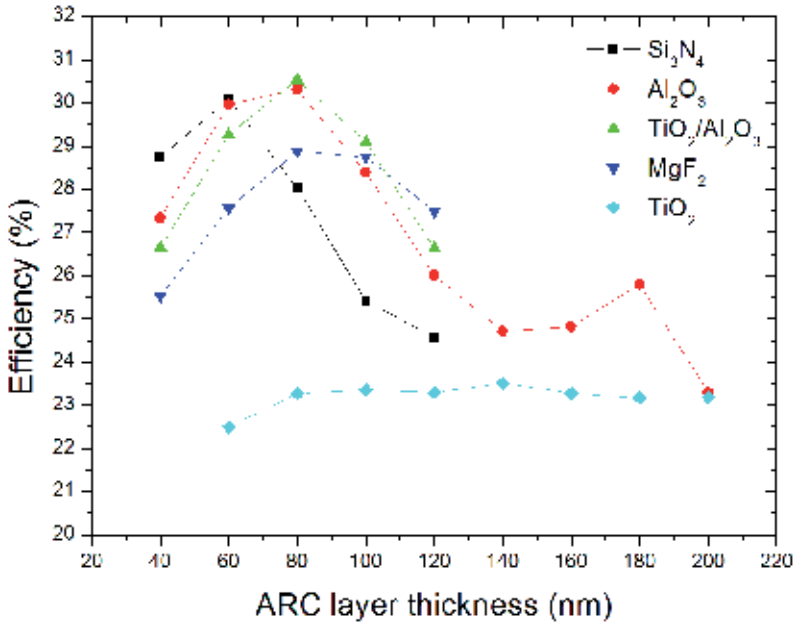


**Figure 10.** Stand-alone solar cell efficiency vs. AR coating thickness for several materials.

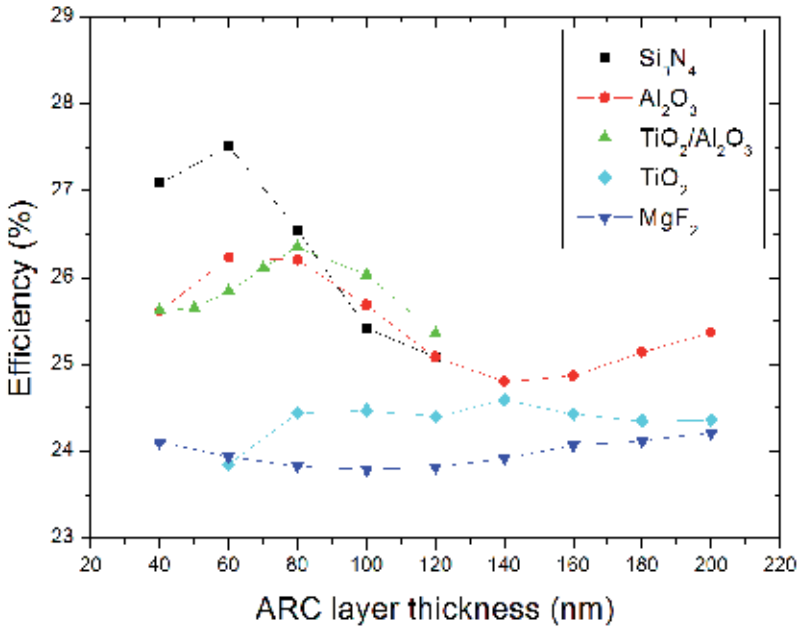


**Figure 11.** CPV system efficiency vs. AR coating thickness for several materials, using the same cell structure as for the plots in Figure 10.

## 6. Current matching: Stand-alone solar cell vs. performance in CPV module

In this section the spectral loss of the optical system is analysed. Several simulations were made starting from a double-junction solar cell in which the thickness of the base of the top cell is increased from 500 nm to 950 nm for the case of a stand-alone solar cell, and from 500nm to 1150nm for a solar cell that is assembled in a module. The obtained results are again specific to each configuration of solar cell and type and materials of a CPV module. Nevertheless, the general tendency of the results that is observed (i.e. the switching from a top-cell limiting configuration to a bottom-cell limiting configuration with increasing top-cell base thickness) is generally valid.

Figure 12 shows the behavior of the efficiency when increasing the thickness of the base of the top-cell of a double-junction solar cell. It can be seen that when increasing the thickness from 500nm until approximately 700nm, also the efficiency increases. This shows (and is confirmed by the plots of the I-V curves not shown here) that the top-cell of the double-junction solar cell is limiting. Increasing the thickness of the base further, from approximately 800nm to 950nm the efficiency decreases, and the bottom-cell is the limiting one. The reason for the drop in efficiency is on one hand that the series resistance of the top-cell increases, and that there is more light absorbed in the top-cell and therefore less light available for current generation in the bottom-cell.

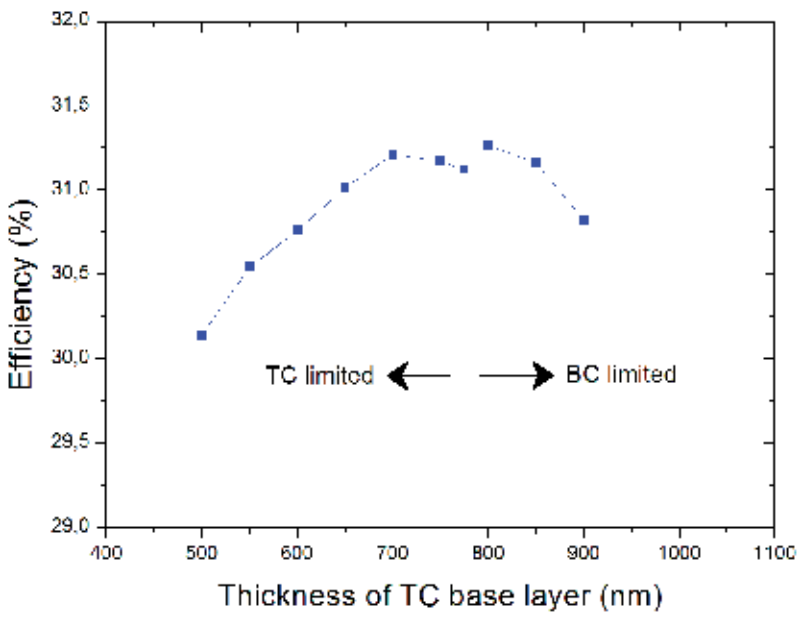


**Figure 12.** Simulation of the efficiency of a stand-alone double-junction solar cell as a function of top cell base thickness.

http://dx.doi.org/10.5772/52707

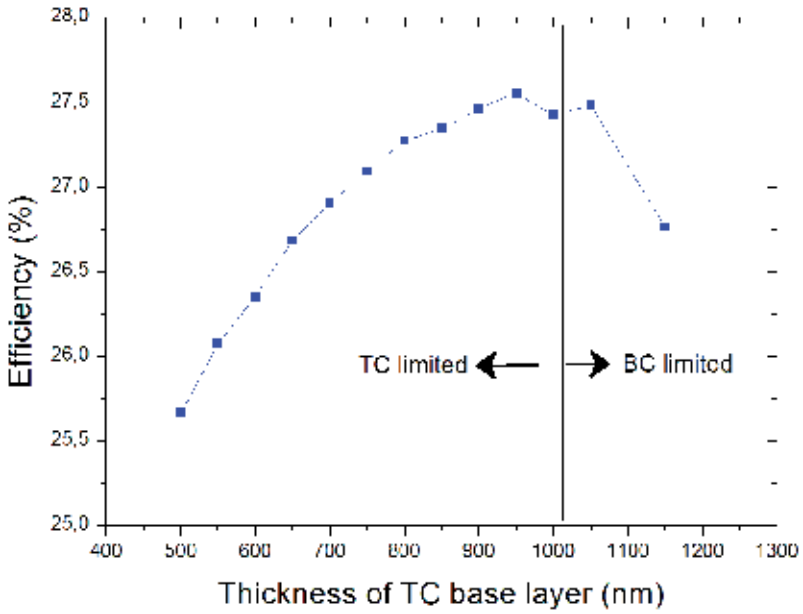


**Figure 13.** Simulation of the efficiency of a double-junction solar cell that is mounted inside a CPV module as a function of top cell base thickness.

The same series of simulations have been done for a solar cell mounted in a double lens CPV system like the one shown in Figure 2 and the result is plotted in Figure 13. Even though the general tendency of switching from a top-cell limiting configuration to a bottom-cell limiting configuration is true in both examples, the thickness at which this switching occurs is different, and occurs at higher thickness when the solar cell is mounted inside a module. This figure shows that when embedding the cell in the CPV system the current matching for the individual solar cell in a dual junction solar cell moves towards around a 1000 nm-thick top-cell base. This can be explained by the fact that part of the sun light gets either absorbed by the materials of the system or get reflected on the interfaces of them, so that less light is available for generating current in the solar cell. It also follows that the efficiency of the solar cell and system is lower than that of only the solar cell.

Continuing with the analysis of the system as a whole, it can be seen that the efficiency of this system is in all the range lower than that of a stand-alone solar cell. As an example two solar cells with different width of the top-cell base will be compared, one of 750 nm and the other one of 950 nm. If the final design of a solar cell is with a 750 nm thick top cell base, its efficiency is 31.21%, and if the final design is with a 950 nm thick top cell base, its efficiency will be 30.82%. If these two solar cells are mounted in the system, the first solar cell will have an efficiency of 27.09%, and the latter one an efficiency of 27.55%. This means that the solar cell with a top-cell base thickness of 750 nm performs better when it is operated in air (i.e. 0.39% higher), whereas the solar cell with a top cell base thickness of 950 nm performs better when it is mounted in the module. According to these simulations, if the thickness of

the base of the top-cell is increased from 650 nm to 950 nm in a solar cell that is going to be operated in the optical system described earlier, the overall system efficiency would be increased by 0.46%. The very important conclusion of this analysis is, once more, that the priority should be to optimize the module efficiency and not only the solar cell efficiency.

The previous simulations can be complemented with simulations of the spectral response of a solar cell. In Figure 14 is plotted the spectral response of the solar cell for a stand-alone solar cell of a 650 nm and a 950 nm thick top-cell base. This figure is similar to the ones measured on real devices, like e.g. in [14]. Figure 15 shows the same plot for a solar cell that is mounted in a CPV system. When increasing the width of the top-cell base, the generated current in the top cell increases (blue curve). This behaviour is also true when the solar cell is inserted in a module, even though it is less enhanced.

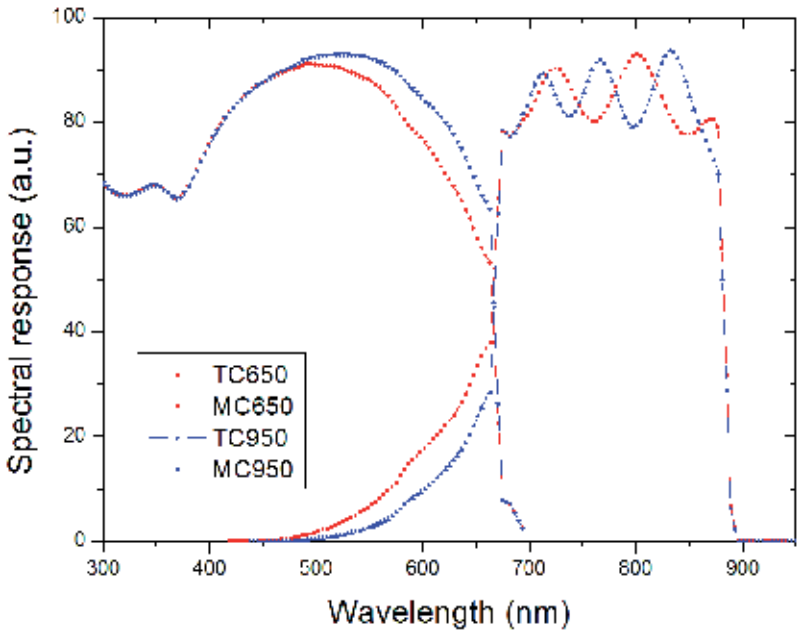


**Figure 14.** Simulation of the spectral response of a double-junction solar cell for two different TC base thicknesses (650 nm and 950 nm).

http://dx.doi.org/10.5772/52707

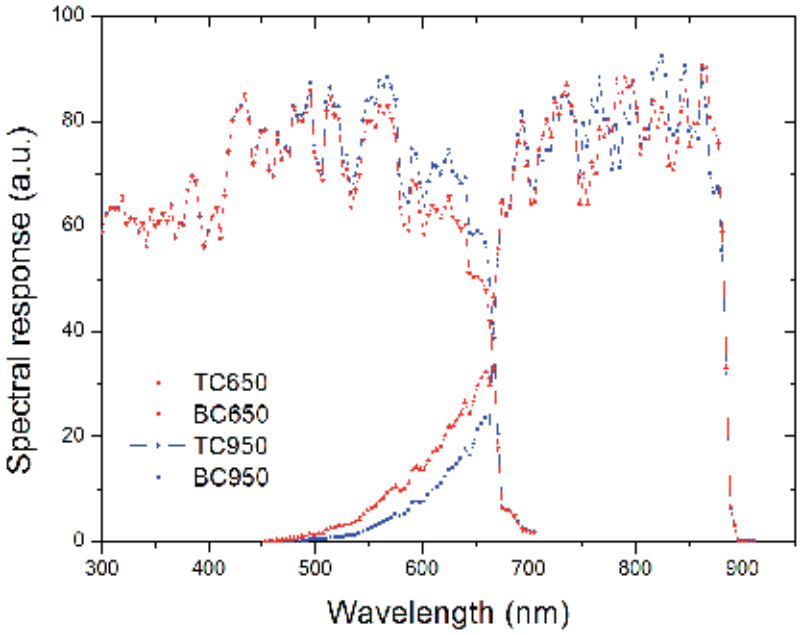


**Figure 15.** Simulation of the spectral response of a double-junction solar cell mounted inside a CPV module. The simulations are made for two different top cell base thicknesses (650 nm and 950 nm).

## 7. Power loss in a CPV module due to a non-matched solar cell

It has been shown in this chapter with the help of a simulation program that the performance of a solar cell depends on the medium in which it operates. A solar cell that is measured in air as a standalone device does not perform in the same way as in a system that is composed of solar cell and optical concentrator system. The system efficiency is typically lower than the efficiency of a standalone solar cell, due to losses that are attributed to (spectral) absorption of the materials and reflections on the interfaces of different type of materials. These losses between a stand-alone solar cell and the efficiency of the system can be minimized, if the right materials are chosen and the solar cell and the optical system are adapted to each other.

In order to get a feeling on how big the impact of the efficiency loss is on the module power output, simple calculations are given. It has been shown in previous sections that due to a wrong choice of anti-reflection coating the loss in efficiency of the CPV system can be 1,71%, and that if the thickness of the base of the top cell is not adapted to the system, it is possible to lose another 0,46% in efficiency. This means that by adapting the ARC and the thickness of the base of the solar cell, it is possible to gain (or not to lose) more than 2% in system efficiency, according to the simulations of the system and parameters described earlier. The simulations were made for a double-junction solar cell, and it can be expected that the loss of 2% that is observed for a non-optimized solar cell will be even higher for a system with a triple-junction solar cell.

As an example, it is assumed that the optimized system efficiency of a CPV module is 30%, whereas the efficiency of the not optimized CPV module is 28%. Assuming that a given CPV module has 10 solar cells of 1 $cm^2$ of active area each and works at a concentration of 500 suns, then the output power would be 127,5 W for 30% system efficiency and 119 W for 28% system efficiency, assuming an irradiation of 850 $W/m^2$. With this simple example it is intended to visualize that a seemingly small difference of 2% in system efficiency has an effect of approx. 6,7% on module level and therefore also on the installation cost of a CPV power plant. The effect that a 2% efficiency difference makes on module level depends on its design (number of solar cells, concentration ratio, etc.), and should be therefore only considered qualitatively.

## 8. Conclusion

In this chapter simulations of double-junction solar cells were discussed. The ISOSIM simulation software is a powerful tool to obtain characteristic curves of solar cells. With this software package it is also possible to understand and predict experimental behaviour of solar cells under real operating conditions. The results obtained in this chapter can be extrapolated to triple-junction solar cells, since typically the third junction is made out of Germanium and is far from limiting the multijunciton solar cell. It has been analysed the efficiency of a solar cell and a system composed of solar cell and additional layers that should represent the optical system of a CPV module. It has been analysed the effect of the anti-reflection coating material and its thickness on the efficiency of the solar cell, and has also been shown that when increasing the width of the base to the top cell, the double-junction solar cell switches from being top cell limiting to bottom cell limiting. These two parameters, the type and thickness of the ARC layer and the thickness of the top-cell base thickness play an important role on the efficiency of the solar cell. When the solar cell is assembled in a CPV module the optimum values of ARC coating material and its thickness and the optimum thickness of the base layer of the top cell changes. This means that in order to obtain maximum module power output, a solar cell and optical system should match each other well, in a way that the design of the solar cell should take into account the optical system of the CPV module or the other way around, the design of the optical system should be adapted to a given solar cell. It is also shown that a small variation in efficiency of a solar cell has a big impact on CPV module power output and therefore also on the installation cost of a CPV power plant.

## Author details

Egbert Rodríguez Messmer

Isofotón S.A, Spain

http://dx.doi.org/10.5772/52707

## References

[1] F. Rubio, M. Martínez, D. Sánchez, R. Aranda, P. Banda, Two years operating CPV plants: Analysis and results at ISFOC, 7th International Conference on Concentrating Photovoltaic Systems, Las Vegas 2011

[2] SolFocus (May 2010). SolFocus and Victor Valley College Complete the Largest Solar Power Plant of its Kind in North America, Available from: http://www.solfocus.com/en/ news-events/press-releases/2010-05-26.php

[3] Amonix.ParquesSolares de Navarra, Flexible Deployment Leads To Largest CPV Solar Power Plant Under The Sun, Available from: http://www.amonix.com/content/success-stories

[4] Concentrix Solar (February 2010). Concentrix Solar enters the US Market with Megawatt CPV Deployment at a Chevron Facility, Available from: http://www.soitec.com/en/solar-energy/

[5] Soitec press release http://www.soitec.com/events/san-diego/press-room.php (accessed 22 December 2011)

[6] H. Lerchenmüller, A.W. Bett, J. Jaus, G. Willeke; Cost and market perspectives for FLATCON-systems, Proceedings of the 20th European Photovoltaic Solar Energy Conference, Barcelona (Spain) 2005

[7] J.A. López Villanueva, V. Díaz, S. Rodríguez Bolívar, J.A. Jiménez Tejada and E. Rodríguez Messmer; A multijunction solar cell simulation program for the development of concentration systems, Proceedings of 6th Spanish Conference on Electronic Devices, San Lorenzo del Escorial, Madrid (Spain) 2007

[8] V. Díaz, J.A. López Villanueva, S. Rodríguez Bolívar, J.A. Jiménez Tejada and E. Rodríguez Messmer; ISOSIM: A Multijunction Solar Cell Simulation Program, Proceedings of the 4th International Conference on Solar Cell Concentrators, San Lorenzo del Escorial (Spain) 2007.

[9] E. Rodríguez Messmer, V. Díaz, J. Miguel-Sánchez, J.A. López Villanueva; Simulation of the Impact of Design Parameters on the Efficiency of Concentrator Systems with the ISOSIM Package, Proceedings of the 33rd IEEE Photovoltaic Specialists Conference (PVSEC), San Diego 2008.

[10] Software Spectra, Inc., (2011), Optical Data from Sopra SA, Available from: www.sspectra.com/sopra.html

[11] Aiken, D. (2000). Antireflection coating design for series interconnected multijunction solar cells, Progress in Photovoltaics: Research and Applications, 8 (2000), pp 563-570

[12] Olson, J. (2003). Growth and characterization of high efficiency III-V multijunction solar cells for terrestial and space applications, Proceedings of the 10th European Workshop on MOVPE, Lecce (Italy) 2003

[13] R.R. King, D.C. Law, K.M. Edmondson, C.M. Fetzer, G.S. KinseyH. Yoon, D.D. Krut, J.H. Ermer, R.A. Sherif, and N.H. Karam; Advances in high-efficiency III-V multi-junction solar cells, In: Advances in OptoElectronics, Volume 2007, 29523, doi: 10.1155/2007/29523(2007).

[14] I. García, I. Rey-Stolle, B. Galiana, and C. Algora; A 32.6% efficient lattice-matched dual-junction solar cell working at 1000 suns, Applied Physics Letters 94, 053509 (2009).

Chapter 12

# Electric Energy Management and Engineering in Solar Cell System

Purnomo Sidi Priambodo, Didik Sukoco, Wahyudi Purnomo, Harry Sudibyo and Djoko Hartanto

Additional information is available at the end of the chapter

http://dx.doi.org/10.5772/52572

## 1. Introduction

Solar cell system has many competitive advantages in comparisson to other renewable energy resources. For instance, wind-turbin is very dependable to geographical location and has very high noise pollution if applied in residential area. Other example is micro-hydro, which depends on altitude and available in very limited locations. Furthermore, nuclear energy should be forgotten since its high radioactive risk. On the other side, solar cell system has characteristics of zero pollution, no radioactive risk, compact, portable and can be installed in any residential areas and has relatively high energy availability in any location on the earth surface in a year round. In general, solar cell array, which cover a residential roof house can supply the basic electrical energy needs of the residences who live in the house, almost a year round. These competitive advantages of solar cell system over other renewable energy resources, make solar cell system the most favorite renewable energy resource.

There are 2 main topics and will be discussed in accordance to energy management of renewable energy resources, based on solar cell system. **The first topic** is how to keep the system sustainable to supply the applied electrical load. As we have already known that solar energy is not available continuosly in a day and year round. For instance, at noon, the availability of solar energy is abundant, however, at night there is not available at all. In the rain or winter season, the availability of solar energy is less than in the dry or summer season. On the other hand, the needs of electrical energy may be in opposite situation of the availability of solar energy. In order to keep the solar cell system able to serve the total electrical load, it is necessary to design the system, which has sufficient number of solar cells and bat-

teries to get and store the electrical energy from solar energy at the most available energy time (noon), and delivering to the consumers at the non-available solar energy time (night). In this first topic, in order to keep sustainable, it is conducted by designing the sufficient number of solar cells and batteries to supply the predicted electrical load.

In the first topic, the sustainability perspective in an energy network is emphasized in the form of designing the sufficient number of solar cells and batteries to supply the predicted electrical load. **The second topic** is sustainability to deliver energy perspective. It is focused on how conducting collaboration between several autonomy units of renewable energy system to build a renewable energy resource grid. Even, if possible, to do integration between autonomy units of solar system and the conventional electrical state own company. Here, we emphasize that the key problem of electric energy management of renewable energy resouces such as solar cell system is sustainability.

## 2. Electric energy management in an autonomy unit of solar cell system: A perspective

There are at least 2 strategic ways to implement renewable energy resources especially solar cell systems to fulfill the national electrical energy needs. The first strategy is to encourage the people to fulfill their own basic residential electric energy need by building private solar cell system. The second strategy is to let the Government as the regulator to drive a consortium of companies to build large plants of solar cell system to fulfill the regional or national electric energy need. Of course, the consortium will require a large amount of financial investment at the starting point, however along with the time, the long term electric cost will be getting lower and more cost effective, since solar cell system requires very minimum maintenance cost and free of solar energy.

A solar cell system as an autonomy energy resource unit must have an energy management control unit, which embeded in the system. In general, there are at least 5 parts should exist in a electrical renewable energy resource system, as shown on Fig 1 below, i.e.: (1) solar cell array; (2) management energy control system; (3) energy storage (s); (4) DC to AC and AC to DC converters and (5) delivery bus. Thus 5 parts should be designed such that the system becomes more efficient to manage the gathered electrical energy and to reach higher sustainability with low investment cost. We need 100% sustainability to fulfill the electrical energy need.

In order to reach 100% sustainability, first of all, the designer has to know how much energy need in average in every single day (prediction). Then, the designer must consider the region, where the solar cell system is located and it relates to the earth latitude. Further, it counts to the statistical condition of how long the total time the sun shines on thus region in a year round. Another important info is the statistical info of the longest duration of NO sunshine days, which relates to the seasons and weather. Thus are the most critical information to determine the requirement of the total number of solar cells and batteries in the system.

http://dx.doi.org/10.5772/52572

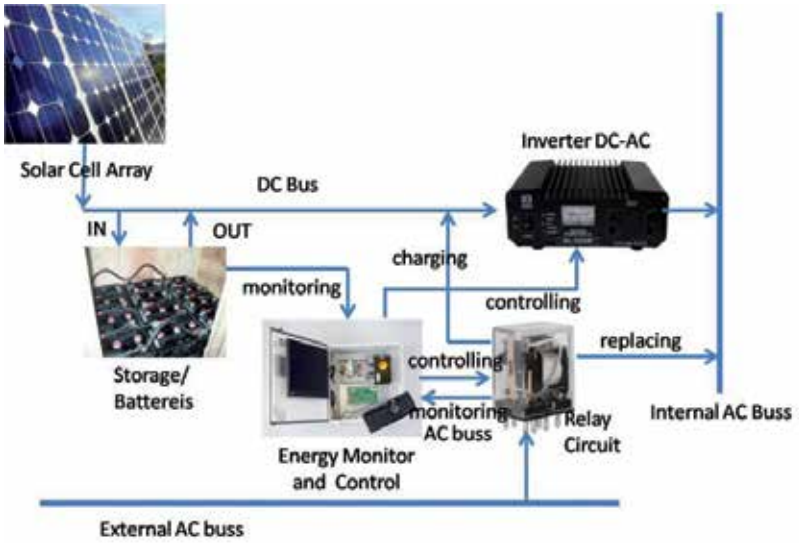


**Figure 1.** Big picture of Solar Cell Based Renewable Energy Unit System.

Solar cell produces DC electrical energy, which fits to be storage in batteries. In designing solar cell system, as explained above, it must be determined the assumption of average need of energy per day, for example A Watt-hour/day. Further, the estimate of statistical condition of how long the total time of NO sunshine days on thus region in a year round must be determined, for example N days. The amount of solar cells and batteries needed by the system is written in the following equation:

$$(1+c)\cdot N\cdot A \quad Watt\,hour \tag{1}$$

where $c$ is a leak energy coefficient of the battery. In general, it has been known that the battery is not perfect to store DC electrical energy, it is always a part of stored energy in battery leaks. This is a inefficiency factor of battery and presented as "$c$" coefficient.

Solar cell system performance fully depends on the performance of thus 5 parts in building the system; which has been listed above (Fig 1). The following is explanation of every part.

## 3. Solar cell and eficiency

The main characteristic of solar cell is I-V curve. It has several derivative parameters such as$I_{sc}$ (short circuit current), $V_{oc}$ (open circuit voltage) and the maximum possible delivered energy $P_{mp}=V_{mp}\cdot I_{mp}$, as shown on the following Fig 2.

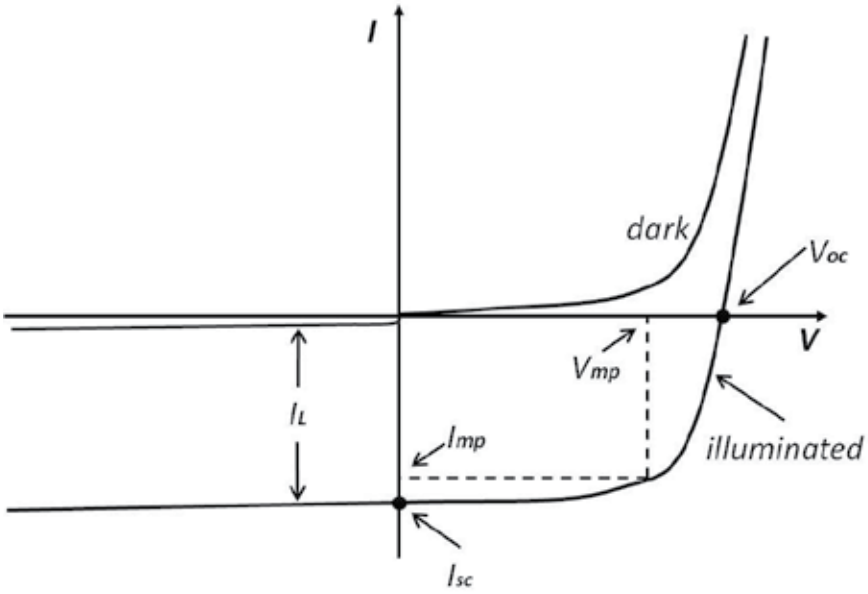


**Figure 2.** The Graph of the I-V characteristics of an ideal diode solar cell when non-illuminated (dark) and illuminated [1].

The main parameter that determines the solar cell efficiency is the maximum square area (power) as form of multiplication I-V ($P_{mp}$=$V_{mp} \cdot I_{mp}$), which is a maximum square formed inside I-V curve as shown on Fig 2 above. The next derivative parameter is fill factor *FF* that represents the ratio PMP to the product $V_{OC}$ and $I_{SC}$. This parameter gives an insight abouthow "square" is the output characteristic.

$$FF = \frac{P_{MP}}{V_{OC} \cdot I_{SC}} = \frac{V_{MP} \cdot I_{MP}}{V_{OC} \cdot I_{SC}} \tag{2}$$

In the case of solar cell with sufficient efficiency, in general, it has FF between 0.7 and 0.85. The energy–conversion efficiency, η can be written as [2]

$$\eta = \frac{V_{MP} \cdot I_{MP}}{P_{in}} = \frac{V_{OC} \cdot I_{SC} \cdot FF}{P_{in}} \tag{3}$$

where $P_{in}$ is the total power of light illumination on the cell. Energy-conversion efficiency of commercial solar cells typically lies in between 12 and 14 % [2]. In designing a good solar cell, we have to consider and put any effort to make those four parameters $I_{SC}$, $V_{OC}$, FF and η as optimum as possible [1]. We like to use term optimum than maximum, since the effort to obtain one parameter to be maximum ,in designing solar cell, will degrade other parameters. Hence the best is considering the optimum efficiency of solar cell.

http://dx.doi.org/10.5772/52572

## 4. Buss system

Solar cell produces DC electric energy. For solar cell system, where the solar cell array has radius not more than 100-m to batteries and electrical loads, it is effective and cost efficient to be connected by DC buss system. By using DC buss system, in order to transfer electrical energy from solar cells to batteries and loads, the parameter needs to be considered is voltage. The DC buss is the most efficient and cost effective, since it does not require electrical conversion from DC to AC. DC buss can be extended for more than 100-m, even can be more than several kms. In order to lower the DC electric power loss in the transmission from solar cells to batteries and loads, the DC transmission voltage should be increased, hence, to deliver the electrical power it requires only a very low current. This method is very popular used in AC electric transmission for long distance by using high voltage AC. The DC electric power transmission loss is written by the following equation:

$$P_L = I_{DC}^2 R_{tr} \tag{4}$$

$P_L$ is power loss in the DC transmission line, $R_{tr}$ is the total transmission line resistance and $I_{DC}$ is the DC current on DC buss transmission line. Hence, to lower power loss and $R_{tr}$ kept same, then $I_{DC}$ must be decrease much lower with consequence of $V_{DC}$ must be increase proportionality to the decrement of $I_{DC}$. To increased voltage $V_{DC}$, in general conducted by using boost converter method.

### 4.1. Boost converter for DC buss system

Boost converter is an electronic circuit for *DC to DC converting*. It functions to increase voltage $V_{DC}$ higher, i.e. by controlling the signal driver duty cycle. *Boost Converter* base circuit requires only 4 fundamental components, which are: inductor, electronic switch, diode and output capacitor, shown on Fig 3. The converter circuit can be operated in 2 modes, which depends on the energy storage capacities and the relative length of the switching period [3]. Those 2 methods are CCM (*Continuous Conduction Mode*) and DCM (*Discontinuous Coduction Mode*), where CCM is for efficient power conversion and DCM is for low power conversion[3].

#### *4.1.1. Continuous Conduction Mode (CCM)*

**Mode 1 ($0 < t \leq t_{on}$),**

Mode 1 starts, when switch S (MOSFET) switched on at $t = 0$ until $t = t_{on}$. The equivalent circuit for Mode 1 is shown on the following Fig 4a. By assuming that the serial resistance value DC voltage source is relatively low, there will be an inductor current transient $i_L(t)$ larger than zero and increase linearly at the beginning of transient. Inductor voltage is $V_L = V_i$.

**Mode 2 ($t_{on} < t \leq T_s$),**

Mode 2 starts, when switch S (MOSFET) switched off at $t = t_{on}$ until $t = T_s$. The equivalent circuit for Mode 2 is shown on Fig 4b. Inductor voltage, $V_L$ in this period is $V_i - V_o$. In this case $V_i < V_o$, it means in Mode 2, $V_L$is in opposite direction to $V_L$ in Mode 1.

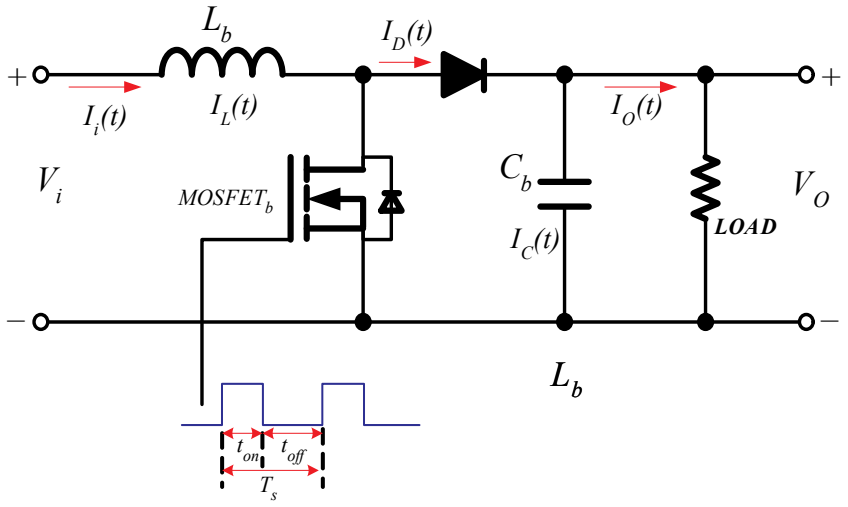


**Figure 3.** Basic DC Voltage Boost Converter Circuit [3]

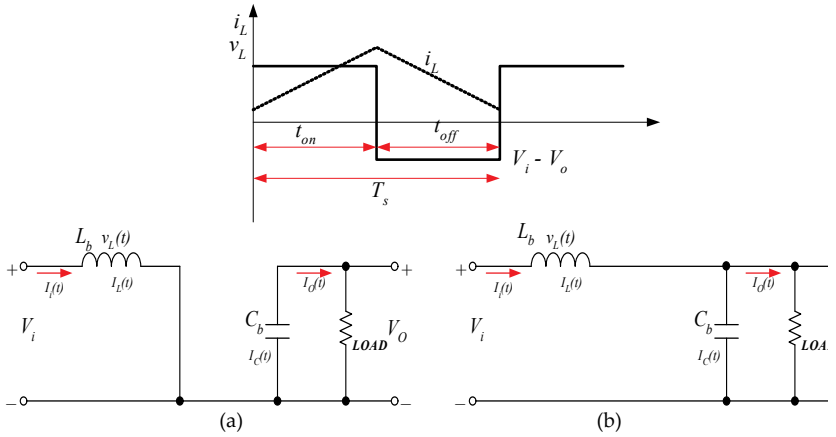


**Figure 4.** *Continuous Coduction Mode*:(a) Close switch, (b) Open switch

In steady state operation, the signal formed due to switching is repeated over all the time. The integral of inductor voltage $v_L$ in one period must be equal to zero, where $T_s = t_{on}+t_{off}$. Therefore, the total summation of inductor voltage at open switch and close switch must be equal to zero.

$$V_i t_{on} + (V_i - V_o) t_{off} = 0 \tag{5}$$

http://dx.doi.org/10.5772/52572

Where:

$V_i$: input voltage

$V_o$ : the average of output voltage

$t_{on}$ : time *on*

$t_{off}$ : time off

$T_s$: switching period

By arranging and separating $V_i$ and $V_o$, and then dividing the both sides by $T_s$, it results in

$$\frac{Vo}{Vi} = \frac{Ts}{toff} = \frac{1}{1 - D} \tag{6}$$

where $D$ is duty cycle.

By assuming that the circuit has 100% efficiency, i.e $P_i = P_o$

$$I_i V_i = I_o V_o \tag{7}$$

$$\frac{Io}{Ii} = 1 - D \tag{8}$$

where

$I_o$ : the average output current

$I_i$ : the average input current

When the switch is close,

$$V_L = V_i; L \frac{di_L}{dt} = V_i; \frac{di_L}{dt} = \frac{V_i}{L}$$

$$\frac{di_L}{dt} = \frac{\Delta i_L}{\Delta t} = \frac{\Delta i_L}{DT} \rightarrow \frac{di_L}{dt} = \frac{V_i}{L}$$

$$\Delta i_{L\ (close)} = \frac{V_i DT}{L} \tag{9}$$

When the switch is open,

$$V_L = V_i - Vo; L \frac{di_L}{dt} = V_i - Vo; \frac{di_L}{dt} = \frac{V_i - Vo}{L}$$

$$\frac{di_L}{dt} = \frac{\Delta i_L}{\Delta t} = \frac{\Delta i_L}{(1 - D)T} \rightarrow \frac{di_L}{dt} = \frac{V_i - Vo}{L}$$

$$\Delta i_{L\ (open)} = \frac{(V_i - Vo)(1 - D)T}{L} \tag{10}$$

At the transient time, where $V_o$ is going to steady state condition, $\Delta i_{L\ (open)}$ or $i_L$ slope at Mode 2 also experience transient following the gradient of $V_o$ transient. At the time $V_o$ achieves steady state condition, then $\Delta i_{L\ (open)}$ achieves steady state as well.

*4.1.2. Discontinuous Conduction Mode (DCM)*

At this mode, the inductor current will drop to zero before finishing one switching period, as shown on Fig 5. As the CCM analysis, the voltage inductor integral during one period is zero.

$$ViDTs + (Vi - Vo)D_1Ts = 0 \tag{11}$$

Then

$$\frac{Vo}{Vi} = \frac{D_1 + D}{D_1} \tag{12}$$

and

$$\frac{I_o}{I_i} = \frac{D_1}{D_1 + D} \tag{13}$$

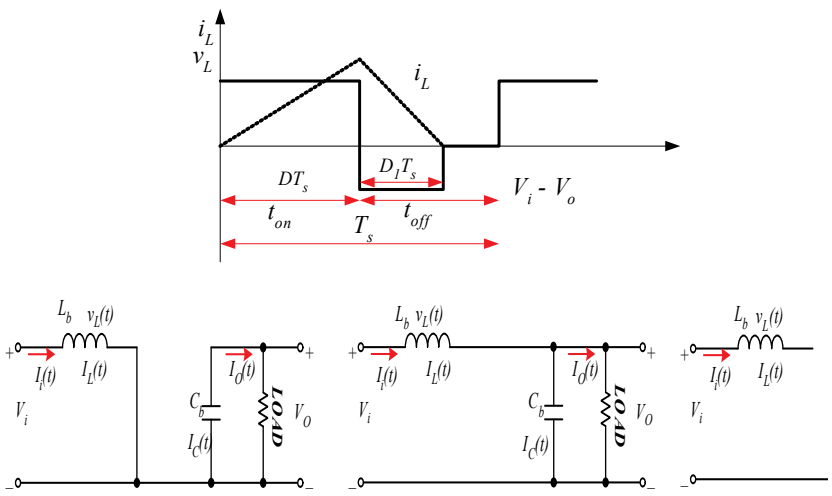


**Figure 5.** Equivalent circuit for DCM mode.

**a.** Mode 1($0 < t \leq t_{on}$);

**b.** Mode 2($t_{on} < t \leq (D+D_1)T_s$);

**c.** Mode 3$(D + D_1)T_s < t \leq T_s$

http://dx.doi.org/10.5772/52572

From Fig 5.c, the average input current is equal to the inductor current,

$$I_i = \frac{V_i}{2L_b} DT_s (D + D_1) \tag{14}$$

By using equation (13),

$$I_o = \left(\frac{V_i T_s}{2L_b}\right) DD_1 \tag{15}$$

In practice, *duty cycle* D should change to respone the $V_i$ change, such that obtaining constant $V_o$. It requires an electronic feedback control system, as a function of loading curent for the change of $V_i/V_d$. This functions to control *duty cycle*. By using equations (12) and (15), we obtain:

$$D = \left[\frac{4V_0}{27V_i}\left(\frac{V_o}{V_i} - 1\right)\frac{I_o}{I_{o,avg,max}}\right]^{0.5} \tag{16}$$

Where $I_{o,avg,max}$ is the average of maximum output current, which is obtained via the following equation:

$$I_{o,avg} = = \frac{T_s V_0}{2L_b} D(1 - D)^2 \tag{17}$$

The average output current will be maximum, when D = 1/3

$$I_{o,avg,max} = \frac{2}{27}\frac{T_s V_o}{L_b} \tag{18}$$

The critical inductance $L_{bc}$, is defined as inductance at the region of boundary, between *continuous* and *discontinuous modes,* and defined as:

$$L_{bc} = \frac{RD(1 - D)^2}{2F_s} \tag{19}$$

where:

*R* : equivalent load, Ohm

*Fs* : switching frequency, Hz

### 4.2. DC to AC inverter for AC buss system

When the distance between renewable energy clusters of solar cells, batteries and electrical loads is relatively far (can be hundred kms) and the electrical loads mostly are AC electrical loads, then it is necessary to consider to use AC buss system, which supported by DC to AC

inverters. By utilizing AC buss system, for long distance electrical transmission, the increase of AC voltage can be conducted by using passive transformator, which is common to be used. However, the integration process of several renewable energy autonomy systems is relatively more complex than integration in DC buss system. The problems in AC buss integration are due to more parameters that must be synchronized, such as voltage, frequency and phase. While in DC buss integration, it is only facing voltage synchronization.

In general, AC electrical power transmission is delivered in 3 (three) phases, especially for 3-phase electrical-mechanical motor loads, in order to be more smooth and more efficient in operation. 3-phase system is inherent in electrical generator based on mechanical generator, by arranging the three generator coils in three different locations by $120^0$ phase angle in the generator. It also happens in the DC to AC inverter 3 phase. The sine generator generates 3 equal sine wave with different phase each of $120^0$. DC-to-AC 1-phase inverter system is the fundamental to develop 3-phase system. The knowledge of working mechanism of 1-phase system is very helpful to understand 3-phase system.

In this chapter, we will discuss the working mechanism of DC to AC inverter 1-phase system in general. Then it is continued by discussion of the methods to synchronize thus three parameters of AC buss system, i.e: voltage, frequency and phase. In general, the use of DC or AC buss depends on the distance between sources, batteries and loads, also the variances of the loads. The ultimate consideration is energy efficiency and cost effective of the solar cell sytem.

*4.2.1. Full bridge inverter*

DC-AC inverter is a vital component in the solar cell system in order to support AC buss system for AC load. DC to AC inverter technology has been developed since the beginning of electronics technology era. At the beginning, DC-to-AC inverter was developed based on sinusoidal oscillator, which is amplified by push-pull amplifier of B class that has maximum efficiency of 50%. The 50% power loss is due to instantaneous drop-voltage at the final transistors on the push-pull amplifier. The fact of the 50% power loss is due to the sinusoidal form of the current and voltage running through the final transistor in DC to AC inverter circuit.

By realizing that push-pull final has maximum 50% efficiency, then full-bridge inverter technology was developed to increase the efficiency of DC to AC inverter. The work mechanism of bridge inverter is based on switching methods, as shown on the circuits of Fig 6 and 7, where at switch "on" the load current ($I_L$) goes through maximum, however the voltage drop ($V_{DR}$) across switch is very minimum. While at switch "off" the load current ($I_L$) goes through minimum, however the voltage drop ($V_{DR}$) across switch is maximum. Hence, it can be expected that power loss in the final transistors in the bridge inverter method is very small, which can be represented in equation:

$$P_L = V_{DR} I_L \quad \text{always minimum} \tag{20}$$

http://dx.doi.org/10.5772/52572

$P_L$ or power loss is always minimum, either when switch "on" or "off".

In order that bridge inverter idea realized, then the power input to the final transistors must be a constant voltage $V_{cc}$ and on-off discrete signal to control bride-inverter switches. The on-off signal is in the form of discrete signal. The advantage of using bridge inverter (either half or full) is improving the electrical power conversion DC to AC efficiency, where the ideal is close to 100 %. The high output efficiency makes the bridge converter technique replaces push-pull B class amplifier for DC to AC inverter. There are at least 2 (two) basic fundamental of bride inverter configurations exist, i.e half bride inverter (Fig 6) and full bridge inverter (Fig 7).

*4.2.1.1. Half-bridge inverter*

The following Fig 6 shows the circuit configuration of half bridge inverter. The circuit consists of 2 switching elements, $S_1$ dan $S_2$. Each element has one anti parallel diode. The switching element can be transistor, MOSFET, or IGBT.

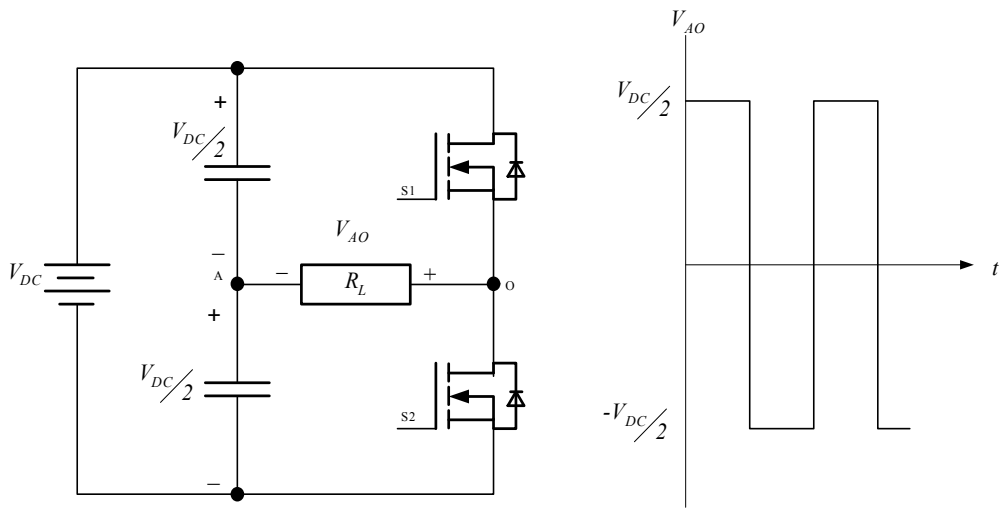


**Figure 6.** The circuit configuration of half-bridge inverterand example of output signal

The basic operation of half-bridge inverter circuit consists of 2 conditions:

1. At $S_1$ ON during 0 - T/2 period, the output voltage will drop on the load with value of $V_{dc}/2$;
2. At $S_2$ On during T/2 – T period, the output voltage will drop on the load with value of $-V_{dc}/2$.

The switching process for $S_1$ and $S_2$ must be designed such that both are not in "ON" condition at the same time. If this happens, it will happen short connection input $V_{dc}$, which will cause damage on the switching elements.

*4.2.1.2. Full-bridge Inverter*

Fig 7 shows the circuit configuration of full-bridge inverter 1-phase. The circuit consists of 4 switching elements: $S_1$, $S_2$, $S_3$, and $S_4$. The circuit operation consists of 2 conditions:

1. At $S_1$ and $S_4$ ON, $S_2$ and $S_3$ OFF, in the first half period, then the output voltage will drop on the load with value of Vdc.
2. While at $S_2$ and $S_3$ ON, $S_1$ and $S_4$ OFF, in the second half periode, then the output voltage will drop on the load with value of -Vdc.

As explained in *half-bridge inverter*, to avoid short condition on $V_{DC}$, the switching process should be designed such that at $S_1$and $S_4$*ON*, $S_2$and $S_3$must be *OFF* and vice versa. For the sake of this purpose, *gate* driver should use *dead time* mechanism.

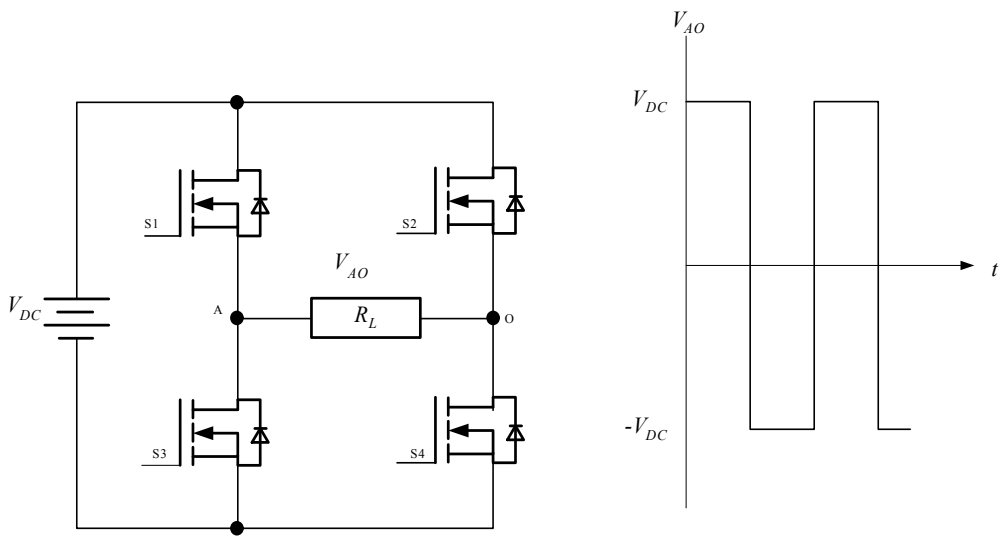


**Figure 7.** The circuit configuration of full-bridge inverterand example of output signal.

From Fig 6 and Fig 7, it can be concluded that the peak-to-peak output voltage of half-bridge configuration is a half of full-bridge one. The square wave output voltage has spectrum as shown on the following Fig 8.

http://dx.doi.org/10.5772/52572

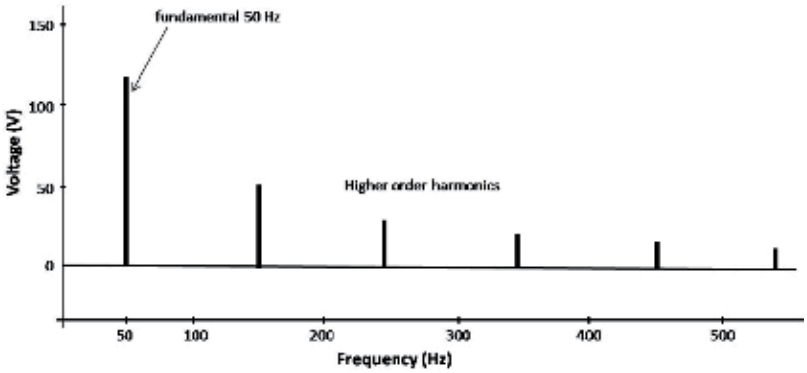


**Figure 8.** Square-Wave Harmonics Analysis of Unfiltered Output[4]

If all spectral components of power exist on the spectrum, are added together and assumed to be the output of the bridge-inverter, then the output efficiency can reach close to 100%. However, the higher order harmonics in the spectrum are not useful, even possible have ruining effects on the electro- mechanical loads. If higher order harmonics are substracted from the total output (by filtering), hence only the fundamental signal left, and the output efficiency is just 70%. To improve the output efficiency (in bridge inverter context), the discrete switch input control can be modified on to: (1) modified sine wave or (2) pulse width modulation (PWM). The following Fig 9 illustrates comparisson between pure sine wave, modified sine wave and square wave.

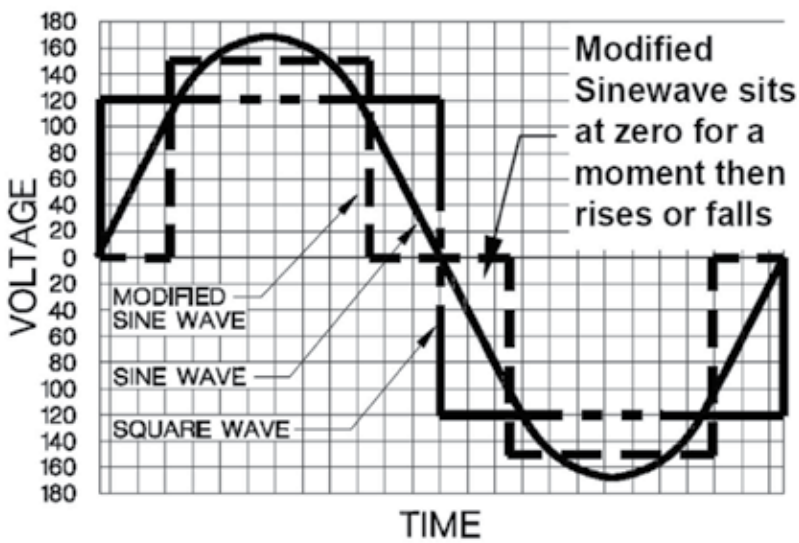


**Figure 9.** Comparisson between pure sine wave, modified sine wave and square wave.

As for instance, after going through filtering process, the square waveoutput signal is still consisting of higher order harmonics as shown on Fig 10, as following.

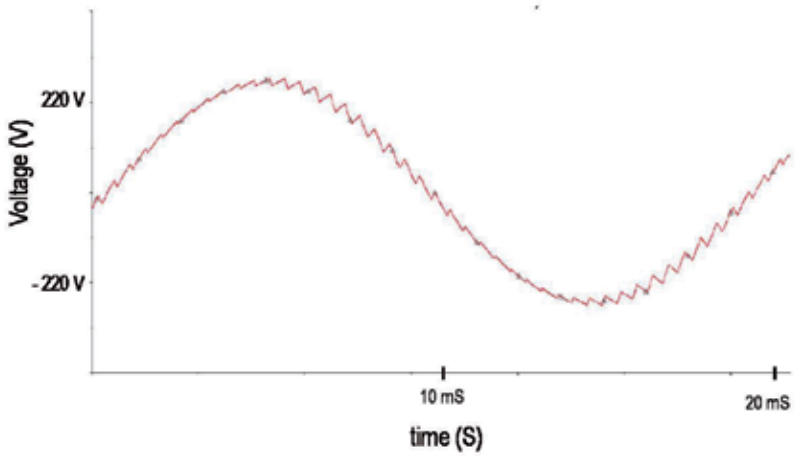


**Figure 10.** Output signal square wave as shown on Fig 6 and 7 (after filtered).

Eventhough modified-sine wave improves the output by suppressing the harmonics more than the square wave, however technically, it is too expensive, because conducting controls on two inputs: switching and Vcc. Furthermore, we will leave this modified-sine wave method.

The method that is proven good to improve output efficiency by suppressing higher order harmonics is pulse width modulation (PWM). In general PWM is the squential of discrete pulse, which is based on pulse width modulation. PWM technique becomes famous to generate pure sinusoidal wave, which is applied for DC to AC inverter and for controlling electrical motor.

*4.2.1.3. Sinusoidal pulse wave modulation*

The basic principal in forming PWM sine wave is by comparing two waves i.e. sinus wave as the reference and triangle wave as the carrier in real time. The sine wave has frequency $f_r$, which will be the inverter output frequency, i.e. 50 Hz or 60 Hz. The carrier signal has frequency $f_c$, which becomes switching frequency in inverter circuit. The ratio between $f_c$ and $f_r$is called frequency modulation ratio, $m_f$, which is defined as:

$$m_f = \frac{fc}{fr} = \frac{ftri}{fsin} \tag{21}$$

The typical switching frequency is between 2 kHz – 15 kHz, and sufficient for power system applications. The higher carrier frequency, the easier conducting filtering that is separating fundamental frequency output from the carrier frequency and its higher harmonics. Howev-

http://dx.doi.org/10.5772/52572

er, the higher the switching or triangle frequency, it will increase interference effect to other electronics instruments (electromagnetic compatibility – EMC). Fig 11 below, shows the basic concept of signal comparisson between reference and carrier signals, or sometimes called as 2-level PWM.

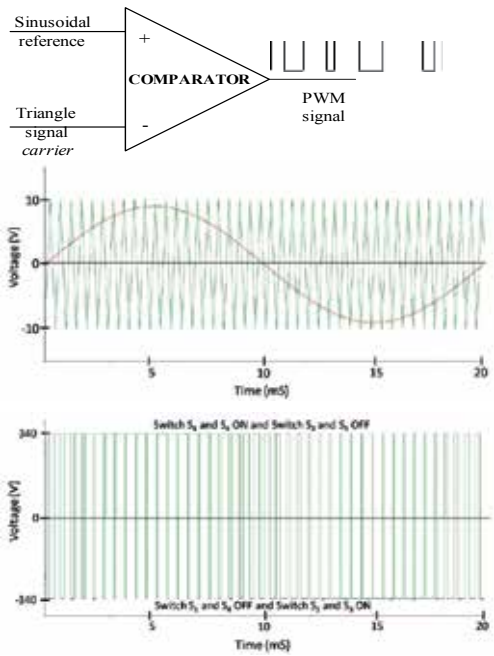


**Figure 11.** Basic concept formation of 2-level sine wave PWM

The comparisson of two input signals (sinusoidal reference and triangle carrier) results in discrete signal that is called as pulse width modulation (PWM), as shown on Fig 11 above. Moreover, the ratio between reference signal and carrier amplitudes, is called as amplitude modulation ratio $m_a$, which is defined as:

$$m_a = \frac{Vm, \quad sinusoidal\ reference}{Vm, \quad triangle\ carrier} \tag{22}$$

Where :

$V_{m,\ sinusoidal\ reference}$ : peak amplitude of reference wave

$V_{m,\ triangle\ carrrier}$ : peak amplitude of carrier wave

The PWM output, as result of comparisson between sinusoidal reference signal and triangle carrier signal, can be represented in the form of *transcendental equation*. Later on $m_a$ can be used to control the output amplitude of the PWM fundamental frequency. Moreover, the

value of $m_a$ can be used to compensate the variation of DC input voltage, such that resulting in constant output AC voltage.

*4.2.2. 3-Level PWM realization*

2-level PWM, which is illustrated on Fig 11, is successful to suppress the higher order harmonics, such that improving inverter efficiency close to 80%. In order to suppress more on higher order harmonics, it is proposed to use 3-level PWM. To realize the 3-level PWM concept, it is required a circuit that can control the synchronization of switch pairs: $S_1$ with $S_4$ and $S_2$ with $S_3$, which are represented by H-bridge on Fig 7. The circuit that realizes 3-level PWM is shown on Fig 12. It is the development of basic concept of 2-level as shown on Fig 11. The 3-level PWM requires 2 equal inputs of sine wave references with $180^0$ phase different. The resulting 3-level PWM signal is shown on Fig. 12 below.

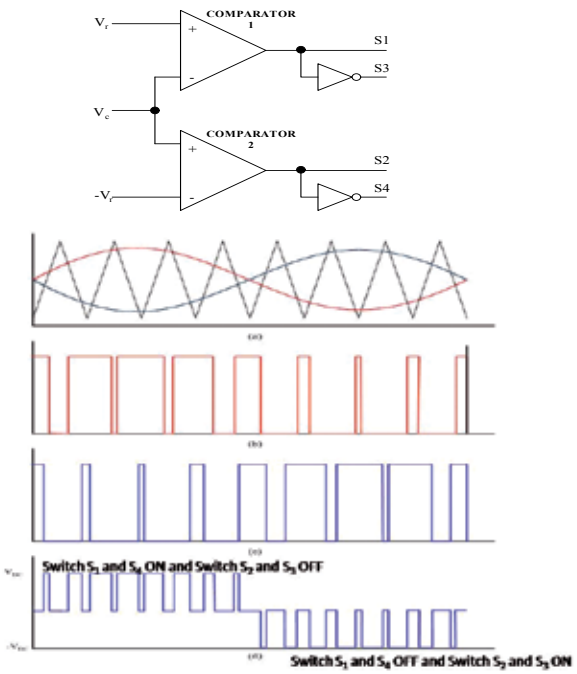


**Figure 12.** Illustration of 3-level PWMGenerator dan process generation of 3-level PWM [4·5]

**a.** Comparisson between 2 sine reference signals dan triangle carrier signal

**b.** Pulse for S1 and S4

**c.** Pulse for S2 san S3

**d.** Output wave

http://dx.doi.org/10.5772/52572

Fig 13 shows the output spectrum of 3-level PWM, which has output efficiency close to 85%, even one reports achieving 90%. If it is compared to the square wave spectrum, which is shown in Fig 8 and has output efficiency of 65-75%, then it can be concluded that 3-level PWM gives us a significant efficiency improvement.

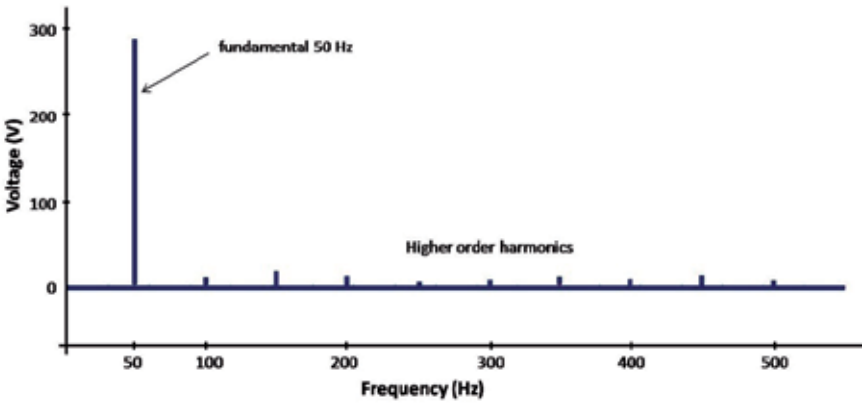


**Figure 13.** level PWM Harmonics Analysis of Unfiltered Output

### 4.3. Filter

Fig 13 shows that 3-level PWM suppresses higher order harmonics much better than square wave. However, the existing higher order harmonics are still able to annoy the performance of electro-mechanical systems. By this reason, those higher order harmonics must be soppress more such that the harmonics becomes very low and not significant. We need a low-pass filter, which has a cut-off frequency $f_c < f_2$ (where: $f_2$ is second harmonic frequency). The filter is realized in the form of passive filter that consists of passive components L and C, as shown on Fig 14 below.

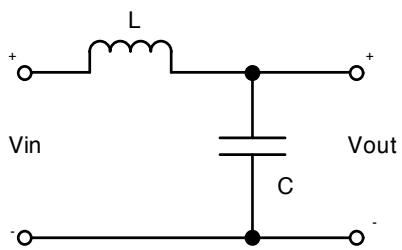


**Figure 14.** A simple low-pass L-C filter to filter out higher order harmonics of PWM.

The inductor value is designed such that the drop voltage on the inductor should be <3% of the inverter output voltage,

$$I_{load,max}.2.\pi.f.L < 0{,}03V_{ac} \tag{23}$$

Where:

$I_{load,max}$ : maximum RMS load current

$V_{ac}$ : RMS output voltage

$f$ : output frequency

For a simple low-pass L-C filter, the cut-off frequency is[6]:

$$f_c = \frac{1}{2\pi\sqrt{LC}} \tag{24}$$

$$C = \frac{\left(\frac{1}{2\times\pi\times f}\right)^2}{L} \tag{25}$$

However, sometimes, as a recommendation, the cut-off frequency should be set up on 1 or 2 octave above the fundamental frequency, i.e. 150 Hz, for 50 Hz system.

The big picture of 3-level PWM inverter 1-phase full-bridge is illustrated on Fig 15 below. Four op-amps that exist on Fig 15 function as combination of 2 NANDS logic circuits and 2 op-amps as shown

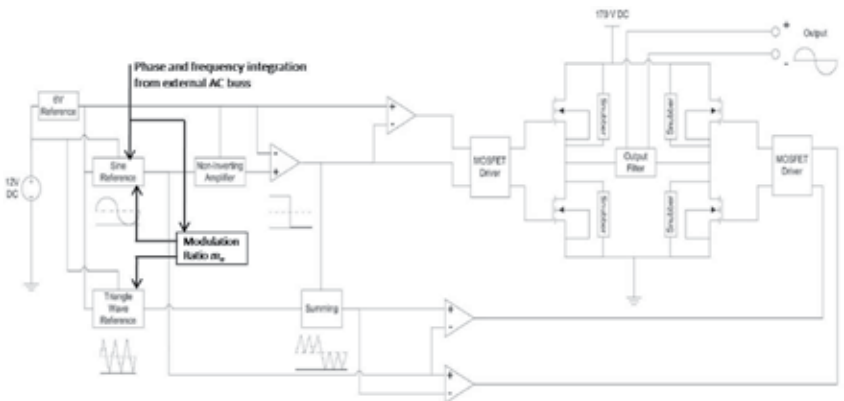


**Figure 15.** Comprehenssive 3-level PWM schematic blocks [4].

on Fig 12. For the sake of integration with external electrical AC buss, the system conducting synchronization of 3 main parameters: frequency (50 or 60 Hz), phase and voltage. To simplify synchronization process, the sensing (monitoring) and controlling those 3 parameters must be conducted by microprocessor system.

http://dx.doi.org/10.5772/52572

## 5. Energy management: Energy flow-in, flow-out and monitoring energy in the baterrays

The keyword for energy management in solar cell system is sustainability. The main rule, if the total electrical energy supply from solar cells to the batteries is less than the total used energy, then to maintain the sustainabilty, there must be energy supply from the external energy resource(s). Moreover, if the total electrical energy supply from solar cells to the batteries is more than the total used energy, then the collected energy from the solar cells must be stored to the batteries, if full, then must be delivered to the external AC buss. This purpose is that the excess of supply energy can be utilized by other outside consumers that connected to common external AC buss. If there exist many autonomy renewable energy system, then they can be coordinated to build an energy grid system, which makes possible to collaborate each other to maintain sustainability altogether. By the existence of a grid system, then a business concept of buying-selling electrical energy supply between autonomy renewable energy systems can be realized.

In order such that Solar cell system can function as autonomy energy system, then it must has an energy management system in the form of an electronic control system, supported by microprocessor circuit or computer system, which monitors the total IN and OUT of electric energy on battery storage. Moreover, at the same time, it monitors the number of available energy in the storage and controlling the flow and contingency electric energy in the system. By monitoring IN and OUT energy and the availability energy in the storage, it is expected that the total energy available in the storage can always be monitored real time accurately. The core components of energy management in solar cell system are batterries and processor system. The following is brief explanation regarding to both components.

### 5.1. Batteray analysis

Electric energy storage is used to store the received energy from solar cells (at noon), in order to be utilized at the time when there is no available electrical energy supply from the solar cell (at night). In general, electric energy storage can be realized in the form of wet and dry batteries, super capacitors and even carrier energy storage in the form of hydrogen gas storage. Priambodo et al [7], have shown that electrical energy received from solar cell array can be stored by converting it into energy carrier in the form of $H_2$ gas by using electrolysis method. Furthermore, the stored $H_2$ gas can be used when there is no available supply electric energy from solar cells, by using fuel cell system. In this chapter, we will limit discussion to battery storage only.

Solar cell system needs battery bank to store the electric energy that collected in at noon. In general, there are two kinds of batteries, wet and dry. The wet battery uses electrolysis method, where it requires a sealed box to keep two plates anode and cathode, which are connected by wet electrolyte which can be base or acid. During charging time, there exists ionization process in electrolyte liquid, while during discharging process, there exists deionization process. The dry battery, actually is not really dry. The dry battery working concept

is still the same with the wet one, however, the dry battery uses electrolyte gel, such that looks more dry. The components of battery are illustrated in Fig 16, as follows.

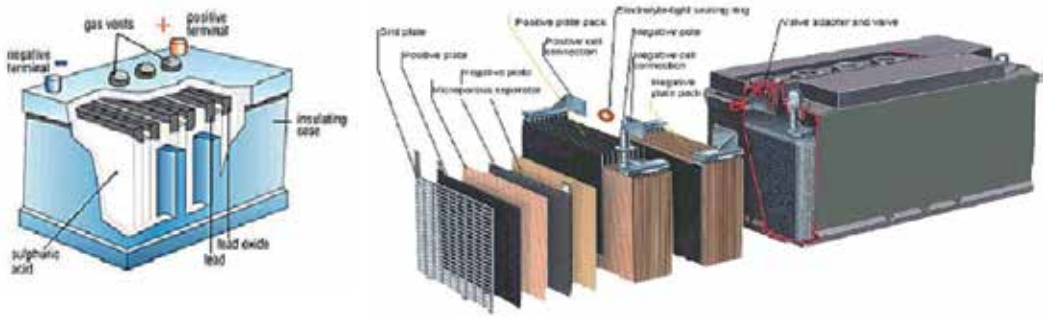


**Figure 16.** Component parts of a batteray

The illustration of chemical process in wet battery is shown in the following equations:

$$\begin{aligned}
&\text{Positive plates: } PbO_2 + 4H^- + SO_4^{2-} + 2e \underset{\text{Charge}}{\overset{\text{Discharge}}{\rightleftharpoons}} PbSO_4 + 2H_2O \\
&\text{Negative plates: } Pb + SO_4^{2-} \underset{\text{Charge}}{\overset{\text{Discharge}}{\rightleftharpoons}} PbSO_4 + 2e^- \\
&\text{Overall reaction: } PbO_2 + Pb + 2H_2SO_4 \underset{\text{Charge}}{\overset{\text{Discharge}}{\rightleftharpoons}} 2PbSO_4 + 2H_2O
\end{aligned} \tag{26}$$

The battery perfomance is determined by at least 5 parameters: (1) the speed to store electric energy in charging process; (2) the battery capacity; (3) battery leak; (4) energy dissipation; and (5) the speed of capability for discharging to the loads. The following is discussion according the analysis methods for those 5 parameters. There are 2 (two) conditions, i.e. charging and discharging, which requires different modelling. The reason to have different models for charging and discharging is to have a simplification, because the whole analysis components are related each other, in complex relation.

*5.1.1. Batteray charging model*

Charging process can be approximated by capacitance circuit model that is illustrated on Fig 17 below. Capacitance C models and illustrates the capacity of the battery, while Resistance R(V,i) models and illustrates the speed of battery charging and charging dissipation. For the sake of simplification, we assume that R is always constant. The lower R, then the faster battery charging process, at the same time it has lower dissipation. The main point, the good battery should has lower R.

http://dx.doi.org/10.5772/52572

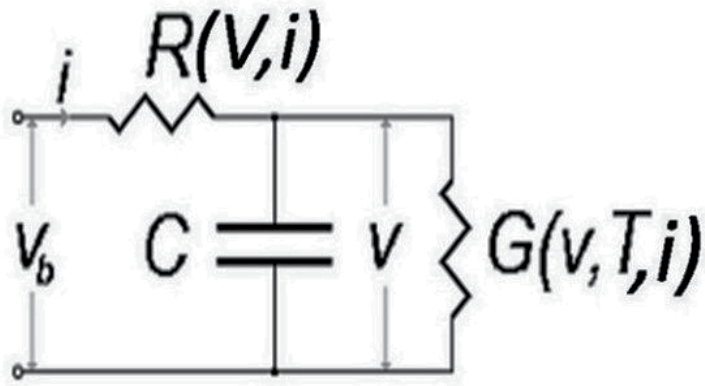


**Figure 17.** Batteray charging model [8].

Current equation for charging model based on the capacitance circuit is:

$$i = C\frac{dv}{dt} + G(V,\ T,\ i)V \tag{27}$$

Battery charging cycle on this model, has characteristic graph, which is shown on Fig 18, below.

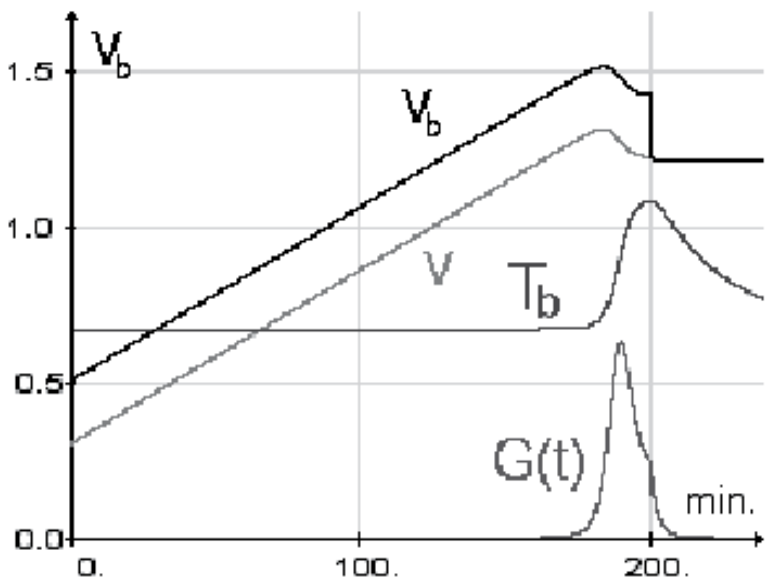


**Figure 18.** Charging Process [8]

When the battery is not full yet, if there is no charging current ($i = 0$), then $G(V,T,i=0)$ illustrates leak conductance (coefficient c), which exist on battery system in passive condition (recall Eq-1). When at $i \neq 0$, then $i^2R$ is dissipation in charging process and $G(V,T,i \neq 0)$ is leak conductance at charging time. If the battery has already been full, then the battery voltage will be constant and the energy charging excess in charging process will change to heat dissipation, which shown by the leak conductance of $G(V,T,i=0)$ function. R and G values show the degree of dis-efficiency of the battery. For the sake of electric management, it is requires accurate information according to R, C and G(V,T,i) function of baterry. The information of those 3 values can be obtained by careful measurements.

*5.1.2. Batteray discharging model*

Discharging process can approximated by using a Constant Voltage Source Circuit Model as illustrated on Fig 19 below. The reason we use Constant Voltage Source circuit model, because there is a fact that at condition of near to empty, the battery (without load) still has voltage that close to peak voltage when battery at the full condition. Based on this fact, it is difficult to use capacitance model for discharging process. At Constant Voltage Source Circuit Model, $V_{DC}$ models Constant Voltage Source of the battery, while Resistance Rs models and represents the battery energy content. Gp represents the battery leak, which is quitely equal to G(V,T,i) function on battery charging model.

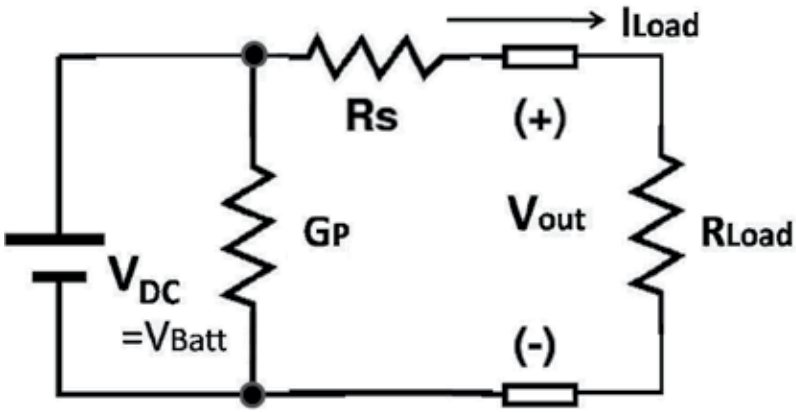


**Figure 19.** Baterry discharging model, Rs represents the battery energy content and Gp represents the battery leak.

By assumption that $V_{DC}$ is constant, then the battery energy $E_{batt}$ can be represented by the value of $R_S$, which represents internal series resistance of the battery at discharging process. $R_S$ can be calculated by the following simple formula:

$$R_s = \frac{V_{Batt} - V_{out}}{I_{load}} \tag{28}$$

http://dx.doi.org/10.5772/52572

It is requires an algorithm to calculate $R_S$ as representation of battery stored energy at real time condition. It is for reader exercise to develop thus $R_s$ as a function of battery stored energy. The illustration of stored energy vs $R_s$ is shown on Fig 20, below:

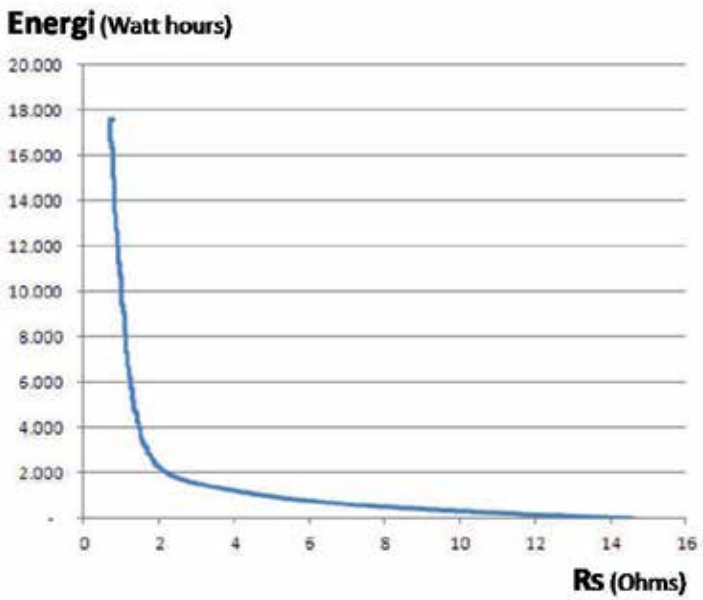


**Figure 20.** Illustration of stored energy vs Rs [9]

By understanding the information in this Chapter, the available information can be used to develop energy management concept for solar cell system. The main point is monitoring flow-in current to and flow-out current from batteries, which then combined with the information according to available energy in batteries, will give accurate information regarding to the energy in the system. The accurate information is required by the system when deciding integration process to keep maintain sustainability and also to conduct the business of selling and buying electric energy in the grid system.

### 5.2. Electronics energy management system

There are many tasks, which have to be done, such that energy management can be conducted accurately. The following, we list the mandatory tasks required in energy management for solar cell system. First of all is current monitoring flow-in to and flow-out from the battery bank. The second one is measuring electrical energy content inside batteray bank by using algorithm of stored energy vs Rs. The third one is an evaluation of the internal energy condition and based on the sustanainability criteria, conducting decission process to do integration with external system (grid). The fourth one, when integration is decided, then synchronization of frequency, phase and voltage must be conducted soon. Those four tasks require algorithms or procedures, which can be very complex for electronic analog circuits.

Hence, the only way is by utilizing microprocessor circuit or even computer system to conduct energy management tasks. The comprehenssive block diagram of Solar Cell Based Renewable Energy Unit System has been already shown on Fig 1. The detail of the circuitries are for the reader exercise to give contributions to realize an electrical energy management for solar cell system.

## 6. Conclusion

Electrical energy management and engineering for solar cell system is started by designing electrical energy requirements, technical specifications of solar cells and batteries, also information of zone latitude and statistical weather of the location. The characterizations to obtain information of solar cell and batteries efficiency are very important to support in designing the system. Furthermore, electrical energy management and engineering for solar cell system, must deal with 4 tasks listed in sub-chapter 5.2. To cover those 4 tasks, then it has to be developed a processing system based on microprocessor or even computer system. If there exist several units of autonomy solar cell systems, then they can be coordinated to build a grid energy system, which can support each other to keep maintain sustainability service. Ultimately, it can be established independent electric energy collaboration and totally eco-friendly.

## Author details

Purnomo Sidi Priambodo, Didik Sukoco, Wahyudi Purnomo, Harry Sudibyo and Djoko Hartanto

Universitas Indonesia, Indonesia

## References

[1] P.S.Priambodo, N.R. Poespawati, D. Hartanto, “Chapter book: Solar Cell Technology”, INTECH Open Access Publisher, ISBN 978-953-307-316-3,www.intechweb.org

[2] M.A. Green, “Solar Cells, Operating Principles, Technology and System Applications,” Prentice Hall, ISBN 0-13-82270, 1982

[3] B.M. Hasaneen and A.A.E. Mohammed, “ Design and Simulation of DC/DC Boost Converter,” 978-1-4244-1993-3/08, ©2008 IEEE

[4] I.F. Crowley, H.F. Leung and S.J. Bitar, “PWM Techniques: A Pure Sine Wave Inverter,” Worcester Polytechnic institute, 2010-2011

http://dx.doi.org/10.5772/52572

[5] A. Rusdiyanto and B. Susanto, "Perancangan Inverter Sinusoida 1 Fasa dengan Aplikasi Pemograman Rumus Parabola dan Segitiga Sebagai Pembangkit PWM," P2Telimek, LIPI, 2008

[6] D. Trowler and B. Whitaker, "Bi-Directional Inverter and Energy Storage System", University of Arkansas, Dept of Electrical Engineering, Texas Instruments Analog Design Contest, May 2008

[7] P.S. Priambodo, F. Yusivar, A. Subiantoro and R. Gunawan," Development of Electrolysis System Powered by Solar-Cell Array to Supply Hydrogen Gas for Fuel-Cell Energy Resource Systems," American Institute of Physics Proceedings on The International Workshop on Advanced Material for New and Renewable Energy, Indonesian Institute of Sciences (LIPI), Jakarta, Indonesia, 9-11 June 2009

[8] D. Casini, and G. Marola "Solar batteray charge for NiMH batteries" International Symposium on Power Electronics, Electrical Drives, Automation and Motion, 2008

[9] D. Sukoco and P.S.Priambodo, "Rancang Bangun Sistem Pengendali Energi Listrik Terbarukan Dengan Monitoring Baterai berbasis Algoritma Numerik," Master Thesis, Dept. of Electrical Engineering, Universitas Indonesia, June 2012

Chapter 13

# Effect of Source Impedance on Hybrid Wind and Solar Power System

Mu-Kuen Chen and Chao-Yuan Cheng

Additional information is available at the end of the chapter

http://dx.doi.org/10.5772/54495

## 1. Introduction

Large wind turbines use mechanical systems, such as geared or gearless devices to increase the speed of the generator. In addition, an inverter is employed to adjust the output voltage to exceed the grid value. With its phase leading the bus phase, wind power can be integrated into the grid bus. The integration can be easily realized owing to negligible impedance of the utility bus. The main issues for wind-power generating systems include fluctuations in output voltage and quality of power supplied to the utility power system. In small renewable energy systems, wind power and solar energy are integrated to improve the reliability of the individual power system. Conventionally, the AC output voltage of the wind turbine is rectified, and then combined with the output voltage of the solar cell to charge the battery and provide power supply to the load. To characterize the battery, the Thevenin battery model considering the nonlinear effect of source impedances was proposed. A battery evaluation test system was employed to validate this model. The curve of test results follows entirely the theoretical calculation [1]-[3]. For photovoltaic application, the inner resistance of solar panel was also included in the theoretical analysis. The maximum power point tracking (MPPT) of solar panel for different insolation levels verified the proposed solar cell model. The MPPT technique adjusted continuously the battery-charging rate and obtained shorter charge time [4]. It was reported that a dual battery configuration with deep-cycle batteries can increase the available capacity. Moreover, the system may achieve optimum utilization of the PV array and proper maintenance of the storage battery [5]. In another research, a microcontroller was employed to adjust the maximum charging current according to the PV power production and battery voltage level. Using this method, better exploitation of the power produced by the PV power source can be achieved. Moreover, battery lifetime can be increased by restoring high state of charge (SOC) in short charging time [6]. Another study compared the performance of equal

rate charging, proportional rate and pulse current charging in charging multiple batteries. The total charging time is shortest when using pulse current charging strategy. All the batteries become fully charged almost simultaneously when they are charged with proportional rate or pulse current method [7]. The optimum size of the PV module for a specific wind turbine to meet the load requirement for the hybrid wind/PV system was investigated in order to minimize the overall cost of the system [8] - [9]. Nevertheless, the effect of source impedance in a small hybrid wind/PV system has not yet been investigated. In this study, theoretical analysis shows that it is difficult to obtain both wind power and solar energy at the same time by traditional methods, which is verified by field test. To overcome such problem, a micro-processor-based controller design for detecting instantaneous voltage variations of both energy sources is proposed, and a charge controller is employed to optimize the charging operation.

## 2. Theory and analysis

Owing to the large variation in the wind and solar energy, the converter is employed to provide the stable power for normal application. When only one energy source supplies the load, as shown in Fig.1(a), the voltage and frequency of the converter output is adjusted to meet the load specification. In Fig. 1(b), both wind and solar energy supply the same load simultaneously. In addition to the load requirement, the voltage and frequency of both converter outputs are adjusted such as the two energy sources can supply the load at the same time. In case of the DC-DC converter, only the output voltage of both converters should be adjusted to charge the same load.

In a small hybrid power system, a battery is usually utilized to store the renewable energy to improve the reliability of the system. Moreover, to simplify the power system, the power source charges directly the battery. Figure 2 shows the conventional charging system, in which the rectified DC voltage charges two batteries. In addition to source voltages $E_w$, $E_1$ and $E_2$, charging currents $I_1$ and $I_2$ are also determined by source resistances $r_w$, $r_1$ and $r_2$ for the wind power and the two batteries, respectively. The output voltage $V_0$ is the summation of $V_{0w}$, $V_{01}$ and $V_{02}$ from wind power and batteries $E_1$ and $E_2$, respectively. According to the circuit theory, the equations for $V_{0w}$, $V_{01}$ and $V_{02}$ are as follows:

$$V_{0w} = E_w\left(\frac{r_1 r_2}{r_w r_1 + r_1 r_2 + r_w r_2}\right) \tag{1}$$

$$V_{01} = E_1\left(\frac{r_2}{r_1 + r_2}\right) \tag{2}$$

http://dx.doi.org/10.5772/54495

$$V_{02} = E_2\left(\frac{r_1}{r_1 + r_2}\right) \tag{3}$$

$$V_0 = V_{0w} + V_{01} + V_{02} \tag{4}$$

As mentioned, $V_{ow}$, $V_{o1}$ and $V_{o2}$ are voltages from wind power and the two batteries, respectively, which contribute to the output voltage $V_o$ independently.

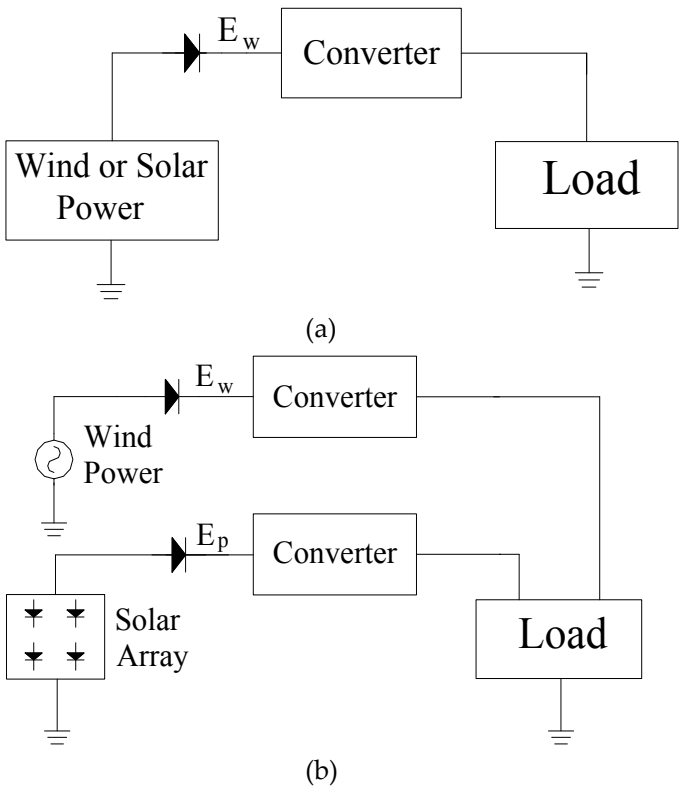


**Figure 1.** (a) Wind or solar power supplies the load through a converter. (b) The wind and solar power use two converters to supply the load at the same time. The voltage and frequency of the converters are adjusted to meet the load requirement.

The following are possible charging situations.

**a.** When $V_{0w} > V_{01} = V_{02}$, the charging current from wind power charges simultaneously both batteries $E_1$ and $E_2$.

**b.** When $V_{0w} > V_{01} > V_{02}$, the charging currents from both wind power and battery $E_1$ charge battery $E_2$.

**c.** When $V_{0w} > V_{02} > V_{01}$, similar to case (b), the charging currents from both wind power and battery $E_2$ charge battery $E_1$.

**d.** When $V_{01} > V_{0w} > V_{02}$, wind power has no effect on the circuit, only battery $E_1$ charges battery $E_2$.

**e.** When $V_{02} > V_{0w} > V_{01}$, similar to case (d), wind power has no effect on the circuit, only $E_2$ charges battery $E_1$.

As seen in above analysis, it is only in case (a) that wind power can charge both batteries at the same time. However, in case (b), when battery $E_1$ also charges battery $E_2$, the voltage drop of $I_1$ $r_1$ and $I_2$ $r_2$ cause increase in $V_{02}$ and decrease in $V_{01}$ respectively. Finally, when $V_{01} = V_{02}$, the charging condition returns to case (a). Case (c) is similar to case (b), so it exhibits self-regulating behavior during the charging process. Cases (d) and (e) are not normal charging conditions.

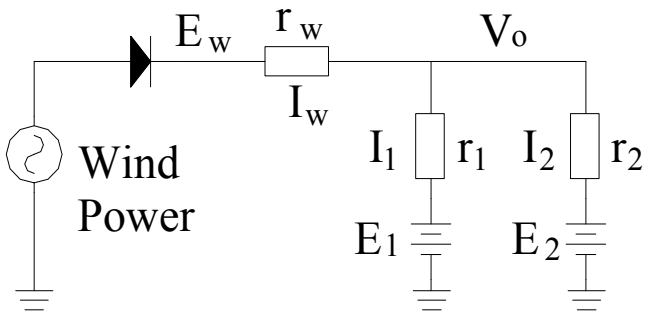


**Figure 2.** Wind power charges both batteries. During the charging process, the increase in charging current $I_1$ leads to increase in internal voltage drop $I_1$ $r_1$, which raises $V_o$, and in turn increases $I_2$. Therefore, this charging configuration comprises a self-regulation mechanism.

Figure 3(a) shows a hybrid wind and PV power generating system. $E_w$, $E_p$, $E_b$, $r_w$, $r_p$ and $r_b$ are factors that determine the charging current. Similar to the above conventional charging conditions, the output voltage $V_0$ is made up of $V_{ow}$, $V_{op}$ and $V_{ob}$ from the wind generator, solar panel and battery, respectively. The related equations are listed below.

$$V_{ow} = E_w\left(\frac{r_b}{r_w + r_b}\right) \tag{5}$$

$$V_{op} = E_p\left(\frac{r_b}{r_p + r_b}\right) \tag{6}$$

$$V_o = E_b + V_{ow} + V_{op} \tag{7}$$

http://dx.doi.org/10.5772/54495

Possible charging conditions are as follows:

**a.** When $V_{ow} > V_{op} > E_b$, both wind and solar energies charge the battery.

**b.** When $V_{op} > V_{ow} > E_b$, both wind and solar energies charge the battery.

**c.** When $V_{ow} > V_{op}$, only wind energy charges the battery.

**d.** When $V_{op} > V_{ow}$, only solar energy charges the battery.

From the above analysis, in cases (a) and (b), there are two energy sources charging a battery at the same time. However, in case (a), the larger current $I_w$ from wind energy may result in a larger internal voltage drop $I_b r_b$ of the battery. Therefore, when $V_{ow} > V_{op}$, the charging condition becomes case (c), and solar energy cannot be utilized to charge the battery. Case (b) shows the same behavior. Contrary to the conventional charging system, the hybrid charging system exhibits a competition effect, meaning that only the larger power source can dominate the charging system.

Figure 3(b) shows the I-V curves of the charging system. Because the source resistance of the wind generator is much smaller than that of the solar panel, the wind I-V curve reduces slowly with increase in charging current. The source resistance of the battery is also much smaller than that of the wind generator. Therefore, the terminal voltage of the battery Vo increases only slightly with increase in charging current. When the solar I-V curve drops to P, which is equal to the terminal voltage of the battery, the solar energy stops charging the battery.

Figure 3(c) shows the V-T curves of the charging system. Before time $T_o$, the battery is in under-charge condition, both power sources behave as the current sources with their ratio of output currents proportional to that of generated power levels. For time $T_o$ to $T_f$, the source resistance of the solar panel lowers gradually the solar charging current and the battery terminal voltage $V_o$ increases slowly. Finally, at time $T_f$, only wind power can charge the battery.

To improve the performance of the hybrid power generating system shown above, a switch control is employed. It is connected to the battery circuit as shown in Fig. 4. In this operation mode, both wind and solar energy can be utilized, although only one energy source can charge the battery at any time. Owing to the different characteristics of wind and solar energy, as shown in Eq. (10), we can adjust the charging duty cycle ratio $k$ of the two energy sources to obtain maximum energy in the battery. The equations are listed below.

$$V_{ow} = E_b + E_w\left(\frac{r_b}{r_b + r_w}\right) \tag{8}$$

$$V_{op} = E_b + E_p\left(\frac{r_b}{r_b + r_p}\right) \tag{9}$$

$$W = kW_w + (1-k)W_p \tag{10}$$

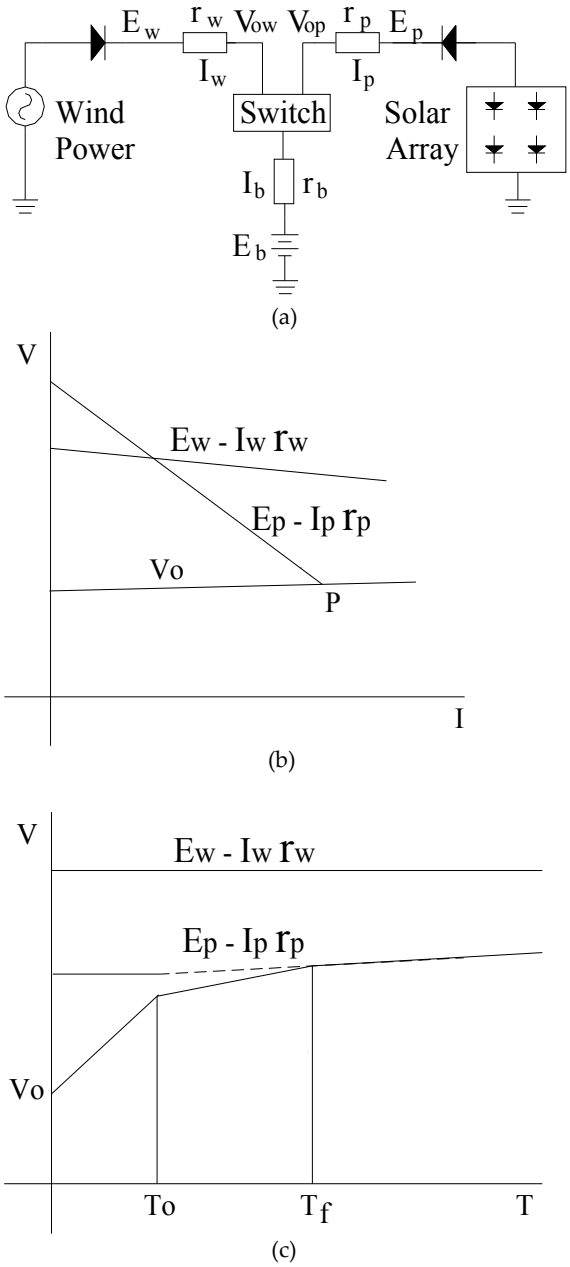


**Figure 3.** (a) Small hybrid wind and PV energy charging system. Two power sources charge a battery. Owing to the internal voltage drop caused by impedance of wind, solar and battery power source, only one power source can contribute to the charging process. (b) I-V characteristics of the charging system. When the solar I-V curve drops to point P, solar power cannot charge the battery. (c) Simplified charging curve of the system. Two current sources charge the battery before time $T_o$. Then, charging speed reduces because of increase in resistance of the solar power circuit. After time $T_f$, only wind power charges the battery.

http://dx.doi.org/10.5772/54495

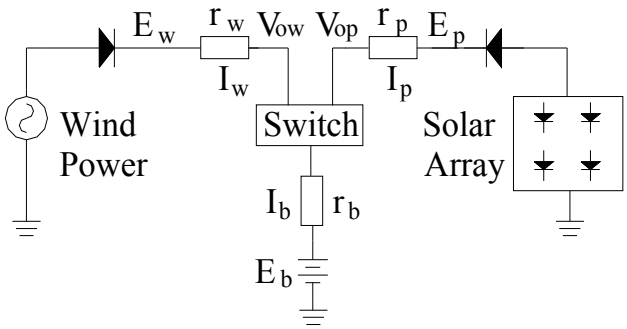


**Figure 4.** Switch-controlled wind and PV energy charging system. The wind and solar power charge a battery alternately. Both power sources can charge the same battery at different times. During solar energy charging, mechanical energy generated by inertia of the wind turbine will be stored and employed to charge the battery during wind energy charging. On the other hand, solar energy cannot be stored but will be lost during wind energy charging. In view of this, we can adjust the wind power charging duration to obtain the maximum energy.

To overcome the drawbacks of the hybrid wind and PV charging system shown above, a microprocessor-controlled power generating system, as shown in Fig.5, is proposed. The different charging modes, which vary with the weather conditions to obtain the maximum energy, are shown in Table 1. With both energy sources, the system operates in the independent charging mode. The wind and solar energy charge batteries $E_{bw}$ and $E_{bp}$, respectively. If there is only one energy source, the system runs in the hybrid charging mode. Either energy source can charge batteries $E_{bw}$ and $E_{bp}$ simultaneously. Owing to the instability of wind energy, if both energy sources co-exist, wind energy exceeds the threshold value, the charging system runs in the wind-enhanced mode. In this case, not only can both energy sources be employed to improve the reliability of power system, the fluctuations in the small wind power generating system can also be reduced.

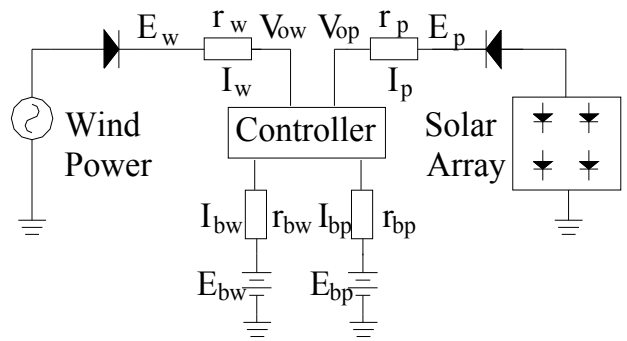


**Figure 5.** Microprocessor-controlled wind and PV energy charging system. Both power sources charge the two batteries. According to the wind and solar energy conditions, the controller regulates the charging conditions for $E_{bw}$ and $E_{bp}$. There is no power loss in this charging system. When there is only one power source, it can charge both batteries. With both power sources and high wind energy, the excess wind energy charges battery $E_{bp}$. The controller improves greatly the reliability of this charging system.

| Energy Source | Ebw | Ebp |
|---|---|---|
| Solar Energy | ▲ | ▲ |
| Wind Energy | ▲ | ▲ |
| Solar and Wind Energy (low wind speed) | ● | ● |
| Solar and Wind Energy (high wind speed) | ▲ | ▲ |
| ● : Independent Charging ▲ : Hybrid Charging | | |
| Ebp : Solar Battery Ebw : Wind Battery | | |

**Table 1.** Microprocessor – controlled charging modes, Under independent charging condition, the solar energy and wind energy charges respectively the corresponding battery. Under hybrid charging condition, both energy sources charge the two batteries simultaneously.

## 3. Results and discussion

### 3.1. Source resistance measurements

To measure battery source resistance, as shown in Fig. 6(a), a 12-V/75-AH battery supplied the load through a switch. We adjusted the load resistance $R_L$ to change the battery discharging current $I_b$. From the voltage difference $E_b - V_o$ and $I_b$, the source resistance $r_b$ can be determined.

Because the solar energy is much smaller than the battery energy and the solar cell internal resistance $r_p$ is much larger than the battery source resistance $r_b$, as shown in Fig. 6(b), the output terminal of the solar panel is directly grounded to measure the solar charging current $I_p$. A 75-W solar cell panel was used in the experiment performed outdoors. From the solar voltage $E_p$ and the current $I_p$, the solar internal resistance can be determined.

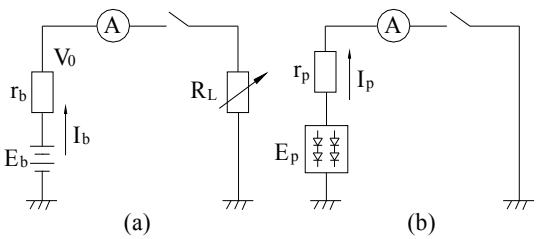


**Figure 6.** (a) Circuit for measuring battery source resistance. Because much energy is stored in the battery $E_b$ and the battery source resistance $r_b$ is small, $R_L$ is employed to limit the discharging current $I_b$. (b) Circuit for measuring solar cell internal resistance. Solar current $I_p$ is varied by adjusting the orientation of the solar cell panel relative to the sun.

As shown in Fig. 7(a), the source resistance of battery decreases with increasing discharge current. The battery source resistance is about 0.02-0.12 Ω for discharging current 1-13 A. The power loss of the source resistance results in temperature rise of the battery. Hence, chemical reaction proceeds more easily with increasing charging current and the resistance to battery charging is reduced.

http://dx.doi.org/10.5772/54495

The source resistance of solar cell panel, as shown in Fig. 7(b), also decreases with increasing short-circuit current However; the source resistance of the solar cell panel is much larger than that of battery. Even though the area of the solar cell panel is large, the thickness of the solar cell structure is too small to increase the efficiency of optical absorption. Conventionally, the thickness of the solar cell active layer is in the micrometer range. Moreover, the resistivity of solar cell is large, which results in high source resistance.

The stator of PMG has 36 slots wound with 40 turns of 0.8-Φ copper wires. The source resistance (one phase) of PMG is found to be 0.5 Ω. It is much smaller than the source resistance of the solar cell panel (about 6-18 Ω). In general, the difference in voltage between wind energy source $E_w$ and solar energy source $E_p$ is not large. According to Eqs. (5) and (6), when the wind turbine is in operation, the wind output $V_{ow}$ is much larger than the solar output $V_{op}$. Therefore, the wind turbine dominates the battery charging behavior.

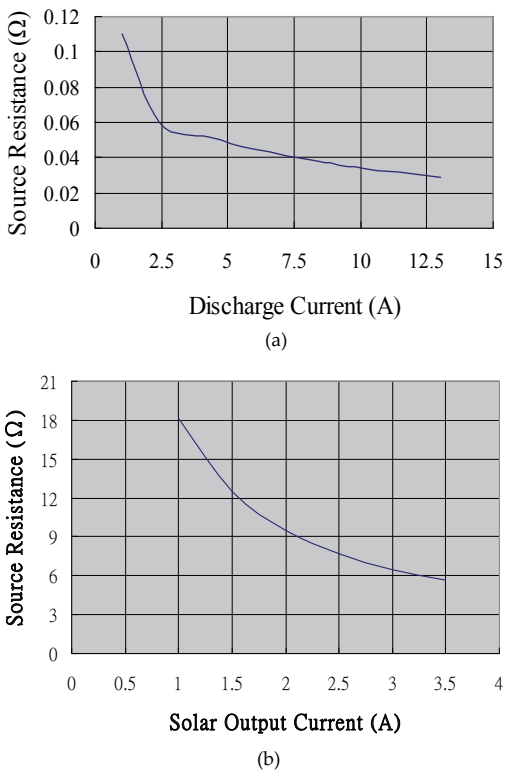


**Figure 7.** Under conventional wind speed, the source impedance of the PMG comes from the resistance of copper winding of the stator. Copper is a good conductor. Therefore, there is only a small variation in resistance when the generator current increases. In (a), the battery stores the chemical energy. Under loaded condition, thermal effect increases with the current in the battery, which speeds up the chemical reaction. Hence, the source resistance of the battery decreases with the current. However, the solar cell is made up of semiconductors. In addition to the high resistance of semiconductors, there is also a large variation in resistance of the solar cell when the current increases, as shown in (b).

### 3.2. Conventional hybrid wind and PV power generating system

In this study, a 250-W permanent magnet alternator driven by wind turbine and a 12-V/75-W solar cell panel were used as the wind and solar energy source, respectively. Both energy sources were output to 12-V/75-AH lead batteries, which were kept in under-charged condition before test. In the experiment, a 100- MHz scope was employed to measure the charging current and battery voltage. A current probe set at 100 mV/A was utilized to sense the charging current. The alternator outputs were converted into DC output by a rectifier module to charge the batteries. As shown in Fig. 8, there was a large variation in current and voltage because of the unstable wind speed. The fluctuations in amplitude of the charging current were attributed to the conventional AC-DC rectification effect. Increase in wind speed also led to increase in charging current. The variation in battery voltage as a result of internal impedance is above 1V.

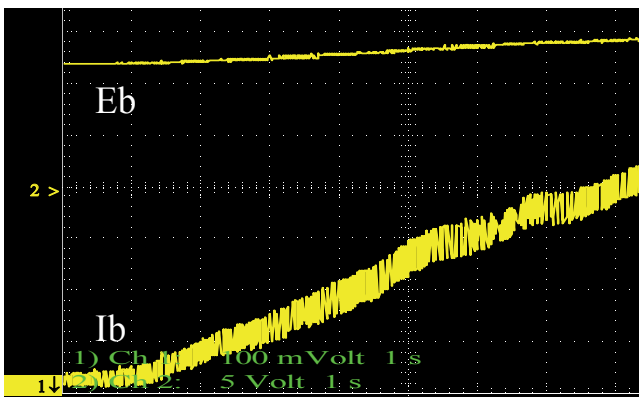


**Figure 8.** Charging current (Ch1: A/div) and battery voltage (Ch2: 5 V/div) of wind power. Owing to the source resistance of the battery, the internal voltage drop increases with the charging current $I_b$. This leads to the increase in the battery voltage $E_b$.

A battery was charged by wind and solar energy sources using the conventional wind and PV charging system, as shown in Fig. 3. In the first 30 minutes, the battery remained in an under-charged condition. As shown in Fig. 9(a), the stable 0.8-A PV charging current is not affected by the large variation in wind charging current. After 1 hour, as seen in Fig. 9(b), the charging curve of solar energy shows an opposite trend as that of wind power. The solar charging current decreases as the wind charging current increases. After 2 hours, as shown in Fig. 9(c), either solar energy or wind power dominates the charging behavior. When the wind charging current exceeds 3 A, the solar energy source does not output any power. Therefore, the system cannot get both wind and solar energy at the same time.

http://dx.doi.org/10.5772/54495

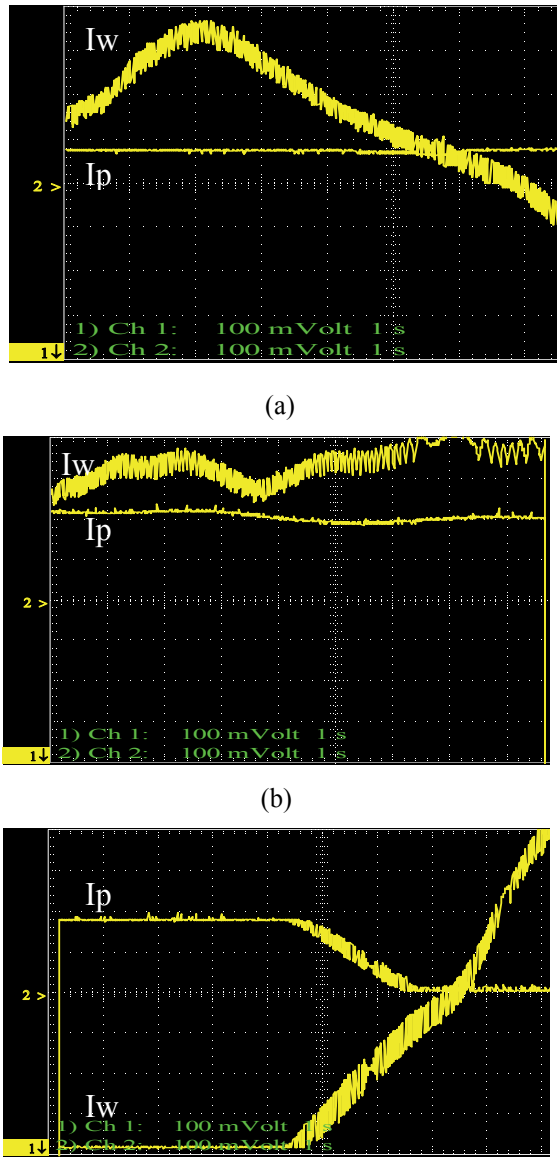


**Figure 9.** Both wind and solar sources charge a single battery. Ch1: wind charging current (A/div), Ch2: solar charging current (A/div). (a) During the first 30 minutes, despite large variations in the wind charging current $I_w$, both energy sources charge the battery simultaneously, indicating that the open-circuit battery voltage $E_b$ is small. (b) After 1-hour charging, competitive behavior occurs. When the wind charging current $I_w$ exceeds 6.5A, the solar charging current $I_p$ decreases. The large wind charging current increases the internal voltage drop of the battery, which leads to decrease in solar charging current. (c) After 2-hour charging, a wind charging current of only 0.5 A can reduce the solar charging current from 1.8 A. This points out that the battery voltage builds up gradually and the small internal voltage drop is enough to exclude the solar charging current. Therefore, the small source impedance of the wind generator dominates the charging operation. A wind charging current of only 3 A can stop the solar charging current.

### 3.3. Switch- control hybrid wind and PV power generating system

In order to acquire both wind and solar energy at the same time, the system is configured as in Fig. 4. As seen in Fig. 10(a)-(c), the wind to solar charging duty cycle ratio is changed to examine the charging behavior at three wind speeds. Owing to fluctuations in wind speed at 3 m/s, the system sometimes stops outputting the wind charging current, as seen in Fig. 10(a), while the charging of battery by solar energy remains very stable. When wind speed increases to 4 m/s, as shown in Fig. 10(b), the wind charging current continues to charge the battery during its duty cycle, but the current decreases during charging. When the solar charging duration is increased to 3.2 seconds, the wind charging current drops to 2 A, as seen in Fig. 10(c) prior to solar charging. Upon completion of solar charging, i.e. after 3.2 seconds, the wind charging current increases to 4 A and falls gradually back to 2 A This phenomenon can be explained as follows. During solar energy charging, the wind turbine is in a no-load condition. Wind energy is thus converted into mechanical energy, which speeds up the alternator. In other words, owing to the inertial momentum, the wind turbine can store mechanical energy, and solar energy is not best utilized or lost during wind charging. Therefore, the charging duty cycle ratio between wind and solar energy can be adjusted to obtain the maximum energy source.

### 3.4. Microprocessor- controlled hybrid wind and PV power generating system

In the above two cases, there is always some energy loss during the power generating system operation. To obtain both wind and solar energy at the same time, a microprocessor and two batteries as shown in Fig. 5 are employed to control the charging operation from both energy sources. Figure 11 displays the circuit in detail, in which controller IC1 and comparator IC2 control the system operation. Depending on the weather condition, wind energy can charge the wind battery $E_{bw}$ directly or the solar battery $E_{bp}$ indirectly through $Q_{ws}$. Both wind and solar energy are sensed by two comparators of IC2. One senses the sunlight to control the load while the other monitors the charging condition of the wind battery. If there has been no wind or sun for some days and both wind and solar energies remain insufficient, the two batteries will be in under-charged condition and utility power supply will be used instead. In view of large variations in wind energy, a current transformer CT is employed to detect the charging current of the wind battery. If the charging current exceeds the specification of the battery, $Q_w$ runs in PWM mode to protect the battery. All functions are controlled by the software of controller IC1.

As shown in Fig. 12, when wind speed is low, about 3 m/s, the system runs in the independent charging mode and the solar battery charging current remains constant at 2A, although there are slight variations in the charging current of the wind battery.

If there is only wind power, as shown in Fig. 14(a), the system runs in the wind- hybrid charging mode, so the unstable wind charging current charges both wind and solar batteries. When the charging current is less than 2 A, as shown in Fig. 14(b), the system remains in the wind- hybrid charging mode and only the wind battery is being charged.

http://dx.doi.org/10.5772/54495

When there is solar energy and a high wind speed at the same time, as shown in Fig. 15, the system runs in the wind-enhanced charging mode. In order to benefit from both energy sources and reduce fluctuations from the wind source, the system runs in the wind-enhanced charging mode when the wind charging current is above 3A. The wind charging current charges the solar battery in addition to the original wind battery, leading to variations in the solar charging current. When the wind charging current is below 3A, the system runs in the independent charging mode. That is, the stable solar charging current of 2A and the fluctuating wind charging current charge the solar battery and the wind battery, respectively.

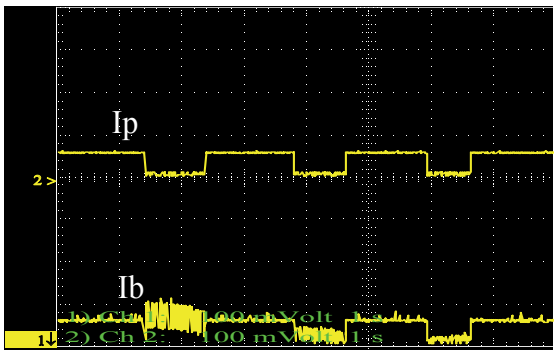


(a)

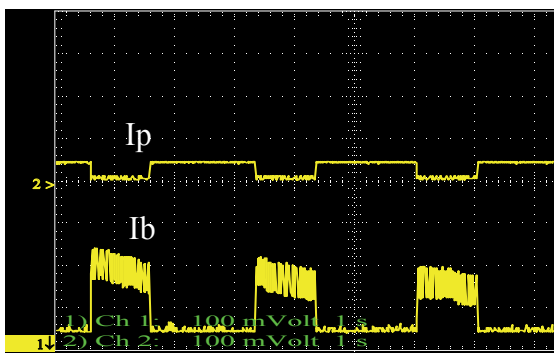


(b)

**Figure 10.** Switch-controlled wind and solar sources charge a battery. Ch1: battery charging current (A/div), Ch2: solar charging current (a),(b), wind charging current (c) (A/div). (a) Wind speed is 3 m/s, but it is unstable. The charging duty cycle ratio between solar and wind power is 2:1. In the absence of wind power, only the solar charging current (0.6 A) charges the battery. In the presence of wind power, the wind charging current gradually decays. Because the wind charging duration is only 0.8 second, steady state cannot be attained. (b) Wind speed is increased to about 4 m/s and solar charging current is decreased to 0.4 A. Wind energy exceeds solar energy. (c) Wind speed is increased to 5 m/s. The charging duty cycle ratio between solar and wind power is changed to 1:2. Moreover, the solar charging duration is extended from 1.8 to 3.2 seconds. In this situation, mechanical energy accumulated by inertia of the wind turbine during solar charging can also be utilized during wind charging. Hence, this configuration can ensure full utilization of wind energy with no loss at all.

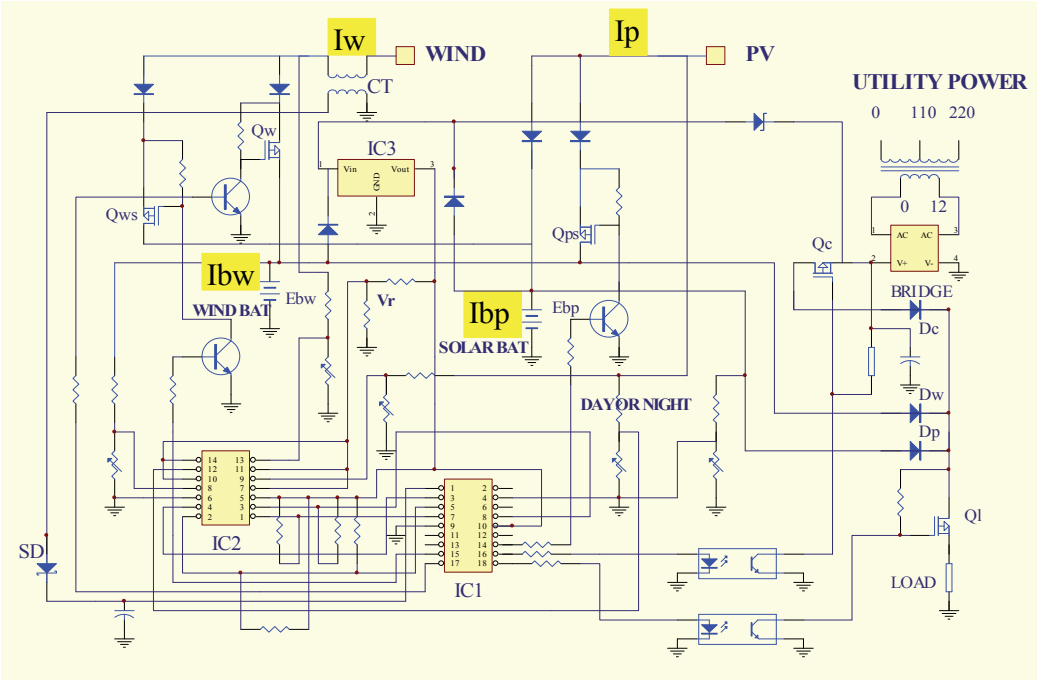


**Figure 11.** Microprocessor-controlled hybrid wind and solar charging circuit. Microprocessor IC1 and Comparator IC2 controls the wind charging current $I_w$ and the solar charging current $I_p$ that fuel the wind ($E_{bw}$) and solar ($E_{bp}$) battery. According to the weather condition, the wind and solar charging currents may charge either the wind or solar battery. Current transformer CT senses the wind charging current to prevent damage to the battery by excess charging current. If the energy of the batteries cannot meet the power required, utility power supply is used instead.

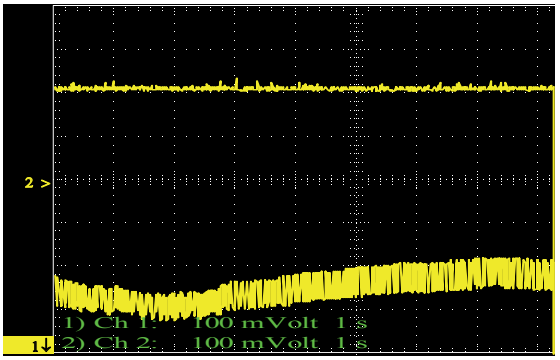


**Figure 12.** Both solar and wind power co-exist. The controller operates in the independent charging mode. The wind charging current charges the wind battery (Ch1: A/div) while the solar charging current charges the solar battery (Ch2: A/div).

http://dx.doi.org/10.5772/54495

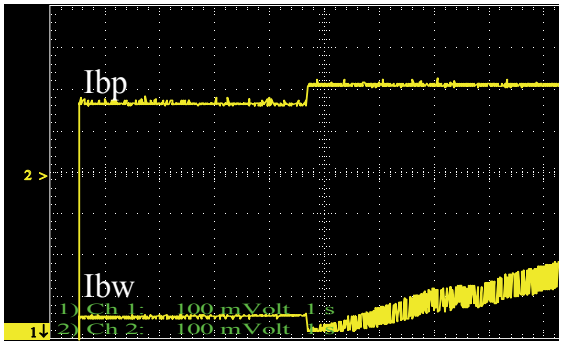


**Figure 13.** The charging system operates in two stages. In Stage 1, only solar energy exists. The solar charging current not only charges the solar battery but also the wind battery. In Stage 2, when wind power also exists, the wind charging current charges the wind battery. Part of the solar charging current is switched back to the solar battery. Ch1, Ch2: A/div.

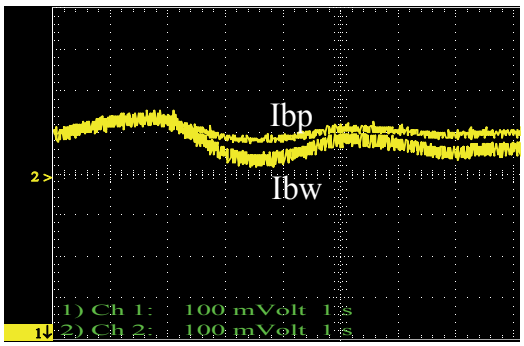


(a)

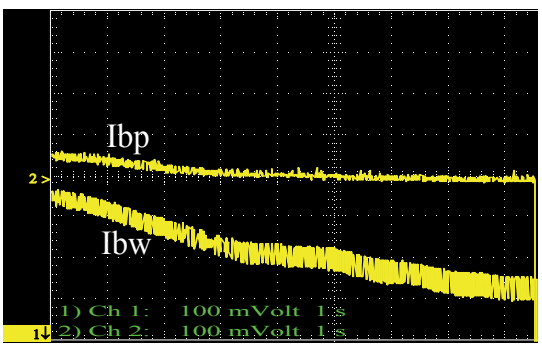


(b)

**Figure 14.** The charging system operates when there is only wind power. (a) When wind speed exceeds 5 m/s, the wind charging current charges both wind and solar batteries. (b) When wind speed drops gradually below 3 m/s, the wind charging current in the solar battery decreases to zero. Ch1, Ch2: A/div

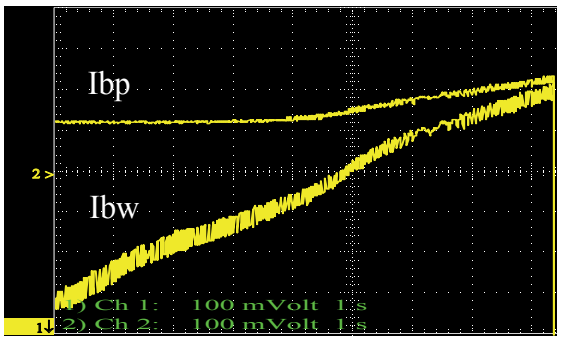


**Figure 15.** Both wind and solar power sources co-exist, but wind speed sometimes exceeds 8 m/s. The charging system operates in two stages. In Stage 1, when wind speed is below 5 m/s, same as that in Fig. 12, the solar and wind charging currents charge the solar and wind battery, respectively. In Stage 2, when wind speed is increased, the wind charging current not only charges the wind battery, but also the solar battery. That is, there are two currents charging the solar battery. Ch1, Ch2: A/div

## 4. Conclusion

In this study, theoretical investigations are performed to examine the effect of source impedance on a small hybrid wind and PV power system. Because of voltage drop in power sources, both energy sources cannot charge a battery simultaneously after initial charging. This study proposed using a switch circuit to increase the utilization of both energy sources. There is only slight solar energy loss when wind power is in operation. To increase energy efficiency by gaining both wind and solar energy, a microprocessor-based hybrid charging system is proposed. Results show that besides increasing the reliability of the power system, the fluctuations in wind energy source are also reduced.

## Author details

Mu-Kuen Chen and Chao-Yuan Cheng

Department of Electrical Engineering, St. John's University, Taiwan

## References

[1] Salameh, Z. M., Casacca, M. A. and Lynch, W. A. "A mathematical model for lead-acid batteries," *IEEE Trans. On Energy Conversion*, vol.7, no.1, pp 93-98, Mar. 1992.

http://dx.doi.org/10.5772/54495

[2] H. G. Zimmerman and R. G. Peterson, "An electrochemical cell equivalent circuit for storage battery/power system calculations by digital computer", Proceedings 13th Intersociety Energy Conversion Engineering Conference, pp. 33-38, 1978.

[3] Harrington, S. and Dunlop, J. "Battery charge controller characteristics in photovoltaic systems," *IEEE AES Magazine*, pp 15-21, Aug. 1992

[4] Masoum, M. A. S., Badejani, S. M. M. and Fuchs, E. F., "Microprocessor-controlled new class of optimal battery chargers for photovoltaic applications," *IEEE Trans. On Energy Conversion*, vol.19, no.3, pp 599-606, Sep. 2004.

[5] Casacca, M. A., Capobianco, M. R. and Salameh, Z. M. "Lead acid battery storage configurations for improved available capacity," *IEEE Trans. On Energy Conversion*, vol.11, no.3, pp 139-145, Mar. 1996.

[6] Koutroulis E. and Kalaitzakis K., "Novel battery charging regulation system for photovoltaic applications," *IEE Proc. Electr. Power Appl.* vol.151, no.2, pp 191-197, March 2004

[7] Jiang Z. and Dougal, R. A. "Control strategies for active power sharing in a fuel-cell-powered battery-charging station," *IEEE Trans. On Industry Applications*, vol. 40, no. 3, pp 917-924, May/Jun, 2004

[8] Borowy, B. S. and Salameh, Z. M., "Optimum photovoltaic array size for a hybrid wind/PV system," *IEEE Trans. On Energy Conversion*, vol.9, no.3, pp 482-488, Sep. 1994.

[9] Chedid, R. and Rahman, S., "Unit sizing and control of hybrid wind-solar power systems," *IEEE Trans. On Energy Conversion*, vol.2, no.1, pp 79-85, Mar. 1997.

*Edited by Arturo Morales-Acevedo*

Over the last decade, photovoltaic (PV) technology has shown the potential to become a major source of power generation for the world - with robust and continuous growth even during times of financial and economic crisis. That growth is expected to continue in the years ahead as worldwide awareness of the advantages of PV increases. However, cost remains as the greatest barrier to further expansion of PV-generated power, and therefore cost reduction is the prime goal of the PV and solar cell investigation. This book intends to contribute to such a purpose by covering a wide range of modern research topics in the solar cell physics and technology fields. The already established -1st generation- silicon solar cell technology, the 2nd generation thin film and the 3rd generation dye sensitized solar cells, including new technologies with very high perspectives for reducing the cost of solar electricity such as CZTS, organic polymer and tandem solar cells based on III-V compounds -under concentrated sunlight- are studied in this book by experts in the field from around the world. At the end, two chapters are also dedicated to the systems engineering, providing a complete PV energy research and application perspectives panorama

ISBN 978-953-51-6313-8

Photo by stevanovicigor / iStock

IntechOpen